PSFC/RR-01-6 **DOE-ET-54512-341**

Observations and Theory of Mode-Converted Ion Bernstein Waves in the Alcator C-Mod Tokamak

E. A. Nelson-Melby

December 2001

Plasma Science and Fusion Center
Massachusetts Institute of Technology
Cambridge, MA 02139 USA

This work was supported by the U.S. Department of Energy, Cooperative Grant No. DE-FC02-99ER54512. Reproduction, translation, publication, use and disposal, in whole or in part, by or for the United States government is permitted.

Observations and Theory of Mode-Converted Ion Bernstein Waves in the Alcator C-Mod Tokamak

by

Eric Alan Nelson-Melby

B.A. (1996) Department of Physics
Cornell University

Submitted to the Department of Physics
in partial fulfillment of the requirements for the degree of

Doctor of Philosophy in Plasma Physics

at the

MASSACHUSETTS INSTITUTE OF TECHNOLOGY

February 2002

Author .....
Department of Physics
4 December 2001

Certified by .....
Miklos Porkolab
Professor of Physics
Director, Plasma Science and Fusion Center
Thesis Supervisor

Accepted by .....
Thomas J. Greytak
Professor of Physics, Associate Department Head for Education

Observations and Theory of Mode-Converted Ion Bernstein Waves in the Alcator C-Mod Tokamak

by

Eric Alan Nelson-Melby

Submitted to the Department of Physics
on 4 December 2001, in partial fulfillment of the
requirements for the degree of
Doctor of Philosophy in Plasma Physics

Abstract

This thesis discusses experimental observations and the theory of mode-converted ion Bernstein waves (IBW) in the Alcator C-Mod tokamak. IBWs are short-wavelength, hot plasma oscillations that can be excited in the core of the plasma through mode conversion of an externally launched fast magnetosonic wave (FW). The balance between ion cyclotron damping of the FW and mode conversion to an IBW as a function of minority ion species concentration is explored. In the mode conversion regime, with appropriate plasma parameters, significant amounts of power can be transferred to the IBW, which can then damp on electrons, producing localized electron heating, current profile control, and current drive. Observations of electron heating in deuterium–helium-3 plasmas at 7.8 Tesla are discussed and compared to theory and full-wave code modeling. An analytic theory based on the internal resonator model [A.K. Ram, et al., Phys. Plasmas, **3**, 1976 (1996)] for mode conversion compares favorably with the experimentally measured mode-conversion efficiency, as do the results of the full-wave code TORIC [M. Brambilla, Plasma Phys. Controlled Fusion, **41**, 1 (1999)]. This thesis also presents direct observations of IBW oscillations, before damping takes place. Measurements are presented of the density fluctuations driven by the wave electric field near mode conversion in three ion species (hydrogen, helium-3, and deuterium) plasmas. This has been achieved with a newly upgraded Phase Contrast Imaging (PCI) diagnostic, which is now able to detect radio-frequency waves through the use of optical heterodyning. The PCI system in C-Mod measures line-integrated density fluctuations using a CO_2 laser which passes vertically through the plasma. The density fluctuation pattern is an inherently 3-dimensional structure, so the full-wave code TORIC has been used to interpret the one-dimensional measurements, which have some unexpected features, such as multiple peaks and troughs in amplitude. Strong IBW signal was often observed to the low-field side of the mode conversion layer. The importance of the parallel electric field for these IBW density fluctuation measurements is identified. IBW wavenumbers from 5 to 12 cm^{-1} have been detected, which is within the range of the code results.

Thesis Supervisor: Miklos Porkolab
Title: Professor of Physics
Director, Plasma Science and Fusion Center

Acknowledgments

I extend my gratitude to all those who have enriched my work: my advisor Miklos Porkolab helped introduce me to the interesting and complex zoo of plasma waves. He helped guide me into an interesting and workable thesis project. When it seemed that I had reached dead ends in my analysis, he encouraged me to dig deeper into the physics. He had a wide range of ideas when I encountered problems in both theory and experiment. Steve Wukitch remembered what it was like to be a grad student and thus helped me have the right perspective while I was taking exams and classes and working on my thesis experiment. Yuichi Takase brought me into the world of RF waves in plasmas during a brief stint as my advisor. Both he and Steve taught me about about RF electronics, taking measurements, and experimental design. Alex Mazurenko's years of hard work on the phase contrast imaging system added immeasureably to this thesis. In addition, he always had interesting adventures in and out of the lab—I look forward to future mountain climbing with him. From Abhay Ram I learned about the importance of being mathematically careful and correct while getting at the root of physics problems. I would like to thank him for many hours of discussions on mode conversion, ion Bernstein waves, dispersion relations, and plasma wave physics. Abe Bers ran an informative and lively plasma electro-dynamics seminar where cross-pollination of ideas occured. He gave me crucial insights along the way. Paul Bonoli helped me navigate the complexities of TORIC. He had insights about issues related to the RF antenna and computational physics. Amanda Hubbard helped me understand the details of electron-cyclotron emmission in C-Mod. She and Steve Wukitch also helped me build upon the work of Peter O'Shea in electron temperature break-in-slope analysis. Ambrogio Fasoli had many good comments on my thesis as one of my readers. I also learned more about basic plasma physics from his well-organized class notes while being a teaching assistant for his introductory plasma course. Chris Rost gave me lucid explanations on the workings of phase contrast imaging. Ashley Shugart and Gary Hallock helped me operate the PCI on my crucial run day (when much of my thesis data was gathered).

Steve Wolfe was always helpful when I had questions about C-Mod, EFIT, or the data-acquisition system. Earl Marmar and Jim Terry gave me a brief introduction into the world of spectroscopy, which helped me determine the H/D ratios and helium levels in the plasma. Davis Lee helped me understand the neutral particle analyzer and charge exchange. He was always there with a word of encouragement and a healthy treat during the long hours in the control room. Réjean Boivin had a way of staying cheerful even in the face of experimental catastrophe. He helped push me to finish during the last grueling months of my thesis writing. I could always count on Jim Reardon for unusual perspectives that forced me to examine my assumptions when I was solving problems. With my office mates Sanjay, Chris, and Howard, I had stimulating conversation on topics ranging from MHD to nuclear power to science education.

Most of all, I give thanks to my wonderful red-headed wife, Guenevere Nelson-Melby, who patiently put up with my new definition of the phrase "almost done." She helped me turn this thesis into something more than a mish-mash of equations and figures by helping me to improve my writing style through her teaching and editing skills.

Contents

List of Figures

List of Tables

Chapter 1

Plasma Fusion and the Alcator C-Mod Tokamak

1.1 Brief outline of thesis

This thesis focusses on the behavior of radio-frequency (RF) waves in a hot, magnetized plasma in a tokamak. It outlines a simple theory of how much power can be transferred to the short-wavelength ion Bernstein waves (IBW) from the launched RF fast magnetosonic wave. It describes the first measurements of the complicated three-dimensional structure of the density fluctuation around the mode conversion region, and elucidates the critical role of the parallel RF electric field in this process.

Chapter 1 is a brief introduction to plasma fusion as a source of energy and the Alcator C-Mod tokamak as a means for exploring the confinement and heating of plasmas to fusion relevant temperatures. **Appendix A** provides more details on current energy use and the future energy outlook.

Chapter 2 is devoted to the theory of waves in hot magnetized plasmas, especially the fast magnetosonic wave (FW) and the ion Bernstein wave (IBW). Through the process of mode conversion, the FW launched with the RF antenna at the edge of the plasma can excite the short-wavelength IBW. Examples are given for both kinds of waves and their damping within the plasma. (**Appendix B** illustrates the mechanism of cyclotron damping in particular.) A theory is developed which predicts how much

power can be converted from the long-wavelength fast wave to the short-wavelength IBW.

Chapter 3 is an introduction to a diagnostic used to observe these waves in the plasma: Phase Contrast Imaging (PCI).

Chapter 4 presents experimental results of the process of mode conversion in a deuterium – helium-3 plasma. The theory developed in Ch. 2 compares favorably to the experimental measurements, where direct electron heating that occurs as the IBW is Landau damped was measured.

Chapter 5 uses the PCI diagnostic to show experimental measurements of mode-converted ion Bernstein waves near the region where the fast wave couples to the IBW. These results are compared to numerical simulations using the ion-cyclotron range of frequencies (ICRF) code TORIC, which solves for the RF electric field in toroidal geometry. This code resolves both the fast wave and the IBW. **Appendix C** describes how the fluctuating electron density is calculated from the TORIC electric field solution, **Appendix D** describes a method for estimating the ion species concentration mix for these plasmas, and **Appendix E** is a compilation of all the experimental data observed with the PCI from the FW–IBW mode-conversion scenarios.

Finally, **Chapter 6** summarizes the conclusions learned from the mode conversion experiments, and contains suggestions to improve the PCI system in order to better explore the physics discussed in Ch. 5.

1.2 Energy Needs and the Plasma Fusion Solution

In the year 1999, the global population reached 6 billion people. Global energy consumption was 4×10^{20} joules, equivalent to the total energy the sun radiates in one microsecond. Currently, approximately 85% of the world's energy needs are met using fossil fuels. Energy demand will grow with the population, and the billions who live in developing countries may reach energy consumption levels comparable to more developed nations. Because of the limited supply of affordable reserves, and the environmental and health problems related to the heavy use of fossil fuel

combustion, longer term energy sources will be needed soon. These sources will need to provide a high enough energy density for manufacturing and urban concentrations, allow for improvement to the standard of living in developing countries, and have minimal environmental impact. Renewable energy sources such as solar and wind power will play a role in the future, but are limited in scope. Fusion energy can, and I believe, will be a significant part of the long-term solution. This thesis furthers the understanding of plasma physics and ways to heat a plasma to fusion-relevant temperatures. (**Appendix A** clarifies the need for fusion energy by discussing current and future energy use, fossil fuel reserves, renewable energies, and the advantages of fusion energy.)

As we seek to produce energy through fusion, our sun — a working example of a fusion reactor — can serve as a model. Stars are at such high temperatures that their matter is in a state that is not usually found on the Earth. When any material is heated to a temperature such that the kinetic energy is comparable to the electron binding energies of the atoms (typically thousands of degrees Celsius), the electrons can be ripped free from the nucleus and the atoms become ions. This ionized gas is called a plasma. When plasmas are heated to millions of degress Celsius, fusion reactions can occur. This happens when some of the ions are traveling with enough energy to overcome the mutually repulsive electromagnetic forces, allowing the strong nuclear force to fuse them together. This releases much more energy than was required to overcome the repulsive barrier. Examples of both kinds of plasmas exist in the sun. The surface of the sun, though a plasma, does not have enough energy for fusion. However, in the inner core of the sun the hydrogen fuel is transformed into helium through a chain of fusion reactions.

In the laboratory, a very successful way to heat a plasma to temperatures comparable to and greater than the core of the sun, is through wave-particle interactions. Energy from an electromagnetic wave is transferred to the plasma particles by launching power from the edge of the plasma and allowing it to be absorbed inside the core plasma, much like a microwave oven transfers energy from a magnetron to food or water.

1.3 Magnetic Confinement Fusion

To understand current experiments in fusion, it is important to examine the problem of plasma confinement, and to look at how it has been approached historically.

To produce usable fusion energy, it is necessary not only to heat the fuel, but to keep it confined at high density. The path toward sustained fusion in a star begins with its formation. As gravity pulls a large amount of material toward a common center, a spherical mass is formed which initially is heated through the transformation of gravitational potential energy into kinetic energy. With enough mass, enough energy is released to eventually "ignite" the star and begin fusion "burning" in the core of the star. At this point the gravitational collapse is halted, due to a balance between the gravitational forces pulling material toward the core and the outward pressure due to kinetic energy released by fusion reactions. Our sun is an example of a star at this stage of development, confining its fusion fuel through gravity. The material at the core of the sun is estimated to have a density of 158 g/cm^3 and a temperature[1] of 16 million K, or 1.4 keV [1].

Achieving controlled fusion on the Earth has been a difficult task. A key to controlled fusion in the laboratory is to hold a plasma at fusion-producing temperatures long enough to allow a significant number of fusion reactions to occur. On the Earth we cannot amass enough material for gravity to confine the plasma.

One approach to confine the hot plasma in the laboratory is through inertial confinement fusion (ICF). There are several methods of achieving the high densities and temperatures needed for fusion in ICF: implosion of a small pellet using lasers or particle beams, imploding metal shells around a pre-formed plasma, and other methods. In the most common method, imploding small pellets of fuel, the fusing plasma is only "confined" for at most a few nanoseconds. For the process to produce net energy, each mini-explosion should release more energy from fusion reactions of

[1]In plasma physics it is common practice to use units of *energy* for *temperature*, thus 1 eV = 1 electron volt is equivalent to 11,600 degrees kelvin. (In this thesis, footnotes are denoted by a small number raised above the text, while a reference to the Bibliography is denoted by a number in square brackets, such as this: [1].)

the fuel than was used to compress and heat it.[2] The U.S. Department of Energy (within its defense related activities) is spending billions of dollars to build a facility to study ICF — the National Ignition Facility. Its goal is to reach ignition (more energy out than in) from exploding fuel pellets.

Another approach to confinement is to use magnetic fields. Since a plasma is composed of electrically charged particles, it responds to electromagnetic forces. With an appropriate configuration of magnetic fields inside a large air-tight structure, a hot plasma can remain trapped in a "magnetic bottle". The magnetic field keeps the plasma from immediately striking the walls of the vacuum vessel. Of course, eventually the energy leaks out due to collisions and other processes which lead to diffusion and transport of particles and heat. To achieve practical fusion power production, particle and energy loss across the magnetic field lines must be understood and controlled. This loss usually is much higher than that predicted by theory based only on collisions. Another problem is that this flow of energy across the magnetic field is a large heat load on whatever material surface is closest to the hot plasma. This heat load can be dissipated without damage, through proper design and use of materials, and clever magnetic field configurations to radiate most of the power before striking physical surfaces.

1.3.1 The History of Magnetic Confinement

The first experimental magnetic confinement devices in the late 1940s and 1950s were all similar in design, relying on the principle that charged particles generally follow magnetic field lines. Because any intersection of the field line with a material surface results in the loss of the particles, early plasma physicists tried to create "infinite" magnetic field lines by using circular paths. The shape of a torus has been at the heart of many of the magnetic confinement devices in the five decades of controlled fusion research. A toroidal magnetic confinement device is basically a

[2]These types of explosions can also shed light on the behavior of matter in an exploding supernova or an exploding hydrogen bomb. Perhaps for this reason, more than for its energy potential, this approach is well-funded.

solenoid joined end to end. (A solenoid is a cylindrical coil of wire designed to produce a strong magnetic field inside the cylinder. By joining the cylinder end to end it becomes a torus.) One of the earliest examples of a toroidal magnetic confinement experiment was the stellarator, a device shaped like a racetrack (two long sections joined by U-curves at each end) and designed by Lyman Spitzer in 1951 at Princeton under the classified Project Matterhorn, part of the nation-wide fusion energy effort Project Sherwood. British scientists were working on the Zero Energy Thermonuclear Assembly, or ZETA (a toroidal pinch, where currents along the metal surface of the torus produce a magnetic field which was supposed to "pinch" and heat the plasma) and other smaller experiments in the 1940s and 1950s.

There have been other ideas to "plug" the ends of a magnetic confinement device rather than wrap the field lines around on themselves. These involved using the magnetic mirror effect whereby charged particles reflect from regions of increasing magnetic field. However, mirror devices were not able to achieve high confinement of particles because of end losses (some particles do not reflect, and escape along the axis of the device). Today, there are no longer large mirror experiments being pursued.

In the early period of fusion research, the Soviet Union was also working on toroidal devices. In the 1950s, Igor Tamm and Andrei Sakharov were working on ideas for a toroidal magnetic fusion device which would become known as a tokamak.[3] In 1968, the Soviet fusion research program announced results from a tokamak named T-3 which achieved electron temperatures over 1 keV, a great improvement over previous experiments with other magnetic configurations. The tokamak concept has since been one of the most widely built and studied experimental configurations in controlled fusion research, with the largest fusion power output and best confinement of all devices so far. This thesis is based on experiments performed in this type of device.

[3]The word tokamak is from a Russian acronym, but it is unclear whether it was originally: **to**roidal'naya **ka**mera **ma**gnitnye **k**atushki, meaning toroidal chamber and magnetic coils, or: **to**roidal'naya **kam**era s **ak**sial'nym magnitym polem, meaning toroidal chamber with axial magnetic field.

1.3.2 Tokamak Geometry

A toroidal magnetic geometry does have some disadvantages. Particles are lost due to drifts which are not present in a linear device. Charged particles follow straight magnetic field lines, but when the field is curved as in a torus, the particles can drift across field lines. Another effect of bending the solenoid into a torus is that the field inside becomes non-uniform in magnitude. The toroidal field magnitude is inversely proportional to the major radius (the distance from the center of the torus), so the side of the plasma closer to the inboard wall is sometimes referred to as the "high-field side" and the part of the plasma farther out from the hot center is the "low-field side". This gradient of the field causes another drift of particles across magnetic field lines. Because of these drifts, additional magnetic fields are needed to keep the ions and electrons from being lost (effectively cancelling the drifts).

The unique features of a tokamak make it fairly easy to reduce these losses. One way to do this is make the fields helical rather than circular. A stellarator produces these helical fields by the use of specially designed (and difficult to manufacture) external magnets. The distinguishing feature of a tokamak is a large toroidal current which produces a poloidal magnetic field (see Fig. 1-1). This is usually accomplished by induction using a transformer in the middle of the torus. The toroidal and poloidal field combine to make a helical field. There are other external coils which produce a vertical field, keeping the plasma from drifting outward. There are also usually coils to fine-tune the shape and position of the plasma.

1.3.3 The Alcator C-Mod Tokamak

The Massachusetts Institute of Technology's Plasma Science and Fusion Center has a long history of tokamak design and construction. Following the successful completion of the Alcator A and Alcator C tokamak experiments, the Alcator C-Mod tokamak [2] began operation in 1993. The name Alcator comes from the Italian words for high-field torus: *Alto Campo Torus*, the name chosen for the first high magnetic field tokamak experiment at M.I.T. by Prof. Bruno Coppi. The Alcator concept is

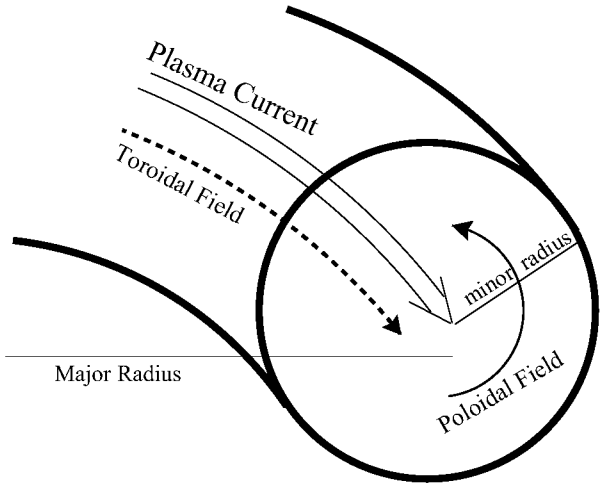

Figure 1-1: The geometry of a tokamak, showing the plasma current, toroidal and poloidal magnetic fields, and major and minor radius.

a smaller and potentially cheaper way to high fusion power density because it uses a more compact machine with higher magnetic fields and densities than the larger tokamaks such as JET in Europe or TFTR at Princeton. The highest central field run to date is just over 8 tesla[4], which means that the field at the edge of the plasma on the high-field side was approximately 12.2 T. This is much larger than the central field (typically 2 – 3 tesla) in the larger machines.

A wide range of plasma parameters has been explored in C-Mod. Typical parameters are: 5.4 tesla central magnetic field, 1 MA plasma current, 3×10^{20} m^{-3} central electron density, and 2 keV central temperatures. The plasma size and shape are usually such that the major radius (the distance from the center of the torus to the center of the plasma, where the field is entirely toroidal) is 67 cm, the minor radius 21 cm, and the plasma is elongated so that it is 1.6 times taller than it is wide. The combination of fields result in nested magnetic flux surfaces that hinder the plasma from hitting the walls, because cross-field transport is much slower than parallel transport. In C-Mod, there is usually a "last closed flux surface" (LCFS) outside of which the field lines are no longer closed in a continuous loop but rather intersect a material surface. Particles that flow beyond the LCFS will travel along the open field lines

[4]1 tesla (1 T) = 10,000 gauss. The Earth's magnetic field is approximately 0.5 gauss.

and quickly be lost from the plasma, hence this region is sometimes known as the "scrape-off layer", or SOL. Figure 1-2 shows a cross-section of the Alcator C-Mod vacuum vessel and protective molybdenum tiles, along with the magnetic flux surfaces from the center out to the LCFS for a typical plasma, as reconstructed from the magnetic equilibrium code EFIT [3], which solves the Grad-Shafranov equation using measured plasma quantities as input.

The C-Mod tokamak is a meticulously engineered system to contain the hot plasma. The vacuum vessel shown in Fig. 1-2 contains the plasma. This vessel is surrounded by the magnet system, the main components of which are 20 toroidal field coils (Fig. 1-3(2)). Each square "coil" is made of 4 separate pieces connected with special sliding joints using felt metal which maintain electrical contact even when the joints move. During a plasma discharge (or "shot"), several hundred kiloamps of current run through these toroidal field (TF) coils, producing immense outward pressure on the square loop. Because the current wraps around the loop several times, advancing slightly in the toroidal direction each wrap, there is also an asymmetry which results in a twisting force on the TF coil. Without something to hold it all together, the TF coils would fly apart during a shot. So the TF coils, which surround the vacuum vessel, are themselves surrounded by a massive cylinder of steel consisting of a cylindrical shell (a single piece of forged steel) and a top and bottom circular plate (each weighing 35 tons, see Fig. 1-3(5)), held together by 96 special alloy drawbars. There are wedge plates (Fig. 1-3(3)) designed to fit between the TF coils. The wedge plates are firmly connected to the steel cylinder with tapered bars. The vacuum vessel is pumped down to a pressure of typically 9×10^{-7} torr (1 billionth of an atmosphere) before a plasma shot. A detailed diagram of the magnetic field coils and the vacuum vessel where the plasma is contained is shown in Fig. 1-3. More information and photographs can be found at the Plasma Science and Fusion Center's web page **http://www.psfc.mit.edu/cmod/**.

The large plasma current present in C-Mod also heats the plasma, but additional heating is needed for high fusion performance. The plasma current heats the plasma through resistive ohmic heating (like a light bulb filament) to $1 - 1.5$ keV. However,

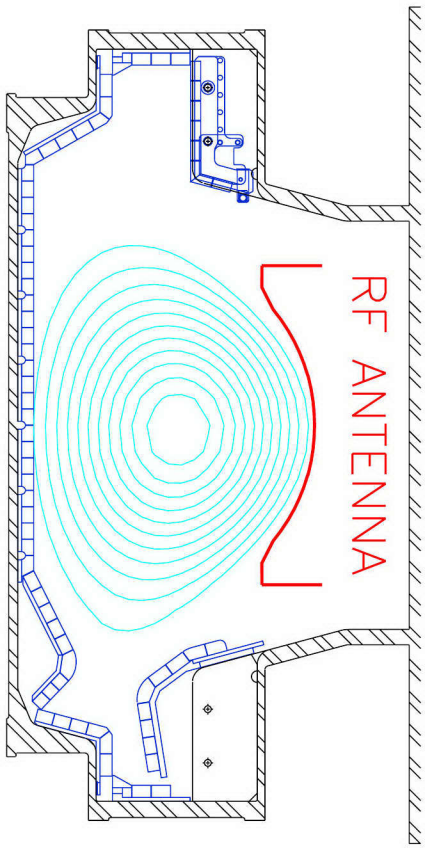

Figure 1-2: A cross-sectional view of the C-Mod tokamak vacuum vessel. Major radius is increasing to the right. The curved surface to the right of the plasma labelled "RF ANTENNA" represents the limiter protecting the antenna (see Fig. 1-4). Also shown are the magnetic flux surfaces (in this case contours of constant poloidal magnetic flux).

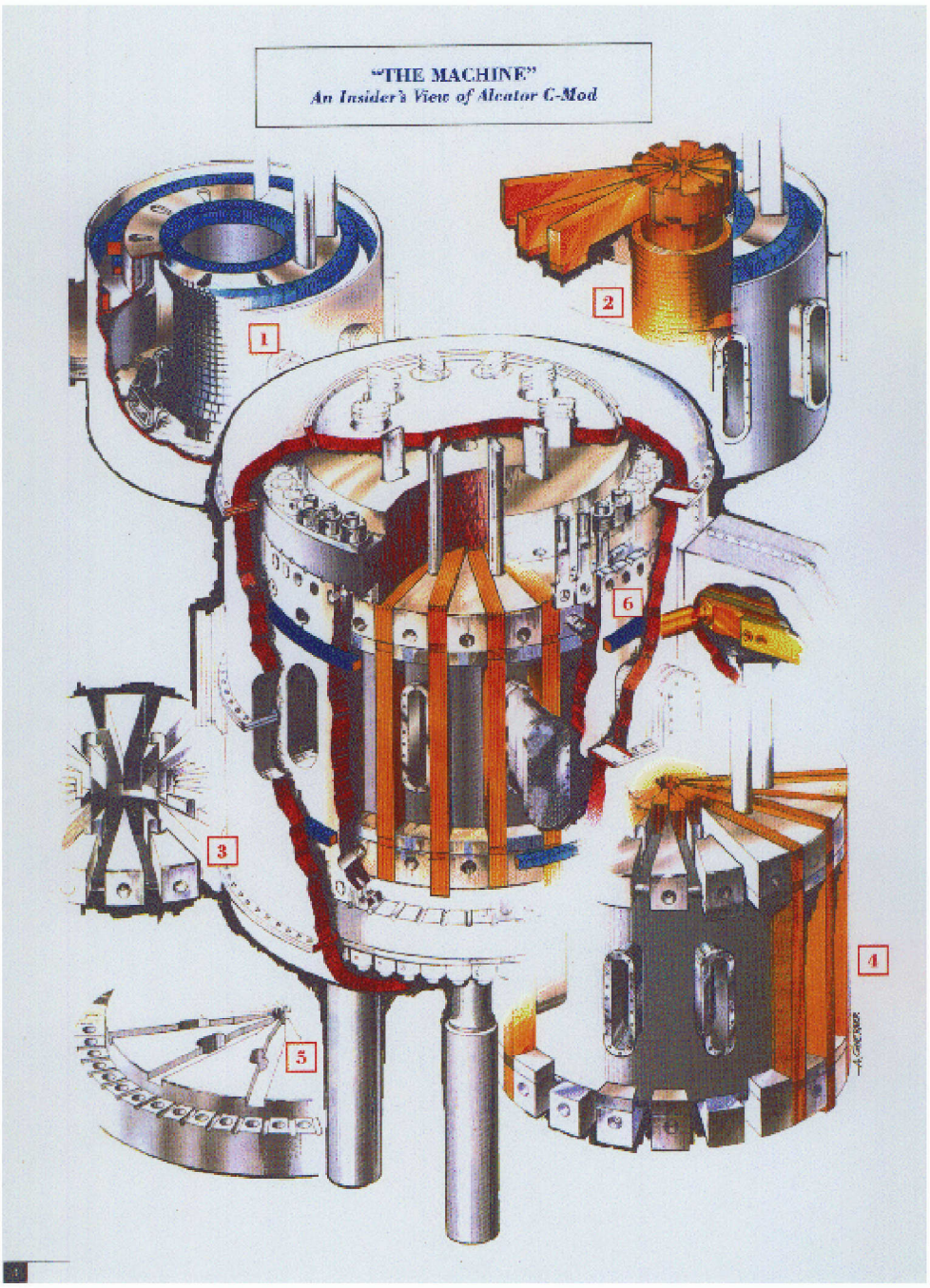

Figure 1-3: The Alcator C-Mod tokamak. (1) Molybdenum tiles covering the inner column. (2) The top arms of three square toroidal field coils (20 total). Also shown are the ohmic coils wrapped around the central magnet arm assembly. (3) A wedge plate which goes in between the toroidal magnet arms. (4) The top and bottom wedge plates, with the vacuum vessel (two horizontal ports are visible) in between. (5) One of the 35 ton stainless steel top and bottom covers. (6) The complete machine on concrete legs and surrounded by a cryostat. Visible above the label 6 is one of the drawbars which hold the covers and cylinder together.

Figure 1-4: A view of the D- and E-port antennas from inside Alcator C-Mod. (Turn the page clockwise 90° to view correctly).

unlike metals, plasma resistivity decreases with increasing temperature, so the ohmic heating becomes less effective at higher temperatures. It is desirable to reach temperatures of 5 – 10 keV in order to study fusion relevant conditions. Therefore, another heating method is needed. The main method of auxilliary heating in C-Mod is to use radio waves launched from antennas on the low-field side. The antennas are made of thick straps of inconel (a nickel-based steel alloy chosen for its high strength) coated with copper (chosen for its high conductivity) encased in a metal box and protected from the plasma by a Faraday shield, composed of metal rods nominally parallel to the total magnetic field at the antenna location. The machine has 10 equally spaced ports around the torus named A through K (skipping I) for diagnostic access and auxilliary heating. Three of these ports are filled with RF antennas. The D- and E-port antennas have two parallel straps, curved to fit the shape of the plasma, and driven 180° out of phase (when one strap has maximum upward going current, the other is at maximum downward current). This launches power equally in both directions toroidally. The third antenna at J-port has four straps which can be variably phased, in order to launch waves with net toroidal momentum and drive electric current in the plasma. Each pair of straps is connected to a large RF transmitter through ∼50 meters of rigid 6-inch and 9-inch diameter coaxial tubing. Each transmitter is capable of coupling approximately 2 megawatts of power into the plasma. The E-port antenna, the resonant loop[5], and the transmitter system are tuned to a frequency of 80.0 MHz, the D-port system is tuned to 80.5 MHz (to avoid cross-talk with the E-port system), and the J-port system can be tuned to any frequency between 40 and 80 MHz. Using all three of these antennas to couple ∼5 MW of RF power to the plasma, central temperatures as high as ∼5 keV have been achieved. All the data in this thesis is from the D and E antenna systems, pictured in Fig. 1-4, where the straps are just visible behind the protective Faraday rods.

To produce practical fusion energy from a magnetically confined plasma, the

[5]Each strap is fed at the top and bottom (with the ground in the center) by coaxial line. The top and bottom lines are connected together in a resonant loop which is an integral multiple of half-wavelengths in order to drive the desired frequency.

plasma must be heated to very high temperatures (10 keV or more). It must also be confined for long enough that significant numbers of fusion reactions can occur. RF waves can help in achieving both these goals. The physics of two kinds of waves that may be useful in a fusion reactor, the fast magnetosonic wave and the ion Bernstein wave, will be explored in the next chapter.

Chapter 2

Waves in Plasmas

The word "plasma" was first used to describe an electromagnetic fluid of electrons and ions in 1922. During the 1920s, at the General Electric Research Laboratory in Schenectady, N.Y., Irving Langmuir, Lewi Tonks and Harold Mott-Smith were investigating the properties of electrical discharges through gases at low pressures. They produced a series of papers about electron and ion interactions with each other and with the anode, cathode, and walls of the discharge tubes. They reported observations of oscillations. They described the different populations of electrons present in such discharges, and noted the difference between the "sheath" region near a physical surface, and the quasi-neutral central region they named "plasma". Robin Herman, in her highly recommended book about the history of fusion energy research [4, pg. 25], described the origin of the word this way:

> Langmuir had been passing electrical discharges through gases and needed a term for the partially ionized gas that resulted. The way the gas contained different particles such as high velocity electrons, molecules, and impurities "reminded him of the way blood plasma carries around red and white corpuscles and germs," wrote a colleague, Harold M. Mott-Smith. So Langmuir proposed the term *plasma*.

The first time the term plasma was used by Langmuir in a widely available journal was, appropriately enough, in a paper about "Oscillations in Ionized Gases" [5] in

1928. The important qualification was made that the Debye shielding length (the distance over which the electric field of a test charge in an otherwise neutral plasma can be felt) should be much smaller than the scale length of the device for the region to be called a true plasma, rather than part of the sheath.

2.1 Wave Dispersion Relations

Ordinary fluids such as air or water can support only a few types of oscillations or waves. For example, sound waves in air are due to the propagation of pressure disturbances. Water surface waves are due to the cohesion (surface tension) and inertia of water. But a plasma can support a whole "zoo" of waves [6]. In a regular fluid, particles carry wave motion, but in a plasma, waves can be supported by electric fields, magnetic fields, electrons, ions, or combinations of fields and particles. The dispersion relation relates the wavelength to the frequency of the wave. This relation can describe the wave motion by providing information about the wavelength and phase velocity for a given frequency, for example.

Even a vacuum can support a type of wave: electromagnetic radiation. The dispersion relation for electromagnetic radiation (including light waves, radio waves, gamma rays, etc.) can be found from Maxwell's equations in vacuum (using SI[1] units):

$$\nabla \times \vec{E} = -\frac{\partial \vec{B}}{\partial t} \tag{2.1}$$

$$\nabla \times \frac{\vec{B}}{\mu_0} = \epsilon_0 \frac{\partial \vec{E}}{\partial t} \tag{2.2}$$

$$\nabla \cdot \vec{B} = 0 \tag{2.3}$$

$$\nabla \cdot \vec{E} = 0 \tag{2.4}$$

[1]Systéme International, with base units for mass in kilograms, length in meters, time in seconds and charge in coulombs. Other units are volt for electric potential, tesla for magnetic intensity, ampere for current, joule for energy and watt for power. This is also sometimes referred to as the "mks" system of units, for meters-kilograms-seconds.

By combining Eq. 2.1 and Eq. 2.2, one obtains the differential equation for the electric field:

$$\nabla \times \nabla \times \vec{E} = -\frac{1}{c^2}\frac{\partial^2 \vec{E}}{\partial t^2}, \tag{2.5}$$

where $c = 1/\sqrt{\epsilon_0 \mu_0} = 2.99792458 \times 10^8$ m/s.

Carrying out Fourier analysis on Eq. 2.5 can transform spatial derivatives into wavevectors and time derivatives into frequencies. Considering just a single wavevector and a single frequency, one can assume that all field quantities vary simply harmonically in time (with angular frequency ω) and space (with wavevector[2] $\vec{k}$, where the wavenumber $k = 2\pi/\lambda$ for wavelength λ): $E \propto e^{i(\vec{k}\cdot\vec{r}-\omega t)}$. If there are no special boundary or initial conditions then Eq. 2.5 transforms simply into:

$$\vec{k} \times \vec{k} \times \vec{E} = -\frac{\omega^2}{c^2}\vec{E}, \tag{2.6}$$

revealing a relationship between electric field, wavevector, and frequency. Then, using a vector identity and Eq. 2.4 one obtains an equation for the wave electric field:

$$\left(\frac{\omega^2}{c^2} - k^2\right)\vec{E} = 0 \tag{2.7}$$

For a solution with $\vec{E} \neq 0$, it is necessary that:

$$\frac{\omega^2}{c^2} = k^2, \text{ or } \frac{\omega}{k} = \pm c, \tag{2.8}$$

which is the dispersion relation for electromagnetic waves in vacuum. This dispersion relation indicates that the phase velocity $v_{\text{ph}} = \omega/k$ is of constant magnitude c. The group velocity (the velocity of energy flow, or of a wavepacket composed of many different wavenumbers) $v_g = d\omega/dk = c$ is the same for any wavenumber, so there is no "dispersion" in the sense that waves of different wavelengths in a wavepacket all propagate with the same phase and group velocities. The situation can be very different in a plasma, as will be seen in the rest of this chapter.

[2]The wavenumber is the magnitude of the wavevector, which indicates the direction of propagation of the phase velocity.

2.1.1 The Cold Plasma Approximation and the CMA Diagram

The reason plasma waves are so different from vacuum waves is that, in the presence of a plasma, the source terms in Maxwell's equations are non-zero. Charge and current density play a significant role in altering the simple character of vacuum electromagnetic waves. Maxwell's equations become:

$$\nabla \times \vec{E} = -\frac{\partial \vec{B}}{\partial t} \tag{2.9}$$

$$\nabla \times \frac{\vec{B}}{\mu_0} = \epsilon_0 \frac{\partial \vec{E}}{\partial t} + \vec{J} \tag{2.10}$$

$$\nabla \cdot \vec{B} = 0 \tag{2.11}$$

$$\nabla \cdot \vec{E} = \frac{\rho}{\epsilon_0} \tag{2.12}$$

where two new source terms appear on the right-hand side. Taking the curl of Eq. 2.9 and substituting into Eq. 2.10 results in a wave equation:

$$\nabla \times \nabla \times \vec{E} = -\frac{1}{c^2}\frac{\partial^2 \vec{E}}{\partial t^2} - \mu_0 \frac{\partial \vec{J}}{\partial t} \tag{2.13}$$

The plasma current $\vec{J}$ due to a plasma wave is related to the particle velocities. Modeling the plasma as a mix of fluids of several kinds of particles (electrons and different ion species),

$$\vec{J} = \sum_s q_s n_s \vec{v}_s \equiv \overline{\sigma} \cdot \vec{E}, \tag{2.14}$$

where the index s in the sum denotes the plasma species, and the conductivity tensor $\overline{\sigma}$ is *defined* by Eq. 2.14 (this relationship is strictly only valid in Fourier space [7]). By substituting the Lorentz force into Newton's second law (neglecting pressure terms as this is a cold plasma model), one obtains the equation of motion for the fluid of species s,

$$m_s d\vec{v}_s/dt = q_s(\vec{E} + \vec{v}_s \times \vec{B}). \tag{2.15}$$

Solving for $\vec{v}_s$ in terms of the components of $\vec{E}$, and plugging into Eq. 2.14 allows one to determine the conductivity tensor elements.

To proceed to obtain a dispersion relation, again Fourier analyze Eq. 2.13 in time and space:

$$\vec{k} \times \vec{k} \times \vec{E} = -\frac{\omega^2}{c^2}\vec{E} - i\mu_0\omega\overline{\sigma} \cdot \vec{E}. \tag{2.16}$$

Define $\mathbf{K} = \mathbf{1} + i\,\overline{\sigma}/\omega\epsilon_0$ to be the dimensionless dielectric tensor, where $\mathbf{1}$ is the identity tensor, and let $\vec{n} = c\vec{k}/\omega$, then Eq. 2.16 becomes the plasma wave equation:

$$(\vec{n}\vec{n} - n^2\mathbf{1} + \mathbf{K}) \cdot \vec{E} = 0. \tag{2.17}$$

To find non-trivial solutions with $\vec{E} \neq 0$, it is necessary that the 3×3 matrix representing the tensor $\vec{n}\vec{n} - n^2\mathbf{1} + \mathbf{K}$ have zero determinant, which determines the dispersion relation for hot plasma waves. In many physical situations one or more components of the wavevector and the frequency are fixed, and the dispersion relation is solved for the remaining components. If the source is driving the wave at a constant frequency the imaginary part of the wavenumber solution, if any, represents spatial damping.[3] Or, if a wavenumber is momentarily imposed, then the frequency can be solved for and the imaginary part represents temporal damping.

The vector equations can be quite complicated in the toroidal geometry of a tokamak. However, by considering a small region where the background plasma density and magnetic field do not vary appreciably, the plasma can be considered homogeneous, and a great simplification can be made. Consider a plane wave with propagation vector $\vec{k}$ in a plasma with local magnetic field $\vec{B}$. Taking a cartesian (x, y, z) coordinate system, let the magnetic field be along the z direction, and the wave propagation vector $\vec{k}$ be in the $x - z$ plane, so that $k_\perp = k_x$ and $k_\parallel = k_z$. The plasma wave equation for the electric field vector can be written out as three equations:

$$\begin{pmatrix} K_{xx} - n_\parallel^2 & K_{xy} & n_\perp n_\parallel + K_{xz} \\ K_{yx} & K_{yy} - n^2 & K_{yz} \\ n_\perp n_\parallel + K_{zx} & K_{zy} & K_{zz} - n_\perp^2 \end{pmatrix} \begin{pmatrix} E_x \\ E_y \\ E_z \end{pmatrix} = 0, \tag{2.18}$$

where $n_\perp = n\sin\theta$, $n_\parallel = n\cos\theta$, and θ is the angle between the wavevector and the magnetic field, with $\cos\theta = \vec{k} \cdot \vec{B}_0/|k||B_0|$.

[3]Since the wave is taken to vary as $\exp(-i\omega + i\vec{k} \cdot \vec{x})$, an imaginary part of the wavenumber k introduces a factor $\exp(-\vec{k}_{\rm im} \cdot \vec{x})$.

In a cold plasma (neglecting the pressure term in the equations of motion), the plasma wave equation in a homogeneous magnetic field can be written in Stix notation [8, ch. 1-4] as:

$$\begin{pmatrix} S - n_{\parallel}^2 & -iD & n_{\perp} n_{\parallel} \\ iD & S - n^2 & 0 \\ n_{\perp} n_{\parallel} & 0 & P - n_{\perp}^2 \end{pmatrix} \begin{pmatrix} E_x \\ E_y \\ E_z \end{pmatrix} = 0, \tag{2.19}$$

The Stix notation dielectric tensor elements are:

$$S = (R + L)/2, \tag{2.20}$$

$$D = (R - L)/2, \tag{2.21}$$

and

$$P = 1 - \sum_s \frac{\omega_{ps}^2}{\omega^2}, \tag{2.22}$$

where

$$R = 1 - \sum_s \frac{\omega_{ps}^2}{\omega(\omega + \Omega_s)}, \tag{2.23}$$

and

$$L = 1 - \sum_s \frac{\omega_{ps}^2}{\omega(\omega - \Omega_s)}. \tag{2.24}$$

Two characteristic frequencies appear which are quite important in determining the wave dynamics. The plasma frequency ω_{ps} for a species of charge Z_s (in units of the fundamental charge e), mass m_s and density n_s,

$$\omega_{ps}^2 = \frac{n_s Z_s^2 e^2}{m_s \epsilon_0}, \tag{2.25}$$

is proportional to the density and is the angular frequency at which simple charge displacement perturbations oscillate in the plasma. The cyclotron frequency

$$\Omega_s = \frac{Z_s e B}{m_s}, \tag{2.26}$$

is proportional to the magnetic field strength and is the angular frequency at which the particles gyrate in a circular motion around the magnetic field lines. Note that the cyclotron frequency Ω_s is a signed quantity: $\Omega_e < 0$ for electrons, and $\Omega_i > 0$

for ions. Thus at the ion cyclotron frequency $\omega = \Omega_i$, $L \to \infty$, and at the electron cyclotron frequency $\omega = |\Omega_e|$, $R \to \infty$.

The ratio of the frequency of the wave to these two characteristic frequencies determines how the plasma affects the propagation characteristics. The wavelength of the wave compared to the plasma's spatial scales also determines how the plasma affects propagation. One of the important plasma lengths is the radius of a particle's circular orbit around the magnetic field, which is known as the gyro-radius or the Larmor radius. This radius depends on the particle's kinetic energy. For a plasma of any given temperature, even though the same kind of particles will gyrate at the same frequency, they will have a range of different radii. If the wavelength is longer than any of these radii, then again, a simplification can be made. The essence of the cold plasma approximation is the assumption that compared to a wavelength, the Larmor radius is infinitesimal, and the component of the phase velocity parallel to the magnetic field is much larger than the thermal speeds of the particles.

Cold plasma waves have a much greater variety of characteristics than vacuum waves. The dispersion relation for normal modes in the plasma is obtained by setting the determinant of the matrix in Eq. 2.19 to zero. This can be expressed as a quadratic equation in n^2:

$$\begin{gathered} An^4 - Bn^2 + C = 0, \quad \text{with} \\ A = S\sin^2\theta + P\cos^2\theta \\ B = RL\sin^2\theta + PS(1+\cos^2\theta) \\ C = PRL \end{gathered} \tag{2.27}$$

Since this is a quadratic equation, there are always two solutions

$$n^2 = (B \pm \sqrt{B^2 - 4AC})/2A \tag{2.28}$$

for a given set of plasma parameters. The solution with the larger phase velocity (smaller n^2) is called the fast wave, and the solution with the smaller phase velocity (larger n^2) is called the slow wave. When the solution is such that one of the roots $n^2 < 0$, then that wave is evanescent — it cannot propagate.

These two roots represent waves that are very different from one another in different plasma parameter regimes. A good way of characterizing the large variety of

waves that can exist for various plasma densities and magnetic field strengths is the Clemmow-Mullaly-Allis (CMA) diagram [8, ch. 2-2]. The CMA diagram is a way of representing the different character of the cold plasma solutions for different regions of parameter space. (For example, in high density and high magnetic field plasmas, the waves are quite different than in low density and low magnetic field plasmas.) All cold plasma waves are represented in this diagram, and many hot plasma waves can be simply described as modifications of these waves. The CMA diagram is separated into different regions by cutoffs and resonances, where the wavenumbers go to 0 or ∞ (infinity), respectively. These bounding regions are all simultaneously visible (Fig. 2-1) for a plasma with an ion to electron mass ratio of 5 (perhaps an actual realization of this "plasma" could be a collection of dust grains where the lighter particles are preferentially negatively charged and the 5 times heavier particles are positively charged).

The reciprocal of Eq. 2.28 is the normalized phase velocity:

$$u^2 = v_{\rm ph}^2/c^2 = 2A/(B \pm \sqrt{B^2 - 4AC}). \tag{2.29}$$

Since A, B, and C are functions of the angle θ relative to the magnetic field, a polar plot of the magnitude of the phase velocity versus angle can illustrate the two solutions present in Eq. 2.29.

Within any region bounded by the resonance and cutoff lines, the wave phase velocity solution will have a similar topology. For example, in the lower right region, below $R \to \infty$ and to the right of $L = 0$, there are no propagating solutions anywhere. In the upper right region, above $L \to \infty$ and to the right of $P = 0$, there are always two solutions, a slow wave with a figure-eight shaped polar plot and a fast wave with a circular shaped plot. The solution near $L \to \infty$ (Fig. 2-2[a]) looks different than the solution near $P = 0$ (Fig. 2-2[b]), but the topology is the same.

The fast magnetosonic wave, often referred to as just the fast wave (FW), corresponds to the small n^2 solution in the upper-right-most region of the CMA diagram (low frequency, high density, and high magnetic field). This is the outer solution in Fig. 2-2, corresponding to nearly X-mode polarization at $\theta \sim \pi/2$ or $3\pi/2$.

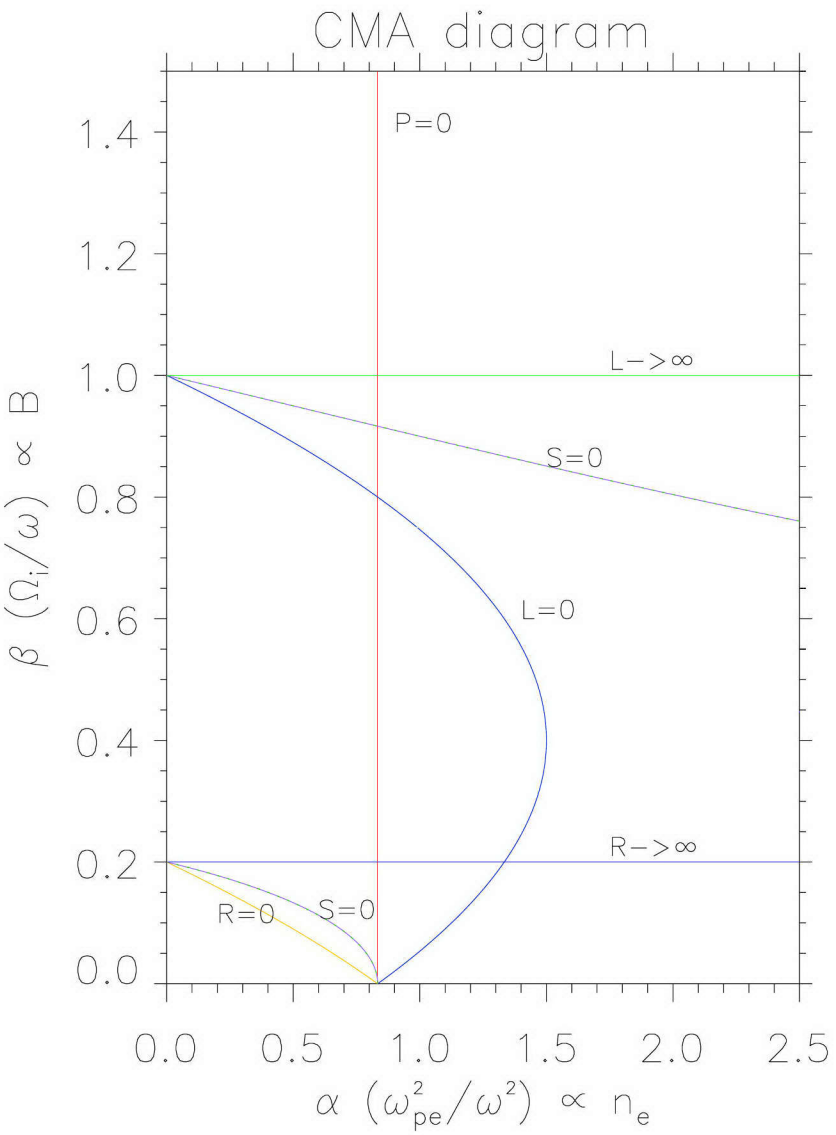

Figure 2-1: CMA diagram for a single ion species plasma with ion to electron mass ratio of 5. Cold plasma resonances and cutoffs are labelled.

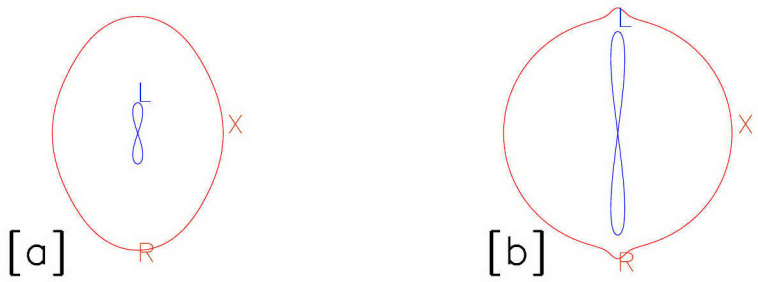

Figure 2-2: Two phase velocity solutions ($v_{\rm ph}/c$ *vs.* θ, with $\theta = 0$ at the top of the plot, increasing counter-clockwise) for the upper-right region of the CMA diagram (Fig. 2-1). [a] $\alpha = 1.76$, $\beta = 1.02$. [b] $\alpha = 0.853$, $\beta = 1.22$. Polarizations at $\theta = 0$ or π (L or R) and $\theta = \pi/2$ or $3\pi/2$ (O or X) are also shown.

When realistic ion to electron masses (such as 3672 for deuterium) are used, the bounding lines in the CMA diagram become harder to see in a linear plot. However, by plotting the x-axis (proportional to plasma density) on a logarithmic scale, the CMA diagram can be a useful tool for investigating wave propagation across a plasma with varying density and magnetic field.

As a specific example of this tool which will apply to the mode conversion cases discussed later in this chapter (Sec. 2.4) and in Ch. 4, consider a majority deuterium plasma with a moderate amount of helium-3 ($n_{\rm He3}/n_e = 0.15$), a scenario denoted by D(^{3}He). This correponds to a C-Mod D(^{3}He) plasma that exhibited mode conversion from the fast wave to an ion Bernstein wave (see Sec. 2.4). Other parameters were: $B_0 = 7.8$ tesla, $n_{e0} = 2.4 \times 10^{20}\,{\rm m}^{-3}$, $f = \omega/2\pi = 80$ MHz, placing the minority helium-3 cyclotron resonance in the center of the plasma. For a magnetic field profile that varies inversely with major radius, and a density profile peaked in the center of the plasma and falling off to very small edge values, the wave trajectory along the major radius from the antenna through the plasma to the high-field side can be

plotted on the CMA diagram. Each point represents a distinct value of density and magnetic field. This is shown in Fig. 2-3.

The trajectory curve passes through many regions in the CMA diagram, bounded in this case by the $L = 0$, $S = 0$, and $L \to \infty$ lines. In Fig. 2-4, the wave phase velocity (normalized to the speed of light) for the fast and/or slow wave as a function of the angle θ for each distinct region in the CMA diagram[4] is plotted. The trajectory curve is shaped like a backwards "C", beginning at region 1 near the antenna on the low-field-side, and ending in region 7 at the high-field-side. The short dashed line along the early and late part of the trajectory (small α) represents very low densities, which may not actually exist at the edge of C-Mod plasmas. Edge probe measurements suggest that the plasma density remains finite for quite some distance away from the last closed flux surface. Although it has never been measured in the antenna box itself, a reasonable estimate is that the plasma density remains of order $10^{18}\,\mathrm{m}^{-3}$ right up to the antenna straps. The heavier dashed portion of the trajectory is for densities greater than or equal to $10^{18}\,\mathrm{m}^{-3}$. The fast magnetosonic wave is the outer curve in regions 1, 4, and 7 (the inner curve is the slow wave, or shear Alfvén wave). In regions 3 and 6 only the fast wave can exist, and in regions 2 and 5, the fast wave is cutoff, while the slow wave could still propagate. The labels on the phase velocity curves correspond to the polarizations for the specific cases of $\theta = 0$ (propagation along the magnetic field), where the wave could be either the L-mode ($n^2 = L$) or R-mode ($n^2 = R$), and $\theta = \pi/2$ (propagation across the magnetic field), where the wave could be either the O-mode ($n^2 = P$) or the X-mode ($n^2 = RL/S$). Note the lack of any propagating O-mode anywhere in this plasma; the frequency is so low that the entire trajectory is far to the right of the $P = 0$ cutoff line, where $\omega \simeq \omega_{pe}$, so $P \ll 0$ and the O-mode is cutoff.

The general CMA diagram allows freedom in both $n_\perp$ and $n_\parallel$. However, if the parallel wavenumber is fixed by the launching structure, as is approximately the case for the two- and four-strap antennas on C-Mod, then the cold plasma dispersion

[4]For those readers with access to the C-Mod computer cluster, an interactive CMA diagram program can be run in IDL at USER10:[MELBY.IDL]CMA.PRO

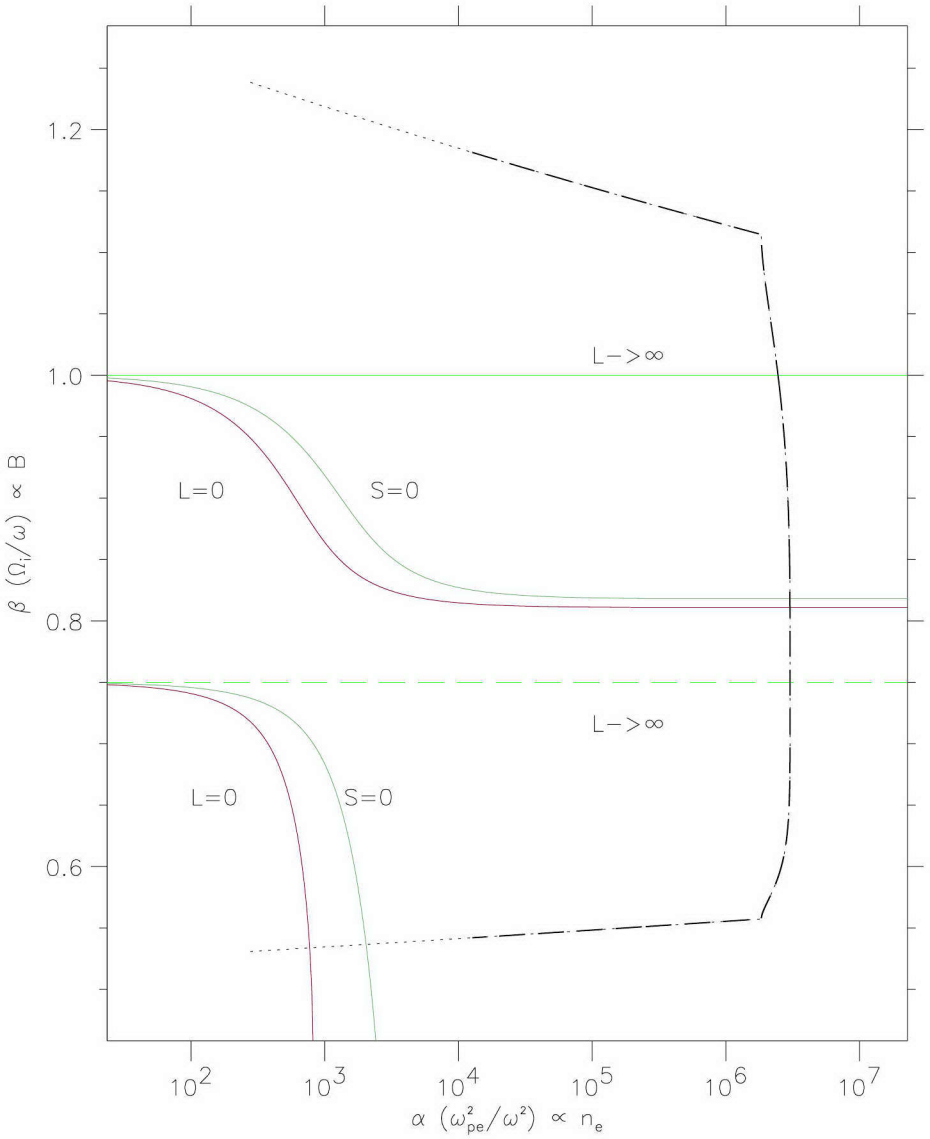

Figure 2-3: CMA diagram for an 80 MHz, 7.8 tesla D(^{3}He) C-Mod plasma, $\beta = \Omega_D/\omega$. The dashed line represents a trajectory along the midplane of the plasma for a typical density and magnetic field profile.

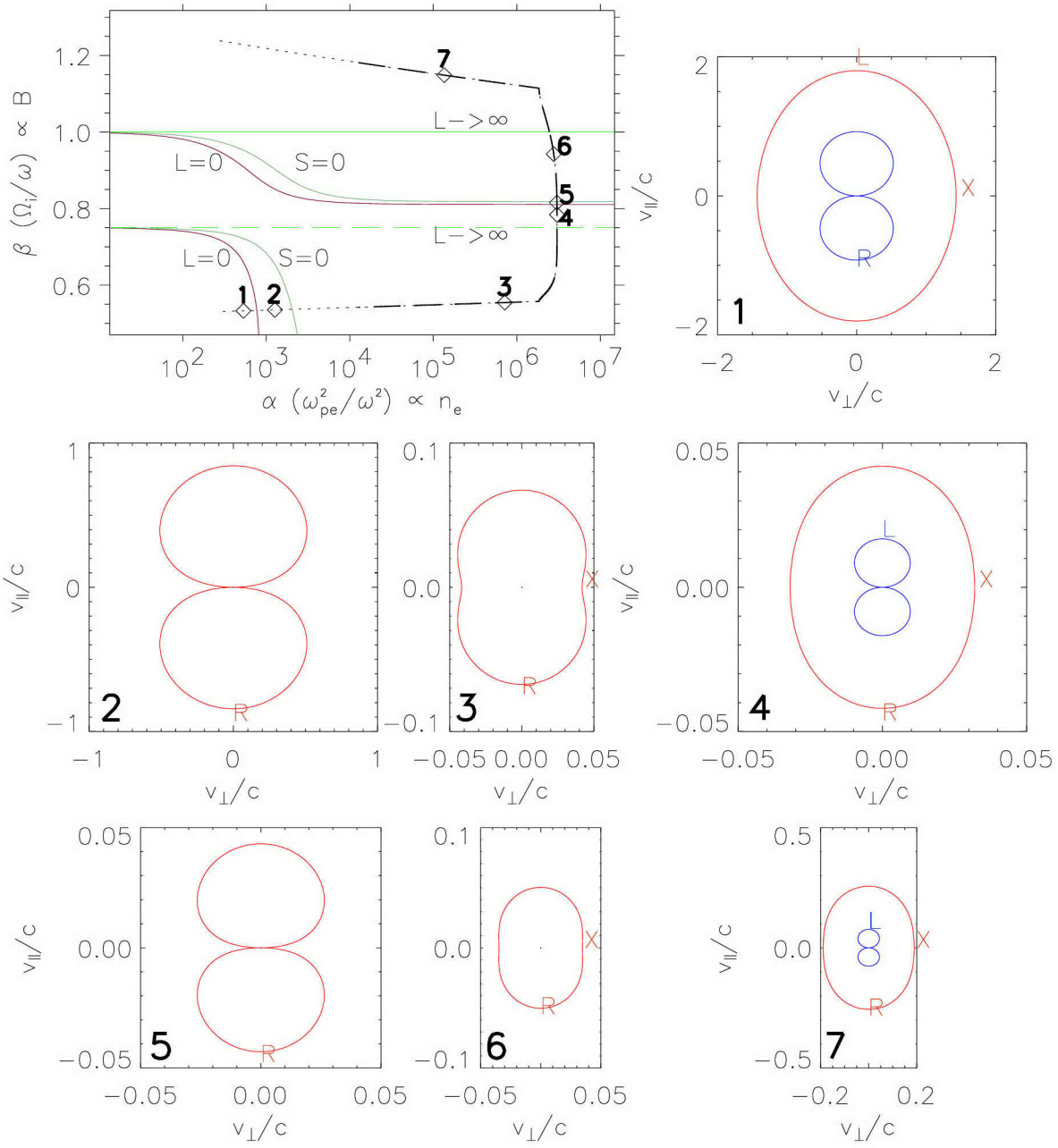

Figure 2-4: CMA diagram for an 80 MHz, 7.8 tesla D(^{3}He) C-Mod plasma, $\beta = \Omega_D/\omega$. Phase velocity solutions are plotted for each region, labelled 1–7. Note that region 5 is between the $L = 0$ cutoff and the $S = 0$ resonance.

relation for the remaining free parameter $n_\perp$ becomes

$$Sn_\perp^4 + [(P+S)n_\parallel^2 - RL - PS]n_\perp^2 + P(n_\parallel^2 - L)(n_\parallel^2 - R) = 0. \tag{2.30}$$

The $S = 0$ resonance is still present (but only for one solution of the quadratic equation, see discussion after Eq. 2.31), but the cutoffs have become $P = 0$, $n_\parallel^2 = R$, and $n_\parallel^2 = L$. From this, a modified CMA diagram may be plotted. Figure 2-5 shows the same region of the CMA diagram as Fig. 2-3, but with a fixed $k_\parallel = 11.2\,\mathrm{m}^{-1}$ ($n_\parallel = 6.7$), a parallel wavenumber typical of the C-Mod two strap antenna at the low-field side. Note that the $L \to \infty$ and $R \to \infty$ resonances no longer affect the wave because they can be factored out of Eq. 2.30 ($S \to L/2$ or $S \to R/2$ in these limits). When $n_\parallel$ and ω are fixed, the only remaining parameter to be solved for in the wave equation is $n_\perp$. Thus the trajectory in density–magnetic field space is no longer represented at each point by a phase velocity polar plot, but rather a single value — this is the dispersion relation.

When $\omega \sim \Omega_{\mathrm{ion}}$ then the fast root of the cold plasma dispersion relation Eq. 2.27 is well approximated by

$$n_\perp^2 = \frac{(L - n_\parallel^2)(R - n_\parallel^2)}{(S - n_\parallel^2)}. \tag{2.31}$$

This dispersion relation is sometimes known as the ICRF (ion cyclotron range of frequencies) equation. Once the dispersion relation is solved, the polarization can be obtained by solving the 3 vector component equations in Eq. 2.19 for the 3 unknowns E_x, E_y, and E_z. For a cold plasma, the ratio of the perpendicular components can be obtained from the middle line alone:

$$\frac{iE_x}{E_y} = \frac{n^2 - S}{D}. \tag{2.32}$$

In the cartesian system as defined, with $\vec{B} = B\hat{z}$ and $k_\perp = k_x$, rotating electric field components can be defined:

$$E^+ = \frac{E_x + iE_y}{\sqrt{2}}, \tag{2.33}$$

and

$$E^- = \frac{E_x - iE_y}{\sqrt{2}}. \tag{2.34}$$

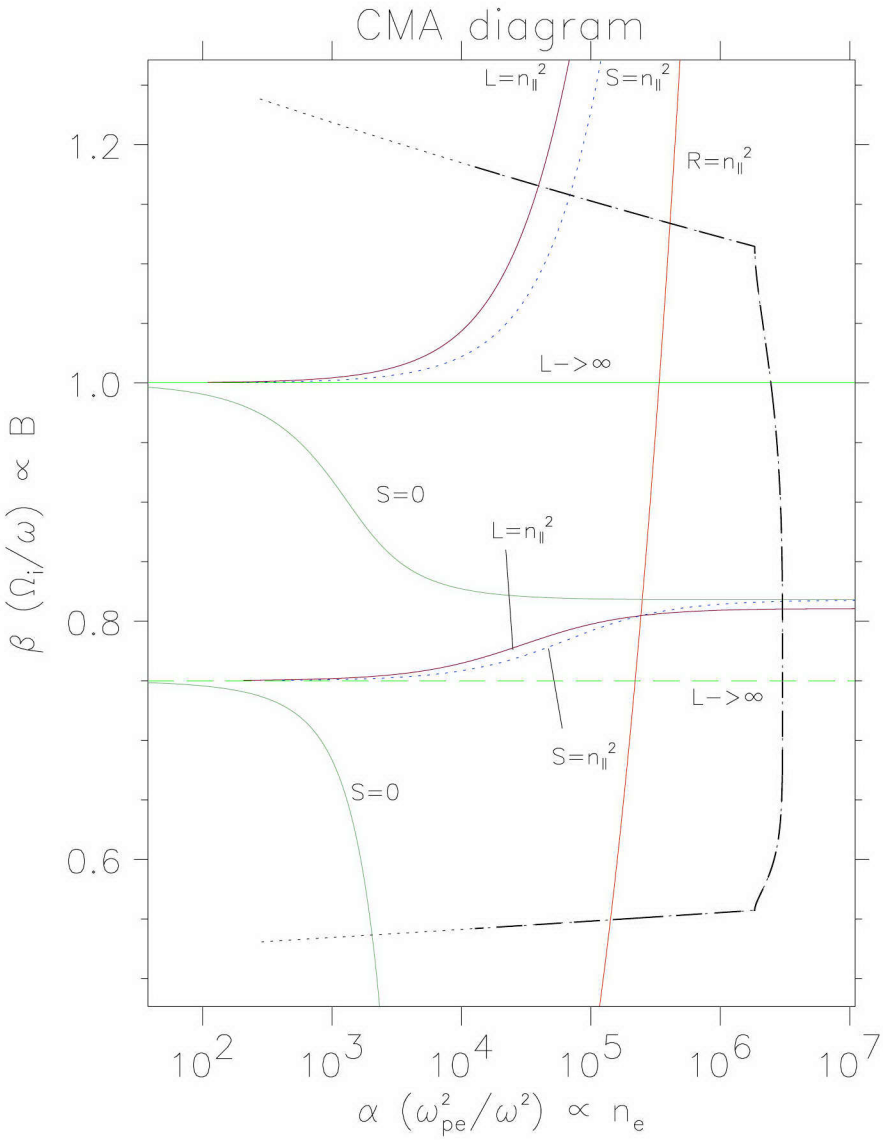

Figure 2-5: CMA diagram with parameters as in Fig. 2-3, but with fixed $n_{\|} = 6.7$. Note how the cutoffs change character from the unrestricted $n_{\|}$ CMA diagram.

The $\sqrt{2}$ normalization is chosen so that the same amount of power will be present in $|E_x|^2 + |E_y|^2$ as in $|E^+|^2 + |E^-|^2$. When the polarization of a wave is entirely E^+ ($iE_x/E_y = -1$), it rotates in the same direction around the magnetic field as the positively charged ions, and is called left-hand circulary polarized (LHCP). If it is entirely E^- ($iE_x/E_y = 1$), it rotates in the same direction as the negatively charged electrons, and is called right-hand circularly polarized (RHCP). The dispersion relation Eq. 2.31 and the corresponding polarization are shown in Fig. 2-6. In the dispersion relation, the location of the cutoffs are also indicated: the $n_\parallel^2 = R$ cutoffs are shown by the vertical dash–dot line, the $n_\parallel^2 = L$ cutoffs by dashed vertical lines, and the $n_\parallel^2 = S$ "resonances" (these are not true resonances in the full cold plasma solution, see discussion below) by dotted vertical lines. Note that there is a small region of propagation between an $n_\parallel^2 = S$ resonance and $n_\parallel^2 = L$ cutoff to the HFS of the left-most $n_\parallel^2 = R$ cutoff, but this should play little role for most applications.

The polarization plot shows the fraction of the power in the perpendicular electric field that is in the LHCP component (solid line) and the RHCP component (dashed line). At the low density edges of the plasma, the wave is more nearly linearly polarized (nearly equal amounts of RHCP and LHCP). As the plasma density becomes significantly high, for most of the plasma cross-section, the fast wave is predominantly RHCP. However, near the $n_\parallel^2 = S$ resonance, a significant portion of the power is LHCP. The impact of this resonance and the enhanced left-hand circular polarization on the wave damping (through wave–particle interactions with the ions) is discussed in Sec. 2.3.1 and Appendix B.

The approximate fast wave dispersion relation, Eq. 2.31 exhibits a resonance at $S = n_\parallel^2$, not $S = 0$. The exact cold plasma dispersion relation for fixed $n_\parallel$ (Eq. 2.30) exhibits a true resonance (for the slow wave root) at $S = 0$, but no resonance at $S = n_\parallel^2$. This can be seen as follows: at $S = 0$, Eq. 2.30 has two solutions, $n_\perp^2 \to \infty$ and

$$n_\perp^2 = \frac{P(L^2 - n_\parallel^4)}{L^2 + Pn_\parallel^2}. \tag{2.35}$$

The first solution corresponds to the slow wave (the shear Alfvén wave at $\omega \ll \Omega_i$, or the ion cyclotron wave at $\omega \sim \Omega_i$), which does have a resonance at $S = 0$. But the

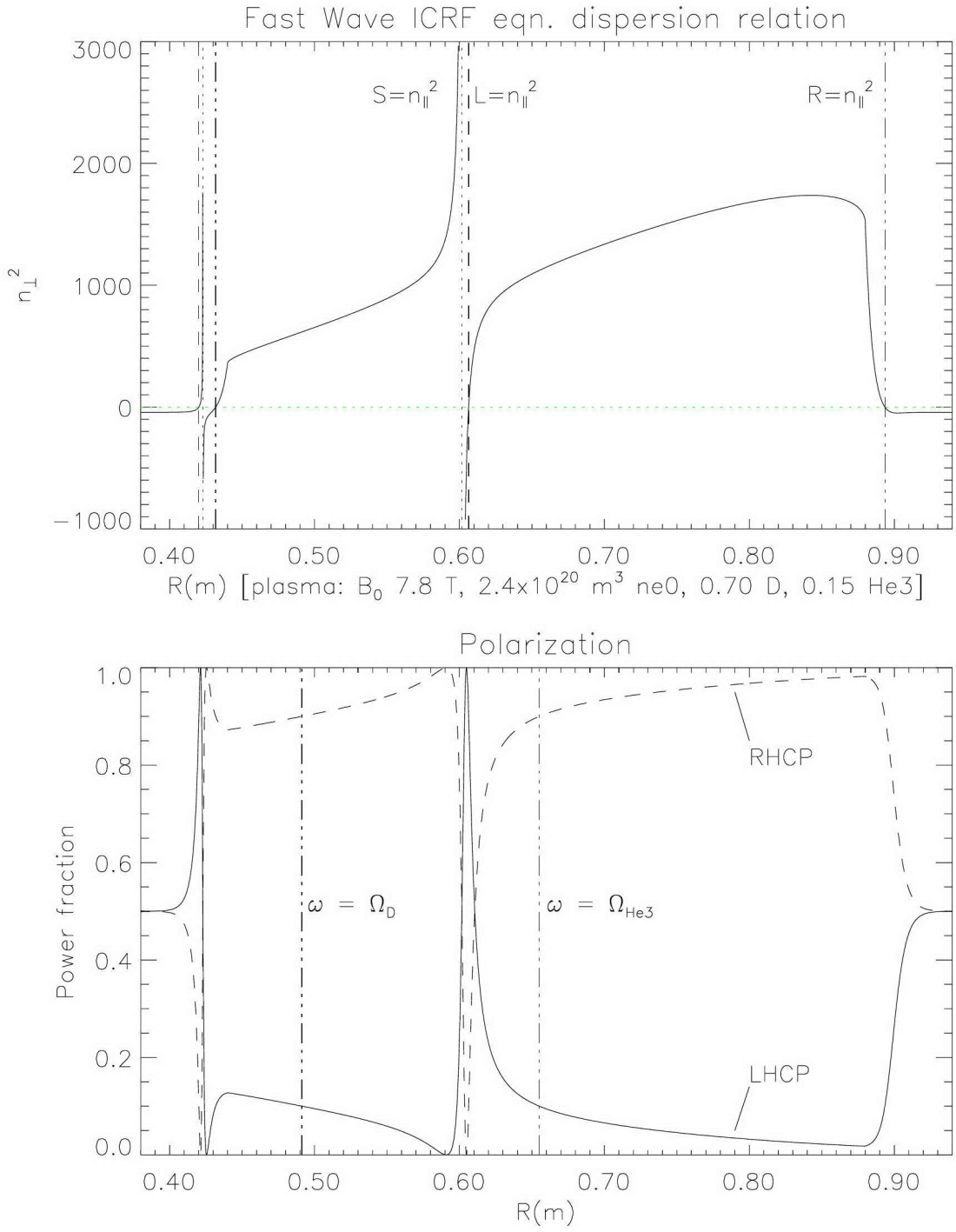

Figure 2-6: Top: The fast wave dispersion relation Eq. 2.31. Bottom: FW polarization [LHCP = $|E^+|^2/(|E_x|^2 + |E_y|^2)$, RHCP = $|E^-|^2/(|E_x|^2 + |E_y|^2)$], showing the predominant RHCP nature, except near the $S = n_\parallel^2$ layers at 0.602 m ($\beta = 0.82$ in the CMA diagram), and at 0.423 m ($\beta = 1.15$) where a significant LHCP component exists.

second solution (Eq. 2.35), corresponding to the fast wave, remains finite at $S = 0$. The fast wave $n_\perp^2$ is positive (propagative) as long as $L^2/n_\parallel^2$ is between $|P|$ and $n_\parallel^2$. This is usually the case because P is large and negative in the ICRF, and $L > n_\parallel^2$ except for the narrow regions between $n_\parallel^2 = L$ and $n_\parallel^2 = S$.

Although it is not a true resonance, the $S = n_\parallel^2$ layer still plays an important role in determining where the cold plasma solution breaks down, and exhibits some of the features of a resonance. At $S = n_\parallel^2$, Eq. 2.30 has two solutions:

$$n_\perp^2 = \frac{-D^2}{2S} \pm \frac{D\sqrt{D^2 + 4PS}}{2S}. \tag{2.36}$$

Because P is large and negative in this regime (since $\omega \ll \omega_{pe}$), both of these solutions are large and complex. The comparison between the ICRF equation (Eq. 2.31) and the fast root of the full cold plasma wave equation (Eq. 2.30) in the vicinity of $S = n_\parallel^2$ is shown in Fig. 2-7. Note that where the approximate dispersion relation becomes infinite at $S = n_\parallel^2$, the exact cold plasma root remains finite. However, the perpendicular wavenumber still becomes very large compared to its value away from this region (at the peak values of $n_\perp^2$, the parameter $k_\perp \rho$ for deuterium at 1 keV and 8 T becomes approximately 1/2, an indication that the finite Larmor radius should not be neglected). It is in this sense that the $S = n_\parallel^2$ layer is similar to a resonance, and when $S = n_\parallel^2$ is called a resonance in this thesis, it is only in this loose sense. Also note in Fig. 2-7 the location of the $S = 0$ layer, indicated by the dot-dashed line. The fast wave is unaffected by the $S = 0$ layer.

In the cold plasma dispersoin relation, a resonance or any location where the wavenumber becomes very large is an indication that the cold plasma theory is insufficient and more physics needs to be taken into account. Kinetic effects will often reveal the presence of another wave near the resonance. In fact, to quote Swanson [9]:

> **Theorem 1:** In an inhomogeneous plasma, linear mode conversion is always involved to some extent in resolving every plasma resonance.

The proof and more mathematical details are given in Refs. [9, 6], but the point for the discussion of the fast wave in this section is that mode conversion will come into

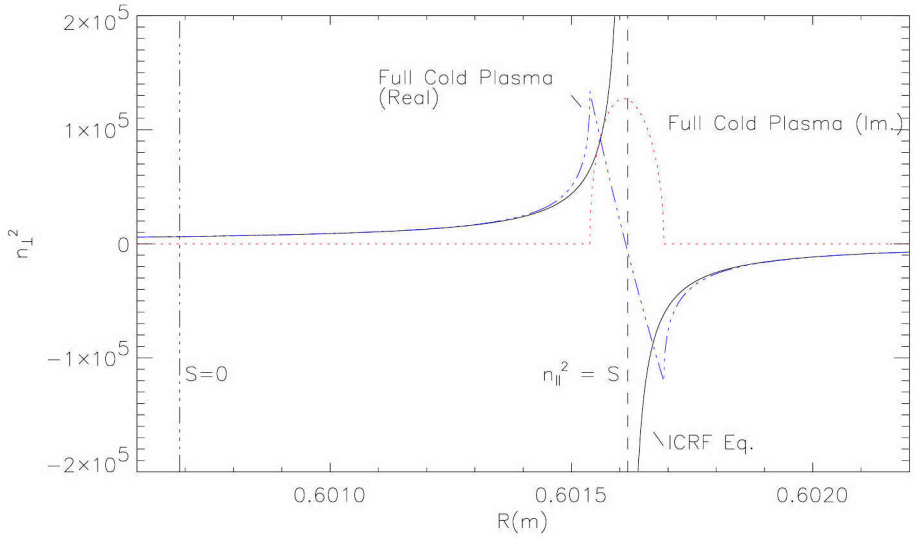

Figure 2-7: The full cold plasma solution (dash-dot line: real part, dotted line: imaginary part) and the ICRF equation approximation (solid line) to the fast magnetosonic wave near the Alfvén "resonance" $S = n_\parallel^2$.

play (see Sec. 2.4). By considering hot plasma effects, the region of large wavenumber shown in Figs. 2-6 and 2-7 can be resolved into a short-wavelength hot plasma wave: an ion Bernstein wave (see Sec. 2.2). From Fig. 2-6 it can be seen that there is an $n_\parallel^2 = L$ cutoff very near the $n_\parallel^2 = S$ "resonance". The fast wave must tunnel through this evanescent gap in order to propagate to the high-field side. This cutoff–resonance pair will be discussed in Sec. 2.5, where the $n_\parallel^2 = S$ layer will be treated as an actual resonance in order to connect with previous physics results, and the location of the $n_\parallel^2 = S$ layer will be important in calculating the efficiency with which the ion Bernstein wave is excited.

In summary, the cold plasma dispersion relation, and in particular the ICRF approximation (Eq. 2.31), describes the behavior of the fast magnetosonic wave quite well. The cutoff and resonant locations do not change much even when more complicated dispersion relations are used. However, a point of weakness in the cold plasma theory has been shown to be near the $n_\parallel^2 = S$ layer, where in order to describe the fast wave and the other main wave of interest in this thesis, the ion Bernstein wave, hot plasma effects will need to be explored.

2.1.2 The Hot Plasma Dispersion Relation

In the cold plasma fluid approximation, all particles of a certain kind are treated as having the same velocity. In a hot plasma, the ions and electrons have a range of velocities, described by the distribution function[5] $f_j(\vec{r},\vec{v},t)$ for species j, where j could represent electrons, different kinds of ions, or a class of particles with a special velocity range. Because of collisions between particles with collision time τ_{ij}, the distributions will usually be Maxwellian if $\tau_{ij} \ll \tau_p$, where τ_p is the particle confinement time. This is almost always the case in a tokamak, but may not be true in a magnetic mirror device, or in a plasma with highly energetic neutral beam injection (for heating and fueling). The Maxwellian distribution may possibly have a different temperature along the magnetic field ($T_\parallel$) and perpendicular to the magnetic field ($T_\perp$). In steady-state the Maxwellian distribution can be defined as:

$$f_{\text{Maxwellian}}(v_\parallel, v_\perp) = n\,\frac{m}{2\pi T_\perp}\exp(-mv_\perp^2/2T_\perp)\sqrt{\frac{m}{2\pi T_\parallel}}\exp(-mv_\parallel^2/2T_\parallel), \qquad (2.37)$$

where $n(\vec{r},t)$ is the density. The normalization is such that $\int d^3v f(\vec{r},\vec{v},t) = n(\vec{r},t)$. The quantity $\sqrt{2T/m}$ is defined as the thermal velocity[6] v_{th}. For a Maxwellian distribution of one velocity component, with the thermal velocity defined this way, 84% of all particles have speeds less than or equal to the thermal velocity, as shown in Fig. 2-8. The distribution of kinetic energy for this velocity component, which is proportional to $v_x^2\exp(-mv_x^2/2T)$, peaks at $v_x = \pm v_{th}$.

When a wave is imposed on a background Maxwellian plasma, the velocities of the particles, and hence the distribution function, will be altered. The Vlasov equation describes the evolution of the distribution function in the presence of an electric and/or magnetic field, neglecting collisions. Assuming that the zeroth order magnetic field is steady-state, and that the first order "perturbed" electric and magnetic fields due to the wave are small, the first order "perturbed" distribution function can be solved with the Vlasov-Maxwell system of equations (see for example [8, ch. 10]). The

[5]The distribution function is the number of particles per unit volume per unit velocity with a given velocity.

[6]Some authors define the thermal velocity to be $\sqrt{T/m}$, but as long as there is consistent use everywhere, the physics results are equivalent.

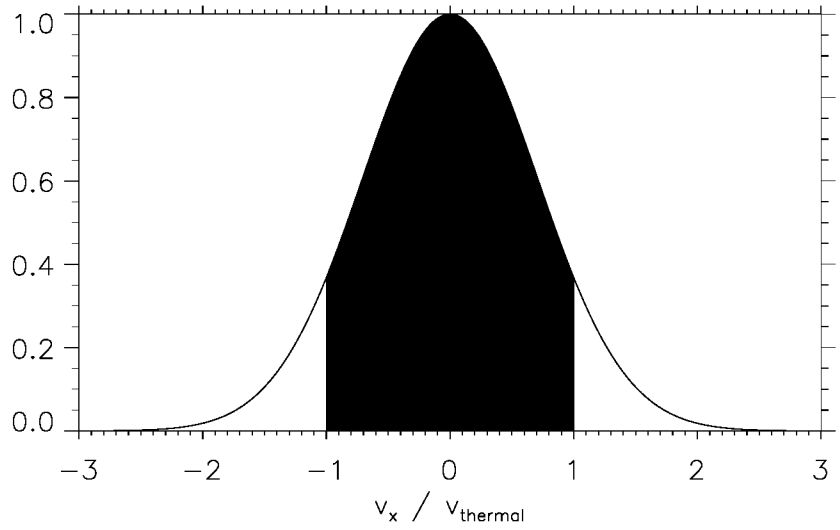

Figure 2-8: An arbitrarily normalized maxwellian distribution function for one velocity component v_x. The filled area represents the particles for which $|v_x| \leq v_{\rm th}$.

perturbed plasma current $\vec{J}$ due to the wave is then related to the first moment of the distribution function,

$$\vec{J} = \sum_s q_s \int d^3\vec{v} f_s(\vec{r}, \vec{v}, t) \equiv \overline{\sigma} \cdot \vec{E}, \tag{2.38}$$

where the index s denotes a sum over plasma species, and the conductivity tensor $\overline{\sigma}$ is defined by Eq. 2.38.

When the zeroth order distribution function in $v_\perp$ is Maxwellian (while still allowing a non-Maxwellian distribution in $v_\parallel$), a special function appears in the solution to the Vlasov-Maxwell system of equations. The dielectric tensor elements can be written in terms of modified Bessel functions $I_n(b)$, where $b = \frac{1}{2}k_\perp^2\rho^2 = k_\perp^2 \frac{T_\perp}{m\Omega^2}$. This defines an average Larmor radius $\rho = v_{\perp \rm th}/|\Omega|$ for the distribution of particles. In this thesis, whenever the Larmor radius is referred to for a distribution of particles, and not a specific particle, it is this ρ that is meant.

If the parallel velocity distribution is Maxwellian as well, and $T_\perp = T_\parallel$ then the dielectric tensor elements can be expressed in terms of the plasma dispersion function [10] $Z(\zeta_{ns})$, where $\zeta_{ns} = (\omega - n\Omega_s)/|k_\parallel|v_{ths}$, and the derivative is $Z'(\zeta_{ns}) = -2[1 + \zeta_{ns}Z(\zeta_{ns})]$. The plasma dispersion function is plotted in Fig. 2-15.

Finally, if there are no zero-order drifts (neglecting the background d.c. plasma current and rotation for example), then the dielectric tensor elements are (see Chen[7] [11, ch. 7.10] or Stix [8, ch. 10-7]):

$$\begin{aligned}
\mathbf{K}_{xx} &= 1 + \textstyle\sum_s \frac{\omega_{ps}^2}{\omega^2} \frac{e^{-b_s}}{b_s} \zeta_{0s} \sum_{n=-\infty}^{\infty} n^2 I_n(b_s) Z(\zeta_{ns}) \\
\mathbf{K}_{yy} &= 1 + \textstyle\sum_s \frac{\omega_{ps}^2}{\omega^2} \frac{e^{-b_s}}{b_s} \zeta_{0s} \sum_{n=-\infty}^{\infty} \{n^2 I_n(b_s) + 2b_s^2 [I_n(b_s) - I_n'(b_s)]\} Z(\zeta_{ns}) \\
\mathbf{K}_{xy} &= -\mathbf{K}_{yx} = -i \textstyle\sum_s \frac{\omega_{ps}^2}{\omega^2} e^{-b_s} \zeta_{0s} \sum_{n=-\infty}^{\infty} n [I_n(b_s) - I_n'(b_s)] Z(\zeta_{ns}) \\
\mathbf{K}_{xz} &= \mathbf{K}_{zx} = -\tfrac{k_\perp}{k_\parallel} \textstyle\sum_s \frac{\omega_{ps}^2}{\omega^2} \frac{\omega}{2\Omega_s} \frac{e^{-b_s}}{b_s} \sum_{n=-\infty}^{\infty} n I_n(b_s) Z'(\zeta_{ns}) \\
\mathbf{K}_{yz} &= -\mathbf{K}_{zy} = -i \tfrac{k_\perp}{k_\parallel} \textstyle\sum_s \frac{\omega_{ps}^2}{\omega^2} \frac{\omega}{2\Omega_s} e^{-b_s} \sum_{n=-\infty}^{\infty} [I_n(b_s) - I_n'(b_s)] Z'(\zeta_{ns}) \\
\mathbf{K}_{zz} &= 1 - \textstyle\sum_s \frac{\omega_{ps}^2}{\omega^2} e^{-b_s} \zeta_{0s} \sum_{n=-\infty}^{\infty} I_n(b_s) \zeta_{ns} Z'(\zeta_{ns})
\end{aligned} \tag{2.39}$$

Note that Ω_s is signed; $\Omega_e < 0$ and $\Omega_i > 0$. Also note that when working with both positive and negative $k_\parallel$, the absolute value of $k_\parallel$ should be used in ζ_{ns}, which is necessary for the analytic continuation of the Z function for negative $k_\parallel$ [8, Ch. 8-14]. Because only the magnitude of $k_\parallel$ is used in ζ_{ns}, the only elements for which the sign of $k_\parallel$ matters are K_{xz}, K_{zx}, K_{yz}, and K_{zy}, which are normally much smaller than the other elements.

Using these dielectric tensor elements, the hot plasma dispersion relation (from setting the determinant of the 3 by 3 matrix in Eq. 2.18 to zero) can be written:

$$\begin{aligned}
(K_{xx} - n_\parallel^2)[(K_{yy} - n_\perp^2 - n_\parallel^2)(K_{zz} - n_\perp^2) + K_{yz}^2)] + \\
K_{xy}[K_{xy}(K_{zz} - n_\perp^2) + K_{yz}(n_\perp n_\parallel + K_{xz})] + \\
(n_\perp n_\parallel + K_{xz})[K_{xy}K_{yz} - (n_\perp n_\parallel + K_{xz})(K_{yy} - n_\perp^2 - n_\parallel^2)] = 0.
\end{aligned} \tag{2.40}$$

In order to better understand the dispersion relation that results from the dielectric tensor elements in Eq. 2.39, the factor which appears in every term in the infinite sums, $e^{-b} I_n(b)$ is plotted in Fig. 2-9 for the first 40 n numbers[8] and for values of b ranging from 0.1 to 10. This factor drops off very rapidly for a given value of $k_\perp \rho$

[7]Note that in Chen's book the definition of ζ_n is $(\omega + n\Omega)/k_\parallel v_{th}$, hence the terms proportional to n in the expressions for ϵ_{xy} and ϵ_{xz} have the opposite sign as in the definition used in this thesis and in Stix. But there are errors as well: there is a typographical error in the use of $\pm$ for the sign of the charge, ϵ_{xz} should have it, but ϵ_{xy} should not. Finally, Chen's expressions incorrectly omit the absolute value of $k_\parallel$ in ζ_n.

[8]$I_n(b) = I_{-n}(b)$ for integral n, and $I_n'(b) = I_{n-1}(b) - \frac{n}{b} I_n(b)$, so it is sufficient to examine the behavior of $I_n(b)$ for $n \geq 0$.

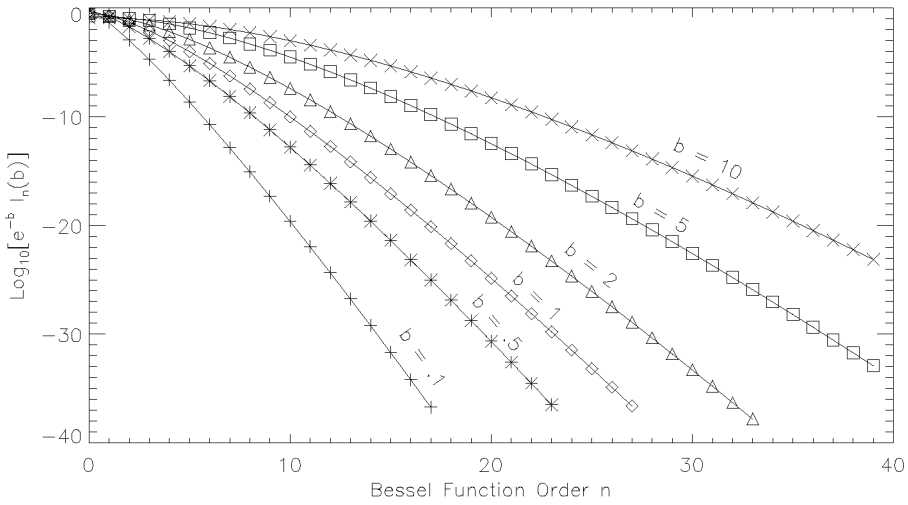

Figure 2-9: The function $e^{-b}I_n(b)$ for various values of b. In the electromagnetic dispersion relation, $b = \frac{1}{2}k_\perp^2\rho_i^2$.

as n increases, thus it is sufficient, even for exact numerical work, to truncate the series at 50 to 100 terms. If one is only interested in waves with wavelength such that $k_\perp\rho < 1$, then it is necessary to keep only a few terms. Note, however, that for fixed n, $e^{-b}I_n(b)$ increases very rapidly as b increases. For example, for $n = 20$, $e^{-b}I_{20}(b)$ increases by 17 orders of magnitude as b increases from 1 to 10. Thus for even small increases in $k_\perp\rho$, it may be necessary to keep many more terms in order to retain a certain degree of accuracy.

To make a connection to cold plasma theory in the Stix notation, the dielectric tensor elements can be related to the zero temperature limits of the elements in Eq. 2.39: as $T \to 0$, $\mathbf{K}_{xx}$ and $\mathbf{K}_{yy} \to S$, $\mathbf{K}_{xy} \to -iD$, $\mathbf{K}_{yx} \to iD$, $\mathbf{K}_{zz} \to P$, and $\mathbf{K}_{xz}$, $\mathbf{K}_{zx}$, $\mathbf{K}_{yz}$, $\mathbf{K}_{zy} \to 0$.

The cold plasma dispersion relation (and the CMA diagram) can be used for preliminary analysis of a certain RF wave heating scenario. If this scenario includes cold plasma resonances, or wave damping calculations are desired, then the hot plasma dispersion relation must also be examined. Some of the most prominent solutions to the hot plasma dispersion relation in the ion cyclotron range of frequencies which do not have a cold plasma counterpart are ion Bernstein waves, which are described in

the next section.

2.2 Ion Bernstein Waves

Ion Bernstein waves (IBWs) can be useful for plasma heating and control, which can increase the temperature and enhance the confinement, resulting in higher fusion power output. They are short-wavelength, hot plasma waves which can damp effectively on electrons, or on ions near cyclotron resonances. They often appear in processes of mode conversion where a longer wavelength electromagnetic wave encounters a resonance, coupling to the nearly electrostatic Bernstein waves, which have a much shorter wavelength. One application of IBWs is local electron power deposition in the central regions of the plasma. In addition, if the source of the wave launches an asymmetric toroidal wavenumber spectrum, a toroidal current could be generated at the location of power deposition [12, 13, 14]. Most tokamak fusion reactor designs rely on some amount of externally driven toroidal current to operate in steady state (the rest being driven through "bootstrap" current, an effect of the steep pressure gradient). Ion Bernstein waves can also be used to create transport barriers by creating a velocity shear. It has been found that a velocity shear in the radial direction (i.e., the plasma flow velocity changes direction across the plasma cross-section) can reduce the size of turbulent eddies in the plasma which allow heat to flow across the magnetic field [15, 16]. Thus velocity shear can improve the energy confinement. IBWs have been used to drive such a flow in the poloidal direction in TFTR[9] [17]. Further applications and experiments with IBWs are described in a fairly recent review article by Ono [18].

2.2.1 The Electrostatic Approximation

Ira Bernstein first mathematically described the waves that bear his name while exploring longitudinal electron oscillations (longitudinal meaning that the direction

[9]The Tokamak Fusion Test Reactor which operated at the Princeton Plasma Physics Laboratory.

of wave propagation is the same as that of the wave electric field) [19] (see also the work of Stepanov [20] around the same time). These longitudinal oscillations had very short wavelengths. Many short-wavelength modes, including IBWs, can be adequately described by a dispersion relation using the electrostatic approximation, where the wavevector $\vec{k}$ is parallel to $\vec{E}$, so that Faraday's law becomes

$$\nabla \times \vec{E} = -\frac{\partial \vec{B}}{\partial t} = 0,$$

and the magnetic portion of the wave can be neglected. The electric field can now be represented as the gradient of a potential, and the wave equation becomes a scalar equation, which can be obtained by taking the divergence of Ampere's law (Eq. 2.10):

$$\vec{k} \cdot \mathbf{K} \cdot \vec{k} = 0. \tag{2.41}$$

In the coordinate system used in this chapter, this becomes

$$K_{xx} k_\perp^2 + 2 k_\perp k_\parallel K_{xz} + K_{zz} k_\parallel^2 = 0. \tag{2.42}$$

This can be written in terms of the plasma dispersion function Z, the modified Bessel functions of argument $b = \frac{1}{2} k_\perp^2 \rho^2$, and a function β (see [8, Ch. 11-10] or [11, Ch. 7.10.3]):

$$1 + \frac{k_\parallel^2}{k_\perp^2} - \sum_s \frac{\omega_{ps}^2}{\Omega_s^2} \frac{\beta_s}{b_s} = 0, \tag{2.43}$$

where

$$\beta_s = -\sum_{n=-\infty}^{\infty} e^{-b_s} I_n(b_s)[1 + \zeta_{0s} Z(\zeta_{ns})] \tag{2.44}$$

and the sum over s is a sum over plasma species.

Bernstein first considered the $k_\parallel = 0$ case (which also applies for $\omega / k_\parallel v_{\mathrm{the}} \gg 1$) in his original paper and revealed what are called "pure" Bernstein modes. The "pure" Bernstein modes are in contrast to "neutralized" Bernstein modes[10] with $\omega / k_\parallel v_{\mathrm{the}} \ll 1$, which allows the electrons to stream back and forth along the magnetic field and neutralize the space charge built up during the wave oscillations by the ion motion [7, Ch. 30.2]. Taking the asymptotic limit of the Z function (for large argument

[10] Also known as electrostatic ion cyclotron waves, see the end of Sec. 2.2.1.

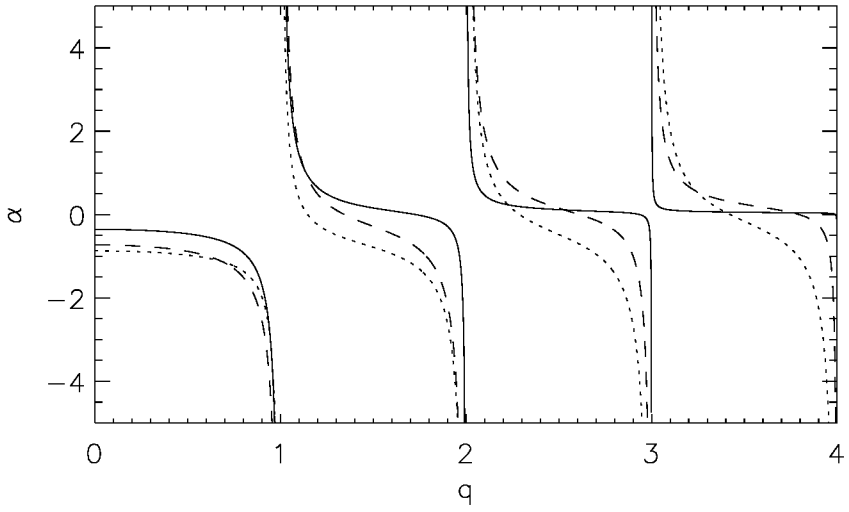

Figure 2-10: The function $\alpha(q,b)$ which appears in the $k_\parallel = 0$ electrostatic dispersion relation, for $b = 0.5$ (solid line), $b = 2.5$ (dashed line), and $b = 10$ (dotted line).

$Z(\zeta_n) \simeq -1/\zeta_n)$, and using the Bessel function identity $e^b = I_0(b) + 2\sum_{n=1}^{\infty} I_n(b)$, the function β becomes[11]:

$$\alpha_s = 2\sum_{n=1}^{\infty} e^{-b_s} I_n(b_s) \frac{n^2}{q_s^2 - n^2} = \beta_s(k_\parallel \to 0), \tag{2.45}$$

where $q_s = \omega/\Omega_s$, the ratio of the wave frequency to the cyclotron frequency of the species s. The dispersion relation becomes:

$$1 - \sum_s \frac{\omega_{ps}^2}{\Omega_s^2} \frac{\alpha_s}{b_s} = 0. \tag{2.46}$$

This function α is discussed and plotted by Bernstein in his discussion of electron Bernstein waves. An example of the function $\alpha(q,b)$ *vs.* q for several values of b is shown in Fig. 2-10.

A simple case to analyze is when $\omega \gg \Omega_{\rm ion}$ ($q_{\rm ion} \gg 1$), which yields the dispersion relation for electron Bernstein waves (EBW). If the electron and ion temperatures are comparable, then $\frac{b_e}{b_i} = \frac{T_e}{T_i}\frac{Z_i^2 m_e}{m_i} \ll 1$. For the first few harmonics of the electron cyclotron frequency, $q_e \sim 1$ to 10. The ion terms can be neglected compared to the

[11]Note the typographical error in Bernstein's original 1958 paper, his definition of α in Eq.(47) is missing a factor of e^{-b}.

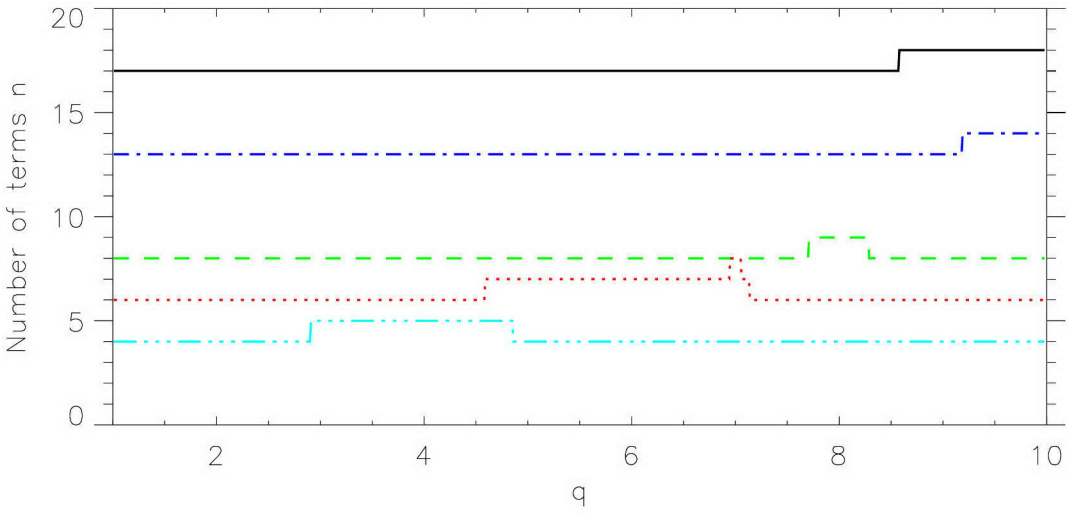

Figure 2-11: The number of terms needed in the function $\alpha(q,b)$ so that subsequent terms are $< 10^{-6}$. Five values of b are shown, starting from the bottom: $b = 0.1$ (dash-dot-dot-dot), $b = 0.5$ (dot), $b = 1.0$ (dash), $b = 5.0$ (dash-dot), $b = 10.0$ (solid).

electron terms as can be seen by examining the ratio of the lowest order ion term: $[2\omega_{pi}^2 e^{-b_i} I_1(b_i)]/[\Omega_i^2 b_i(q_i^2-1)]$, to a typical electron term: $[2\omega_{pe}^2 e^{-b_e} I_n(b_e) n^2]/[\Omega_e^2 b_e(q_e^2 - n^2)]$. This ratio is

$$\frac{\text{1st ion term}}{\text{nth electron term}} = \frac{n_i}{n_e}\frac{T_e}{T_i}Z_i^2 \frac{(q_e^2-n^2)}{n^2[(Z_i m_i/m_e)^2 q_e^2 - 1]}\frac{e^{-b_i}I_1(b_i)}{e^{-b_e}I_n(b_e)}. \tag{2.47}$$

Since $b_i = b_e \frac{T_i m_i}{T_e m_e Z_i^2}$, the ion $e^{-b_i}I_1(b_i)$ function in the numerator will usually be much smaller than the electron function in the denominator. In addition, the factor involving q_e is much smaller than one. For the first electron term, $n = 1$, the ratio (2.47) is always small ($\sim m_e/m_i$). For higher order terms, this ratio is a decreasing function of b_e.

To verify that ion terms do not contribute much to the dispersion relation, first one can determine how many terms are required in the α_e sum in order to accurately calculate α_e. This is shown in Fig. 2-11, for several different values of b_e and a range of q_e, with the accuracy defined by finding the first term with magnitude less than or equal to 10^{-6}. Note that even for $b = 10.0$, only ~ 20 terms are needed to evaluate α to an accuracy of 10^{-6}.

For a given q_e and b_e, if the ratio of the first ion term to the last retained electron term (the nth term, with n given by Fig. 2-11) is small, then the ion terms will not change the dispersion relation significantly from that obtained using the electron sum alone. This is shown in Fig. 2-12. It can be seen that at low b_e (Fig. 2-12(a)), the ion terms can approach the order of magnitude of the last retained electron term, but it is still smaller. As b_e gets larger, the approximation of dropping the ion terms is even better.

Thus, by neglecting all ion motion, the EBW dispersion relation becomes:

$$\frac{\Omega_e^2}{\omega_{pe}^2} = \frac{\alpha_e}{b_e}. \tag{2.48}$$

From the form of α it can be seen why there are Bernstein waves associated with every cyclotron harmonic of every plasma species. For a propagating solution, $b_e \propto k_\perp^2$ must be positive, and α_e/b_e must equal a positive constant, Ω_e^2/ω_{pe}^2, which is usually of order 1 for tokamak plasmas. (For example, in a typical C-Mod plasma, $\Omega_e^2/\omega_{pe}^2 = 1.2$).

It can immediately be seen that there are no solutions for $q < 1$, because α is negative. Thus there are no Bernstein modes below the fundamental cyclotron frequency. In fact, wherever $\alpha < 0$ there is a gap where no EBW can propagate. When $\alpha > 0$, a value of b_e can be found to balance α_e to satisfy Eq. 2.48. Even near very high harmonics (very large values of q) a solution can be found. For large q, most of the terms in the infinite sum in α are small. But when q_s is close to (and slightly larger than) an integer n, then nth term remains finite, because the very large and positive factor $n^2/(q_s^2 - n^2)$ compensates for the very small factor $e^{-b}I_n(b)$ (see Fig. 2-9 for large n).

For frequencies in the ICRF, $\omega \ll \Omega_e$ so $q_e \ll 1$. Since $b_i/b_e \ll 1$, and ion Bernstein waves of interest have $b_i \sim 1$, then $b_e \ll 1$ and it is sufficient to consider only the $n = 1$ term in α_e, and $\alpha_e \simeq -b_e$. The IBW electrostatic dispersion relation for $k_\parallel = 0$ then becomes:

$$1 + \frac{\omega_{pe}^2}{\Omega_e^2} = \sum_i \frac{\omega_{pi}^2}{\Omega_i^2}\frac{\alpha_i}{b_i}. \tag{2.49}$$

If there is only one ion species present, then the discussion of solutions for EBWs can also be applied to IBWs near ion cyclotron harmonics, except that the positive

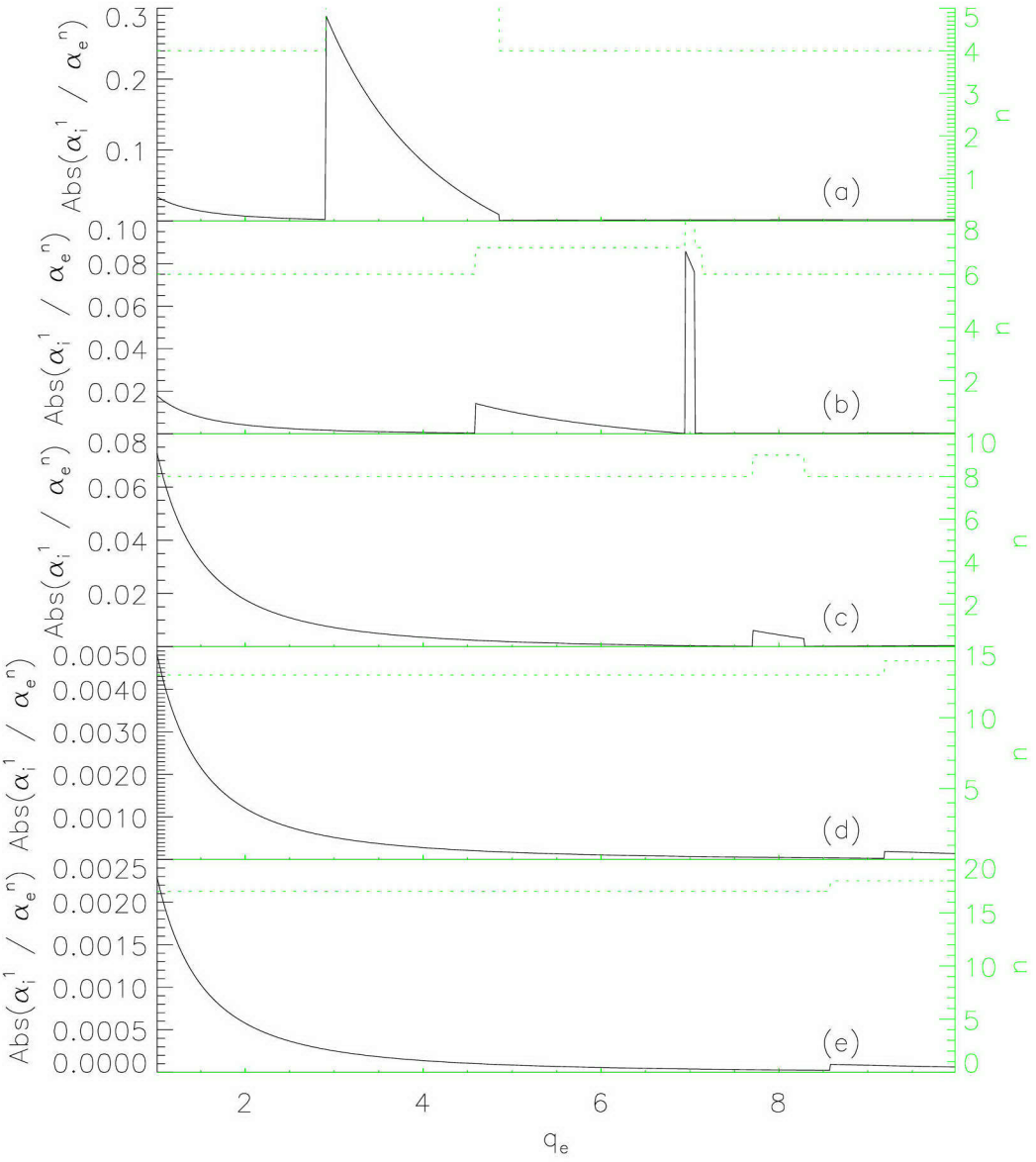

Figure 2-12: The magnitude of the ratio of the 1st ion term in Eq. 2.46 to the nth electron term (n determined as in Fig. 2-11). Five values of b_e: (a) $b_e = 0.1$ (b) $b_e = 0.5$ (c) $b_e = 1.0$ (d) $b_e = 5.0$ (e) $b_e = 10.0$

constant that must equal α_i/b_i is rather small:

$$\frac{1+\omega_{pe}^2/\Omega_e^2}{\omega_{pi}^2/\Omega_i^2} = \frac{\alpha_i}{b_i}, \tag{2.50}$$

since $\frac{\omega_{pi}^2}{\Omega_i^2} = \frac{\omega_{pe}^2}{\Omega_e^2}\frac{m_i}{m_e Z_i} \gg 1$. This corresponds roughly to an EBW with $\Omega_e^2/\omega_{pe}^2 \to \infty$.

Thus by comparing with the EBW dispersion relation for large Ω_e^2/ω_{pe}^2 (see Ref. [21]), it can be seen that in the electrostatic dispersion relation for ion Bernstein waves, there exist solutions between each cyclotron harmonic, beginning at a long wavelength just below any given harmonic and becoming shorter and shorter wavelength (larger $k_\perp$) as the next lowest harmonic is approached (see for example Fig. 2-13).

In a plasma with multiple ion species, IBWs can exist between the cyclotron harmonics of the same or different species, for example between the 3rd harmonic of one species and the 2nd harmonic of the other. In addition, there is a new type of IBW between the fundamental cyclotron frequencies of distinct ion species. As an example, for a D(^{3}He) plasma at 7.8 T ($n_{e0} = 2.4\times10^{20}\,\mathrm{m}^{-3}$, $n_{\mathrm{He3}}/n_e = 0.2$, $T_e = T_i = 3\,\mathrm{keV}$), the electrostatic IBW dispersion relation Eq. 2.49 is illustrated in Fig. 2-13, for both $k_\parallel = 0$ and $k_\parallel = 14.9\ \mathrm{m}^{-1}$. These are compared to the full electromagnetic dispersion relation (obtained by solving Eq. 2.40 numerically) in Fig. 2-14. Note that an ion Bernstein wave branch exists between each separate cyclotron harmonic pair. In a single-species plasma, no IBW can exist below the fundamental cyclotron frequency, and indeed this is the case for $\omega < \Omega_D$. If the plasma were composed of helium-3 alone, there could also not exist any IBW for $\omega < \Omega_{\mathrm{He3}}$. However, between the fundamental cyclotron frequencies of the two species, there exists, in a limited range, an unusual ion Bernstein wave, also referred to as an ion-ion hybrid wave. This was first described by Buchsbaum [22], and more will be said of this wave in Sec. 2.4.2, including a discussion of the full electromagnetic dispersion relation as a function of space for changing plasma parameters. This hybrid wave has low wavenumber near the $S = 0$ cold plasma slow-wave resonance (which is also the resonance condition for the lower-hybrid and upper-hybrid waves which exist in higher frequency regimes than in the ICRF). When electromagnetic corrections to the dispersion relation are taken into account, it is seen that this IBW can couple to the fast magnetosonic wave

in this region (see Fig. 2-14(a) and Fig. 2-17).

It is interesting to note that the inclusion of finite $k_\parallel$ affects the electrostatic dispersion relation for the ion-ion hybrid wave much more than those associated with higher harmonics. In fact, it can be seen that near $k_\perp \rho_D \sim 1$, the imaginary part becomes comparable to the real part. It is here that, were electromagnetic corrections taken into account, the fast magnetosonic wave would be seen to have comparable wave number. There is also very strong damping (comparable real and imaginary parts) already at $k_\perp \rho_D \sim 3$ — however, the magnitude of the damping is incorrect, as can be seen from comparison with the full electromagnetic dispersion relation (shown in Fig. 2-14(b)). The electrostatic dispersion relation with finite $k_\parallel$ can overestimate the imaginary part of $k_\perp$ by orders of magnitude. In fact, for most of the region plotted in Fig. 2-14(a), the real part of $k_\perp$ from the simpler $k_\parallel = 0$ dispersion relation agrees better with the full solution than the $k_\parallel \neq 0$ electrostatic equation. However, neither electrostatic dispersion relation gives a good estimate of the damping — for this, the electromagnetic effects are important.[12]

Another interesting feature of ion Bernstein waves is displayed in Fig. 2-13: the group velocity is the opposite sign as the phase velocity! When this occurs the wave is called a backward wave. This can be seen by choosing any point on an IBW branch, along the curved solid lines. The slope of the line connecting this point to the origin is proportional to the phase velocity $\omega/k_\perp$. In this plot this is always positive (there also exist solutions for $k_\perp < 0$, which are just mirror images about the axis $k_\perp = 0$). The slope of the ω *vs.* $k_\perp$ dispersion relation curve at that point is proportional to the group velocity $d\omega/dk_\perp$. In this plot this is always negative.

As mentioned at the beginning of this section, there are different types of ion Bernstein waves, depending on the value of $\omega/k_\parallel v_{\mathrm{the}}$. For $\omega/k_\parallel v_{\mathrm{the}} \ll 1$ the waves are called electrostatic ion cyclotron waves (the predominant term in U.S. research)

[12]This has been pointed out by Marco Brambilla [7, Ch. 30.4] and is used in TORIC [23, 24] in order to more properly treat electron Landau damping of the IBW. Basically, for finite $k_\parallel$, the leading electromagnetic correction cancels a part of the electrostatic (e.s.) expression, explaining both why Re $k_\perp$ is better approximated by the $k_\parallel = 0$ e.s. relation and why the finite $k_\parallel$ e.s. relation overestimates the damping.

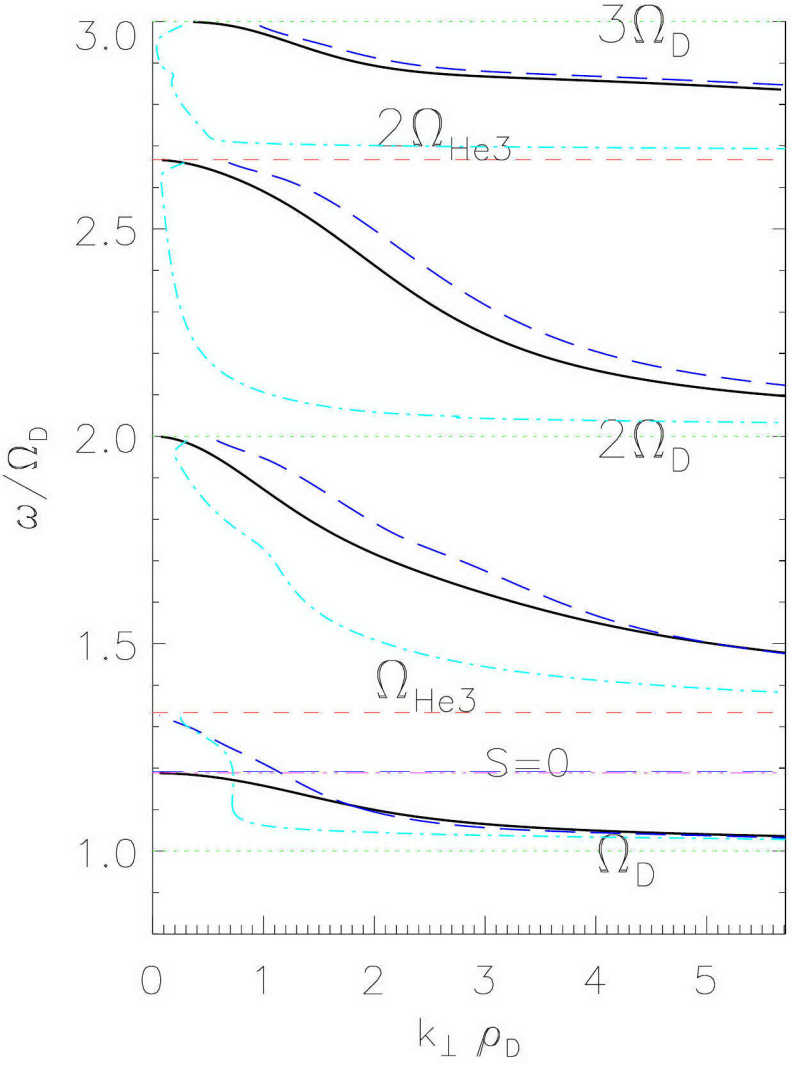

Figure 2-13: Electrostatic IBW dispersion relation for both $k_\parallel = 0$ and $k_\parallel = 14.9$ m^{-1}. Solid lines are the electrostatic pure ion Bernstein wave ($k_\parallel = 0$) dispersion relation (Eq. 2.49). Dotted horizontal lines are labelled as the fundamental, 2nd harmonic and third harmonic deuterium cyclotron frequencies, dashed lines are the fundamental and 2nd harmonic helium-3 cyclotron frequencies, and the dot–dash line is the ion-ion hybrid resonance frequency where the Stix dielectric tensor element $S = 0$. Just above this line is the dashed line representing $n_\parallel^2 = S$, applicable to the $k_\parallel \neq 0$ case. Also plotted is Eq. 2.43 for the case of $k_\parallel = 14.9$ m^{-1} ($\omega/k_\parallel v_{\mathrm{the}} = 0.81$ to 1.00 for $\omega/\Omega_D = 1.05$ to 1.3), the long dashed line representing the real part of $k_\perp$ and the dot-dash line representing the imaginary part (multiplied by -1 to fit on the same plot).

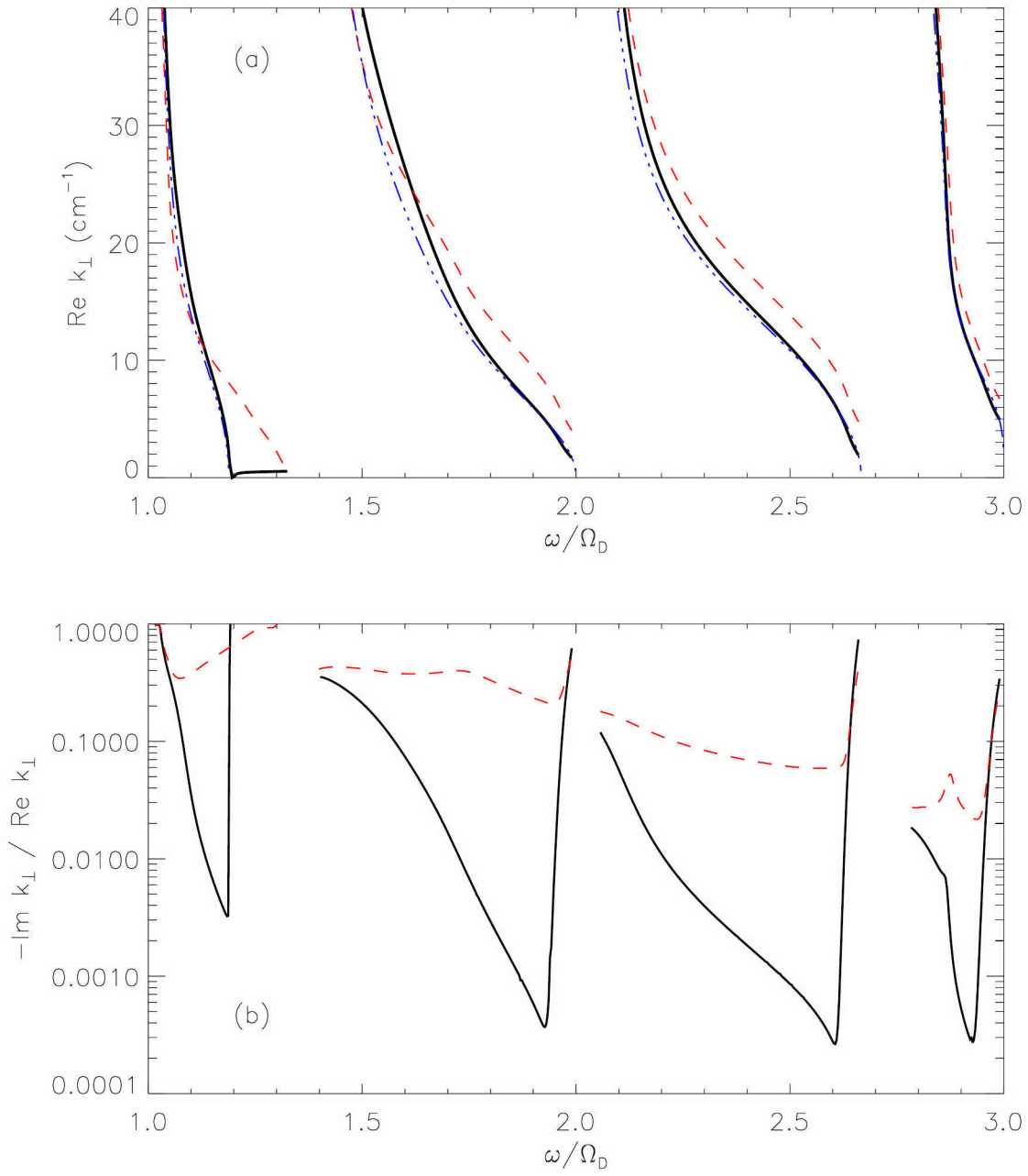

Figure 2-14: The same electrostatic IBW dispersion relations from Fig. 2-13 compared to the full electromagnetic solution (plotted with frequency along the horizontal axis). The solid line is the full solution, the dashed line is the electrostatic solution with $k_\parallel = 14.9$ m^{-1}, and the dot-dashed line is the $k_\parallel = 0$ electrostatic solution (which predicts Im $k_\perp = 0$). (a) Real part of $k_\perp$. Note that between the ion-ion hybrid layer ($\omega/\Omega_D \approx 1.19$) and the fundamental ^{3}He layer ($\omega/\Omega_D = 4/3$) there is no propagating IBW solution, so the fast wave is shown for the full electromagnetic solution. (b) -Im $k_\perp$ / Re $k_\perp$. The electrostatic solution overestimates the damping.

or "neutralized" IBW (the predominant term in European research), because the electrons are able to move quickly enough to neutralize the space charge of the wave. Electron Landau damping of these waves is weak in most situations. These were the first IBWs observed experimentally, usually in linear plasma devices and detected with probes (see Refs. [25, 26, 27, 28, 29, 30, 31, 32]). At the other extreme, for very small $k_\parallel$, $\omega/k_\parallel v_{\rm the} \gg 1$ and the waves are known as "pure" IBWs. Schmitt [33] observed pure IBWs by using a long wire in the center of a Q-machine aligned very closely to the total magnetic field, so that the waves would propagate as close to perpendicular to the field as possible. Here the backward wave nature of the IBW was clearly verified. Finally, there is a regime in between where $\omega/k_\parallel v_{\rm the} \sim 1$, in which case the IBWs are electron Landau damped. These are the kinds of IBWs observed in Alcator C-Mod in this thesis, whose behavior in a tokamak can be complicated (see Ch. 5).

2.3 Wave Damping

Waves will undergo spatial damping when the wavenumber solution is complex, meaning that k has a non-zero real and non-zero imaginary part (if it is purely imaginary over an extended region, then the wave is evanescent and could reflect with no damping). Mathematically, wave damping can be explained by the appearance of an imaginary part in the dielectric tensor elements through the plasma dispersion function $Z(\zeta_{ns})$. As can be seen in Fig. 2-15, this happens when the argument ζ is small enough. Physically, this can be explained through wave – particle resonances, where the motions of particles are such that in the particle's frame of reference, the electric field is nearly constant, or varying slowly enough that the energy gained and lost to the fluctuating electric field does not average to zero.

2.3.1 Cyclotron Harmonics and Finite Larmor Radius Effects

In the cold plasma approximation, the Larmor radius of the gyrating particles is treated as infinitesimal. However, if the perpendicular kinetic energy is high enough

that the diameter of the orbit begins to be even a small fraction of the wavelength, then the plasma wave must be treated including finite Larmor radius (FLR) effects, and all cyclotron harmonics can affect the wave.

Equation 2.39 for the hot plasma dielectric tensor elements contains terms depending on all cyclotron harmonics through $\zeta_{ns} = \frac{\omega - n\Omega_s}{k_\parallel v_{ths}}$. It was demonstrated that the factors $e^{-b}I_n(b)$ fall off rapidly with increasing values of n, and the infinite series can be truncated for a good approximation. However, if one is interested in cyclotron damping of the wave at a certain cyclotron harmonic $n \neq 0$, then those terms including n must be kept. The reason is that the plasma dispersion function $Z(\zeta_n)$ has maximum imaginary part for $\zeta_n = 0$, or $\omega = n\Omega$, as shown in Fig. 2-15. The imaginary parts of the dielectric tensor elements involving the x and y coordinates are what produce the cyclotron damping. From this it is clear why second harmonic (n=2) or higher damping requires finite $k_\perp \rho_{ion}$, otherwise the terms which produce the damping would be negligibly small. Even fundamental cyclotron damping (n=1) requires a small but non-zero temperature, because at $T = 0$, $\rho = 0$ and there is no imaginary part. The plasma heating schemes that take advantage of ion cyclotron damping use waves that are in the ion cyclotron range of frequencies and are commonly referred to as ICRF waves.

Of course, just having a large imaginary part of the Z function does not guarantee damping. The Z function is multiplied by other factors in the dielectric tensor elements which are determined by the plasma parameters, and these must be finite in order for significant damping to occur. For minority cyclotron damping, this is effectively the same as requiring the correct polarization of the electric field near the cyclotron resonance.

Cyclotron damping is strongest in the vicinity of a cyclotron resonance, and an expression for the fast wave damping decrement[13] across the minority ion cyclotron resonance can be written as [34]:

$$2\eta = \frac{\pi}{2}\frac{\omega_{pM}}{c}\frac{n_m}{n_M}\frac{Z_m}{Z_M}R\,|E^+|^2/|E_y|^2, \tag{2.51}$$

[13] If $k = k_{re} + ik_{im}$, and $E \propto \exp(ikx)$, then the power decrement at a distance x will be $P \propto |E|^2 \propto \exp(-2k_{im}x)$. The accumulated power decrement from 0 to x will be $\exp(-2\int_0^x k_{im}dx) \equiv \exp(-2\eta)$.

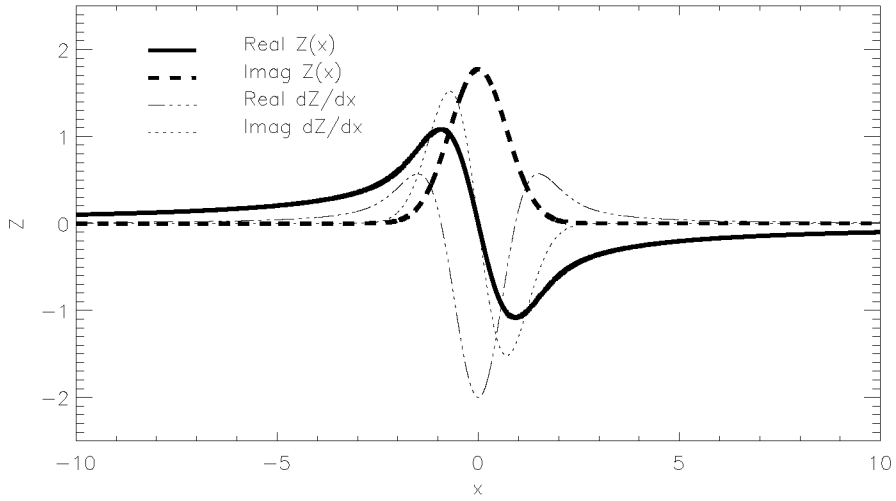

Figure 2-15: The plasma dispersion function $Z(\zeta_n)$ and its derivative $Z'(\zeta_n)$, real and imaginary parts. At the origin $Z(0) = i\sqrt{\pi}$.

where R is the tokamak major radius, M is the majority species index, m is the minority, and Z is the charge state. The polarization, including first order hot plasma effects, is:

$$\frac{|E^+|^2}{|E_y|^2} = \frac{(1-f)^2}{1+\sigma_1^2}, \tag{2.52}$$

where

$$\sigma_1^2 = \frac{\pi}{4}\left(\frac{n_m}{n_M}\frac{M}{m}\frac{Z_m^2}{Z_M^2}\right)^2 \left(1 - \frac{\omega_{cM}^2}{\omega^2}\right)^2 \left(\frac{\omega}{k_\parallel v_{thi}}\right)^2 \tag{2.53}$$

and

$$f = \frac{\omega}{\omega_{cM}}. \tag{2.54}$$

In the minority ion heating regime with small minority concentration n_m/n_M, $\sigma_1^2 \ll 1$ and if the frequency is set to the minority cyclotron frequency $\omega = \omega_{cm}$, then $f = (Z_m M)/(Z_M m)$ and the polarization factor depends only on the charge and mass ratio of the majority and minority ion species. For example, at the minority cyclotron resonance, for D(^{3}He) plasmas, $f = 4/3$ so the polarization factor $|E^+|^2/|E_y|^2 = 1/9$ for the minority heating regime. For D(H) plasmas, $f = 2$ and $|E^+|^2/|E_y|^2 = 1$, and for both H(^{3}He) and D(T) plasmas, $f = 2/3$ and $|E^+|^2/|E_y|^2 = 1/9$. Thus, all other factors being equal, D(H) plasmas should produce the strongest minority cyclotron

damping.

Ion Bernstein waves in tokamak plasma experiments are highly damped at ion cyclotron harmonics [18]. Usually in C-Mod plasmas where mode-converted IBWs are present in the plasma, Landau damping reduces the wave amplitude to negligible values before reaching a cyclotron resonance layer. However, if the mode-conversion layer is close to a cyclotron layer, then a combination of electron Landau and ion cyclotron damping will play a role in the wave damping. The integrated IBW power decrement across the nth ion cyclotron harmonic resonance layer (for weak damping) is [18]:

$$\Gamma_n \equiv \int \mathrm{Im}\, k_\perp dx = \frac{k_\perp R\pi}{|k_\perp \partial K_{xx}/\partial k_\perp|}\left(\frac{\omega_{pi}^2}{\Omega_i^2}\right)\frac{I_n(b_i)e^{-b_i}}{b_i}, \tag{2.55}$$

where R is the magnetic field gradient scale length (usually the same as the major radius R_0), and b_i is the same as that defined in section 2.2.1, and the index i refers to the resonant ion species.

The cyclotron damping presented in this section is based on the mathematical details of the dispersion relation. Appendix B presents a physical picture of cyclotron damping, and shows why it requires a finite value of $k_\perp\rho$ to be effective, especially for higher harmonics.

2.3.2 Landau damping

Landau damping can affect waves even in unmagnetized plasmas (i.e. $\Omega_e = \Omega_i = 0$), and can be present in magnetized plasmas through the $n = 0$ terms in the dielectric tensor elements.

It was seen in Sec. 2.3.1 that when the argument of the Z function $\zeta_n = \frac{\omega - n\Omega}{k_\parallel v_{th}}$ was small enough, damping was introduced. For cyclotron damping at the nth harmonic, this occurred when $\omega \approx n\Omega_i$, which requires a non-zero magnetic field.

When $n = 0$, the argument of the Z function cannot be made zero for finite frequency. However, if $\zeta_0 = \frac{\omega}{k_\parallel v_{th}}$ is small enough, there can still be a significant imaginary component to the Z function, and hence collisionless damping. This is Landau damping (from $\mathbf{K}_{zz}$), transit-time damping (from $\mathbf{K}_{yy}$ — also called transit-

time magnetic pumping (TTMP)) and the coherent combination of the two (from the cross-terms $\mathbf{K}_{yz}$ and $\mathbf{K}_{zy}$) (see Eq. 2.39). Because the electrons have a much greater thermal velocity than the ions, these processes are usually more important for electrons. Porkolab [35] has shown that for the ICRF regime, the transit-time term and the cross-term cancel for arbitrary phase velocities, and the remaining collisionless damping could be viewed to come entirely from Landau damping (this was noted earlier by Stix [36] for a limited regime). Because some of these dielectric tensor elements also contain the derivative of the Z function, which is zero at the origin, ζ_0 cannot be too small, or there won't be much of an imaginary part. In $\mathbf{K}_{zz}$ the $n = 0$ term relevant to Landau damping contains the factor $\zeta_{0s}^2 Z'(\zeta_{0s})$, which has the largest amplitude imaginary part for $\zeta_{0s} = \pm 1.225$. However, if other multiplying factors depend on $k_\parallel$, there may be another value of ζ_{0s} which produces the strongest damping. An example is given by the total electron Landau damping of the fast wave in the ICRF in a Maxwellian plasma [34] (see also Ref. [37]):

$$\frac{4\pi k_{\perp im}}{k_{\perp re}} = 2\pi \frac{\sqrt{\pi}}{2} \beta_e \zeta_{0e} e^{-\zeta_{0e}^2} \left(1 + \frac{1}{\alpha^2}\right), \tag{2.56}$$

where β_e is the electron beta, the ratio of the electron pressure to the magnetic pressure $\beta_e = 2\mu_0 n_e T_e / B^2$, and α is:

$$\alpha = \frac{T_e}{m_i c^2} \left(\frac{\omega^2 - \Omega_i^2}{\omega_{pi}^2}\right) \left(S - n_\parallel^2\right) |K_{zz}|. \tag{2.57}$$

The ratio of imaginary to real parts has been written this way because it is closely related to the distance over which the wave will be strongly damped: $4\pi k_{\perp im}/k_{\perp re} = \lambda/\delta_{1/e}$ where $\delta_{1/e}$ is the distance the wave must travel for the power to fall to $1/e \approx 0.37$ of its original value. Thus even when $k_{\perp im}/k_{\perp re}$ is as little as 8%, the $1/e$ folding length is already one wavelength, and when $k_{\perp im}/k_{\perp re} = 0.5$, the $1/e$ folding length is 16% of a wavelength. In this expression for the electron Landau damping of the fast wave the strongest damping occurs when $\zeta_{0e} = \sqrt{2}/2 \approx 0.707$.

The ion Bernstein wave can also experience strong electron Landau damping if $\omega/k_\parallel v_{\text{the}} \sim 1$. A general expression is given by Ono [18], but a very useful special

case for D(^{3}He) mode-converted IBWs (see Ch. 4) is given in Ref. [37]:

$$k_{\perp im}^{\mathrm{IBW}} \simeq \frac{24}{7}\left(\frac{\Omega_D^2}{\omega_{pD}^2}\right)^2 \frac{(\omega^2-\Omega_D^2)(\omega^2-\Omega_{\mathrm{He3}}^2)\omega^2 n_\parallel^2 n_{\perp\mathrm{IBW}}^2}{2v_{thD}^2 c_A^2 \Omega_D^2 k_{\perp\mathrm{IBW}}(k_{\perp\mathrm{IBW}}^2-k_{\perp\mathrm{FW}}^2)} \frac{k_\parallel^2 v_{the}^2 \sqrt{\pi}\zeta_{0e} e^{-\zeta_{0e}^2}}{2\omega_{pe}^2|1+\zeta_{0e}Z(\zeta_{0e})|^2}, \quad (2.58)$$

where $c_A^2 = B^2/(\mu_0 \sum_j n_j m_j)$ is the Alfvén velocity (the sum over j is over ion species). Since ω is between Ω_D and Ω_{He3} for the mode-converted IBW, the imaginary part of the wavenumber is the opposite sign as the real part, as it should be for a backwards wave.

The imaginary part of the wavenumber due to electron Landau damping of both the IBW and the FW is shown in Fig. 2-16 and Fig. 2-17, for example.

Landau damping is a subtle process, and difficult to describe using the single particle picture of Appendix. B, because it depends on the differing effects of two classes of particles: those with velocities slightly higher than the phase velocity of the wave, and those with velocities slightly lower. For an enlightening discussion on the physical basis of Landau damping,[14] see Chen [11, Ch. 7.4–7.6], Stix [8, Ch. 8-2], and Ref. [40]. Suffice it to say that when the wave phase velocity is near the thermal velocity of a plasma species, Landau damping on that species will occur (i.e. when $\frac{\omega}{k_\parallel v_{\mathrm{th}}} \sim 1$).

2.3.3 Collisional damping

A wave can damp away if the particles which are carrying the energy (ions in the case of an IBW) collide with other particles, losing phase information and dissipating energy. In a hot plasma such as in Alcator C-Mod, the collision frequency between particles is very low. Collisional damping of the mode-converted IBWs is not expected to play any significant role, as it is excited in a very hot region of the plasma and damps away through electron Landau damping before it has a chance to reach colder regions of the plasma.

In the IBW review paper by Ono [18, Sec. B.2], he presents an expression for the imaginary part of the wavenumber which arises due to collisional damping. Ion

[14] The physics of Landau damping is still an active area of research. See for example Refs. [38, 39] for more on the physical basis of linear Landau damping.

collisions are the most important effect on IBW, and the damping due to ion species i can be represented as

$$\mathrm{Im}\, k_\perp^i = \sum_j \frac{\nu_{ij}}{2v_{g\perp}} f_i \frac{1}{[A + B/(k_\perp \rho_i)^2]}, \tag{2.59}$$

where the sum over j is over all ion species, and ν_{ij} is the 90° collision frequency between the i and j ion species, $v_{g\perp}$ is the perpendicular group velocity, and f_i is the fraction of the wave energy density due to species i. For unlike species ($i \neq j$), $B = 0$ and $A = 1$. For like species ($i = j$), $B = 1$ and $A = 0$.

The group velocity $v_{g\perp}$ of the IBW will be of the order of the ion thermal velocity, slowing down as $k_\perp \rho_i$ increases (see Fig. 2-13). In order to make an estimate of the collisional damping to see if it could compete with the Landau damping (Eq. 2.58), calculate two cases, one near the beginning of the wave and the second near where the wave would be damped away by Landau damping. In case (1) the group velocity is of order the ion thermal velocity and $k_\perp \rho_i \sim 1$, and in case (2) the group velocity has slowed down to ~ 1 percent of the ion thermal velocity and $k_\perp \rho_i \sim 10$. Take a plasma with two ion species, D and ^{3}He. Rather than partitioning the energy between the two, make an overestimate by assuming $f_D = f_{\mathrm{He3}} = 1$. Finally, use a general estimate of an ion–ion collision frequency [41, Eq. 11.24]:

$$\nu_{ii} = \frac{n_i Z^4 e^4 \ln \Lambda}{12\pi^{3/2} \epsilon_0^2 M^{1/2} T_i^{3/2}}, \tag{2.60}$$

where M is the mass of the ion and Z the charge state. To estimate the 90° collision frequency, a factor of four times the Coulomb logarithm ($4 \ln \Lambda$) can be dropped [41, Eq. 11.19] ($\ln \Lambda$ for C-Mod is typically ~16 to 17).

For ion density of order $3 \times 10^{20}\,\mathrm{m}^{-3}$, temperature $T_i \sim 2$ keV, and ^{3}He ions ($M = 3\,m_p$, $Z = 2$), the 90° ion–ion collision frequency is approximately 370 sec^{-1} (or 28 sec^{-1} for deuterium). This means that Im $k_\perp^{\mathrm{He3}}$ from collisions is approximately $6 \times 10^{-6}\,\mathrm{cm}^{-1}$ for case (1) and $0.05\,\mathrm{cm}^{-1}$ for case (2). These values are small compared to the imaginary part of $k_{\perp \mathrm{IBW}}$ shown in Fig. 2-17 due to collisionless damping. For example, with 20% ^{3}He at a value of $k_\perp \rho$ corresponding to case (1), $k_\perp \rho = 1$ ($b = 0.5$) and Im $k_{\perp \mathrm{IBW}} = 0.04\,\mathrm{cm}^{-1}$, which is much larger than the estimated

collisional damping for case (1). Similarly, for case (2): $k_\perp \rho = 10$ ($b = 50$) and Im $k_{\perp \mathrm{IBW}} = 14\,\mathrm{cm}^{-1}$, which is again much larger than the estimated collisional damping of 0.05 cm^{-1}. When the upshift in $k_\parallel$ is taken into account (seen from ray-tracing of the IBW), the collisionless damping is even more pronounced, and thus collisional damping can be neglected.

2.4 Fast Waves, Ion Bernstein Waves and Mode Conversion

The fast magnetosonic wave launched by the C-Mod antenna can be coupled to an ion Bernstein wave in the plasma if the conditions are right. The requirement is that there exists a location in the plasma where both waves have the same, or nearly the same, wavenumber. In the dispersion relation, this is where two separate roots coalesce in a certain region. When this occurs, the fast wave can excite an ion Bernstein wave and convert a significant fraction of its power to this short-wavelength mode. This process is called linear mode conversion, and can be illustrated by the spatial dispersion relations of each type of wave.

The fast wave to IBW mode conversion problem has been studied for more than 30 years now. The possibility of a process where one wave transfers energy to another at a resonance was first conjectured by Stix in 1960 [42], and more explicitly described as mode conversion of a fast electromagnetic wave to a slow electrostatic wave in 1965 [43]. Then the possibility of heating at the ion-ion hybrid resonance was studied experimentally [44] and theoretically [45]. The dispersion relation and tunneling factor for the fast wave to ion Bernstein wave mode conversion process at the ion-ion hybrid layer was described theoretically in 1976 [46] and 1977 [47], and also observed experimentally in a tokamak for a D(H) plasma in 1977 [48]. Since then Swanson in particular (see Refs. [49, 9, 6]) has developed the mathematical theory of mode conversion, especially with applications to the ion-cyclotron range of frequencies. For more recent developments in the theory of FW to IBW mode conversion, see Sec. 2.5.2.

2.4.1 IBWs in a Single Species Plasma

In a plasma with a single ion species, ion Bernstein waves can propagate (possibly with some damping) between each cyclotron harmonic. The collisionless damping of the wave can be calculated from a dispersion relation which takes into account kinetic effects.

The electrostatic dispersion relation Eq. 2.43 contains solutions which correspond to ion Bernstein waves, including cyclotron and Landau damping. However, to get a more accurate estimate of the complex wavenumber solution, the full electromagnetic hot plasma dispersion relation Eq. 2.40 can be solved. (Note that all plasma species' distribution functions are assumed to be Maxwellian, and that this solution is from a *linearized* Vlasov-Maxwell system of equations.) This has been done with a code written by Dr. Abhay Ram and run on a Cray SV1 supercomputer operated by the National Energy Research Scientific Computing Center (NERSC) located at the Lawrence Berkeley National Laboratory (see **http://hpcf.nersc.gov/**). It solves for $k_\perp$ as a function of position along the midplane (horizontal coordinate changing from R_{min} to R_{max}, vertical coordinate staying constant at the plasma center) for a given plasma profile and constant $k_\parallel$. For the results in this chapter, 10 Bessel function terms were retained for the electrons, and 100 for each ion species. An initial guess for the complex root of the equation $D(k_\perp) = 0$ is entered for each solution to be followed through the plasma. Once the solution is found using a complex root solver module, it is used as the initial guess for the next step along the desired major radial path. The plasma model used for Figs. 2-16 and 2-17 was typical of the D(^{3}He) 7.8 T plasmas on C-Mod: central electron density $n_{e0} = 3 \times 10^{20}\, m^{-3}$, central electron ($T_{e0}$) and ion temperature $T_{i0} = 3$ keV, toroidal field on axis ($R_0 = 66$ cm) 7.8 tesla (no poloidal field was included in the code), varying with major radius $B(R) = B_0 R_0 / R$. The fast wave is launched with a frequency of 80 MHz and a parallel wavenumber of $k_\parallel = 0.15$ cm^{-1}. This means the argument of the Z function is of the right order for electron damping: $\frac{\omega}{k_\parallel v_{\rm the}} \sim 1.0 - 1.4$ from the center to half-way out ($r/a = 0.5$). The profiles were modeled with analytic functions which approximated actual C-Mod

profiles, peaking on axis and falling to some fraction of the central value at the plasma edge (minor radius a = 22 cm). Letting r be the minor radius in centimeters, the density profile was: $n_{e0}(0.042 + (1 - 0.042)(1 - (r/a)^2)^{0.5})$ and the temperature profile was (for both electrons and ions): $T_0(0.13 + (1 - 0.13)(1 - (r/a)^2)^2)$.

Although the argument of the Z function is of the right order to introduce damping, the more important effect which increases the damping as the IBW propagates away from the mode conversion layer is that $k_\perp$ is increasing, hence the modified Bessel functions are rapidly increasing, which are multiplying factors of the Z functions in the dispersion relation.

Once the fast wave has tunneled through the evanescent gap at the edge and is propagating in the plasma in this scenario, it does not change very much. For a pure deuterium plasma in C-Mod at 7.8 T with an electron density of $3 \times 10^{20}\,\mathrm{m}^{-3}$ and (ion and electron) temperature of 3 keV, the fast Alfvén wave (FW) launched at a frequency $f = (\omega/2\pi) = 80$ MHz from the low-field side has a nearly constant wavelength in the plasma of approximately 12 cm (wave number 0.5 cm^{-1}). (See Fig. 2-16.) There are no cutoffs other than the $n_\parallel^2 = R$ cutoffs on the edges of the plasma, and there is no wave resonance. There is a small amount of direct electron Landau damping of the fast wave near the core of the plasma, as seen by the broad hump centered around 69 cm, as well as a small amount of fundamental cyclotron damping (a finite $k_\perp \rho_i$ effect) centered around the deuterium cyclotron resonance at 49 cm. Note the imaginary part of the fast wave has been multiplied by 1000 to make it visible on the same plot. The fast wave imaginary $k_\perp$ reaches its largest value of about 0.0007 cm^{-1} at 69 cm.

An ion Bernstein wave (IBW) could also exist in this plasma, with a wave number ranging between 10 and 100 cm^{-1}. This is the IBW which, at low $k_\perp$, is associated with the second harmonic layer of deuterium ($\omega = 2\Omega_D$) at 98 cm (which is outside the plasma). Thus in the pure D plasma at 7.8 T, the IBW wavenumber does not actually coincide with that of the fast wave, so it will not be excited in the plasma by mode conversion. Note that both the real and imaginary parts of the Bernstein wave grow quickly as the wave approaches the deuterium cyclotron resonance located

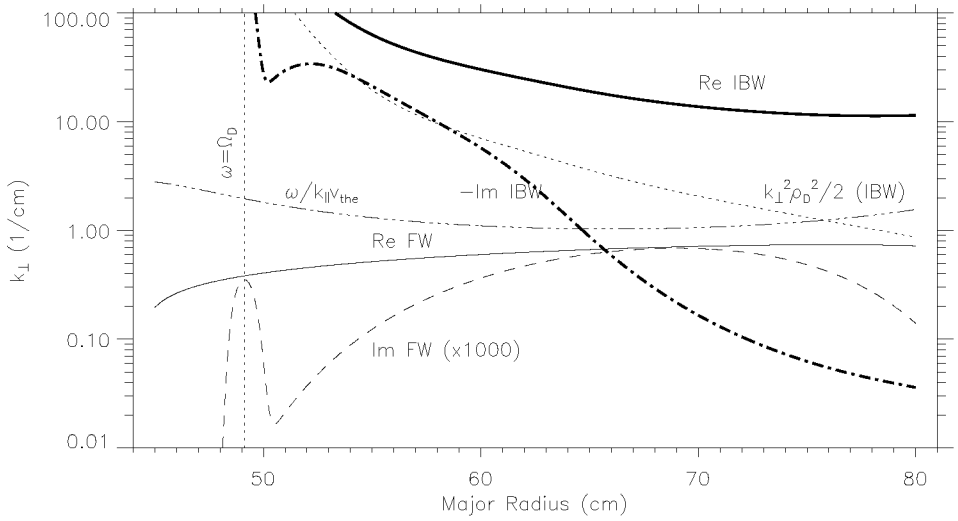

Figure 2-16: Fast wave and IBW wavenumber for a pure deuterium plasma. FW: thin solid line – real, dashed line – imaginary. IBW: thick solid line – real, dot-dashed line – -imaginary. Note that the imaginary part of the fast wave has been multiplied by 1000, and the imaginary part of the IBW by -1. Also plotted is the (dimensionless) magnitude of $k_\perp^2 \rho_D^2/2$ for the IBW (dotted line) and $\omega/(k_\parallel v_{the})$ (dot-dot-dot-dashed line).

at about 49 cm major radius (the center of the plasma in this model is at 66 cm), indicating that this IBW would damp away before it reached the deuterium resonance. The imaginary part corresponding to the positive real part is negative (this is because the ion Bernstein wave is a backward wave, i.e., the phase velocity is the opposite sign as the group velocity). So, in order to show it on the same log plot, it has been multiplied by -1.

Although this is an accurate dispersion relation for the assumed constant $k_\parallel = 0.15\,\mathrm{cm}^{-1}$, the antenna actually launches a spectrum of parallel wavenumbers, which because of the toroidal geometry and the magnetic topology, will change as the wave propagates across the plasma. The first order effect is that for a given toroidal mode number n, $k_\parallel \simeq n/R$, where R is the major radius, so there will be an upshift of $k_\parallel$ towards the high-field-side. The spectrum can also be decomposed into poloidal mode numbers which will further complicate the picture. See Sec. 2.5.2 and particularly Eq. 2.74 for more details on the parallel antenna spectrum. In addition, experience

from ray-tracing of ion Bernstein waves [50] suggests that there would be a change in the poloidal spectrum of a given IBW ray, causing a rapid upshift of $k_{\|}$ and a corresponding further increase in damping. In this section this variation of $k_{\|}$ is neglected, in order to illustrate the main features of the FW – IBW mode conversion process without further complication.

If an antenna were installed at the low field side designed to launch the appropriate polarization, then the IBW could be directly excited and propagate inside the plasma. This has been tried on several machines [51, 52, 14, 53, 54, 55] but not on Alcator C-Mod. Direct-launch ion Bernstein wave heating experiments are often plagued with difficulties such as parasitic losses to other modes, scattering off of fluctuations at the edge, and damping near the edge before reaching the core, which is most often the desired target location for IBW damping. Because of these disadvantages, a more attractive solution to achieving IBW excitation and damping in the core of the plasma is to use the fast magnetosonic wave, which can be coupled to the plasma at the edge, and then mode-converted to an ion Bernstein wave somewhere in the plasma, as described in the next section. The location of IBW damping can then be controlled by varying plasma parameters. Experimental results of this process on C-Mod are presented in Ch. 4.

2.4.2 IBWs in Two Ion Species Plasmas

In a plasma with two distinct ion species (i.e. with different charge to mass ratios), there are more possibilities for the propagation, excitation, and damping of IBWs. Continuing with the example of Sec. 2.4.1, with the addition of helium-3 to the background deuterium plasma, the IBW associated with the 2nd harmonic of deuterium would no longer be able to propagate to the fundamental deuterium resonance; the damping becomes significant by the time it reaches the fundamental ^{3}He cyclotron resonance. (See Fig. 2-17). This is a general feature of Bernstein waves: they can usually only propagate *between* cyclotron resonances (as shown in Fig. 2-13 as a function of frequency).

A new feature also appears in the fast wave dispersion relation between the D

and ^{3}He cyclotron resonances which is not present in a single ion species plasma: a cutoff–resonance pair. Beginning from the low-field side antenna (strap located at R = 0.93 cm), the fast wave would first encounter an $n_\parallel^2 = L$ cutoff ($k_\perp \to 0$), then a narrow evanescent layer, then the ion-ion hybrid, or Buchsbaum [22] resonance ($n_\parallel^2 = S$). This resonance first appears very near the helium-3 cyclotron resonance at the magnetic axis, then moves to the high-field side (towards the deuterium cyclotron resonance) as the helium-3 concentration increases. A new ion Bernstein wave branch also appears, beginning at the ion-ion hybrid resonance and continuing to the deuterium cyclotron resonance. In the vicinity of that resonance the ion Bernstein wave and the fast wave converge, having the same wavenumber (both real and imaginary parts). This is where linear mode conversion can occur.

The location of the mode conversion layer depends on the ion species mix. It will be closer to the minority species. The width of the evanescent gap (between $n_\parallel^2 = L$ and $n_\parallel^2 = S$) will be small when near either one of the cyclotron resonances, and will grow to some maximum in between the two resonances. Also, the damping rate of both the fast wave and IBW will depend on where the IBW is excited, relative to the cyclotron resonance. The specific case of D(^{3}He) will be illustrated in the rest of this section.

Another new feature in Fig. 2-17, compared to the pure D dispersion relation, is that the imaginary part of the fast wave is enhanced around the ^{3}He cyclotron resonance, representing the minority ion cyclotron damping. This bump would be even broader if an enhanced minority ion temperature (representing the high energy quasi-linear "tail" on the ion distribution function) were included in the model. The maximum damping is slightly to the high-field side of the cyclotron resonance.[15]

The presence of a closely spaced cutoff and resonance causes the incoming fast wave to reflect some power back to the low-field side, transmit some to the fast wave branch on the high-field side, and convert some of its power to the ion Bernstein

[15]Although the plasma dispersion function Z has a maximum imaginary part right at the cyclotron resonance, in the expression for k, the Z function appears with complex factors which vary with major radius, producing the maximum Im $k_\perp$ just to the HFS of resonance.

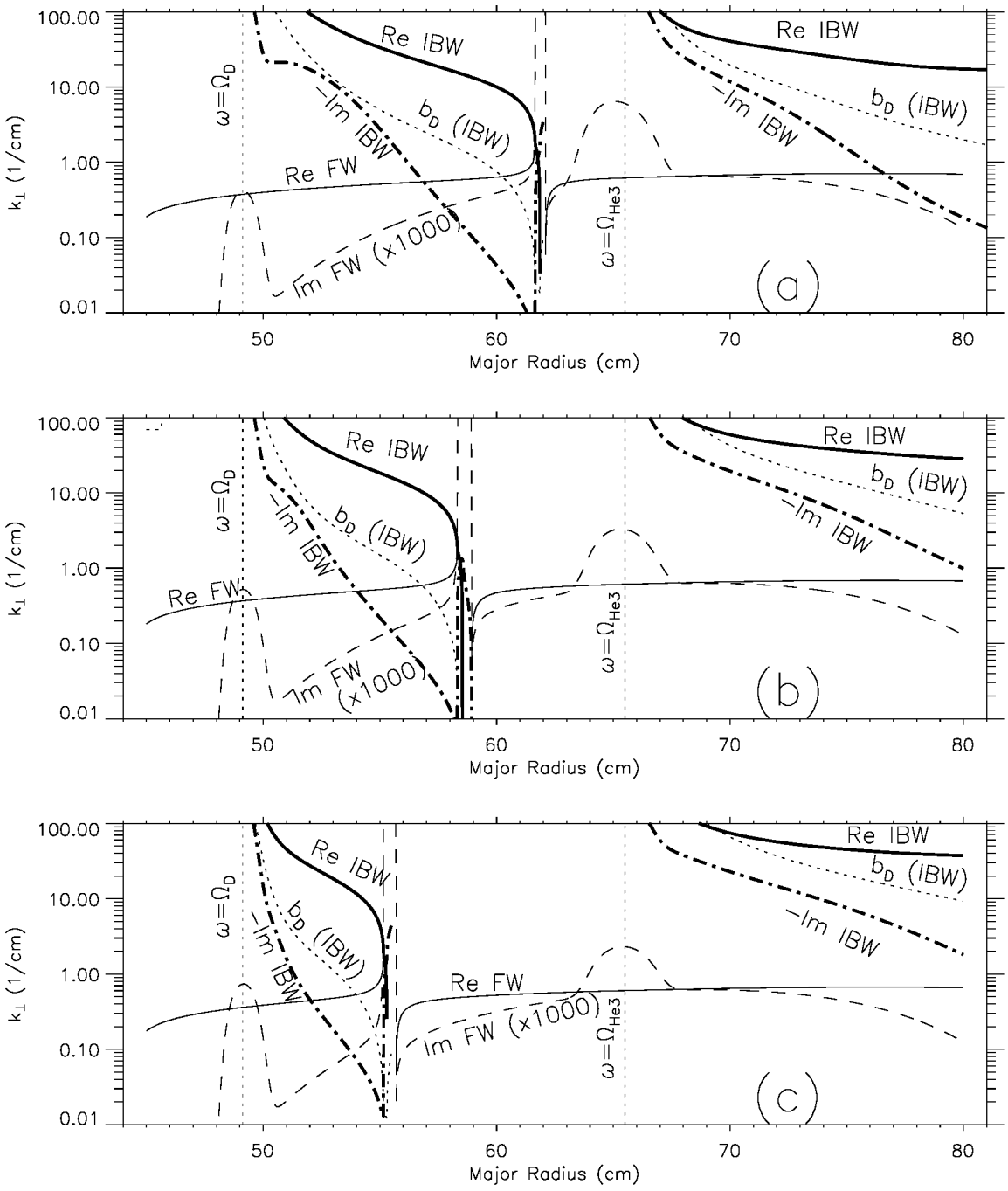

Figure 2-17: Fast Wave and IBW for D(^{3}He) Plasmas: parameters same as in Fig. 2-16 but with increasing ratios of n_{He3}/n_e: (a) 10% (b) 20% (c) 30%. Also plotted (dotted line) is $b_D = k^2_{\perp \mathrm{IBW}} \rho_D^2/2$.

wave (see section 2.5). (Of course, some power will also be lost to ion cyclotron damping on the minority helium-3 ions). Just how much power can be coupled to the ion Bernstein wave (the mode-conversion efficiency) has been the subject of much theoretical and experimental work (Refs. [56, 57, 37, 58, 59, 23, 60, 61, 62]). Chapter 4 will present experimental analysis of D(^{3}He) plasmas at 7.8 T, showing the measured mode conversion efficiency as a function of concentration.

Three main effects are visible in Fig. 2-17 as the concentration is increased from 10% to 30%. The minority concentration here and throughout this thesis will be relative to the electron density, i.e. n_{He3}/n_e. Since the helium-3 is doubly ionized, it contributes two electrons for every ion, while the majority deuterium can only contribute one, therefore 20% He^3 means that 40% of the electrons comes from helium-3 and 60% from deuterium.

1) The ion-ion hybrid layer moves away from the helium-3 cyclotron resonance as n_{He3}/n_e is increased. In general, as ion concentrations change, the hybrid layer moves towards the cyclotron layer of the species whose concentration is decreased, and away from the one that is increased.

2) The evanescent layer, i.e. the gap between the cutoff and the resonance, changes size as the concentration is increased. In general, the gap starts small near one of the cyclotron resonances, grows as it is pushed away from the resonance, then shrinks again as it approaches the other ion cyclotron resonance layer. This has important implications for the mode conversion efficiency.

3) The minority ion cyclotron damping (represented by the imaginary part of the fast wave perpendicular wave number near 65 cm) decreases as the concentration increases. (Note, however, that the potential for damping on deuterium, near 49 cm, is increasing — deuterium is becoming the minority species as helium-3 becomes the majority.)

The position of mode-conversion, the evanescent distance, and the peak FW damping near the helium-3 resonance are shown in Table 2.1 (for constant $k_{\|}$ and $B = (B_0 R_0)/R$).

Although the fast wave wavenumber is maximum at the $n_{\|}^2 = S$ layer for the cold

^{3}He Concentration	R(mode conversion)	Cutoff–resonance gap	Max. Im $k_\perp$
10%	61.66 cm	0.43 cm	0.0064 cm^{-1}
20%	58.33 cm	0.59 cm	0.0033 cm^{-1}
30%	55.16 cm	0.53 cm	0.0023 cm^{-1}

Table 2.1: Wave parameters *vs.* ^{3}He concentration.

plasma dispersion relation, the coupling between the FW and the IBW in the hot plasma dispersion relation can actually occur some distance away. The cold and hot plasma dispersion relations are compared in Fig. 2-18, along with the locations of several critical layers. Note that the $S = 0$ layer is a resonance for the slow wave cold plasma root (not shown) corresponding to root with the opposite sign before the radical in Eq. 2.28 as the fast wave. For the ion Bernstein wave the condition $S = 0$ is not particularly significant. For most purposes dealing with the fast wave, the cold plasma dispersion relation is sufficient to describe the wavenumber quite accurately. The local dispersion relations discussed in this section describe the propagation and damping of the FW and IBW. If the wavenumbers of these two waves coincide, the dispersion relation indicates that the FW to IBW mode conversion process is possible. However, it cannot tell us with what efficiency the FW can excite the IBW. For this a more global analysis is necessary.

2.5 Mode Conversion Efficiency

In order to usefully exploit the FW to IBW mode conversion process for plasma heating and control it is necessary to know how much power can be converted to the IBW. This is the question of mode conversion efficiency and is addressed in this section, first by a relatively simple theory developed more than 30 years ago, and then by a more sophisticated model that has emerged only in the last few years.

2.5.1 Budden Tunneling

A useful estimate of the fraction of power that is reflected, transmitted, and mode-converted at a cutoff-resonance pair can be made using Budden tunneling theory.

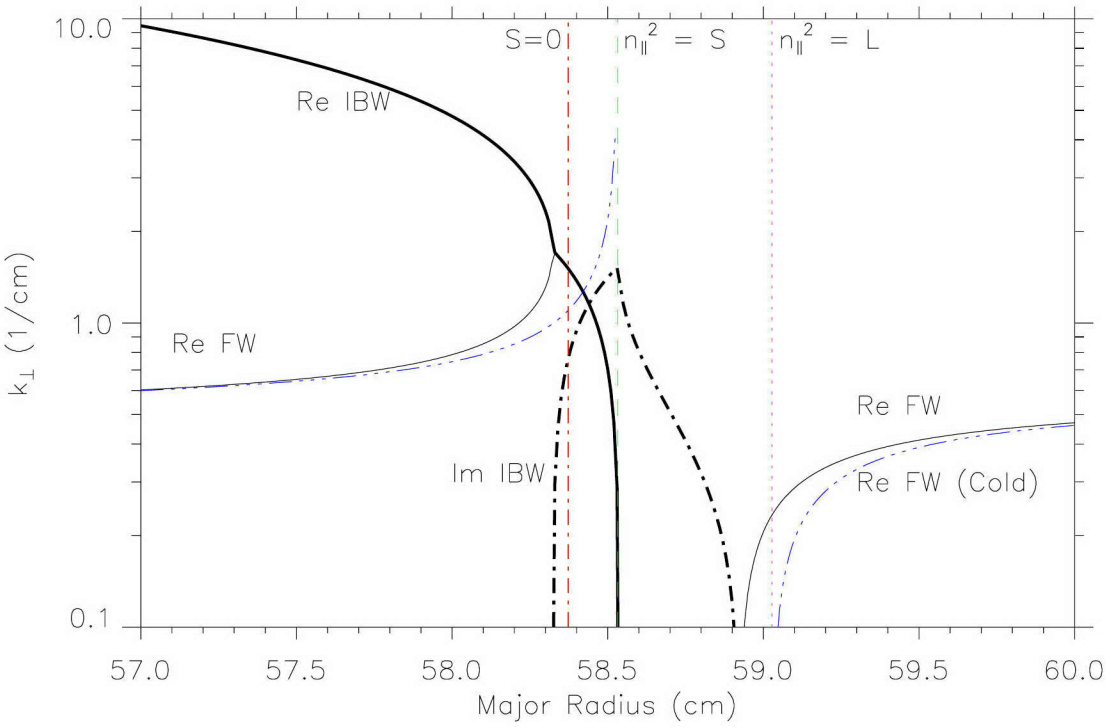

Figure 2-18: Close-up view of the coupling between the FW and IBW for the 20% ^{3}He case (Fig. 2-17(b)). Solid line: hot plasma; dot-dot-dot-dash line: cold plasma (FW only). The vertical lines show the locations of: $S = 0$ (dot-dash), $n_\parallel^2 = S$ (dash), and $n_\parallel^2 = L$ (dot).

First discussed by K.G. Budden in his book *Radio Waves in the Ionosphere* [63], the problem of a resonance (represented by an infinity in the index of refraction) and a resonance–cutoff pair (represented by an infinity near a zero) has since been studied extensively [64, 8] not just for waves propagating in the ionosphere, but also in tokamaks and other magnetic confinement devices [65, 66].

The simplest case is to assume a normally incident plane wave on the cutoff-resonance surface, with wave amplitudes varying in only one dimension. The fast wave dispersion relation in Fig. 2-17 shows the characteristics of a cutoff-resonance pair at the mode-conversion layer. The essential features of this region are captured by the (cold plasma) fast wave dispersion relation (Eq. 2.31):

$$n_\perp^2 = \frac{(L - n_\parallel^2)(R - n_\parallel^2)}{(S - n_\parallel^2)} \equiv Q(x) \tag{2.61}$$

with a cutoff at $n_\parallel^2 = L$ and a resonance at $n_\parallel^2 = S$. In deriving this dispersion relation, spatial derivatives across the static magnetic field were Fourier transformed into $ik_\perp$. Let z be along the static magnetic field, x be along the perpendicular component of the wave propagation vector (across the magnetic field), and y be the vertical direction. Let the origin ($x = 0$) be at the $S = n_\parallel^2$ resonance. To examine the appropriate differential equation for the wave electric field (which in this one-dimensional treatment is a plane wave proportional to $e^{-i(\omega t - kx)}$), treat $k_\perp$ as $-i\frac{d}{dx}$ [16] and the dispersion relation becomes

$$\frac{d^2 E_y}{dx^2} + \frac{\omega^2}{c^2} Q(x) E_y = 0. \tag{2.62}$$

To more easily examine this differential equation both analytically and numerically, it is advantageous to use dimensionless quantities. Let the normalized distance s be

[16] This is justified because in the cold plasma model the same wave equation could have been derived without the step of Fourier transforming spatial derivatives in the first place [67]. Going the other direction, treating d/dx as $ik_\perp$, is known as WKB theory, and relies on the assumption that the wavelength is smaller than the plasma inhomogeneity scale lengths. The treatment described in this section and in Sec. 2.5.2 is a full-wave analysis, solving a 2nd order differential equation with boundary conditions, and does not rely on any assumption of wavelength and inhomogeneity scale length. For more on the justification of treating $k_\perp$ as $-id/dx$ and the question of energy conservation, especially when the plasma model does contain dissipation, see Refs. [68, 69] and particularly references in [69].

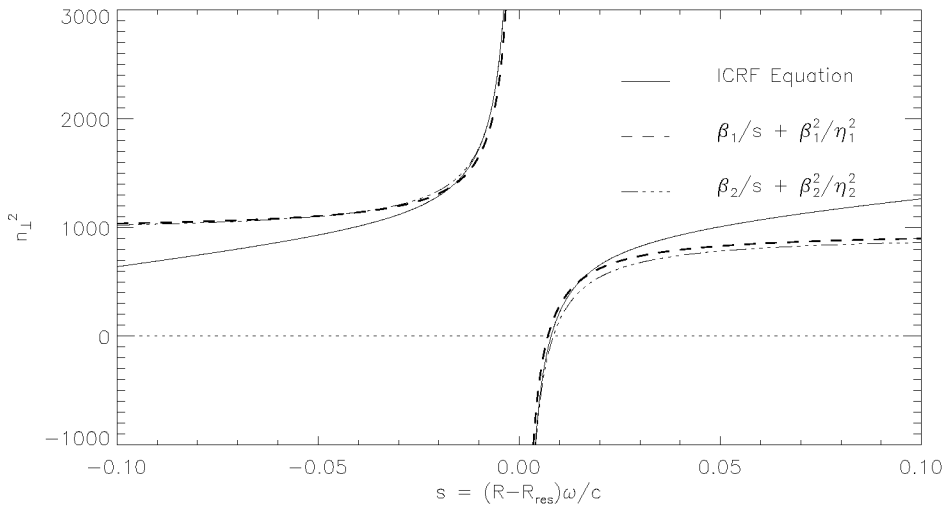

Figure 2-19: Cold Plasma Fast Wave dispersion relation with fits to a Budden potential. Plasma parameters are the same as Fig. 2-17 for the case of 20% ^{3}He. The solid line is the actual ICRF dispersion relation. The dashed line is the Budden potential (Eq. 2.64) with $\beta_1 = -6.9$ and $\eta_1 = 0.22$ determined from a least squares functional fit. The dot-dash line is the Budden potential with $\beta_2 = -8.0$ and $\eta_2 = 0.26$ determined from the linearization procedure (see Eq. 2.68).

the free space wavenumber times the distance, $s = x\omega/c$. Then Eq. 2.62 is of the form that Budden treated:

$$\frac{d^2E_y}{ds^2} + Q(s)E_y = 0, \tag{2.63}$$

if the "potential" function $Q(s)$ can be described simply as

$$\frac{\beta}{s} + \frac{\beta^2}{\eta^2}. \tag{2.64}$$

Of course, this functional form does not well match the actual $n_\perp^2$ far away from the resonance since the simplified form asymptotes to the same constant value for $s \to \infty$ and $s \to -\infty$, whereas the actual form is changing on either side of the resonance due to the non-uniform magnetic field and plasma density. Nevertheless, close to the resonance the index of refraction can approximated by (Eq. 2.64) (see Fig. 2-19 for a least squares fit within $-0.1 < s < 0.1$, and $-1000 < n_\perp^2 < 3000$).

A recent summary of the mode-conversion problem was published by Monakhov et al. [59], whose explanation in section II of their paper is summarized and elaborated

upon in the following paragraph. The idea is to linearize the dielectric tensor elements around the resonance, so that the ICRF dispersion relation takes the form of a Budden type potential near the resonance, with Budden parameters determined directly from plasma parameters and their derivatives, without the need for a fit to the dispersion relation.

Starting again from another form of the ICRF equation:

$$n_\perp^2 = \frac{(L - n_\parallel^2)(R - n_\parallel^2)}{(S - n_\parallel^2)} = \frac{(S - n_\parallel^2)^2 - D^2}{(S - n_\parallel^2)} \equiv Q(x), \tag{2.65}$$

and expanding the dielectric tensor elements linearly around the resonance at $x = 0$: $S \approx S(0) + S'(0)x, D \approx D(0) + D'(0)x$. Then, since $S(x = 0) = n_\parallel^2$, $Q(x)$ becomes:

$$Q(x) \approx \frac{[S'^2x^2 - (D + D'x)^2]}{S'x} = S'x - \frac{D^2}{S'x} - \frac{2DD'}{S'} - \frac{D'^2x}{S'}. \tag{2.66}$$

Since we are only interested in the region very near the resonance ($x \ll 1$), neglect terms proportional to x:

$$Q(x) \approx \frac{-2DD'}{S'} - \frac{D^2}{S'x} \tag{2.67}$$

The differential equation for the electric field then becomes:

$$\frac{d^2E_y}{dx^2} + k_{\perp\infty}^2(1 - \frac{\Delta}{x})E_y = 0, \tag{2.68}$$

where $k_{\perp\infty}^2 = -(2\omega^2DD'/c^2S')$, $\Delta = -(D/2D')$, and the prime refers to differentiation along the x direction. All quantities are to be evaluated at $x = 0$. Equation 2.68 is now of the form Budden treated (Eq. 2.63 and 2.64) with $\beta = -\frac{c}{\omega}k_{\perp\infty}^2\Delta$ and $\eta = k_{\perp\infty}\Delta$. Figure 2-19 shows that this linearization procedure produces a reasonable approximation to the cold plasma dispersion relation near the resonance.

Once the $n_\perp^2$ "potential" function has been simplified in this way, an exact analytic solution to the differential equation can be found. This solution is applicable everywhere, even at the resonances and cutoffs. This type of differential equation for the wave electric field has analytic solutions known as Whittaker functions (a confluent hypergeometric function[17]). By setting appropriate boundary conditions,

[17]By taking the general hypergeometric differential equation and letting two of the singularites coalesce, it becomes the *confluent* hypergeometric equation.

the case of the incoming wave first encountering the resonance or the cutoff can be treated. For example, if the wave first encounters the resonance and then the cutoff, this would correspond to high-field side incidence in a tokamak. In Alcator C-Mod the more relevant case is when the wave encounters first the cutoff and then the resonance (low-field side incidence). In this case, the appropriate boundary condition is to construct a solution which has an asymptotic form far away from the resonance to the high-field side representing a left-traveling wave (propagating away from the resonance). This is the transmitted wave. Then find the asymptotic form of this solution far away from the resonance on the low-field side. This turns out to be a sum of two waves, a left-traveling (incident) wave and a right-traveling (reflected) wave (see Eqs. (21.71)–(21.74) in Ref. [63]). The magnitude of the (complex) ratio of the amplitudes of the reflected wave term to the incident wave term is the reflection coefficient, $|R|$. Similarly the ratio of transmitted to incident amplitude is the transmission coefficient, $|T|$.[18] It turns out that these coefficients do not depend on the parameter β, but only on η: $|T| = e^{-\frac{1}{2}\pi\eta}$ and $|R| = 1 - e^{-\pi\eta}$. The power in the reflected and transmitted wave sum to less than that in the incident wave!

$$|R|^2 + |T|^2 = 1 - e^{-\pi\eta} + e^{-2\pi\eta} < 1. \tag{2.69}$$

The power that is "lost" can be attributed to mode conversion, which, when finite temperature effects are taken into account, is the power that goes into the short-wavelength ion Bernstein wave. (See also the interesting discussion on this "energy loss" in both of Budden's books, sec. 21.16 in [63] and 19.5 in [64]).

For low-field-side incidence, the mode-converted power fraction,

$$1 - |R|^2 - |T|^2 = e^{-\pi\eta}(1 - e^{-\pi\eta}) \equiv C, \tag{2.70}$$

reaches a maximum of 0.25 when $|T|^2 = e^{-\pi\eta} = 0.5$, or when $\eta = \ln 2/\pi \approx 0.22$. (In actual experiments the mode conversion fraction can be higher than 25%; see the next section on the internal resonator model). If η becomes much larger than 0.22, then

[18] In the Monakhov and many other papers, the R and T refer to *power* coefficients, i.e. the square of the magnitude of the Budden definitions.

the evanescent gap is too large and there is not much transmitted or mode-converted power. If η is much smaller than 0.22, then most of the power tunnels through the gap and again there is not much mode-converted power. Thus, for an experiment to successfully examine the mode-conversion process, a minimum requirement is that plasma parameters be set up such that near the desired mode-conversion region, the Budden tunneling parameter η is near 0.22.

The reflection, transmission, and mode-conversion coefficients are obtained from the asymptotic forms of the solution, far from the resonance. It is of interest to note that the analytic solution shows that the electric field does not diverge at the resonance. To examine the electric field behavior near the resonance-cutoff region for small ($\eta = 0.02$), ideal ($\eta = 0.22$), and large ($\eta = 1.5$) evanescent gap, it is instructive to look at the Whittaker function near the origin. Most formulas and expansions for the Whittaker function $W_{k,m}(x)$ are difficult to evaluate when $2m$ is an integer, as in the Budden relevant case where we are interested in $W_{k,1/2}(x)$. However, a good treatment of this case is found in Buchholz [70] or Slater [71]. The result of evaluating the Whittaker functions near $x = 0$ for these three cases with the software package *Mathematica* is shown in Fig. 2-20. In Fig. 2-20(a), the gap is too small for much power to be mode-converted, and the wave passes through nearly unchanged. In Fig. 2-20(c), the gap is too large — most of the power is reflected and little is transmitted or mode-converted. Fig. 2-20(b) represents the ideal case where 25% of the power is mode-converted.

For *high-field-side* incidence (never tried on C-Mod, and quite difficult for most tokamaks as it requires an antenna to be installed on the inside of the torus), the behavior is quite different. Here,

$$|R| = 0,\ |T| = e^{-\frac{1}{2}\pi\eta},\ |R|^2 + |T|^2 = e^{-\pi\eta} < 1. \tag{2.71}$$

Again, the reflected and transmitted power do not add up to the incident power, so there is some that is mode-converted, $C_{\text{power}} = 1 - e^{-\pi\eta}$. In this case, for the best mode conversion, it is desirable to have η as large as possible so that very little power tunnels through to the propagating region on the low-field-side.

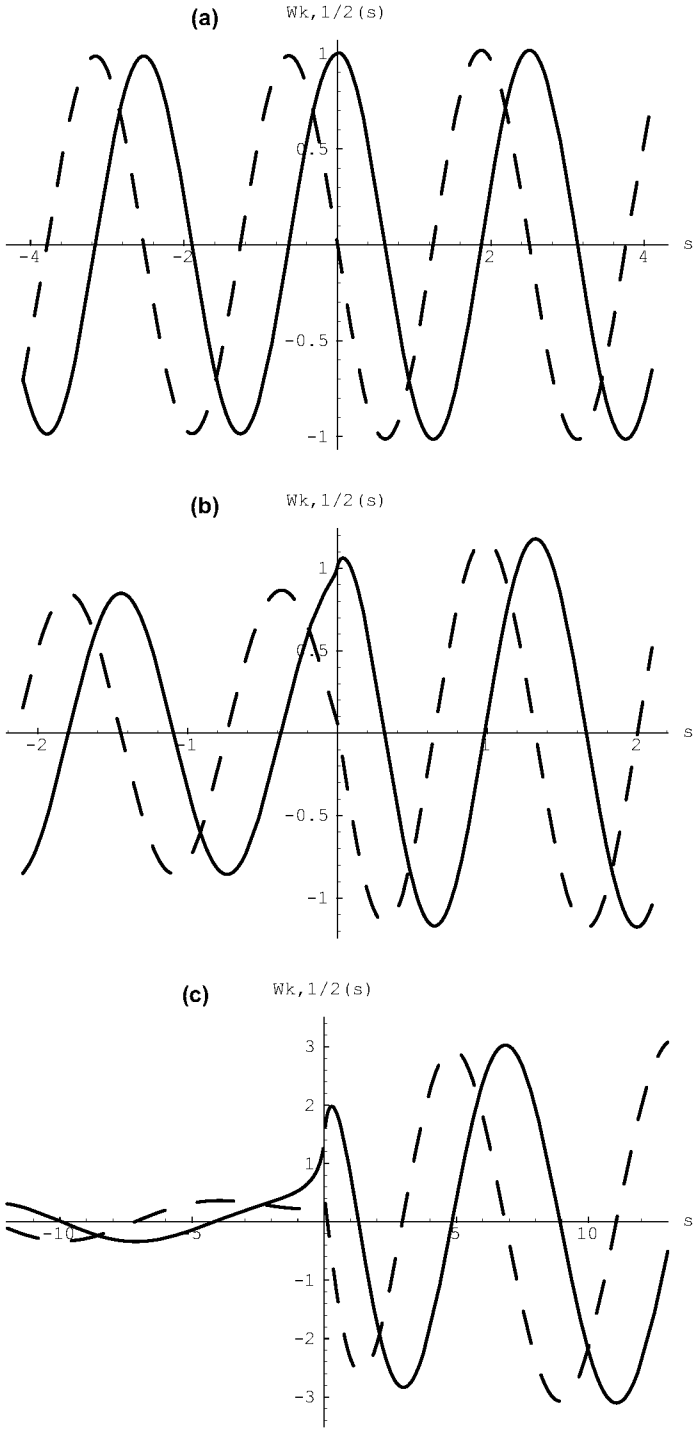

Figure 2-20: Whittaker functions $W_{k,1/2}(z(s))$, where $k = -i\eta/2$ and $z = 2i\beta s/\eta$. Real part: solid line, Imaginary part: dashed line. (a) $\eta = 0.02, \beta = 0.05$, (b) $\eta = 0.22, \beta = 1.0$, (c) $\eta = 1.5, \beta = 1.0$.

An interesting effect has been seen by van Duin and Sluijter [72] when the perpendicular wave number is modeled with a more complicated potential function than simply the Budden type Eq. 2.64. For example, they find that when the wave number is allowed to be different on one side of the cutoff-resonance pair than on the other, then high-field-side incidence no longer leads to complete transmission and mode-conversion. The find that up to 10% of the power can be reflected if the evanescent gap is not too large.

For a more complicated model of the waves coming from the curved C-Mod antenna, the plane wave undergoing mode-conversion may not be normal to the resonant surface. The full case of oblique incidence has been treated by Budden [73] and White and Chen [66]. Rather than introduce that further complication, a more important consideration in C-Mod plasmas is the existence of a high-field-side cutoff. The power transmitted through the cutoff–resonance pair does not go off to infinity, as in the Budden model, but reaches and reflects from the high-field-side cutoff at the edge of the plasma (or even closer in, for high $k_{\|}$). This is treated in the next section.

In summary, Budden tunneling theory can tell us under what conditions low-field-side incidence should result in strong mode conversion. This is when the evanescent gap is such that $\eta \approx 0.22$, in which case the mode conversion efficiency is 25%.

2.5.2 Internal Resonator Mode Conversion Model (including many toroidal and poloidal modes)

Although the Budden problem is of great interest for the fast wave to IBW mode conversion process in a tokamak, it is not the entire story. The cutoff–resonance pair cannot truly be treated in isolation, because as can be seen from the ICRF equation dispersion relation illustrated in Fig. 2-6, there is an $n_{\|}^2 = R$ cutoff on the high-field-side (HFS) edge of the plasma. In a "multiple-pass" picture, this would cause any wave power that tunnels through the gap to reflect back, which will also then mode-convert and tunnel, etc. However, for global analysis of the problem, the idea of multiple passes through the mode conversion region is not appropriate. (Figure 4-

12 compares mode conversion efficiency measurements to both the internal resonator theory predictions and those made by single- and multiple-pass models.)

In order to properly treat the HFS cutoff and reflected power coming back to the mode conversion layer, it is best to go back to the differential equation governing the electric field. In work done by Ram, Bers, Schultz and Fuchs [58], a second order differential equation that describes the propagation of the fast wave through the cutoff–resonance pair and reflection from the HFS cutoff (by using a simple model dispersion relation described below), is solved in terms of known analytic functions. The boundary conditions assumed are: on the low-field-side (LFS) there is an incoming and reflected wave, and no outgoing wave from the high-field-side (complete reflection at the HFS cutoff). Thus the quantity to be solved is the reflection coefficient R, from which the mode conversion coefficient C can be obtained by the requirement that all the incident power is either reflected or mode-converted: $1 = R + C$. The differential equation solved is similar to the Budden equation (2.63), but the potential function is different on the LFS and HFS of the resonance, in order to better fit the actual fast wave dispersion:

$$\frac{d^2E}{d\xi^2} + Q(\xi)E = 0, \tag{2.72}$$

where $\xi = \frac{\omega x}{c}$ is the normalized distance from the fast wave resonance at $n_\parallel^2 = S$, where $x = 0$. Ideally, $Q(\xi) = \frac{(L-n_\parallel^2)(R-n_\parallel^2)}{(S-n_\parallel^2)}$, but there is no analytic solution for even a simple model density and magnetic field profile. However, the potential

$$Q(\xi) = \begin{cases} \gamma - \frac{\beta}{\xi}, & \text{if } \xi > 0, \\ \alpha\xi + \tilde{\gamma} - \frac{\beta}{\xi}, & \text{if } \xi \leq 0, \end{cases} \tag{2.73}$$

allows a solution to be constructed as follows: for the region $\xi > 0$, the solutions are Whittaker functions (Fig. 2-20), as in the Budden tunneling case. For the region $\xi \leq 0$, three separate solutions corresponding to near the HFS cutoff (Airy functions), near the resonance (Whittaker functions) and in between (WKB solutions), are matched together (using uniform asymptotic matching), and finally that solution is matched to the positive ξ region. This gives an electric field solution which describes the mode-conversion problem in this "internal resonator" formed by the cutoff–resonance–cutoff triplet.

Since this is only a one-dimensional model, toroidal effects are neglected. The two-dimensional nature of the problem could be mocked up in this model by considering rays above and below the midplane. In this chapter only one ray along the midplane will be considered as representative of the problem. However, instead of just computing the mode-conversion coefficient for one parallel wavenumber, the coefficients of the whole spectrum of toroidal and poloidal mode numbers to model the two-strap antenna are summed according to their weight in the power spectrum. For a given poloidal mode number m_θ and toroidal mode number n_ϕ the parallel wavenumber varies with minor radius r and major radius R and can be expressed as:

$$\begin{aligned} k_\parallel &= \frac{\vec{k}\cdot\vec{B}}{|B|} \\ &= \frac{n_\phi B_\phi}{R|B|} + \frac{m_\theta B_\theta}{r|B|}, \end{aligned} \tag{2.74}$$

where $|B| = \sqrt{B_\theta^2 + B_\phi^2}$ and B_ϕ is the toroidal magnetic field and B_θ the poloidal.

An important note about the sign of B_ϕ and B_θ

The values of n_ϕ, m_θ, B_ϕ and B_θ in Eq. 2.74 can be positive or negative. Since n_ϕ and m_θ are defined relative to a *toroidal* coordinate system, the signs of B_ϕ and B_θ must also be consistent with that coordinate system. A wave with a positive n_ϕ number has a phase velocity in the positive ϕ direction, which is defined to be the clockwise direction when the torus is viewed from above. Since in Alcator C-Mod the usual scenario is to have both toroidal current and toroidal field in the clockwise direction when viewed from above[19], and there is no data in this thesis dealing with "reversed field" runs, the toroidal field and toroidal current (and hence poloidal field) in Eq. 2.74 will be taken to be positive.

An example of applying this model potential to actual C-Mod data can be seen by using a data point from Ch. 4. The plasma and resonator parameters are modelled af-

[19]In the C-Mod database, this would be a negative field and negative current, because they are defined relative to a cylindrical system with the azimuthal direction going counter-clockwise when viewed from above.

ter a C-Mod D(^{3}He) discharge (shot[20] 960131008 at time 0.73665 sec). This discharge was estimated (see Sec. 4.3) to have a helium-3 concentration $n_{\rm He3}/n_e \simeq 22.4\%$, a residual hydrogen concentration $n_H/n_e \simeq 5\%$, and $n_D/n_e \simeq 50.2\%$. Other plasma parameters were: $B_{\rm tor} = 7.77$ T at $R_0 = 0.673$ m, minor radius at the edge $a_0 = 0.214$ m, plasma current $I_p = 1016$ kA, central electron density $n_{e0} = 2.20 \times 10^{20}$ m^{-3}, central electron temperature $T_{e0} = 2.12$ keV, $T_D = T_H = 1.72$ keV, and $T_{\rm He3} = 1.79$ keV.[21] Both the ion and electron density and temperature profiles were modelled from experimental data with a 4-parameter fit of the form:

$$A_0[\frac{A_a}{A_0} + (1 - \frac{A_a}{A_0})(1 - (r/a_0)^b)^c], \tag{2.75}$$

where r is the minor radius from the center of the plasma, $\frac{A_a}{A_0}$ is the ratio of the edge value to the central value, and b and c are inner and outer exponents. This functional form fits a wide range of profiles, with the best fits for temperature profiles usually having $c \sim 2$ to 4.5, $b \sim 1.3$ to 3 (in this example, $c_T = 2.56$, $b_T = 2.09$, and $T_a/T_0 = 0.087$). Density profiles are usually flatter in the center, with $c \sim 1$ to 3 and $b \sim 1.5$ to 5 (in this example, $c_n = 1.30$, $b_n = 2.65$ and $n_a/n_0 = 0.60$). Beyond $r = a_0$, the temperature and density are assumed to fall off exponentially, with a characteristic e-folding length of 5 mm. This is an area for future improvement in the model, as the edge temperature and density on the high-field-side have never really been measured on C-Mod. There are plans to attempt it in the future.

The temperature data is measured from electron cyclotron emission and is described in Sec. 4.2. The density data is taken from a two-frequency laser interferometry measurement, with several vertical chords of line-integrated density measurements used to reconstruct a profile which is smooth.

The ICRF dipole antenna launches a spectrum of toroidal and poloidal mode numbers. By considering the current in the straps, the width of each strap, and

[20]The C-Mod shot number designation consists of four parts: the first two or three digits are the number of years since 1900, the next two digits are the month of the year, the next two are the day of the month, and finally the last three digits is the shot number for that day. For example, the 3rd shot on February 22nd, 1998 is: 980222003, and the 15th shot on June 23rd, 2000 is: 1000623015.

[21]The slightly higher minority temperature comes from an assumed simple model for minority tail temperature, $T_{\rm min} \propto n_e/n_{\rm He3}$, see Sec. 4.4.1.

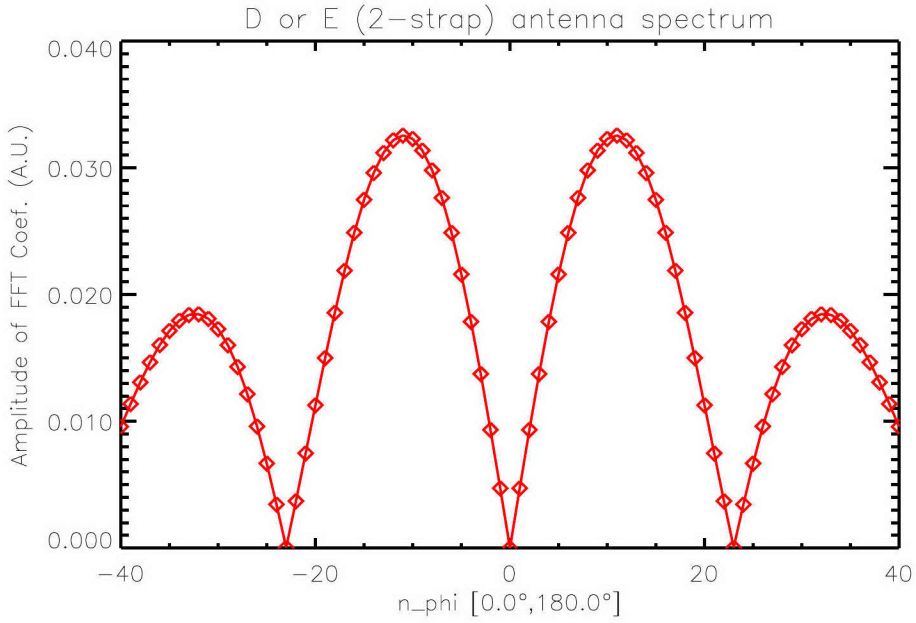

Figure 2-21: The spatial Fourier transform of the current distribution in a [0,π] phased two-strap antenna. The amplitude of the Fourier coefficient *vs.* toroidal mode number n_ϕ is plotted.

the spacing between the straps, a toroidal mode number vacuum spectrum can be computed by taking the spatial Fourier transform of the current distribution in the toroidal direction. This is shown for the D and E antennas on C-Mod in Fig. 2-21. This "vacuum" spectrum peaks at $n_\phi \sim \pm 10$ to ± 11. A similar treatment of the poloidal extent of the current in the antenna yields an m_θ spectrum symmetric about $m = 0$ which peaks at $m = 0$ and falls off rapidly for higher m numbers (see Fig. 2-28).

The power spectrum that is actually coupled to the plasma is significantly different from the vacuum spectrum. Because of the large evanescent gap between the antenna and the low-field-side $n_\parallel^2 = R$ cutoff for large $n_\parallel$, the high n_ϕ modes do not couple well to the plasma. A full solution to the coupling problem should include a self-consistent plasma/antenna interaction calculation, with a full hot plasma model to include damping. This is too complicated for the purpose of this cold plasma internal resonator model. (It would also take too long to be useful in routine analysis). A simple estimate of the effect of the evanescent gap on a mode with a given n and m can be made by computing the damping decrement $\exp(-2\int_0^x k_{im} dx)$, where x is the

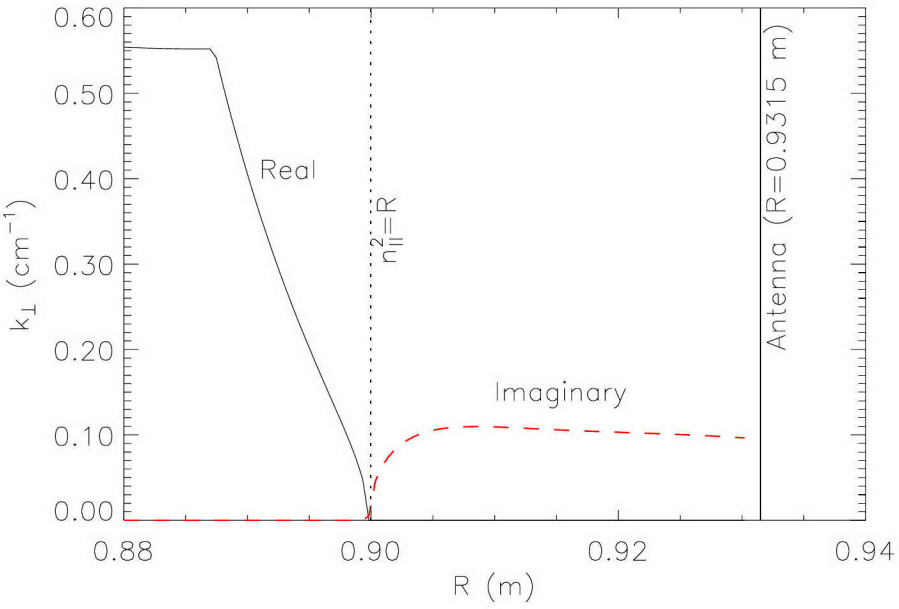

Figure 2-22: Real (solid line) and imaginary (dashed line) parts of the fast wave $k_\perp$, as determined from a 1st order $k_\perp\rho$ expansion dispersion relation. The location of the RF antenna strap (solid vertical line), and the cold plasma $n_\parallel^2 = R$ cutoff (vertical dotted line) are also shown.

width of the gap between the antenna strap and the $n_\parallel^2 = R$ cutoff. An example is shown in Fig. 2-22 with $n = 9$ and $m = -1$, for which the edge damping factor is 0.55. This factor is an indication of the coupling to the plasma and will be used in order to weight this mode compared to other n and m numbers.

Because the internal resonator model only considers power that arrives at the $n_\parallel^2 = S$ resonance in order to calculate the mode-conversion coefficient, a more accurate estimate can be made by calculating the "single-pass" damping the FW experiences between the low-field-side edge and the $n_\parallel^2 = S$ resonance. This is a combination of direct electron Landau damping and ion cyclotron damping. Both of these damping mechanisms are represented by the imaginary part of $k_\perp$ for the fast wave as shown in Fig. 2-23, as determined from a 1st order $k_\perp\rho$ expansion dispersion relation [37]. The broad hump near the center of the plasma is electron Landau damping, and the larger, narrower peak at 0.665 m is the minority ^{3}He cyclotron damping. From a power

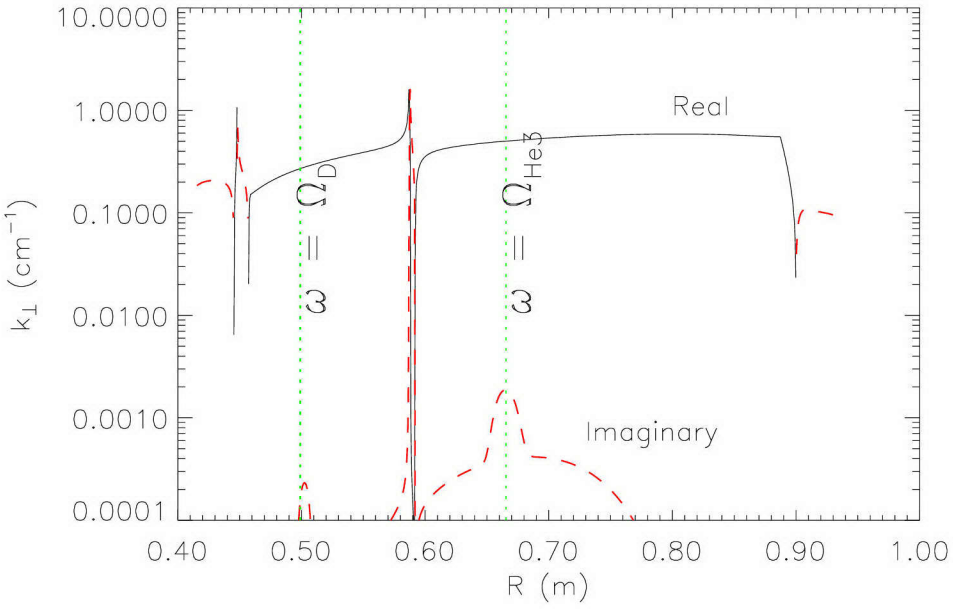

Figure 2-23: Real (solid line) and imaginary (dashed line) parts of the fast wave $k_\perp$. Also shown are the locations of the cyclotron resonances (vertical dotted lines) for ^{3}He (R=0.665 m) and D (R=0.499 m).

decrement calculation $\exp(-2\int_{x_1}^{x_2} k_{im} dx)$, where x_1 is the location of the $n_\parallel^2 = R$ cutoff on the low-field-side, and x_2 is the $n_\parallel^2 = L$ cutoff immediately to the low-field-side of the $n_\parallel^2 = S$ resonance, 98.4% of the FW power remains after a single pass through this region. This is very weak damping because the ^{3}He concentration is very high (22%). At lower concentrations, the single-pass damping is higher (see Fig. 4-11). However it is always weaker than D(H) minority cyclotron damping, because the polarization is not as favorable for producing large E^+.

The most important boundary conditions to account for in obtaining the best fit to the potential Eq. 2.73 are the high-field-side cutoff (at $\xi = \xi_R$), the $n_\parallel^2 = S$ resonance (at $\xi = 0$) and the nearby $n_\parallel^2 = L$ (at $\xi = \xi_L$) cutoff. By expanding around $\xi = 0$ as in Sec. 2.5.1, the parameter β can be expressed in terms of the cold plasma dieletric tensor elements S, D, and their spatial derivatives at $\xi = 0$:

$$\beta = \frac{\omega}{c}\frac{D^2}{S'}|_{\xi=0}. \tag{2.76}$$

Now use the fact that at the $n_\parallel^2 = L$ cutoff at ξ_L, the potential must be zero $Q = 0$,

which determines γ:

$$\gamma = \frac{\beta}{\xi_L}. \tag{2.77}$$

This determines the two low-field-side model parameters β and γ. Now, as with the original Budden form (Eq. 2.64), a tunneling parameter η can be defined:

$$\eta = \frac{\beta}{\sqrt{\gamma}}. \tag{2.78}$$

In order to obtain the two high-field-side parameters α and $\tilde{\gamma}$, first the location of the $n_\parallel^2 = R$ cutoff at ξ_R must be determined. If it is not actually found in the calculated profile region (as could be the case for very low values of $k_\parallel$), it is assumed to be 4 e-folding lengths beyond the high-field-side edge at $r = a_0$. By fixing ξ_R, the parameters α and $\tilde{\gamma}$ are related because $Q = 0$ at ξ_R:

$$\tilde{\gamma} = \frac{\beta}{\xi_R} - \alpha\xi_R. \tag{2.79}$$

Thus all that remains is to calculate α. This is done by first making an initial estimate by calculating the derivative of $n_\perp^2$ near the HFS cutoff, and then using that to perform a least-squares fit on the HFS portion of the FW dispersion relation to obtain the best α.

Once the parameters α, β, γ, and $\tilde{\gamma}$ are determined, the mode conversion coefficient $C = 1 - R$ can be determined from an analytic expression for the reflection coefficient R (see Eq. 11 in Ref. [58]):

$$R = \left| \frac{c_{II}}{d_{II}} - (1 - e^{\pi\eta})e^{-2i\theta} \right|^2 e^{-2\pi\eta}, \tag{2.80}$$

where θ is the phase of the complex number $\Gamma(-i\eta/2)$ (the Gamma function; see Ref. [74] for numerical evaluation of Γ, ψ, $I_n(b)$, etc.). c_{II} and d_{II} are the coefficients of the linearly independent pair of Whittaker functions which make up the electric field solution near the resonance (on the low field side). Their ratio is[22]:

$$\frac{c_{II}}{d_{II}} = e^{-2i\theta} \frac{(c_I/d_I)e^{2i\tilde{\theta}}[A + i\pi + i\pi\coth(\pi\eta/2)] - [A + i\pi\coth(\pi\eta/2) - i\pi\coth(\pi\tilde{\eta}/2)]}{(c_I/d_I)e^{2i\tilde{\theta}}A - [A - i\pi - i\pi\coth(\pi\tilde{\theta}/2)]}, \tag{2.81}$$

[22]Note the typographical errors in Eq. 14 and Eq. 16 of Ref. [58] which are corrected in Eq. 2.81 and Eq. 2.83.

where

$$A = \frac{1}{2}\ln\left(\frac{\tilde{\gamma}}{\gamma}\right) + \psi_R\left(\frac{i\tilde{\eta}}{2}\right) - \psi_R\left(\frac{i\eta}{2}\right) + i\frac{\pi}{2}\left[\coth\left(\frac{\pi\tilde{\eta}}{2}\right) - \coth\left(\frac{\pi\eta}{2}\right)\right], \qquad (2.82)$$

$\tilde{\theta}$ is the phase of $\Gamma(-i\tilde{\eta}/2)$ (with $\tilde{\eta} = \beta/\sqrt{\tilde{\gamma}}$), and ψ_R is the real part of the Psi function. The function ψ (also called the digamma function) is related to the Gamma function: $\psi(z) = \frac{d\ln\Gamma(z)}{dz}$. c_I and d_I are the coefficients of the Whittaker functions for the electric field solution near the resonance on the high field side. Their ratio is:

$$\frac{c_I}{d_I} = -i\left(\frac{\alpha}{8i\tilde{\gamma}^{3/2}}\right)^{-i\eta}\exp(\frac{\pi\eta}{2})\exp(\frac{4i}{3\alpha}\tilde{\gamma}^{3/2}). \qquad (2.83)$$

The most important result from this calculation can be seen from noting that $|c_I/d_I| = 1$ and hence $|c_{II}/d_{II}| = 1$, which can then be expressed as a complex phase $c_{II}/d_{II} = \exp[i(\pi + \phi)]$. By substituting this expression in Eq. 2.80, it can be shown that the mode conversion coefficient has a minimum of 0 and a maximum of 4 times the Budden result:

$$C(\eta, \phi) = 4e^{-\pi\eta}(1 - e^{-\pi\eta})\cos^2\left(\frac{\phi}{2} + \theta\right). \qquad (2.84)$$

The phase ϕ depends on the details of the inhomogeneous plasma on the high-field-side, but if $\eta = \ln 2/\pi \approx 0.22$ (for which the phase of $\Gamma(-i\eta/2) \approx 0.520\pi$), and the phase $\phi \approx \pm\pi$, then the mode-conversion efficiency can be 100%! Of course, if this is the case for one toroidal mode number, it will probably not be the case for others, so that the average mode-conversion efficiency across all modes will average out to some lower value. Nevertheless, the result that the maximum possible mode-conversion is 4 times the Budden result[23] can be very useful in exploring new regimes for efficient mode conversion.

The mode conversion coefficient C, including all the phase information, is relatively insensitive to small changes in β and γ. However, starting with almost any

[23]This can also be shown by considering a perfectly reflecting boundary on the high-field side of the evanescent layer, which was the inspiration for the internal resonator work [67]. A similar expression was obtained much earlier by Ngan and Swanson (Eq. 202 in Ref. [49]), but only from a single-pass picture which did not properly treat the wave solution as a whole on the HFS. In any case, the reflecting boundary problem leaves the phase undetermined.

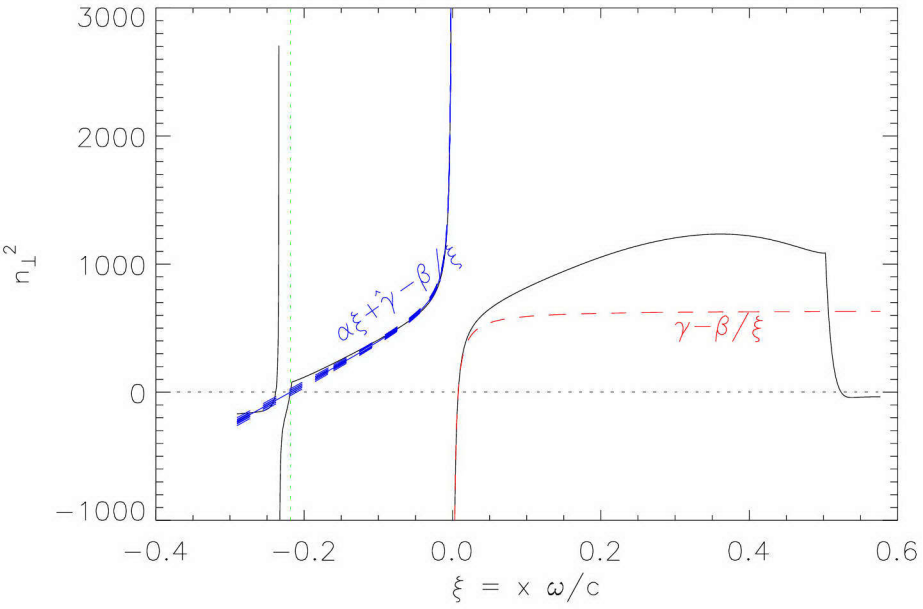

Figure 2-24: The fast wave dispersion relation (solid line) $n_\perp^2 = (L - n_\parallel^2)(R - n_\parallel^2)/(S - n_\parallel^2)$, along with the model potential (dashed line) $n_\perp^2 = Q(\xi)$, given by Eq. 2.73. Also plotted (horizontal dotted line) is the line $n_\perp^2 = 0$; the intersections between the dispersion relation and this line are the cutoffs — the vertical dotted line shows the location of the high-field-side cutoff that forms part of the resonator.

initial value of C, by changing α and $\tilde{\gamma}$ by $\sim 20\%$, C can vary from 0% to 100%. Thus it is important to determine the location of the high-field-side cutoff and the nature of the FW dispersion relation on the HFS as accurately as possible. In practice, a 2% variation in both parameters seems to cover the uncertainty in the fit that is due to irregular profile shape and lack of knowledge about the HFS density edge. Figure 2-24 shows the model potential fit to the ICRF dispersion relation, including the uncertainty on the HFS (Fig. 2-25 is a closer look at the HFS cutoff region). There is approximately a 1 cm variation in cutoff location (45.7 ± 0.5 cm) for a $\pm 2\%$ change in the values of α and $\tilde{\gamma}$.

Using this procedure for the case shown in Fig. 2-23 with $n = 9$ and $m = -1$ yields: $\alpha = 3121.7$, $\beta = 4.944$, $\gamma = 640.5$, and $\tilde{\gamma} = 659.7$, predicting a mode-conversion efficiency of 98%. The range of values from trying $\alpha \times (1 \pm 0.02)$ and $\tilde{\gamma} \times (1 \pm 0.02)$ were 90% to 99%.

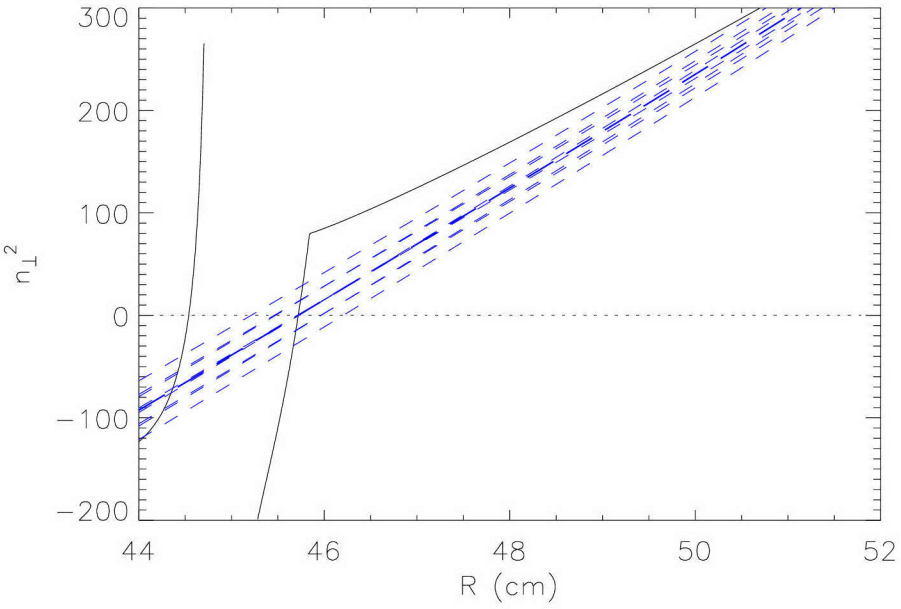

Figure 2-25: The fast wave dispersion relation (solid line) near the HFS $n_\parallel^2 = R$ cutoff, with the model fit, exhibiting the variation that occurs in small changes in α and/or $\tilde{\gamma}$.

Strictly speaking, it is not correct to treat each m_θ number independently, as the m numbers are coupled for a given n because of the toroidal geometry and the non-circular plasma shape (m is only conserved in cylindrical geometry). However, if the inverse aspect ratio a_0/R_0 is small (for C-Mod $a_0/R_0 \sim 1/3$), the m numbers can be treated as approximately independent. The result of running the internal resonator model fitting procedure for a range of m numbers for $n_\phi = 9$ and $n_\phi = 15$ are shown in Fig. 2-26 and Fig. 2-27, respectively. The m-spectrum response reveals an interesting aspect of the plasma's effect on the vacuum spectrum. Although the vacuum spectrum is completely symmetric, power is shifted preferentially into positive m's (as can be seen in Fig. 2-28), because the positive m numbers have a higher coupling factor than the negative m numbers. This introduces a slight up-down asymmetry into the launched FW power spectrum, which may play a role in helping to explain asymmetries observed in mode-conversion scenarios (see Ch. 5).

By adding the results for each m number, weighted by the shifted spectrum, a

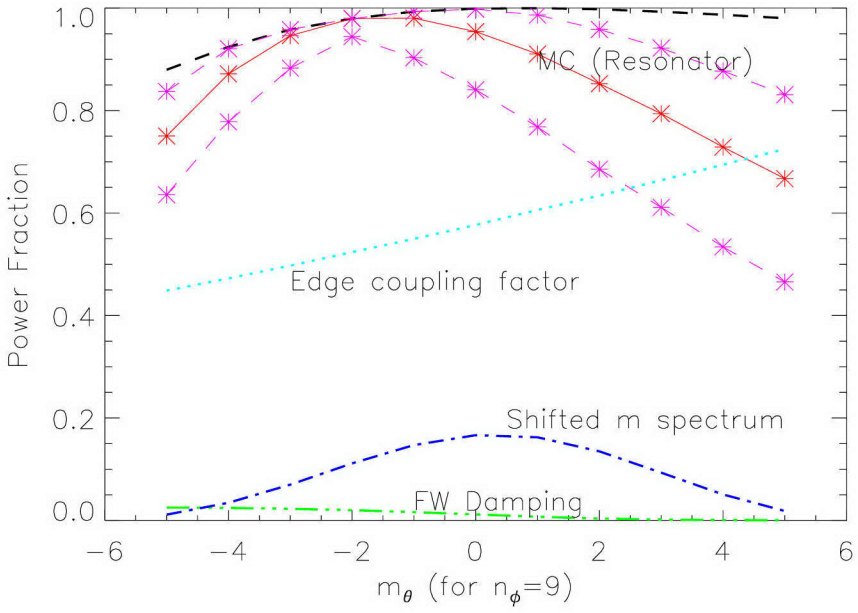

Figure 2-26: Mode-conversion efficiency predictions for the C-Mod antenna m spectrum, for $n_\phi = 9$. The stars (*) connected by the solid line is the MC efficiency prediction, bracketed by the dashed lines which represent the 2% variation in α and $\tilde{\gamma}$. The dashed line above these is the maximum envelope (4 $\mathrm{MC_{Budden}}$). The dotted line is the edge coupling factor, which shows an asymmetry in m number, resulting in the dot-dash line representing the shifted antenna m-spectrum. The lowest dot-dot-dot-dash line is the single-pass damping the fast wave experiences before reaching the MC layer.

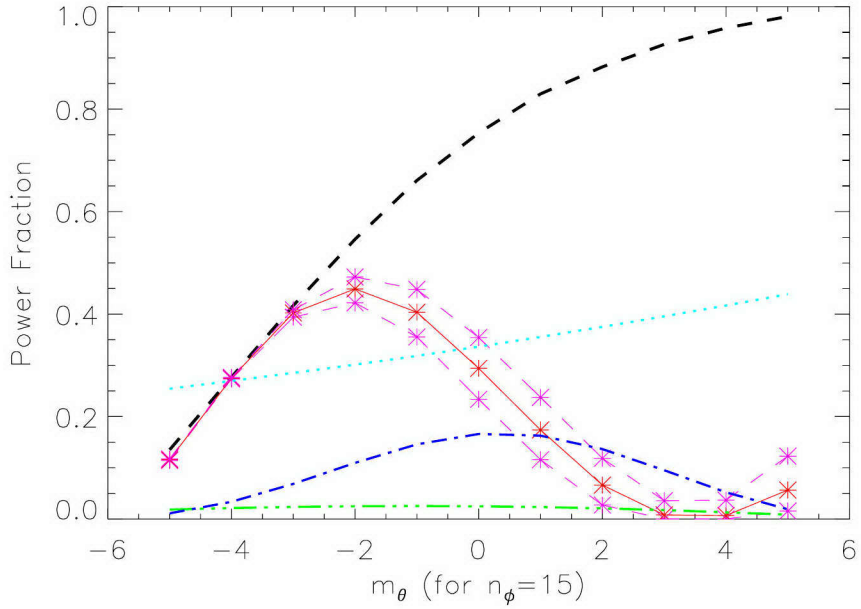

Figure 2-27: The same quantities as in Fig. 2-26 are plotted, but for $n_\phi = 15$.

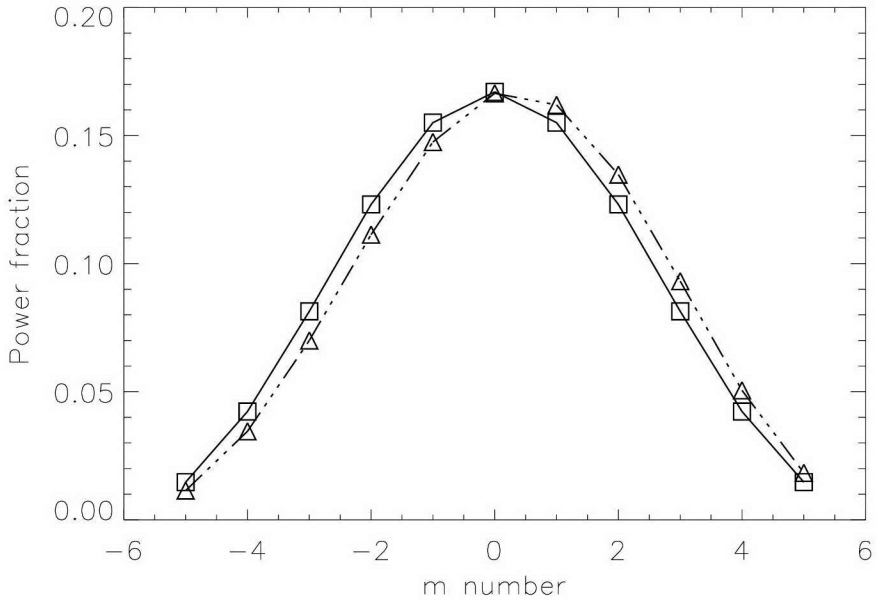

Figure 2-28: The poloidal mode number power spectrum, showing the magnitude squared of the Fourier coefficient f_P for each m number. Squares connected by solid line: vacuum spectrum. Triangles connected by dot-dot-dot-dash line: vacuum spectrum multiplied by edge coupling factor. Both are normalized so that $\sum_m f_P = 1$.

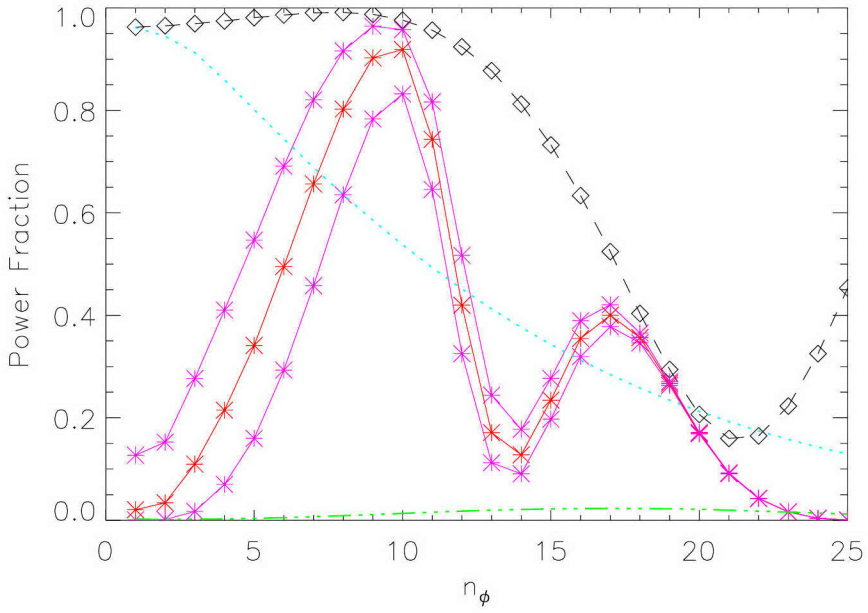

Figure 2-29: The same quantities as in Fig. 2-26 and 2-27 are plotted, but as a function of n_ϕ. The edge coupling factor, which is a monotonically decreasing function of n_ϕ, is arbitrarily normalized.

net result for a given n number can be calculated. The result of this calculation for n numbers from 1 to 25 is shown in Fig. 2-29. Note that this is sufficient to describe negative n numbers in this model, since the only dependency on n and m is through $n_\parallel^2$, for which $(+n, -m)$ and $(-n, +m)$ are equivalent, and $(-n, -m)$ and $(+n, +m)$ are equivalent. Note that the lowest n numbers couple the most effectively into the plasma, but there is not much power at low n due to the $[0, \pi]$ phasing of the two-strap antenna, where the vacuum spectrum peaks at around $n_\phi = 10$. When the information in Fig. 2-29 is combined with the toroidal vacuum spectrum in Fig. 2-21 (by applying the edge coupling factor times the vacuum spectrum as a weighting function when summing the different n numbers), a final answer for this plasma scenario can be calculated. In this case the weighted mode-conversion fraction is 52.4%, ranging from 41.1% to 62.5% with the 2% variation in α and $\tilde{\gamma}$. The weighted mode-conversion envelope (the maximum mode-conversion fraction, ignoring the high-field-side phase information) is 90.8%. The weighted fast wave single pass damping from both ion

cyclotron and electron Landau damping is 1.3%. In this case it does not make much difference, but if the single-pass damping were higher, it would be more accurate to multiply the MC factor by 1 minus the fast wave damping, to account for the loss in power before reaching the mode-conversion layer. These results agree reasonably well with the experimental measurement of the plasma on which this scenario was based (see Sec. 4.4.1 for all the measurements compared to this theory), for which the power fraction absorbed by electrons through electron Landau damping of the mode-converted IBW was estimated as $48.5 \pm 5.8\%$.

Figure 2-29 shows the effects of favorable and unfavorable phase in the high-field-side resonator. The MC efficiency rises and falls with n number. This is due to the $\cos^2(\phi/2 + \theta)$ factor in Eq. 2.84. Variation in many other factors will also produce this characteristic sinusoidal (bounded by the maximum envelope) behavior: density (see Fig. 5-3), density profile shape, ion species concentration, magnetic field, etc.

At low minority concentration, so that the MC layer is near the minority cyclotron resonance, it is possible that the internal resonator model theory may not apply. This would be the case if the Doppler-broadened minority cyclotron resonance begins to overlap the mode conversion region near $n_\parallel^2 = S$. The Doppler-broadened cyclotron resonance width is approximately [34]:

$$\Delta = \frac{k_\parallel v_{\mathrm{thm}} R}{\sqrt{2}\omega}, \tag{2.85}$$

where R is the tokamak major radius and v_{thm} is the thermal velocity of the minority ion species. From Eq. 2.85, it can be seen that this overlap may occur for large $k_\parallel$ or large minority tail temperature.

For example, two different n_ϕ numbers can produce very different results, for a plasma with parameters the same as in Fig. 2-24 except that $n_{\mathrm{He3}}/n_e = 0.08$ and the minority ^{3}He temperature is the same as the majority. Figure 2-30(a) shows the 1st order $k_\perp \rho$ finite Larmor radius (FLR) dispersion relation for the FW and IBW, with $n_\phi = -11$ and $m_\theta = 2$. The FW and IBW wave numbers coincide, and the predicted MC efficiency is 66%. However, by changing n_ϕ from -11 to -24 as in Fig. 2-30(b), the minority resonance has destroyed the possibility of mode conversion — the FW and

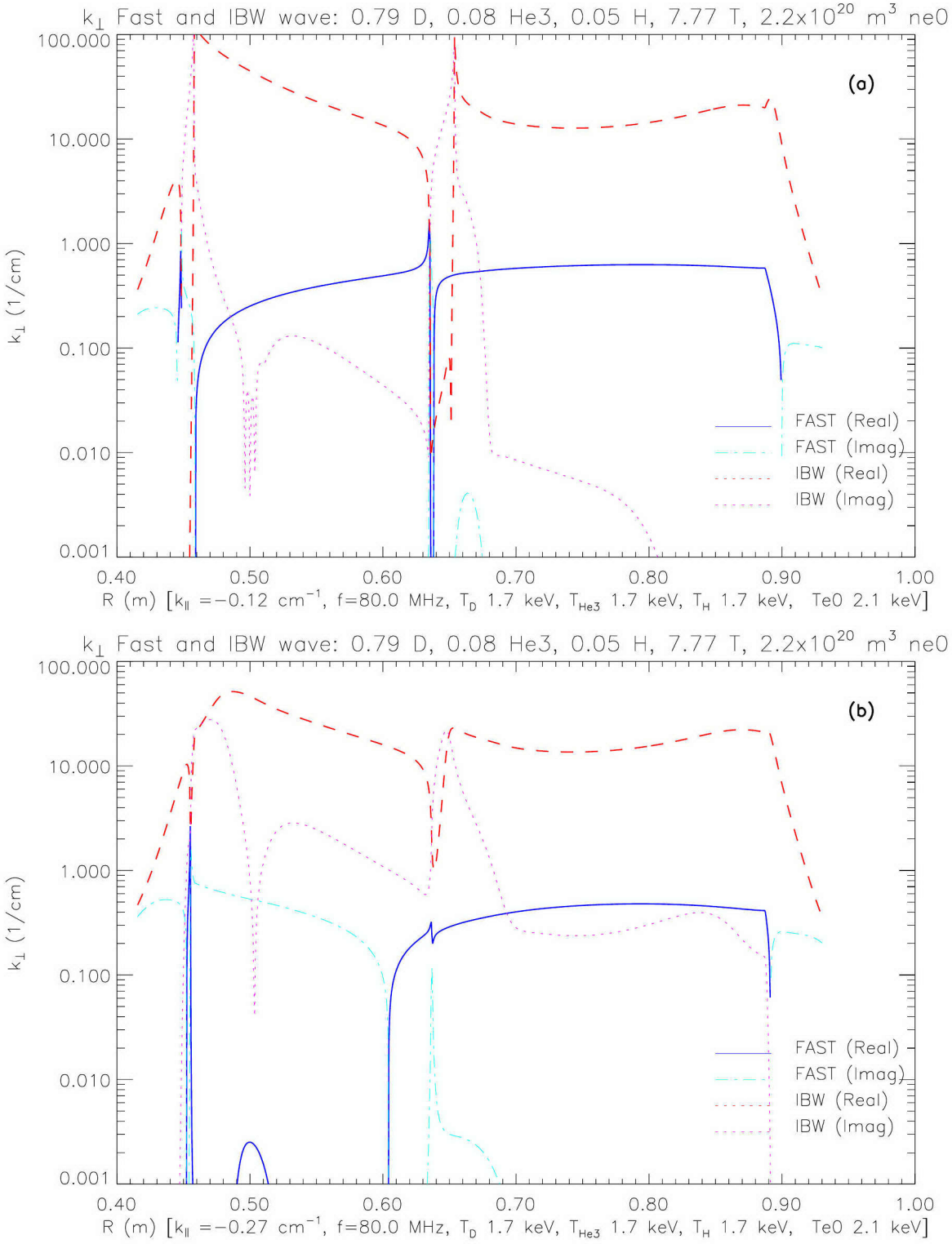

Figure 2-30: The FLR dispersion relation showing the FW (solid line: real part, dot-dash line: imaginary part) and the IBW (dashed line: real part, dotted line: imaginary part). (a) $n_\phi = -11$, $m_\theta = 2$, ($k_\parallel$ at the low-field-side edge is -0.12 cm^{-1}). (b) $n_\phi = -24$, $m_\theta = 2$, ($k_{\parallel\,\mathrm{LFS}}$ = -0.27 cm^{-1}).

IBW do not coincide. In this case, no matter what the cold plasma internal resonator model might predict, the MC efficiency is taken to be zero.

An example of the effect of high minority temperature is shown in Fig. 2-31, which corresponds to the same parameters as Fig. 2-30(a), but with 5% ^{3}He. In Fig. 2-31(a), the minority temperature is 1.72 keV (same as the majority) and the predicted MC efficiency is 86%. However, by increasing the ^{3}He temperature to 10 keV, the FW imaginary part has increased and the FW and IBW no longer coincide. The cold plasma internal resonator model would still predict 86% efficiency, but by using hot plasma knowledge, the MC power for this case would be set to zero.

The theory outlined in this section can be used to explore new regimes for favorable fast wave to ion Bernstein wave mode conversion, and predict approximately how much power can be expected to appear in the IBW. Because it is based mostly on analytic expressions, an answer can be produced fairly quickly, and it can even be used for between-shot analysis, in order to guide mode conversion experiments on the tokamak.[24]

2.6 TORIC: a full-wave ICRF code

In order to compare experimentally measured quantities in a toroidal device to theory, it is often insufficient to only consider one-dimensional models as have been discussed so far in this chapter. The shape of the metal chamber and the last closed flux surface has important implications for the boundary conditions of the RF waves. Yet calculating the electric field solution in toroidal geometry for the full electromagnetic dispersion relation is still computationally out of reach[25]. However, with appropriate approximations for the ICRF regime, a simpler model can be solved in a reasonable amount of time. The ICRF code TORIC [23, 24], written by Marco Brambilla at IPP-Garching, and now routinely run at MIT, includes toroidal geometry in the wave

[24]For those readers with access to the C-Mod computer cluster, an interactive program can be run in IDL which includes the FW and IBW dispersion relations, mode conversion, and the internal resonator model at USER10:[MELBY.IDL]RF_SCENARIOS.PRO (run the module "gui").

[25]At Oak Ridge National Laboratories, there has been a code developed which approaches this ideal [75, 76], but which still has difficulties and requires a large supercomputer.

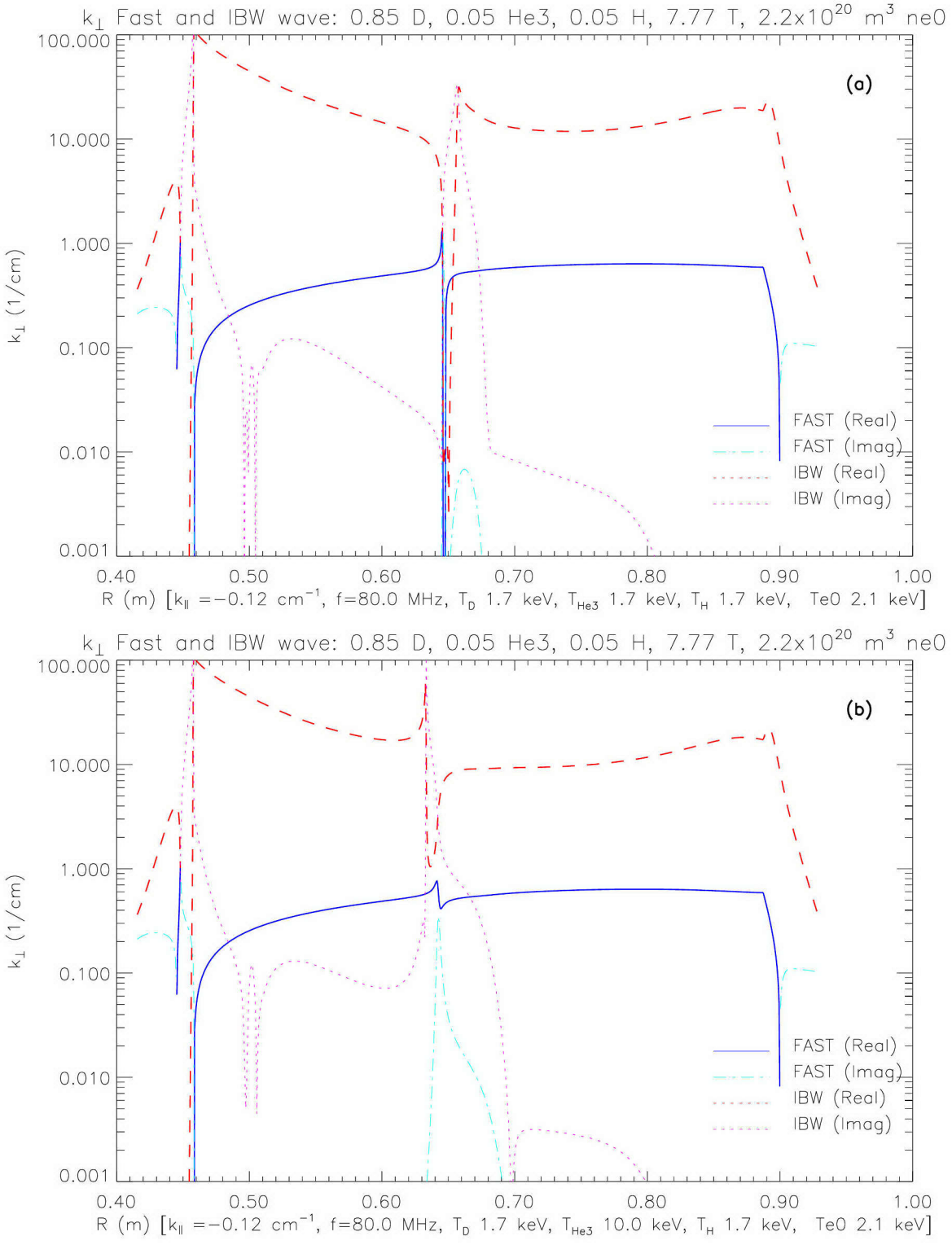

Figure 2-31: The FLR dispersion relation showing the FW (solid line: real part, dot-dash line: imaginary part) and the IBW (dashed line: real part, dotted line: imaginary part). (a) $T_{\mathrm{He3}} = 1.72$ keV. (b) $T_{\mathrm{He3}} = 10$ keV.

equations in order to solve for both fast waves and IBWs (the ion-ion hybrid wave and the IBW associated with $\omega = 2\Omega_i$) in a tokamak.

The dispersion relation used is a $k_\perp \rho_i < 1$ expansion, but it is connected to an asymptotic form for large $k_\perp \rho_i$, that has been shown to agree quite well with the full electromagnetic dispersion relation in most instances [24, Sec. 7.3]. The wave equations have source terms consisting of a zero-order and second-order (in $k_\perp \rho$) plasma current, and an imposed antenna current. The equations are Fourier transformed into toroidal modes n and poloidal modes m, solved, and then inverse-transformed into real space (involving the inversion of a very large, block-diagonal matrix). The coordinate system used in the code, (ψ, η, ζ), varies with position, because it is oriented to the local magnetic field. ψ is the radial coordinate perpendicular to magnetic flux, ζ is tangent to the total magnetic field, and η is orthogonal to ζ, lying in the magnetic surface. The electric field solution the code returns as output is E_ζ, E^+, and E^-, where E^+ and E^- are the LHCP and RHCP components, respectively (the analogies in cartesian coordinates are defined in Eq. 2.33 and Eq. 2.34). E^+ and E^- can be expressed as linear combinations of E_ψ and E_η (see Eq. C.1).

Each component of the electric field solution in toroidal geometry E_α, where α could stand for ψ, η, or ζ, is assumed to have a form:

$$E_\alpha = \sum_{n_\phi=-\infty}^{+\infty} A_{n_\phi} e^{i n_\phi \phi} \sum_{m_\theta=-\infty}^{+\infty} E_\alpha^{m_\theta}(n_\phi;\psi) e^{i m_\theta \theta}, \tag{2.86}$$

where θ is the poloidal angle and ϕ is the toroidal angle. The factor A_{n_ϕ} is some complex weighting factor to be determined from the antenna spectrum (which depends on the toroidal structure and phasing of the antenna) in order to properly combine the different toroidal mode number solutions. This factor is not calculated by TORIC, but can be determined by examining many toroidal mode solutions and matching to an antenna spectrum (see Sec. 5.5.5 for an example of 12 modes run for the same plasma scenario). Currently, there must be one TORIC run for each toroidal mode number solution. Because of the assumed toroidal symmetry, the n_ϕ modes can be solved for independently. The same cannot be said for the m_θ modes, because the curvature in the toroidal direction and the non-circular cross-section couple the different poloidal

modes together. Because of the large computational cost in running TORIC, usually only the dominant toroidal mode in the antenna spectrum is solved for, which is usually sufficient to exhibit the character of the full solution. The infinite sum in poloidal mode numbers is truncated to include as many m_θ numbers as needed to resolve the short-wavelength features in the electric field solution (or as many as the available memory and disk space allow). For example, to resolve a $k_\perp \rho_i \sim 1$ wave half-way from the center at $r/a \sim 0.5$, the number of poloidal modes needed can be estimated as follows: let $k_\perp \sim m/r$ with $k_\perp \rho_i \sim 1$ so $m \sim r/\rho_i$. With $r = 10$ cm and $\rho_i = 0.1$ cm, this indicates that mode numbers m_θ from -100 to +100 should be kept.

The memory required for a TORIC run solving for one toroidal mode number scales linearly with the number of radial elements, and with the square of the poloidal mode numbers retained in the sum. To date, the largest number of modes $N_m = 2m_{\max} + 1$ run while retaining sufficient numerical resolution in the radial grid (240 radial elements) is 255 ($-127 \leq m \leq 127$, including $m = 0$). The number of poloidal angle slices in the spatial grid must be an integral power of 2 and should be at least as large as $4m_{\max}$ in order to resolve the highest poloidal mode numbers. Large memory runs have been done on the NERSC (see Sec. 2.4.1) supercomputers, and on the Digital Equipment Corp. (DEC) *Alpha* workstations at the Alcator C-Mod computer cluster using the frontal method (see Sec. 2.6.1).

TORIC can solve for both the fast wave and IBW at the same time, and can predict the amount of power mode-converted from the FW to the IBW which is subsequently damped through electron Landau damping. The code was recently upgraded to improve the treatment of Landau damping [23]. Although the code attempts to distinguish between the different Landau damping sources, it is often difficult to separate the direct electron Landau damping of the fast wave from the Landau damping of the IBW in the vicinity of the mode-conversion layer, so the total electron Landau damping predicted by the code is used to compare to experimental results (see Ch. 4 and Ch. 5). An example of the electric field solution and the damping predicted by TORIC for the D(^{3}He) plasmas at 7.8 T discussed in this chapter is shown in Figs. 2-33 – 2-35, for which $n_{\mathrm{He3}}/n_e = 0.24$.

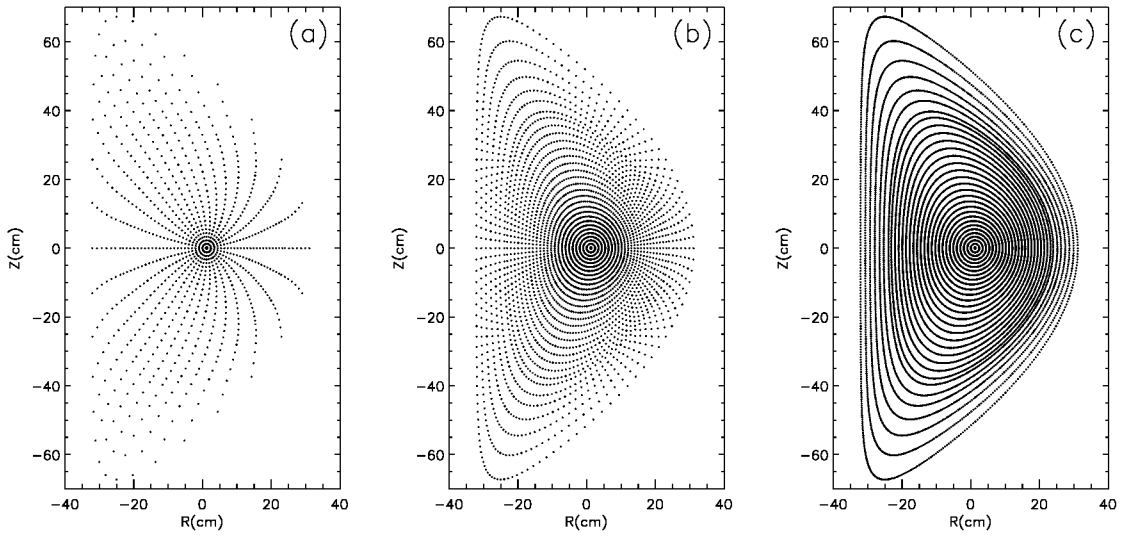

Figure 2-32: The spatial grid set up by TORIC to solve for the RF electric field and 2-D power deposition profiles, showing every poloidal point but only every 8th radial magnetic flux surface. (a) 32 points in θ for 15 m_θ modes, (b) 128 points for 63 modes, (c) 512 points for 161 modes.

The importance of including enough poloidal modes in the Fourier expansion is also illustrated by comparing the results for three runs, using 15, 63, and 161 poloidal modes. The same number of radial elements was used for each run, representing 243 magnetic flux surfaces (50 points to represent the vacuum region between the plasma/vacuum interface and the vessel wall). 32 poloidal slices were used for the 15 mode case, 128 for the 63 mode case, and 512 for the 161 mode case. The spatial grids for these runs are shown in Figs. 2-32(a)–(c). The vessel wall in the default TORIC model follows a flux surface outside the plasma with an elongation and triangularity to approximate the C-Mod shape. The magnetic equilibrium is usually represented by a fairly simple model (see Appendix C). TORIC has been upgraded through the work of Jeff Spaleta at PPPL and Paul Bonoli at MIT to use more realistic magnetic equilibria obtained from the magnetic equilibrium code EFIT, but the simpler model

has been used in this thesis.

The electric field solution for the component E^- (RHCP part) is shown in Fig. 2-33. Only the inner 94% of the flux surfaces are plotted, due to problems with the electric field at the edge which, if plotted, would mask the nature of the field in the center. In the current version of TORIC, the electric field sometimes has large spikes in amplitude or discontinuities at the plasma/vacuum interface, especially with high numbers of poloidal modes. Note that the mode conversion region near $R = -10$ cm becomes better resolved as the number of poloidal modes kept is increased. This is where the fast wave converts energy into the ion Bernstein wave, which subsequently Landau damps on electrons. A close-up of the region of Landau damping is shown in Fig. 2-34. Again, note that as the number of poloidal modes is increased, this region becomes better resolved. With only 15 poloidal modes, this region is up/down symmetric, with features following flux surfaces. Once 161 poloidal modes are used, the true character of the mode conversion region is revealed, with up/down asymmetries apparent. Also, the region of strong damping can be seen to be spread out in major radius. This will be further elaborated upon in Ch. 5, with implications for experimental observations.

The 2-D power deposition profiles for the various damping mechanisms can be integrated in the minor radial direction to obtain a 1-D profile as a function of flux surface (in TORIC the flux variable is the minor radius divided by the edge radius). This is shown in Fig. 2-35, illustrating the two dominant damping mechanisms: ^{3}He minority ion cyclotron damping (Fig. 2-35(a)), and total electron Landau damping, both from the fast wave and the IBW (Fig. 2-35(b)). The 1-D profile can then be integrated, yielding a prediction of the amount of power deposited in the plasma through each specific mechanism. With only 15 poloidal modes, there is spurious minority cyclotron damping, due to E^+ "spillover" along flux surfaces which intersect the ion cyclotron resonance layer. As the number of poloidal modes is increased, the spurious damping is reduced. The Landau damping correspondingly increases. A poloidal mode number scan for this scenario has been performed by Paul Bonoli, who has worked with Marco Brambilla in order to improve and expand TORIC. The results

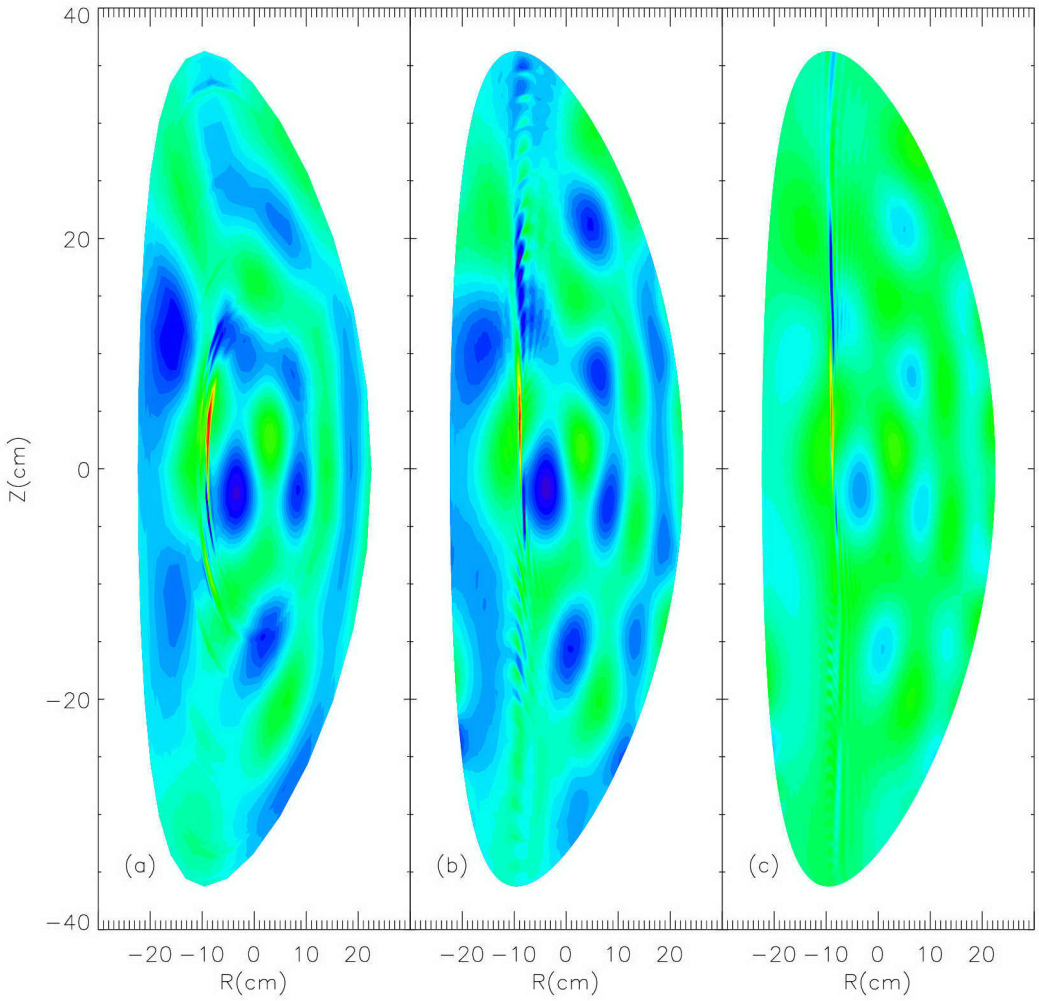

Figure 2-33: The electric field component E^- in a D(^{3}He) plasma at 7.8 tesla, 24% ^{3}He, as computed by TORIC for three different sets of poloidal mode numbers kept in the Fourier expansion. This is a contour plot, showing the positive and negative values of E^- together (Note: the aspect ratio has not been preserved, in order to show in more detail the mode conversion region). (a) $-7 \leq m \leq 7$, (b) $-31 \leq m \leq 31$, (c) $-80 \leq m \leq 80$.

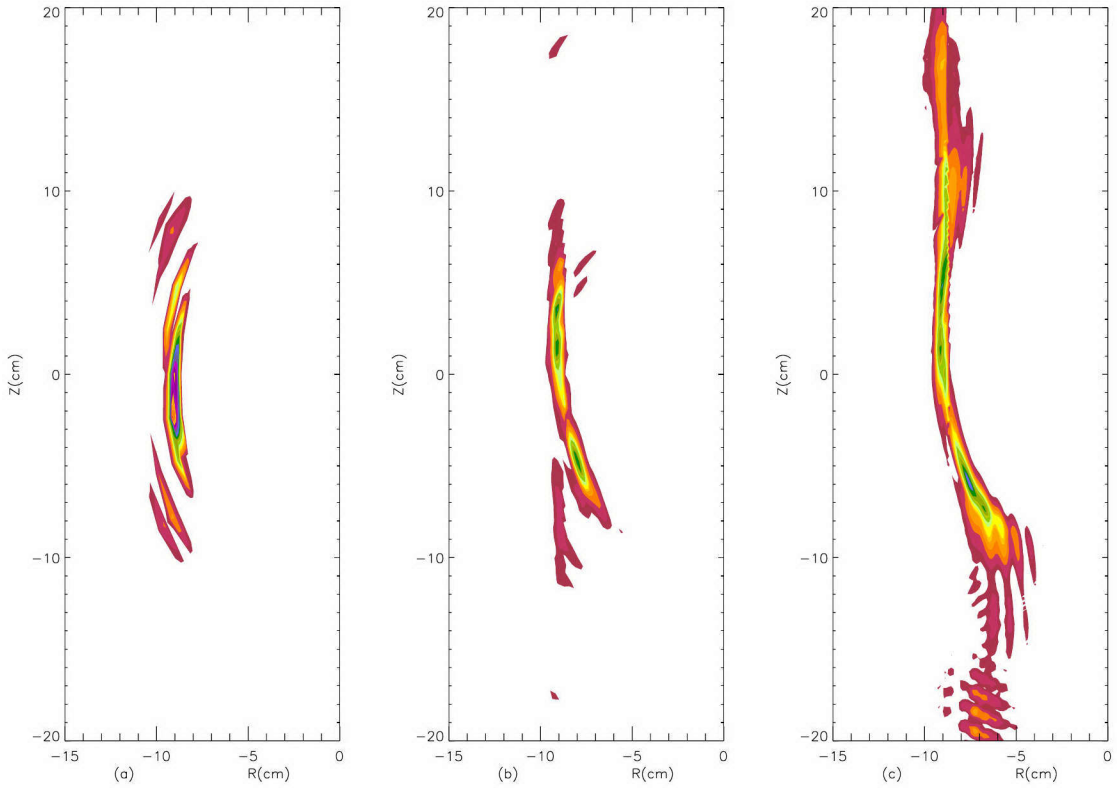

Figure 2-34: A contour plot of the total computed electron Landau damping in a D(^{3}He) plasma at 7.8 tesla, as computed by TORIC for three different sets of poloidal mode numbers kept in the Fourier expansion. (a) $-7 \leq m \leq 7$, (b) $-31 \leq m \leq 31$, (c) $-80 \leq m \leq 80$.

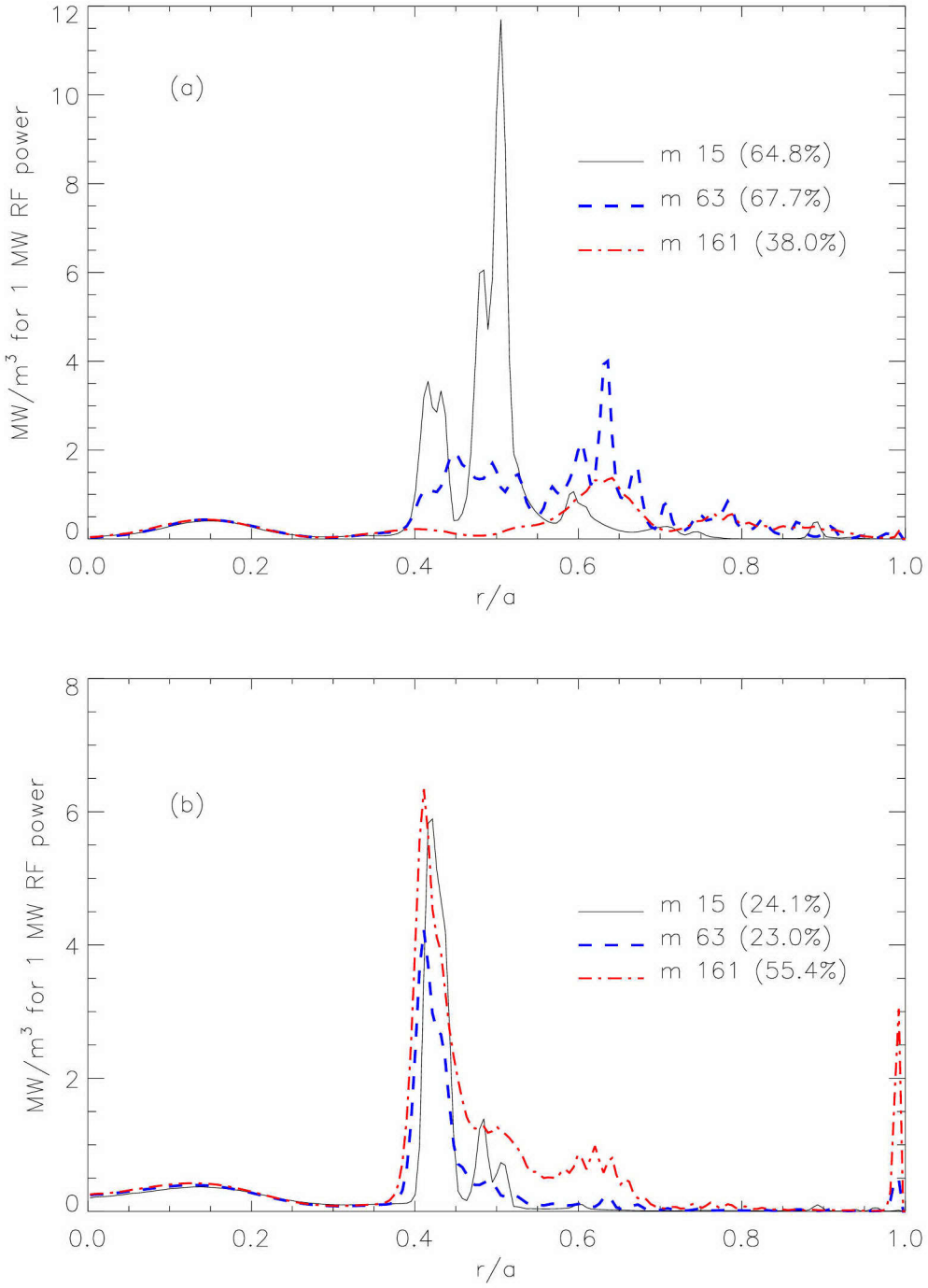

Figure 2-35: Power deposition profiles from TORIC runs for a D(^{3}He) plasma at 7.8 tesla and 24% ^{3}He. (a) Power density profile of minority ^{3}He ion cyclotron damping. (b) Power deposition to electrons through Landau damping. Simulations are shown with three different numbers of poloidal modes. Solid line: $-7 \leq m \leq 7$; Dashed line: $-31 \leq m \leq 31$; Dot-Dash line: $-80 \leq m \leq 80$. Next to each m label is the integrated power share of the total incident 1 MW of RF power for the corresponding damping mechanism.

N_m	N_T	P_D	P_{He3}	P_{cld}
15	32	11.09%	64.83%	24.08%
31	64	10.10%	64.80%	25.08%
63	128	9.32%	67.70%	22.98%
127	256	7.39%	47.54%	45.07%
161	512	6.55%	38.00%	55.40%

Table 2.2: Power distribution for a D(^{3}He) plasma at 7.8 T, 24% ^{3}He, showing the shift as the number of poloidal modes is increased. N_m is the number of poloidal modes kept, N_T is the number of points in the theta direction (the number of poloidal slices), P_D is the fraction of the incident power damping on the fundamental deuterium ion cyclotron resonance, P_{He3} is the fraction damping on the (minority) helium-3 cyclotron resonance, and P_{cld} is the total electron Landau damping fraction.

are shown in Table 2.2, which indicates that at 161 poloidal modes, the solution is nearly converged, but that when larger runs become possible in the near future, more than 161 modes should be used.

TORIC is a useful tool for exploring the physics of ICRF waves in a tokamak geometry. It has been used to study the mode conversion of FW to IBW, and the partitioning of deposited power to various plasma components. However, because of the large memory and size requirements for sufficient resolution of the IBW, the full antenna spectrum has not yet been simulated. There are plans (and ongoing work) which should make the running of TORIC possibly hundreds of times faster, which will allow the exploration of a wide range of plasma parameters.

2.6.1 Running TORIC on the Alcator C-Mod computer cluster

The most computationally intensive step in the TORIC code is the inversion of a very large complex matrix, the size of which is proportional to the square of the number of poloidal modes. Recently, the newer version of TORIC that includes the more correct treatment of electron Landau damping has been modified by Paul Bonoli to run using a frontal method, whereby a large portion of this computation can be done on disk rather than entirely in memory. This allows more poloidal mode numbers to be run

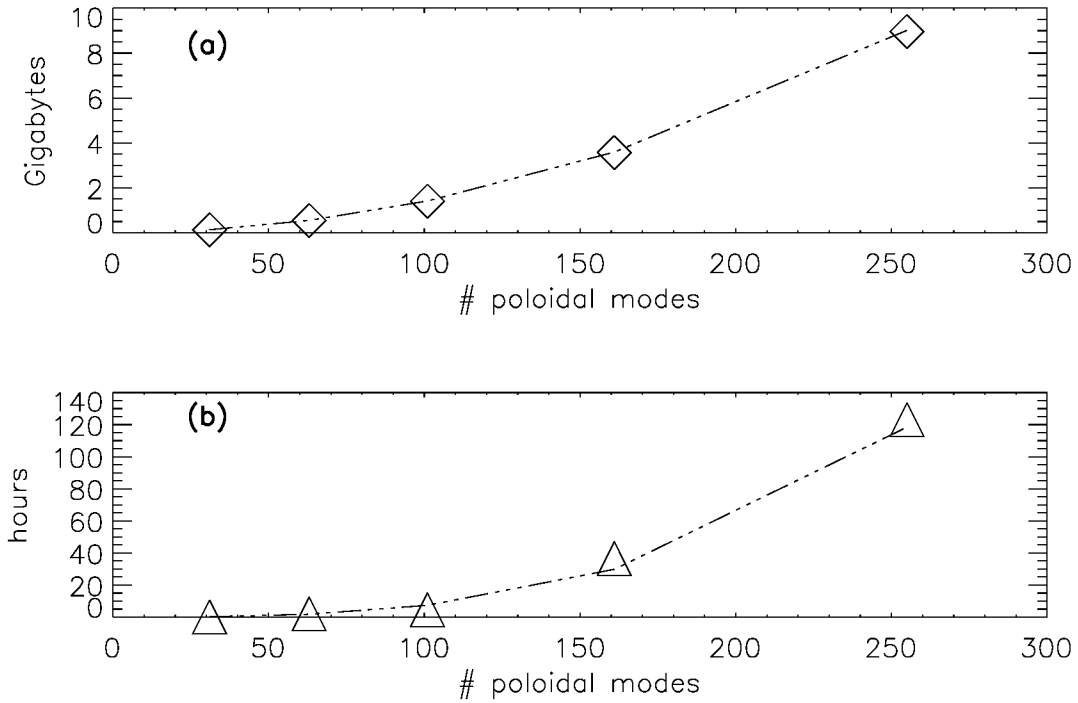

Figure 2-36: Scaling of memory and time requirements as a function of poloidal modes kept in TORIC runs. (a) Size of the temporary file in gigabytes (1 gigabyte = 10^9 bytes). The dot-dot-dot-dashed line is a geometric fit: $1.386 \times 10^{-4}\, N_m^2$ (b) Actual run-time (on an *Alpha* workstation), in hours. The line is an approximate geometric fit: $7.14 \times 10^{-6}\, N_m^3$.

than before (even more than on the NERSC Cray supercomputer, which was limited to ~161 modes). Simulations with 161 poloidal modes can now be routinely run, completing the calculation in about 36 hours (for one toroidal mode). Figure 2-36 shows the scaling of the size of the temporary matrix inversion file that is created on disk and the time required to run, as a function of the number of poloidal modes kept in the Fourier expansion.

Recently, a new Beowulf cluster of ~36 computers was installed at the Plasma Science and Fusion Center in order to run large computer codes and quickly perform between-shot analysis. In the future, TORIC may be able to take advantage of this cluster to run even higher resolution runs very quickly. To take full advantage of the multiple processors in the cluster, TORIC will need to be reconfigured so that many

parts of the code (or at least the large matrix inversion) can be run in parallel on many processors.

2.7 Summary of Chapter 2

The Alcator C-Mod antennas are designed to heat the plasma by launching the fast magnetosonic wave (FW) into the plasma. The theory of plasma waves in a cold, homogeneous plasma is sufficient to show the presence of resonances and cutoffs in the dispersion relation of the FW. The CMA diagram can be used as a tool to examine the effects of an inhomogeneous plasma (by treating each point along a density and magnetic field profile as locally homogeneous) on the wave behavior for a wide range of plasma parameters. At a wave resonance, the hot plasma dispersion relation is needed to resolve the infinity in the wavenumber. The presence of wave damping can also be demonstrated from the hot plasma dispersion relation. The resolution of the ion-ion hybrid resonance for the FW indicates that another mode can be excited in the plasma — an ion Bernstein wave. A return to cold plasma theory using second order differential equations can predict the efficiency with which the FW converts to an IBW. An "internal resonator" model considering the effects of the high-field side cutoff for the FW is an improvement over the simple Budden tunneling theory for mode conversion efficiency predictions. Finally, all of these effects can be treated simultaneously in a full-wave numerical ICRF code such as TORIC, which solves for the RF electric field (and the damping on electrons and ions) in the plasma.

Chapter 3

Phase Contrast Imaging

Chapter 2 presented the theory of electromagnetic waves in a hot, magnetized plasma, especially the fast magnetosonic wave and the mode-converted ion Bernstein wave. In order to test the theory, and find areas that need improvement and deeper exploration, measurements of the wave properties need to be made. These include the wavelength, the electric field amplitude, and the damping rate. It is extremely difficult to measure the RF wave electric field directly in the core of a hot (several keV) plasma. However, the wave fields also drive electron density fluctuations. There is a long history of diagnostic tools that are able to measure density fluctuations in fluids and in plasmas. Phase Contrast Imaging (PCI) is a sensitive method that is particularly well-suited to measure electron density fluctuations in a hot plasma.

Phase Contrast Imaging [77, 78, 79] relies on the interference of scattered and appropriately phase-shifted unscattered radiation passing through a phase object, such as a plasma with electron density fluctuations causing the scattering. It is sometimes referred to as "internal reference interferometry", because it is similar to laser interferometry where a beam is split with one path passing through the plasma as the signal and another beam outside the plasma as the reference. In PCI, the entire beam is sent through the plasma, the reference is the average of the whole beam, and the signal is obtained from a small portion of the beam. The PCI system on the Alcator C-Mod tokamak uses a 10.6 μm wavelength CO_2 laser, expanded to a width of 15 cm, passing through the central portion of a 42 cm wide plasma. After passing

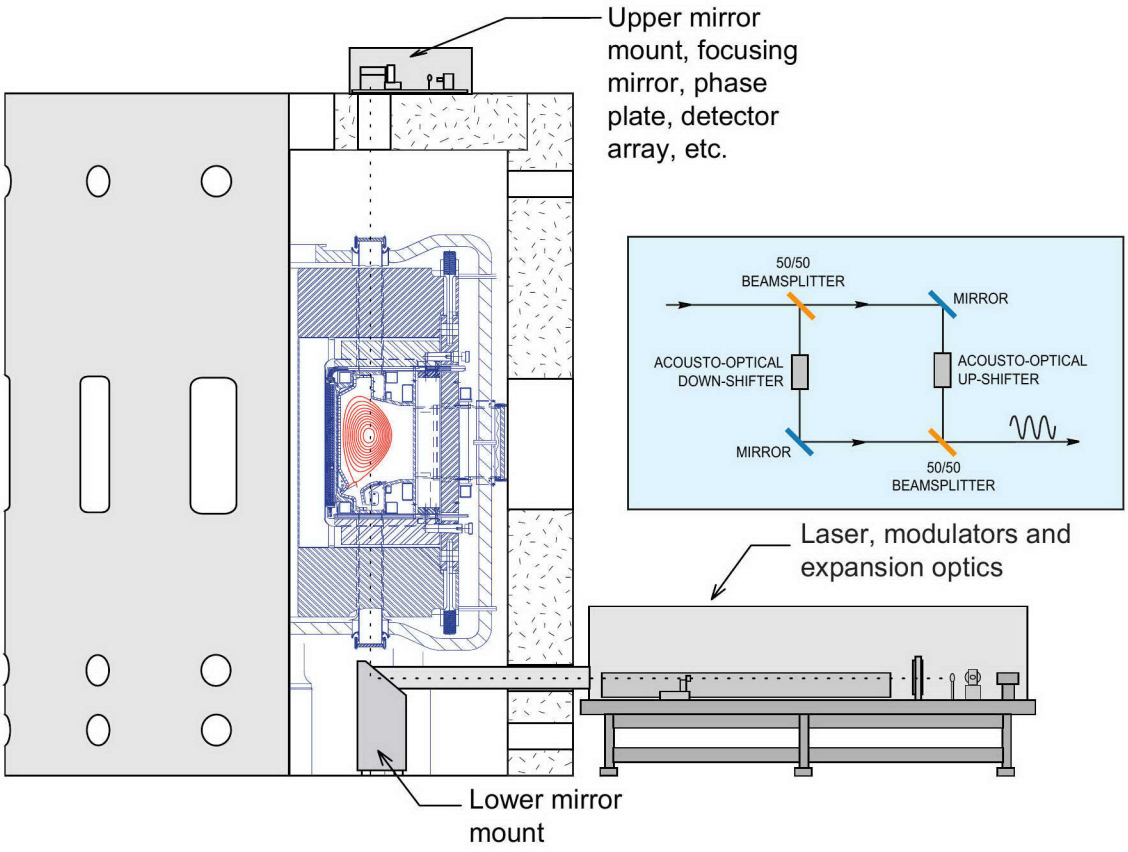

Figure 3-1: Cutaway view of the C-Mod tokamak and the PCI system. Inset shows how the laser intensity is modulated at RF frequencies. The dotted line is the path of the laser. Note that the lower and upper mirror mounts are physically isolated from the machine, to reduce vibrations in the system. The cross-hatched thick outer layer is a concrete "igloo" used to attenuate the neutron flux coming from the machine during a discharge.

through the plasma and the rest of the system, the infrared laser light is imaged onto a 12 element (soon to be upgraded to 32 elements) HgCdTe photoconductive linear array. The layout is shown in Fig. 3-1.

A density perturbation in the plasma can affect the phase and intensity of the laser. If the laser beam encounters a density perturbation which is purely sinusoidal and propagating perpendicular to the beam, the laser electric field can then be represented by a uniform intensity background with some phase variations and can be decomposed into three plane waves: the unscattered wave, and the left and the right scattered waves of small amplitude (see Fig. 3-2). Just after passing through a density

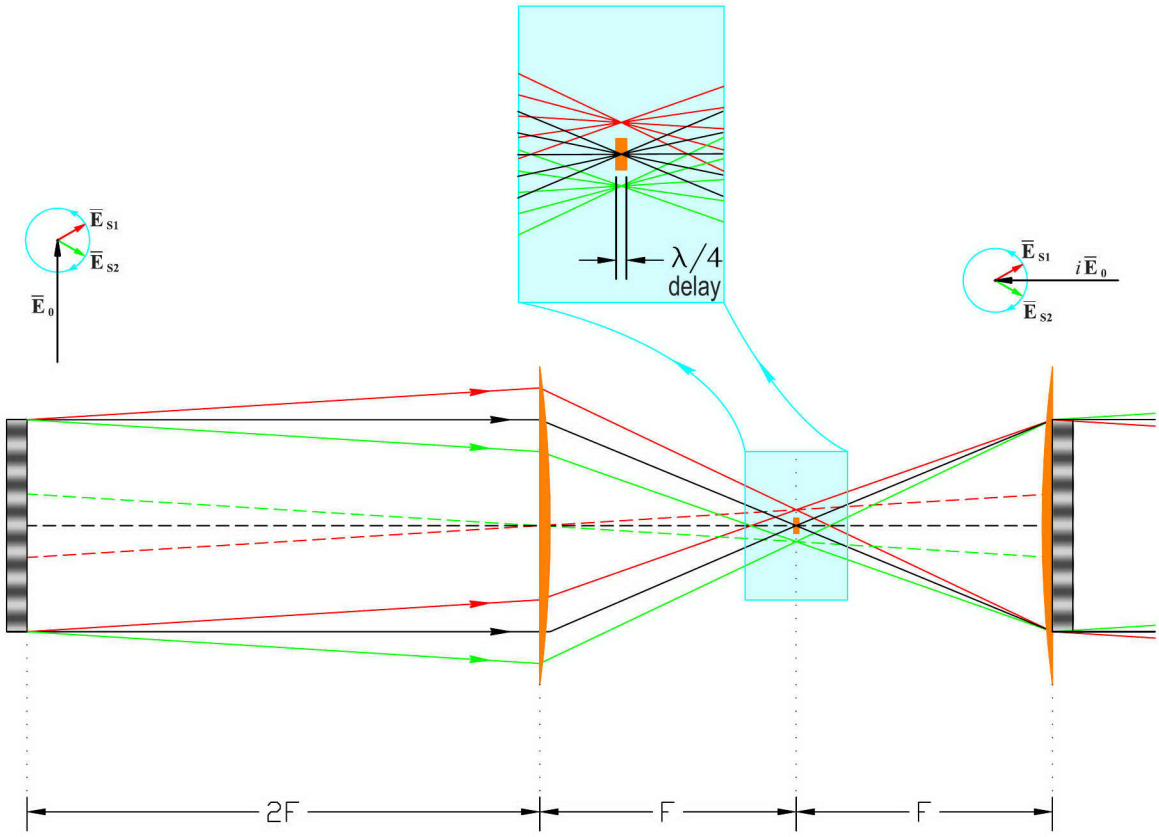

Figure 3-2: The physical basis of Phase Constrast Imaging. On the left is shown a plasma layer with a sinusoidal density perturbation, and on the right is the image of the plasma, after passing through the PCI system. The phase shift shown in the center of the figure is accomplished with a groove in a reflecting plate.

perturbation, the (complex) amplitude of the laser field can be written as the sum of these three waves:

$$E_1 = E_0 + E_0\frac{i\Delta}{2}e^{ik_p x} + E_0\frac{i\Delta}{2}e^{-ik_p x}, \tag{3.1}$$

where the x direction is along the density perturbation (across the beam) and the z direction is parallel to the laser beam. Δ is the amplitude of the small phase variation (see Eq. 3.8) introduced by the density perturbation of wavenumber k_p. The phase shift Δ alters the original laser intensity[1] $I_0 = |E_0|^2/(2\mu_0 c)$ only to second order in

[1]Taking the laser intensity to be the magnitude of the time-averaged Poynting flux, $I = \langle S \rangle = \frac{1}{2}\mathrm{Re}\frac{E\times B^*}{\mu_0} = \frac{|E|^2}{2\mu_0 c}$, where the phase velocity has been taken to be c, to very good approximation (see Eq. 3.6).

Δ:

$$I_1 = |E_1|^2/(2\mu_0 c) \simeq I_0(1 + \Delta^2 \cos^2 k_p x). \tag{3.2}$$

A special phase plate can make the intensity variation more easily detectable. After leaving the plasma the laser beam is focussed by an off-axis parabolic mirror onto a reflective plate with a partially reflecting narrow groove where the main beam spot is focussed. The groove is $\lambda/8$ deep ($1.325\ \mu m$) so that the main beam travels $\lambda/4$ (90° of phase) farther than the scattered portions of the beam. The extra distance travelled causes the contribution of the scattered light to be in phase with the unscattered light when imaged on the detectors. The electric field of the laser can now be written as:

$$E_2 = iE_0 + E_0\frac{i\Delta}{2}e^{ik_p x} + E_0\frac{i\Delta}{2}e^{-ik_p x}, \tag{3.3}$$

where the unscattered field has been phase-shifted by $\pi/2$. Now the lowest order laser intensity modification introduced by the density perturbation is linear in Δ,

$$I_2 = |E_2|^2/(2\mu_0 c) \simeq I_0(1 + 2\Delta \cos k_p x), \tag{3.4}$$

and can be more easily detected to indicate the presence of density fluctuations in the plasma.

The Argand diagrams on the left and right of Fig. 3-2 are meant to represent the electric field vectors of the unscattered and scattered portions of the beam. On the left, just after passing through a thin layer of density perturbation which varies sinusoidally across the beam, the electric field of the unscattered beam (long vertical arrow) remains unchanged, but the right and left scattered portions of the beam (small diagonal arrows) point at different angles depending on the position x along the perturbation. However, they always sum to a small vector perpendicular to the unscattered vector. The net effect is that as one moves along the perturbation, the laser electric field would rock back and forth slightly, changing phase, but the amplitude would remain nearly constant. On the right, after the unscattered beam has reflected off the phase plate, it has been rotated 90° in phase. So now as one moves along the (reversed) image of the perturbation, the small vector which is the sum of the scattered portions is always parallel or anti-parallel to the large unscattered

vector, so the net effect is that the laser electric field vector changes in magnitude according to how much phase variation there was in the original perturbation.

To calculate the phase variation Δ introduced by plasma density fluctuations, one can start with the dispersion relation for the laser electromagnetic wave. Because the laser beam propagates mostly perpendicular to the background magnetic field, it can be treated as a mixture of the O-mode and X-mode of propagation (see Ch. 2.1.1), the exact mix depending on the laser polarization. Because of the high frequency of the laser ($\omega_{CO_2} = 1.78 \times 10^{14}$ rad/sec), $\omega/\omega_{ce} \ll 1$ and $\omega/\omega_{pe} \ll 1$ for C-Mod plasmas, so both the O-mode dispersion relation $n_\perp^2 = P$ and and the X-mode dispersion relation $n_\perp^2 = RL/S$ reduce to the same approximate dispersion relation:

$$n^2 \simeq 1 - \frac{\omega_{pe}^2}{\omega^2}. \tag{3.5}$$

Even for very high densities of $5 \times 10^{20}\,\mathrm{m}^{-3}$, the plasma frequency is still much lower than the laser frequency ($\omega_{pe}^2/\omega^2 = 5 \times 10^{-5}$), so that in the solution for the laser wavenumber k, the plasma density can appear linearly:

$$k = \frac{\omega}{c}\sqrt{1 - \frac{\omega_{pe}^2}{\omega^2}} \simeq \frac{\omega}{c}(1 - \frac{\omega_{pe}^2}{2\omega^2}). \tag{3.6}$$

The propagation of a small portion of the laser beam through the plasma can be represented by a plane wave proportional to the factor $exp[-i(\omega t - kz)]$, with k given by Eq. 3.6. The entire laser will oscillate in time at the same rate, and it is only differences in phase experienced by different portions of the beam that matter for the phase contrast, so the phase accumulated due to the spatial variation of density is:

$$\phi = -\int kz\mathrm{d}z = -L\frac{\omega}{c} + \int \frac{n_e e^2}{2m_e\epsilon_0 c\omega}\mathrm{d}z, \tag{3.7}$$

where the integration length through the plasma is L. The first term is just a constant phase shift experienced by all portions of the beam and does not give any phase contrast. The second term is the phase shift of interest which produces the phase contrast (and is the amplitude Δ described above for a sinusoidal density perturbation). By taking out the constant factors from the integral and using the laser free-space wavelength

$$\lambda_0 = 10.6\,\mu m = \frac{2\pi c}{\omega},$$

and the classical electron radius

$$r_e = \frac{e^2}{4\pi\epsilon_0 m_e c^2},$$

the phase variation can be written as:

$$\tilde{\phi} = \lambda_0 r_e \int n_e \mathrm{d}z. \tag{3.8}$$

For the CO_2 laser, the factor $\lambda_0 r_e = 2.99 \times 10^{-20}\,\mathrm{m}^2$. Therefore, for line-integrated signals as described in Ch. 5 of order $10^{15}\,\mathrm{m}^{-2}$, this means that $\tilde{\phi} = 3 \times 10^{-5}$, a very small phase shift indeed.

Phase Contrast Imaging can thus be used as a sensitive tool to measure small density fluctuations in the plasma. It is a non-perturbing measurement and it can operate in all fusion-relevant densities and temperatures, even fusion-reactor relevant parameters. Because of the line-integration described in this section, the PCI is most sensitive to perturbations whose constant-phase wavefronts are perpendicular or nearly perpendicular to the beam, otherwise the positive and negative amplitudes of the perturbations will average out to negligible values. Complications can arise when the wavelength of the perturbation λ_p becomes comparable to the geometric mean of the laser wavelength λ_0 and the plasma thickness L. That is, the simple line-integration treatment and PCI theory in this section is strictly only applicable if $\lambda_p^2 \gtrsim 4\lambda_0 L$. The maximum integration length in a C-Mod plasma would be approximately 70 cm, so for the CO_2 laser this inequality is $\lambda_p \gtrsim 0.39$ cm, or $k_p \lesssim 16\ \mathrm{cm}^{-1}$. This condition is satisfied for all the IBW features observed both in the experimental data and in the code results presented in Ch. 5. See Refs. [78, 79] for more details.

3.1 Frequency and Wavenumber resolution

The detectors are sensitive up to 10 MHz, and high-pass filters are used to pass through only $\gtrsim 2$ kHz fluctuations, thus avoiding a large steady state signal and the noisy lowest frequency range of fluctuations. There are also 500 kHz low-pass filters to avoid aliasing, as the voltages from the detectors are sampled and digitized at 1 MHz

(500 KHz Nyquist frequency), so the system is sensitive to frequencies from 2 to 500 kHz. The longest wavelength that can be effectively imaged is approximately the beam width, thus setting a lower bound for detectable k numbers of about 0.4 cm^{-1}. Short wavelength detection is limited in practice by the number of channels and their spacing, setting an upper limit in k between 5 – 10 cm^{-1}, depending on how large a portion of the beam is imaged on the 12 detectors. In the IBW experiments described in Ch. 5, images were taken with both a wide beam (7 cm) in order to better measure spatial structure, while sacrificing k resolution, and with a narrow beam (3.5 cm) in order to measure the IBW wavenumber with better k resolution, while sacrificing spatial coverage.

3.2 Detecting RF signals

The system just described is totally insensitive to fluctuations at C-Mod RF transmitter frequencies of between 40 – 80 MHz. However, the PCI system has recently been upgraded in order to measure high-frequency fluctuations, while at the same time retaining the ability to measure low (2 – 500 kHZ) fluctuations.

To accomplish these RF measurements, the laser is modulated in intensity at a frequency near the radio-frequency of interest. This is done by splitting the beam, upshifting one half and downshifting the other, using acousto-optical (AO) frequency shifters[2] (see inset in Fig. 3-1), and then recombining the two halves into one beam before entering the plasma. The modulation frequency is chosen to be a few hundred kHz different from the RF frequency, for example 80.3 MHz. When the 80 MHz signal in the plasma is illuminated by the 80.3 MHz modulated laser, the image intensity (which is the product of both) reveals a 300 kHz beat oscillation, the frequency at which the detectors see the signal. This method is also known as "optical heterodyning", and was first suggested by Stefano Coda for use on C-Mod [78]. The process is illustrated in Fig. 3-3.

Note that the envelope of the final signal from the detector is smaller than the am-

[2]Also called acousto-optical modulators.

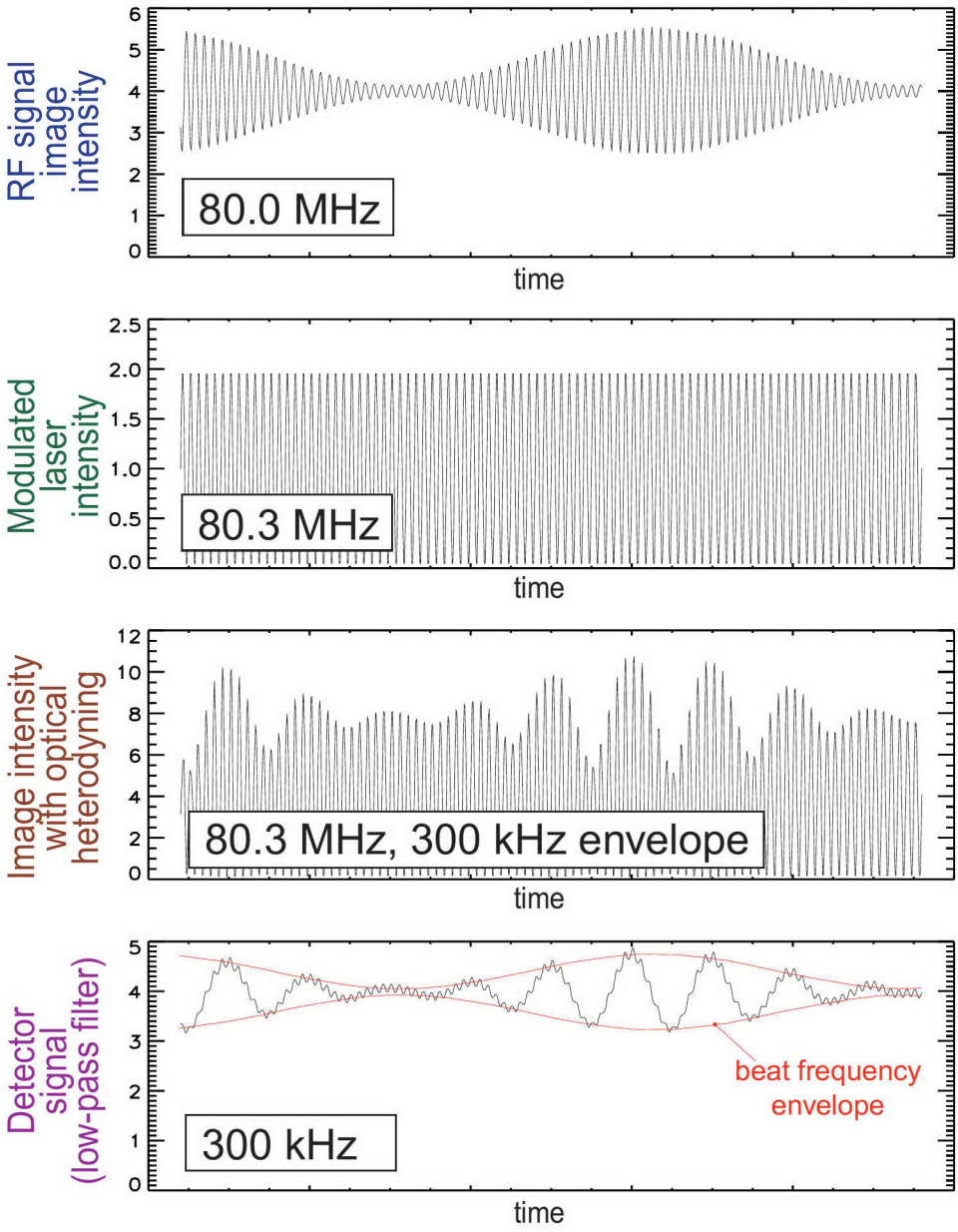

Figure 3-3: The RF optical heterodyning process, on a *simulated* varying-intensity 80.0 MHz signal.

plitude of the original density fluctuation in the plasma. This effect can be seen mathematically as follows. If the laser intensity (dropping the constant factor $1/(2\mu_0 c)$ for convenience) before being split is $I_0 = \langle E_0^2 \rangle$, where the $\langle\,\rangle$ denotes a time average over a laser period, then $E_0 = \sqrt{2I_0}\cos\omega t$ is the time-varying laser electric field amplitude. If the laser power is split equally, then the electric field E_1 of the half of the laser beam that is up-shifted by a frequency ω_s will be:

$$E_1 = \sqrt{\eta_1 I_0}\cos(\omega + \omega_s)t, \tag{3.9}$$

where η_1 is the fraction of power entering the AO modulator that is diverted and frequency-shifted (the rest is lost in a beam dump). The electric field E_2 that is down-shifted will be:

$$E_2 = \sqrt{\eta_2 I_0}\cos[(\omega - \omega_s)t + \psi], \tag{3.10}$$

where ψ is the phase difference due to any additional distance that the down-shifted beam travels compared to the up-shifted beam. In the setup used on C-Mod, the acousto-optical modulators were not of equal efficiency: $\eta_1 = 0.25$ and $\eta_2 = 0.80$. However, this still produces a large intensity modulation at twice the shift-frequency ω_s. When the beams are recombined, the electric field of the total beam is varying at two different frequencies:

$$\begin{aligned} E_1 + E_2 = &(\sqrt{\eta_1 I_0}\cos\omega_s t + \sqrt{\eta_2 I_0}[\cos\omega_s t\cos\psi + \sin\omega_s t\sin\psi])\cos\omega t \\ &+(-\sqrt{\eta_1 I_0}\sin\omega_s t + \sqrt{\eta_2 I_0}[\sin\omega_s t\cos\psi - \cos\omega_s t\sin\psi])\sin\omega t. \end{aligned} \tag{3.11}$$

Since $\omega_s \ll \omega$, when a time average over the laser period $2\pi/\omega$ is taken, the $\cos\omega_s t$ and $\sin\omega_s t$ factors will not change much, and the final laser intensity will be modulated at a frequency $\omega_m = 2\omega_s$:

$$I_L = \langle (E_1 + E_2)^2 \rangle = I_0 \frac{\eta_1 + \eta_2}{2}\left[1 + \frac{2\sqrt{\eta_1\eta_2}}{\eta_1 + \eta_2}\cos(2\omega_s t - \psi)\right]. \tag{3.12}$$

Note that because of the inefficient modulators, the average laser intensity is no longer I_0 but rather $I_0' = I_0(\eta_1 + \eta_2)/2 = 0.525 I_0$. The modulation factor $\alpha_m = 2\sqrt{\eta_1\eta_2}/(\eta_1+\eta_2)$ is equal to 1 when both shifters are 100% efficient ($\eta_1 = \eta_2 = 1$). This would mean that the minimum intensity during modulation is 0 and the maximum

intensity is $2I_0$. However, for the C-Mod setup, $\alpha_m = 0.85$, so that the minimum intensity is 15% of I_0', and the maximum intensity is $1.85\, I_0'$.

When this modulated laser intensity passes through the plasma and the PCI system, the final result will have intensity variations at several different frequencies. Suppose the line-integrated density fluctuations in the plasma result in a laser intensity variation of:

$$I_{\text{image}} = I_L \left[1 + A_1(t) + A_2(t) \cos \omega_{\text{rf}} t\right], \tag{3.13}$$

where $A_1(t)$ is the slowly varying amplitude of low-frequency background fluctuations, and $A_2(t)$ is the slowly varying amplitude of the high-frequency RF fluctuation. When the laser intensity is sinusoidally modulated as in Eq. 3.12, this results in an image intensity

$$\begin{aligned} I_{\text{image}} = I_0' \Big[& 1 + A_1(t) + \alpha_m (1 + A_1(t)) \cos(\omega_m t - \psi) + A_2(t) \cos \omega_{\text{rf}} t \\ & + 0.5 \alpha_m A_2(t) \left(\cos[(\omega_{\text{rf}} + \omega_m)t - \psi] + \cos[(\omega_{\text{rf}} - \omega_m)t + \psi]\right) \Big]. \end{aligned} \tag{3.14}$$

Because the detectors are only sensitive up to $\sim$ 10 MHz, the high frequency RF terms involving $\omega_{\text{rf}} \sim 80$ MHz or ω_m (which is usually chosen to be a few hundred kHz different from ω_{rf}) average to zero, and what remains is converted to voltage by the detectors, digitized at 1 MHz and stored with Aurora-14 digitizers:

$$I_{\text{image}}^{\text{detected}} = I_0' \left\{ 1 + A_1(t) + \frac{\alpha_m}{2} A_2(t) \cos\left[(\omega_{\text{rf}} - \omega_m)t + \psi\right] \right\}. \tag{3.15}$$

The origin of the smaller final heterodyned signal is seen to be the factor $\alpha_m/2$, which for the C-Mod setup is 0.425. So when an RF signal is detected, to recover the amplitude of the original density fluctuation causing the signal, it should be multiplied by a factor $\frac{2}{\alpha_m} = 2.35$.

3.3 Absolute Calibration

Before each plasma discharge, an absolute calibration and test of the PCI system is performed by measuring a controlled density perturbation (a sound wave propagating in air). This occurs in the laser box enclosure as shown in the lower right of Fig. 3-1. A speaker mounted on the bottom of the table produces a short 1 millisecond

sound burst at 15 kHz, causing a pressure wave to pass through the laser beam which slightly changes the index of refraction of the air. The result on the raw signal from the 12 PCI channels is shown in Fig. 3-4. This signal is fit to a test signal to determine the amplitude and start time of the sound burst on each channel. The short vertical lines at the beginning of the sound burst on each channel shows where the fit determined the start of the sound wave for each channel. Channel 1 is the portion of the laser beam closest to the speaker, and Channel 12 the farthest. The time delay from channel to channel accurately determines the channel spacing, and combined with the speed of sound in air (taken to be 340 m/s), the wavenumber resolution. The overall delay from time $t = 0$ determines the positions of the channels relative to some fixed reference point. In this way it was determined that for the shot shown in Fig. 3-4, the channel positions ranged from 65.59 cm to 68.89 cm major radius, and the channel-to-channel spacing was 0.30 cm. This means that a spatial Fourier transform of the data would yield 12 wavenumber bins ranging from -10.46 cm^{-1} to 10.46 cm^{-1}, with resolution $\Delta k = 1.74$ cm^{-1}. (Actually there are 13 wavenumber bins usually plotted, but because of spatial aliasing, the -10.46 cm^{-1} bin is identical to the +10.46 cm^{-1}.)

An example of a two-dimensional Fourier transform of the PCI data to turn information about spatial structure and time behavior into information about wavenumber and frequency is shown in Fig. 3-5. The first 2000 samples (2 msec) of the sound burst calibration were used, to avoid the reflected wave that bounces off the top of the laser box enclosure and other surfaces. A sound speed of $\omega/k \simeq 340$ m/s is consistent with the faint diagonal band of signal from 0 to -5 cm^{-1}, with the main sound burst signal centered roughly on the 340 m/s line.

One of the main sources of noise and uncertainty in the measurements is the laser itself. For the PCI data presented in this thesis, a double-tube CO_2 gas discharge laser was used, which was subject to instabilities, high frequency noise, and unsteady power output. A sound burst measurement for nearly every shot (sometimes the speaker would fail or the sound burst would not be visible for some or all otherwise functioning channels) allows a comparison of the plasma signals to a known density

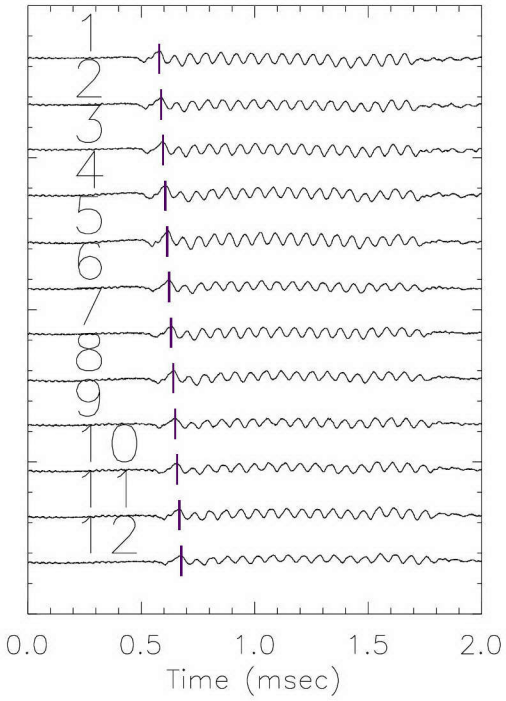

Figure 3-4: The sound wave used for absolute calibration and testing of the PCI system. The 12 separate PCI channels are shown on the same plot.

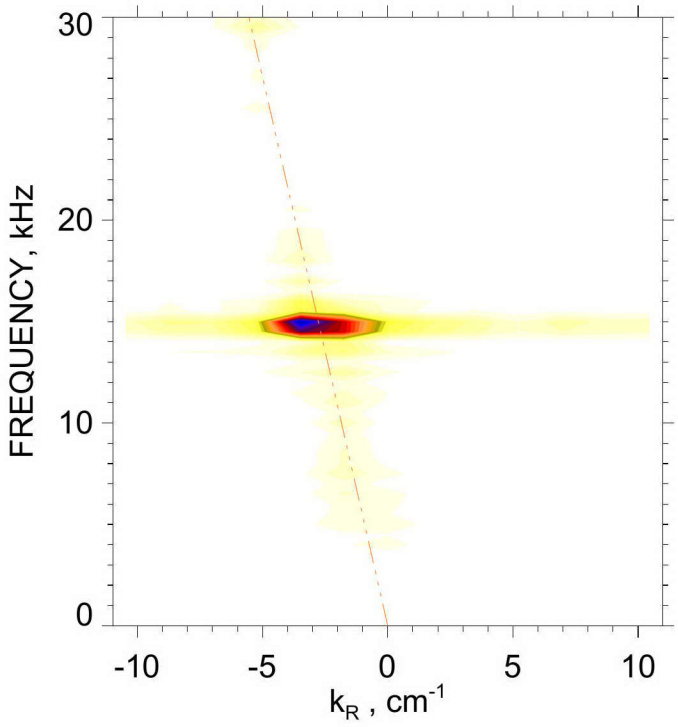

Figure 3-5: 2-D Fourier transform of the PCI sound wave signal from Fig. 3-4. The speaker frequency is 15 kHz. The dot-dash diagonal line is the sound velocity $\omega/k =$ 340 m/s, for negative k.

perturbation. For the sound system in the laser enclosure, using a spherical wave front model of the sound wave and Eq. 3.8, an expected line-integrated signal of the sound burst at a certain distance from the speaker can be calculated. The equivalent line-integrated signal that would have to be measured in the plasma to produce a signal as strong as the sound wave signal is [79]:

$$\int \tilde{n}_e dz\Big|_{\text{reference}} = \frac{7.83 \times 10^{12}}{\sqrt{d}} \text{cm}^{-2}, \tag{3.16}$$

where d is the distance in cm from the speaker to the PCI integration chord of interest. This can be used for calibration as follows: suppose a plasma signal is measured along a chord 20 cm away from the speaker that is 60% as strong as the sound wave measurement along that chord that was taken before the shot. Then this represents a signal strength of $\int \tilde{n}_e dz = 10^{16}\,\text{m}^{-2}$.

For more information on the C-Mod PCI system, other phase effects similar to PCI, and other physics results using the PCI, including low frequency fluctuations and RF fast wave observations, see Alexander Mazurenko's thesis [79], and also the 14th RF topical conference proceedings [80].

The PCI system on C-Mod can now be used to measure the density fluctuations associated with RF waves, with signal levels as small as $\sim 1 \times 10^{15}\,\text{m}^{-2}$ (the actual threshold depending on the bandwidth used in the Fourier transforms, and the RF noise pickup level, which was typically of order $5 \times 10^{14}\,\text{m}^{-2}$). Signals have been detected from both the D- and E-port antennas (the PCI diagnostic is located directly in front of the E-port antenna). Future experiments may try to measure a signal from the J-port antenna, as well. This may be difficult to observe a strong enough signal, as the J antenna is located 144° away toroidally.

Chapter 4

Deuterium – Helium-3 Mode Conversion Experiments

In order to better understand the validity of the mode conversion theory (both the internal resonator model and TORIC) and the prediction that significant amounts of power can be transferred from the fast Alfvén wave to the ion Bernstein wave, several experiments have been run on Alcator C-Mod with ion-ion hybrid layers present in the plasma. This chapter presents results of mode conversion experiments in D(^{3}He) plasmas, before the PCI diagnostic was operational. Although there are no observations of the density fluctuations associated with the mode-converted IBWs, indirect effects of the IBWs were observed through electron heating.

4.1 Experimental setup

In January and February of 1996 and February of 1998, a series of plasmas was run on Alcator C-Mod with central toroidal field of ~7.8 tesla consisting of deuterium and varying amounts of (doubly-ionized) helium-3, in order to study the transition between minority ion cyclotron heating and mode conversion. As the ^{3}He concentration in the plasma increases, mode conversion of the fast wave to an ion Bernstein wave becomes more important and direct electron heating in the vicinity of the mode conversion region should occur through electron Landau damping of the ion Bernstein

wave.

In this scenario the D ion-cyclotron resonance is on the high-field side at a major radius of 49 cm, while the ^{3}He ion-cyclotron resonance is at 65 cm, near the magnetic axis. Figure 2-17 shows the wave dispersion relations for this type of scenario (for fixed $k_\parallel$). For Alcator C-Mod parameters, the gap between the cutoff and the resonance through which the fast wave must tunnel in order to mode-convert is of the right size to allow efficient coupling of power to the IBW. The 1996 run has been discussed in Peter O'Shea's thesis [60] and in Ref. [61]. I have used some of the same shots from 1996 in addition to the 1998 run in order to get more complete coverage of the full range of helium-3 concentration.

4.2 Experimentally Measured Electron Power Deposition

An experimentally measurable quantity that can be directly related to the process of FW to IBW mode conversion is the electron power deposition profile. This is because with the right conditions, the electrons are heated directly by the IBW through electron Landau damping. There are several other ways that RF power could be transferred to the electrons. One way is through electron Landau damping of the fast wave. However, this heating mechanism is weak for the electron temperatures typical of these D(^{3}He) C-Mod plasmas. Also, this mechanism is greatest where the electron temperature is greatest — on axis. Thus when the mode conversion layer is off-axis, the two mechanisms can easily be separated. Another way the electrons are heated by the FW is indirectly through the ions. With a helium-3 cyclotron layer present in the plasma, ^{3}He ions can absorb RF power. The energetic ions can then collide with and heat the electrons. However, by using a prompt "break-in-slope" method described in the next section, this heating mechanism can also be separated from the electron Landau damping of the mode-converted IBWs. Also, in the mode conversion regime (high ^{3}He concentration), the minority ion cyclotron damping is weaker than

in the low ^{3}He concentration regime.

The dominant parallel wavenumbers from the two-strap antennas used in these experiments had magnitudes from 11 to 15 m^{-1}. This means that the mode-converted IBWs in D(^{3}He) plasmas at 7.8 T should damp predominantly on electrons via Landau damping, because $\omega/k_{\|}v_{\rm the} \sim 1-2$ already near the mode-conversion layer, thus the IBW is already nearly in resonance with a large portion of the electrons. This figure of merit ($\omega/k_{\|}v_{\rm the}$) should decrease as the IBW propagates away from the mode conversion layer, due to the upshift of $k_{\|}$, causing even stronger Landau damping. If the mode-conversion layer is off-axis, then there will be no interference from the other direct electron heating mechanism: fast wave Landau damping on the hot core electrons. Thus the power deposited on electrons can be attributed to RF FW power converted to IBWs. By examining the electron temperature and its response to sudden RF power changes, an electron power deposition profile throughout the plasma can be measured.

A high time-resolution electron temperature diagnostic was operational during the D(^{3}He) plasma run days. As electrons gyrate around the magnetic field, they emit microwaves (for fields from 4-8 tesla, the electron cyclotron frequency $f_{ce} = 112-224$ GHz). Microwave receiving horns were placed on the low-field-side of the plasma, and a grating polychromator (GPC) was used to observe microwave radiation at 9 specific frequencies (at the 2nd harmonic of the electron gyrofrequency), corresponding to 9 major radial locations within the plasma. The channel positions can be determined only through accurate knowledge of the total magnetic field throughout the plasma. This system is further described in Peter O'Shea's thesis [60] and Ref. [81]. Usually the data was sampled at a rate of 20,000 samples per second, or 50 μsec between samples. Thus when looking at typically 1 to 2 milliseconds around an RF power transition for a prompt electron temperature response (a time much smaller than the energy confinement time of 20 to 30 msec for these plasmas), the temperature data contains a sufficient number of samples (20 to 40) to find a linear slope before and after the power transition.

4.2.1 Electron Temperature "Break-In-Slope" Technique

The local RF heating power density can be determined from the change in the time rate of change of the temperature. This is known as break-in-slope analysis.

A simple model for a hot plasma is that of a mixture of two magnetized fluids: negatively charged electrons and postively charged ions. The fluid model energy conservation equation for electrons can be written (neglecting terms involving the drift velocity due to any steady-state electric field):

$$\frac{3}{2} n_e \frac{\partial T_e}{\partial t} + \nabla \cdot \vec{q}_e = P_e^{RF} - P_e^{rad} + P_e^{OH} + Q, \tag{4.1}$$

where n_e is the electron density, T_e is the electron temperature, $\vec{q}_e$ is the electron heat flux, P_e^{RF} is the RF power density absorbed by the electrons, P_e^{rad} is the power density radiated from the electrons (mostly through bremsstrahlung), and P_e^{OH} is the ohmic power density (due to the presence of a large plasma current and the finite resistivity of the plasma) absorbed by the electrons, and Q is the heat exchanged between electrons and other plasma species, through collisions.

Consider this equation for a region of plasma during RF heating compared to a time just after the RF power source is shut off (with a typical shut-off time of 100 – 200 microseconds). Electric field solutions for the D(^{3}He) scenarios from TORIC suggest that the IBW propagates only a few centimeters before damping completely away. An order-of-magnitude estimate for the group velocity of the IBW is the ion thermal velocity [18]. Thus for a 2 keV plasma, after the RF power is shut off, the energy in the IBW should take less than a microsecond to travel even 5 cm, so the shut-off can be considered instantaneous in the following analysis.

Characteristic times for changes in $P_e^{\rm rad}$, Q, and $P_e^{\rm OH}$ are of the order of the energy confinement time τ_E or longer. If the change is abrupt enough, and the plasma does not have much time to transport the heat away, then the only source term that changes significantly in Eq. 4.1 is P_e^{RF}. However, for almost all C-Mod shots, there are other abrupt changes in electron temperature, known as sawteeth because of the gradual rise in temperature and sudden crash[1], a cycle which repeats itself throughout

[1]Although the sawtooth crash and its extremely rapid timescale are not yet fully understood, the

most of the discharge. Characteristic times associated with the heat flux ($\nabla \cdot \vec{q}_e$) after a sawtooth crash are quite fast, typically 100 – 200 microseconds for the heat pulse to propagate half-way out from near the center. This can be a large perturbing influence on the determination of the electron temperature slope before and after an RF transition. By considering only times that are not too near the sawteeth crashes, this effect can be mitigated.

Peter O'Shea discussed all these terms and their relative influence on the local temperature time evolution in detail [60, Ch. 6], and found that the upper limit for the time window for slope-fitting after an RF transition to achieve reasonable accuracy in applying the break-in-slope method is approximately 1.4 msec. Thus by taking a window of approximately only ± 1 msec around the RF power transition, the change in the electron temperature can attributed to *direct* ICRF electron heating (i.e. not indirectly through ion heating and subsequent ion–electron collisions or heat transport mechanisms).

Even in the absence of RF power transitions, the time behavior of the electron temperature between sawteeth crashes is not always linear, as can be seen in Fig. 4-1, which shows a few typical sawteeth during RF heating. The inner channels show the temperature increasing until the sawtooth threshhold is reached, when there is a crash of a few hundred eV, producing a heat pulse which propagates to the outer channels very quickly. If the break-in-slope method is attempted on a channel just when the heat pulse is passing by, or on the inner channels toward the top of the sawtooth period when the temperature often begins to level off, the slope may appear to change before and after the RF transition, even though there may be no direct connection to the RF. A more accurate determination of the actual response to the RF power transition can be made by comparing how the temperature was changing during the previous few sawteeth periods.

For example, for a sudden RF turn-on, the electron temperature response is shown

phenomenon is probably due to a magnetohydrodynamic instability which develops near the core at the magnetic flux layer where the magnetic field angle is such that the field line completes one toroidal circuit around the machine for one poloidal circuit.

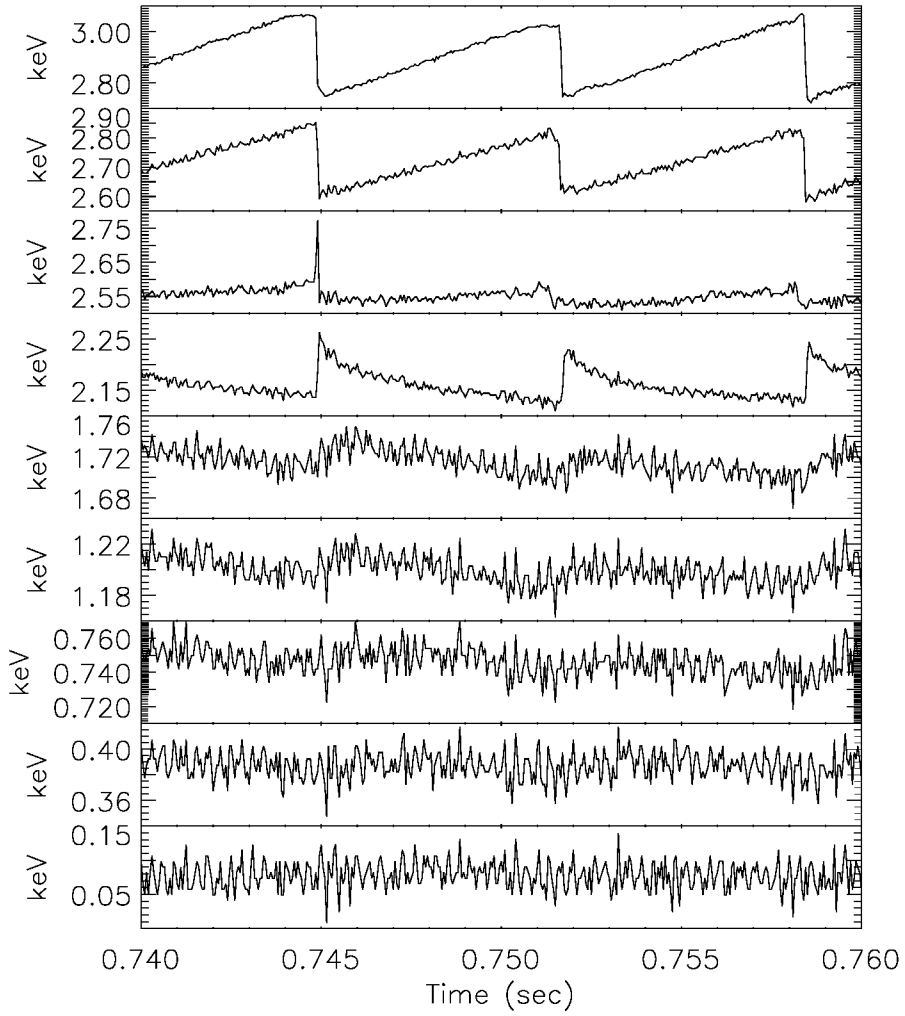

Figure 4-1: Electron temperature sawteeth during constant RF heating, as measured by the 9-channel GPC ECE diagnostic. Central channel on top, increasing in major radius to the outermost channel on the bottom.

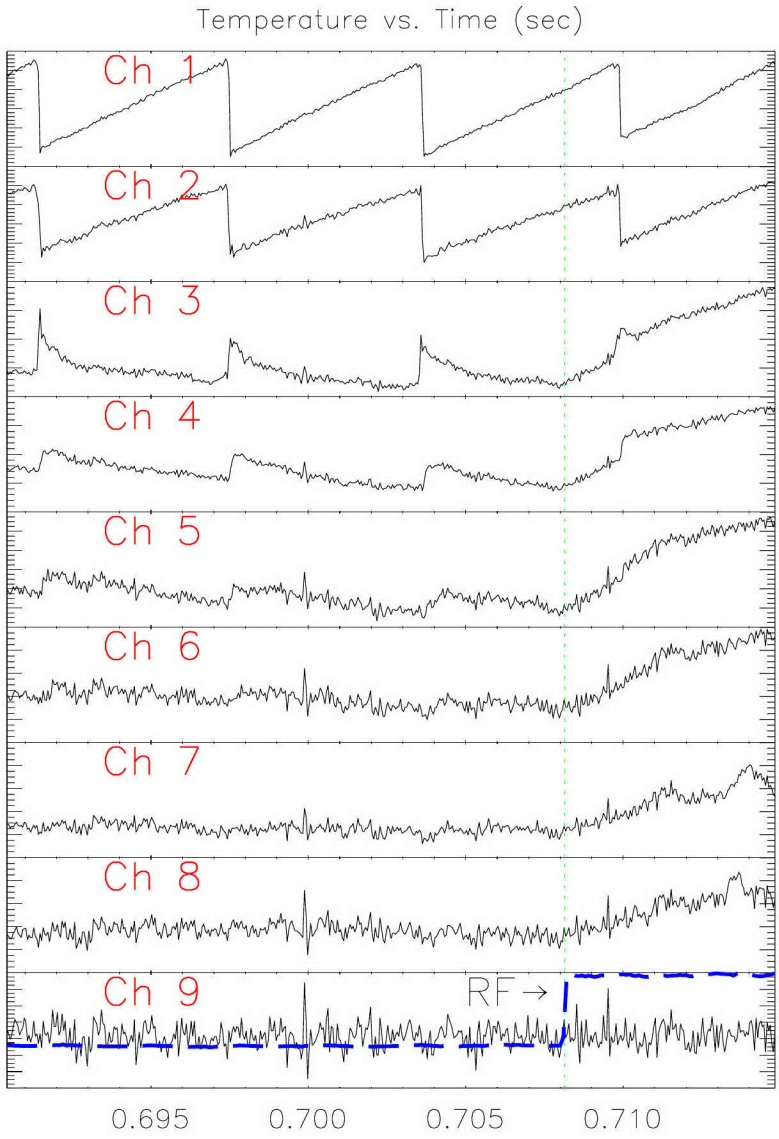

Figure 4-2: The "break-in-slope" of the electron temperature due to an RF power transition at 0.70815 sec. Channel 1 is located farthest to the high-field-side (near the center in this case) and channel 9 farthest out in major radius. Also shown over channel 9 is the RF power trace (dashed line), with the vertical dotted line indicating the transition time.

in Fig. 4-2. Even without the expected response from the previous few sawteeth, it can be seen that the strongest prompt electron heating is on channels 3 through 6. Many times the response is more subtle, and is only drawn out by comparing the expected slope from previous sawteeth. For example, on channel 1 in Fig. 4-2, it can barely be seen that there is a change in slope during the sawtooth period around the RF transition. However, when compared to the previous two sawteeth, the change in slope becomes clearer. By subtracting the average of the previous two sawteeth from the transition sawtooth (see Fig. 4-3 and Fig. 4-4), and taking a ± 1.2 msec time window around the transition, a least-squares linear fit of $\partial T_e/\partial t$ before and after the abrupt change in RF power gives the "break-in-slope" $\Delta\frac{\partial T_e}{\partial t}$. The error is estimated by calculating the slope 30 times, and each time applying random weighting to all the fitting points, then setting the uncertainty in the slope to be the standard deviation of the resulting fits.

In order to calculate a power density from this change in slope, the density profile (obtained from interferometry) at the RF transition time is multiplied by the change-in-slope profile. Assuming the density remains constant during the $\sim$2 msec time window, this can be used to calculate how much of the RF power was being absorbed by the electrons:

$$\frac{3}{2}n_e\Delta\frac{\partial T_e}{\partial t} = \Delta P_e^{RF}. \tag{4.2}$$

The fraction of RF power absorbed by electrons is given by:

$$\frac{\Delta P_e^{RF}}{P_{\text{after}} - P_{\text{before}}}, \tag{4.3}$$

where P_{before} and P_{after} are the RF power absorbed by the entire plasma before and after the transition. Usually the fraction of RF power leaving the antenna that is actually absorbed by the entire plasma (both ions and electrons) is not well known, but is quite high in those cases analyzed when most of the power could be accounted for (e.g., in D(H) plasmas with minority heating). The discrepancy could be due to parasitic absorption [82] (by excitation of electrostatic modes for example) at the plasma edge (outside the last closed flux surface) or heating of machine or antenna surfaces. Assuming these losses are small, the net RF power leaving the transmitters

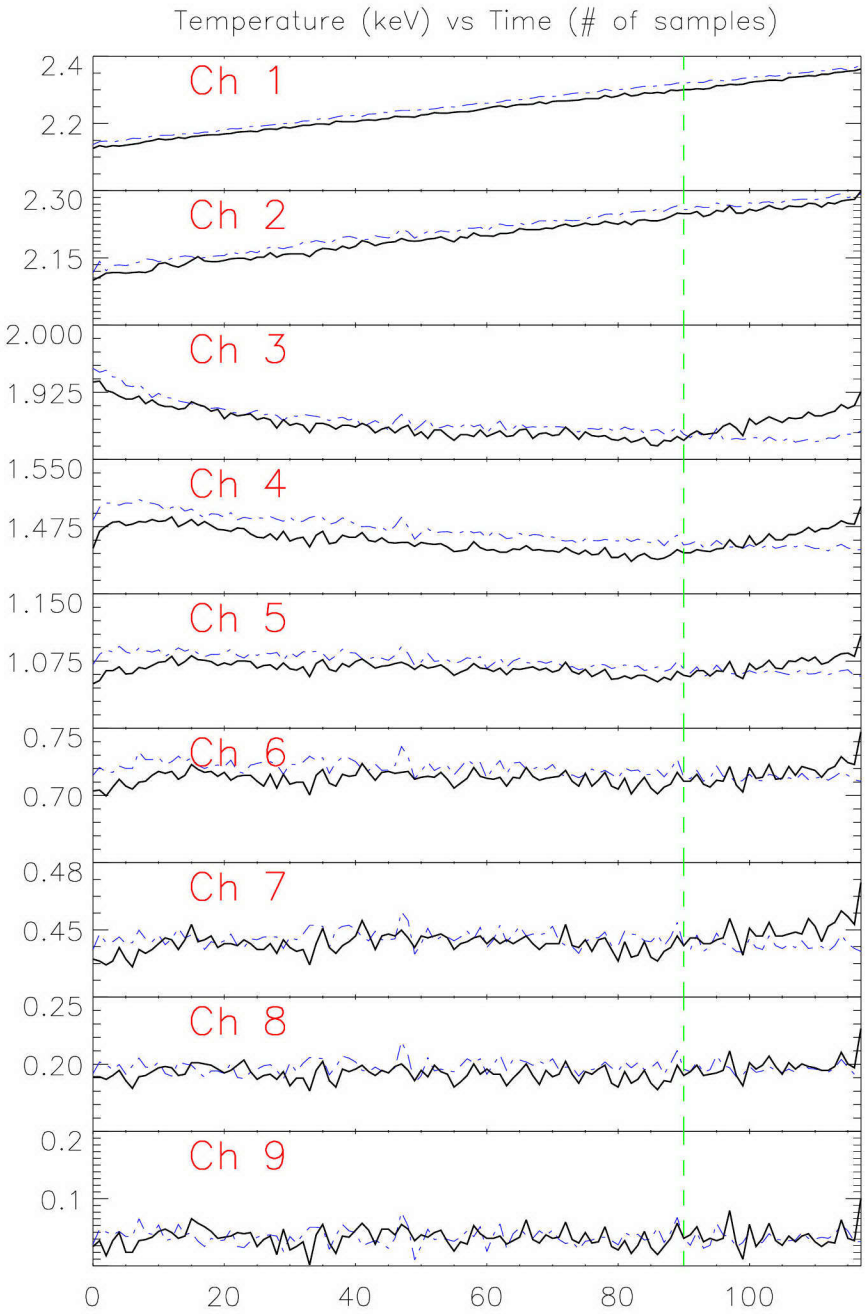

Figure 4-3: Solid line: sawtooth during the RF power turn-on (indicated by the vertical dashed line). Dot-dash line: average of previous two sawteeth, during steady RF power.

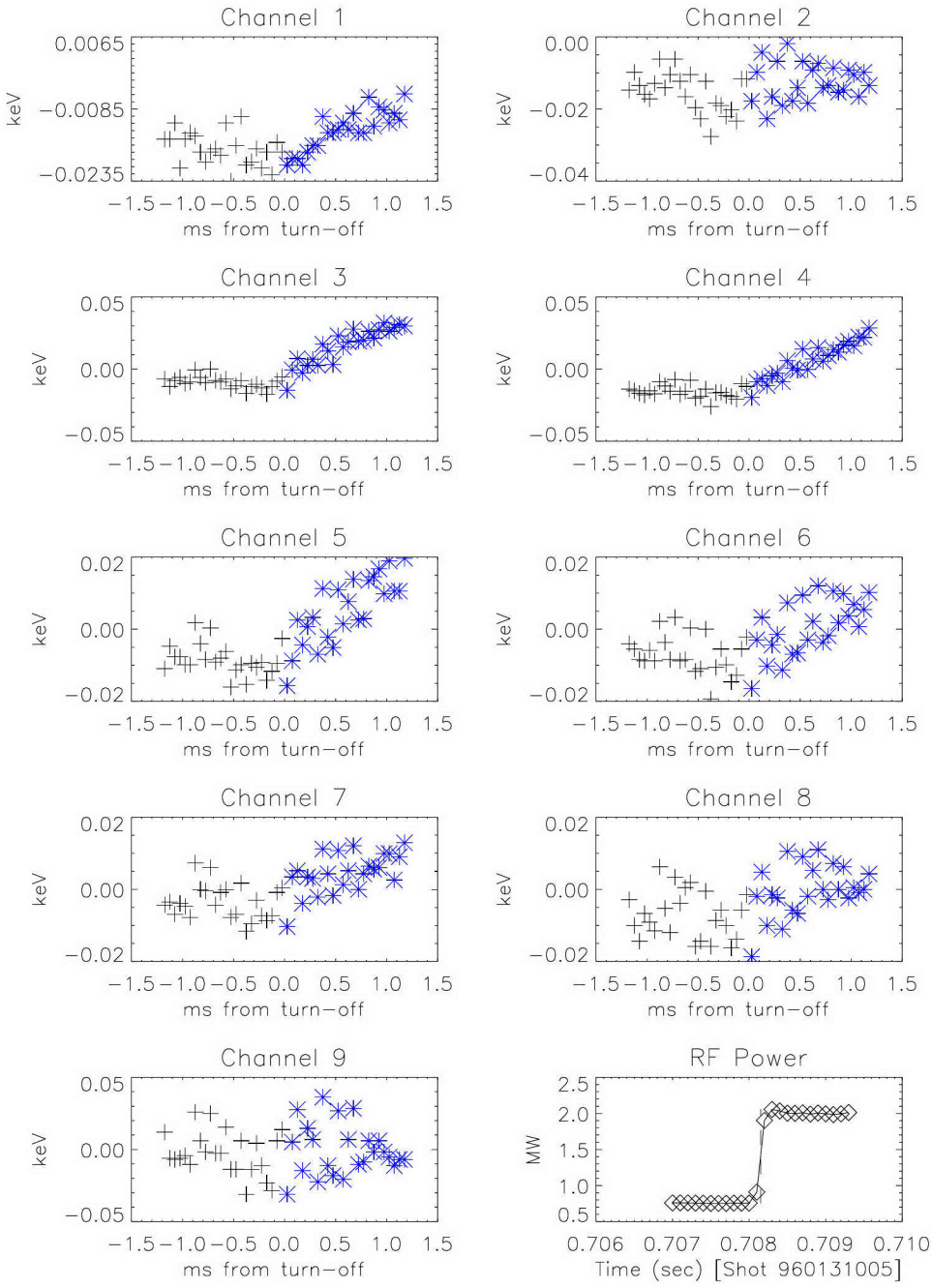

Figure 4-4: The sawtooth-corrected prompt electron temperature response (transition sawtooth minus average of previous two sawteeth). Pluses: data points for slope-fit before transition, stars: data points after the transition.

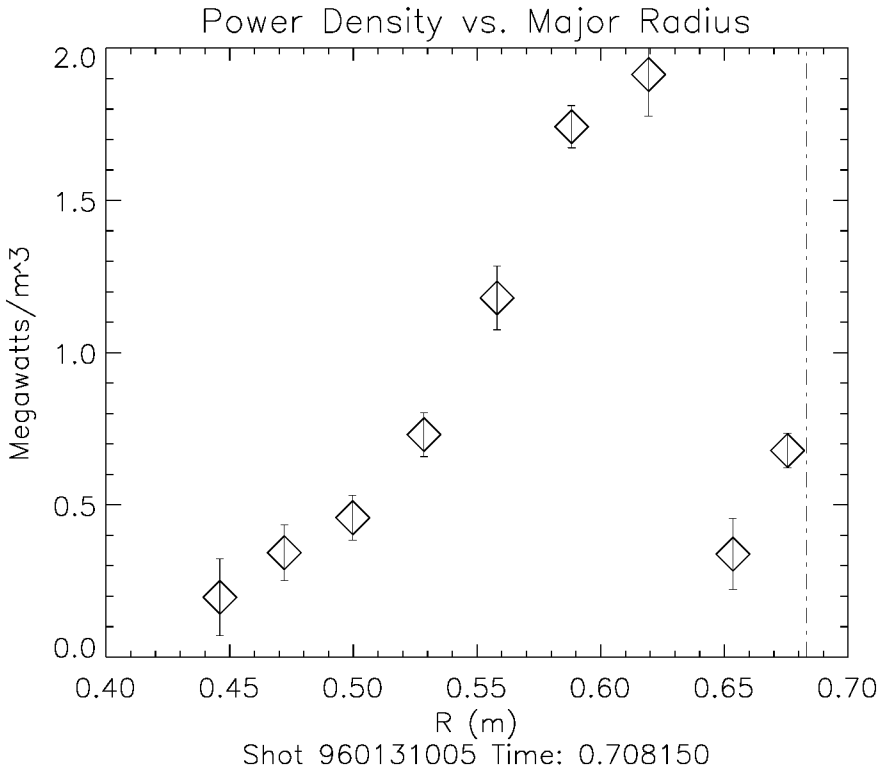

Figure 4-5: Electron power deposition profile (MW/m^3) *vs.* major radius. Integrated power accounts for $53 \pm 3\%$ of the launched RF power.

measured by directional couplers in the coaxial line can be used for P_{before} and P_{after}.

For the slopes calculated in Fig. 4-4, the measured RF power deposition profile is shown in Fig. 4-5. The GPC diagnostic usually measures temperature on the low-field-side (LFS), but in these D(^{3}He) scenarios the mode-conversion layer and hence the expected direct electron heating is on the high-field-side (HFS). However, because energy transport is so rapid along the magnetic field, heat that is deposited on a magnetic flux surface at the HFS will quickly be distributed everywhere along that surface, thus appearing on the LFS for the GPC to measure.

The RF power density profile is integrated (with a simple linear interpolation between points) using the EFIT[2] volume element calculation to obtain the total RF power deposited to electrons. This power divided by the net RF power involved in

[2]A computer code which calculates a magnetic equilibrium for the plasma from magnetic measurements at the edge (see Ref. [3]).

the transition is the RF power fraction absorbed by electrons. Then, assuming that direct electron Landau damping (which is stronger near the hot center of the plasma) is a small contribution to the total, this integrated RF power fraction to electrons can be equated to the mode-conversion efficiency. This is compared to theory in Sec. 4.4.

4.3 Estimating the Helium-3 Concentration

In order to calculate what mode conversion efficiency should be expected from theory, it is necessary to know the exact ion species mix in the plasma. The amount of power that is mode-converted or damped on minority ions is a function of the Helium-3 concentration (among other plasma parameters). There are few reliable methods of measuring the various ion concentrations in the core of a hot tokamak plasma. Most spectroscopic methods rely on cold edge measurements where partially ionized atoms can still exist. Charge exchange methods can measure higher energy ions that exchange electrons with neutral atoms, becoming neutral themselves and hence unconfined. If they then make it outside the plasma to a neutral particle analyzer, some estimate of that ion species' concentration can be made. To date, charge exchange for helium-3 ions has not been applied on C-Mod. (See Appendix D for possible future methods of measuring the ion species concentrations.)

Peter O'Shea discussed in his thesis [60, Apdx. A] several other methods of estimating the ^{3}He concentration, including attributing the density rise after the helium gas valve was opened to helium arriving in the core, looking at the increase in the effective average charge of the plasma ions, and finding a linear scaling between the amount of time the gas valve was open to the amount of helium ions present in the plasma.

Another method is to use knowledge of the location of the prompt electron heating, which should be close to the mode-conversion layer, to extract a helium concentration in the core of the plasma. By running TORIC with several different ^{3}He concentrations, and comparing the location of the peak heating to the location of the $n_\parallel^2 = S$ resonance layer for $m_\theta = 0$, $n_\phi = 10$ (the dominant mode numbers in the

C-Mod antenna spectrum), the correlation between peak heating location and ^{3}He concentration is confirmed, as shown in Fig. 4-6.

The dominant effect is that as the concentration is increased, the location of peak heating moves farther to the HFS. There is another trend evident about the location of the $n_\parallel^2 = S$ layer relative to the location of peak heating. At low concentrations, it is somewhat to the right of the peak, and at higher concentrations it moves toward the peak and even past it, to the high-field-side for a concentration of 28% (Fig. 4-6(d)). Thus the following procedure was used in order to estimate the ^{3}He concentration for an experimentally measured profile: the profile mapped to the high-field-side was plotted along with the location of the $n_\parallel^2 = S$ layer for various levels of ^{3}He. The ^{3}He concentration range was taken to be that for which the location of the peak heating was within ~ 1 cm of the expected location. This is the origin of the estimated ^{3}He level (and error bars) used in Sec. 4.4 as inputs to theory and for identifying the helium-3 concentration of the data points.

As a check that this method of determining the ^{3}He concentration is consistent with other independent methods, the value of the helium-3 density determined this way (by multiplying the value of n_{He3}/n_e determined from the location of peak heating by the measured value of n_{e0}) is plotted against the time the gas valve was open in Fig. 4-7. There should be a linear relationship between n_{He3} and the gas valve time, which is approximately verified in the figure. However there is still a large variation even for the same gas-puff time, which may be an indication that the amount of helium that reaches the core is not always the same for the same gas-puff time.

Another method of determining the helium-3 concentration in the core is by examining the central density before and after a helium gas puff. For large helium gas puffs, the total density rise after the puff can be attributed to helium reaching the core if the density was in steady-state before the puff. This analysis on a few shots (not shown) are also consistent with the method using the location of the $n_\parallel^2 = S$ layer and the expected peak heating location from TORIC.

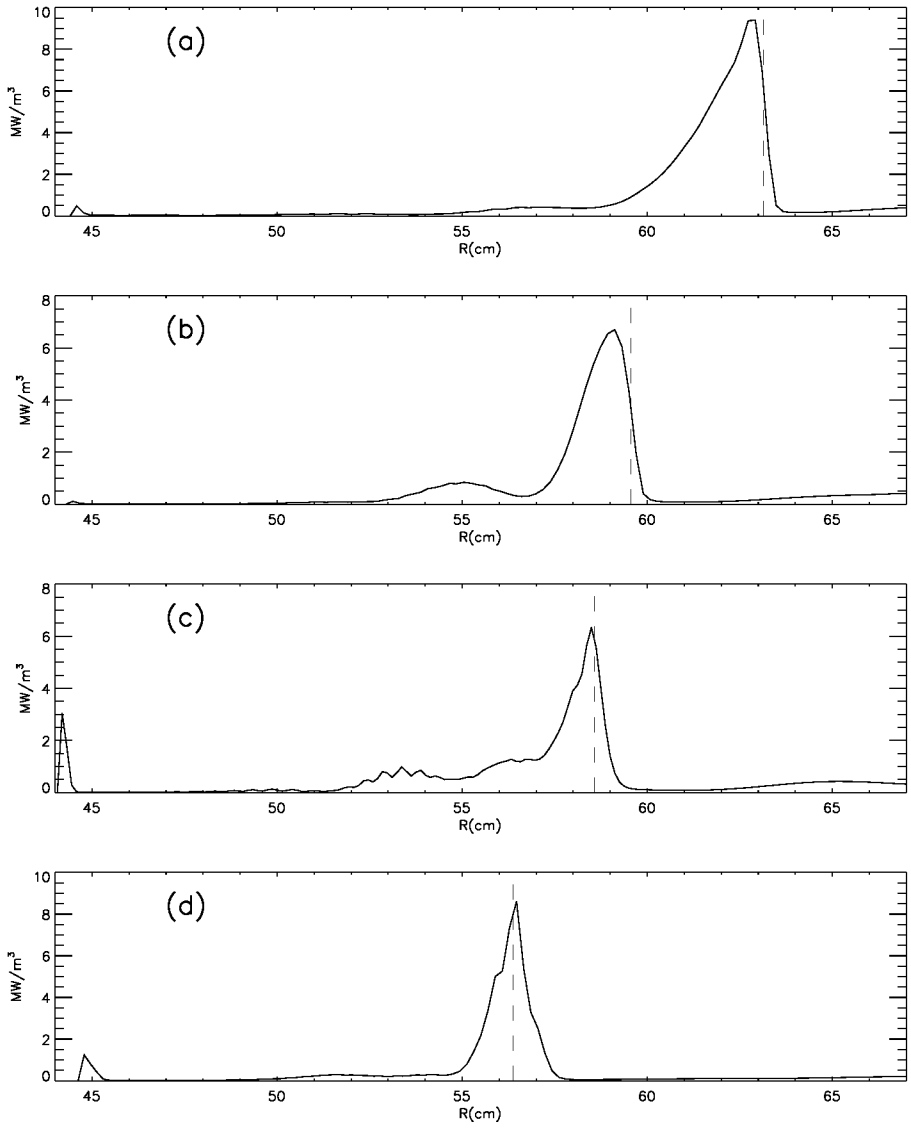

Figure 4-6: Power deposition profiles for electron heating through Landau damping from TORIC. Four different values of n_{He3}/n_e are shown: (a) 13.7% (b) 19.65% (c) 24.0% (d) 28.0%. In each case the vertical dashed line indicates the location at which $n_{\parallel}^2 = S$ on the midplane for $n_\phi = 10$, $m_\theta = 0$. The peaks near the dashed lines are electron Landau damping of the IBWs, and the lower values near the center ($R \sim 67$ cm) are direct electron Landau damping of the FW.

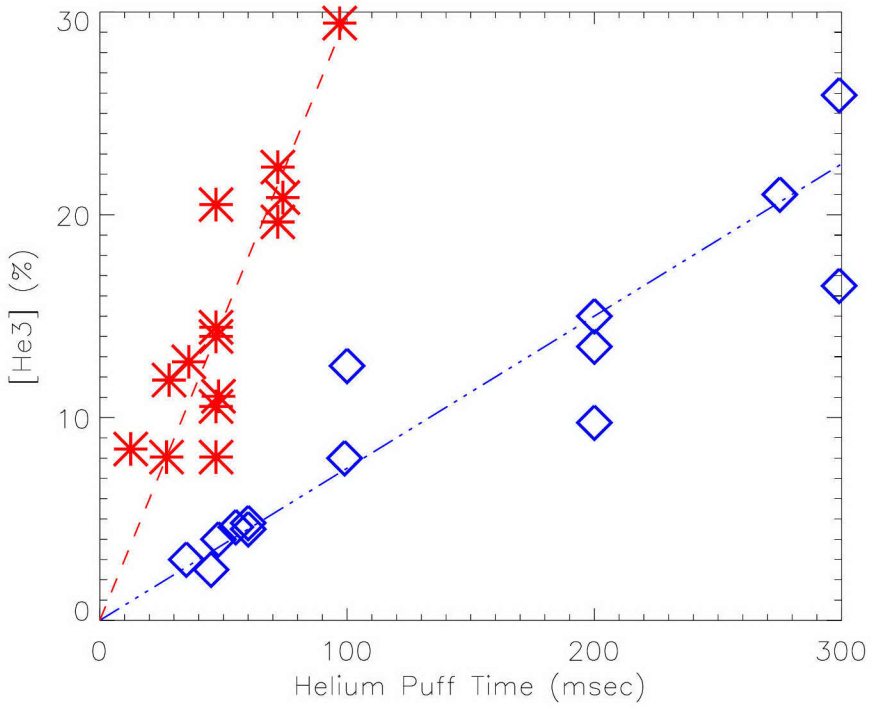

Figure 4-7: Helium-3 density (using n_{He3}/n_e as determined from peak heating location and measured n_e) *vs.* gas-valve time. Diamonds: 1998 data, with dash-dot line the least squares linear fit (including the origin in the fit). Stars: 1996 data, with dashed line the least squares linear fit (including the origin in the fit). Some valve parameters changed between 1996 and 1998.

4.4 Comparison of Experiment to Theory

The results of applying the experimental analysis described in this chapter on 28 different power transitions with varying ^{3}He concentrations and suitable sawteeth nearby to compare to is shown in Fig. 4-8. The peak heating was usually in the range of 1.5 to 8 MW/m^3, and the location of the peak heating ranged from $\sim$ 0.65 m (on axis) to $\sim$ 0.56 m ($r/a \simeq 0.6$). Occasionally for a few points in the profiles the values are negative. This means that the change in slope was the opposite direction as expected from the RF power change, and the analysis has failed. However, negative values occurred only for a few points and did usually not affect the integrated value greatly.

4.4.1 Mode Conversion Efficiency from the Internal Resonator Model

By integrating the power deposition profiles in Fig. 4-8 and dividing by the amount of RF power in the transition, the mode conversion efficiency can be obtained. Then, applying the internal resonator model as described in Sec. 2.5.2 for each data point, the mode conversion efficiency prediction can be compared to the experimental data.

One parameter that is important in determining the theoretically expected mode conversion efficiency, especially at low concentration, is the minority temperature. Because ion cyclotron heating preferentially deposits power on the minority ion species, the ICRF heating can drive a high-energy "tail" on the minority ion distribution function. Assuming this tail can be described as a high-temperature Maxwellian distribution, the dispersion relations described in Ch. 2 can still apply. Detailed modeling could be done using a Fokker-Planck code which follows the evolution of the ion distribution functions through the heating process[3], but here a simple model is used which approximates the more detailed quasi-linear theory. The assumption is

[3]This has been done by Peter O'Shea (see Ch. 7 in Ref. [60]), from which he concluded that for ^{3}He minority heating, with its poor polarization, the tail temperature was more or less the same as the thermal background ions.

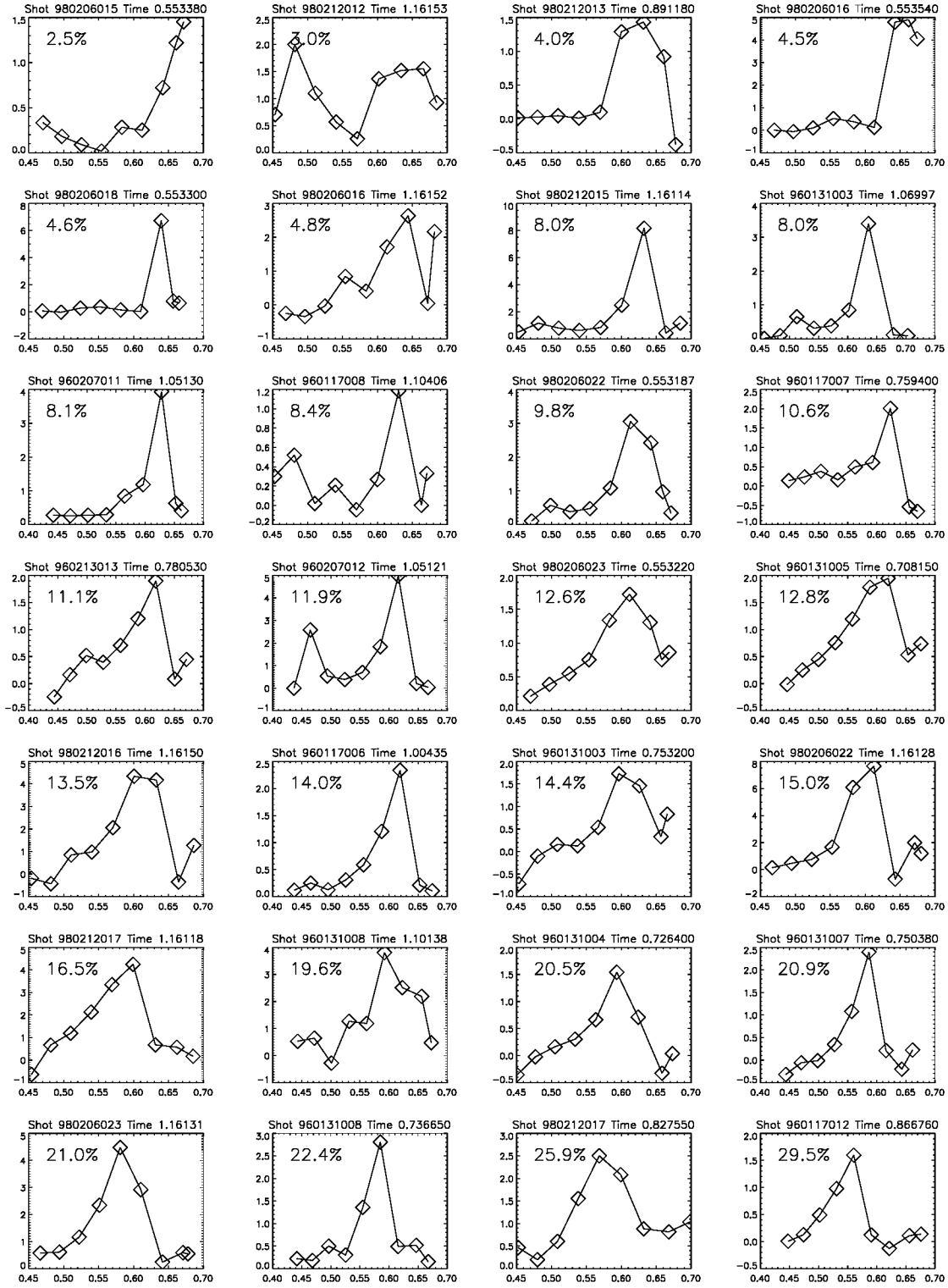

Figure 4-8: Experimentally measured electron power deposition profiles (in MW/m^3), with ^3He concentration (indicated in the upper left of each plot), increasing from left to right, and top to bottom. The horizontal axis is the major radius, in meters.

that the minority tail temperature decreases with increasing concentration[4],

$$T_{\mathrm{He3}} = \frac{40\,\mathrm{keV}}{100\,n_{\mathrm{He3}}/n_e}, \tag{4.4}$$

unless this formula predicts $T_{\mathrm{He3}} < T_D$, in which case $T_{\mathrm{He3}} = T_D$. For example, at 1% ^{3}He concentration, the tail temperature would be 40 keV, at 5% 8 keV, and at 10% 4 keV. Other temperatures in the numerator of Eq. 4.4 were tried, but using 40 keV allowed the internal resonator theory mode-conversion efficiency prediction to fit the experimentally measured electron power deposition fraction quite well (see Fig. 4-10). Changing this factor would affect the low concentration results the most — increasing it would depress the predicted mode conversion efficiency, as there would be a larger Doppler-broadened cyclotron resonance, and hence fewer (n_ϕ, m_θ) pairs in the antenna spectrum for the internal resonator model to actually apply (see Sec. 2.5.2). However, even large variations in this temperature factor did not affect the results of the internal resonator theory for helium-3 concentrations above 10 to 15%.

The point by point comparison between the internal resonator theory and the experimental data is shown in Fig. 4-9. The agreement is reasonable, especially considering that this is a one-dimensional model! There are 11 points for which the difference between the percent of power to electrons from data and that predicted by theory is less than 10%, 9 points for which the difference is between 10% to 20%, 4 points between 20% to 30%, and 4 points between 30% to 40%.

As mentioned in Sec. 2.5.2, the amount of power mode-converted in the resonator model depends sensitively on the density at the edge, which is not well known, especially on the high-field-side. Thus, allowing a 2% variation in the two most sensitive parameters of the model (producing an approximately 1 cm uncertainty in the location of the high-field-side cutoff), and connecting the upper and lower limits of the theory points together, the trend predicted by the theory can be compared to the data points. This is shown in Fig. 4-10. The trend is not smooth at the edges because

[4]The quasi-linear theory to predict the effective minority ion tail temperature was worked out in Ref. [36]. In a very simplistic limit ($\xi \gg 1$), the minority temperature is inversely proportional to the minority density.

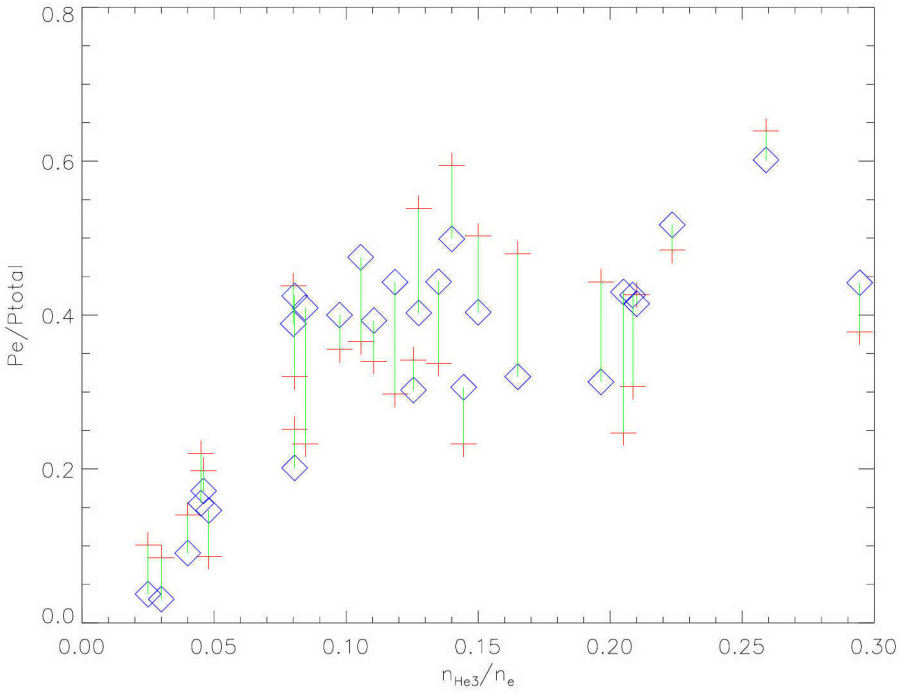

Figure 4-9: Mode conversion efficiency defined as the fraction of the total launched power that is damped on electrons (through MC IBW). The pluses are the experimental data points (for error bars, see Fig. 4-10), and the diamonds are the internal resonator theory prediction (weighted over all n and m numbers). The only free parameter for the theory is the helium-3 minority temperature (see text). The solid line connects the two, showing the discrepancy point by point.

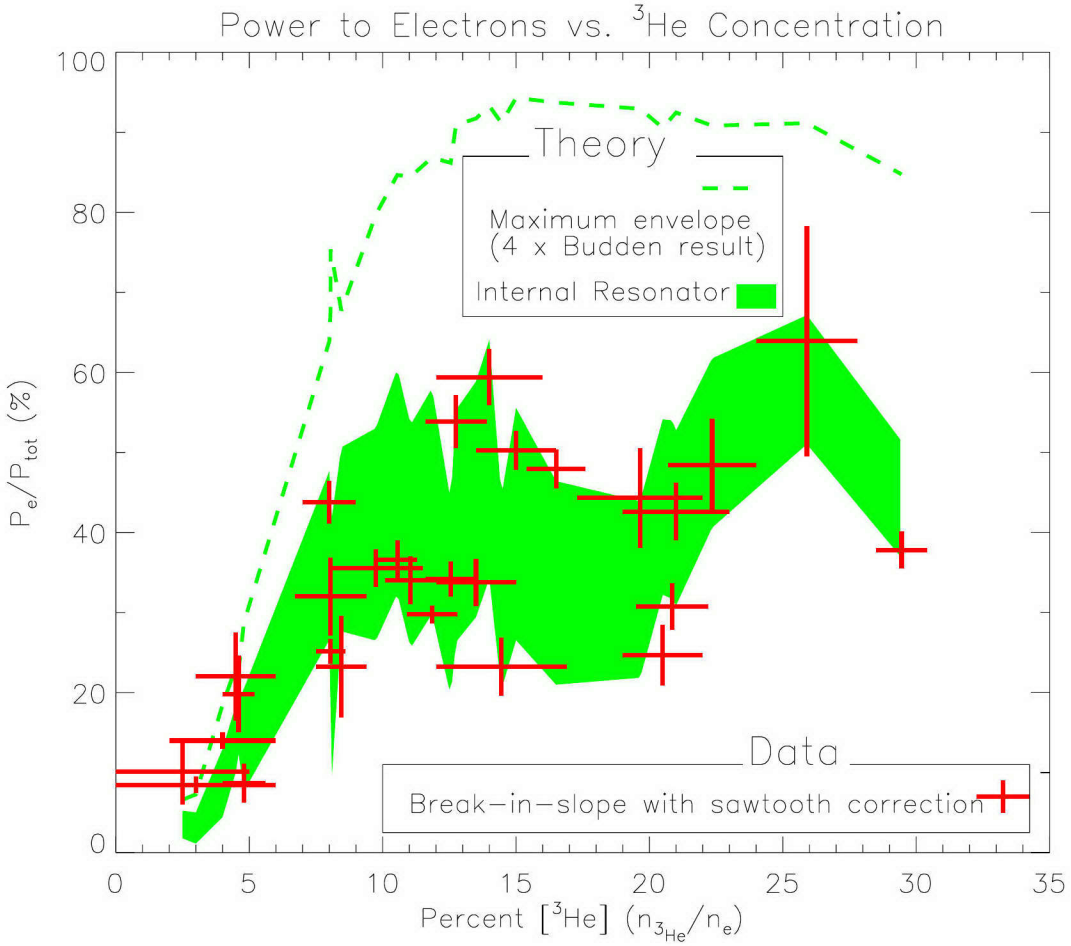

Figure 4-10: Mode conversion efficiency: internal resonator theory and experimental data. Pluses: experimental data points showing uncertainty in concentration and power fraction. Filled background: range of resonator theory, given by a 2% variation in α and $\tilde{\gamma}$. Dashed line: 4 times the simple Budden tunneling result.

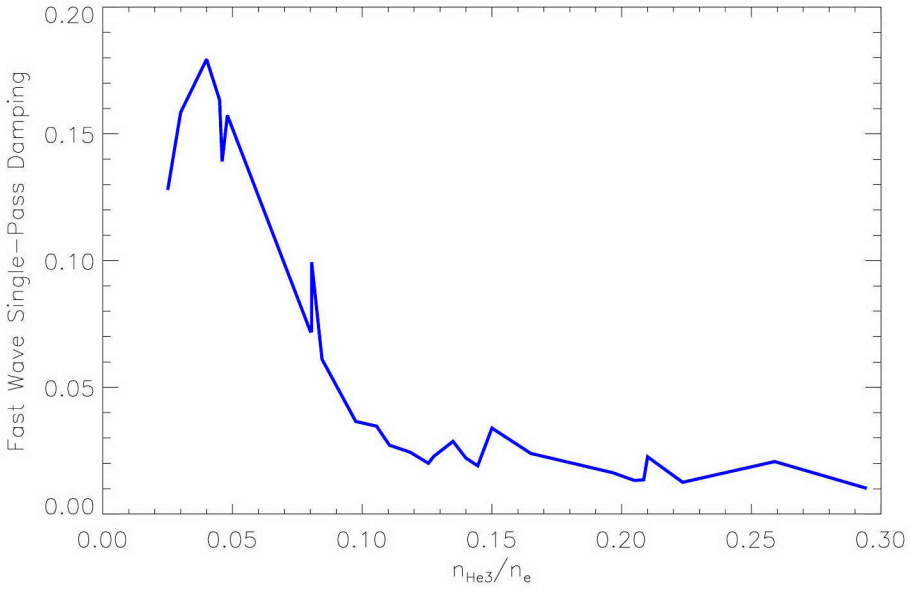

Figure 4-11: Fast wave single-pass damping (mostly cyclotron damping) before arriving at the mode-conversion layer, *vs.* helium-3 concentration. Strongest single-pass damping at 4% ^{3}He.

the points that are connected are for theory predictions of individual data points, for which the ^{3}He concentration is not the only parameter that is changing. The ^{3}He concentration is one of the main factors determining the mode conversion efficiency, but there are also variations in density, density profile, and magnetic field from point to point. This can account for some of the large differences in data, even for nearly the same concentration. Some of the variation is also due to the large error bars in both power fraction and helium concentration, which are very difficult to determine experimentally. This means that the ^{3}He concentration used in the theory may be off by several percent and thus be giving an answer that is not the appropriate one to compare to the data.

The single-pass fast wave damping due to integrating the imaginary part of $k_\perp$ from the plasma edge to the $n_\parallel^2 = L$ cutoff is dominated by the cyclotron damping. This is plotted in Fig. 4-11 as a function of helium-3 concentration, which indicates that the strongest ion heating should occur near $n_{\mathrm{He3}}/n_e \approx 0.04$. The minority ion cyclotron damping should not contribute much to the experimentally measured

profiles using the break-in-slope technique, which selectively tries to measure only prompt electron heating. However, the damping in Fig. 4-11 also includes some direct electron Landau damping of the fast wave, which would show up in the experimental break-in-slope profiles. This is not accounted for in the internal resonator mode-conversion theory, which could explain the slight underestimate of the theory at low concentration where some of the data points lie above even the maximum 4×Budden envelope. For example, at the 0% to 5% n_{He3}/n_e level, the experimental power fraction to electrons of ~10% could be mostly due to direct electron Landau damping near the magnetic axis, while the theoretically expected mode-conversion fraction is at most a few percent.

Figure 4-12 compares the internal resonator theory to an even simpler theory. As mentioned in Sec. 2.5.1, the amount of mode-converted power in a single-pass through the mode conversion region depends on whether the cutoff or resonance is encountered first. For LFS incidence (cutoff first), some fraction of the power is transmitted (T), some is reflected ($R = 1 - 2T + T^2$), and the rest is mode-converted ($C = T(1 - T)$). For HFS incidence (resonance first), no power is reflected, the same amount is transmitted as from the LFS (T), and the rest is mode-converted ($C = 1 - T$). The lowest dashed line ($T(1 - T)$) in Figure 4-12 shows the amount of power mode-converted (assuming it all ends up damping on electrons) from just a single-pass from the LFS. (A weighted sum of all m and n numbers is used for the calculation.) The next highest dashed line is the result of considering two passes: first, some power is mode-converted by passing through the MC region from the LFS, and some is transmitted (the reflected portion is assumed to be lost). The transmitted portion is assumed to reflect from the HFS edge, and to encounter the MC layer from the HFS, where a fraction $(1 - T)$ of the incident power is mode-converted (the transmitted power is also assumed to be lost). The total power thus mode-converted from two passes is $2T(1 - T)$. Note that this is the most direct comparison to the internal resonator theory, which also assumes that power reflected from the mode-conversion region is lost to the low-field side. This prediction generally falls within the range of the internal resonator theory prediction, but cannot explain the large

variation in the data as the helium-3 concentration is increased.

The dot-dashed line in Fig. 4-12 is the result of a calculation in which the single-pass fast wave damping on the helium-3 cyclotron layer (i.e., on helium ions)[5] is included. Let the single-pass damping of the fast wave on ions in the low-field side region (between the mode conversion layer and the LFS edge) be F. Then, when a certain amount of power leaves the antenna, a fraction $(1 - F)$ will continue on to encounter the mode-conversion layer. By considering the two passes as described in the previous paragraph, a certain amount of that power will be mode-converted, and a certain amount will continue back through the LFS region (this includes the amount first reflected when the MC layer is encountered from the LFS, and the amount transmitted when it is encountered from the HFS). This remaining power will encounter the cyclotron layer again, then what is left is assumed to reflect perfectly off the LFS edge (at the $n_\parallel^2 = R$ layer), and start the whole process over again. By adding the contribution to the mode-converted power from an infinite number of passes, a convergent infinite series is obtained whose sum can be expressed in terms of the Budden single-pass transmission factor T and the single-pass fast wave damping on ions F:

$$C_\infty = \frac{2T(1-T)(1-F)}{F(2-F) + 2T(1-T)(1-F)^2}. \tag{4.5}$$

Note that $1 - C_\infty$ is the amount of power predicted to go to the ions in this model where there are only two competing damping mechanisms: mode conversion, in which power ends up on electrons, and cyclotron damping, in which power ends up on ions. If $F = 0$, then $C_\infty = 1$, indicating that all the power goes to electrons if there is no fast wave damping, and if $F = 1$ then $C_\infty = 0$, indicating that no power reaches the electrons if it is all damped on ions first. This factor is calculated for each n and m number for which the mode-conversion should apply (see Figs. 2-30 and 2-31 for examples where it would not apply), and then the weighted sum is shown by the dot-dashed line in Fig. 4-12. It is interesting to note that this prediction ends up

[5]This is calculated from the imaginary part of the fast wave from a first order $k_\perp \rho$ dispersion relation. This includes some contribution from direct electron Landau damping, which would end up on electrons, not ions. However, the dominant contribution is from the cyclotron damping, so no attempt to correct this small discrepancy is made in the calculation of F.

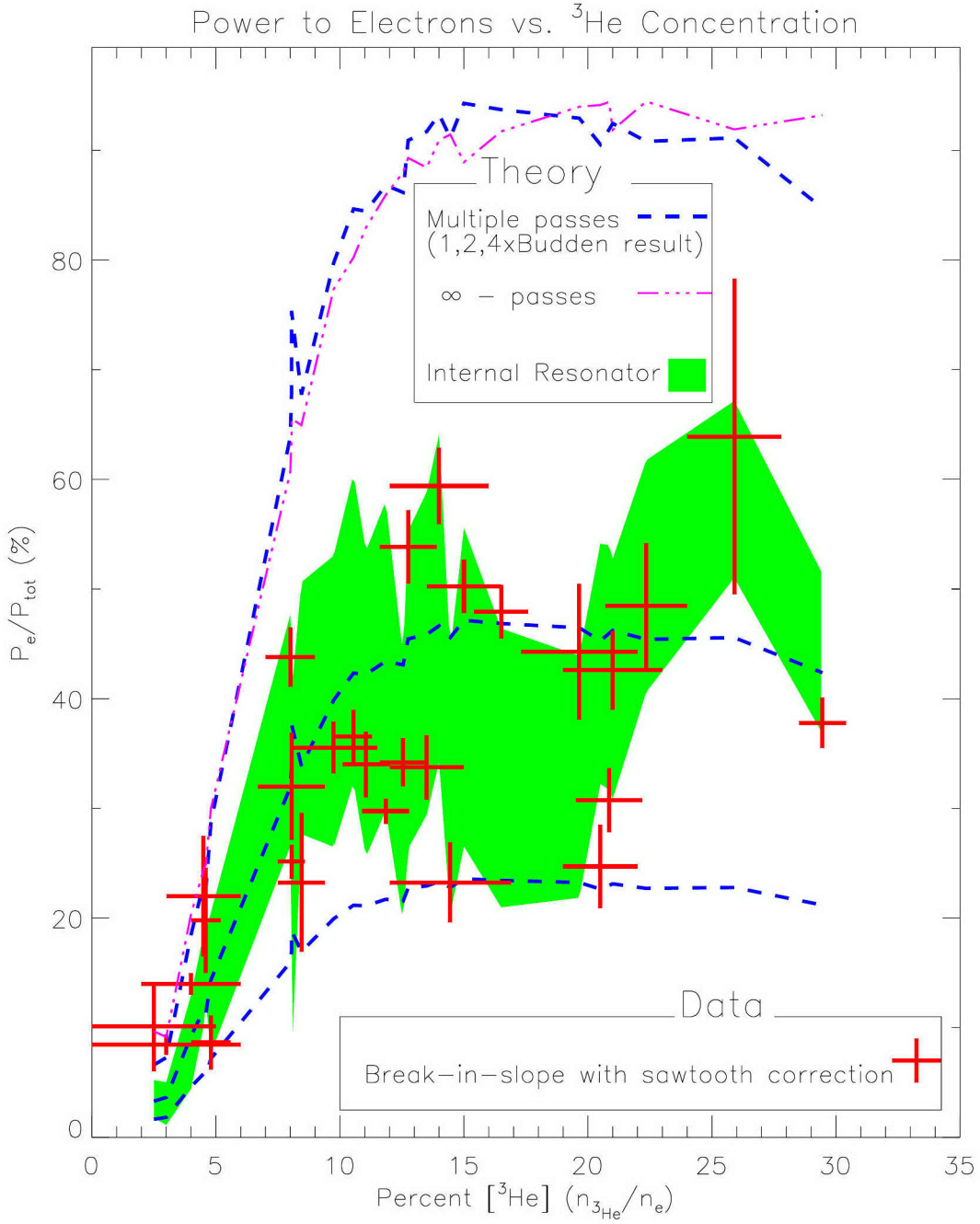

Figure 4-12: Mode conversion efficiency showing the comparison between the internal resonator theory and a simple multiple-pass theory. Pluses are experimental data points, the filled background represents the range of the resonator theory, and the dashed and dot-dashed lines are from the multiple-pass theory. The three dashed lines are: (bottom) single-pass through the MC region, (middle) double-pass through the MC region (first LFS then HFS), and (top) four times the single-pass result (the maximum envelope from internal resonator theory). The dot-dashed line is the infinite-pass model (which considers the balance between mode-conversion and cyclotron damping).

being almost the same as the maximum expected mode conversion from the internal resonator theory (disregarding the phase) of $4T(1-T)$ (see Eq. 2.84), which is shown by the highest dashed line. It is clear that the infinite-pass model does not agree with the experimental data. This could be partially due to the presence of other damping mechanisms, such as edge losses and ion damping on the HFS of the MC layer. It is also due, in part, to having ignored the phase information and the interference of the RF electric field as it passes through the plasma and encounters the cutoffs and resonances.

The internal resonator theory described in Sec. 2.5.2 and compared to experimental data from D(^{3}He) plasmas in this section offers a qualitative explanation of the results, which show large variation in mode-conversion efficiency as a function of helium-3 concentration. It emphasizes the importance of considering the phase of the electric field, which is ignored in a single- or multiple-pass picture of RF wave propagation and damping in the plasma. It can be used to quickly explore new regimes for efficient mode conversion.

4.4.2 TORIC results

The previous section has illustrated the importance of considering the global field solution as opposed to viewing the RF waves as just passing through the resonances and cutoffs. The global field solution in two dimensions can be calculated by a full-wave code such as TORIC. Of course, much more information than just the mode-conversion efficiency can be obtained from TORIC. (For example, the density fluctuation can be predicted and compared to PCI observations, as shown in Ch. 5). However, for the purposes of this chapter, the fraction of power deposited to electrons from TORIC using full toroidal geometry and two dimensions will be compared to the data and the one-dimensional resonator theory.

As described in Sec. 2.6, many poloidal modes are needed in a TORIC simulation in order to properly resolve the short-wavelength mode-converted ion Bernstein wave. An example of such a run using 155 poloidal modes comparing the electron power deposition to one of the experimentally determined profiles (the 19.6% ^{3}He case in

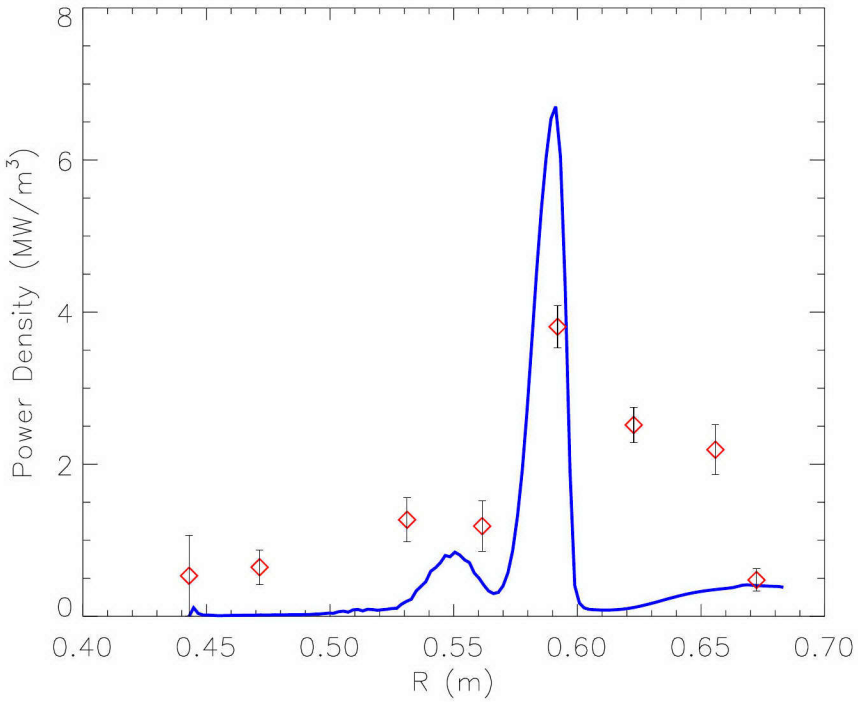

Figure 4-13: Electron power deposition profile (on the high-field-side). Solid line: TORIC prediction ($n_\phi = 10$); diamonds: experimental data, obtained by using the "break-in-slope" technique.

Fig. 4-8, which corresponds to C-Mod shot 960131008 at time 1.10138 sec) is shown in Fig. 4-13.

The position of peak heating in the experimental points is at the same location as the peak in the TORIC profile. The value of peak heating is smaller than the peak heating predicted by TORIC (as is usually the case). This is partially due to the fact that the GPC channels average over $\sim$1 cm radially and $\sim$3 cm vertically. Another reason the experimental profiles are usually lower (and broader) than the TORIC predictions are that the TORIC result is for only one toroidal mode number. Other toroidal mode numbers are slightly different, and when summed together would result in a broader and lower profile. Finally, the experimental profiles are usually broader than the actual direct electron heating profile because the heat transport effects are not completely removed by the break-in-slope analysis.

The two inner points (at ~0.65 and ~0.62 m) that are much higher than the TORIC prediction could be due to some indirect effect of the ion cyclotron damping appearing in the break-in-slope through collisional heating of the electrons. Examining all the experimental profiles in Fig. 4-8 reveals that there are occasionally unexpected points such as these two, usually near the axis (which may be due to the ion cyclotron damping effect just mentioned, or possibly due to sawtooth interference) or out near the edge, on the high-field side (which may be real electron heating due to a second mode conversion layer on the high-field side sometimes present in these D(^{3}He) scenarios, where a kinetic shear Alfvén wave is excited). However, on the whole, the profiles match with the expectation that there is a sudden onset of heating corresponding to the flux surface that first intersects with the roughly vertical electron Landau damping region, followed by a rapid fall-off to the high-field side as the IBW wave power is damped away.

Integrating the power deposition profiles from TORIC produces predictions that can be compared to the experimental data points. A series of runs with only 15 poloidal modes was completed several years ago. These results are shown by the open diamonds in Fig. 4-14. At higher concentrations, the TORIC results with only 15 poloidal modes are completely unresolved and the power fraction predictions are practically meaningless. Higher resolution runs are shown by the filled diamonds, but only for one dominant toroidal mode number of +10. To get a more accurate prediction, many toroidal mode numbers should be run, and the power deposition from each added with the proper weighting (related to the predicted loading), to get a prediction appropriate for the C-Mod antenna spectrum. As the computing resources become available, this could more easily be performed. However, even one toroidal mode number includes hundreds of poloidal mode numbers so a wide range of $k_{\|}$ is included in the TORIC analysis. Note that the TORIC points fall in the range of the data (and the internal resonator theory, see Fig. 4-10), except for the highest concentration points near ~30% ^{3}He. The pair of connected points at 29.45% ^{3}He are the results of two different n_ϕ numbers, the upper one for $n_\phi = 10$ and the lower one for $n_\phi = -10$. This is to give an indication of the possible range of values

from the full spectrum of n_ϕ numbers. To get a complete answer, TORIC should be run for a full spectrum of n_ϕ numbers, and the results should be summed according to each n_ϕ mode's partial loading in the C-Mod antenna spectrum. More data should be taken at these high concentrations, with well diagnosed plasmas (especially the density profile and the helium-3 concentration).

4.5 Future Observations with PCI

Unfortunately, since the installation and upgrade of the phase contrast imaging system to directly observe ICRF waves in early 2000, there have not been suitable D(^{3}He) plasmas at 7.8 tesla, due to an administrative limit of 6 tesla to protect the toroidal field coils from damage, after a major arc ocurred while running at 7.8 tesla in the last high-field campaign in February of 1998. When high-field runs resume in the future, the PCI diagnostic can be used to test the TORIC predictions of the D(^{3}He) mode conversion process by measuring the density fluctuation associated with the resonance and FW–IBW coupling region. In addition, the J-port antenna could be run at lower frequency in order to place the D(^{3}He) mode conversion layer in the plasma with a lower central field, and the PCI diagnostic could attempt to view the mode-conversion process 144° away toroidally, if the FW and/or the IBW propagate that far. However, other experiments have been designed to look at mode-conversion with the PCI below 6 tesla, using H–D–^{3}He plasmas. These experiments will be discussed in Ch. 5.

4.6 Summary of Chapter 4

The D(^{3}He) FW to IBW mode conversion scenario at 7.8 T in Alcator C-Mod is very efficient at exciting the ion Bernstein wave in the core of the plasma. The IBW deposits its power through electron Landau damping in a region of a few centimeters. The internal resonator theory and TORIC predictions agree reasonably well with the data. This scenario would be a good candidate for mode conversion current drive

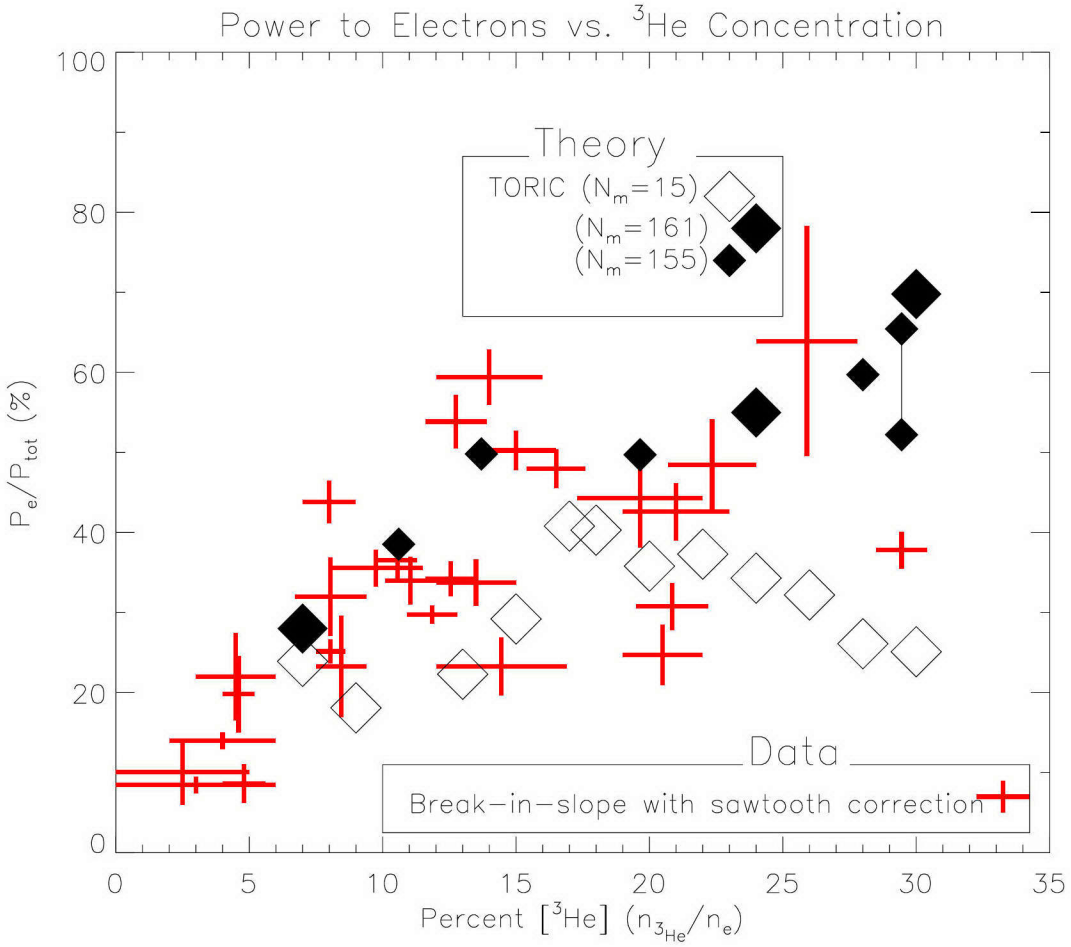

Figure 4-14: Mode conversion efficiency: TORIC predictions and experimental data. Pluses: experimental data points showing uncertainty in concentration and power fraction. Diamonds: TORIC prediction for $n_\phi = 10$ (except for the pair of small diamonds connected by a line – the lower one is $n_\phi = -10$ and the upper one is $n_\phi = 10$). Open diamonds are for only 15 poloidal modes, large filled diamonds are for 161 poloidal modes and 240 radial elements, small filled diamonds are for 155 poloidal modes and 160 radial elements.

and flow drive experiments, by phasing the antenna to drive a toroidal current (i.e., 90° phasing of adjacent antenna straps). Also, with very localized heating, a poloidal flow could be driven. These effects could result in better control of heat and particle transport, resulting in improved confinement.

Chapter 5

Mode Conversion Experiments in H–^{3}He–D Plasmas

This chapter presents the results of experiments which make major contributions toward the understanding of mode conversion in toroidal geometry. In all of these three ion species plasmas, TORIC code results show that there is a curved region of strong IBW electric field that extends back toward the low-field side (LFS) of the fast wave mode-conversion layer, roughly along a magnetic flux surface. The parallel electric field plays an important role in the IBW PCI observations. The source of the up/down asymmetries in the electric field solutions for specific toroidal mode numbers are clarified. This chapter also raises questions which are not yet completely answered, representing a challenge to theory and suggesting directions for future work.

As mentioned at the end of Ch. 4, the PCI has not yet been able to study the FW to IBW mode conversion process in D(^{3}He) plasmas at 8 T. However, indirect evidence of mode-converted IBWs (through Landau damping on electrons) was discussed. More direct measurements are now possible in C-Mod with the new capability of the PCI system to detect RF waves in the plasma (see Sec. 3.2). An experiment was designed (with H–^{3}He–D plasmas at 6 T) to observe mode-converted ion Bernstein waves directly in a hot tokamak plasma with phase contrast imaging for the first time.

5.1 Previous IBW measurements in tokamaks

Previous efforts to measure ion Bernstein waves directly in magnetic fusion experiments have relied on small-angle laser scattering (see Refs. [83, 84, 85, 86, 87, 88, 51, 89]). These experiments include observations of mode-converted ion-ion hybrid waves, as well as IBWs associated with higher ion-cyclotron harmonics, even up to the eighth harmonic (although the higher harmonics were measured with probes, not laser scattering [87, 18]). The laser scattering method is well-suited to measure the wave number and hence the dispersion relations for IBWs. In some experiments, estimates were made of the magnitude of the density fluctuation associated with the waves. However, laser scattering only allows the observation of a small volume of plasma and a small range of wavenumbers, beginning with already fairly short wavelength features. This means that the transition from the long-wavelength fast wave to the short-wavelength ion Bernstein wave is not easily observable. PCI allows the observation of a large region of plasma and a wide range of wavenumbers simultaneously. Since a mode-converted ion Bernstein wave is excited near a resonance where the FW and IBW wavenumbers coincide (typically 1 to 3 cm^{-1} for C-Mod), it is important to resolve small wavenumbers as well as large ones to get a complete picture of mode conversion, propagation, and damping.

5.2 Experimental Design

In order to directly image the effects of a mode-converted IBW in the tokamak, the plasma must be designed so that there exists an ion–ion hybrid layer in (or near) the view of the PCI laser. Mode conversion occurs in the vicinity of the hybrid layer, which in a cold plasma is given by the condition $n_\parallel^2 = S$ (see Sec. 2.1.1), for a given parallel wavenumber $n_\parallel = ck_\parallel/\omega$. The C-Mod two-strap antenna launches a spectrum of parallel wavenumbers, which may evolve as the wave propagates through the plasma, so that there may be an extended region where mode conversion can occur. However, the dielectric tensor element S is usually large enough that for most

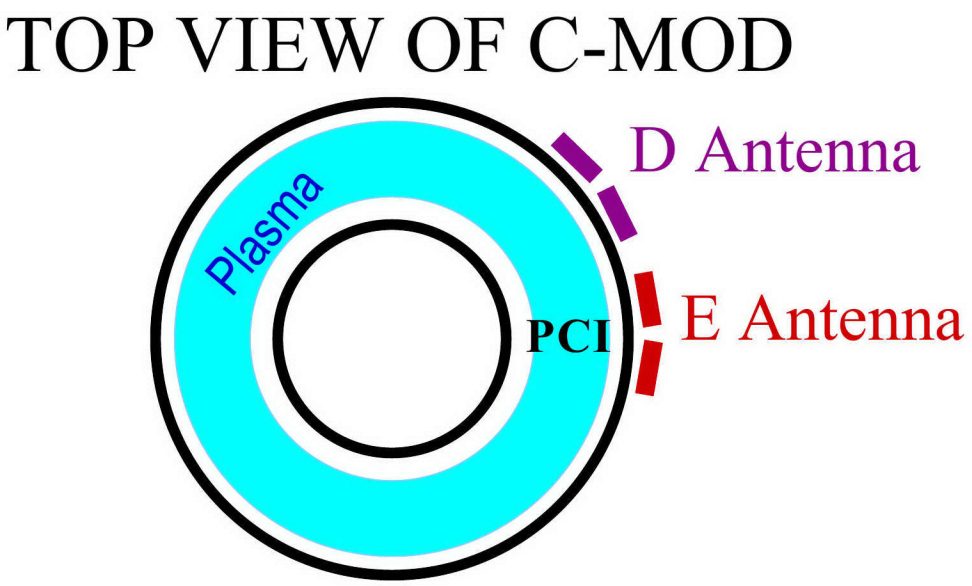

Figure 5-1: Top view of C-Mod showing the location of the PCI diagnostic directly in front of the E-port antenna, which is 36° away from the D-port antenna.

FW wavenumbers, this region is restricted to a few centimeters in C-Mod. Because the PCI viewing chords are limited by the extent of the vertical access port to be between 60 cm and 79 cm major radius, the mode-conversion region should be somewhere near the center[1] of the plasma (which is usually at 67 cm), so that the beginning (i.e., where the IBW is "launched" from the FW), and possibly the end (i.e., where the IBW is damped away) of the IBW signal amplitude across the major radius can be observed.

In addition to having a mode-conversion layer present in the vicinity of the PCI viewing window, the fast wave must couple a significant amount of power to the IBW for it to be observed. This means that the evanescent gap (between the $n_\parallel^2 = L$ cutoff and the $n_\parallel^2 = S$ resonance) must be of the right size to allow efficient mode conversion (see Sec. 2.5).

The fast wave antennas closest to the PCI diagnostic (the PCI is located at E-port) were chosen for these experiments because they offered the greatest chance of success. These were the D-port antenna with fixed frequency of 80.5 MHz, and the E-port

[1]Recent TORIC simulations (see Sec. 5.5) has shown that perhaps it is sufficient to merely have the MC layer to the HFS of the PCI viewing window, because the short-wavelength oscillations will appear to the LFS of the FW mode-conversion layer.

antenna at 80.0 MHz. (See Fig. 5-1 for a top view of C-Mod, showing the location of the relevant ICRF ports). Working within the constraints of these frequencies and a maximum central magnetic field of 6 tesla, a set of plasma parameters was found which in theory would ensure good mode conversion. In a plasma consisting of hydrogen and helium-3, a mode conversion layer between the H and ^{3}He fundamental cyclotron layers could exist near the center of the plasma. Because the majority of C-Mod experiments are conducted using deuterium plasmas, and experience has shown that it is difficult to reduce the background deuterium level to negligible levels after running with deuterium plasmas, a certain amount of deuterium must also be expected. With fields below 6 T, the deuterium cyclotron resonance will not actually be in the plasma, but the presence of deuterium affects the location of the $n_\parallel^2 = S$ layer, and the width of the evanescent gap. In fact, some amount of deuterium is advantageous to reaching a broader range of parameters with good mode conversion possibilities, as can be seen in Fig. 5-2. There is another reason why the presence of deuterium is actually desirable for the purposes of observing the oscillations due to the IBW. Peter O'Shea discussed the effect of deuterium on H–^{3}He mode conversion experiments in his thesis [60, Ch. 8.3]. It turns out that the IBW is more weakly damped when there is deuterium present in the H(^{3}He) plasma (most likely because the group velocity is increased with the presence of deuterium), resulting in broader power deposition profiles. This also means that for the PCI observations, the IBW oscillations should be visible over a larger distance.

Thus with a comparable mix of deuterium, helium-3, and hydrogen with central magnetic fields from 5.3 T to 6 T, the mode conversion region is near the center. The exact location and mode conversion efficiency depends sensitively on the exact species mix.

5.2.1 Expected Mode Conversion Efficiency

As was shown in Sec. 2.5, the maximum mode-conversion efficiency that could reasonably be expected is four times the simple Budden tunneling result. The tunneling width η depends on many plasma parameters, but for this regime it was most sensi-

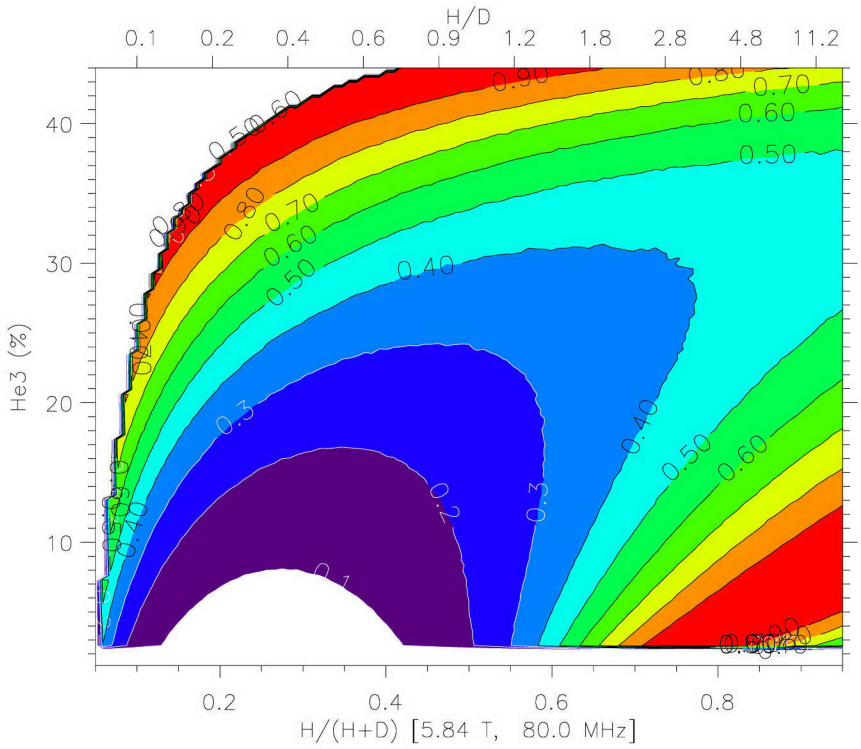

Figure 5-2: The numbers on the contour lines indicate the maximum expected mode conversion (MC) efficiency (4 times the Budden result) as a function of H, D, and ^{3}He concentration. For example, in the region between the lines labeled 0.3 and 0.4, the maximum MC efficiency rises from 30% to 40%. The expected MC efficiency rapidly falls to zero at the edges of the plot (where the contour labels pile up) at the lower right and the upper left because there the MC layer is too close to the cyclotron layer of a minority species and the MC efficiency is assumed to be zero due to interference from the Doppler-broadened cyclotron layer.

tive to the plasma density, the parallel wavenumber, and the ion concentrations. In order to search for good regimes of operation for H–^{3}He mode conversion, a plot of "concentration space" can be examined for regions of maximum Budden tunneling. Figure 5-2 shows the result of such a calculation for a central electron density of $2.4 \times 10^{20}\,\mathrm{m}^{-3}$, central toroidal field of 5.84 T, an RF frequency of 80 MHz, toroidal mode number n_ϕ of 10, and poloidal mode number m_θ of 0. There are only two free parameters because plasma neutrality demands that the concentrations are related:

$$2n_{\mathrm{He3}} + n_D + n_H = n_e. \tag{5.1}$$

There are two regions of strong mode conversion. In the lower right corner is a regime corresponding to a majority hydrogen plasma with very little deuterium, and a moderate amount ($n_{He3}/n_e \sim 10\%$) of helium-3. However, this regime was not the primary target for these mode-conversion experiments as it would be difficult to maintain such a low deuterium concentration, and also the mode conversion layer would be too far beyond the PCI viewing window to the high-field side (HFS).[2] (See Fig. 5-45 for a plot of the mode conversion location in concentration space.) Another broad operating regime is along the top of the plot, corresponding to high ^{3}He concentration and comparable amounts of H and D. This regime has the further advantage of locating the mode conversion near the center of the PCI viewing window for magnetic fields of 5.5 T to 5.9 T. It was also found that lowering the density from the normal 2–3$\times 10^{20}$ m^{-3} to $\sim 1 \times 10^{20}$ m^{-3} should increase the mode conversion efficiency everywhere in this operating space (Fig. 5-3), so a low target density was sought for these experiments. (The internal resonator theory prediction exhibits the characteristic oscillation with plasma parameters described in Sec. 2.5.2.)

5.3 The Dispersion Relation: Phase velocity *vs.* Group velocity

The FW to IBW mode conversion process can be illustrated by the dispersion relation for these waves. The dispersion relation for this three species mix is very similar to the D(^{3}He) cases shown in Fig. 2-17. The ion–ion hybrid pair in this case is H–^{3}He. The presence of the third species, deuterium, can alter the location of mode conversion and the efficiency, but it does not change the fundamental shape of the dispersion relation. Figure 5-4 demonstrates the expected mode conversion process for a plasma with the following parameters: $n_{e0} = 2.4 \times 10^{20}\,\mathrm{m}^{-3}$, $T_{e0} = 1.5$ keV, $B_0 = 5.84$ T, 33%

[2]Although later analysis of the helium-3 concentration (see Appendix D) seems to suggest that the plasmas were often in or near this regime for the mode conversion experiments. TORIC results (see for example Fig. 5-50) also indicate that this regime can produce IBW oscillations within the PCI viewing window, even though the $n_\parallel^2 = S$ layer for the FW is to the HFS of the PCI.

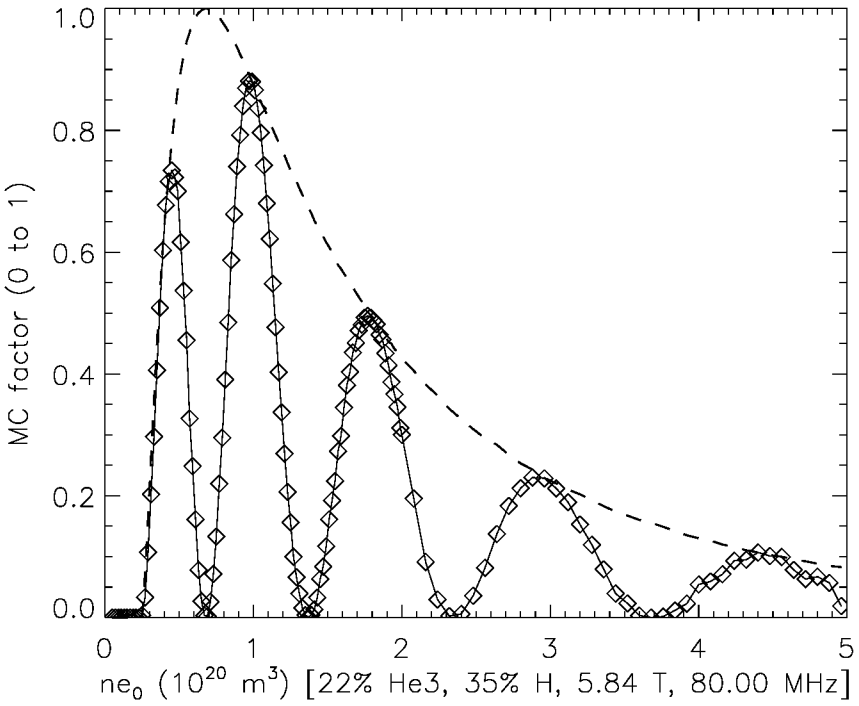

Figure 5-3: The maximum expected mode conversion efficiency as a function of density (dashed line). Also shown is the internal resonator model result (solid line with diamonds, see Sec. 2.5.2) for one toroidal and poloidal mode number. Plasma parameters were: 35% H, 22% He3, 21% D, 5.84 tesla, $n_\phi = 10, m_\theta = 0$. Below a density of 0.25×10^{20} m^{-3}, there is no mode conversion possible because the $n_\parallel^2 = R$ cutoff has moved to far to the LFS (beyond the $n_\parallel^2 = S$ layer).

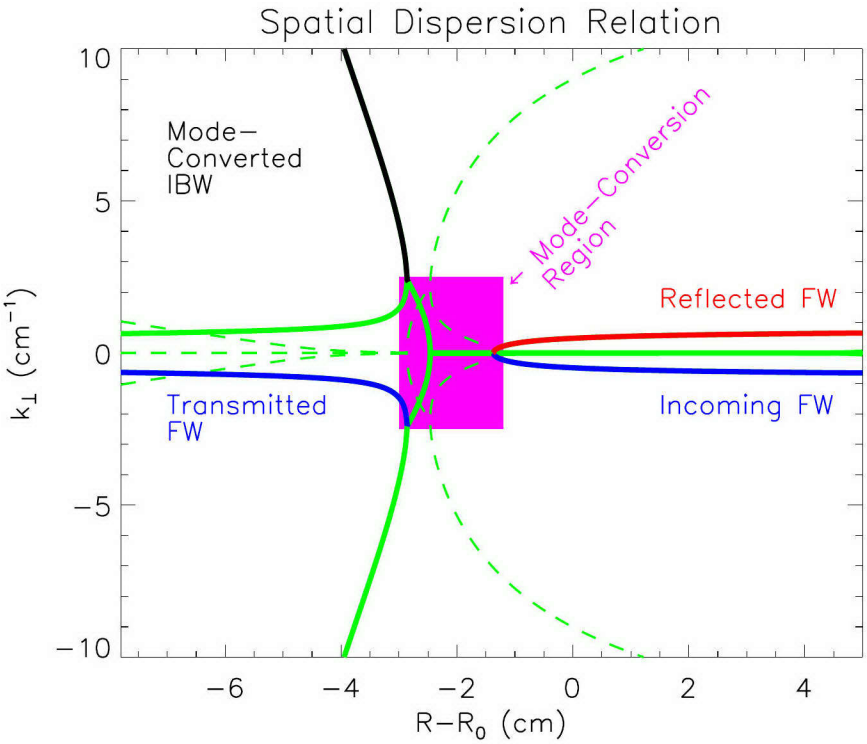

Figure 5-4: The full electromagnetic dispersion relation, showing the fast wave (FW) and ion Bernstein wave (IBW) branches connected by a mode-conversion region. The dashed line is the imaginary part of $k_\perp$. For the fast wave, this is practically zero on this scale outside the mode conversion region, but the IBW has a pure imaginary (i.e., evanescent) $k_\perp$ to the LFS of the mode conversion region, and a small imaginary part (electron Landau damping) to the HFS.

H, 21% D, 23% ^{3}He, $T_{i0} = 1.4$ keV, $f = 80.0$ MHz, $R_0 = 0.66$ m, $a_0 = 0.22$ m, and profiles with the following shapes: letting r be the minor radius, the density profile was $n_e(r)=n_{e0}(0.042 + (1 - 0.042)(1 - (r/a)^2)^{0.5})$ and the temperature profile was (for both electrons and ions): $T(r)=T_0(0.13 + (1 - 0.13)(1 - (r/a)^2)^2)$. 100 terms in the Bessel function sums (see Eq. 2.39) were retained for each ion species, and 10 for electrons (see Sec. 2.4.1 for more on the electromagnetic dispersion relation code used to produce this plot). $k_\perp$ for both the FW and IBW near mode conversion is shown, for fixed $k_\parallel = 0.14\,\mathrm{cm}^{-1}$. The perpendicular direction is in the major radial direction (along the midplane, i.e. $Z = 0$ cm). A negative k number means phase propagation away from the antenna, which is the direction of decreasing major radius, hence $k < 0$. Positive k number is phase propagation towards the antenna. For the fast wave, the group velocity is nearly in the same direction as the phase velocity, so that the initially excited wave is represented by the negative k number branch at ~ -1 cm^{-1}. Upon reaching the mode-conversion region near $R = 0.64$ m, part of the fast wave power reflects back to the antenna (along $k \sim 1\,\mathrm{cm}^{-1}$), and part of the fast wave tunnels through, propagating to the HFS. Part of the power is also mode-converted to an IBW, beginning at $k \sim 2\,\mathrm{cm}^{-1}$, and rapidly decreasing in wavelength. Although the IBW's (initial) group velocity is in the same direction as the transmitted FW, because it is a backward wave, its phase velocity is towards the antenna (positive k). The sign of the group velocities can be seen from the slope of the curves[3], which is the same for the incoming FW, transmitted FW, and mode-converted IBW. Only the reflected FW has a different sign.

Note that this dispersion relation is for an assumed constant $k_\parallel$, and for a path along the midplane. In reality, as the IBW propagates away from the mode conversion region, the parallel wavenumber will evolve, and the propagation path may depart from the midplane. This has been studied with ray-tracing of the IBW [50, 90]. As

[3]The group velocity can be related to how the normalized frequency (ω/Ω_i) changes with respect to the normalized wavenumber ($k_\perp \rho_i$). In Fig. 5-4, even though the frequency is fixed, the cyclotron frequency changes due to the 1/R dependence of the toroidal field. (The density and temperature do not change much in the region covered in Fig. 5-4.) So a change along the horizontal axis can be viewed as a frequency change.

the IBW parallel wavenumber becomes such that $\omega/(k_{\|}v_{\rm the}) \sim 1$, the group velocity can radically change direction, with the wave energy propagating mostly in the poloidal direction, and may even turn back towards the mode conversion region [90]. This effect may also be discernible in TORIC code results (see Sec. 5.5.4), although questions still remain about the validity of direct comparison between the TORIC results and ray-tracing from a local dispersion relation.

5.4 Data: Phase Contrast Imaging of IBWs

Considerable theoretical effort has been devoted to understanding the process of mode-conversion and exactly how much power can be transferred to the plasma through the IBW in hot fusion plasma experiments [50, 37, 59, 23]. The PCI data can help validate and test ICRF theory and codes concerning fast wave mode conversion to an IBW and subsequent damping, because the PCI measurements are related to the structure and magnitude of the RF wave fields near mode conversion. Initial RF PCI results have been presented at the APS meetings [91, 92] and in Ref. [80].

The important aspects of the PCI observations, especially as compared to expected theory, are summarized in this paragraph. Near mode conversion, according to the local dispersion relation, the fast wave and IBW share a wavenumber of approximately 2 to 3 cm^{-1}. The IBW wavelength becomes shorter (wavenumber becomes larger) as it propagates away from the mode conversion layer. PCI signal structure with effective wave numbers (from Fourier analysis of the line-integrated PCI signal) ranging from +4 to +10 cm^{-1} has been observed, in these three ion species plasmas.[4] Positive wavenumbers indicate that the phase velocity is towards the antenna. The observed PCI signal scales linearly with the RF electric field (i.e., the square root of RF power). This is consistent with the linear relationship between n_{e1} and $E_{\rm RF}$ for small amplitude perturbations as described in Appendix C. The PCI signal structure moves across channels as expected during toroidal field ramps. The measured

[4]If spatial aliasing is taken into account, wavenumbers as high as +12 cm^{-1} can be inferred in some shots from the channel-to-channel phase advance.

line integrated amplitudes are of the same order of magnitude as that predicted by TORIC. One of the most interesting and unexpected features of the measurements is that the signal amplitude was not monotonically decreasing, as might be expected for an IBW that is launched with a given amplitude which then decays due to Landau damping. Instead, the PCI observations exhibited a complex structure of peaks and troughs in amplitude, separated by 1 to 2 cm, a spatial scale which is in between the wavelengths expected for the propagating fast wave and the propagating IBW. A possible explanation for these features is offered in Sec. 5.5, using the ICRF code TORIC.

5.4.1 RF heterodyne signal and RF pickup tests

In this thesis, the relevant PCI signal is only a small part of the total measurement, which must be separated out and studied separately. The PCI diagnostic was still sensitive to low-frequency fluctuations at the same time that it was being used to look for an RF signal. Because the background plasma fluctuations fall off in amplitude with increasing frequency [79], it is desirable to place the RF heterodyne frequency at the high end of the resolvable frequencies of the PCI system, which for these experiments ranged from ~2 to 500 kHz. A frequency of approximately 350 kHz was chosen because it was in a region with low background "noise" and because it was far enough below the Nyquist frequency that several points per period were sampled.

In order to observe oscillations at the RF frequency of 80.0 MHz from the E-port antenna and/or 80.5 MHz from the D-port antenna, the acousto-optical (AO) modulator frequency (as described in Sec. 3.2) was set to 40.075 MHz (placing the D-port heterodyne frequency at 350 kHz and E-port at 150 kHz) or 40.18 MHz (placing E-port at 360 kHz and D-port at 140 kHz). Figure 5-5 shows an example of a plasma discharge where both transmitter frequencies were detected simultaneously.

In order to verify that the coherent signal at the expected RF frequency is due to the heterodyning of a real RF signal in the plasma, and not merely RF pickup in the circuitry or detectors, a shot was taken with part of the laser beam blocked. The part of the beam passing through the less efficient ($\eta_1 = 0.25$) AO modulator (see

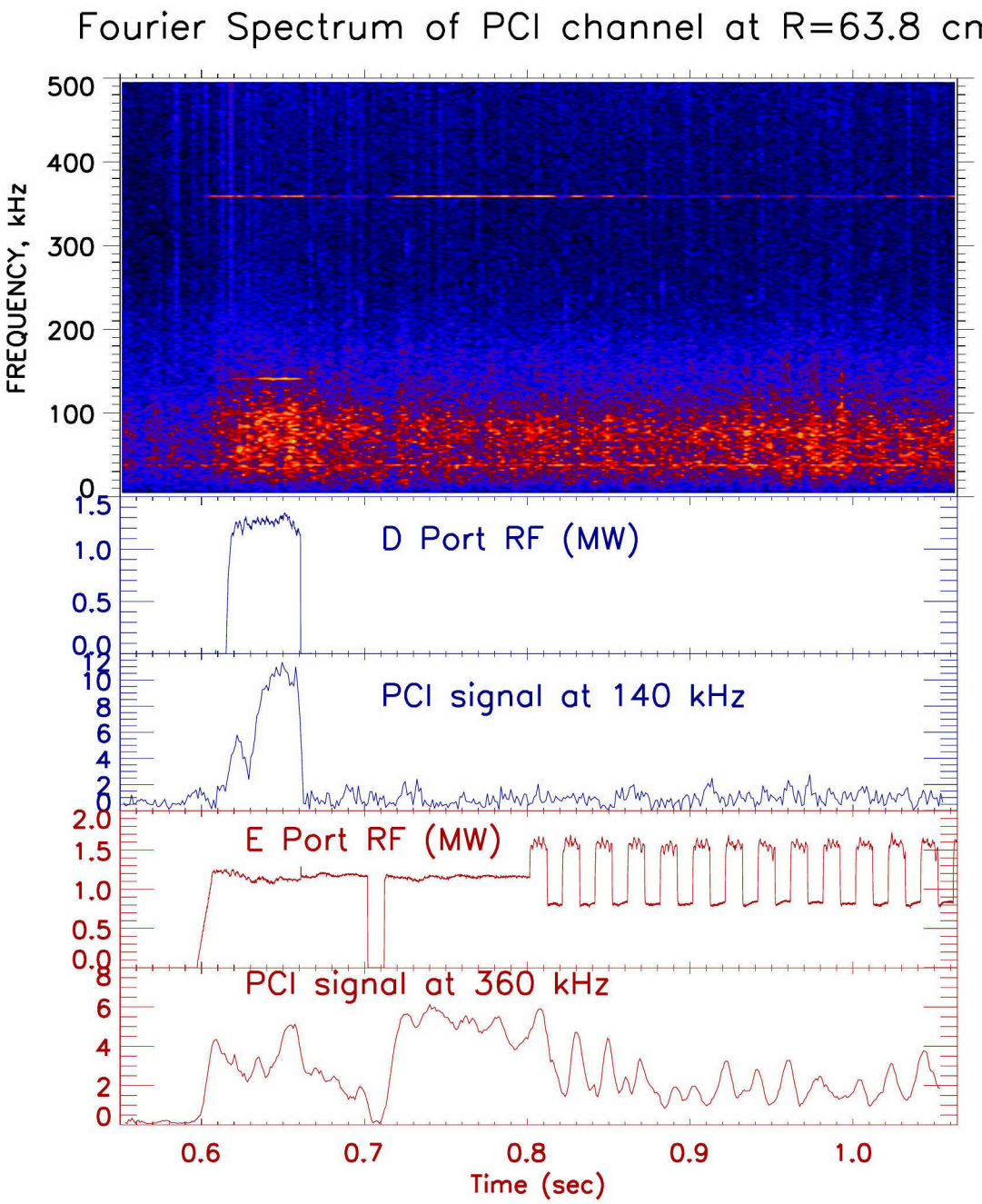

Figure 5-5: The PCI signal for one channel, Fourier-transformed in time (C-Mod shot 1000623020). Broadband fluctuations are seen from 10 to 130 kHZ, and a strong coherent signal is seen at 360 kHz (corresponding to the E-port antenna, bottom two panels), and briefly at 140 kHz (corresponding to D-port antenna, middle two panels). The PCI signal amplitude is plotted in arbitrary units.

Sec. 3.2) was blocked, while the half of the beam passing through the more efficient ($\eta_2 = 0.80$) modulator was allowed to pass through the plasma onto the detectors. Thus the average laser intensity fell to $0.4\,I_0$ as opposed to $0.525\,I_0$ during regular RF modulation. Figure 5-6 shows the result of an overlapping "windowed" Fourier analysis on the 12 PCI channels. In this case this means that a fast Fourier transform (FFT) was performed every 600 samples on the 2548 samples surrounding a certain time point. Since the digitizers take one sample every microsecond, the window width was 2.548 msec. The number of samples are chosen so that, as near as possible, an integral number of RF heterodyne periods falls within the FFT window. In this case, the expected RF heterodyne frequency from the previous shot was 359.105 kHz, so that 2548 samples represents 914.9995 periods. The Fourier amplitude of the desired frequency, converted to m^{-2} units using the sound wave calibration (see Sec. 3.3), is plotted in the left-hand column.[5] The E-port RF power (in MW) is shown at the bottom left on the same time scale as the PCI signal (which has a vertical scale from 0 to $5.81 \times 10^{14}\,\mathrm{m}^{-2}$). Note that there is a slight increase on the PCI signal as the RF power turns on. The Fourier amplitude for a nearby frequency to show the characteristic noise level in that frequency range is plotted in the right-hand column. (This is not the expected frequency for the D-port antenna; the lower right plot merely shows that there was no D-port power for this shot).

The PCI signal on channel 1 (R=68.66 cm) for these two frequencies is compared in Fig. 5-7. As the RF power turns on at 0.6 seconds, the expected frequency bin shows an increase in signal even though part of the beam is blocked. This could be due to residual RF pickup in the electronic circuitry, or an intensity modulation of the beam through non-linearities of the AO modulator producing higher harmonics of the driving frequency. Whatever the source of this noise, it is fairly low compared to the strong signals received on other shots (typically of order $2\text{–}3\times10^{15}\,\mathrm{m}^{-2}$). Another

[5]For each PCI channel, the voltage of the digitized signal is Fourier transformed. The appropriate frequency bin for the RF heterodyne frequency is identified, and the magnitude of the Fourier coefficient for that bin, multiplied by 2 (to take into account the symmetric part of the FFT spectrum above the Nyquist frequency), is compared to the sound wave voltage level (calculated in the same way, for the 15 kHz sound burst frequency) in order to convert the voltage to equivalent line-integrated m^{-2}.

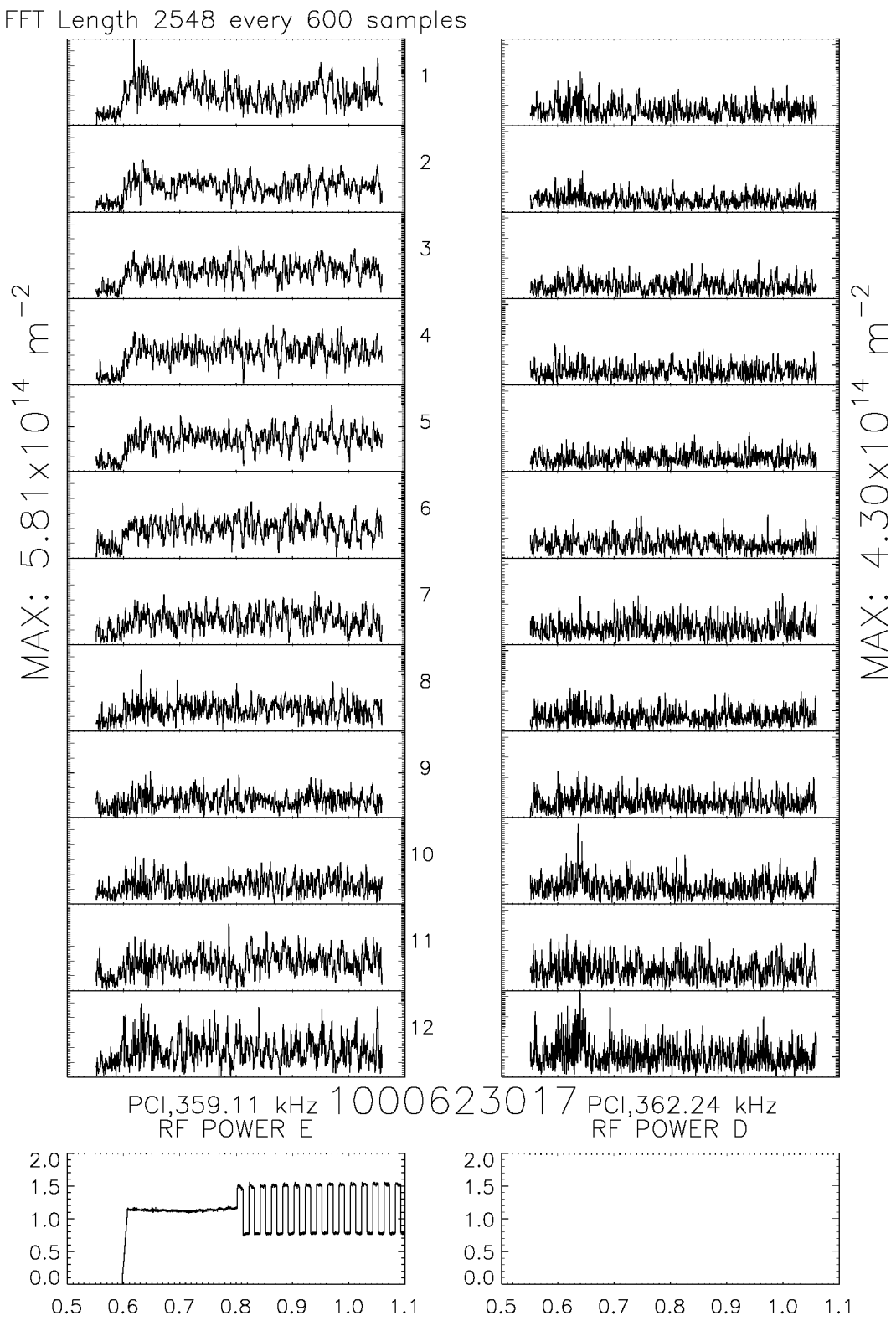

Figure 5-6: A test with the part of the laser beam blocked, in order to measure non-heterodyne RF noise pickup.

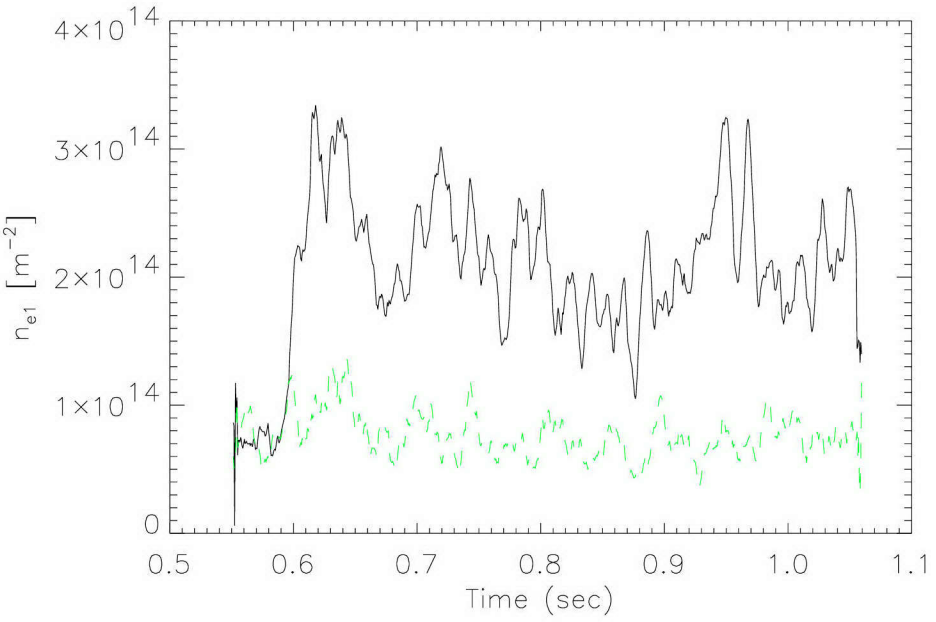

Figure 5-7: The PCI signal from channel 1 of Fig. 5-6, smoothed with a window of 15 data points. The larger signal (solid line) is the signal at the expected RF frequency of 359.11 kHz, and the smaller signal (dashed line) is the amplitude at 362.24 kHz.

indication that a signal is a real RF signal from the plasma and not just pickup is that the signal strength varies from channel to channel and with time. This can be seen in the data presented in this chapter and in Appendix E.

5.4.2 IBW oscillations in the filtered PCI signal

If the PCI is measuring a wave phenomenon, one expects to see oscillations at the wave frequency. Examining the raw PCI voltage does not reveal the oscillating RF heterodyne signal because the low frequency oscillations are usually of much higher amplitude. However, the ambient plasma fluctuations in the range of 300 to 500 kHz are usually not very strong, especially in low-confinement mode (L-mode). All the plasmas in the mode conversion experiments were deliberately kept in L-mode (as opposed to high-confinement, or H-mode), to simplify the analysis.[6] Thus by using a

[6]The plasma was kept in L-mode despite the ∼1–2 MW of RF power by using the inner wall as a limiter, or using an upper X-point (instead of the usual lower X-point) in the magnetic equilibrium

bandpass filter around the heterodyne frequency of interest, a coherent signal can be visualized (see Fig. 5-8).

By comparing the signal from channel to channel, information about the spatial structure and wavenumber can be obtained. The amplitude varies from channel to channel, and in time. The amplitude *vs.* time for each channel could be used to generate a contour plot of the signal structure during the shot, such as in Fig. 5-15 and Appendix E. However, a much faster and more reliable method is to take a windowed Fourier transform, taking care to use an appropriate number of samples for the expected RF frequency. Because the exact RF frequency seemed to drift somewhat during the course of the run day (probably due to thermal drift inside the RF signal generator used to drive the AO modulators), a large time window on a channel with strong signal was used for an FFT to determine the appropriate RF frequency for each shot. Then the windowed FFT analysis was done using a smaller time window. Three factors needed to be balanced in the choice of the length of the time window: good time resolution (requiring as small a window as possible), a good match with the RF heterodyne frequency (requiring a number of samples which is as near an integral number of RF periods as possible), and a large signal to noise ratio (requiring as large a window as possible). In practice this resulted in a time window of 5 to 7 msec.

5.4.3 Dependence of PCI signal on RF power

Information about the RF electric field amplitude in the plasma can also be obtained from the RF PCI system (an example of measurements compared to theory is presented in Sec. 5.5.7). The PCI diagnostic is absolutely calibrated before each discharge with a sound wave passing through air across the laser beam (see Sec. 3.3). The signal level can then be related to the total line-integrated electron density perturbation in the plasma. If the RF electric field amplitude is small enough so that the linearization procedure of Appendix C is valid (to obtain n_{e1} in terms of E_{RF}),

(the X-point is on the flux surface just outside the last closed flux surface), for which it has been found that H-mode is more difficult to attain.

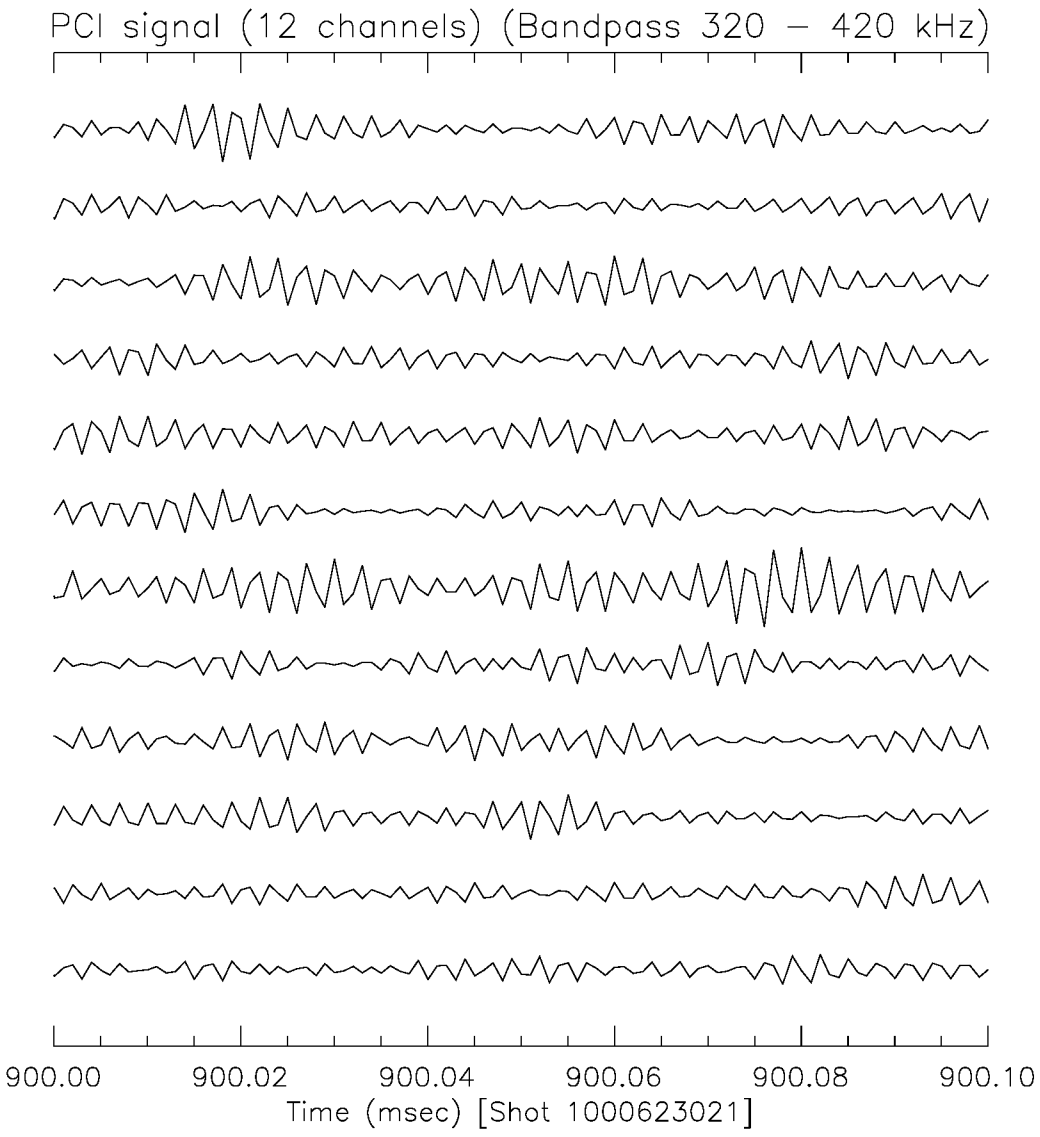

Figure 5-8: The raw PCI signal voltage is processed through a digital bandpass filter (heavily attenuating all signals except in the range of 320 to 420 kHz), for a plasma discharge which exhibited a particularly strong RF signal at 359.106 kHz.

then the amplitude of the RF density fluctuation should scale linearly with the RF electric field, or as the square root of RF power. During a shot when the RF power was raised from 0 to 700 kW in 40 msec, while other plasma parameters remained roughly constant, this behavior was observed as shown in Fig. 5-9, confirming the linear nature of the density fluctuation. This means that the analysis in this chapter based on the linear theory is valid.

5.4.4 Observed wavenumbers and Spatial Structure

Information about the wavelength of the oscillation can be obtained by comparing the signal on multiple PCI channels. As can be seen in Fig. 5-8, the phase of the oscillation at the RF heterodyne frequency advances from channel to channel. Just as a one-dimensional (1-D) Fourier transform in time can accurately produce information about the frequency components of the signal, a 2-D Fourier transform of the multiple-channel raw PCI data can convert information about the temporal and spatial behavior of the signal into frequencies and wavenumbers. This transform (with a time window of 2048 samples) is shown in Fig. 5-10, for a plasma discharge with the D-port RF antenna energized (which is driven at 80.5 MHz). The actual observed frequency is shown on the left, corresponding to the RF frequency shown on the right. The phase advance from channel to channel of the Fourier-transformed 350 kHz harmonic was approximately the same across the 12 channels, accounting for the fairly narrow peak in k-space. Other discharges displayed broader spectra, sometimes with multiple wavenumbers clearly visible.

Note that, unlike the previous fast wave observations [79, 80], only a positive wavenumber peak is observed, with no corresponding negative wavenumber. This indicates that only an oscillation with phase velocity towards the antenna on the LFS is observed. At first this seems to verify the backward wave nature of the IBW, since the group velocity could be expected to be directed away from the antenna. However, the actual picture may be more complicated, as is explained in Sec. 5.5.4.

Figures 5-11 and 5-12 show an example of a plasma discharge where several wavenumbers were simultaneously visible. The width of the beam was 3.56 cm and

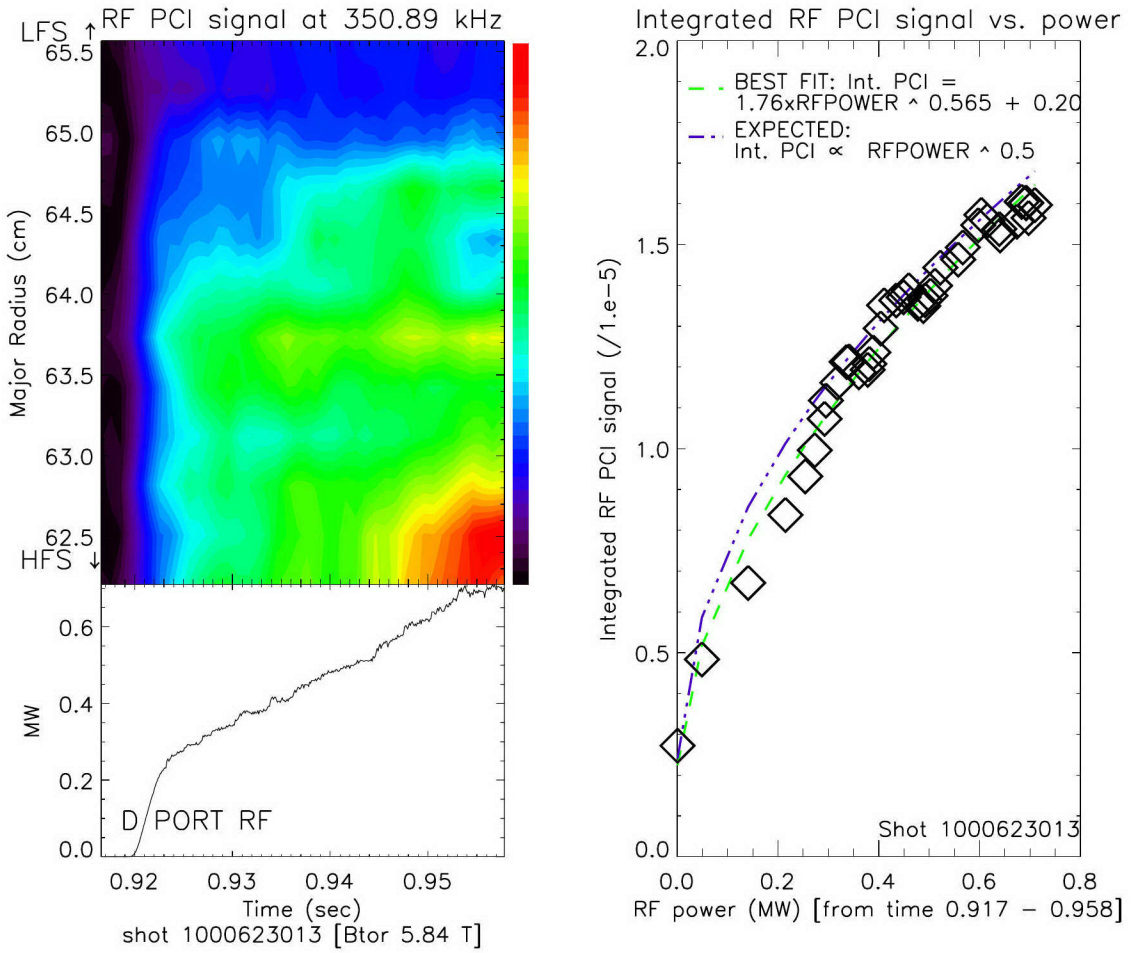

Figure 5-9: RF PCI signal scales with electric field E_{RF} (i.e. $\sqrt{P_{RF}}$). On the left is a contour plot of the 12 PCI channels during a power ramp of the D-port antenna. The quantity plotted is the Fourier amplitude of the RF heterodyned frequency of 350.89 kHz for the 80.5 MHz original signal. The pattern does not change significantly, remaining strongest on the HFS at 62 cm, but the overall signal strength increases as the power is raised. On the right, the total integrated PCI signal across the 12 channels *vs.* the RF power is shown. The data is consistent with a scaling linear in E field. The signal is not zero at zero power due to the finite Fourier window and a non-zero background signal level at 350.89 kHz.

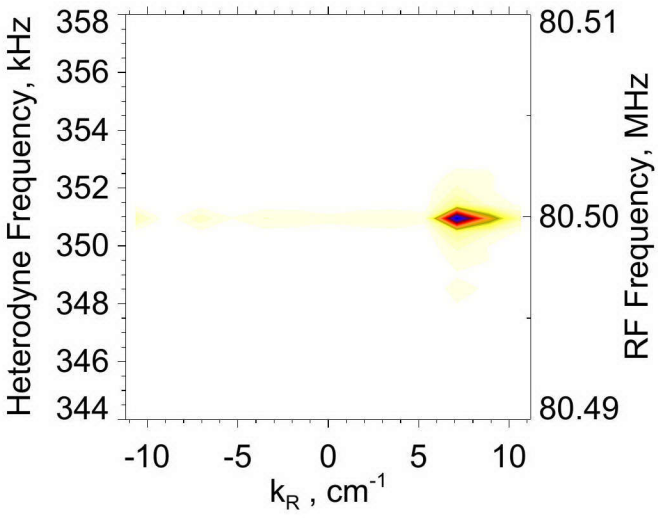

Figure 5-10: Ion Bernstein Wave observation with $k_R = +7$ to $+9$ cm^{-1}.

the channel spacing was 0.296 cm, so that the resolvable wavenumbers ranged between $\pm 9.79\,\mathrm{cm}^{-1}$, with uncertainty in each spatial Fourier transform bin of $\pm 0.815\,\mathrm{cm}^{-1}$. (13 bins are plotted, but the 13th is just a copy of the first).

There are three fairly well-separated peaks in Fig. 5-11 at the RF heterodyne frequency of 351 kHz. Note that the right-most peak, at 9.79 cm^{-1}, is at the edge of the contour and seems to spill over into the negative side of the plot. This is because the extreme edge on the right is copied onto the edge on the left, illustrating the aliasing that occurs when the wavelength is too short for the channel spacing. If the frequency of a signal were above the Nyquist frequency of 500 kHz, say 600 kHz, it would appear below the Nyquist frequency, at 400 kHz. Similarly, if the wavenumber of a signal is +6 cm^{-1}, and the channel spacing is such that only ± 5 cm^{-1} can be resolved, then it will "wrap around" and appear as if the signal were at -4 cm^{-1}. Both of these effects are limited, however. There is a filter in the PCI detection system which attenuates signals above 500 kHz. Very high wavenumbers with several complete wavelengths across a single detector element will tend to average out to zero. Wavenumbers that are near but beyond the spatial Nyquist wavenumber will still appear, but the amplitude becomes weaker with higher wavenumber. This spatial aliasing tended to occur

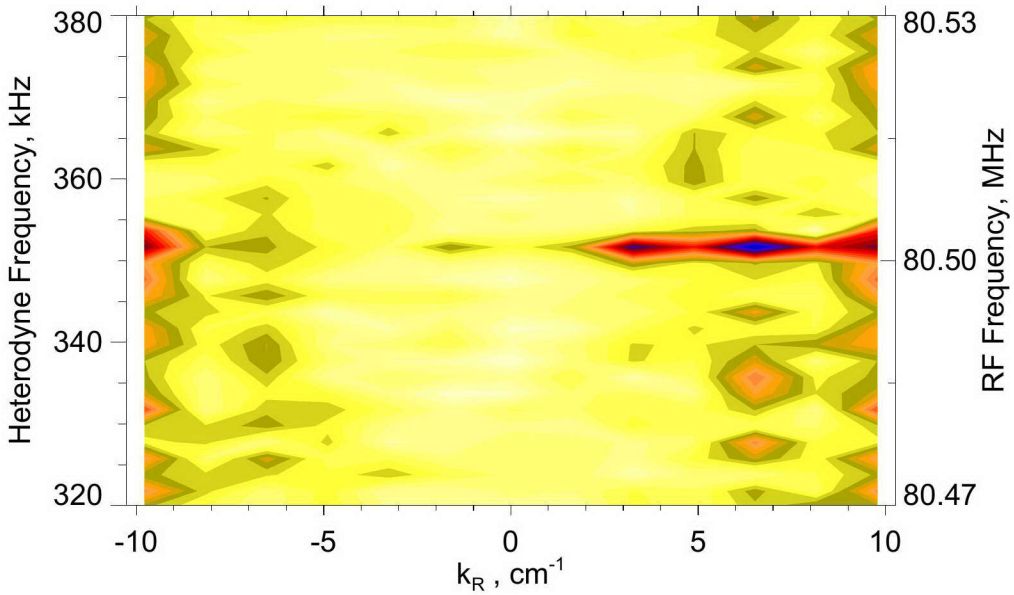

Figure 5-11: A 2-D Fourier transform (time and space into frequency and wavenumber) of the PCI data for shot 1000623009. Note the strong peaks at 3.26 ± 0.82, 6.52 ± 0.82, and 9.79 ± 0.82 cm^{-1} (for 351 kHz).

on many of the wide beam (∼7 cm) shots, where the high positive wavenumbers expected for the IBW signal appeared as negative wavenumbers. Even for the narrow beam (∼3.5 cm), there was some spatial aliasing taking place. For this and other reasons explained in Sec. 5.5.7, it is recommended that for future IBW observations in C-Mod, the channel spacing should be reduced by a factor of 2 to 3.

The spread of wavenumbers visible in Fig. 5-11 corresponds to two or three separate regions in space, as can be seen in Fig. 5-12. An effective wavenumber between each channel is calculated using the channel to channel phase advance. There are several separate peaks in the 2-D FFT (Fig. 5-11) because there are separate groups of slightly different wavenumbers.

The spatial structure present in Fig. 5-12 (shown by the dot-dash line) is a good example of the unexpected features of these experiments. There are two main peaks in amplitude, centered at 65.5 cm and 63.5 cm. In most of the plasma measurements of these H–^{3}He–D plasmas, amplitude peaks of this same spatial scale were observed. In some cases with a wider beam (∼7.2 cm), there were as many as 4 peaks seen.

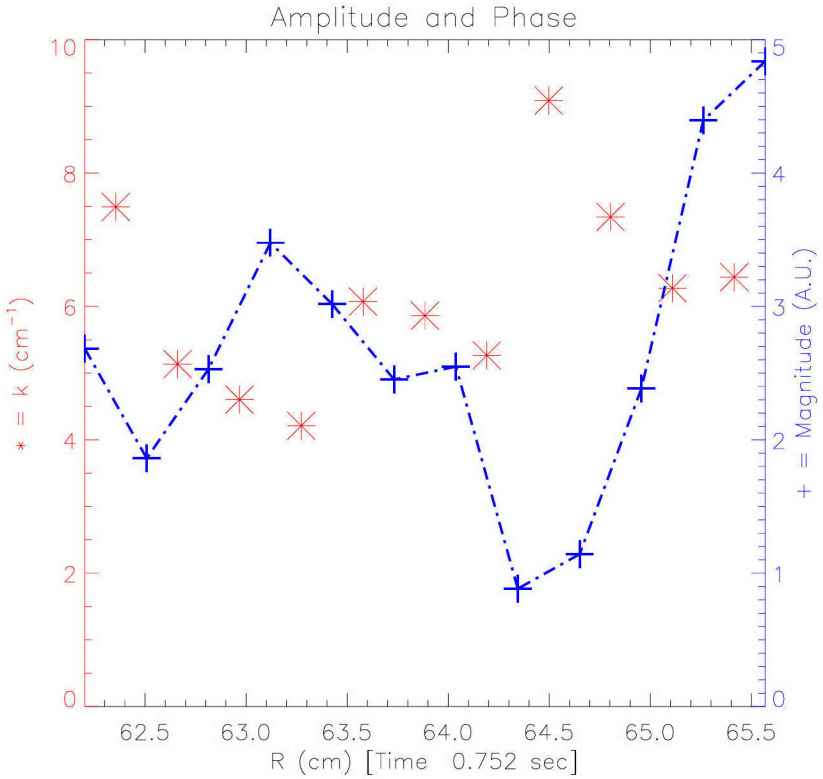

Figure 5-12: The amplitude and phase of the Fourier-transformed PCI signal as shown in Fig. 5-11, for the frequency bin near 351 kHz. The amplitude points are connected by the dot-dash line with vertical scale on the right. The phase between adjacent channels is represented by an effective k number $k_{ab} = (\psi_a - \psi_b)/dR$, where ψ is the phase of the Fourier component and dR is the channel spacing. The vertical scale for the k numbers is on the left, showing only the positive portion of the possible wavenumbers.

These type of features, which were persistent throughout the two run days[7] devoted to these experiments, could be due to separate regions of IBW oscillations in the poloidal cross-section, which are located at different major radial locations. This could be consistent with ICRF code results from Refs. [93, 94] and Ref. [76], which predict different regions of mode conversion away from the midplane for some scenarios. It is also consistent with code results from TORIC, and a particular instance of PCI data is compared to TORIC in Sec. 5.5.7. More extensive comparison between code results and the PCI data may be able to determine the correct physics to include and clarify the strengths and weaknesses of ICRF toroidal full-wave codes.

Simultaneous observation of FW and IBW wavenumbers

As mentioned in Sec. 5.1, one of the main advantages of the PCI system over a laser-scattering system is its capability to resolve multiple wavenumbers simultaneously. This is especially important when attempting to observe ICRF waves in the mode-conversion regime. Figure 5-13 shows a plasma discharge (shot 1000623014) where both the outgoing fast wave (negative wave number) and an ion Bernstein wave (large positive number, or aliased into large negative numbers) were observed. The signal was stronger near the time of peak RF power. Because the laser beam in this case was wide ($\sim$7.3 cm^{-1}, channel spacing 0.612 cm), the smallest five wavenumber bins in the spatial Fourier transform were 0., $\pm$0.86, and $\pm$1.71 cm^{-1}. The FW wavenumber is in the -0.86$\pm$0.31 cm^{-1} bin, which is in good agreement for the FW dispersion relation for the plasma parameters of shot 1000623014, predicting a FW wavenumber of -0.6 cm^{-1}. As discussed above, spatial aliasing of the high positive IBW wavenumbers can be expected, especially for large channel spacing. Thus the strong peak at -3.42 cm^{-1} is probably an IBW wavenumber of 6.84 cm^{-1}, which is consistent with observed IBW wavenumbers when a narrow beam is used, where

[7]Only the 23 June 2000 run day will be discussed in this thesis. A second run day on 12 December 2000 was an attempt at exploring the changes in the mode conversion with low current (400 kA). However, there was a power outage the night before and the run day was plagued with problems. Only 3 or 4 useful shots were obtained, and there was no significant difference in the observed PCI pattern. Future experiments could further explore these low current plasmas.

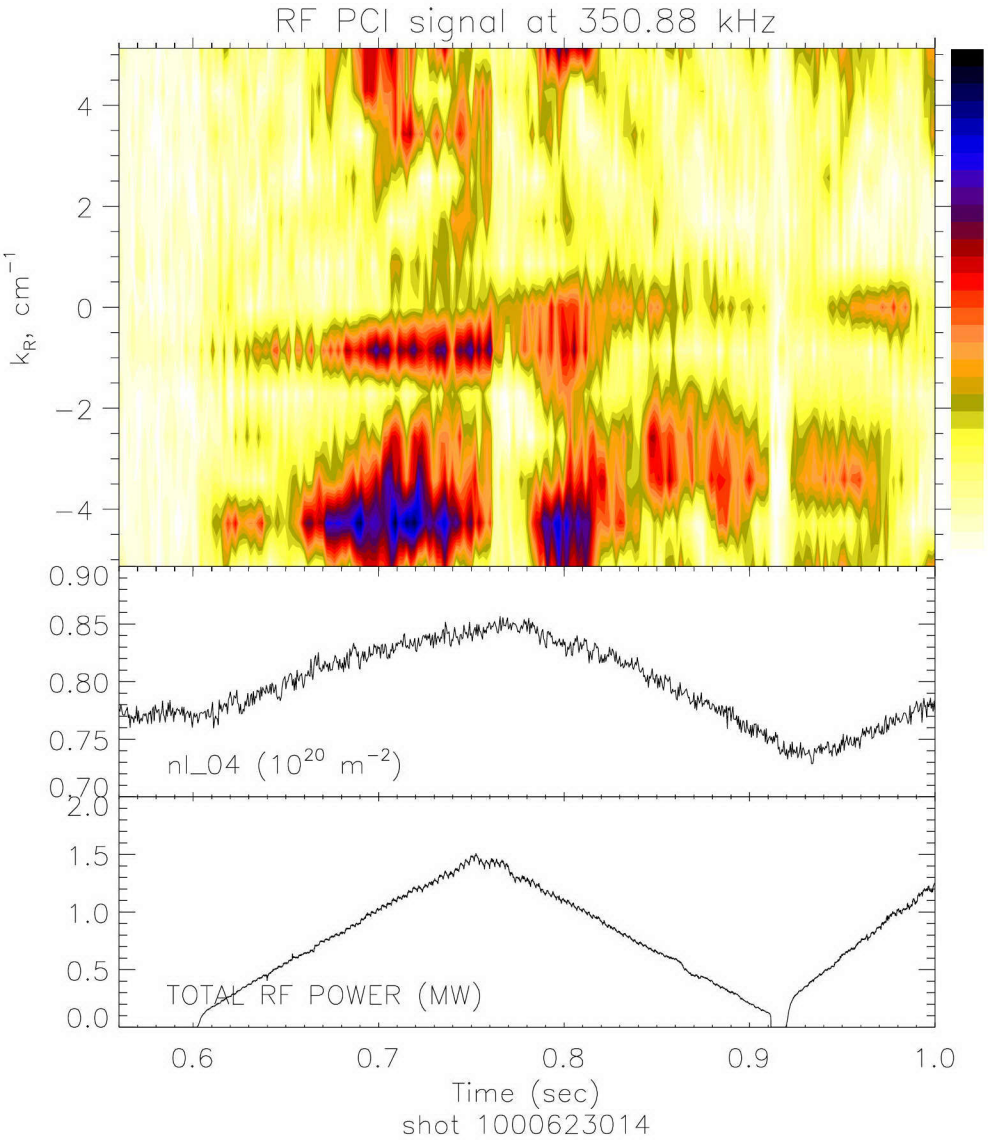

Figure 5-13: A plot of the wavenumber spectrum in the RF PCI signal as a function of time. The top panel is a contour plot of the Fourier amplitude, with the bar on the right showing the magnitude of the signal strength, increasing from bottom to top. From 0.65 to 0.75 sec, two distinct wavenumbers are visible: -1 cm^{-1} remaining fairly constant in time, representing the outgoing FW; and a broad region varying from +3 cm^{-1} to -4 cm^{-1} (most likely aliased from large positive wavenumbers), changing character with time, representing the mode-converted IBW. Bottom two panels: line-integrated density using interferometry, and the D-port RF power (which is the same as the total RF power in this time window).

wavenumbers up to $\sim$10 cm^{-1} are observable without aliasing. The IBW is represented by a spread of wavenumbers in the Fourier spectrum, meaning that the wavenumber is changing rapidly across the laser beam. This could be consistent with the dispersion relation and ray-tracing results, which also predict a change in wavenumber as the IBW propagates. This could also be consistent with the presence of multiple wavenumbers present in the PCI viewing window from several mode-converted IBWs with different n_ϕ numbers, or in different vertical locations.

5.4.5 Toroidal Field Ramp

The location of the mode conversion layer depends on the toroidal field (the dependence is nearly linear for these plasmas). Thus for a true mode-conversion related ICRF signal, the strong signal features should move across the channels during a B field ramp. Lowering the field, for example, moves all the cyclotron resonances to the high-field side, including the ion–ion hybrid layer which remains in between the cyclotron layers. Of course, the pattern will not be exactly the same for different toroidal fields, because of the different mode-conversion efficiency and the exact details of the 3-D pattern of strong density fluctuations. The PCI line-integrated signal will also depend sensitively on the angle of the constant-phase surfaces, which could affect the strength of the signal that is ultimately observed. Even with these limitations, it can be seen in Fig. 5-14 and Fig. 5-15 that the PCI signal structure moves in the expected direction and by the expected distance for a central toroidal field ramp from 5.9 T to 5.6 T.

Figure 5-14 is similar to Fig. 5-6, but in 5-14 it can be seen that the expected D-port signal at 350.87 kHz is roughly 7 times higher than the background noise level, as shown in the left column for the nearby frequency of 347.11 kHz. The RF power was modulated in order to look for evidence of direct electron heating (see Sec. 5.4.7 for an example of electron heating near the PCI signal). The amplitude *vs.* time and space is shown in a contour plot in Fig. 5-15. It can be seen that when the RF power first turns on, there is a strong signal, with peaks at 65.2 cm, 64.2 cm and 62.5 cm. Then there is

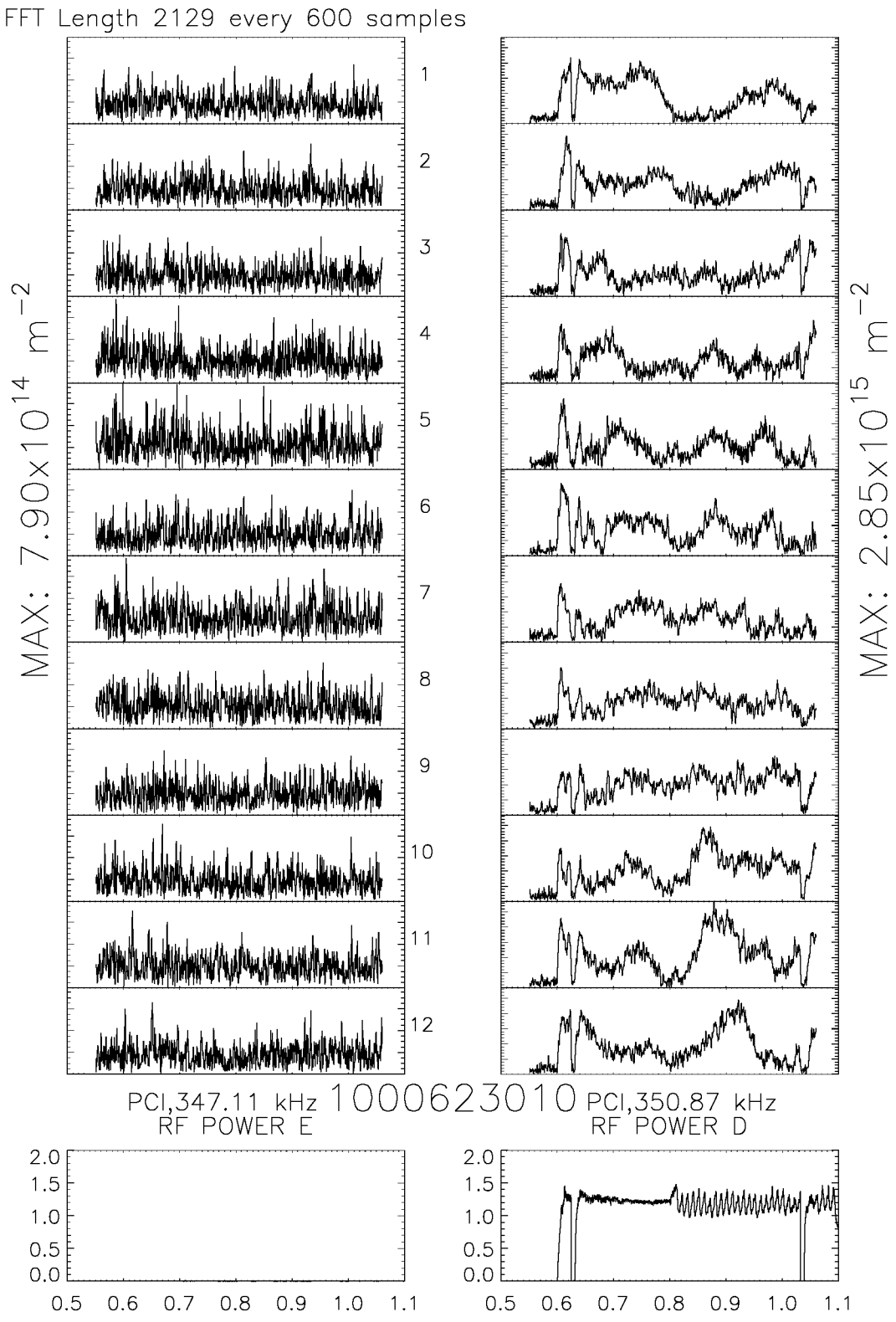

Figure 5-14: The RF PCI signal during a B field ramp with D-port RF power. Note that the signal amplitude in the right column (the expected RF PCI signal) is 7 to 10 times higher than the background noise level. A contour plot of the amplitude data in the right column is shown in the upper panel of Fig. 5-15.

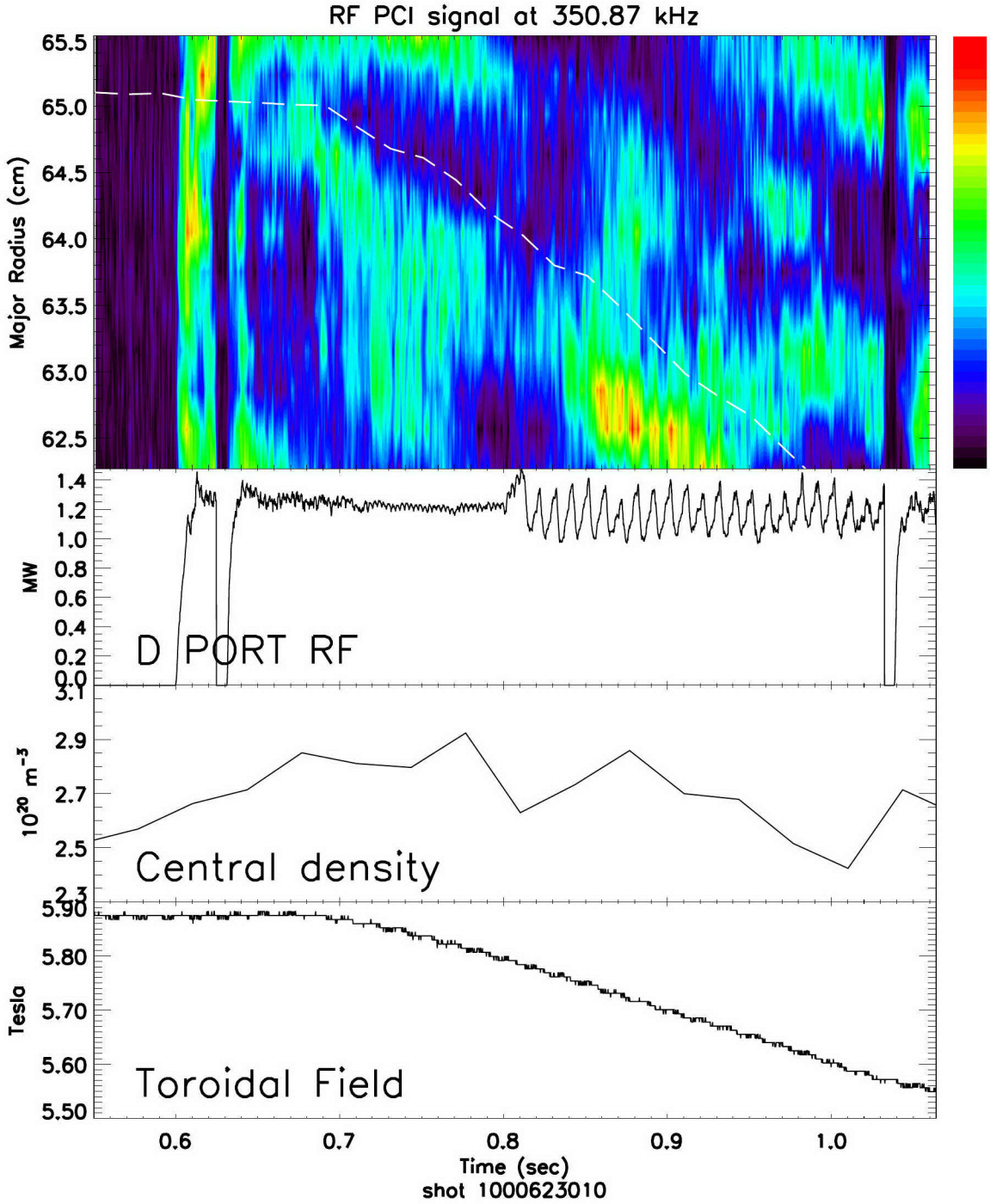

Figure 5-15: Top: contour plot of the amplitude of the 12 PCI channels *vs.* time (contour levels shown by bar on the right, increasing from bottom to top). Bottom 3: D-port RF power (MW), n_{e0} as measured by Thompson scattering, and the toroidal field at 66 cm.

a brief RF transmitter trip,[8] and when the power turns back on, the signal is no longer as strong. This could be due to the change in density (and other parameters) which could decrease the mode-conversion efficiency, and change the pattern enough (even a few millimeters is sufficient, see Sec. 5.5.7) to alter the observed signal strength. At 0.7 sec, the toroidal field begins to decrease in magnitude. The dashed line shows the location of the mode-conversion layer ($n_{\parallel}^2 = S$) for a constant ion concentration mix (26.7% ^{3}He, H/D = 1.9). The actual ion concentration mix in the plasma is not accurately known,[9] but an estimate from several methods described in Appendix D would suggest that the ^{3}He concentration is actually much lower, which would place the location of the MC layer farther to the HFS (and outside the PCI viewing window). Nevertheless, the assumed constant ion species mix serves to illustrate the relative shift in MC layer position as the toroidal field is decreased. At 0.86 sec, the signal at the HFS edge of the PCI view is quite strong until it moves out of view. During this time, it changes position just as would be expected for the B field ramp.

5.4.6 PCI signal restructuring with changes in plasma parameters

The line-integrated PCI signal is very sensitive to small changes in the orientation and radial position of the fluctuating density fronts of constant phase. If the mode-conversion layer moves radially, then the pattern changes. Even with a fixed toroidal field, the mode-conversion layer can move across the channels when the ion concentration mix changes. For example, increasing ^{3}He at the expense of H and D will move the layer to the low-field side, or increasing the H/D ratio with fixed ^{3}He will move the layer to the high-field side. Changes in plasma shape and position with respect to the machine can also cause the pattern within the PCI window to change.

[8]There are probes placed in the RF transmission line and around the antenna straps to detect problems such as high reflected power, or phase imbalance between antenna elements. When a dangerous situation is detected, the transmitter shuts down to prevent damage. After a short time, the circuitry is designed to try to come to full power again.

[9]In the future, as the ICRF codes are validated and become more capable of modeling the expected PCI signal from various ion concentration mixes, the PCI observations can be used themselves as a very accurate determination of the core ion concentrations.

Changes in density can shift the relative balance between FW and IBW by changing the mode-conversion efficiency. Finally, changes in temperature (especially the electron to ion temperature ratio) can change the propagation characteristics of the IBW, again changing the observed PCI pattern. Ray-tracing studies of IBWs [50] indicate that the distance a mode-converted IBW can propagate is dependent on the ratio of the electron to ion temperature. The role of the electron and ion temperatures (and their ratio) in the IBW propagation and damping, and the effect on the PCI signal is one of the open questions that needs to be further explored. Perhaps this will require the development of a better ion temperature diagnostic on C-Mod.

Shot 1000623011 is an example of a plasma discharge where the changes in the ion concentrations alone do not seem to be able to explain the observed shifts in the PCI pattern. Figure 5-16 shows the RF PCI results for the D-port expected heterodyne frequency of 350.86 kHz (the toroidal field remained constant at 5.84 T during the PCI window). As can be seen from the contour plot of the amplitude *vs.* space and time, the strong features move to the HFS during the initial power ramp, then stay relatively steady for approximately 200 msec (barring a brief interruption in RF power), and then seem to move again to the HFS as the E-port RF power turns on at 1.02 sec. Yet the best estimates of the concentration changes in the core of the plasma suggest that the pattern should move to the LFS. The H/D ratio falls, and both less H or more D would move the mode-conversion layer to the LFS. The measured effective charge is fairly constant (perhaps slightly rising) and the ^{3}He gas puff valve is at a constant voltage during the PCI time window, so that the ^{3}He density should remain roughly constant. Since the central density is rising, probably due to increased deuterium, the relative concentration of ^{3}He ions would fall slightly (which would push the MC layer to the HFS), but not enough to counterbalance the effect of the falling H/D ratio (which pushes the MC layer to the LFS). In other shots as well, there were often changes and restructuring in the PCI signal that are difficult to explain using the available plasma parameter measurements.

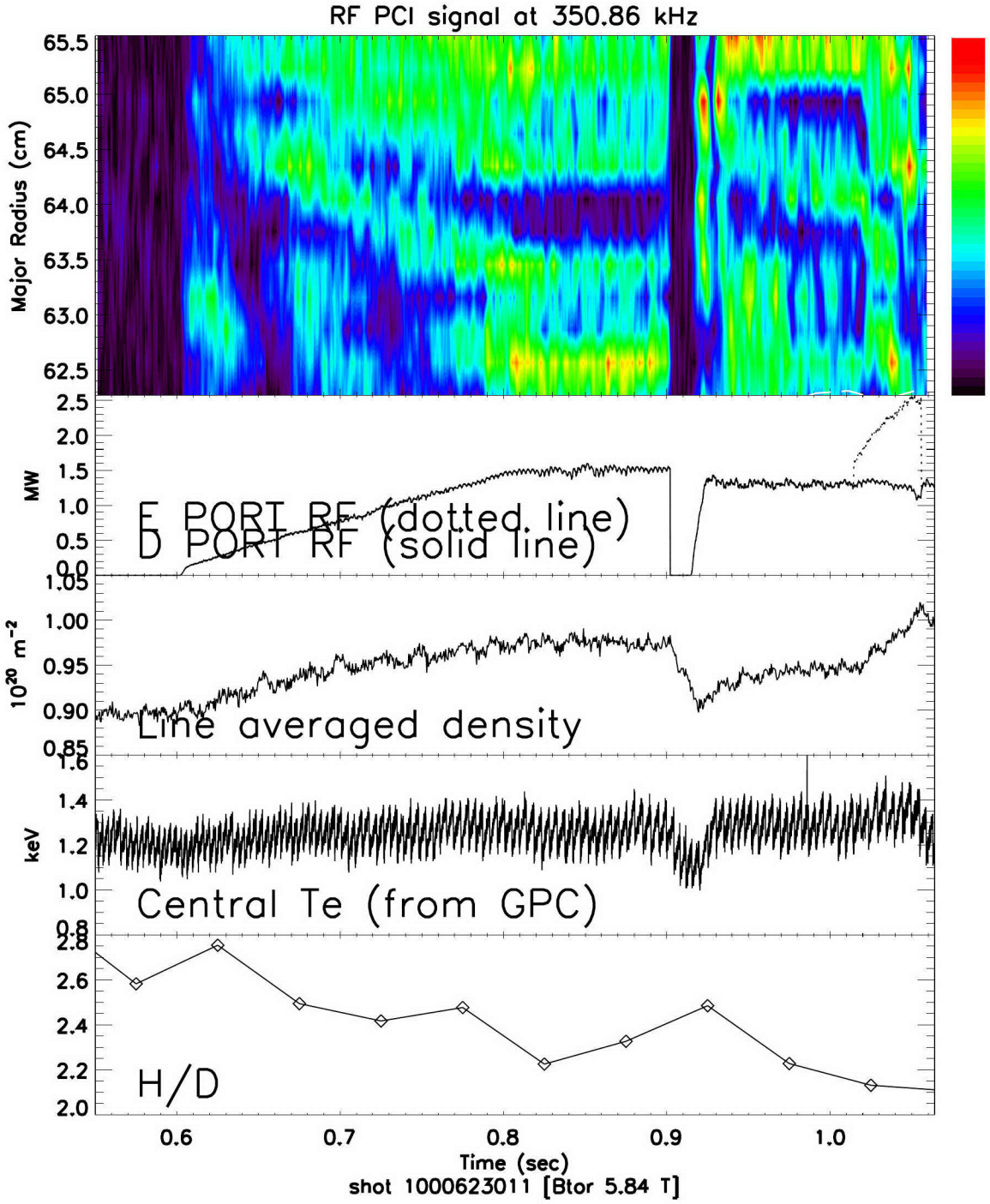

Figure 5-16: The RF PCI signal for the D-port heterodyne frequency. Top panel: contour plot (contour levels increasing from bottom to top in bar on the right) of the PCI signal amplitude across the 12 channels. Bottom four: D-port RF power ramping up, with a short pulse of E-port RF power at 1.0 sec. Line integrated density from interferometry. Central temperature channel from the GPC-ECE diagnostic. H/D ratio as measured by spectroscopy at the edge.

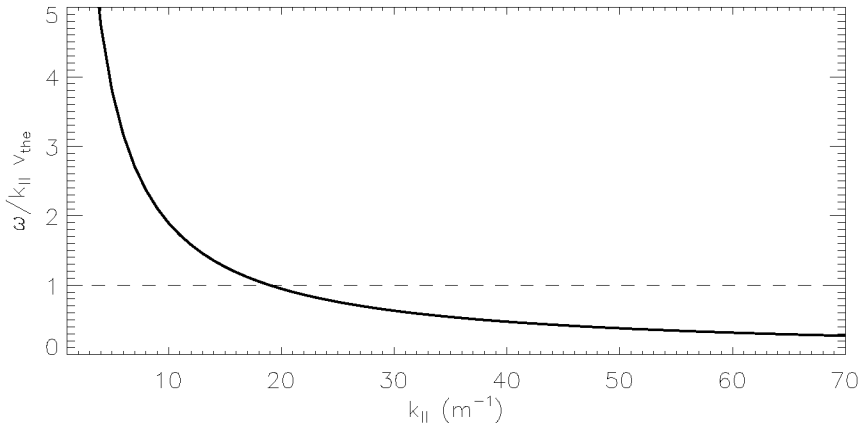

Figure 5-17: The electron Landau damping (ELD) parameter $\omega/(k_{\|}v_{\mathrm{the}})$ as a function of $k_{\|}$ for C-Mod relevant frequency (80.0 MHz) and temperature (2 keV). Strong ELD of the mode-converted IBWs should occur for $\omega/(k_{\|}v_{\mathrm{the}}) \sim 1$.

5.4.7 Electron heating

The mode-converted IBWs in this regime should be accompanied by direct RF electron heating. This is because in these three species C-Mod plasmas at a few keV temperature, the mode-converted IBWs should damp through electron Landau damping (ELD) (see Sec. 2.3.2) soon after they are "launched" inside the plasma by the fast wave. The critical parameter for electron Landau damping, $\omega/(k_{\|}v_{\mathrm{the}})$, is shown as a function of $k_{\|}$ in Fig. 5-17 for 80.0 MHz and 2 keV. As the IBW propagates away from the mode-conversion layer, the $k_{\|}$ will become larger (mostly due to an $|m_\theta|$ increase, see Sec. 5.5.4). The dashed line in Fig. 5-17 is where the ELD parameter is 1, which is where strong damping should occur. For the 2 keV temperature plotted in the figure, this occurs at $k_{\|} \approx 20$ m^{-1}.

Experimental confirmation of the expected electron Landau damping is shown in Figs. 5-18 through 5-20. The direct electron heating was determined with the break-in-slope technique as described in Sec. 4.2.1. Figure 5-18 shows just the region in the PCI viewing window for the high-current (1 MA) shot 1000623021. The resulting power densities for three channels is shown as the squares (in MW/m^3). The electron cyclotron emission (ECE) diagnostic used for the temperature measurements

receives localized microwave radiation from 9 spatially separated channels, usually on the low-field side. Because the transport of heat is so rapid along a magnetic flux surface, heat that is deposited on the HFS would also appear on the LFS, where the temperature was measured. In order to compare with the PCI channel locations, the ECE channels were mapped to the HFS along a magnetic flux surface (except for the right-most channel, which was already in the PCI viewing window). This requires precise knowledge of the total magnetic field and an accurate magnetic equilibrium reconstruction. There were some uncertainties involved in the positions because of small uncertainties in the calibrated magnetic field. Nevertheless, the main feature is clear: there is strong (3 MW/m^3) electron power deposition in the vicinity of the strongest PCI signal, which is much higher than any expected direct electron Landau damping of the FW. Still, this is near the same location as any expected direct ELD of the FW, so other instances where the heating is farther off-axis is shown in Figs. 5-19 and 5-20.

Figure 5-19 shows the entire HFS region of the plasma, comparing the electron power deposition profile with the PCI signal for three shots. Note that in each case there is an off-axis peak in electron heating which is to the HFS of the PCI viewing window (the PCI only extends to 62 cm major radius in these cases). This could be consistent with the mode-converted IBW propagating along the midplane across the PCI window, and then damping to the HFS. Yet from the estimated ^{3}He concentration for these shots (see Appendix D), the mode-conversion layer is to the HFS of the PCI viewing window — which would not allow for any IBW signal within the PCI viewing window if the IBW propagates only to the HFS of the fast wave mode conversion layer. However, the location of the PCI signal (to the LFS of the mode conversion layer) and the peak electron heating (near the mode conversion layer) are consistent with TORIC results (see Sec. 5.5). From the picture suggested by TORIC, the IBW is excited at the fast wave mode conversion layer, then propagates along a magnetic flux surface above and below the midplane toward the low-field side. Thus electron Landau damping of the mode-converted IBW occurs along the flux surface which intersects the midplane at the location of peak heating, which is also near the mode

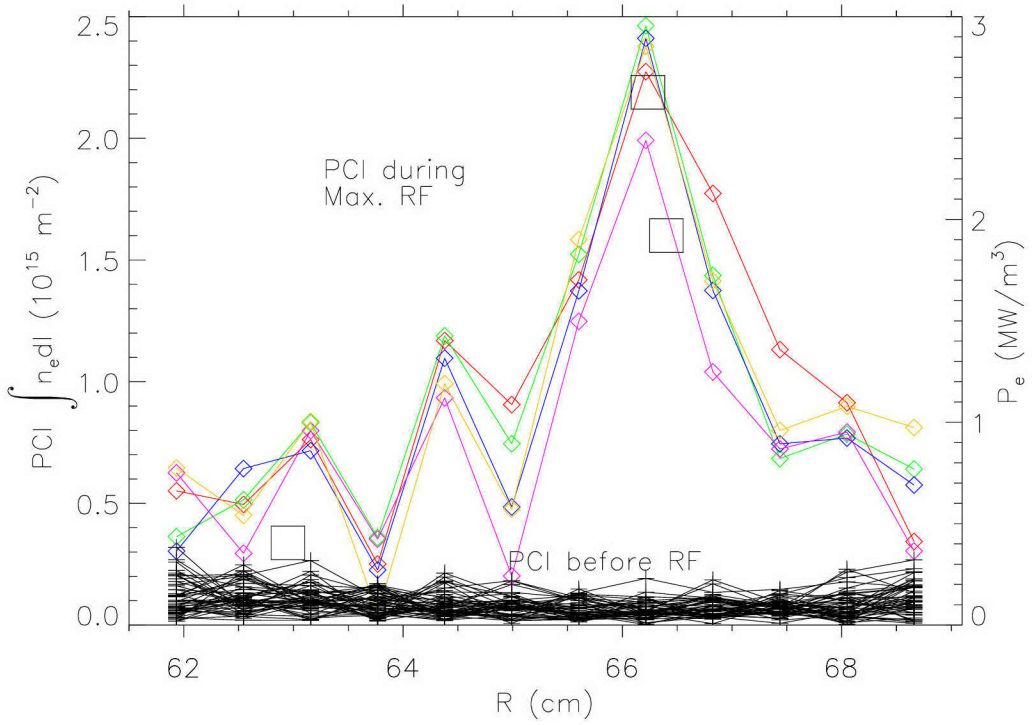

Figure 5-18: IBW signal amplitude (small diamonds) decays to the high-field-side (from large to small R). The signal is shown for several time slices of shot 1000623021, showing the persistence of the peaks and troughs over time. Direct electron heating as obtained from "break-in-slope" analysis (power density shown as large squares, with scale on the right) is measured near the location of the peak signal. Also shown is the PCI signal amplitude at this frequency before the RF power turns on (plus signs).

conversion layer. Yet the PCI viewing the region near the center of the plasma can still observe IBW oscillations because they have traveled back along the flux surface to the LFS.

Figure 5-20 compares two shots which were meant to be identical in all plasma parameters except the plasma current. Shot 1000623020 had a plasma current of 800 kA, and shot 1000623021 had a plasma current of 1 MA. According to experience from ray-tracing, the higher current should result in a more rapid upshift in $k_{\|}$ (due to the stronger poloidal field), and hence a shorter propagation distance. However, unexpectedly, the biggest change was in the location of the peak electron heating, as can be seen by comparing the top and bottom plots in Fig. 5-20. This could be because the helium-3 concentration seemed to change somewhat (see Appendix D) between shot 20 and 21, which would move the mode conversion layer. But it could also have to do with the changes in the damping of the IBWs with higher current. This could be the subject of an interesting future experiment: reproducible, constant plasma parameter shots with increasing (and decreasing) plasma current to observe the effects on the PCI signal and the electron heating.

The total power absorbed by the electrons can be obtained in the same manner as described in Sec. 4.2.1 by integrating the power density profile throughout the plasma. Integrated electron power deposition profiles for these three-ion-species plasmas have shown experimentally ~20% to 50% of the total RF power absorbed by electrons. Detailed comparison with either TORIC or the internal resonator model (as was done for D(^{3}He) plasmas in Sec. 4.4.1) would require more exact knowledge of the ion species concentration mix, especially the ^{3}He concentration.

5.4.8 PCI structure of both D- and E-port antennas at the same time

Valuable information about the toroidal propagation of the FW and IBW can be gained by comparing the PCI signal for the D-port and E-port antennas under identical plasma conditions. This is because the PCI diagnostic is directly in front of

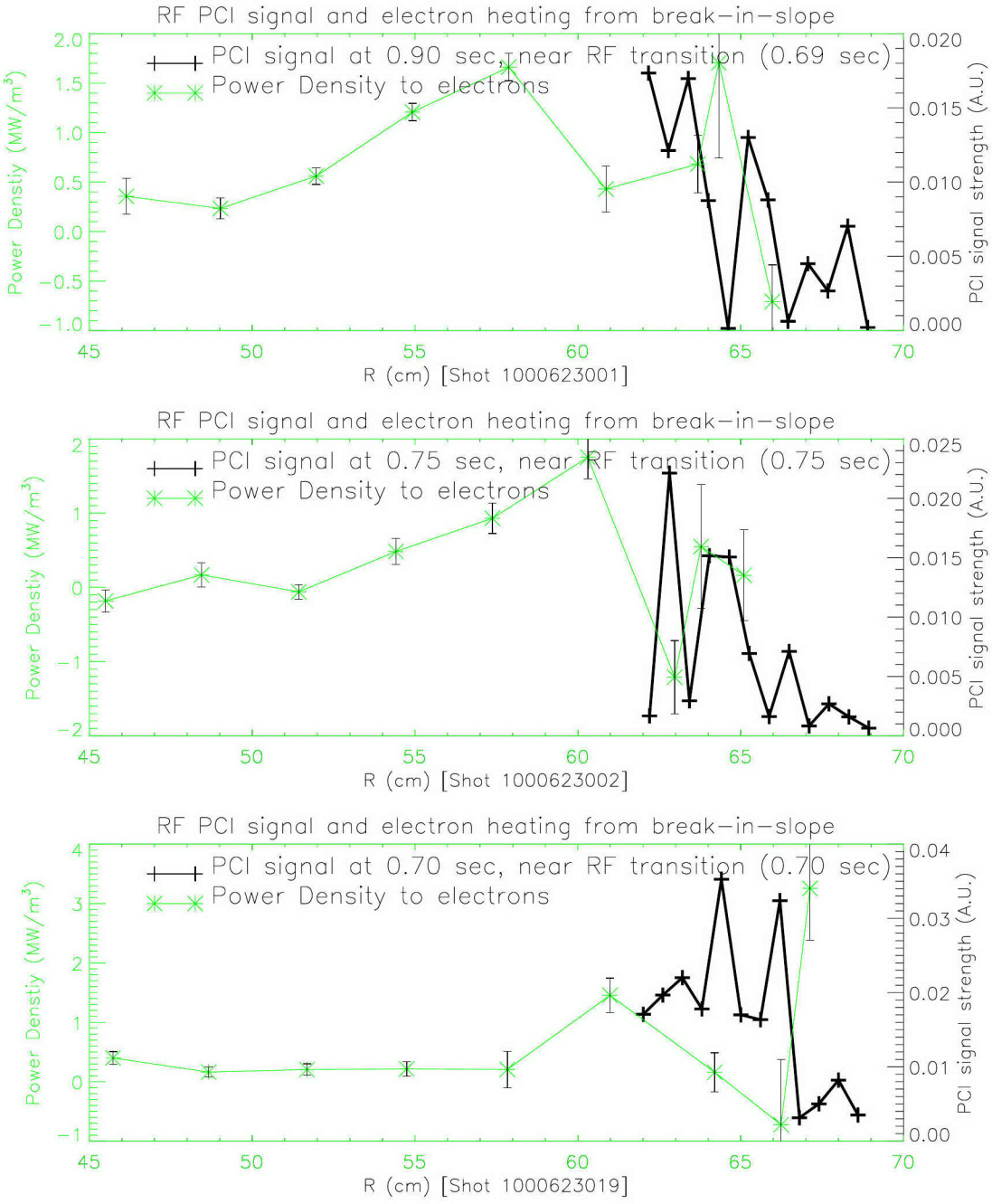

Figure 5-19: The electron power deposition profile compared to the PCI signal. From top to bottom: shot 1000623001, 002 and 019. The pluses connected by the thick lines are the PCI data, and the stars (with error bars) connected by the thinner line are the electron power deposition data points.

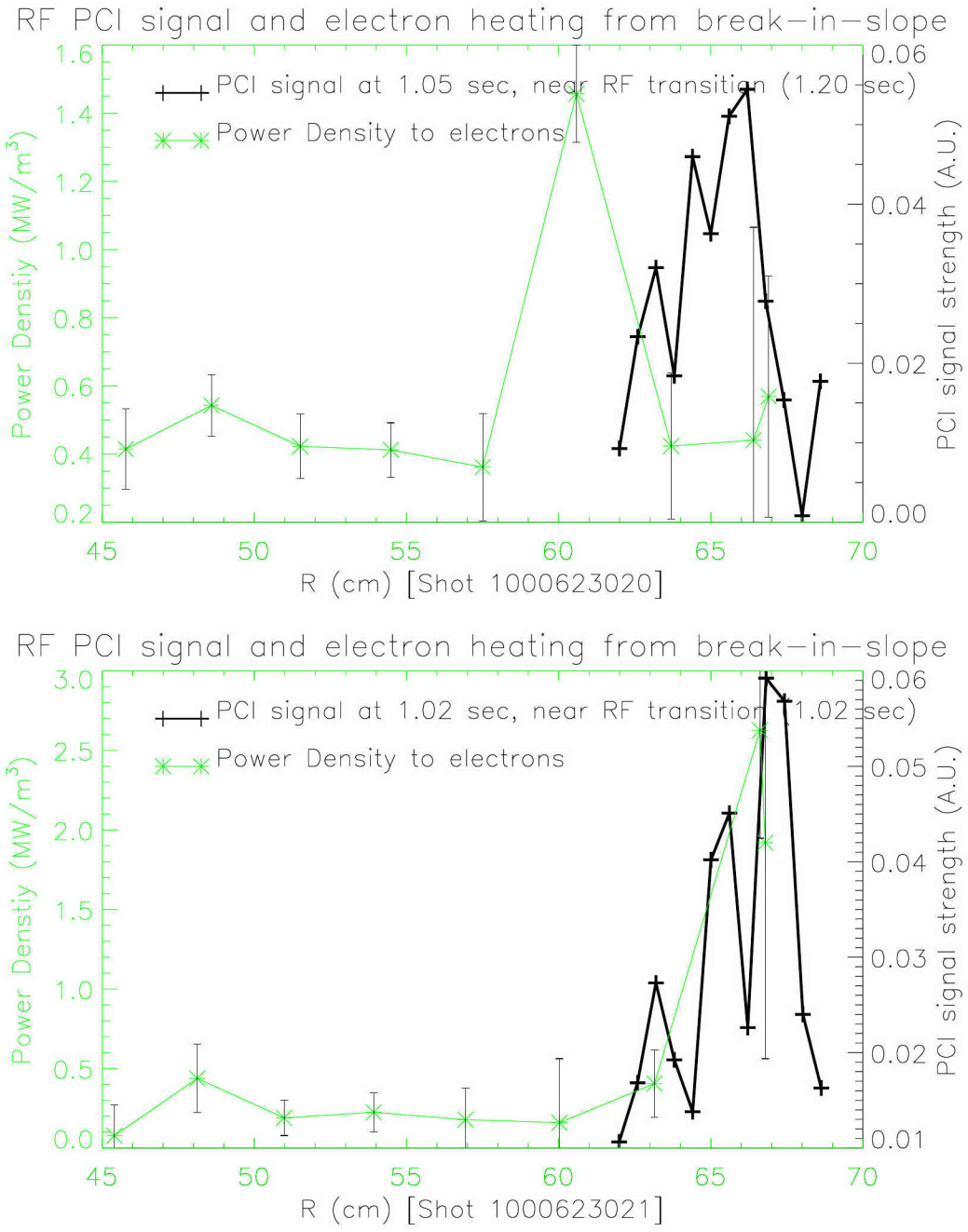

Figure 5-20: The electron power deposition profile compared to the PCI signal. Top: shot 1000623020 (I_p = 800 kA); bottom: shot 1000623021 (I_p = 1 MA). The pluses connected by the thick lines are the PCI data, and the stars (with error bars) connected by the thinner line are the electron power deposition data points.

E-port, but 36° away from D-port (see Fig. 5-1).

Shot 1000623020 is an example of a discharge where both the D- and E-port antennas were radiating about the same amount of power during the PCI window. Figure 5-21 shows the contour plot of the signal amplitude for each antenna. Note that the estimated mode-conversion layer position is shifted by 0.4 cm to the LFS for E-port (80.0 MHz) compared to D-port (80.5 MHz), because of the lower frequency. Because of this shift, the pattern would not necessarily be the same even if the antennas were located at the same toroidal location. In addition, because of the toroidal separation, the observed pattern of the two antennas might be expected to be quite different. This is due in part to the fast wave cancellation immediately in front of the two-strap antenna, so that the launched IBW power will be different at 0° compared to 36°. (See Ref. [79] for examples of TORIC simulations of the 3-D propagation and damping of the fast wave alone.) In addition, there could be differences due to ray-tracing effects of the IBWs as they propagate toroidally away from the mode-conversion region. However, there are some similarities between the signals from the two different antennas, as can be seen in Fig. 5-23. For example, the node at 64.4 cm is present for both D- and E-port, and it persists in time even when the rest of the pattern shifts slightly (see Fig. 5-21). If the E-port signal were multiplied by a factor of 3, then the structure would look fairly similar. The difference in magnitude may be due to the node of the FW present along a line equidistant from the two straps of the antenna (the PCI view is along this line for the E-port antenna), which in turn could result in less IBW power near the PCI from E-port as compared to D-port. Some of the difference could also be due to the higher ambient noise at the lower heterodyne frequency of 141 kHz as compared to 359 kHz, which may add to the Fourier amplitude of the RF signal, but this alone cannot explain the discrepancy in signal magnitude. Perhaps with more detailed 3-D modeling using TORIC (see Sec. 5.5.7), the differences due to toroidal distance from the antenna could be more closely examined. This would be very interesting for the implications of toroidal propagation and damping, to see how far around the machine the FW and IBW power can reach. It would also help to verify the proper method for summing the

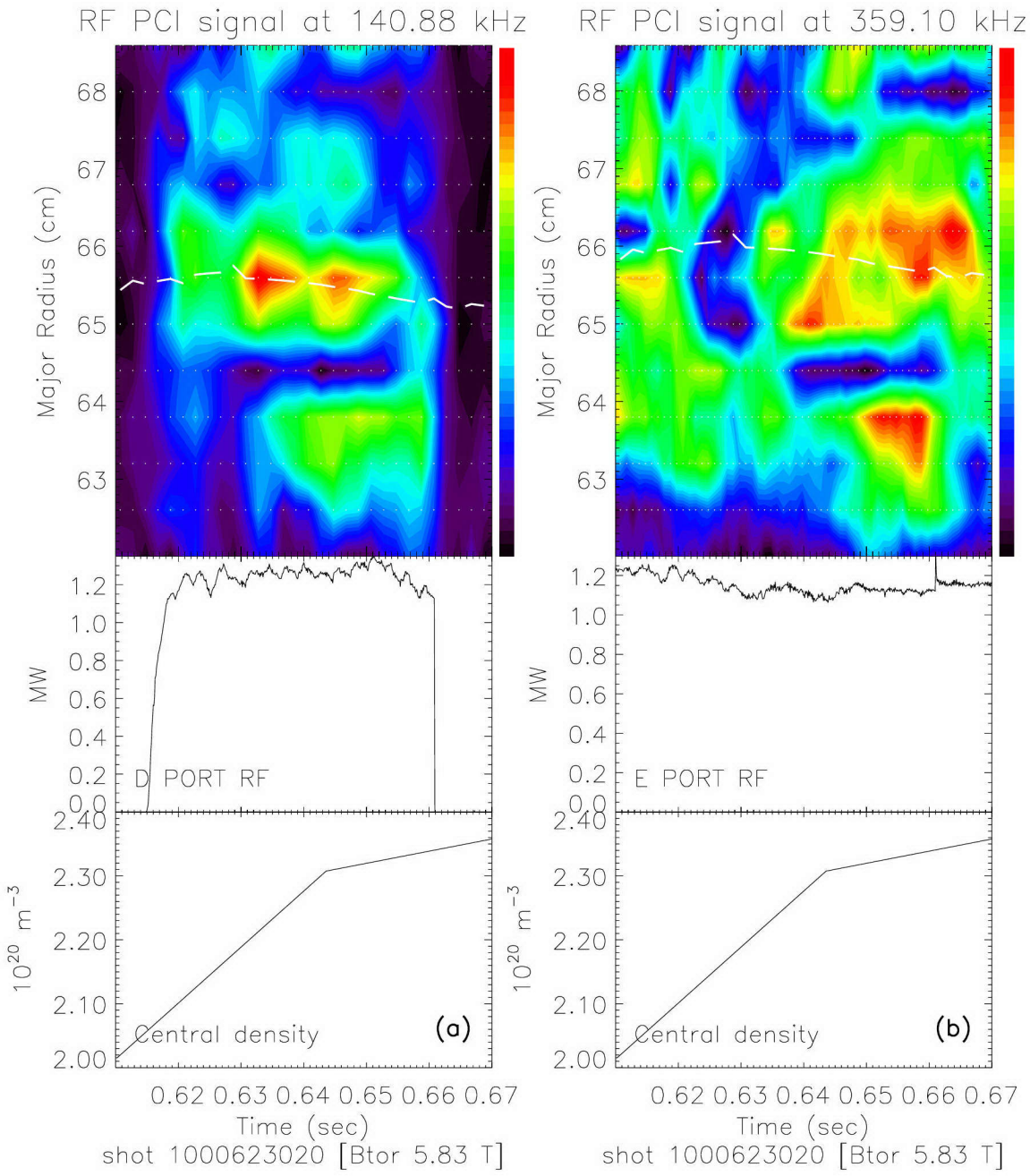

Figure 5-21: The PCI signal for both D- and E-port antennas during the same shot. On the left (a) is the signal at 140.88 kHz, the heterodyne frequency for 80.5 MHz (D-port), and on the right (b) at 359.10 kHz, the heterodyne frequency for 80.0 MHz (E-port). The dashed line within the contour plot shows the time behavior and relative shift (because of the frequency difference) in the location of the (shifted) mode-conversion layer (for n=10, m=0, then shifted by 8 cm) for each case. In both cases, as can be seen in Appendix E, the actual MC layer is much further to the HFS.

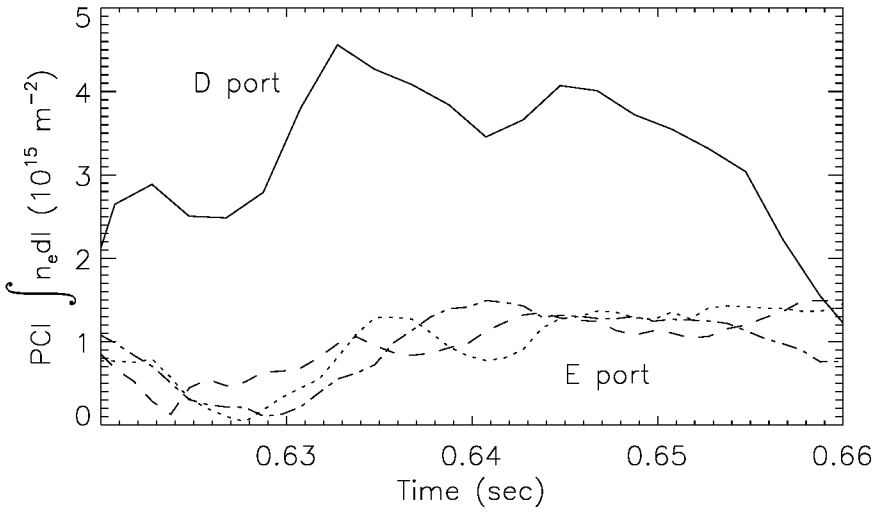

Figure 5-22: The time history of the strongest signals from D- and E-port. Solid line: D-port signal at 65.60 cm. Dotted line: E-port signal at 66.19 cm, dashed line: E-port signal at 65.60 cm, and dash-dot line: E-port signal at 65.00 cm.

toroidal mode number solutions in order to reconstruct the entire antenna spectrum in the superposition of the TORIC solutions (see Sec. 5.5.5).

5.4.9 Summary of the RF PCI data

A complex structure of peaks and troughs in amplitude, with a range of wavenumbers consistent with both a fast wave and ion Bernstein wave has been observed in H–^{3}He–D plasmas in C-Mod with the RF PCI system. The signal scales linearly with the RF electric field. Tests were performed to ensure that the signal is truly due to the RF optical heterodyning process, and not just RF pickup. The signal structure moves across channels as the torodial field is changed. Electron Landau damping has been observed in the vicinity of the IBW PCI signal. If the ion concentrations presented in Appendix D are correct, then in all cases IBW signal has been seen to the low-field side of the fast wave mode conversion layer. IBW signal from both ICRF antennas nearest the PCI port has been observed. There has also been some puzzling observations concerning PCI signal restructuring which indicate that the

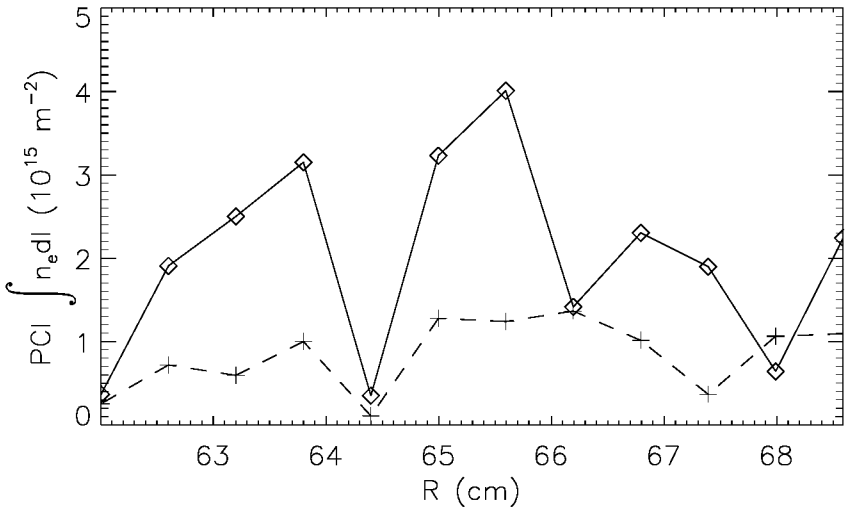

Figure 5-23: The D-port (diamonds, solid line) and E-port (pluses, dashed line) signal amplitudes *vs.* space at time slice 0.647 sec. Vertical scale (for both Fig. 5-22 and 5-23) is in units of 10^{15} m^{-2}.

line-integrated pattern across the width of the PCI laser beam can be very sensitive to small changes in plasma parameters. This undesired effect could be reduced by increasing the PCI channel density (see Sec. 5.5.8).

5.5 Theory: TORIC predictions for comparison to PCI data

From the dispersion relation with fixed or only slowly varying $k_{\|}$, the mode-converted ion Bernstein wave would be expected to propagate away to the high-field side, with the perpendicular wavenumber rapidly increasing, accompanied by a small amount of Landau damping (as shown in Fig. 5-4). However, this simple picture is not consistent with many aspects of the observed data. The observed IBW wavenumbers were often fairly constant across the PCI viewing window. The observed amplitude shows multiple peaks and troughs. From the simplest picture, one would expect a monotonic decrease in amplitude towards the high-field side. Finally, although the

ion concentrations were not known accurately enough to make this claim definitively, the evidence suggests that there was often a strong IBW signal to the low-field side of the estimated location of the FW to IBW mode-conversion layer. This would be very strange because the IBW is not expected to propagate to the low-field side of the mode-conversion layer (note the large imaginary part of $k_{\perp \mathrm{IBW}}$ beyond R-R_0=-2 cm in Fig. 5-4). These features can be explained by TORIC simulations, as described in this section.

5.5.1 Electric field solution for a three species plasma

A set of plasma parameters was chosen that was fairly typical of these H–^{3}He–D plasmas for detailed study using the full-wave code TORIC (see Sec. 2.6). These were: central field 5.8 T, plasma current 800 kA, 33% H, 23% ^{3}He, 21% D, central electron density $2.4 \times 10^{20}\, m^{-3}$, electron temperature 1.5 keV, ion temperature 1.4 keV, major radius 67 cm, minor radius 23.8 cm, Shafranov shift on axis 1.2 cm, elongation 1.65, triangularity -0.3, parabolic profiles for density and temperature (the same form as Eq. 2.75) with inner exponent of 2, outer exponent of 0.2 for density and 1.0 for temperature, and edge/central value of 0.14 for ion temperature, 0.27 for electron temperature, and 0.33 for density. The estimates of the helium fraction discussed in Appendix D suggest that the ^{3}He concentration chosen for this TORIC run is quite high, and may only be applicable to the first few shots of the day. However, a few TORIC runs performed with different ion concentrations (see Sec. 5.5.9) suggest that the features described in this section are quite general to these three species, 6 tesla mode conversion scenarios.

The electric and magnetic fields represent the full solution to the problem of RF wave excitation in the plasma. Once E_{RF} and B_{RF} (and their spatial derivatives) are known, the charge density, the current density (and hence the dielectric tensor), and the Poynting flux can be calculated. For the calculations in this section, B_{RF} was calculated from numerical differentiation of E_{RF} and Faraday's law (recalling that all

field quantities are assumed to vary as $\exp[-i\omega t]$):

$$\nabla \times \vec{E}_{\mathrm{RF}} = i\omega \vec{B}_{\mathrm{RF}}. \tag{5.2}$$

A range of toroidal mode numbers from -15 to +15 were run, representing most of the power in the two-strap antenna spectrum (see Fig. 2-21, which should be squared for the power spectrum). An example of the electric field solution for the toroidal mode number $n_\phi = 10$ is shown in Fig. 5-24 (showing the LHCP and RHCP parts of the wave) and Fig. 5-25 (showing the parallel electric field and the Poynting flux component in the major radial direction). This is the highest poloidal mode run completed so far using TORIC, retaining ± 127 m_θ numbers. Only the electric field in the plasma is shown because the problems with the electric field at the edge of the plasma seem to be exacerbated with higher poloidal mode numbers.

The real and imaginary parts of the right-hand circularly polarized (RHCP) component (E^-) and left-hand circularly polarized (LHCP) component (E^+) are shown in Fig. 5-24. Note that, as expected from Fig. 2-6, the fast wave is mostly RHCP except near the $n_\parallel^2 = S$ resonance (at $R \approx -2.6$ cm on the midplane). Near that location in major radius, a short wavelength IBW is present in approximately equal amounts in both E^+ and E^-. When these solutions are animated,[10] the wave fronts move in the direction of the phase velocities. The IBW phase velocity in this poloidal cross-section view is directed toward the antenna (consistent with the IBW wavenumber PCI observations, see Sec. 5.4.4). The FW phase velocity is complicated, composed of standing wave and traveling wave patterns in different regions. The strongest feature is a circulation of power between the reflection layer associated with the mode-conversion layer and the low-field side edge of the plasma. In the animation, the phase velocity is directed towards the center of the plasma in the region below the midplane, and towards the antenna in the region above the midplane. For the fast wave, the group velocity is nearly in the same direction as the phase velocity, and the power is mostly

[10]With the assumed time dependence, the actual field is the real part of $E_{\mathrm{complex}} e^{-i\omega t} = E_r \cos\omega t + E_i \sin\omega t$, where E_r is the real part of the field and E_i is the imaginary part. Animating through at least one cyclotron period consists of cycling through time so that ωt advances through at least 2π in phase.

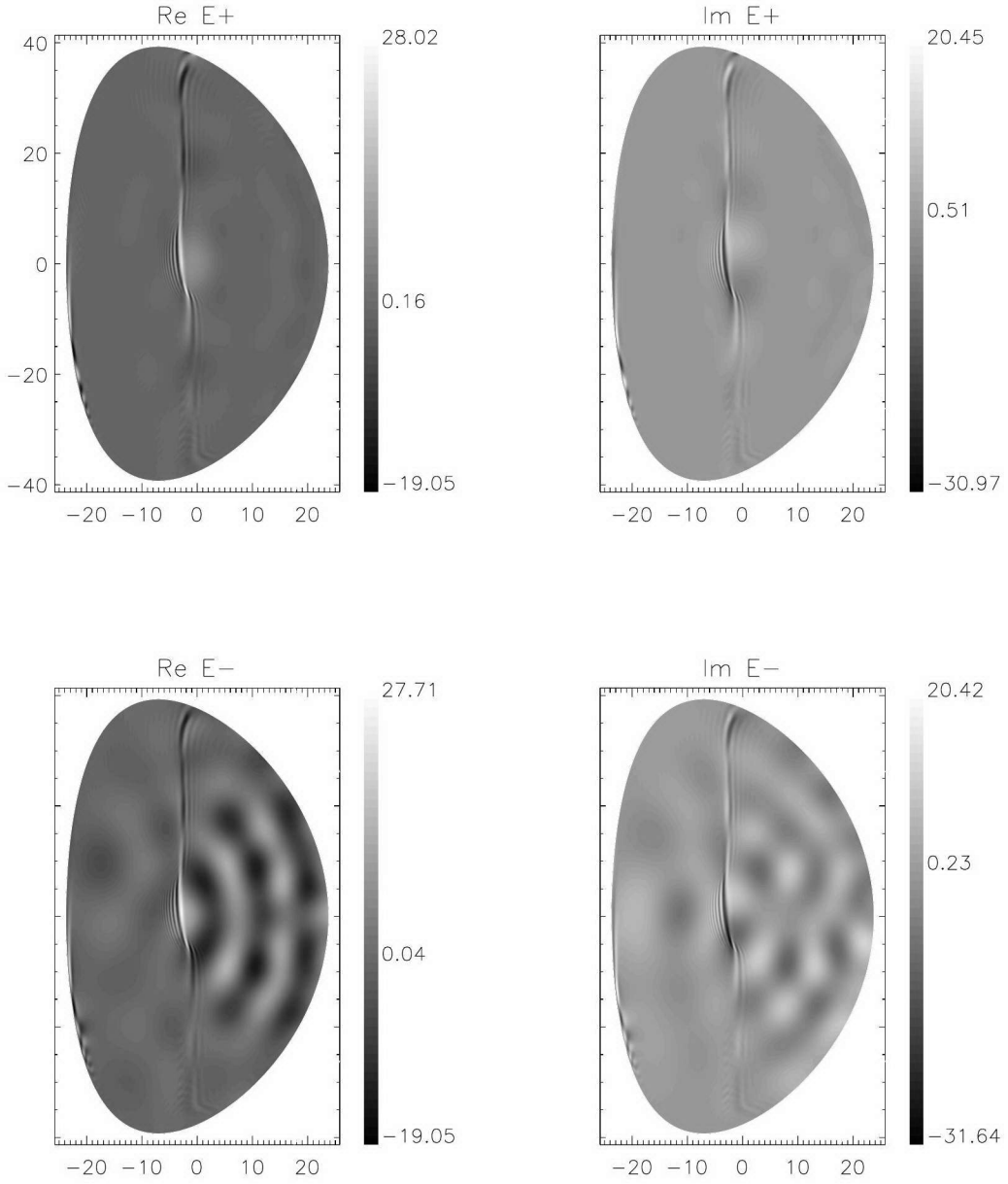

Figure 5-24: Electric field solution from TORIC, using 255 poloidal mode numbers, $n_\phi = 10$. Upper left and right: Real and Imaginary part of E^+. The maximum, minimum, and closest to zero values are identified for the contour levels on the bar on the right of each plot. The units are in kV/m per kA in the antenna. Bottom: Real and Imaginary parts of E^-. Vertical and horizontal scale is cm from the center of the plasma.

carried by the electromagnetic Poynting flux $\vec{S} = (\vec{E} \times \vec{B})/\mu_0$, where $\vec{E}$ and $\vec{B}$ here are the actual physical fields (i.e., Re $\vec{E}\exp(-i\omega t + in_\phi \phi)$). The Poynting flux time-averaged over a cyclotron period indicates power flow that is not simply oscillating back and forth at the RF frequency. For the complex field amplitudes (without the $\exp(-i\omega t)$ dependence) this is given by:

$$\langle \vec{S} \rangle = \frac{1}{2} Re \frac{\vec{E} \times \vec{B}^*}{\mu_0}, \tag{5.3}$$

where the factor of $1/2$ comes from the time-average of $\cos^2(\omega t)$ and $\sin^2(\omega t)$, and B^* denotes the complex conjugate of B. The major radial component of the Poynting flux $\langle S \rangle_R$ is shown in the lower right of Fig. 5-25. From this it can be seen that the flux in the major radial direction is large and negative below the midplane (i.e., directed away from the antenna), and large and positive above the midplane (directed toward the antenna). The combination of the vertical and major radial components of the Poynting flux is shown in Fig. 5-26 , with the length of the arrow proportional to the magnitude. This verifies the circulation of power as seen in the animation of E^+ and E^-. This direction of circulation (clockwise in the poloidal cross-section) persists for other toroidal mode numbers, even those with opposite sign. This could be consistent with the discussion of up/down asymmetries in Ref. [95], where the direction of power flow in a cold plasma with artificial damping did not depend on the sign of the toroidal mode number, but did change direction when the toroidal field was reversed. Unfortunately, TORIC cannot yet be run with a reversed field, but this suggests that the circulation may become counter-clockwise if the direction of the toroidal field were reversed. See Sec. 5.5.2 for more on the expected (a)symmetries.

The magnitudes of the perpendicular components are much larger than the parallel electric field component $E_\parallel$, shown in the upper part of Fig. 5-25. This is expected from cold plasma theory, where the ratio of $E_\parallel$ to the perpendicular component E_x (in local Cartesian coordinates) is (see Eq. 2.19):

$$\frac{E_\parallel}{E_x} = \frac{n_\perp n_\parallel}{n_\perp^2 - P}. \tag{5.4}$$

In the ICRF the wave frequency is much smaller than the electron plasma frequency ($\omega \ll \omega_{pe}$), so the dielectric tensor element $P \simeq -\omega_{pe}^2/\omega^2$ is very large, and $E_\parallel$ is

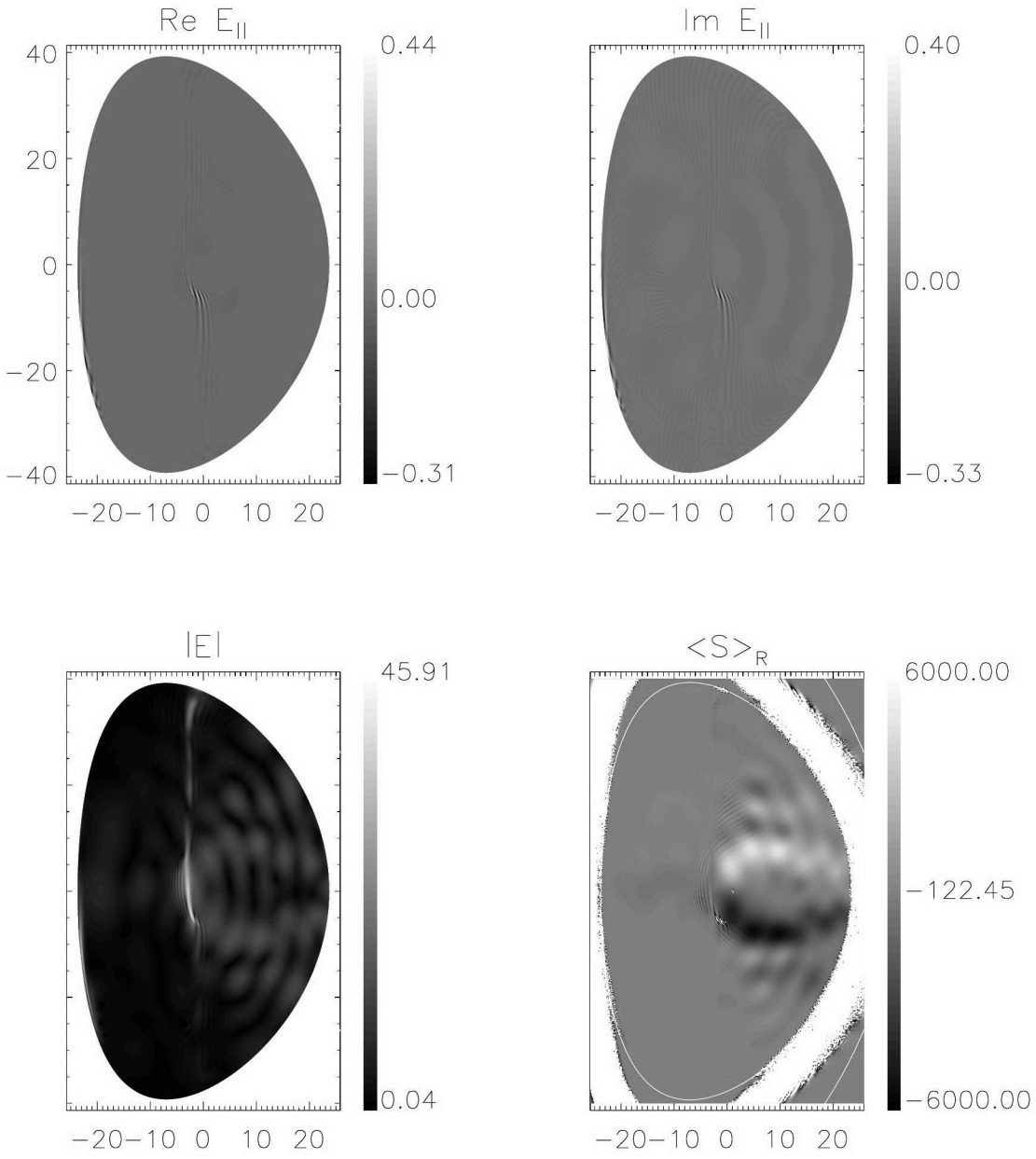

Figure 5-25: Electric field solution from TORIC, using 255 poloidal mode numbers, $n_\phi = 10$. Upper left and right: Real and Imaginary part of $E_\parallel$. The maximum, minimum, and closest to zero value is identified for the contour levels on the bar on the right of each plot. The units are in kV/m per kA in the antenna. Bottom left: magnitude of total E field, bottom right: Poynting flux in the major radial direction, units are MW/m^3 per kA^2 in the antenna. Because of problems with the field at the edge, the Poynting flux has been set to the maximum contour value outside the plasma.

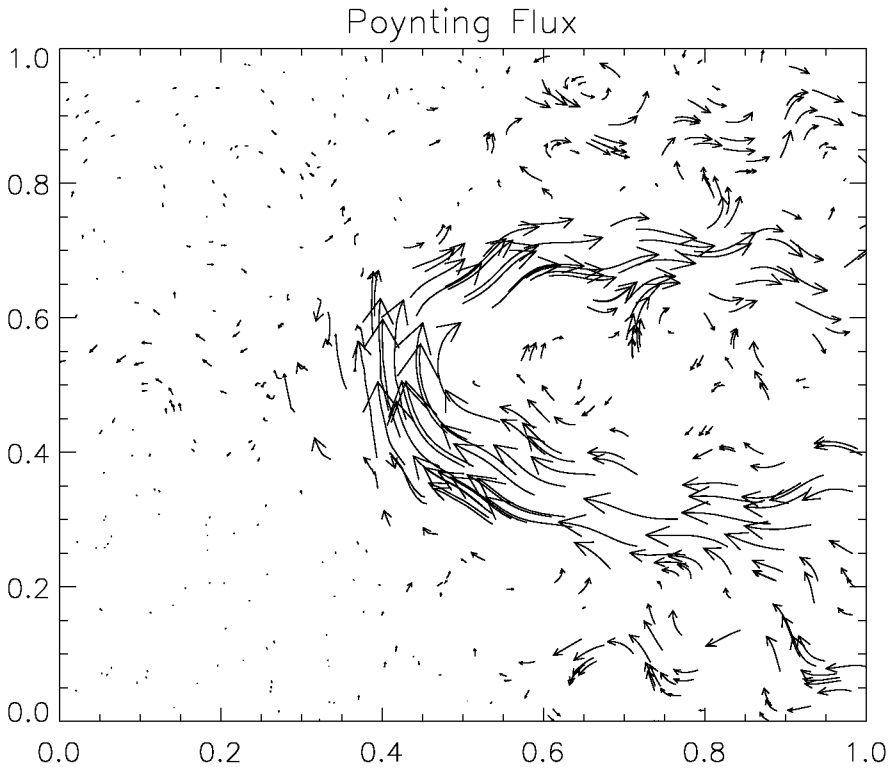

Figure 5-26: Poynting flux in the poloidal plane, arrows showing the projection in the poloidal cross-section. The length of the arrow is proportional to the Poynting flux magnitude. The plotting range corresponds to $-15 < R - R_0 < 17$ cm and $-20 < Z < 20$ cm.

very small. Because in C-Mod, $\omega_{pe} \sim |\Omega_{ce}|$, and $\omega \sim \Omega_{ci}$, P is roughly proportional to $(m_i/m_e)^2$, which for deuterium is 1×10^7. Thus for a typical $n_{\perp \mathrm{FW}} \sim 30$ and $n_{\parallel \mathrm{FW}} \sim 8$, the parallel electric field can be estimated:

$$E_{\parallel}^{\mathrm{cold}}/E_x \sim 2 \times 10^{-5}. \tag{5.5}$$

When a more complicated wave equation accounting for finite temperature is used in TORIC, the ratio of the magnitude of the parallel electric field to $|E^-|$ for the FW ranges from 10^{-4} to 10^{-3}.

There is also region of strongly enhanced $E_{\parallel}$ below the midplane, to the LFS of the midplane FW mode-conversion layer. This corresponds to an ion Bernstein wave excitation and coincides with the region of strong electron Landau damping as predicted by TORIC (see Fig. 5-27). A possible explanation for this IBW behavior is described in Sec. 5.5.4.

Global Power Balance

In TORIC, all the power that leaves the antenna is ultimately damped on one of the plasma species — there are no other loss mechanisms. The situation is assumed to be already in steady-state, where the stored electromagnetic energy is constant.[11] This may be a source of discrepancy with the actual experiment, as there are probably other (very difficult to measure) power loss mechanisms at the edge of the plasma and around the antenna box itself.

As shown in Fig. 5-27, there is a region of strong electron Landau damping near the center of the plasma. This accounts for a large fraction of the wave damping. The other main damping mechanism in this plasma is hydrogen cyclotron damping. The $\omega = \Omega_H$ layer is roughly a vertical line at 8 cm to the LFS of the center, and the Doppler-broadened cyclotron layer can be seen in Fig. 5-28. (The small region of hydrogen damping near the $E_{\parallel}$ peak, if correct, may be due to the enhanced E^+ from the IBW.) The global power balance can be calculated by integrating the 2-D profiles

[11] For an interesting discussion on the physics of the time-dependent problem, beginning with zero RF field and seeing how the field evolves when the antenna is turned on, see Ref. [96].

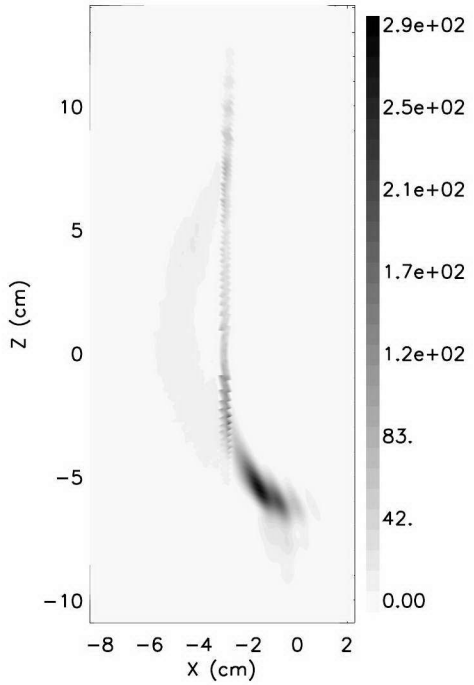

Figure 5-27: The electron Landau damping predicted by TORIC for $n_\phi = 10$. The quantity plotted is in units of MW/m^3 per m^2 area, per MW from the antenna. The strongest region of damping is in the same location as large magnitude $E_\parallel$. (X = R-R_0)

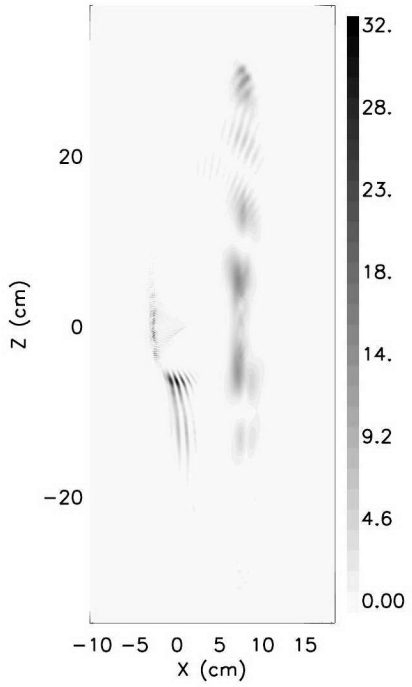

Figure 5-28: The hydrogen cyclotron damping predicted by TORIC for $n_\phi = 10$. The quantity plotted is in units of MW/m^3 per m^2 area, per MW from the antenna. The hydrogen cyclotron layer is at X=8 cm (X = R-R$_0$).

over the plasma volume, thus obtaining the total absorbed power for each mechanism. For this case, the majority of the power transferred to the plasma is through electron Landau damping (65.22% of the total damped power) and hydrogen fundamental cyclotron damping (32.00%). The remaining few percent is in deuterium second harmonic ($\omega = 2\Omega_D$), helium-3 fundamental ($\omega = \Omega_{He3}$), and stochastic damping of the IBW at high wavenumber (see Refs. [24, 97]). With a sufficient number of poloidal modes, TORIC can resolve both the FW and IBW and the relative magnitude of each around the mode conversion layer. It solves for all three electric field components, and can predict the global power balance. Thus the density fluctuation pattern can be calculated and compared to the PCI measurements.

5.5.2 Cold plasma expected symmetries

From cold plasma theory, the expected symmetries of the natural modes in the plasma can be examined, and the physics of many of the features described in Sec. 5.5.1 can be explained. In Ref. [95], a simple wave equation is derived for a cold plasma in a 2-D slab geometry with the toroidal field in the z direction (and no poloidal field). The wave propagation vector is assumed to be in the (x,z) plane, with simple harmonic dependence in the z direction: E, B $\propto \exp(ik_z z)$. Assuming that $E_{\|} = 0$, the RF magnetic field in the longitudinal direction satisfies the following wave equation:

$$\left(\frac{\omega}{c}\right)^2 B_z + i\left[\frac{\partial B_z}{\partial y}\frac{\partial}{\partial x}\left(\frac{D}{(S-n_z^2)^2 - D^2}\right) - \frac{\partial B_z}{\partial x}\frac{\partial}{\partial y}\left(\frac{D}{(S-n_z^2)^2 - D^2}\right)\right] + \nabla\cdot\left(\frac{(S-n_z^2)\,\nabla B_z}{(S-n_z^2)^2 - D^2}\right) = 0. \quad (5.6)$$

In the cold plasma, there is no dissipation so that S and D are real. Under these conditions it can be shown that Eq. 5.6 is invariant under the transformation $B_z(x,y) \Rightarrow B_z^*(x,-y)$. This is equivalent to the electric field transformation:

$$\begin{aligned} E_x(x,y) &\Rightarrow E_x^*(x,-y) \\ E_y(x,y) &\Rightarrow -E_y^*(x,-y) \end{aligned} \quad (5.7)$$

By defining E^+ and E^- the same way as in Eq. 2.33 and 2.34, this implies that E^+ and E^- both transform as E_x in Eq. 5.7. This means that the real part of E^+

and E^- will be even about the midplane (y=0 in this coordinate system, or Z=0 in the cylindrical coordinate system used in this chapter and in Appendix C), and that the imaginary part will be odd. This feature of the cold plasma solution with no dissipation persists even in the TORIC solution which includes dissipation, as can be seen by examining E^- for the fast wave in Fig. 5-24. Equations 5.6 and 5.7 also imply that for the Poynting flux, the following transformations apply:

$$\begin{aligned} \langle S \rangle_x(x,y) &\Rightarrow -\langle S \rangle_x(x,-y) \\ \langle S \rangle_y(x,y) &\Rightarrow \langle S \rangle_y(x,-y). \end{aligned} \tag{5.8}$$

Of course, once dissipation is introduced (through the anti-Hermitian part of the dielectric tensor), the strict symmetries implied by the above transformations no longer apply. However, the basic symmetries remain for the fast wave in the TORIC solutions in this mode-conversion case where the single-pass damping is weak. Eq. 5.8 can even explain why there is a circulation of power in the plasma — this is the "natural" state with no dissipation. When strong damping is introduced, neither the circulation of power nor the odd symmetry about the midplane in the imaginary part of E^+ and E^- is observed in the TORIC solution. (For example, a D(H) scenario with 5% H).

Reference [95] also discusses a natural shift of the launched antenna m number spectrum when coupled to the plasma due to the magnetic field gradient and density gradient, even in the absence of a poloidal magnetic field. This is due to currents induced because of the $\vec{E} \times \vec{B}$ force (of the wave fields alone). This is apparently not related to the m shift discussed in Sec. 2.5.2 and shown in Fig. 2-26. That shift did require a poloidal field. See also Ref. [98] for a discussion of the poloidal asymmetries in a cold plasma in the process of coupling antenna power at the edge to the plasma.

Of course, cold plasma theory is of little use for explaining the asymmetries of the IBW solution, which is explicitly a hot-plasma mode. The asymmetries of the fast wave which are introduced by direct electron Landau damping and cyclotron damping, and the shift due to coupling of the wave from the antenna to the plasma [95] could help explain some of the observed differences in the TORIC solutions for IBW

excitation above and below the midplane for different toroidal mode numbers. However, the main features of the up/down asymmetries seem to be adequately explained by IBW ray-tracing, as discussed in Sec. 5.5.4.

5.5.3 Density fluctuation

In order to use TORIC (or any ICRF code) to explain some of the observations of the PCI data, it is necessary to calculate the expected RF fluctuating density n_{e1}, because the PCI measures electron density perturbations, not the electric field directly. Appendix C describes a procedure for calculating n_{e1} from the electric field, without resorting to wavenumbers and dielectric tensor elements. It turns out that the density flucuation is proportional to the divergence of the electron velocity. The parallel electron velocity $v_{e\|}$ is directly proportional to $E_\|$ and has a multiplying factor of order Ω_e/ω which the perpendicular velocity components lack (see Eq. C.15). The perpendicular velocity components are proportional to linear combinations of the perpendicular field components, which are usually larger than the parallel field by factors of 10^3 to 10^4. However, when $E_\|$ becomes larger than $\frac{m_e}{m_i}E_\perp$, it becomes the dominant contribution to the RF fluctuating density. This is certainly the case for the IBW short-wavelength oscillations below the midplane shown in Fig. 5-25, where $E_\|/E_\perp \sim 0.01$. In fact it seems that based on the TORIC simulations, $E_\|$ of the IBW was the dominant contribution to the PCI signal for all the mode-conversion experiments.

Figure 5-29 shows the relative contribution to the velocity gradient from the three components of the velocity (all plotted on the same scale), in the local "Stix" coordinates described in Appendix C. The plasma scenario is the same as that described previously in this section, but only 161 poloidal modes were used, and $n_\phi = 15$ not 10. Here it can be seen that the part proportional to the parallel electric field E_ζ is roughly a factor of 3 larger than the perpendicular parts. It is also interesting to note that the fast wave structure visible from the E_η contribution (Fig. 5-29(a)) is not present in the E_ζ part (Fig. 5-29(c)).

The calculation in toroidal non-orthogonal coordinates which TORIC uses inter-

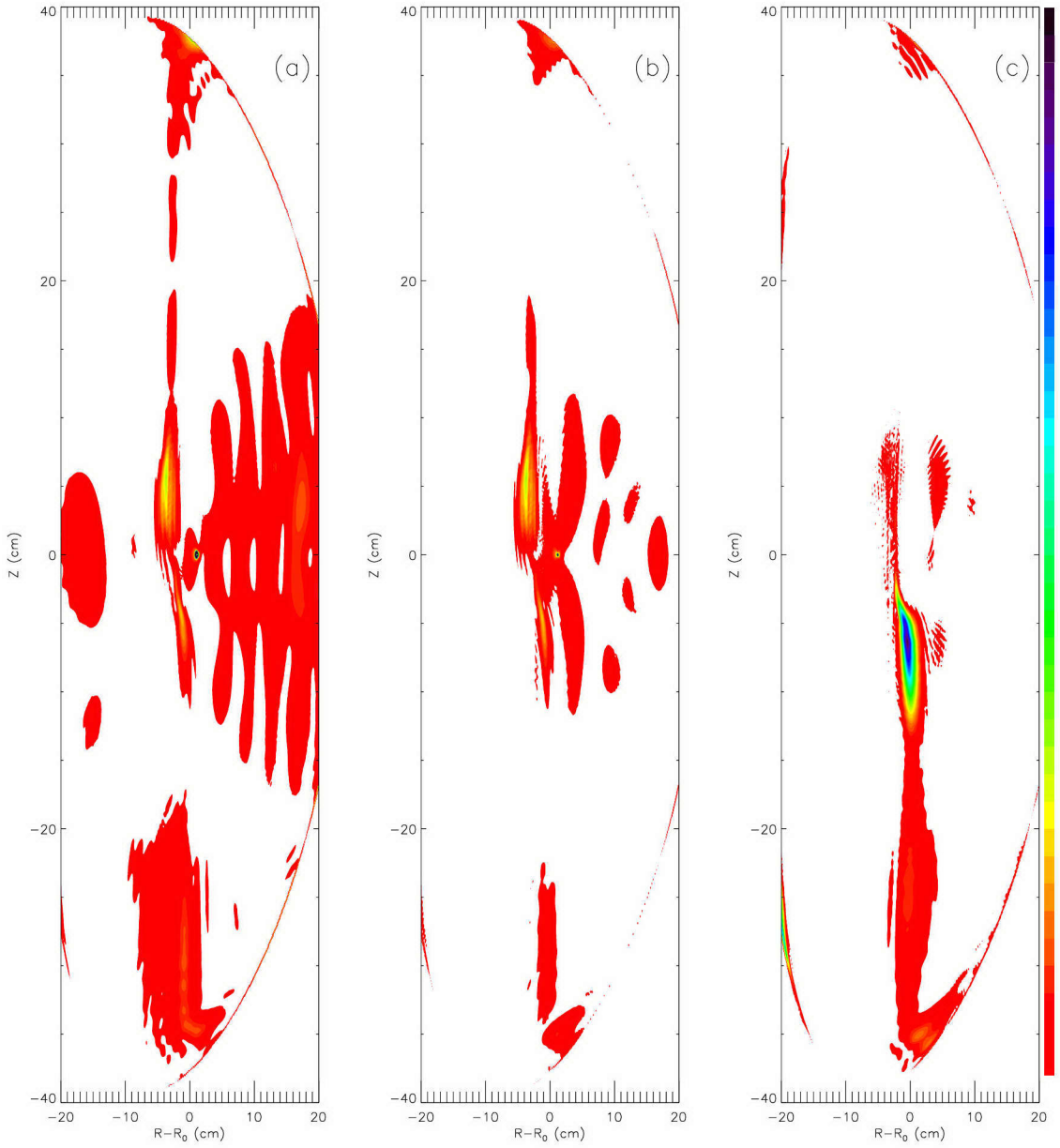

Figure 5-29: The relative contribution to the RF fluctuating density from the three parts of the gradient of the perturbed velocity (in local magnetic coordinates). Magnitudes are shown: (a) $\nabla \cdot \vec{v}|_\psi$ (b) $\nabla \cdot \vec{v}|_\eta$ (c) $\nabla \cdot \vec{v}|_\zeta$. The largest contribution comes from (c), the parallel gradient of the parallel velocity $(\partial_\zeta + \nu_\zeta)v_\zeta$. To the right of (c) is the linear scale for the contours, increasing from bottom to top.

nally is only done here for illustrative purposes. There are more numerical uncertainties introduced with this method, especially near the magnetic axis where there can be singularities in some of the components if not treated carefully. This method also relies on the reconstruction of various quantities associated with the non-orthogonal divergence operator, which are not automatically output by the code. For these reasons the calculations of n_{e1} for multiple n_ϕ modes to compare to the PCI data was performed in cylindrical coordinates (see Sec. C.2.1).

5.5.4 Up/down asymmetries in the IBW solutions and IBW ray-tracing

The region of the TORIC solution where the short wavelength IBW solutions appear reveals some asymmetries about the midplane (Z=0). Figures 5-30 through 5-32 show the region around the IBW wavefields for the real parts of E^+, E^-, and $E_\parallel$. Two toroidal mode number solutions are shown; on the left of each plot is the positive mode number $n_\phi = 13$, and on the right is $n_\phi = -13$. It is clear that the IBW is much stronger above the midplane for negative n_ϕ, and below the midplane for positive n_ϕ. This effect has also been seen in the full-wave code developed at Oak Ridge National Laboratory which treats the ICRF problem to all orders in $k_\perp \rho_i$ (see Ref. [76]). In their code (as in TORIC) they have seen IBW structure to the low field side of the cold plasma $n_\parallel^2 = S$ mode conversion layer. They also note that the up/down asymmetry practically disappears when the poloidal magnetic field is neglected. This has also been seen in TORIC. In a run with greatly reduced toroidal current (300 kA) but otherwise the same parameters as the case studied in this section, the IBW wavefronts and the electron Landau damping was up/down symmetric and vertically straight, without the curvature evident in Fig. 5-27. Thus this effect is clearly tied to the presence of a poloidal magnetic field. Studies of IBW ray-tracing offer a possible explanation for the physics underlying this up/down asymmetry, and the reason why there appears to be IBW wavefields to the low-field side of the cold plasma fast wave mode conversion layer.

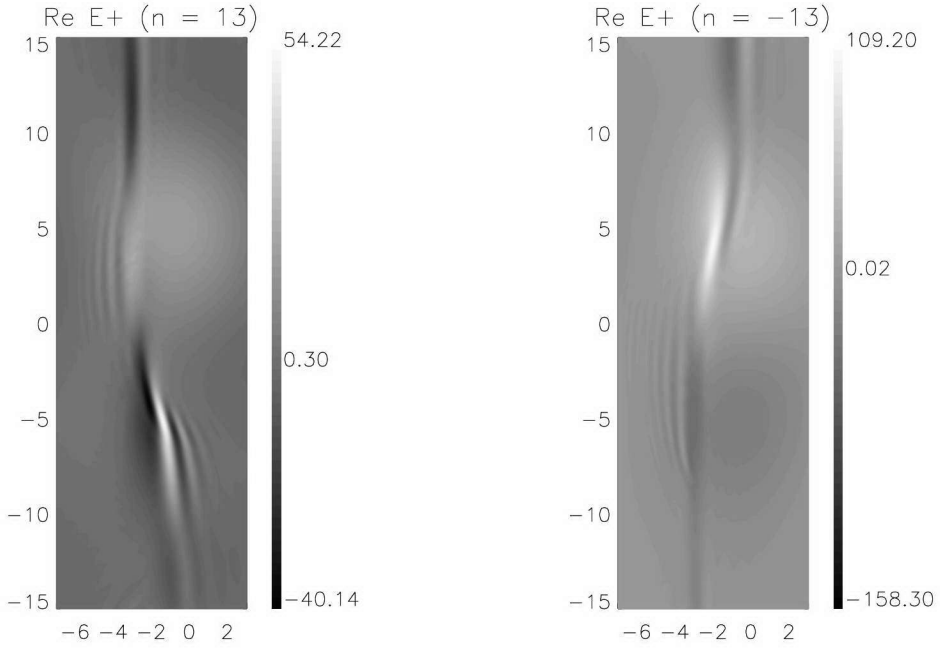

Figure 5-30: Real part of E^+ from TORIC, using 161 poloidal mode numbers. Left: $n_\phi = 13$, right: $n_\phi = -13$. (Axes in cm, contour levels in kV/m per kA in the antenna.)

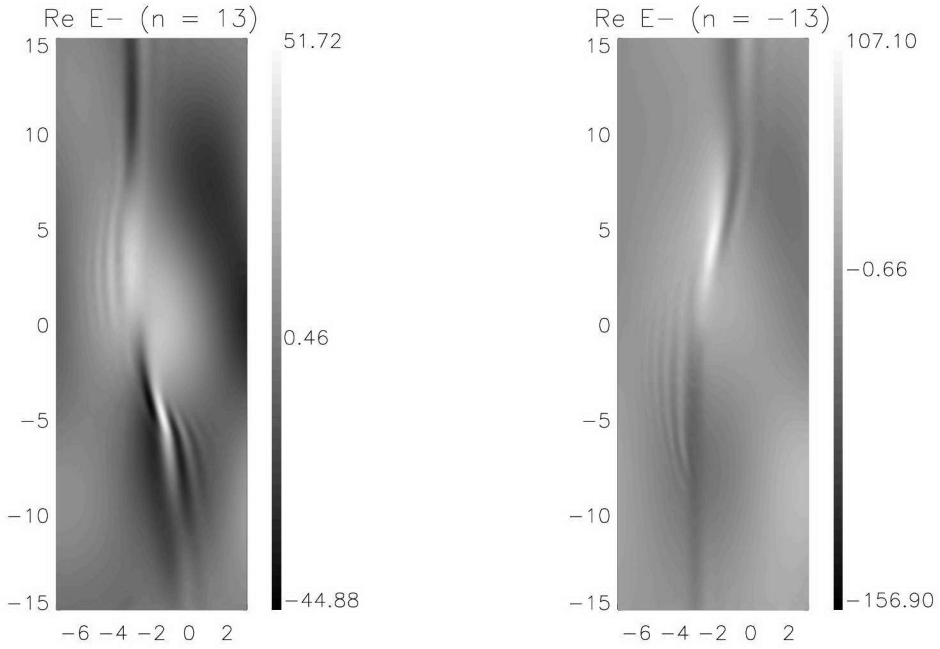

Figure 5-31: Real part of E^- from TORIC, using 161 poloidal mode numbers. Left: $n_\phi = 13$, right: $n_\phi = -13$.

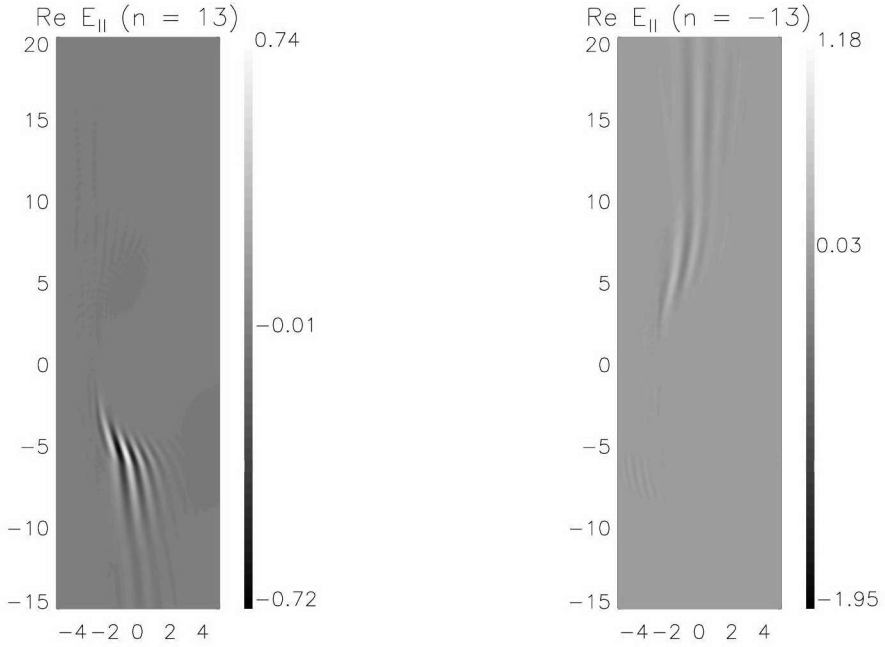

Figure 5-32: Real part of $E_\parallel$ from TORIC, using 161 poloidal mode numbers. Left: $n_\phi = 13$, right: $n_\phi = -13$.

Ray-tracing allows one to follow the evolution of the phase velocity and group velocity (the direction of energy flow) of a short-wavelength wave. If the damping is fairly weak, an estimate of the power deposition and the distance the ray travels before it is completely dissipated can also be made. Reference [50] presents some analytic results concerning the propagation and damping of mode-converted IBWs in toroidal plasmas. Several points are very relevant to understanding the TORIC solutions where IBWs are present. **(1)** The mode-converted IBW's minor radial group velocity is larger than its poloidal group velocity immediately after mode conversion, but when it begins to experience Landau damping, the ray can radically change direction and the poloidal group velocity becomes larger than the radial group velocity. The toroidal group velocity can also change direction. In the numerical results in Ref. [50], the ray is found to have almost completely damped away when $\omega/(k_\parallel v_{\rm the}) \sim 1$. In the mode conversion scenarios for these H–^{3}He–D plasmas in C-Mod, Landau damping can begin to play a role almost immediately after mode conversion. **(2)** There is an upshift in the magnitude of the poloidal mode number m as the ray propagates. Above

the midplane, the m number becomes more negative, while below the midplane, the m number becomes more positive. Very near the midplane, the m number does not change as rapidly as it does far away. **(3)** Before Landau damping becomes important, the IBW ray paths above and below the midplane are mirror images of each other in the poloidal cross-section, but travel in opposite toroidal directions.

These insights from ray-tracing can help explain some of the features of the TORIC solution. Figure 5-33 shows the fluctuating density calculated from the TORIC electric field solution for $n_\phi = 13$. Figure 5-33 shows the region near the center of the plasma, where the strongest contribution to the fluctuating density comes from the short-wavelength IBW below the midplane. The nearly vertical dot-dash line labelled $n_\parallel^2 = S\,(m = 0)$ is the cold-plasma fast wave mode conversion layer, where the FW wave number becomes large and is expected to convert some power into the IBW. The antenna launches fast wave power with a range of m numbers, but the $m = 0$ component is the strongest. Because of the fast wave focussing (visible in Fig. 5-24, for example), the strongest excitation of the IBW is expected near the center of the plasma, just to the high-field side of this layer. Then, according to the ray-tracing picture (see Ref. [90] for an example of an H(^{3}He) plasma with FW to IBW mode conversion in Tore supra), IBW rays below the midplane turn around and propagate to the low-field side, m numbers rapidly increasing. The waves shown in Fig. 5-33 have a phase velocity towards the antenna (consistent with the PCI data) and a decreasing wavelength representing m numbers from 39 (at $R - R_0 \simeq -2$ cm) to 53 (at $R - R_0 \simeq 2$ cm). Since the propagation direction is mostly in the poloidal direction, $k_\perp$ can be approximated by m/r, and this means that $k_\perp$ is increasing from 7.2 to 9.8 cm^{-1}. For the three ion species present in the plasma, this means that $k_\perp \rho$ is close to 1 ($k_\perp \rho_D \sim 0.89$ to 1.25, $k_\perp \rho_H \sim 0.63$ to 0.89, and $k_\perp \rho_{\mathrm{He3}} \sim 0.54$ to 0.77). This may seem to violate the $k_\perp \rho < 1$ expansion that is solved by TORIC, but there is a quasi-electrostatic dispersion relation used to deal with short-wavelength IBWs and their Landau damping in TORIC (see Ref. [24, Sec. 7.3]). The dotted line labelled $n_\parallel^2 = S(m = +53)$ represents the approximate line behind which (i.e., to the low-field side of) the shortest wavelength IBW in this region should not be able to propagate.

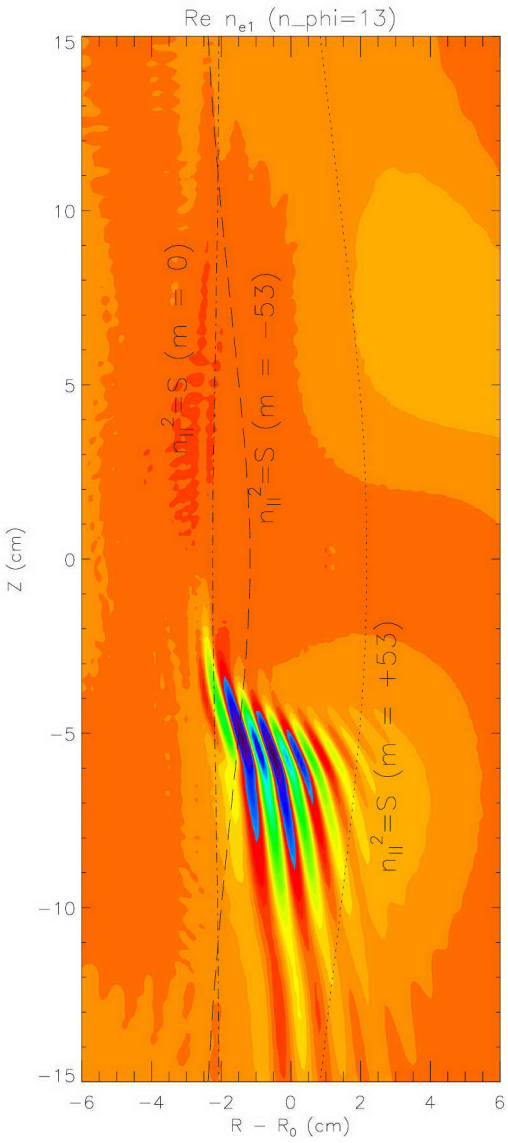

Figure 5-33: Real part of n_{e1} from TORIC, using 161 poloidal mode numbers, for $n_\phi = +13$. Also plotted are the $n_\parallel^2 = S$ layers for $m = 0$, which is the FW mode conversion layer, $m = +53$ (dotted line) — to the LFS of this layer the IBW shown below the midplane cannot propagate, and $m = -53$ (dashed line) — to the LFS of this layer corresponding IBWs above the midplane cannot propagate.

Indeed, the wave seems to be damped away by that point. This picture can now help explain why there is no corresponding IBW above the midplane for this n_ϕ. Because n_ϕ is positive, when there is a finite poloidal magnetic field present, positive m_θ numbers will increase $n_\parallel$, while negative m numbers will decrease $n_\parallel$ (see Eq. 2.74). Also, except for regions of very low density at the edge, S increases as the major radius R increases (i.e. to the LFS). Thus the location at which $n_\parallel^2$ is equal to S moves to the LFS as $n_\parallel^2$ increases. The line behind which the IBW above the midplane (which should have large negative m numbers) cannot propagate is not pushed back as far to the low-field side, because $n_\parallel^2$ is not as large. The dashed line in Fig. 5-33 shows the $n_\parallel^2 = S$ layer for $m = -53$. This line is much closer to the original FW mode-conversion region than for the $m = +53$ line. Thus, there is not a strong IBW above the midplane because it would be evanescent before traveling very far back.

If this picture is correct, and the location of the $n_\parallel^2 = S$ layer for the high $|m|$ number IBWs determines how far the IBW can propagate, then the situation should be reversed for the corresponding $-n_\phi$ toroidal mode number. Figure 5-34 shows the TORIC solution for $n_\phi = -13$. Indeed, now there is only a strong IBW above the midplane, with m numbers ranging from -42 to -56. Again, the phase velocity (towards the antenna) is consistent with the PCI measurements.

Ray-tracing can also suggest why $E_\parallel$ is so much larger for the IBW than for the FW. Because the IBW becomes more nearly electrostatic (i.e. $\vec{k} \parallel \vec{E}$) as it propagates away from the region of coalescence with the FW, and $k_\parallel$ becomes larger (i.e., the wavevector becomes more aligned with the local magnetic field), the component of the IBW electric field along the magnetic field also gets larger.

Although it seems that changing the sign of n_ϕ produces a solution which is a mirror image about the midplane,[12] this is not always the case in the TORIC solutions. For low values of n_ϕ, large values of $|m|$, and a moderate poloidal field, the poloidal part of $k_\parallel$ can be large enough that it alone can push the $n_\parallel^2 = S$ layer back, regardless of the sign of n_ϕ. For example, Fig. 5-35 shows the solution for $n_\phi = -4$,

[12]This is claimed in the code results presented in Ref. [76], but they only showed results for large n_ϕ.

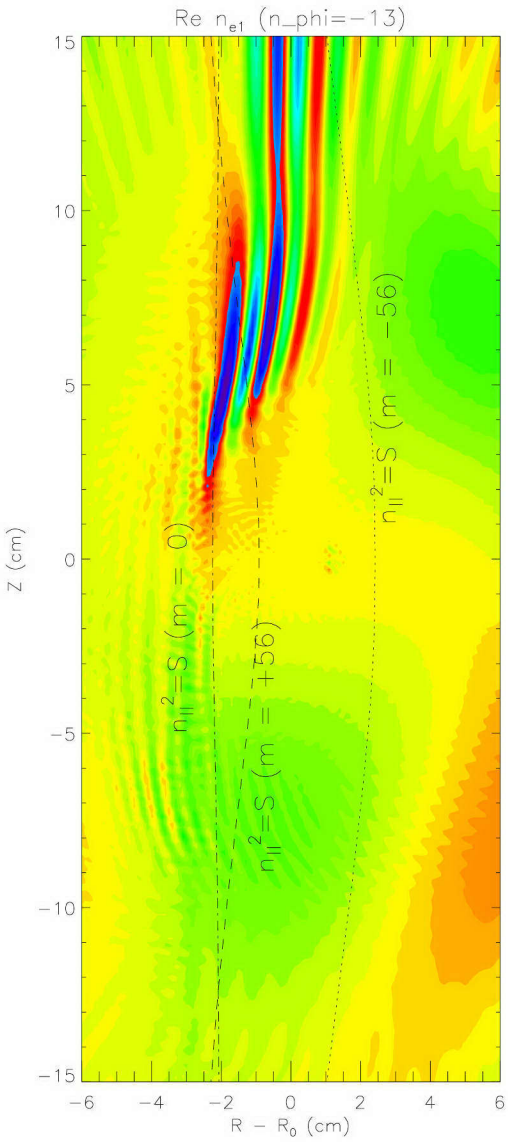

Figure 5-34: Real part of n_{e1} from TORIC, using 161 poloidal mode numbers, for $n_\phi = -13$. Also plotted are the $n_\parallel^2 = S$ layers for $m = 0$, which is the FW mode conversion layer, $m = -56$ (dotted line) — to the LFS of this layer the IBW shown above the midplane cannot propagate, and $m = +56$ (dashed line) — to the LFS of this layer corresponding IBWs below the midplane cannot propagate.

which exhibits high $|m|$ IBWs both below and above the midplane. The region of IBWs below the midplane at minor radius 10 cm and major radius 66.6 cm (where the poloidal field is 0.42 T and the toroidal field 5.86 T) has an m number of 81. Because the n number is -4, the contribution to $k_\parallel$ (see Eq. 2.74) from the poloidal part is 0.57 cm^{-1}, and from the toroidal part is -0.06 cm^{-1}. Above the midplane, at the same minor and major radius, and the same poloidal and toroidal field, the m number is -69. The contribution to $k_\parallel$ from the poloidal part is -0.43 cm^{-1}, and from the toroidal part is -0.06 cm^{-1}. In both cases, the poloidal contribution $mB_\theta/(r|B|)$ is much larger than the toroidal contribution $nB_\phi/(R|B|)$, accounting for the similar locations for the $n_\parallel^2 = S$ lines. In this case, IBWs can be seen propagating to the HFS on the midplane, and to the LFS both above and below the midplane.

Local dispersion relation roots compared to TORIC solution

There is still an unresolved question concerning the TORIC results for these IBW-like oscillations. For the given plasma parameters in the region of the short-wavelength features, there are no propagating modes found in the local hot plasma electromagnetic dispersion relation with the perpendicular and parallel wavelengths that appear to be in the TORIC solution. The short-wavelength IBW-like oscillations (shown in Figs. 5-33 and Fig. 5-50 for example) have electron Landau damping parameters $\omega/(k_\parallel v_{the})$ which are firmly in the range of strong Landau damping, and yet the waves seem to propagate for several wavelengths, as many as 7 full wavelengths in the case of Fig. 5-50. For example, for the case described in Fig. 5-33, in the middle of the IBW oscillation, $\omega/(k_\parallel v_{the})$ is approximately 0.34. According to standard wave theory, the wave should be heavily damped. And in the case of Fig. 5-50 $\omega/(k_\parallel v_{the}) \sim 0.48$. These values were calculated using Eq. 2.74[13] with magnetic fields and the toroidal mode number n_ϕ from the TORIC model, and approximating m_θ from the wave field solution, assuming an $\exp(im_\theta\theta)$ dependence for the electric field in the region where the

[13]Strictly speaking, the $k_\parallel$ used in TORIC is $k_\parallel^{mn_\phi} = \frac{m}{N_\tau}\sin\Theta + \frac{n_\phi}{R}\cos\Theta$ (see Appendix C and Eq. (55) in Ref. [24]). However, by using r for N_τ, $B_\theta/|B|$ for $\sin\Theta$, and $B_\phi/|B|$ for $\cos\Theta$, the answer is nearly the same. In any case, a range of $k_\parallel$ is explored in Fig. 5-37.

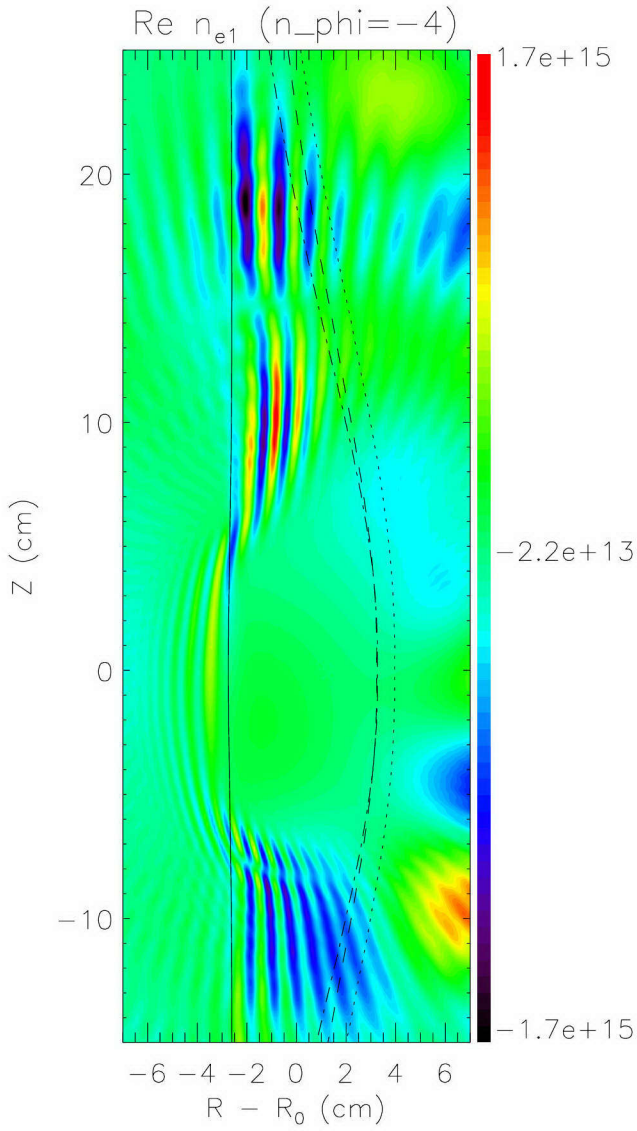

Figure 5-35: Real part of n_{e1} from TORIC, using 161 poloidal mode numbers, for $n_\phi = -4$. Also plotted are the $n_\parallel^2 = S$ layers for $m = 0$ (solid line), which is the FW mode conversion layer, $m = -90$ (dotted line), which is the highest m number in the uppermost IBW region (above 16 cm), $m = -79$ (dashed line), which is the highest m number in the upper IBW region from 6 cm to 15 cm, and $m = +90$ (dot-dash line), which is the highest m number in IBW region below the midplane.

short-wavelength oscillation is propagating mostly in the θ direction. The m numbers are known to be positive below the midplane, not only from ray-tracing experience, but also from directly animating the solution. This is also consistent with PCI observations. However, attempts to find this short-wavelength mode from the local hot plasma electromagnetic dispersion relation have failed to find any propagating root.

For example, for the $n_\phi = 13$ case (as seen in Figs. 5-30 to 5-33), a point in the middle of the propagating IBW oscillation was chosen for analysis using the local dispersion relation Eq. 2.40. At $R - R_0 = -0.73$ cm, $Z = -5.45$ cm, the plasma parameters are: minor radius $r = 5.5$ cm, $m_\theta \simeq 50$, $B_\theta = 0.3$ T, $B_\phi = 5.9$ T, $T_e = 1.42$ keV, $T_i = 1.33$ keV, and $n_e = 2.37 \times 10^{20}$ m^{-3}. Because $B_\phi \gg B_\theta$, the perpendicular wavenumber can be approximated by the wavenumber in the poloidal cross-section (i.e., perpendicular to B_ϕ). With this m_θ number, $k_\perp \simeq m/r \simeq 9.1$ cm^{-1}. Then by using n_ϕ, m_θ, and the magnetic field, the parallel wavenumber can be calculated: $k_\parallel = 65.86$ m^{-1}, so $\omega/k_\parallel v_{the} = 0.34$. However, in order to find roots that are close to those used in TORIC, $k_\parallel$ is chosen to be 17.99 m^{-1} so that $\omega/k_\parallel v_{the} = 1.25$.[14]

Let the left-hand side of Eq. 2.40, which is a complicated transcendental function of $k_\perp$ for given $k_\parallel$, ω, etc., be $D(k_\perp)$. Then a root of this equation ($k_\perp$ such that $D(k_\perp) = 0$) represents a possible mode of oscillation in a uniform plasma with the given plasma parameters. A graphical method to search for all the roots in a given region of the complex $k_\perp$ plane is to plot contour levels of the real and imaginary parts of $D(k_\perp)$. An intersection of the zero level contours for the real and imaginary parts represents a point where $D(k_\perp) = 0$ and hence the $k_\perp$ at that location is a solution to the wave equation. Figure 5-36 illustrates this procedure for the set of plasma parameters described above, using the modified parallel wavenumber.

Three roots are labelled by the letters a, b, and c. The values of $k_\perp$ corresponding to these roots are: $k_\perp^a = 17.04 - 17.23\,i$, $k_\perp^b = 17.45 + 17.15\,i$, and $k_\perp^c = 0.3644 +$

[14]This value of $\omega/k_\parallel v_{the}$ is chosen because, as has been pointed out by Paul Bonoli, in the version of TORIC used for all the code runs in this thesis, there was a feature which forced the electron Landau damping parameter $\omega/k_\parallel v_{the}$ to be 1.25 for the purposes of calculating the IBW damping. Also, in other places in the code, $k_\parallel$ with $m = 0$ was used in calculating certain quantities associated with determining if an IBW is propagative or not. For $n_\phi = 13$ at $R = 66.3$, using $k_\parallel$ with $m = 0$ results in $\omega/k_\parallel v_{the} = 1.15$, which is not too different from 1.25.

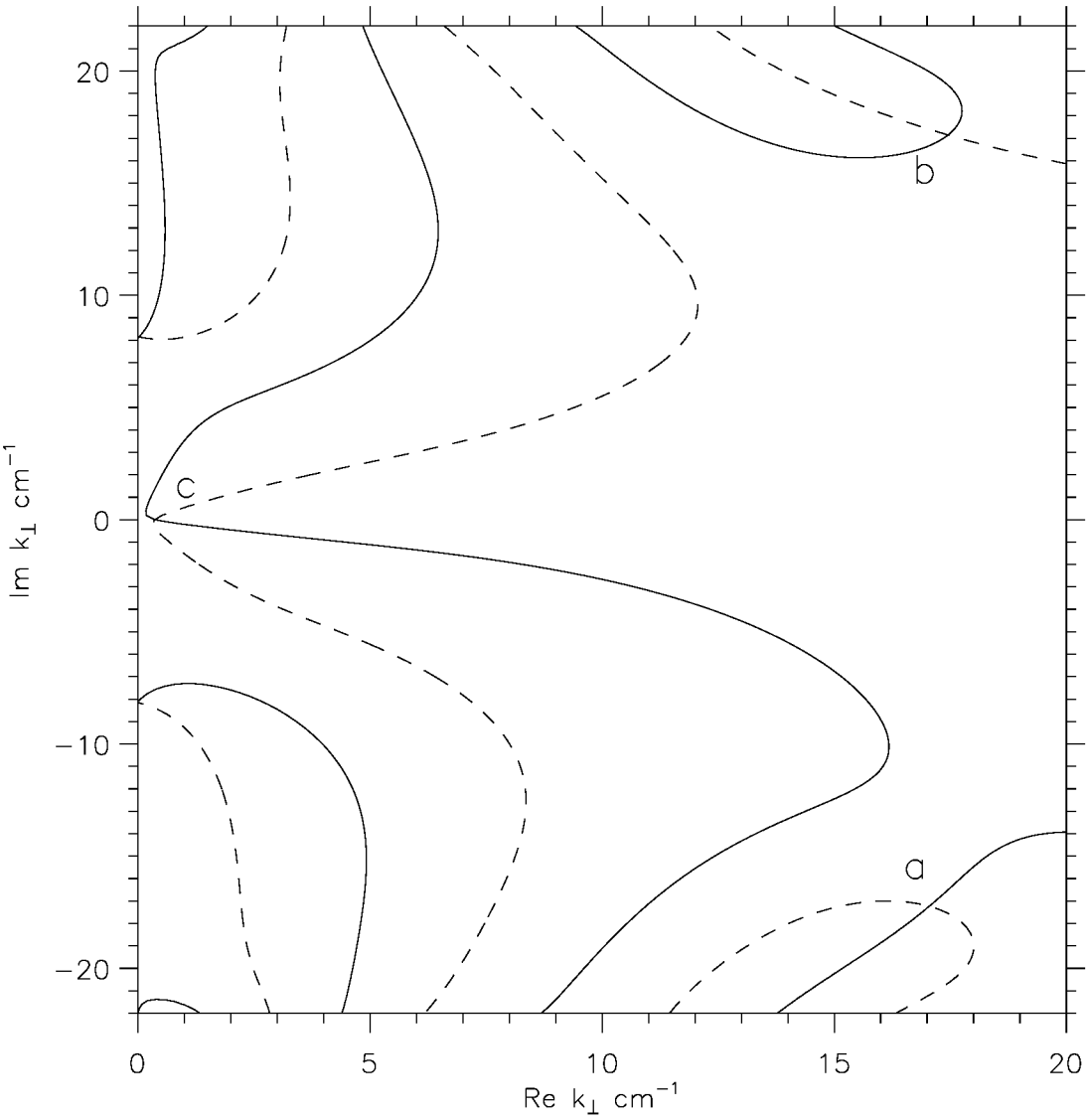

Figure 5-36: A graphical method for finding dispersion relation roots. Plasma parameters are described in the text — note that $\omega/k_{\|}v_{the} = 1.25$ is used for this plot. Along the solid lines the real part of $D(k_\perp)$ is zero, and along the dashed lines the imaginary part of $D(k_\perp)$ is zero. Intersections represent roots, three of which are labelled a, b, and c. (The roots at $0 \pm 9\,i$ cm^{-1} are evanescent.) Note that there is no root in the region as expected from TORIC, with Re $k_\perp \simeq 9.1$ cm^{-1} and small imaginary part.

$6 \times 10^{-8}\, i$. Root c is the fast wave at that location, with a wavelength of 17.2 cm, which agrees quite well with the fast wave in the TORIC solution in that region (see Fig. 5-33). Root a might be identified as an IBW-like root, but it is heavily damped — the imaginary parts are comparable to the real parts. Root b is similar to root a but it has a positive imaginary part, so it is not a backward wave. There is no root near Re $k_\perp \simeq 9.1$ cm^{-1}, which is the estimated real part of $k_\perp$ for the IBW-like region in the TORIC solution.

In order to examine the behavior of each of these roots for various values of $\omega/k_\parallel v_{the}$, the root found from Fig. 5-36 was used as the initial guess for a complex root solver program, which tracked the root through a range of $k_\parallel$, spanning a range of $\omega/k_\parallel v_{the}$ from 0.3 to 2.25. Figure 5-37 shows the values of $k_\perp$ as a function of $\omega/k_\parallel v_{the}$.

Even allowing for a large variation in $k_\parallel$ it still seems that there is not a propagating mode in the local dispersion relation corresponding to the oscillations seen in TORIC to the low-field side of the $n_\parallel^2 = S\,(m = 0)$ layer. The finite Larmor radius dispersion relation (1st order in $k_\perp \rho_i$) also predicts a wavelength that is much shorter than that predicted by TORIC (in any case, if it is not in the full electromagnetic dispersion relation, any root that the FLR dispersion relation finds is spurious). Recent ray-tracing runs simulating the exact parameters from the TORIC cases have failed to reproduce the behavior as seen in the TORIC solutions (and as described in Ref. [90]). Instead, rays that are launched just to the high-field side of the fast wave mode conversion layer damp quickly within at most a centimeter or two, and do not turn back and follow along a flux surface for many centimeters as in the TORIC results. The lack of propagating roots in the local hot plasma electromagnetic dispersion relation can explain the failure of ray-tracing for this specific TORIC plasma to reproduce the features seen in the electric field solution. However, it seems that the general features learned from ray-tracing still can indicate some of the physics of this mode that is found in TORIC.

The presence of a mode in TORIC which cannot be found in the local dispersion relation could have something to do with the global, driven nature of the electric wave-

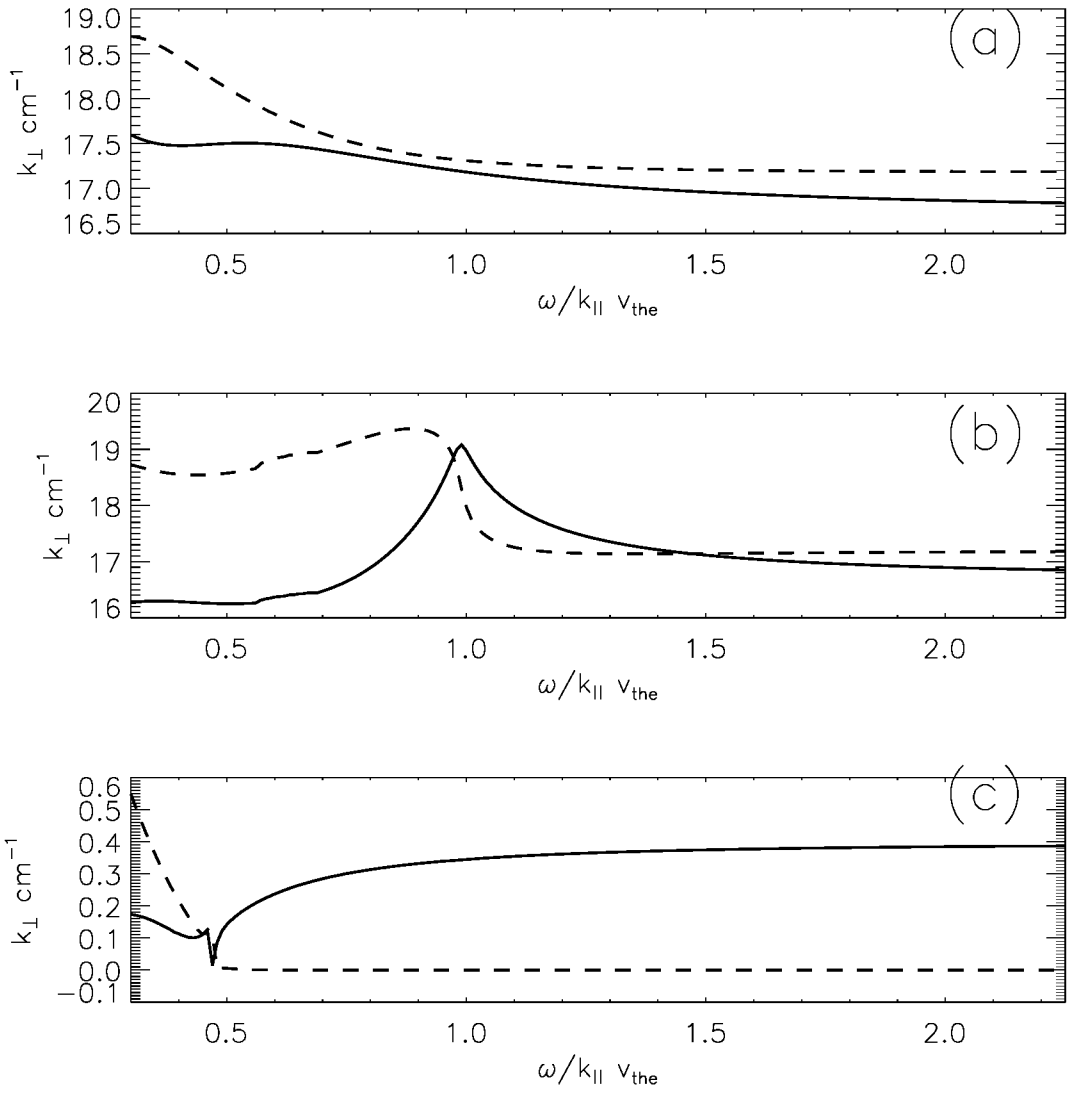

Figure 5-37: The roots found in Fig. 5-36 and their variation with $\omega/k_{\|}v_{the}$. The real parts of $k_{\perp}$ are shown by solid lines, and the imaginary parts by dashed lines. The plots are labelled with the same letters as for the original roots. (a) is the IBW-like heavily damped oscillation (the imaginary part has been multiplied by -1 in the plot). (b) is the root found with large positive imaginary part. It is also heavily damped everywhere, although there is a region between $\omega/k_{\|}v_{the} = 1$ to 1.4 where the real part is larger than the imaginary part. (c) is the fast wave root. When $k_{\|}$ is too large, the $n_{\|}^2 = R$ cutoff causes the fast wave to be evanescent below $\omega/k_{\|}v_{the} < 0.33$.

field solution in TORIC, as opposed to the local, natural mode solution that appears in both ray-tracing and the local dispersion relation. The mathematical problem that is solved by TORIC (a second order differential equation with boundary conditions) may result in different solutions than those obtained from the local dispersion relation (an algebraic equation) [8, Ch. 5-1]. It is interesting to note that in the TORIC solutions, when the code attempts to split the electron Landau damping (ELD) into that from the IBW and the FW, there is an artificial vertical line (corresponding to the $n_\parallel^2 = S$ line for $m = 0$) to the LFS of which there is no IBW-ELD. However, when the total ELD is plotted (the sum of the FW-ELD and IBW-ELD), this artificial division disappears and a smooth, continuous feature appears (such as in Fig. 5-27). This suggests that although there is an IBW dispersion relation used internally in the code,[15] there is not expected to be a short-wavelength IBW-like oscillation to the LFS of the $n_\parallel^2 = S$, $m = 0$ layer. Yet the wave equation that is solved by TORIC finds an IBW-like mode between the $n_\parallel^2 = S$, $m = 0$ layer and the $n_\parallel^2 = S$, $m = m_{\max}$ layer, where $m_{\max}$ is the maximum m number present in the oscillation. Perhaps it is a "toroidal" ion Bernstein wave, with modified wavenumber and damping compared to the local dispersion relation solution. On the whole, the experimental data seems more consistent with the TORIC results than with the ray-tracing and local dispersion relation simulations of these three-species C-Mod plasmas. Further investigation into this puzzle could be the topic of another thesis, or a future publication.

One final example of the up/down asymmetry of the IBW solution which seems to illustrate point **(3)** from the ray-tracing results is shown in Fig. 5-38. According to the ray-tracing results, the IBW rays above the midplane should travel in the opposite toroidal direction as those below the midplane. The Poynting flux only represents the flow of electromagnetic energy, but the IBW energy is also carried in large part by the kinetic energy of the particles, making the IBW group velocity calculation more

[15]The quasi-electrostatic dispersion relation employed in the code to find the IBW roots is only used when Re $n_\perp^2|_{IBW} > 0$, and then only to add a modification to the FLR coefficient in the integro-differential equation for the electric field [24, Sec. 7.3]. The actual electric field is a result of solving the differential equations, not from calculating the polarizations from a local dispersion relation.

complicated than simply calculating the Poynting flux. Nevertheless, examining the sign of the Poynting flux component in the toroidal direction for $n_\phi = 10$ (so that the phase velocity is in the positive toroidal direction) shows that for the IBW region near the center of the plasma, $\langle S \rangle_\phi$ is negative above the midplane and positive below.

The results in this section show that experience from ray-tracing of IBWs can help explain why there are short-wavelength IBW features to the low-field side of the FW mode-conversion layer, and why there are up/down asymmetries in specific toroidal mode number solutions. In effect, when high poloidal mode numbers are used, the TORIC simulation is in a way performing ray-tracing, connecting the short-wavelength IBW and the longer wavelength FW with the proper phase and amplitude. The backward wave nature of the IBW is somewhat more complicated to define in a 3-D geometry, where the direction of the group velocity and the direction of the phase velocity are not necessarily co-linear. In fact, in some projections, the phase velocity components and group velocity components are in the same direction, while in others they point in opposite directions.

5.5.5 Summation of toroidal mode number solutions

The previous section showed the results of calculating the RF fluctuating density for several different n_ϕ numbers. In the C-Mod two-strap antenna, a range of toroidal mode numbers are launched into the plasma, each coupling with different efficiency, and each contributing differently to the total density pattern existing in the experiment and measured by the PCI. This section presents a method for summing the different solutions together to approximate the total pattern.

Reconstructing the full 3-D solution from TORIC after running many toroidal modes requires knowledge of the (possibly complex) weighting factor A_{n_ϕ} in Eq. 2.86 for the total electric field. Calculating this factor by using the simple vacuum spectrum (the Fourier transform of the two current straps) shown in Fig. 2-21 did not reproduce the expected toroidal electric field pattern near the antenna strap in the vacuum region — which is that of an oscillating dipole field with large amplitude near the straps and weaker amplitude away from the straps. Rather than consisting solely

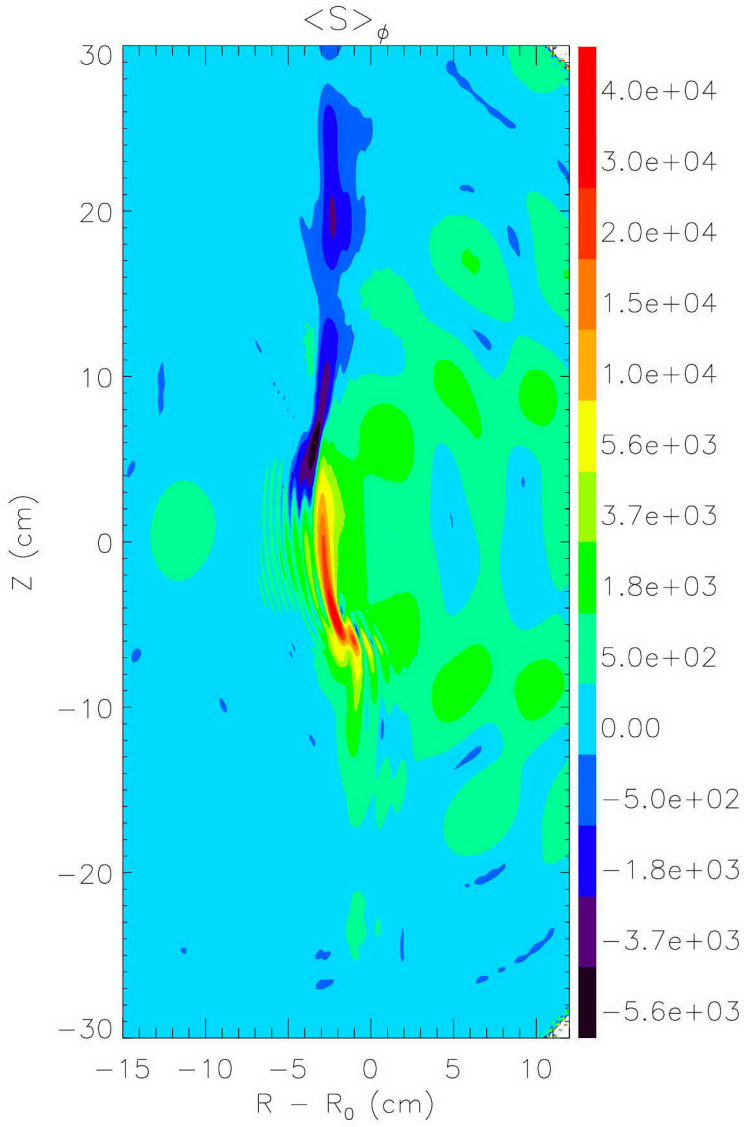

Figure 5-38: Toroidal component of the Poynting flux, as calculated from TORIC results, using 161 poloidal mode numbers, for $n_\phi = 10$. Units are W/m^2 per ampere^2 in the antenna strap.

of two bare straps, the actual antenna is surrounded by a complicated structure of conductors in which image currents of the straps are imposed during RF operation. The simple vacuum spectrum does not accurately model the antenna geometry. The proper way to improve the modeling of the full electric field solution would be to improve TORIC's treatment of the antenna geometry. For example, in the poloidal direction, modeling of the feeder currents to the poloidal strap could be included. Even better, the boundary conditions should be obtained from a full 3-D antenna modeling code. In this way the proper toroidal Fourier coefficient for each toroidal mode number solution could be found. Attempts to add the different toroidal mode numbers together using just the real part of the complex impedance (the part of the loading due to power dissipation in the plasma) also did not yield satisfactory results.

A method used previously [79] which had some success in comparing the 3-D TORIC solution to experimental measurements of the fast magnetosonic wave, is to pick the factors A_{n_ϕ} in such a way that the electric field at the major radius of the antenna looks like the expected dipole field pattern as in Fig. 5-39. Moving away from the antenna, the field is assumed to decay away to zero approximately 12° from the center of the nearest strap.[16] In between the straps, the field connects smoothly from negative to positive. There has been no measurement of the field nor detailed modeling at this location in the tokamak, but the field just described is assumed to reproduce the major features of the two-strap antenna.

Because of the time and computing resources needed to run TORIC with sufficient resolution to correctly solve for the IBW, only twelve toroidal mode numbers were used for the summation in this section. These were 4,6,8,10,13,15, and the corresponding negative toroidal mode numbers. Figure 5-40 shows the solution for the vertical field (E_Z in the cylindrical coordinate system of Appendix C) for each of these toroidal mode numbers. The magnitude of the vertical field along the midplane is shown ($Z = 0$, $-26.5 < R - R_0 < 26.5$ cm), with units as output by TORIC, which are

[16] In fact, measurements of the magnetic field around an antenna mock-up in the laboratory have shown that the field does decay as one moves away toroidally [99], although there were a few low amplitude oscillations around zero (i.e., it is heavily damped, but not critically damped).

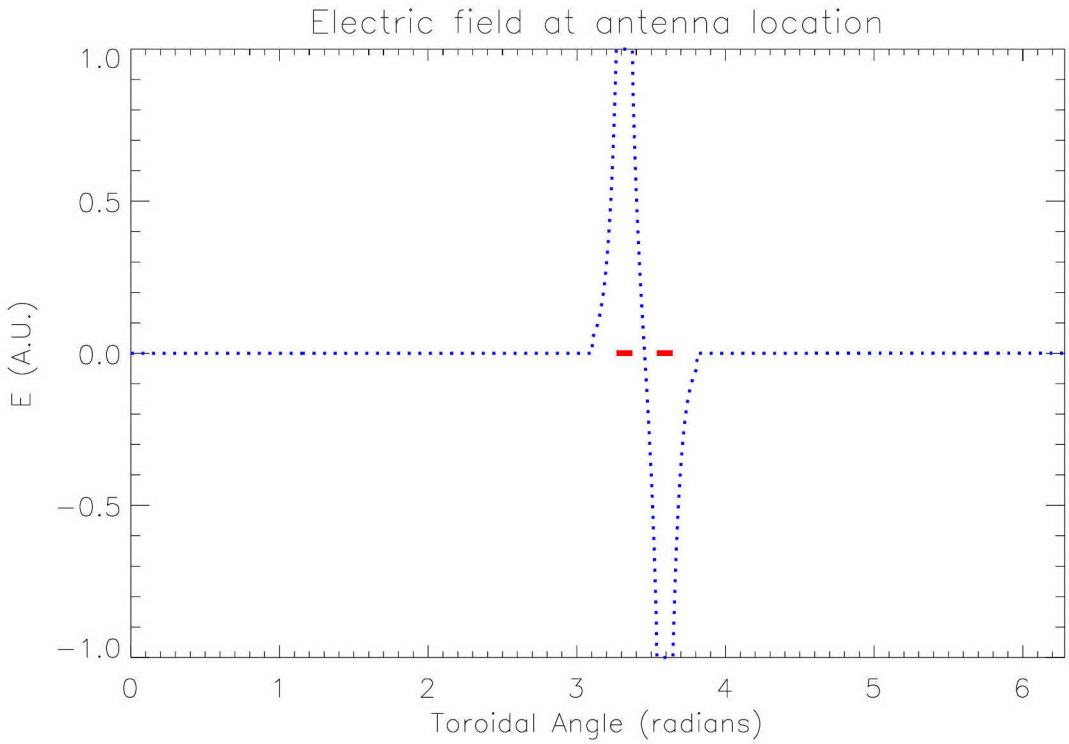

Figure 5-39: The model dipole field used for constructing the 3-D TORIC solution. This is the assumed electric field variation in the toroidal direction just in front of the antenna. The positions of the two straps and their toroidal extent is shown by the short solid lines around 3 radians. The straps are phased [0,π]. The real part of the electric field at time $t = 0$ is shown by the dotted line (the imaginary part is zero). Thus when animated, the fields in front of the straps oscillate out of phase.

volt/m for 1 ampere of current in the strap. No weighting according to an antenna spectrum has been done, yet there is a very large variation (the vertical axis is a logarithmic scale) in the electric field at the edge for different n_ϕ numbers, as well as large variation in the ratio of the field at the edge to the field inside the plasma. This can be partially explained by the different complex loading impedance for each mode, where the real part represents resistive damping, and the imaginary part represents inductive or capacitive parts of the loading. With a different impedance for each mode, the same amount of current can result in different electric fields. The balance between reflection and mode conversion changes for different modes, helping to explain the magnitude of the standing wave pattern between the LFS edge and the mode conversion region near the center.

Reference [98] gives insight into the problem of how the various wavenumbers in the antenna spectrum couple to the plasma. In that paper it can be seen (especially from Eqs. (11) through (13)) that the electric field at the antenna is a complicated function of the toroidal and poloidal wavenumbers. Each n_ϕ solution in TORIC shown in Fig. 5-40 represents the proper weighted sum of 161 poloidal mode numbers, but just one toroidal mode number. The appropriate weighting factors for the sum of these twelve toroidal mode number solutions was calculated as follows: the twelve functions $\exp(in_\phi\phi)$ for the twelve toroidal mode numbers were used as basis functions with complex coefficients to attempt to reproduce the toroidal field pattern shown in Fig. 5-39 (using a least-squares fitting routine). The complex coefficients thus obtained are the A_{n_ϕ}. Because only 12 modes were available, the reconstruction did not reproduce the desired field very accurately. In particular the field away from the straps did not decay to zero. For example, the large peaks in amplitude between 0 and 1 and 5.5 to 6.3 radians in Fig. 5-41 do not match the desired functional form in Fig. 5-39, probably because not enough high n_ϕ modes were retained to accomplish the destructive intereference at that end of the torus opposite the antenna straps. The modelling performed for the fast wave (with only 15 poloidal modes) by Alex Mazurenko [79] suggest that at least 40 toroidal mode numbers should be kept. Even with this imperfect reconstruction, the toroidal field pattern on the midplane at the

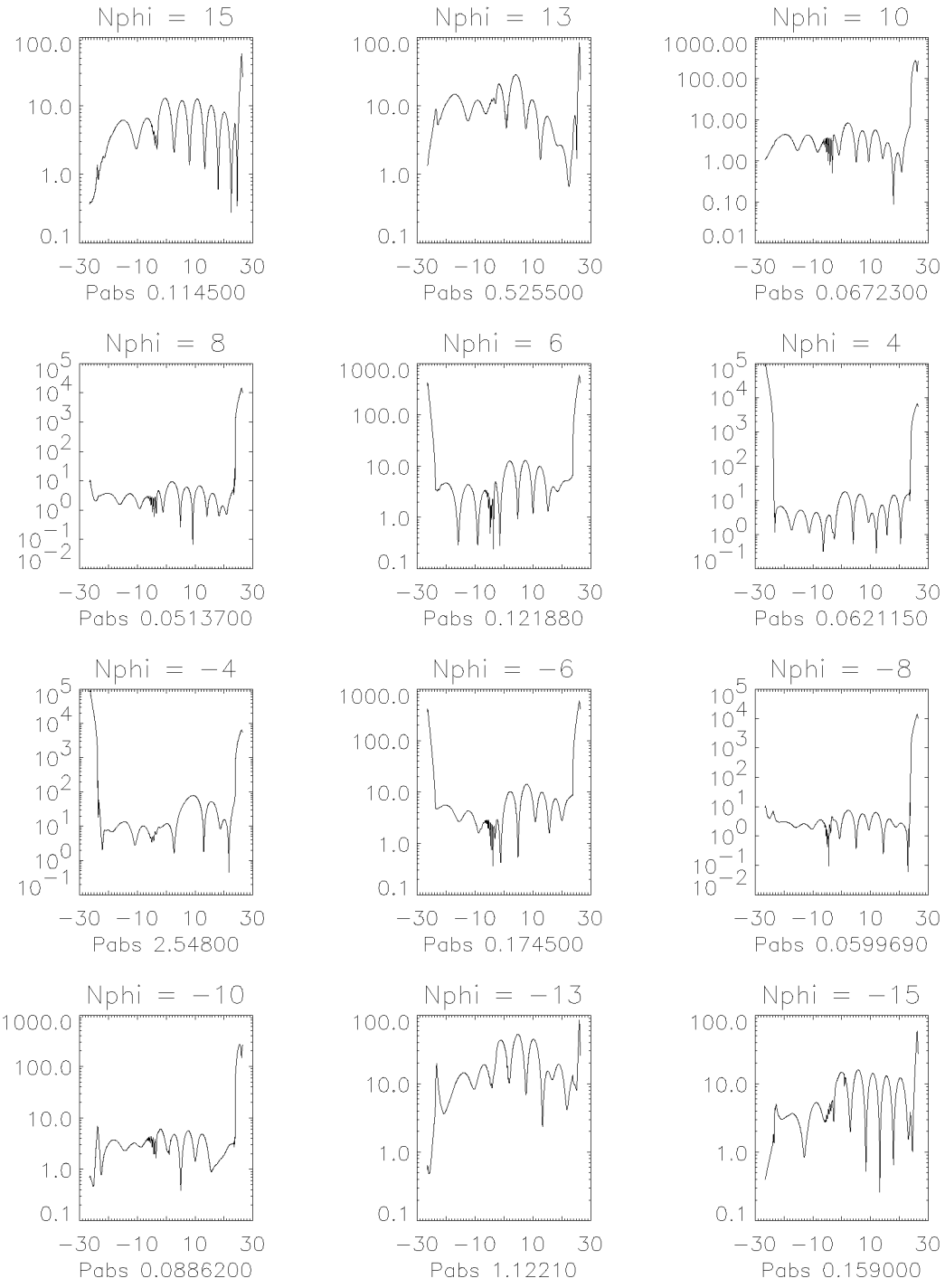

Figure 5-40: The magnitude of the vertical electric field component along the midplane, for 12 different n_ϕ numbers (labeled above the plot). The vertical axis is V/m for 1 amp of current in the antenna, and the horizontal axis is $R - R_0$ cm. Below each plot is shown the total absorbed power in the plasma in watts, which is equivalent to the loading in ohms.

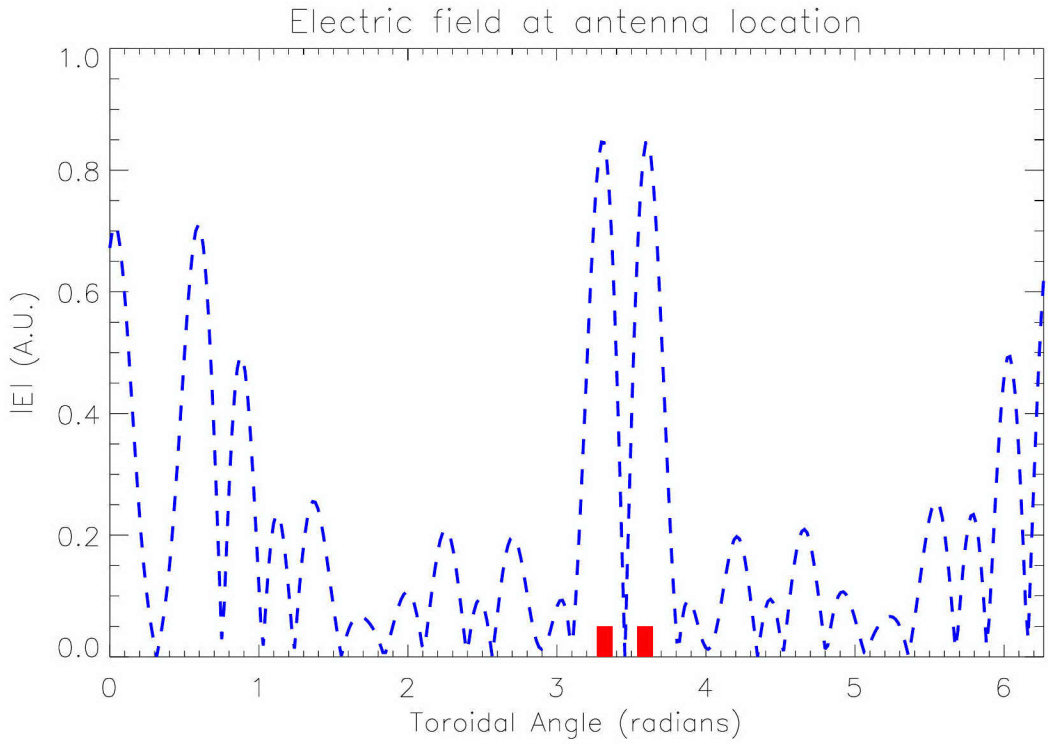

Figure 5-41: The magnitude of the vertical electric field pattern for the weighted sum of 12 toroidal mode numbers from TORIC. The positions of the two antenna straps is shown by the solid bars. Compare this with the dipole field in Fig. 5-39 — 12 n_ϕ modes are not enough to accurately reproduce the mode dipole field. The magnitude is not yet calibrated to a specific power level.

antenna location exhibits the main features of a dipole field — two large out-of-phase peaks in amplitude in front of the straps (between 3 and 4 radians in Fig. 5-41). The A_{n_ϕ} coefficients used showed that the coupling to the plasma effectively shifted power in the vacuum spectrum to larger toroidal mode numbers (i.e., the positive peak moved to higher positive n_ϕ and the negative peak moved toward more negative n_ϕ). Thus the higher toroidal mode numbers contributed more to the total electric field in this mode conversion scenario than the lower toroidal mode numbers. This is consistent with 1-D full-wave code results from FELICE.[17]

The poloidal cross section of the 3-D solution at a specific location in the tokamak

[17]This code was also written by Marco Brambilla and is a forerunner to TORIC. It can calculate the power coupled to the plasma as a function of parallel wavenumber.

can be examined by choosing a specific toroidal angle ϕ, and summing the entire poloidal cross section of each n_ϕ solution with the weighting factor $A_{n_\phi} e^{i n_\phi \phi}$. For example, the location directly in front of the two-strap antenna (exactly between the straps) corresponds to the PCI diagnostic location when the E-port antenna is energized. Figure 5-42 shows the real part of the RF fluctuating density calculated in this way. Note the strong IBW feature in the density fluctuation both above the midplane (predominantly from the negative n_ϕ) and below (predominantly from the positive n_ϕ). The basic features of the sum can be discerned by simply examining the solutions for $n_\phi = \pm 13$ (see Figs. 5-33 and 5-34). This is because the higher n_ϕ numbers contributed the most to the sum when the procedure was followed as described in this section. By summing the fields in this way, the overall amplitude is as yet uncalibrated to a specific power leaving the antenna or a specific amount of current in the antenna straps. One method of doing this is described in the next section.

5.5.6 Using the Poynting flux for power calibration

In order to compare magnitudes of the density fluctuations measured in the experiment to the TORIC solution, the expected theoretical values must be calibrated according to how much power was launched from the antenna (or by how much current is in the antenna strap, a less-well-known quantity experimentally).

In the process of finding the appropriate complex weighting factors A_{n_ϕ}, the electric field solution from each n_ϕ was normalized so that the complex field amplitude at the edge was $1 + 0\,i$. When the different n_ϕ electric field solutions are summed together, the total should be multiplied by a factor proportional to the square root of the RF power launched from the antenna, which is a well-known experimentally measured quantity. This factor can be estimated from the integration of the Poynting flux leaving a box surrounding the antenna. This was done near the antenna so that it was in the propagating fast wave region, where the Poynting flux represents most of the energy flow. The box consisted of a top and bottom arc, two rectangular sides (on either side toroidally of the main electric field peaks shown in Fig. 5-41), and

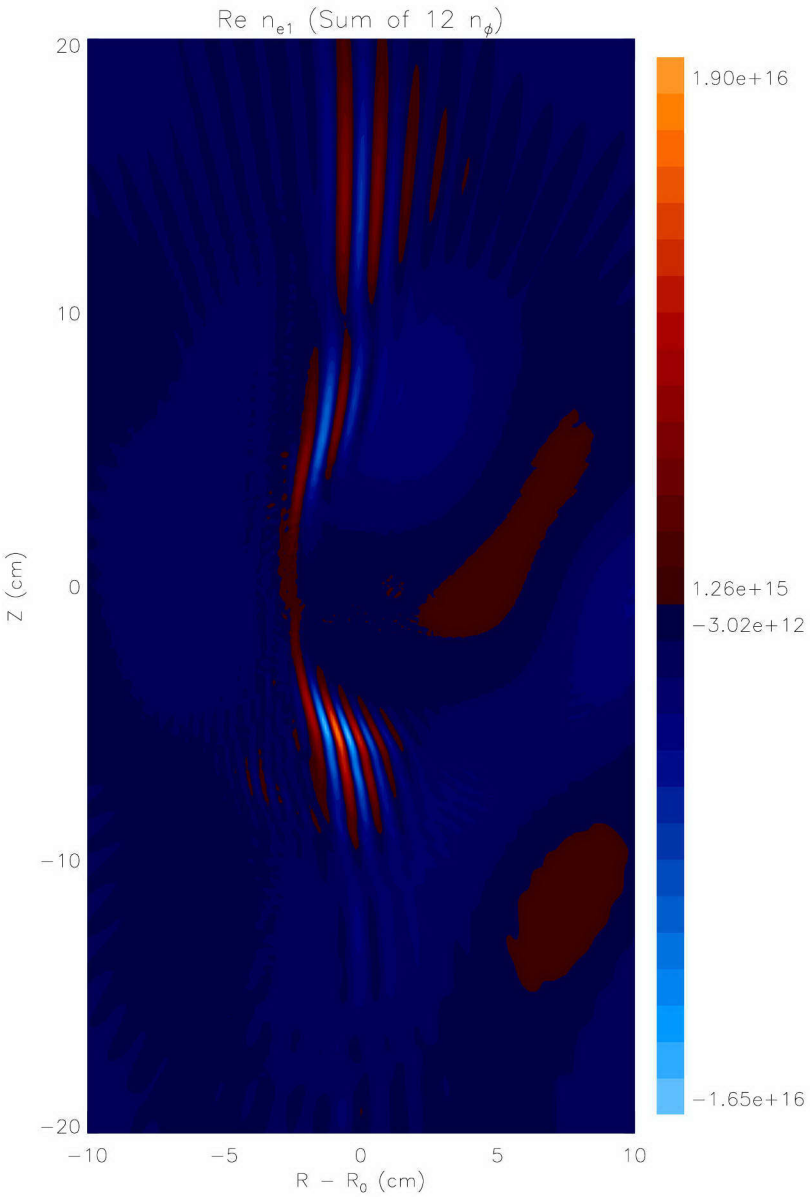

Figure 5-42: The real part of n_{e1} as calculated from the weighted sum of 12 TORIC solutions, for the n_ϕ numbers as described in this section. The contours are shown to the right, with units of m^{-3}. The magnitude has been calculated using the Poynting flux, for a power of 1 MW leaving the antenna.

a cylindrical arc of constant major radius (the surface just in front of the antenna), extending from the bottom to the top of the antenna. Figure 5-25 shows an example of the major radial component of the Poynting flux for $n_\phi = 10$. It can be seen that above the midplane the Poynting flux in the major radial direction is towards the antenna, while below the midplane it is away from the antenna. Integrating this over the surface in front of the antenna yielded a small net amount of power leaving the antenna area (there was an excess in the negative R direction). This was not a very satisfactory way of calculating this factor, because it depended critically on the difference between two large numbers. There were other problems as well: the Poynting flux suffered from numerical inaccuracies, especially just above, below, and to the sides of the antenna. This was because the Poynting flux was calculated using numerical differentiation of the electric field solution (see Eq. 5.2). These areas immediately adjacent to the antenna were not included in the Poynting flux integration. Another problem was the uncertainty in deciding the appropriate surface over which to integrate the Poynting flux. For example, for a surface consisting of a complete 360° cylindrical arc around the torus, along with the top and bottom annuli, the resulting power calibration factor was 20 times smaller (thus the electric field multiplying factor would be ~4.5 times smaller) than from using the surface surrounding the antenna as described above. All of these uncertainties are indications that comparison to experimentally measured magnitudes of density fluctuation levels should rely on more extensive antenna modeling. This would include a better way of summing the electric field solutions for different n_ϕ numbers.

5.5.7 Line-integrated TORIC results compared to PCI data

The PCI diagnostic integrates the contributions from the density fluctuation along vertical chords. If a strong region of density fluctuation above the midplane is the same amplitude as, but 180° out of phase with, another strong region below the midplane, the PCI will not see it. Similarly, if there is a strong region of density fluctuations with wavefronts tilted 60° with respect to the vertical, the peaks and troughs will mostly cancel out, leaving a small PCI signal. Thus regions with vertically

extended constant phase fronts will contribute most to the line-integrated signal. Fig. 5-43 shows the result of line-integrating the two-dimensional poloidal cross section from Fig. 5-42 along vertical chords. Note the region of strong density fluctuation near the center — this is from the strong IBW regions below and above the midplane and to the LFS of the FW mode conversion layer. The smaller peaks to the LFS of the center are due to the mostly standing-wave FW pattern. To the HFS of center, these FW peaks are greatly reduced, indicating that reflection and absorption has occurred near the center, as expected from a cutoff–resonance pair (see Sec. 2.5.1). The small region of short wavelength fluctuation at the HFS edge ($R - R_0 \simeq -23$ cm) is due to a kinetic Alfvén wave excited at the $n_\parallel^2 = S$ layer there. So far, the PCI has only been used to look at the central region of the plasma.

The actual PCI channels have a finite width over which spatial averaging is done. If a very short wavelength fluctuation were imaged on one detector element, such that several complete wavelengths fit across its width, the net contribution would be zero. When a significant fraction of a wavelength falls on one detector, the net contribution to the signal on that channel will depend sensitively on the exact channel location. To simulate the effect of the finite channel width, the real and imaginary parts were separately averaged over 0.6 cm, and then the magnitude and phase were calculated for each channel. The resulting pattern of peaks and troughs can be compared to some of the PCI data, which often exhibited multiple peaks and troughs separated by 1 to 2 cm. The ion concentration mix for the 12 n_ϕ TORIC runs was chosen as an estimate of what may have been present in the core of the plasma for a particular plasma discharge (shot 1000623019). However, the uncertainty in the ^{3}He concentration is very large (in Appendix D, which was actually completed after the twelve TORIC runs, the estimated ^{3}He concentration for shot 19 is lower). In order for an optimal comparison of the density fluctuation pattern as measured by the PCI to that predicted by TORIC, the TORIC pattern has been shifted to the high-field side by 3 cm. The result of applying this averaging procedure to the central region is shown in Fig. 5-44, which also shows the PCI data at time 0.855 sec for shot 1000623019. The major radius (R_0) used in TORIC was 67 cm in this case, so

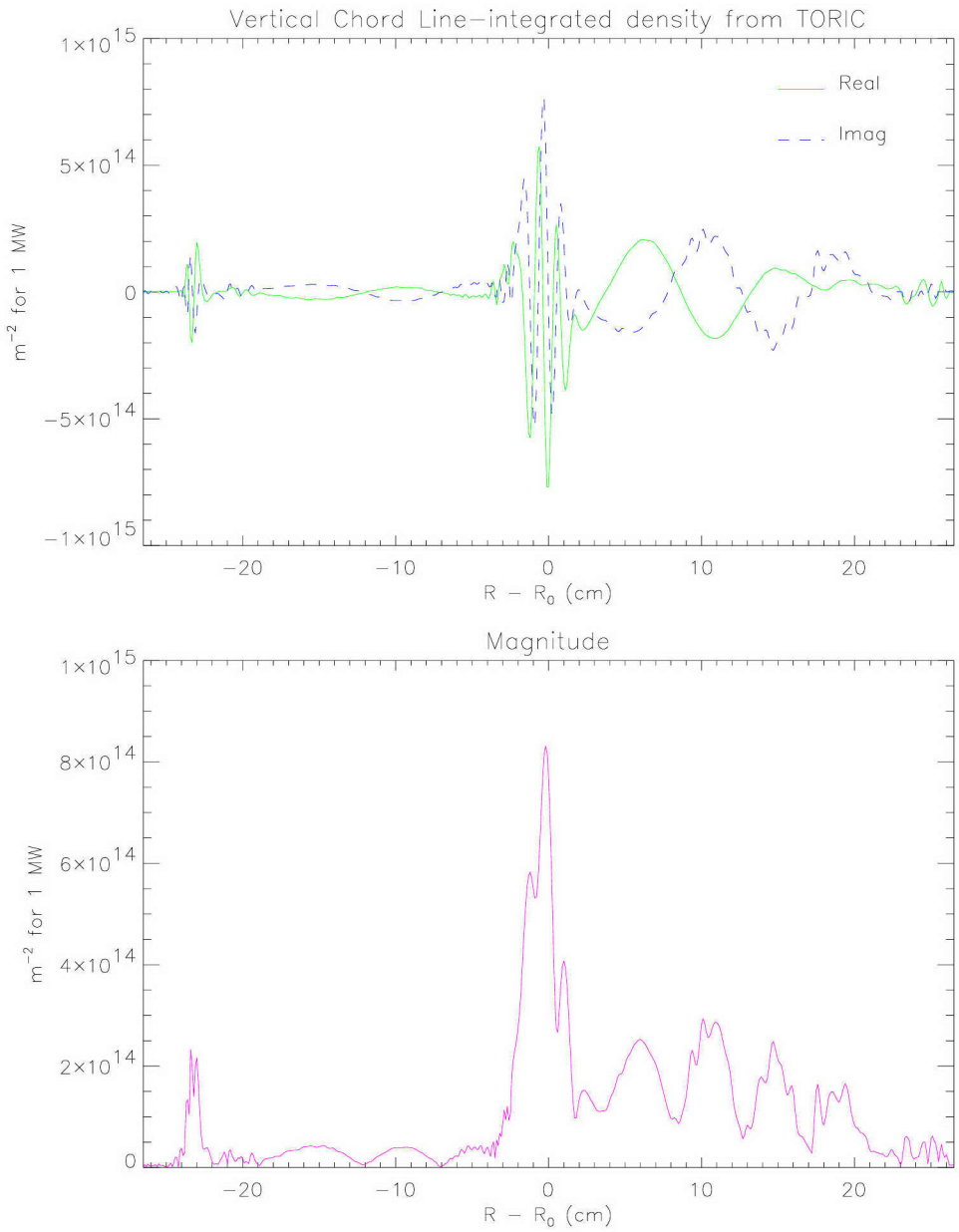

Figure 5-43: The line-integrated (along vertical chords) density fluctuation pattern of Fig. 5-42. Top: real (solid line) and imaginary (dashed line) parts. Bottom: magnitude $\sqrt{real^2 + imaginary^2}$.

the peak feature just below 64 cm is actually predicted to be just below 67 cm for this scenario. In addition, the TORIC magnitude has been multiplied by a factor of 4.5 to better match the experimental data, indicating that the Poynting flux power calibration method underestimates the magnitude of the density fluctuation.

The effective wavenumber obtained by comparing the phase difference between two adjacent channels is shown for the PCI and TORIC in the bottom half of Fig. 5-44. Because of the large channel width, the phase from the TORIC simulated channels has actually wrapped around completely (the spatial aliasing discussed in Sec. 5.4.4). It can be seen that near the region of strongest amplitude, the wavenumbers are different by only a few cm^{-1}.

Because of the 3 cm shift in the TORIC data, this is not an exact comparison of the same plasma parameters in the experiment and in the code prediction. However, it is still a plausible explanation for the source of the multiple peaks and troughs separated by 1 to 2 cm, accompanied by positive wavenumbers from about 4 to 10 cm^{-1}. The 3 cm shift could be accounted for by a decrease in the ^{3}He concentration, an increase in the H/D ratio, or both (all of which would move the mode conversion layer to the HFS). See Fig. 5-45 for a plot of the location of the mode conversion layer for different H–^{3}He–D mixes and what could be responsible for a 3 cm shift. In addition, there could be mismatches between the experiment and code model in the Shafranov shift, the equilibrium position of the plasma within the machine, the total magnetic field, etc., any of which could contribute to a shift in major radial location of the strong IBW signal. Finally, the positions of the PCI channels could be off by a small amount (although probably no more than a few mm). The channel positions are determined from the sound burst calibration method described in Sec. 3.3.

Because the exact ion concentration mix is uncertain, it is not clear that the change in helium-3 concentration to bring the TORIC results in rough agreement with the data from shot 19 corresponds to the actual concentration (indeed Appendix D would suggest that it should be reduced even further than shown in Fig. 5-45). However, there is further evidence that the 3 cm shift resulting in a new ion concentration mix does result in a situation which is consistent with the data. Figure 5-19 shows that

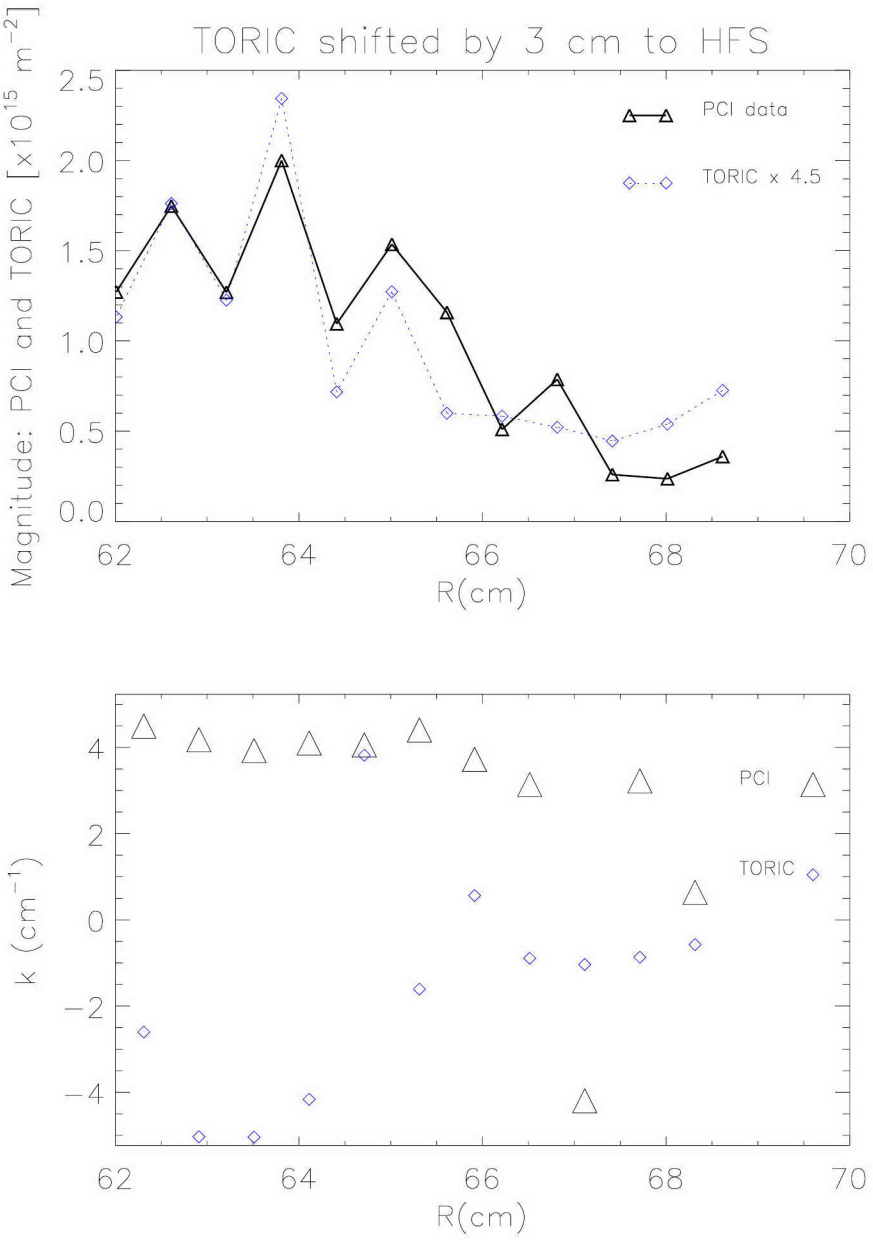

Figure 5-44: The line-integrated density fluctuation pattern from TORIC, shifted by 3 cm and multiplied by 4.5 in order to compare the shape to actual PCI data. Top: magnitude of $\int n_{e1} dl$, in units of 10^{15} m^{-2}. The triangles connected by the solid line are the twelve channels of the PCI. The diamonds connected by the dotted line are the results of the shifted TORIC prediction, multiplied by a factor of 4.5. Bottom: the effective wavenumber from channel to channel phase advance. The triangles are the PCI data, and the small diamonds are the TORIC results. Note that because of spatial aliasing, many of the TORIC wavenumbers in the large magnitude region are wrapped around to the negative side.

the peak off-axis electron heating for shot 19 was around 61 cm major radius. From all the TORIC runs for these three-species plasmas, it can be seen that the location of the peak off-axis electron heating corresponds roughly to the mode conversion layer location. From Fig. 5-45, it can be seen that the 3 cm shift places the MC layer at roughly 61 cm major radius. Thus a plasma mix such as 15.4% ^{3}He and H/D = 0.61 could be consistent with shot 19.

The peak magnitude of the line-integrated PCI signals for these scenarios was usually between 2×10^{15} and 8×10^{15} m^{-2}. The magnitude of the predicted TORIC signal compared to the PCI data in Fig. 5-44 is a factor of 4.5 to 20 times too small when using the Poynting flux calibration, depending on what surface is used to estimate the power entering the plasma. However, if instead of summing the normalized fields according to the dipole pattern of Fig. 5-41, a single toroidal mode is taken with the units as returned by TORIC, then the line-integrated magnitude is too large. The TORIC electric field amplitudes must be multiplied by the amount of current in the antenna strap in order to compare to a specific amount of power leaving the antenna. The antenna current is not measured with as much confidence as the power, but for ~1 MW leaving the D-port or E-port antennas, the current in the strap was approximately 200 to 400 amperes (the exact value depending on the total loading). Multiplying the TORIC results by 200 amperes yields line-integrated density magnitudes that are factors of 2.5 to 6 times too high, depending on the toroidal mode number n_ϕ. When the total loading is calculated by performing a sum of the partial loading of each of the 12 n_ϕ numbers, weighted by the square of the Fourier coefficient of the vacuum spectrum, the answer is probably too low: 0.27 ohm. The estimated loading in the experimental run day devoted to these mode conversion experiments ranged from 5 to 10 ohm. There is probably a significant source of loading present in the experiment that is not accounted for in TORIC. This could be through power loss at the edge by the excitation of waves through non-linear processes (TORIC is a strictly linear code), or power dissipation in some physical object, or other "anamolous" loading. Thus both methods (Poynting flux power calibration and antenna current calibration) of determining the magnitude predicted by TORIC have

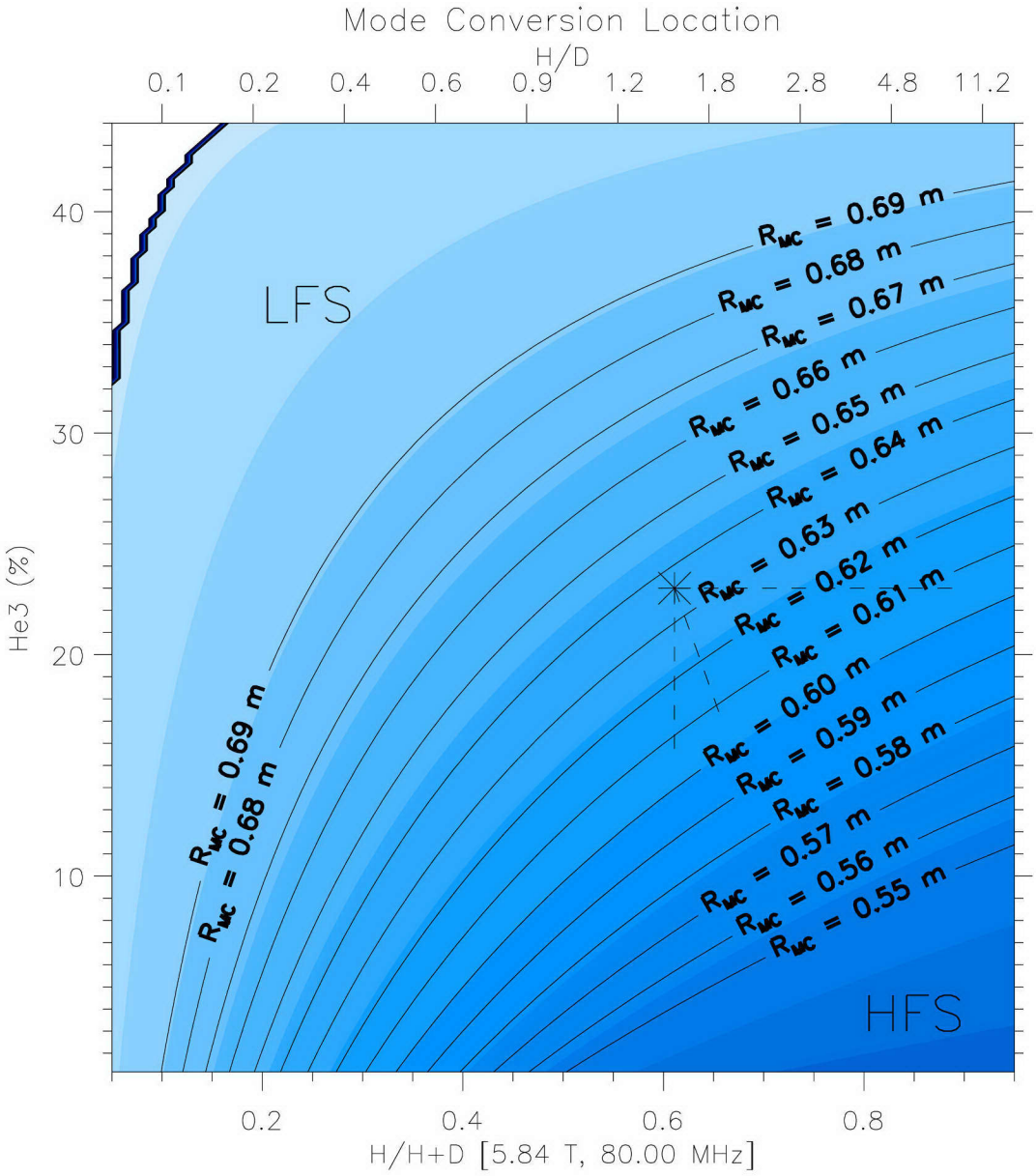

Figure 5-45: A contour plot of the location of the fast wave mode conversion layer ($n_\parallel^2 = S$ for $m = 0$, $n = 10$) as a function of ion species concentration mix. The lower right corner is towards the HFS, while the upper left is towards the LFS. The labeled solid lines are contours of constant location from 55 to 69 cm, every 1 cm. The PCI viewing window for these plasmas covered at most 62 to 69 cm. The plasma modeled in the TORIC results of this section, with $n_{\rm ion}/n_e = 33\%$ H, 23% ^{3}He, and 21% D, (H/H+D = 0.61) is indicated by the star. The mode conversion location for this set of parameters is at 63.6 cm. There are many possible routes which would result in a 3 cm shift to the HFS, three of which are indicated by dashed lines. These are: keeping the ^{3}He fixed, and changing H/H+D to 0.90, keeping H/H+D fixed and changing ^{3}He to 15.4%, and changing both H/H+D to 0.66 and ^{3}He to 16.9%.

problems, but it is interesting to note that they bracket the experimentally measured magnitude — one is too high, the other is too low. Perhaps more extensive antenna modeling and accounting for the full loading of the antenna, or more numerically accurate Poynting flux calculations will bring the code results and the measurements in better agreement.

Suggestions for improvement in the comparison between experimental data and TORIC code results

Although this preliminary comparison between experiment and theory is promising, because it can explain the origin of the spatial structure and wavenumbers observed in the experiment, and is within an order of magnitude in amplitude of the line-integrated density fluctuation, several steps need to be done before more fruitful comparisons can be made. **(1)** The version of TORIC which can be coupled to an EFIT magnetic equilibrium should be used in order to better describe the background plasma, especially the exact boundary conditions of the plasma shape and distances to the antenna and the walls. **(2)** The antenna model in TORIC should be improved, or if possible, coupled to a 3-D antenna model which can produce boundary conditions to be used by TORIC in determining the electric field in the plasma. **(3)** Better measurements of the ion species concentrations in the core plasma need to be made, especially the ^{3}He concentration. Many current methods relying on spectroscopy are strictly only measuring the ion concentration at the edge, which may not be the same as in the core (see Ref. [100, Ch.5] for a discussion of the effect of sawteeth crashes on the H/D ratio, for example). Section D.2 discusses some ideas for helium-3 concentration measurements. **(4)** The intensity of the sound wave as a function of distance from the speaker used for the PCI sound wave calibration should be measured with a sonometer, rather than what is currently done: using a published value from the manufacturer for the speaker response, combined with a spherical sound wave model to estimate the sound intensity as a function of distance from the speaker. **(5)** More PCI channels should be used, and the channel spacing should be reduced to at least 0.1 cm, in order to adequately cover the short wavelength IBW

features. **(6)** Electron power deposition profiles using an ECE radiometer with higher resolution than 9 channels should be used in conjunction with the PCI observations and the TORIC simulations to confirm the location of the strong electron Landau damping.

5.5.8 Sensitivity of PCI measurements to small plasma changes

Because the width of each PCI channel is a significant fraction of the wavelength of the IBW features as shown in Fig. 5-43, the actual measured pattern can be quite sensitive to small shifts in position or angle of the plasma relative to the PCI laser beam. For example, Fig. 5-46 shows the result of line-integration through the central region of the density fluctuation pattern shown in Fig. 5-42 for three sets of chords. The first set (solid line) is exactly vertical, and is just a close-up view of the magnitude in Fig. 5-43. The second set (dashed line) is for a set of chords tilted 0.01 radians (0.57°) clockwise (rotated about the intersection of the corresponding vertical chord with the midplane), and the third (dot-dashed line) is for a set of chords tilted 0.01 radians counter-clockwise. It can be seen that the long-wavelength regions due to the fast wave hardly change at all, while the main feature centered around 67 cm changes character for this small change in chord integration angle with respect to the midplane. Thus if the plasma tilts slightly, the same two-dimensional density pattern can look quite different on the one-dimensional PCI measurement. Or if the PCI laser is not exactly aligned vertically through the plasma, the result will not be quite as expected from the TORIC modelling with vertical chords.

Another example of the sensitivity of the PCI measurements to small plasma changes can be seen in Fig. 5-47. This figure shows the effect of small shifts in the relative location of the plasma and the PCI laser. Each panel shows the background line-integrated pattern from TORIC, along with the magnitude of each of the 12 simulated PCI channels after averaging real and imaginary parts over 0.6 cm. It can be seen that small shifts of order 1 mm or less can cause the pattern to appear quite different, even for exactly the same density pattern. This could occur in an actual plasma discharge from small shifts in the plasma position as a whole, or from small

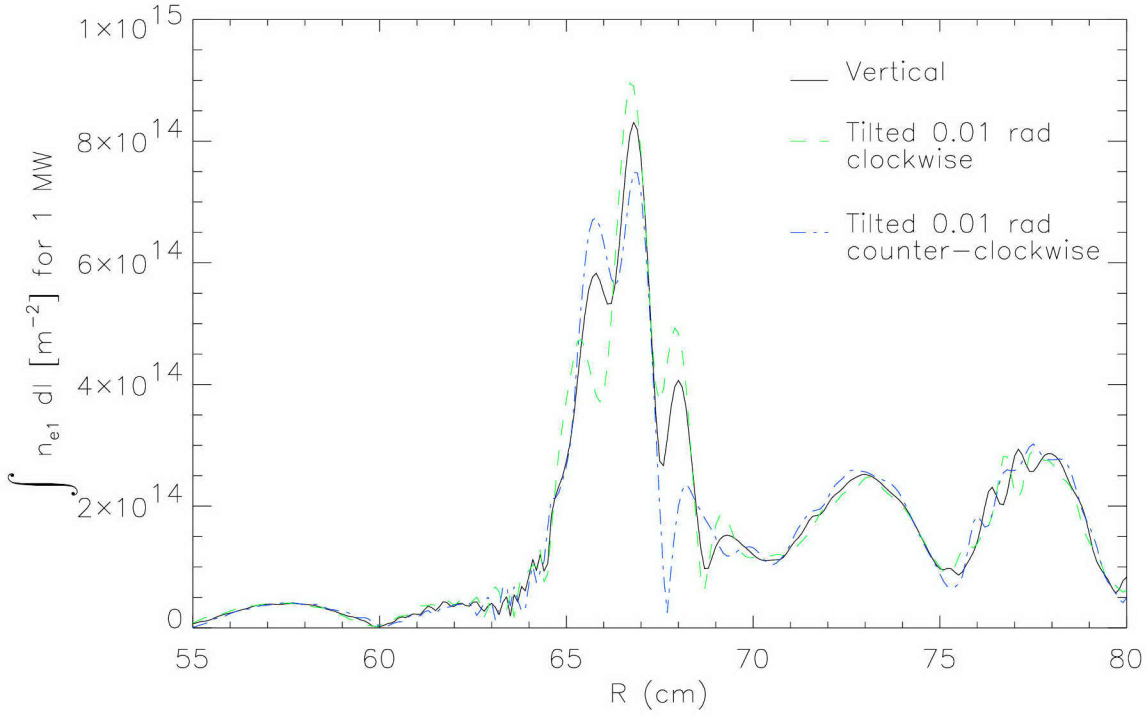

Figure 5-46: The line-integrated density fluctuation pattern obtained from Fig. 5-42 for three sets of chords: exactly vertical (solid line), tilted 0.01 radians (0.57°) clockwise (dashed line), and tilted 0.01 radians counter-clockwise (dot-dashed line). Units are for 1 MW leaving the antenna, using the Poynting flux calibration.

changes in ion concentration ratios, or anything else which would slightly move the mode conversion region relative to the PCI laser. This can help explain some of the puzzling abrupt changes in the observed PCI data when there are seemingly no large changes in plasma parameters (for example, see the contour plots in Fig. 5-15 and 5-21, and the figures in Appendix E). Increasing the channel density (point **(5)** at the end of the previous section) would reduce this undesired sensitivity to small shifts in position by averaging over a much smaller width.

5.5.9 Line-integrated density pattern for several ion species mixes

As the ionic species content of the plasma changes, the mode conversion region will change location. Figure 5-45 shows the expected fast wave mode conversion position for a given magnetic field as a function of ^{3}He concentration and H/D ratio. The mode conversion efficiency will change as well (see Fig. 5-2). The line-integrated density pattern can also appear very different on the PCI diagnostic measuring the same region in a variety of plasmas with different ion species concentrations. The line-integrated experimentally measured density fluctuations show a wide variety of patterns (see Appendix E), including anywhere from one to four peaks of comparable intensity. In order to sample a small portion of the possible configurations that are predicted by the TORIC results, several runs were completed for the same toroidal mode number, but for different ion species mixes.

Figure 5-48 shows the results of decreasing the ^{3}He concentration, while keeping the H concentration about the same, with the net effect of moving the mode conversion layer to the high-field side. The solid line is the same scenario as has been extensively discussed in this chapter, while the dashed line and the dotted line represent plasmas containing smaller amounts of helium. The relative height of the three peaks present in the original solution change significantly as the pattern is moved to the HFS by the change in ion concentrations.

Figure 5-49 are the results from a slightly different plasma scenario. The plasma

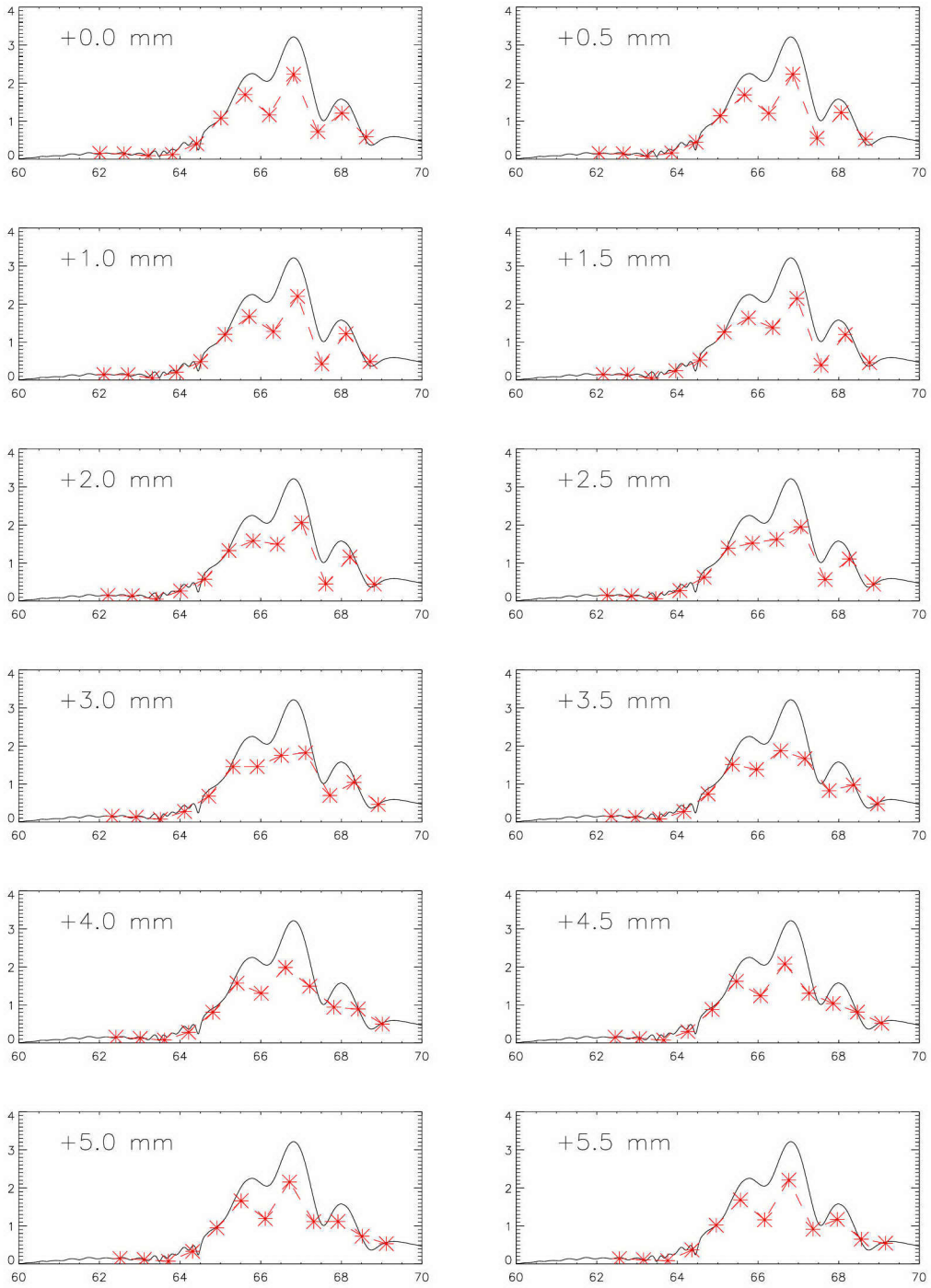

Figure 5-47: The effect of small shifts in the relative location of the plasma and the PCI laser. The solid line in each panel is the line-integrated density fluctuation pattern from TORIC (amplitude only, arbitrary units), *vs.* the major radius. Shown by the stars connected by the dashed line is the magnitude the twelve PCI channels would see (0.6 cm wide), when the beam is centered at a specific major radius. The relative shift from the upper left panel is shown in the upper left corner of each panel, increasing from left to right and top to bottom.

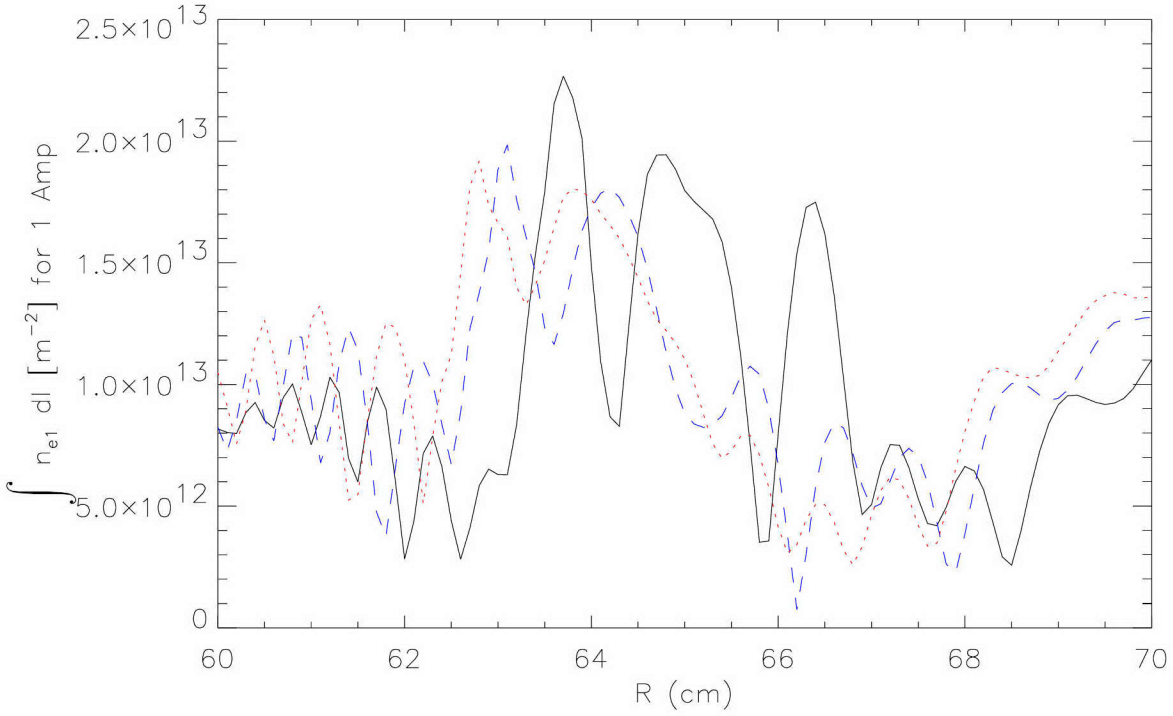

Figure 5-48: The line-integrated density pattern from a single toroidal mode number TORIC solution ($n_\phi = 10$), for three different ion concentration mixes. Solid line: 21% D, 33% H, 23% ^{3}He. Dashed line: 25% D, 35% H, 20% ^{3}He. Dotted line: 29% D, 35% H, 18% ^{3}He.

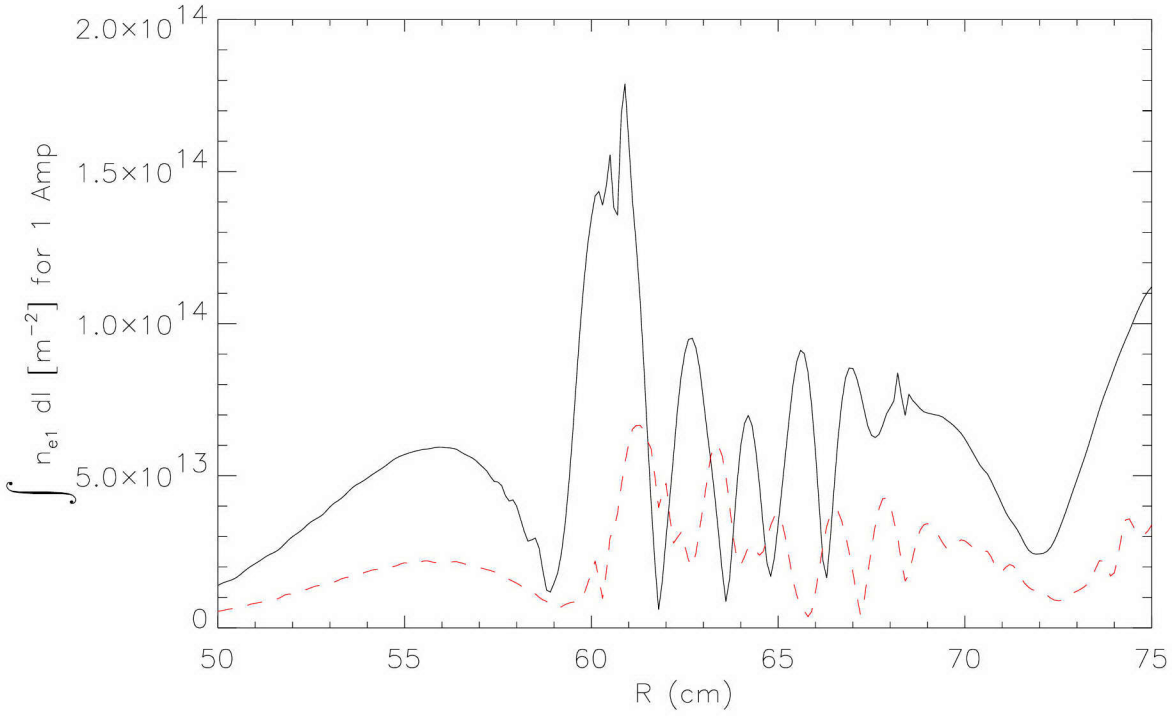

Figure 5-49: The line-integrated density pattern from a single toroidal mode number TORIC solution ($n_\phi = 13$), for two different ion concentration mixes. The density profile is more peaked than those used in previous figures. Solid line: 21.8% D, 40.2% H, 19.0% ^{3}He. Dashed line: 28.9% D, 42.5% H, 14.3% ^{3}He.

parameters are similar to those used previously, but both the density and temperature profile are more peaked (better matching the experimentally measured profiles for shot 1000623019): for the density profile, the inner exponent (see Eq. 2.75) was 1.05 instead of 2.0, and the outer exponent 0.85 instead of 0.2. For the temperature profiles, the inner exponent was 1.93 instead of 2.0 and the outer exponent was 2.73 instead of 1.0. The magnetic field on axis (at $R = 66.8$ cm) was 5.77 T. The peak density was only 2.19×10^{20} m^{-3}, instead of 2.4×10^{20}.

Finally, Fig. 5-50 shows a scenario with very low helium-3 concentration, which was typical of the estimated n_{He3}/n_e for the latter part of the day (see Appendix. D). The main plasma parameters for this TORIC run were: $B_0 = 5.78$ T at $R_0 = 66.7$ cm, $I_p = 775$ kA, 63.6% H, 22.0% D, 7.2% ^{3}He, $n_{e0} = 2.27 \times 10^{20}$ m^{-3}, $T_{e0} = T_{i0} = 1.51$ keV, density profile (see Eq. 2.75): $b = 1.03$, $c = 0.96$, temperature profile: $b = 2.09$, $c = 2.98$, $f_0 = 80.0$ MHz, and $n_\phi = 13$. (Some of the parameters are based on a time slice of shot 1000623020 during the PCI window). The spatial grid consisted of 320 radial elements and 512 poloidal slices, and 161 poloidal mode numbers were used. These plasma parameters places the cold plasma $n_\parallel^2 = S$ mode conversion layer for $n_\phi = 13$, $m_\theta = 0$ at -11 cm, about halfway out to the HFS edge from the center. There is an IBW oscillation visible in the density fluctuation just to the HFS of the $n_\parallel^2 = S$ layer for $m = 0$ (the dot-dashed line in Fig. 5-50). This oscillation becomes stronger (because it develops a larger $E_\parallel$ component) to the LFS. It is interesting to note that the strong region of oscillation stays close to one specific magnetic flux surface, as was the case for all other TORIC examples shown in this section. In this case with far off-axis mode conversion, the IBW oscillation continues back almost to the magnetic axis — which could explain why a strong signal would still appear on the PCI diagnostic which views the central region of the plasma, even when the fast wave mode conversion region (for $m_\theta = 0$) is to the high-field side of the PCI viewing window. This is illustrated in Fig. 5-51, which shows the line-integrated pattern as a function of major radius ($R_0 = 66.7$ cm in this simulation).

The same picture described in Sec. 5.5.4 with the positive and negative m numbers contributing differently to $n_\parallel^2$ applies in this case as well. Since the n_ϕ number is

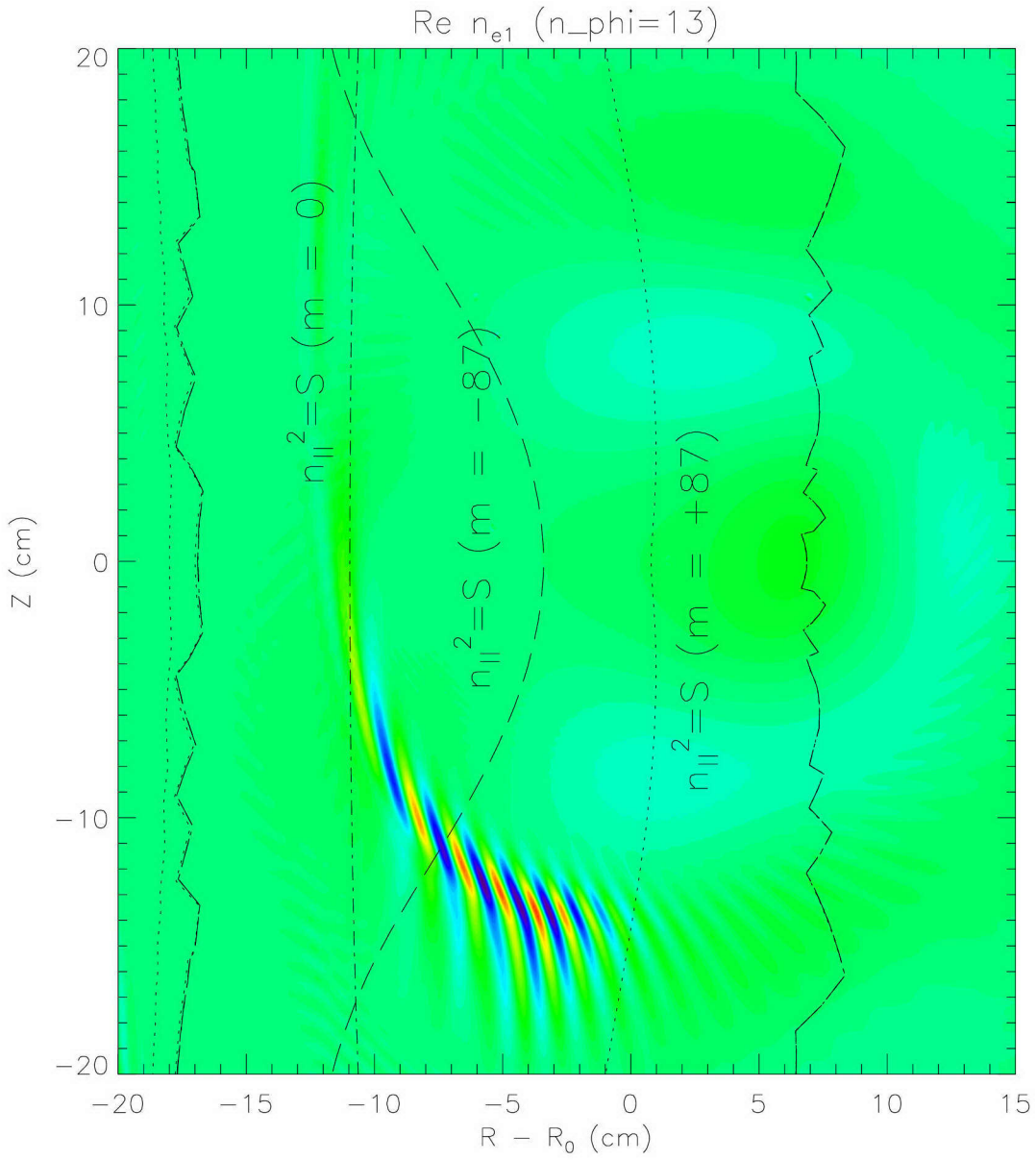

Figure 5-50: Real part of n_{e1} from TORIC, using 161 poloidal mode numbers, for $n_\phi = +13$, for the low n_{He3}/n_e case described in the text. Also plotted are the $n_\parallel^2 = S$ layers for $m = 0$, which is the FW mode conversion layer, $m = +87$ (dotted line) — to the LFS of this layer the IBW shown below the midplane cannot propagate, and $m = -87$ (dashed line) — to the LFS of this layer any corresponding IBWs above the midplane cannot propagate. The jagged lines are artifacts of the contour plotting procedure, effectively showing $S \to \infty$ contours, i.e. the ion cyclotron layers. The hydrogen resonance is at +7 cm and the helium-3 resonance is at -17 cm.

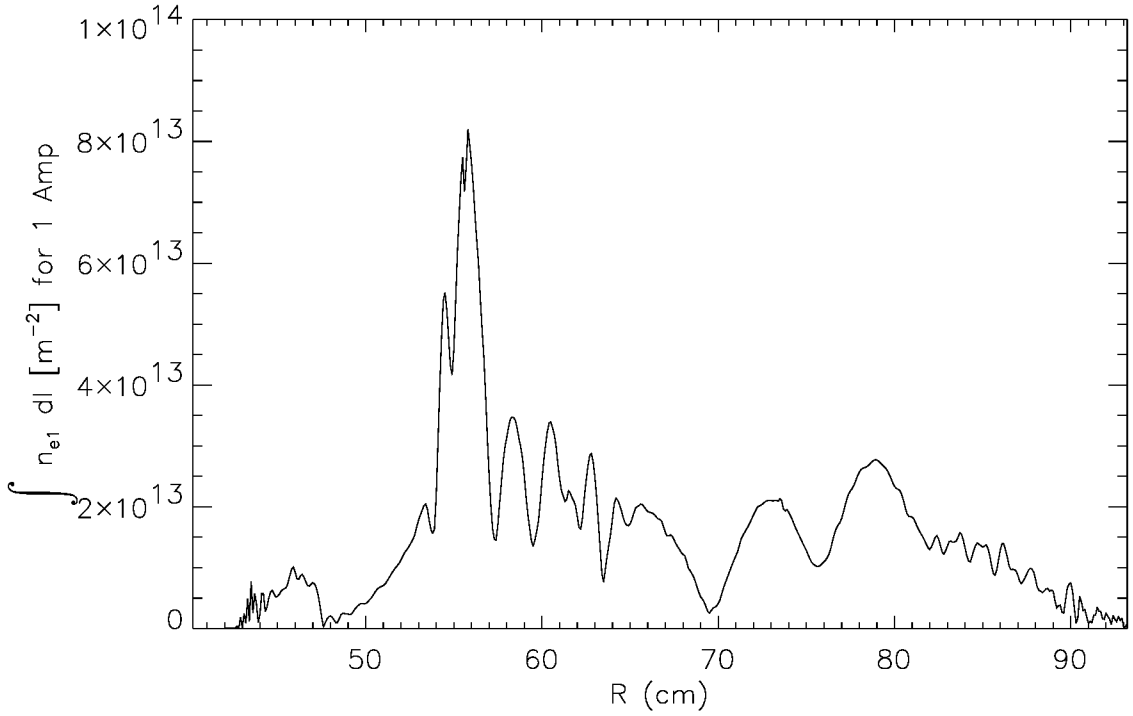

Figure 5-51: The line-integrated density pattern from a single toroidal mode number TORIC solution ($n_\phi = 13$), for a plasma with the fast wave mode conversion layer far to the HFS. Ion concentrations (n_i/n_e): 63.6% H, 22.0% D, 7.2% ^{3}He.

positive ($n_\phi = 13$), the positive m numbers present in the oscillation (the maximum m before damping away near $R \simeq R_0$ is +87) add to the magnitude of $n_\parallel^2$. This pushes the region in which the IBWs can propagate further to the LFS, and indeed the oscillation has damped away before reaching much beyond the $n_\parallel^2 = S$ layer for $m = +87$.

5.6 Summary of Chapter 5

Ion Bernstein waves have been imaged for the first time in Alcator C-Mod. The IBW has been measured across several wavelengths, tracing the progress from near mode-conversion to damping. There are many interesting features of the IBW PCI observations, including multiple peaks and troughs in amplitude. All the PCI signal observed so far is to the low-field side of the fast wave mode-conversion layer. Some of these features can be explained using results from the full-wave ICRF code TORIC along with experience from ray-tracing of IBWs for a hint at the underlying physics (such as m number increase below the midplane and decrease above the midplane). Further work in order to compare the absolute amplitude of the RF electric field and mode conversion efficiency with theory will require more detailed 3-D modeling using more complete knowledge of the exact plasma parameters, especially the ^{3}He concentration in the plasma and the edge density profile right up to the antenna strap (on the low-field side), and up to the wall (on the high-field side). However, results already obtained provide data for validating the complicated ICRF codes and theory for describing ion Bernstein waves together with fast magnetosonic waves.

Chapter 6

Conclusions

Significant amounts of power have been transferred from the plasma edge, via a fast wave antenna, to mode-converted ion Bernstein waves in the core plasma. Localized electron heating has been observed. Prospects for current drive and flow drive experiments using mode-converted ion Bernstein waves appear promising. However, PCI observations and TORIC simulations suggest that the problem of mode-conversion in a bounded, toroidal plasma is a complicated problem. The electric field pattern inside the tokamak during RF heating with a mode-conversion layer present in the plasma is a complicated three-dimensional structure, and the PCI diagnostic has only begun to reveal some of its complexity.

6.1 Conclusions from mode conversion in D(^{3}He) and H–^{3}He–D plasmas

Mode conversion in D(^{3}He) plasmas at 7.8 T appears to have the possibility for high mode conversion efficiency (>60%), and strong localized damping. The electric field pattern has yet to be studied with the PCI diagnostic, but it seems from the electron power deposition profiles that the IBW power damps on a narrow range of flux surfaces. Mode conversion in H–^{3}He–D plasmas at 5.8 T has been observed with the PCI diagnostic and through electron heating. The mode conversion efficiency is

somewhat lower than for D(^{3}He) plasmas, but perhaps that is because the optimum mix of ion species, electron density, magnetic field, and other plasma parameters has not yet been explored. The PCI observations suggest that there exist IBW oscillations with wavenumbers from 4 to 10 cm^{-1} extending several centimeters to the low-field side of the fast wave mode-conversion layer. TORIC simulations offer a possible explanation: the mode-converted ion Bernstein waves excited by the fast wave with low m number near the $n_\parallel^2 = S$ ($m = 0$) layer flow along a narrow range of flux surfaces toward the low-field side. Along this path, the magnitude of m increases and electron Landau damping dissipates the oscillations before the $n_\parallel^2 = S$ layer for large m.

6.2 Failure to observe D(H) mode conversion in C-Mod

There have been some attempts to observe mode-converted IBWs in D(H) plasmas (through direct electron heating), but only a weak signal was observed [101].[1] Simple Budden tunneling theory can help explain why for a typical C-Mod plasma, mode conversion to ion Bernstein waves in a D(H) plasma is weak. Figure 6-1 shows the results of calculating the mode conversion efficiency as a function of central density for a D(H) plasma with 25% H, $B_0 = 5.64$ T, $n_\phi = 10$, $m_\theta = 0$, and RF frequency 80.0 MHz. The dashed line is the maximum expected mode conversion efficiency (see Sec. 2.5.2), which is just 4 times the Budden tunneling result for the single-pass mode conversion efficiency. Also shown by the solid line is the internal resonator theory result.

Because most C-Mod shots have central densities of $2 - 3\times10^{20}$ m^{-3}, or even higher, the expected MC efficiency for D(H) plasmas is quite low (<10%). This is because the gap between the $n_\parallel^2 = L$ cutoff and the $n_\parallel^2 = S$ resonance is too large at

[1] See also the presentation at:
http://www.pppl.gov/publications/pics/aps_dpp_99/taylor.pdf. It is also noted that TORIC simulations in this regime were very sensitive to small changes in plasma parameters, especially the density perhaps showing internal resonator-type effects.

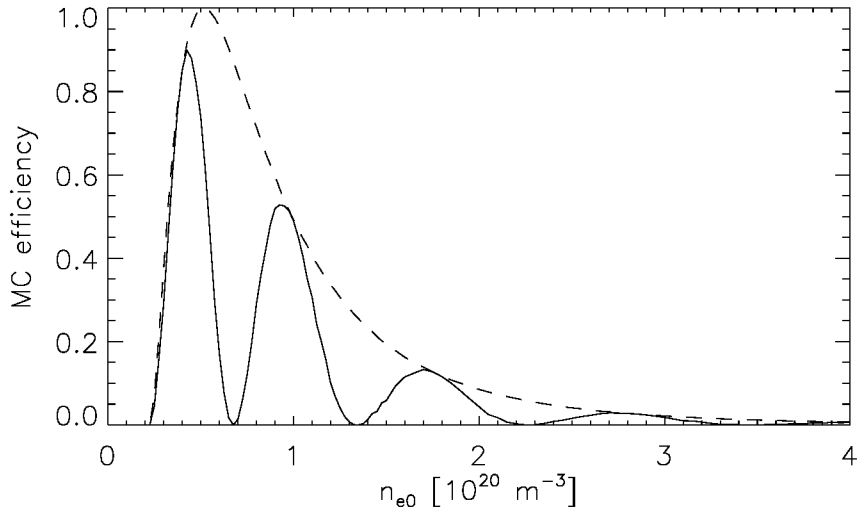

Figure 6-1: The expected mode conversion efficiency for D(H) plasmas as a function of central electron density. The dashed line is four times the Budden result, and the solid line is the internal resonator prediction for $n = 10$, $m = 0$.

these densities. As the density is decreased, the gap narrows, allowing stronger mode conversion. However, at approximately 0.2×10^{20} m^{-3}, the $n_\parallel^2 = R$ layer from the HFS has moved beyond the mode conversion region, so that the fast wave reflects off the $n_\parallel^2 = R$ layer before it can mode-convert, and the mode conversion efficiency drops to zero. Therefore, for future efforts (in D(H) plasmas) to observe mode-converted ion Bernstein waves and their effects on electrons, the central electron density should be lowered to $5 - 6 \times 10^{19}$ m^{-3}, and a high fraction of hydrogen should be used to avoid ion cyclotron damping on the Doppler-broadened hydrogen cyclotron layer.

6.3 Future Work

There are several things that could be done with the PCI and TORIC modeling to better explore the IBW oscillations that seem to extend to the low-field side of the mode conversion layer. These have been discussed in Sec. 5.5.7. Other suggestions for improving the RF PCI system have been made in Alex Mazurenko's thesis [79]. Some of these near-term upgrades would include increasing the number of channels (the

liquid nitrogen cooled detector has 32 elements, only 12 of which are currently used), and decreasing the channel spacing (if low laser power becomes an issue, increasing the efficiency of the AO modulators could help).

Some very interesting experiments could be performed with little or no change to the current PCI system. For example, it would be interesting to see what happens when the mode conversion layer is placed to the low-field side of the magnetic axis, and examine both in the TORIC code simulations and with the PCI diagnostic, what happens to the IBW oscillations in the toroidal geometry — would they also move along flux surfaces, but towards the high-field side? This was not possible before because the machine was limited to 6 T central magnetic field. With higher magnetic field, the same ion concentration mixes already explored on the 23 June 2000 run day could place the mode conversion layer further to the low-field side.

Another interesting set of experiments could be performed with only minimal changes to the RF heterodyne system attempting to observe an IBW or FW signal from the J-port antenna, which is located 144° away from the PCI diagnostic at E-port. The transmitters for the J-port antenna are tunable in frequency, allowing more freedom to place the mode conversion layer within the plasma for a greater variety of magnetic fields. The observation of density fluctuations (or lack thereof) from J-port would be a stringest test for the 3-D electric field pattern reconstructed from TORIC. This could help improve the antenna modeling and the summation of the independent toroidal modes from the antenna spectrum. The J-port antenna is a four-strap antenna fed by two transmitters, so it is capable of launching a wide variety of antenna phasings, not just the $[0,\pi]$ phasing of the D- and E-port antennas. PCI observations of RF density fluctuations from J-port under various phases would provide information concerning the toroidal propagation, and any asymmetries that exist between the positive and negative toroidal mode numbers. (For example, there are expected asymmetries in the ICRF between co- and counter-current drive [95].)

A more complete examination of the IBW behavior with different toroidal current should yield results very useful for comparison with theory. For example, TORIC runs suggest that when the current (and hence the poloidal field) is reduced enough, then

the curved region of IBW oscillations become more straight and vertical. This should be observable with the PCI, and perhaps in the electron power deposition profiles. Also, higher plasma current might be expected to affect the IBW quite strongly. So far only one shot (1000623021) has been performed at 1 MA, and soon C-Mod should be capable of 1.5 MA and more.

Less practical, but possibly more interesting ideas are described in this last paragraph. A main feature of the IBW code results from TORIC was that large positive toroidal mode numbers (for the current and magnetic field in the clockwise direction when viewed from above) produced strong IBW oscillations below the midplane, while negative toroidal mode numbers produced corresponding (but not perfectly symmetric about the midplane) oscillations above the midplane. For small toroidal mode numbers the oscillations seemed to appear both above and below the midplane. The capability of the J-port antenna to launch power preferentially in the positive or negative toroidal directions presents an opportunity to test this theory. If a horizontal (tangential) PCI could be built from say, K-port to H-port, or some other nearby ports, then the wavefronts propagating away from the J-port antenna above and below the midplane could be distinguished. This would allow the PCI to confirm or disprove the predicted up/down asymmetries in the TORIC solutions for specific toroidal mode numbers. Also if more vertical PCI chords were placed on either side of the J-port antenna, the toroidal directivity could easily be measured for various phases of the antenna straps.

Appendix A

Global Energy Consumption

One of the reasons the United States of America rose to world dominance in the 20th century was its exploitation of oil for energy. The high standard of living enjoyed by U.S. citizens (and others in the "developed" world) is in part due to this plentiful energy source. As other less developed countries seek to raise their standards of living in the 21st century, they will require larger amounts of energy as well. Figure A-1 shows the world's energy consumption by major geographical region in the year 1997. The source of data for this figure and elsewhere in this appendix, unless otherwise noted, is from the Department of Energy's web site, under the Energy Information Administration.[1] The regions shown are: North America, Central & South America, Western Europe, Eastern Europe & Former U.S.S.R., Middle East, Africa, and Far East & Oceania. Energy units are given in Quads, where 1 Quad = 1 Quadrillion (10^{15}) Btu, or British thermal units.[2]

Note that North America uses far more energy per capita than any other region in the world (twice that of Europe, which has a comparable standard of living). Most of this is due to energy use in the United States. Figure A-2 shows the energy

[1] See the Energy Information Administration web page **http://eia.doe.gov/** for current information on energy in the U.S. and the world.

[2] 1 Btu is the amount of heat required to raise the temperature of one pound of water one degree Fahrenheit, or approximately 1055 joules. So 1 Quad is equivalent to 1.06×10^{18} joules, 2.93×10^{11} kWh, or the detonation energy of 252 megatons of high explosive. Put another way, if Quabbin reservoir (a large freshwater reservoir in central Massachusetts which supplies drinking water to much of Eastern Massachusetts) were filled with gasoline (a volume of 1.6 km^3), burning it would release about 53 Quads of energy.

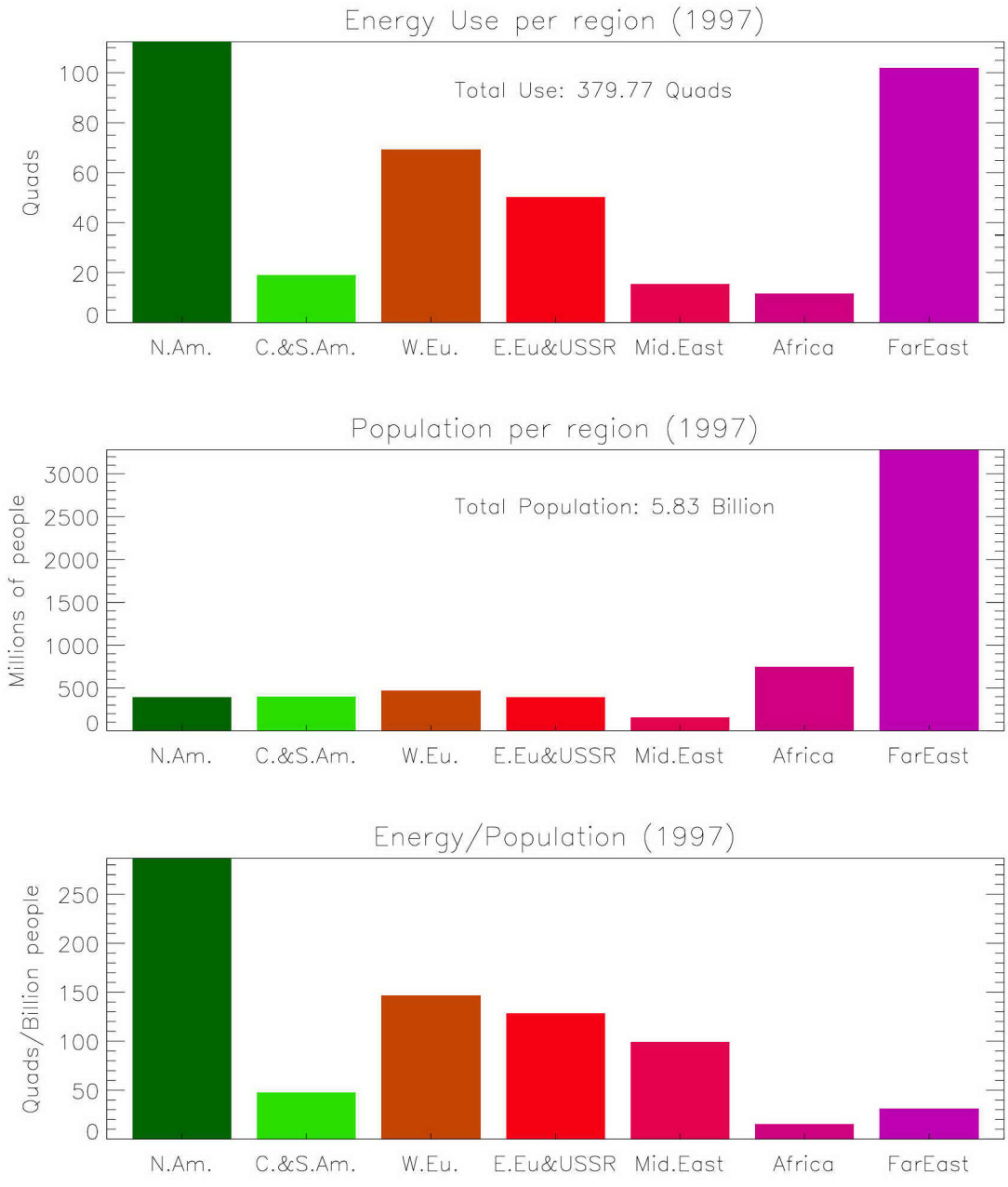

Figure A-1: Top: Energy consumption by region. Middle: Population of region. Bottom: Energy use per capita.

consumption data for the U.S. and eight other countries. Two reasons why the U.S. uses twice as much energy per person as Japan and Europe is because Americans drive more and drive less efficient cars. The U.S. also lacks a culture of energy conservation and recycling, although this seems to be improving. If the entire world were to use as much energy per person as in Western Europe (about 147 Quads/Billion people), then the world energy consumption, at 1997 rates, would be 856 Quads rather than the actual use of 380 Quads. If everyone used as much as the United States, the world use would be 2050 Quads annually. A more reasonable future scenario might be that the U.S. is able to decrease its energy use per capita to that of Europe and Japan as the rest of the world rose to that level. Then, assuming the world population levels off at approximately 10 billion, the world's yearly energy needs would be approximately 1500 Quads/year, or about 4 times the current use. To achieve a prosperous, equitable future, there is clearly a need for more energy.

A.1 Fossil Fuels & Renewable Energy

We are living in the age of fossil fuels. Most of the electricity in the United States is produced from burning coal, natural gas, and other fossil fuels. About 85% of the energy used in the world in recent years has come from fossil fuels (coal, natural gas, and petroleum). Our main methods of transportation use gasoline refined from oil. Figure A-3 shows the contributions from various energy sources to the 1997 U.S. energy consumption. Of the 94 Quads of energy used that year, 38.1% came from petroleum, 24.4% from natural gas, 22.2% from coal, 7.4% from nuclear (fission) electric, 4.2% from hydroelectric, 3.2% from biomass (burning wood chips and other organic material), and 0.4% from geothermal, wind and solar power.

Renewable energy (solar, biomass, wind, hydro, etc.) only accounts for about 7.8% of U.S. energy production. These forms of energy are currently more expensive than fossil fuels. They produce lower power densities than do fossil fuels and fission power plants, requiring greater surface area for the same amount of power (especially wind and solar). Solar power is intermittent and is weaker at higher latitudes and in

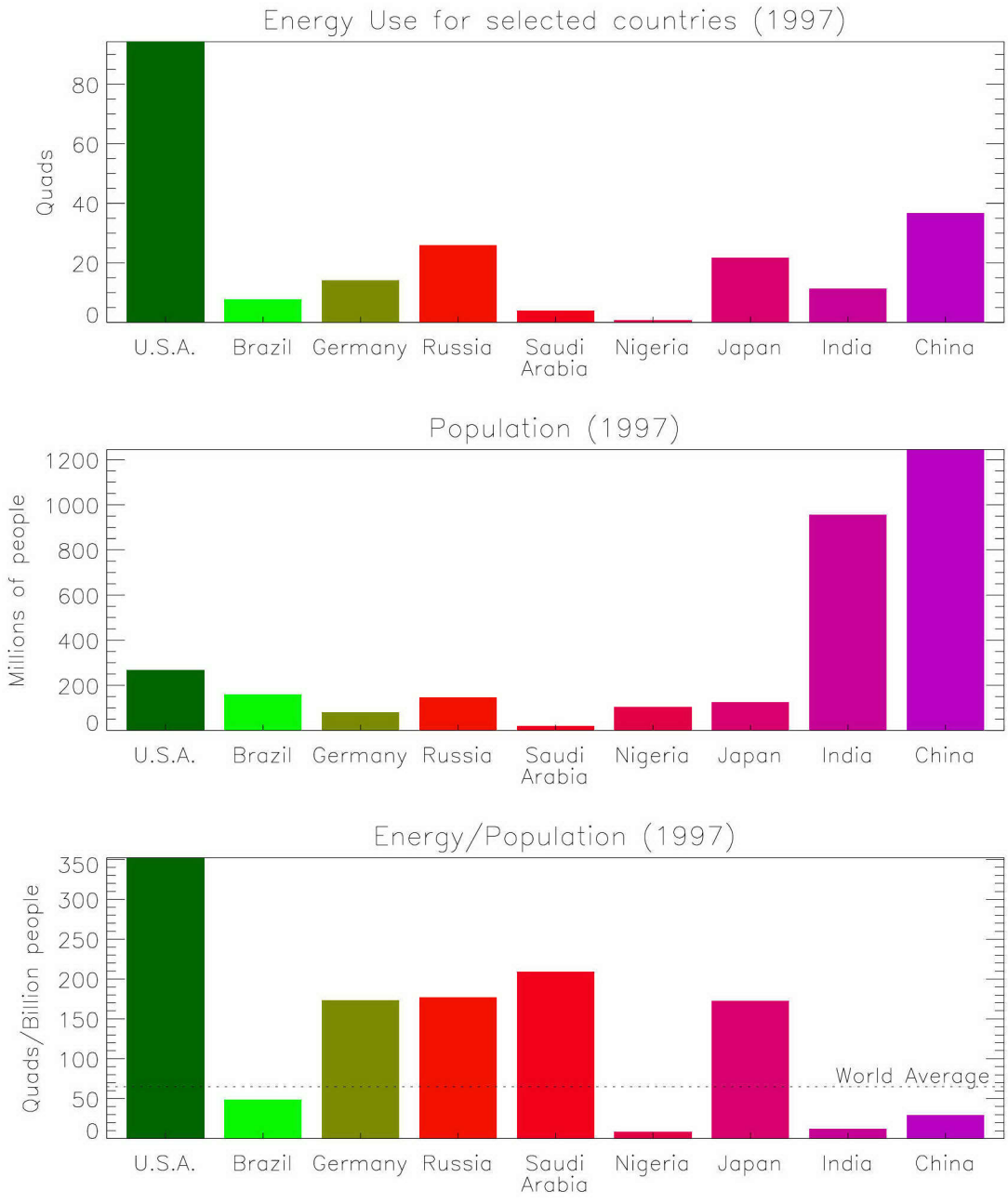

Figure A-2: Top: Energy consumption for 9 countries. Middle: Population of country. Bottom: Energy use per capita.

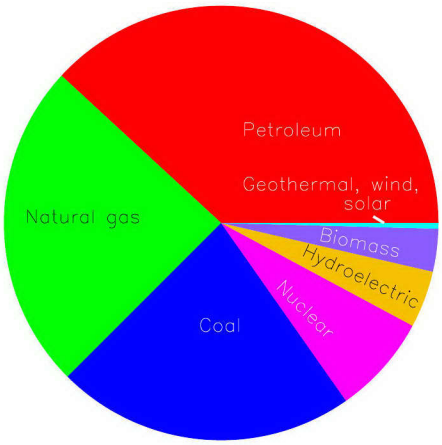

Figure A-3: United States energy use (total 94 Quads) in 1997, by source.

the winter. Renewable energy cannot, with present technology, meet the majority of our power needs.

They are not even, strictly speaking, truly "renewable" energy. Once an energy source is transformed to do useful work, there is always attendant waste heat[3] and the original amount of energy cannot be recovered. Almost all sources of renewable energy are called such because the sun renews the fuel so quickly (except for geothermal, which mainly relies on the decay of radioactive isotopes deep inside the Earth, or tidal, which relies on the gravitational attraction of the moon). When we use energy from the sun, either directly through photovoltaic, solar heating, etc., or indirectly through biomass (which has already used the sun's energy through photosynthesis), or wind or hydro power (using the sun-driven hydrological cycle), the energy used cannot be recovered. But the sun is continuously supplying more energy (through the process of fusion), and should do so for another 5 billion years. On a very long time scale, even fossil fuels are renewable, because more petroleum and coal could be produced via the same process by which the bulk of our current supply was produced

[3]Several ways of stating the second law of thermodynamics [102] are: 1) In any process in which a thermally isolated system goes from one macrostate to another, the entropy tends to increase. 2) Kelvin's formulation: It is impossible to construct a perfect heat engine. 3) Clausius formulation: It is impossible to construct a perfect refrigerator.

hundreds of millions of years ago during the Carboniferous, Permian, and Cretaceous periods. This, however, would take millions of years. Because of a finite readily available supply, fossil fuels are "non-renewable".

A.1.1 Solar Energy

It has been said that all our energy needs could be met using solar energy. However, that would require a huge sacrifice of land. A portion of our energy needs could be met with a smaller sacrifice: covering rooftops with some kind of solar collectors. If the price of electricity and fuel oil were higher and the initial capital costs involved with installation could be recovered in a few years, there would be greater incentive to install solar collectors to produce electricity or direct heating of water. This would still not be an option for everyone, as solar power is most useful only in a limited part of the globe where sunlight is intense and constant.

To estimate the amount of energy that could be directly captured from sunlight falling on the earth, first calculate the solar constant: the amount of solar radiation passing through a unit surface area at the Earth's location. The total output of the sun, or solar luminosity $L_\odot$ is 3.846×10^{26} watts, and the average radius of the Earth's orbit is 1 astronomical unit (AU) or 1.496×10^{11} meters. So at the Earth the solar power per m^2 is $L_\odot/(4\pi AU^2) = 1.37$ kW/m^2. About 39% percent is reflected by the atmosphere before it reaches the surface, and because the Earth is spherical, the surface power density away from the equator is further reduced. For example, at Boston's latitude of 42° N, the power must be multiplied by a factor of $\cos 42° = 0.74$. Sunlight can only be gathered during the daytime and when there is not too much cloud cover. This can be expressed by the useful number of sunlight gathering hours during the 8766 hours of the year. For the United States, taking an average of about 2800 hours[4], and an average latitude of 40°, this results in approximately 200 W/m^2 of useful solar energy. This is close to the estimate made by a Science Council of Canada report on energy [103], which stated that "Solar power varies with latitude,

[4]From a 1965 U.S. Geological Survey chart on mean yearly sunshine hours.

cloudcover and season. More than 90 per cent of all Canadians live below 50°N, where the average solar radiation is about 150 watts/m^2, with four to eight times as much power in June as in December."

If this energy is to be used to produce electricity (through photovoltaic panels, for example), then there will be further losses through conversion efficiency. Even direct use to heat water and extract energy from the water will not be 100% efficient. So assuming a good conversion efficiency of 40%, there is available approximately 80 W/m^2 average during the year, or 700 kWh/year/m^2.[5] In the U.S. Energy Information Administration report, it was stated that there were 69 million households owned in 1997, and an additional 33 million rented. If every one of the 69 million houses were covered with solar panels, and assuming an average roof surface area of approximately 50 m^2, then approximately 2.42 trillion kWh of energy could be produced annually in the U.S. from solar energy.[6] This is equivalent to 8.26 Quads. In a study on the potential of solar photovoltaic power in the Netherlands [104], it was estimated that the total roof surface of 5.8 million residential dwellings amounted to 288 km^2 (hence an average of 50 m^2 per household), with an additional 87 km^2 of commercial buildings that could be used. Assuming roughly the same ratio of commercial to residential surface area in the U.S., an additional 2.89 Quads could be produced from commercial building owners, for a total of 12.46 Quads. However, of the 94 Quads used in 1997, only 35.4 Quads were used by the residential and commercial sector; the rest was divided between the transportation sector (24.7 Quads), and the industrial sector (33.8 Quads), as shown in Fig. A-4.

Thus, even with all available commercial and residential surface area covered by solar panels, it would not even satisfy that sector's own energy needs, and would only provide 13% of the energy needs of the U.S. Of course, there could be large solar collector complexes covering other land areas, but just as with hydroelectric or wind

[5]This agrees with the estimate of 600 700 kWh/year/m^2 from the 2001 Draft National Energy Efficiency and Conservation Strategy report from the Energy Efficiency and Conservation Authority of New Zealand, available at **http://www.eeca.govt.nz/**

[6]This would be sufficient to cover the 1 trillion kWh household electricity consumption in 1997, but not enough to replace the household direct fossil fuel consumption.

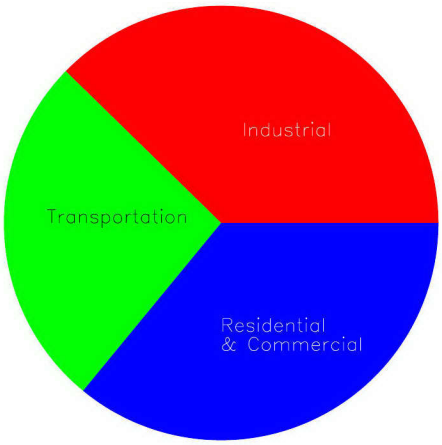

Figure A-4: United States energy use (total 94 Quads) in 1997, by end use sector.

power, that would come with an environmental price that many people might not want to pay. To supply the remaning 81.54 Quads using solar energy, an additional 34,130 km^2 would need to be covered in solar collectors, or enough to cover the entire states of Massachusetts and Connecticut. Future energy demands will most likely continue to require large amounts of concentrated power production near large manufacturing and urban areas.

A.1.2 Wind Energy

A potentially very useful energy source which has not yet been widely utilized is wind power. Harnessing the energy present in wind is another way of using solar energy. A small fraction of the sun's power falling on the earth is converted into wind power. This is a constant (on average), worldwide energy resource. In recent years, there have been more and more wind turbines built and installed producing electricity. The rapid growth of wind power across the world has been impressive (see Fig. A-5). Estimates of the global capacity for windpower are difficult to make, but it has been said by various groups that study renewable energy in the U.S. (for example, the American Wind Energy Association) that there is enough wind energy potential in

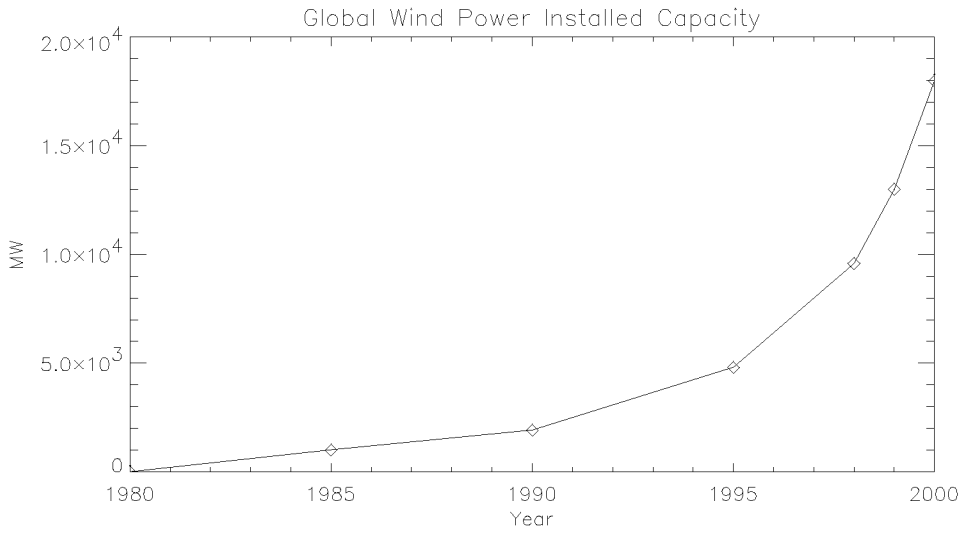

Figure A-5: Global wind power installed capacity (in megawatts) has grown rapidly in the last two decades.

the midwestern states of the U.S., such as Montana and Nebraska, to supply a large fraction (estimates range from 20% to 50%) of the nation's electricity. The Foundation for Alternative Energy, a non-governmental organization based in Slovakia, presents a good case for increasing renewable energy use in the world.[7] They estimate that there is the global potential to produce 46 trillion kWh of energy annually with wind energy. This is approximately 180 Quads, or enough for 1.2 billion people at the comfortable Western European/Japanese energy usage rate of 150 Quads/year/billion. Of course, at the present time wind power represents a miniscule portion of the energy portfolio, but there is clearly much room for growth. There is an interesting feature of wind power which makes it particularly attractive for small-scale local use in conjunction with solar power. In most windy areas, the wind blows stronger in the winter than in the summer. Thus there is the potential for more wind power just at the time of year when solar power is at its ebb, and when wind power is weaker, solar power is strong.

[7]See **http://www.seps.sk/zp/fond/dieret/dieret.html**. There is also a good discussion of wind, solar, and other renewable energies.

Fuel	World Yearly Use (1999)	World Reserves	Years left
Coal	4.74×10^9 short tons/yr	1.09×10^{12} short tons	230 yrs
Natural Gas	8.42×10^{13} ft^3/yr	5.18×10^{15} ft^3	62 yrs
Petroleum	2.74×10^{10} Barrels/yr	1.00×10^{12} Barrels	36 yrs

Table A.1: Global Fossil Fuel Reserves

A.1.3 The Problems With Fossil Fuel

There are many disadvantages of our current heavy reliance on fossil fuels for energy. They release significant amounts of carbon dioxide and other greenhouse gases into the earth's atmosphere. Global climate research is beginning to reveal a definite effect on the climate due to human activity. In the last century, the global average temperature has risen approximately 0.6° C (1.1° F). This year (2001) there have been reports from both the U.S. National Academy of Sciences and the U.N. Intergovernmental Panel on Climate Change that confirm the reality of global warming and the large role that carbon dioxide emissions play in the rapid temperature increase of the last few decades. Burning coal also releases more soot, pollution, and radioactive particles than would a properly running nuclear fission plant producing an equivalent amount of power.

Aside from all the environmental and health problems caused by burning fossil fuels, there is another issue. The finite supply is being depleted rapidly. Table A.1 shows the Energy Information Administration's (year 2000) estimated global reserves of the three main types of fossil fuels (these numbers are somewhat conservative, compared to estimates from other groups). If world usage rates remained as they were in 1999 for each type of fuel independently, and there were no new reserves discovered, the right-most column shows how many years before the estimated reserves are depleted.

Of course as one source of fuel runs out, the use of the remaining types will increase. One can obtain a more complete estimate of the end of the fossil-fuel age by taking into account the growth in population, and probable growth in global energy per capita. In order to compare different fuels, it is necessary to convert all quantities to equivalent Quads. Assume that the different fossil fuels can be freely interchanged

to meet total energy demands (this is not really possible – there are many uses of petroleum for which coal would be a poor substitute). Energy content varies with quality and exact type and grade of fossil fuel, but overall averages extracted from recent Energy Information Administration data are: 1 Quad is equivalent to 1.89×10^8 Barrels of oil, 9.55×10^{11} ft^3 of natural gas, or 4.9×10^7 short tons of coal. Using these conversion factors, the combined total energy content of the fossil fuel reserves in Table A.1 is 32,960 Quads.

Figure A-6 shows two possible scenarios for future fossil fuel consumption. In both, the world population projection is based on the medium-growth scenario from a year 2000 report by the United Nations' Population Information Network.[8] The first scenario (shown by the dashed line) assumes that the energy use per capita stays constant at 64.6 Quad/year/billion people, while the second (dash-dot line) projects a linear growth of the energy per capita from the current 65 Quad/year/billion to the Western European and Japanese values of approximately 150 Quad/year/billion by the year 2050. The corresponding fossil fuel energy demand (assuming a constant 85% share of total energy demand from fossil fuels) grows much more slowly for the constant energy per capita case, up to 510 Quad/year by the year 2050. For the case of linear growth in energy per capita, the total fossil fuel energy demand grows to 1200 Quad/year by 2050. For this case, global fossil fuel reserves are completely depleted by the year 2046! For the case of constant energy per capita, by the year 2050 fossil fuel reserves are down to 11,013 Quad. If the population then held steady at 9.3 billion, and the energy per capita fossil-fuel use remained at 54.9 Quads/year/billion (85% of the total energy demand), the fossil fuel age would come to an end in the year 2072. Recent optimistic estimates [105] of global oil reserves would change the entry for petroleum in Table A.1 from 1 trillion Quad to 2 trillion Quad of energy left. However, this would only add another 4 years to the fossil fuel lifetime under the growing demand per capita scenario, or another 10 years to the steady demand

[8]See **http://www.undp.org/popin/**. There are a range of projections based on assumptions of fertility, with the low estimate placing the world population at 7.9 billion people by the year 2050, the medium estimate at 9.3 billion and the high estimate at 10.9 billion.

per capita. Even if there were vast new reserves discovered before the middle of the century, it may become necessary due to ecological damage or political pressure to phase out fossil fuel use before the end of cheap fossil fuels.

A.2 Nuclear Fission

As fossil fuels become scarce and expensive, power from nuclear fission will probably play more of a role. In 1998, 17% of the world's electricity was produced with nuclear power. However, just as there is a limited supply of fossil fuels in the Earth, the supply of uranium-235, one of the main fission fuels, is also limited. It is estimated that with terrestrial resources of uranium (i.e., without attempting to recover the much more dilute and hence expensive traces of uranium in seawater), there is enough recoverable fuel for conventional nuclear fission power to last another century or so [106]. U-235 is the fissile isotope found in natural uranium, which is predominantly composed of U-238 (about 99.27% of natural uranium is U-238). U-238 is not useful for fission by itself, but can be "bred" into fissile plutonium-239 through neutron capture and two subsequent beta decays. Fission power plants that breed their own fuel in this way could extend the life expectancy of fission power considerably. However, breeders increase the dangers of nuclear weapons proliferation by producing plutonium, from which a nuclear bomb could be constructed with as little as 10 kilograms. Most of the waste from fission plants are currently stored near the reactors themselves. There are plans to bury all the waste from U.S. nuclear power in Yucca Mountain in Nevada, but there are still doubts about that repository's long-term geological stability, and the human race's ability to maintain nuclear waste safe for thousands of years.

Professor Henry Kendall, a Nobel-prize winning physicist at M.I.T. who died in 1999, was a founding member of the Union of Concerned Scientists and was involved in arms control and nuclear safety issues. He said that perhaps the prevention of nuclear weapons proliferation would not be possible unless we abandon fission energy. Public perception after the Chernobyl accident, and the problem of biologically active fission product isotopes (such as iodine, strontium, and cesium), or other radioactive

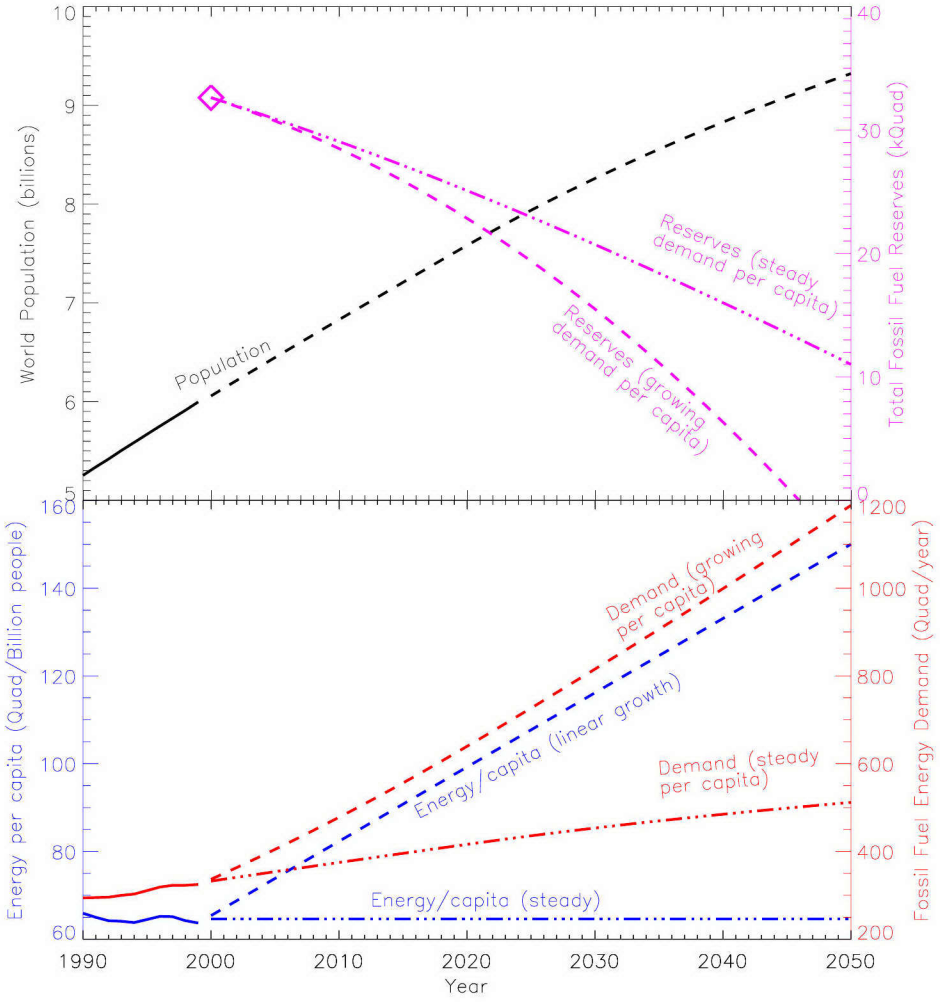

Figure A-6: Two possible future scenarios for fossil fuel lifetime. Top: Projected world population and fossil fuel reserves. Bottom: Energy use per capita and fossil fuel share (85%) of global energy demand.

isotopes, some with half-lives of order tens of thousands of years, may preclude the large scale use of nuclear fission power in the future.

A.3 Fusion Energy

In the year 2001, there are still no net-power-producing fusion experiments on the Earth. Yet fusion power is responsible for the vast majority of light we see in the sky, night or day. Whereas fission is the breaking apart of large heavy nuclei such as uranium and plutonium into two or three smaller unpredictable end products, fusion is the merging together of two (or three) light nuclei such as hydrogen or deuterium into a few well-known end products, most of which are not radioactive. However, there are often bare neutrons ejected as end products of fusion reactions, and high energy nuclei or neutrons striking material surfaces can activate the material and cause it to become radioactive. With wise choices of plasma-facing materials, the radioactivity of the reactor after its useful power-producing lifetime can be safely dealt with in a time of order one hundred years, rather than one thousand years or even tens of thousands of years as for fission waste.

Fusion of very light nuclei releases more energy per unit mass than fission. One of the most promising fusion reactions for first generation fusion power reactors is the deuterium (the isotope of hydrogen with one extra neutron) – tritium (a proton with two neutrons) reaction:

$$\mathsf{D} + \mathsf{T} \longrightarrow \mathsf{He}^4 + \mathsf{n},$$

where the ^{4}He nucleus comes out of the reaction with 3.5 Mev of extra kinetic energy, and the neutron with 14.1 Mev. The D–T reaction has a maximum cross section[9] at about 50 or 60 keV. However, with good energy confinement, ignition could be reached already at 5 to 10 keV. Ignition is reached when the fusion power in charged products (which should remain confined by the magnetic field) absorbed within the plasma is sufficient to heat the plasma to fusion temperatures. Any uncharged fusion

[9]The number of fusion reactions per unit volume is equal to the product of the reactant densities and the cross section multiplied by the velocity, averaged over a Maxwellian temperature distribution.

products, such as neutrons, would pass right through the magnetic bottle and hit the walls, where their energy could be extracted to drive a thermal cycle to produce electricity, as in any fossil fuel or nuclear power plant. Other reactions involving H, D, ^{3}He, ^{6}Li, ^{7}Li, and B require even higher temperatures to reach high reaction rates.

Fusion energy is non-renewable because the sun is not producing a continual supply of hydrogen or deuterium. Most of the hydrogen in the universe was created in the first moments after the big bang. Free neutrons that were not taken up to become part of heavier nuclei decayed with a half life of 10.4 minutes into protons. Stars start out containing mostly hydrogen, but once the hydrogen is fused into helium or heavier elements, there is no going back. Deuterium can be produced through hydrogen fusion in stellar interiors, but it is immediately consumed in subsequent fusion reactions. Most of the deuterium in the universe was created in the first 15 minutes after the big bang. However, even though fusion fuels were formed billions of years ago and there is no ongoing renewal of light elements, hydrogen is the most abundant element in the universe, and the next three are ^{4}He, D, and ^{3}He. So fusion fuels are abundant and all around us. In the Earth's oceans, the deuterium to hydrogen concentration ratio is approximately 1.5×10^{-4}, and 96.5% of sea water is water (the rest is mostly salts). Every gallon of sea water thus contains approximately 0.061 grams of deuterium. Assuming an initial supply of tritium for the D–T reaction to go forward in a fusion reactor, further tritium can be created in some sort of lithium[10] filled blanket surrounding the fusing plasma through the reactions:

$$\mathsf{n(fast)} + \mathsf{Li}^7 \longrightarrow \mathsf{He}^4 + \mathsf{T} + \mathsf{n(slow)} - 2.5 \text{ Mev}$$

and

$$\mathsf{n(slow)} + \mathsf{Li}^6 \longrightarrow \mathsf{He}^4 + \mathsf{T} + 4.8 \text{ Mev}.$$

The first reaction is endothermic, requiring energy to go forward. By placing a layer of lithium-7 first, then lithium-6 in the blanket, fast neutrons (14.1 Mev) can fuse in the first layer, producing tritium and a slow neutron. The neutrons that make it past the first layer can be captured in the next layer, producing more tritium and

[10]Natural lithium is approximately 7.5% ^{6}Li, and the rest ^{7}Li.

extra heat. The net result of this chain of reactions is that one nucleus each of D, ^{6}Li, and ^{7}Li has been used to produce three ^{4}He, one T and 19.9 Mev of energy. The helium-4 is the "ash" of fusion reactions, as it cannot easily be fused with other nuclei because it is very stable and has a high binding energy per nucleon. The tritium can periodically be recovered from the blanket and used for fuel in the D–T reaction. So from the deuterium in one gallon of sea water, 0.19 grams of lithium-6, and 0.22 g of lithium-7, 6.7×10^{10} joules can be produced, assuming this chain of reactions occurs for every D–T fusion event. To get this much ^{6}Li, 2.5 g of natural lithium is required, which is mostly ^{7}Li. To get 1 Quad of energy, 18 million gallons of sea water and 45,000 kg of natural lithium must be processed to extract the D, ^{6}Li and ^{7}Li. Note that unlike when energy is extracted from fossil fuels, most of the raw material here would not be consumed — most of the volume of water will remain and the remaining lithium-7 can be used for other purposes where the isotopic content is unimportant. Lithium is a fairly abundant metal, but if this were the only fusion reaction used in the future, lithium would become the limiting fuel.

An even longer term solution to the problem of obtaining fuel for fusion would be to use the D – D reaction, which has two possible branches, each occuring roughly equally:

$$\mathrm{D} + \mathrm{D} \longrightarrow \mathrm{T}(1.01\ \mathrm{Mev}) + \mathrm{H}(3.02\ \mathrm{Mev})$$

or

$$\mathrm{D} + \mathrm{D} \longrightarrow \mathrm{He}^3(0.82\ \mathrm{Mev}) + \mathrm{n}(2.45\ \mathrm{Mev}).$$

This reaction requires a temperature of at least 30 keV for ignition and has a lower cross section than the D–T reaction, but it would be a good candidate for a second generation fusion reactor. The charged fusion products come out with very high velocities, and it is doubtful that they could all be contained long enough in the plasma to fuse. However, the D–T cross section is large, so assume that the T produced in one branch of the D–D reaction will remain confined long enough to subsequently fuse, releasing an additional 17.6 Mev. The net result of these reactions are that 50% of the time, three D nuclei have been used to produce H, ^{4}He, and a neutron plus 21.6 Mev, and 50% of the time, two D nuclei have been used to produce ^{3}He and a

neutron plus 3.27 Mev. Using this D–D reaction chain in a second generation fusion reactor, the deuterium in one gallon of sea water could produce 1.5×10^{10} joules, or 1 Quad of energy from 72 million gallons (which is 1.7 million barrels or 2.7×10^5 m^3). Most of the water processed for deuterium will be put back in the ocean, as only 1 molecule out of 6500 is DHO instead of H_2O. The world's oceans contain approximately 1.3×10^9 km^3 of water. Using this D–D reaction chain, this represents an energy reserve of 4.8 *trillion* (4.8×10^{12}) Quads. Even at the very high current U.S. energy usage rate of 350 Quads/billion people/year and a world population of 10 billion, the deuterium in the ocean would last 1.4 billion years.

In summary, fusion energy has a nearly unlimited supply of fuel, especially when compared to fossil fuels. It has the potential of producing high densities of power, unlike most renewable energies. A fusion power reactor can be designed to produce much less radioactive waste, and isotopes with much shorter half-lives, than a nuclear fission reactor. Fusion does indeed look like a very viable option for our large future energy needs.

Appendix B

Single Particle Orbits in the Presence of a Wave Field: A physical picture of cyclotron damping

A physical picture of cyclotron damping can be illustrated by examining single particle orbits (charge q, mass m, background magnetic field $B_0 \neq 0$) in the presence of a plasma wave. If the factor $k_\perp \rho$ is non-zero, then the particle can lose or gain a significant amount of energy in just a few orbits. Single particle orbits in a homogeneous magnetic field can be described as a combination of unhindered velocity along the field ($\vec{v}_\parallel$), and circular gyro-motion in the plane perpendicular to the field ($\vec{v}_\perp$). If the parallel velocity is non-zero, then this is a helical orbit, following the magnetic field line. The gyro-frequency Ω is determined solely by the charge q and mass m of the particle, and the magnetic field strength B: $\Omega = qB/m$. Note that this means the electrons and ions (opposite charges) rotate in opposite directions, and $\Omega_e < 0$ for electrons and $\Omega_i > 0$ for ions. The particle-specific Larmor radius $\rho = v_\perp/|\Omega|$ is the radius of the circular orbit.

If the amplitude of the wave is small (in the sense that $|\vec{k} \times \vec{E}|/\omega \ll B_0$) then the

magnetic portion of the wave can be neglected, and only the electric field perturbs the particle's helical orbit. The particle's trajectory in space, $(x(t), y(t), z(t))$ can be determined from the following set of non-linear coupled first order differential equations:

$$\begin{aligned} dx/dt &= v_x \\ dy/dt &= v_y \\ dz/dt &= v_z \\ dv_x/dt &= \tfrac{q}{m}(E_x(t) + v_y B_0) \\ dv_y/dt &= \tfrac{q}{m}(E_y(t) - v_x B_0) \\ dv_z/dt &= \tfrac{q}{m} E_z(t) \\ \vec{E} &= \vec{E}_1 \exp(-i\omega t + ik_\perp x(t) + ik_\parallel z(t)) \end{aligned} \tag{B.1}$$

where the wave electric field vector $\vec{E}_1 = (E_x, E_y, E_z)$. $\vec{E}_1$ can be arbitrarily specified for illustrative purposes, but in an actual plasma $\vec{E}_1$ has only one free component, chosen as an initial condition, with the other two components determined by the general dispersion relation Eq. 2.17. By normalizing spatial quantities to some initial Larmor radius $\rho_0 = v_{\perp 0}/|\Omega|$ (thus the normalized distance is $x' = x/\rho_0$), time to the cyclotron frequency (normalized time $t' = t\Omega$), and velocities to an initial perpendicular velocity ($v' = v/(\rho_0\Omega)$), this set of equations can easily be numerically integrated to find the particle trajectory and increase (or decrease) in kinetic energy, neglecting any change in the electric field amplitude. Note that with these normalizations, the electric field is measured in units[1] of $\rho_0\Omega B_0$, and for a typical amplitude of the launched RF wave in C-Mod of order 10 kV/m this value is $E_0' = 0.002$.

The set of equations B.1 can be solved in normalized units and the evolution of the particle's kinetic energy can be traced. For example, consider a proton in the presence of a purely left-hand circularly polarized (LHCP) wave (electric field rotating in the same sense as the positive ions) at the fundamental cyclotron frequency $\omega = \Omega_i$ and with $k_\parallel = 0$. The initial phase of the particle's orbit relative to the electric field is very important. If $k_\perp \rho_i \simeq 0$ then the particle will experience approximately the same

[1]From $dv/dt = qE/m$, transform to normalized velocity and time: $dv'/dt' = qE/(m\rho_0\Omega^2) = E/(\rho_0\Omega B_0) \equiv E'$.

electric field during its entire orbit. If its velocity begins in the same direction as the electric field vector, it will remain that way throughout the orbit (since the wave period equals the cyclotron period), and will continually gain energy. If, on the other hand, it begins with its velocity opposed to the electric field, it will continually lose energy. Finite Larmor radius effects will complicate the matter somewhat, because now the particle will sample regions separated far enough in space so that the phase and direction of the electric field are not constant in the particle's frame. Figure B-1 shows the resulting change in kinetic energy of the proton after two cyclotron orbits for two different initial phases with Larmor radius such that $k_\perp \rho_i = 0.1$. This would be the value of $k_\perp \rho_i$ for thermal ions in a typical C-Mod shot at 5.4 Tesla and 3 keV. At any given guiding center of a particle orbit there will be many particles, each with different phases. The energy gain (or loss) as a function of initial phase, along with the phase averaged energy gain is shown in Fig. B-2. For this case of rather small $k_\perp \rho$, the average energy gain over all phases is much smaller than the maximum when the velocity and field begin in phase. As $k_\perp \rho$ increases, there is more net power absorption from the wave. An interesting result is that for very energetic particles (large ρ) or very short wavelengths (large $k_\perp$), even right-hand circularly polarized waves (RHCP) can begin to give net energy to the ions gyrating in a left-handed sense relative to the magnetic field! This is shown in Fig. B-3 for three different polarizations, where the solid line is pure LHCP, the dotted line is pure RHCP, and the dashed line is a linearly polarized wave. In fact, at $k_\perp \rho = 3$, it would be better to heat ions with a RHCP wave rather than a LHCP wave. However, for a typical launched wavenumber of $k_\perp = 0.5$ cm^{-1}, $k_\perp \rho = 3$ only for particles with 6 cm Larmor radius, which is much larger than the typical millimeter scale for thermal ions at a few keV. However, alpha particles at 3.5 Mev energy would have a Larmor radius of 5 cm or $k_\perp \rho = 2.5$, which is where the RHCP heating is the strongest. The fast magnetosonic wave has predominantly right-hand polarization in the plasma (see Fig. 2-6), suggesting it could damp on alpha particles if C-Mod were to try deuterium–tritium (see appendix A.3 for more on the D–T reaction) plasma shots.

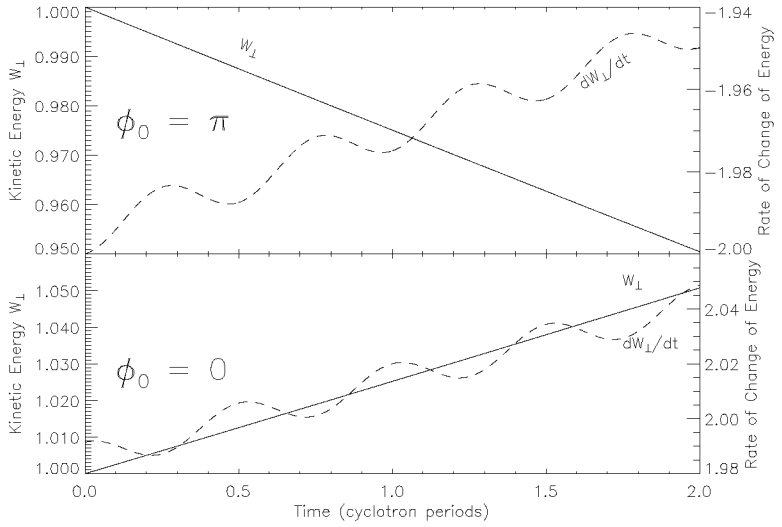

Figure B-1: Change in perpendicular kinetic energy for two different initial phases. Upper: $\phi_0 = \pi$ (velocity opposite E_0). The particle loses 5% of its initial energy after two periods. The rate of change of energy, $dW_\perp/dt = q\vec{v}_\perp \cdot \vec{E}$, is negative but decreasing in magnitude. Lower: $\phi_0 = 0$ (velocity aligned with E_0). The particle gains 5% of its initial energy after two periods. $dW_\perp/dt$ is positive and increasing in magnitude. (Note all quantities are in arbitrary units).

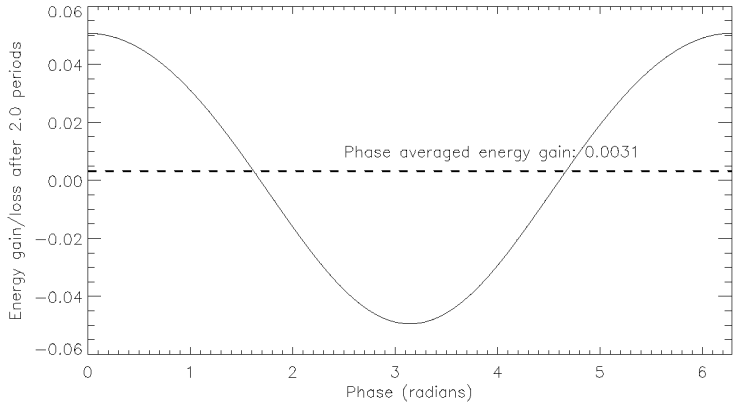

Figure B-2: Kinetic energy gain after two cyclotron periods as a function of initial phase ϕ_0. The net integrated result over all phases is a slight energy gain.

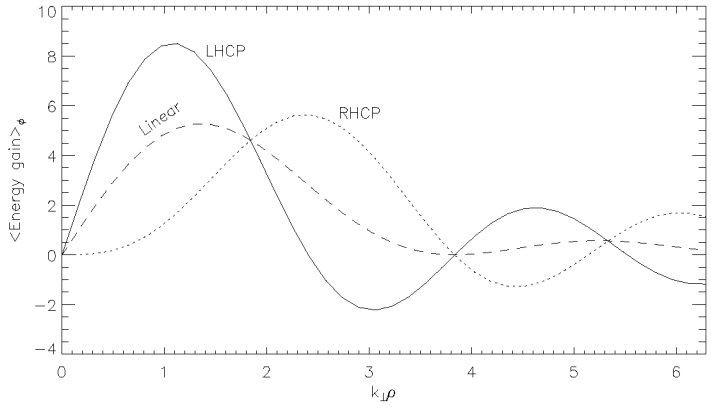

Figure B-3: Phase averaged energy gain (arbitrary units) for three different polarizations, as a function of $k_\perp\rho$.

For very small $k_\perp\rho_i$, the ion cyclotron damping is poor. However there is an interesting effect which can be seen from this single particle picture, also seen in quasi-linear theory, where the heating improves as the temperature increases. For a normal Maxwellian distribution of particles at a few keV temperature, the range of $k_\perp\rho$ present in the plasma for a given perpendicular wave number is quite small. However, minority ion cyclotron heating can often raise the temperature of the ion species being heated far above that of the bulk background plasma. This results in better absorption. Figure B-4 is a closer look at Fig. B-3 for $k_\perp\rho \leq 2$, showing normalized Maxwellian distributions for hydrogen ions at 3 and 80 keV as a function of $k_\perp\rho$ for $k_\perp = 0.5$ cm^{-1} and $B_0 = 5.4$ T. It can be seen that the 80 keV distribution can access a much higher energy gain for the same amount of cyclotron orbits as the 3 keV case.

Even though the energy gain from LHCP waves is maximum at $k_\perp\rho = 1.1$, the Maxwellian distribution indicates that there are very few particles at that energy in the plasma, even with a temperature of 80 keV. Figure B-5 shows the energy gain multiplied by the distribution function and the total integrated energy over the distribution for the three polarizations and two different temperatures. It can be seen that successful ion heating depends on the amount of left-hand polarization that can be achieved. Normally the fast magnetosonic wave has only a small LHCP component

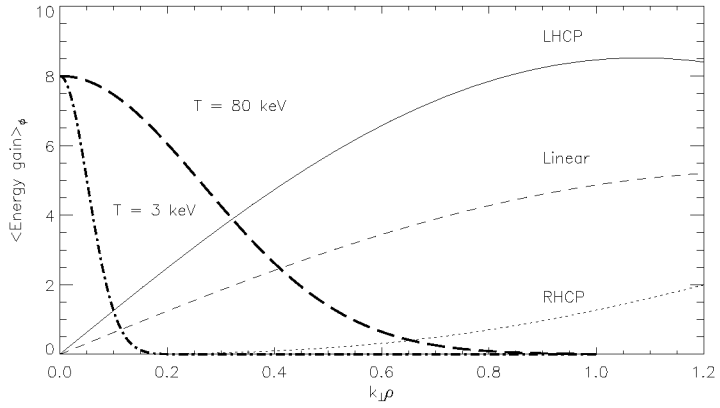

Figure B-4: Phase averaged energy gain as a function of $k_\perp\rho$ for three different polarizations. Also plotted are (arbitrarily normalized) Maxwellian distributions for 3 and 80 keV.

near the cyclotron resonance layer. This can be enhanced by the introduction of a small amount of a minority ion species (for example helium-3 in a majority deuterium plasma, as was shown in Fig. 2-6). If the minority ion species concentration is not too large, then the enhanced E^+ that occurs near the $n_\parallel^2 = S$ resonance will be near the doppler-broadened ion cyclotron resonance of the minority species, allowing strong cyclotron damping. As the concentration is increased, the region of enhanced E^+ moves away from the cyclotron layer, resulting in decreased minority ion heating (see also Fig. 4-11).

In this appendix it was shown that in order to have effective cyclotron damping, high temperature and significant left-hand circular polarization is needed. This can be achieved in a tokamak plasma using the fast magnetosonic wave by introducing a small amount of an ion species which has a distinct charge to mass ratio from the background plasma ions. This is the basis for the successful minority ion cyclotron heating schemes.

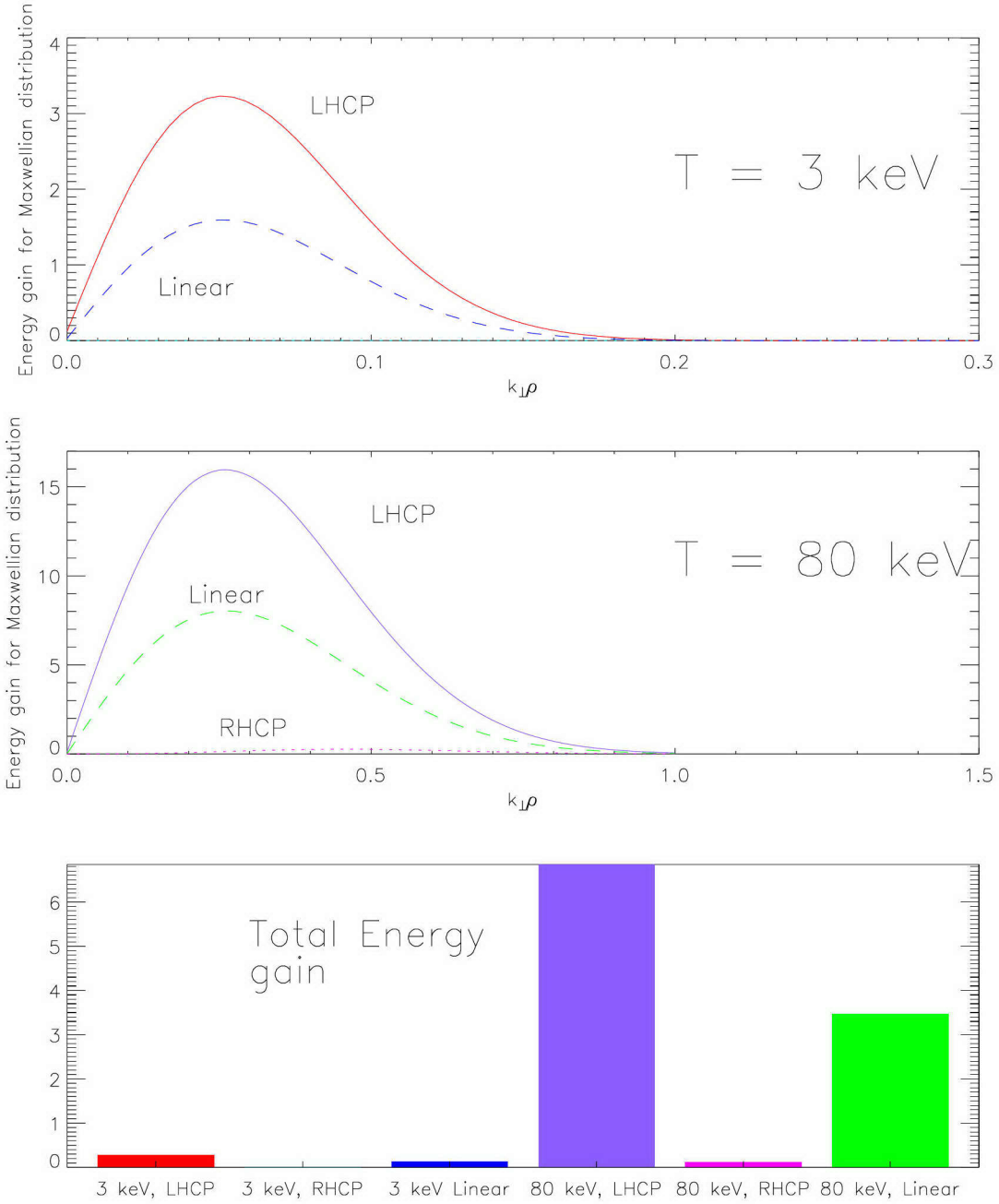

Figure B-5: Maxwellian weighted energy gain as a function of $k_\perp \rho$. Upper: 3 keV temperature, Middle: 80 keV temperature (note vertical scale is 4 times higher), Bottom: Total integrated energy gain for the three polarizations and two temperatures. (Energy units are arbitrary).

Appendix C

Using TORIC to obtain the RF fluctuating density

Most of the intuition developed over the years about the fast magnetosonic wave and ion Bernstein waves are from knowledge of the electric field. However, the PCI diagnostic measures electron density fluctuations. How these two are related is the subject of this appendix.

C.1 TORIC coordinates

One of the main results from the ICRF code TORIC (see Sec. 2.6) is the RF electric field solution. The output consists of three components: the right-hand circularly polarized component E^-, the left-hand circularly polarized component E^+, and the parallel electric field $E_\parallel$. These are referenced to the local total magnetic field, which changes direction from point to point when there is a non-zero poloidal field. The coordinate system used internally in the code is ψ, η, and ζ, where ψ is the radial coordinate perpendicular to magnetic flux, ζ is tangent to the total magnetic field, and η is orthogonal to ζ, lying in the magnetic surface (also known as "Stix" coordinates). The quantity θ which appears in the following expressions is the poloidal angle, which is in general not orthogonal to ψ, due to the non-circular equilibrium shape. E^+ and

E^- are expressed in terms of E_ψ, E_η, and E_ζ:

$$E^\pm = \frac{1}{\sqrt{2}} e^{\pm i\tau} \left(E_\psi \pm i E_\eta \right), \tag{C.1}$$

where the factor $\exp(\pm i\tau)$ is related to the magnetic equilibrium:

$$e^{\pm i\tau} = \frac{1}{\kappa N_\tau} \left(\frac{\partial Z}{\partial \theta} \mp i \cos\Theta \frac{\partial X}{\partial \theta} \right), \tag{C.2}$$

where

$$\kappa^2 = 1 - \frac{\sin^2\Theta}{N_\tau^2} \left(\frac{\partial X}{\partial \theta} \right)^2, \tag{C.3}$$

$$N_\tau^2 = \left(\frac{\partial X}{\partial \theta} \right)^2 + \left(\frac{\partial Z}{\partial \theta} \right)^2, \tag{C.4}$$

and $\tan\Theta$ is roughly the ratio of the poloidal field to the toroidal field (see Ref. [24] for more details). The magnetohydrodynamic (MHD) equilibrium can be thought of as a series of nested flux surfaces, labeled by the radial coordinate ψ, and the equilibrium is represented by:

$$X = X(\psi, \theta) \qquad Z = Z(\psi, \theta), \tag{C.5}$$

where in the simple MHD model used for the TORIC runs in this thesis, X and Z are expressed in terms of the Shafranov shift Δ, the triangularity δ, and the ellipticity η, which are flux functions (functions only of ψ, not θ):

$$\begin{aligned} X(\psi, \theta) &= \Delta(\psi) + a\,\psi \cos(\theta - \delta(\psi) \sin\theta) \\ Z(\psi, \theta) &= a\,\psi\,\eta(\psi) \sin\theta \end{aligned} \tag{C.6}$$

where a is the minor radius of the plasma (the radius at $\psi = 1$).

C.2 Density fluctuation

The RF electric field will perturb the electron density, driving a fluctuation at the RF frequency. If this density $n_{e1}(x,t)$ is much less than the background density $n_{e0}(x)$, then the electron fluid continuity equation can be linearized:

$$\frac{\partial n_{e1}}{\partial t} + \nabla \cdot (n_{e0} \vec{v}_{e1}) = 0. \tag{C.7}$$

For the waves of interest in this thesis, the term $\vec{v}_{e1} \cdot \nabla n_{e0}$ can be neglected compared to $n_{e0} \nabla \cdot \vec{v}_{e1}$, so Eq. C.7 becomes

$$\frac{\partial n_{e1}}{\partial t} + n_{e0} \nabla \cdot \vec{v}_{e1} = 0. \tag{C.8}$$

By assuming the fluctuation is simply harmonic in time $n_{e1}(x,t) = \exp(-i\,\omega t) n_{e1}(x)$, a Fourier transform in time of Eq. C.8 results in an expression for the RF fluctuating density in terms of the perturbed electron velocity:

$$n_{e1}(x) = \frac{-i}{\omega} n_{e0} \nabla \cdot \vec{v}_{e1}. \tag{C.9}$$

To replace the electron velocity with an expression involving the electric field, the (first order) linearized electron fluid force balance equation can be used:

$$n_{e0} m_e \frac{\partial \vec{v}_{e1}}{\partial t} = -n_{e0} e (\vec{E}_1 + \vec{v}_{e1} \times \vec{B}_0), \tag{C.10}$$

where the pressure gradient term $-\nabla p_{e1}$ has been neglected, because it is of order n_{e1}/n_{e0} smaller than the other terms for the temperatures and fields of interest in C-Mod. (The zeroth order equation, which may include a steady-state electric field due to the ∇p_{e0} term, is not fluctutating at the RF frequency so it is not relevant to the PCI measurements). The left-hand side of Eq. C.10 is usually smaller than the two terms on the right, but it has been included for increased accuracy.

C.2.1 Cylindrical coordinates

In order to express n_{e1} in terms of the electric field solution from TORIC, it can be seen from Eq. C.9 and Eq. C.10 that spatial derivatives of the electric field will be involved. In order to more easily perform the numerical differentiation and the line-integration to compare what the PCI diagnostic measures with the theory from TORIC, cylindrical coordinates are used: major radius R (or equivalently $X = R - R_0$), toroidal angle ϕ, and vertical distance above the midplane Z. The components of the electric field in terms of the TORIC solution components are [97]:

$$E_X = \frac{1}{N_\tau} \left\{ \frac{\partial Z}{\partial \theta} E_\psi + \frac{\partial X}{\partial \theta} \left(E_\eta \cos\Theta + E_\zeta \sin\Theta \right) \right\}$$

$$
\begin{aligned}
E_Z &= \frac{1}{N_\tau}\left\{-\frac{\partial X}{\partial\theta}E_\psi + \frac{\partial Z}{\partial\theta}\left(E_\eta\cos\Theta + E_\zeta\sin\Theta\right)\right\} \\
E_\phi &= -E_\eta\sin\Theta + E_\zeta\cos\Theta.
\end{aligned} \tag{C.11}
$$

Combining Eq. C.9 and Eq. C.10 relates the components of the perturbed velocity to the RF electric field (and the steady-state background magnetic field), and Eq. C.9 can be written in cylindrical coordinates:

$$
n_{e1} = \frac{in_{e0}}{\omega}\left[\frac{v_{e1X}}{R} + \frac{\partial v_{e1X}}{\partial X} + \frac{1}{R}\frac{\partial v_{e1\phi}}{\partial\phi} + \frac{\partial v_{e1Z}}{\partial Z}\right]. \tag{C.12}
$$

This is the expression that is used in order to compare the PCI data of Ch. 5 to the theory predictions of TORIC.

C.2.2 Stix coordinates

A more natural representation of the electric field and the electron velocity is in a frame of reference with one component along the total magnetic field, and the other two perpendicular to the field. This is because of the very different behavior of the plasma response along and across the magnetic field. This separation into perpendicular and parallel components also reveals the important role of the parallel electric field for the IBW PCI measurements.

The density fluctuation is proportional to the divergence of the electron velocity. The divergence in the non-orthogonal coordinates that TORIC uses is complicated, but a shorthand notation can be used (see Ref. [97] for the full expressions):

$$
\nabla\cdot v = \left(\partial_\psi + \nu_\psi\right)v_\psi + \left(\partial_\eta + \nu_\eta\right)v_\eta + \left(\partial_\zeta + \nu_\zeta\right)v_\zeta. \tag{C.13}
$$

Now Eq. C.10 can be used to relate the electron velocity to the RF electric field. Because ζ is in the direction of the total magnetic field, v_ζ will be directly proportional only to E_ζ, but the η and ψ components are coupled together:

$$
\begin{aligned}
v_\zeta &= -i\frac{\Omega_e}{\omega}\frac{E_\zeta}{B_0} \\
v_\psi &= \frac{-i\frac{\Omega_e}{\omega}\frac{E_\psi}{B_0} - \frac{\Omega_e^2}{\omega^2}\frac{E_\eta}{B_0}}{1-\frac{\Omega_e^2}{\omega}} \\
v_\eta &= \frac{-i\frac{\Omega_e}{\omega}\frac{E_\eta}{B_0} + \frac{\Omega_e^2}{\omega^2}\frac{E_\psi}{B_0}}{1-\frac{\Omega_e^2}{\omega}}
\end{aligned} \tag{C.14}
$$

Since in the ICRF, $\Omega_e/\omega \gg 1$ and the perpendicular components are comparable in magnitude $E_\psi \sim E_\eta$, Eqs. C.14 can be approximated:

$$\begin{aligned} v_\zeta &= -i\frac{\Omega_e}{\omega}\frac{E_\zeta}{B_0} \\ v_\psi &= \frac{E_\eta}{B_0} \\ v_\eta &= -\frac{E_\psi}{B_0} \end{aligned} \tag{C.15}$$

The parallel derivative of the parallel velocity has a large multiplying factor of $\Omega_e/\omega \sim m_i/m_e$ which the perpendicular derivatives of the perpendicular velocity components lack. For the fast wave, E_ζ is still so much smaller than the perpendicular components that it does not contribute greatly to the density fluctuation. However, near the mode conversion region and the IBW wavefields, the $(\partial_\zeta + \nu_\zeta)v_{e1\zeta}$ contribution to the density fluctuation is the largest of the three, as can be seen in Fig. 5-29.

The most interesting result from this calculation is that for the FW to IBW mode conversion problem, the largest contribution to the perturbed density is from the parallel gradient term, which is due to the derivative of the parallel electric field. This is unusual because in the ICRF, the parallel electric field is the smallest component (sometimes set to zero in ICRF codes and theory), and markedly different in appearance in the poloidal cross-section. Thus the IBW PCI measurements can be a stringent test for ICRF theory, where the parallel electric field must be calculated correctly to compare favorably to the experimental data. For more details and examples, see Sec. 5.5.

Appendix D

Determining the ion concentration mix

This appendix outlines various methods for determining the ion concentration mix in the H–^{3}He–D plasmas of Ch. 5. The fraction of the plasma ions made up of helium-3 is particularly difficult to measure, as there are few accurate methods to detect the amount of doubly-ionized helium in the core of the plasma. The hydrogen and deuterium were measured with a high-resolution spectrometer observing Balmer-α line radiation[1] around 656 nm. The H/D ratio was obtained by examining the difference in the intensity of the line radiation between the two isotopes.

D.1 Helium-3 concentration

For the mode conversion experiments, there were several methods used to estimate the amount of ^{3}He present in the plasma, none of which were definitive by themselves. However, by comparing the relative trends among the different methods, a consistent

[1]The Balmer series of atomic line radiation is for transitions from higher excited states ($n > 2$) to the first excited state ($n = 2$). The α line is the smallest transition, from the $n = 3$ to $n = 2$ state. For hydrogen, the wavelength of the photon emitted from the Balmer-α transition is at 656.2793 nm. The radiation is slightly shifted to 656.1032 nm for deuterium, due to the heavier mass. The analysis technique and the diagnostic instrument were developed by Earl Marmar at the PSFC. I modified the analysis program to adapt to the large hydrogen levels present on run day 1000623, hopefully resulting in more accurate H/D ratios than were initially reported by the automatic analysis routine (which assumed small H/D) and stored in the C-Mod database.

history during the run day was obtained. The next few sections outline these different methods, and then Sec. D.1.6 will present the synthesis of all methods for an estimate of the ^{3}He concentration.

D.1.1 Gas puff time

The simplest estimate of the relative amount of helium in each plasma discharge can be made using the amount of time the helium gas-puff valve was open. Figure 4-7 compared the ^{3}He density in D(^{3}He) plasmas determined from identification of the peak electron heating to the gas valve time. This showed that the helium density in the plasma was roughly linearly proportional to the gas valve time. Unfortunately, for the year 2000 run campaign, the nature of the gas valve changed again (as it did between the 1996 and 1998 run campaigns), so that the scalings from that plot cannot be used. In addition, the programming for the valve was radically changed midway through the 23 June 2000 run day. The amount of helium leaving the gas reservoir through the valve into the vacuum vessel depends on the voltage applied to the valve. From shot 1 to shot 11, the programming consisted of a strong voltage pulse lasting 100 to 200 msec in the early part of the shot (usually before the RF power was turned on), and then a lower "maintenance" voltage level for the rest of the shot, in order to make up for any helium losses in the course of the discharge. From shot 12 to shot 21, however, the voltage programming was placed under feedback-control, with the aim of maintaining a constant overall density during the shot. The result was that the voltage of the valve was a complicated function of time, with only short bursts of maximum voltage. The amount of gas leaving the valve is a non-linear function of the voltage applied, so in order to make a consistent estimate of the shot to shot trend, only the time duration of the maximum voltage pulse was considered. Figure D-1 shows the trend throughout the day, which can be used as a relative measure of the helium concentration from shot to shot. If the proper scaling factor can be determined, it could also be used as a measure of the absolute density.

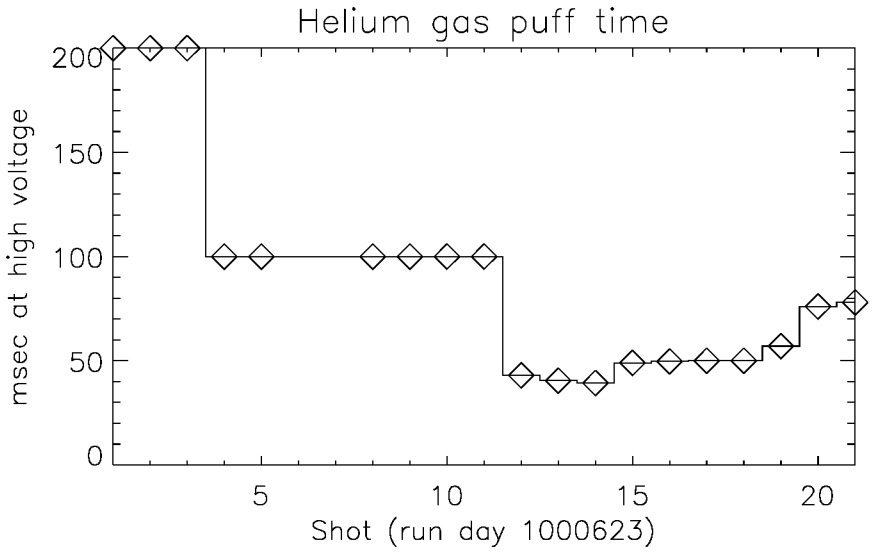

Figure D-1: The amount of time the helium-3 gas puff valve was open at high voltage during the 23 June 2000 run day. Diamonds indicate the successful (i.e. non-dud or fizzle) helium shots.

D.1.2 Electron density rise

Another fairly simple method to determine the amount of helium-3 that has arrived in the *core* of the plasma is to monitor the electron density rise after the helium gas puff. If the plasma density in the core was in steady-state with the walls of the machine and the divertor before the gas puff (not always a very good assumption), then the rise in central electron density can be attributed to the doubly-ionized helium-3 that has arrived in the core of the plasma after being released from the valve at the edge. If the density was not in steady-state (i.e., the density was still rising at the time the helium puff began), a rough estimate can still be made of the helium-3 contribution by attributing the rise in density to the electrons from helium, although some will probably come from other sources. Then the fraction n_{He3}/n_e can be calculated from this density rise by dividing by the total central electron density, and then dividing by two (because each helium atom contributes two electrons). Figure D-2 shows the results of this analysis for the 23 June 2000 run day. Note that the general trend agrees with the gas puff time in Fig. D-1.

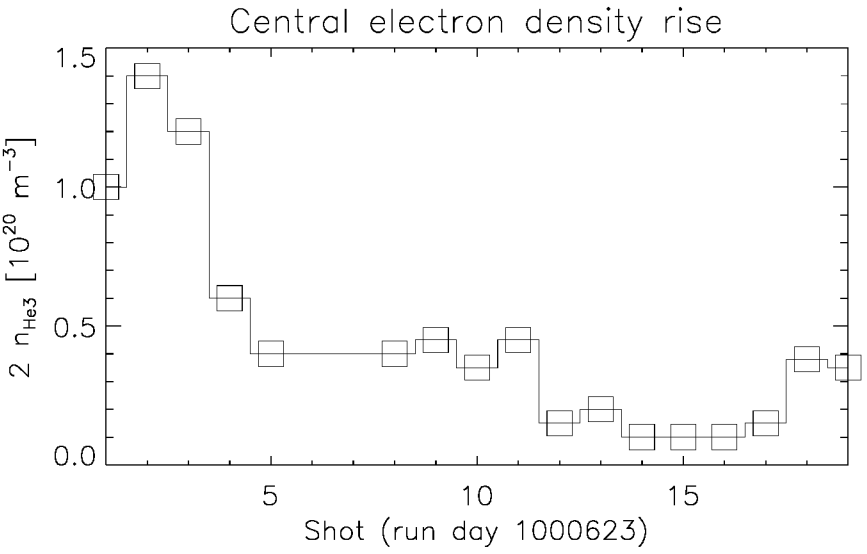

Figure D-2: Central electron density rise after the helium gas puff, attributed to helium-3 arriving in the core (2 electrons for every ^{3}He atom). Squares show the shots for which this method was successfully applied.

D.1.3 Hydrogenic light deficit

A less obvious method that can be used to cross-check the other methods, especially the density rise method, is based on the spectroscopic emission of Balmer-α line radiation[2] from hydrogen and deuterium. By studying many shots before and after the June 23rd run day, it was found empirically that there was a correlation between the total density and the intensity of emitted Balmer-α radiation. This relationship is shown in Fig. D-3. Two main regions are evident (with different slopes) where an increase in density results in an increase in emission. The difference between the longer, lower region and the upper region seems to be somewhat correlated to the small difference in magnetic field between the two regions (upper region: $B_0 \approx 5.2$ T, lower region: $B_0 \approx 5.4$ T).

Knowledge of this relationship between the total density and the hydrogenic brightness can be used to determine if there is a large fraction of non-hydrogenic

[2]These measurements were not the same as that used for the H/D ratio determination. This diagnostic measured the total intensity from both H and D. The diagnostic measurements were provided by Jim Terry at the PSFC.

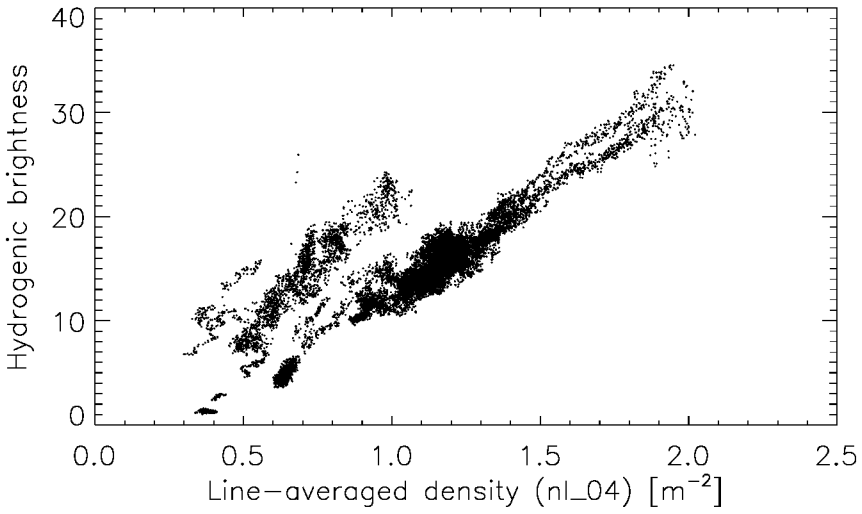

Figure D-3: The correlation between the Balmer-α emission from hydrogen and deuterium and the line-integrated density. Each point is a time slice from a certain shot, and approximately 70 shots are represented.

ion species present. For example, with a large amount of helium-3 present, the density will be higher than expected for the given amount of hydrogenic light, because not all of the density is H or D. For the purpose of trying to determine the amount of helium present in the plasma, the exact nature of the relationship between the density and the brightness is unimportant, as long as it is roughly a one-to-one function. Figure D-4 shows an example of a shot (1000623002) with a large helium gas puff. Four separate segments are shown, corresponding to different times in the shot. The long segment beginning at the origin (green in the color version of this thesis) is from the early part of the shot (0.03 to 0.3 sec), before the helium gas puff. The hydrogenic brightness increased nearly linearly with the density rise. The second segment (magenta) is during the helium gas puff (0.3 to 0.42 sec). During this time, the density rose, but the brightness fell. The fourth segment (cyan) is separated from the other three segments in the plot. This was during the later part of the shot, during the maintenance voltage level on the gas puff valve (1.0 to 1.45 sec). The RF power was on during this time. The last segment (blue) was during the ramp-down phase of the shot, when the density was falling (1.55 to 1.65 sec). This segment is parallel to

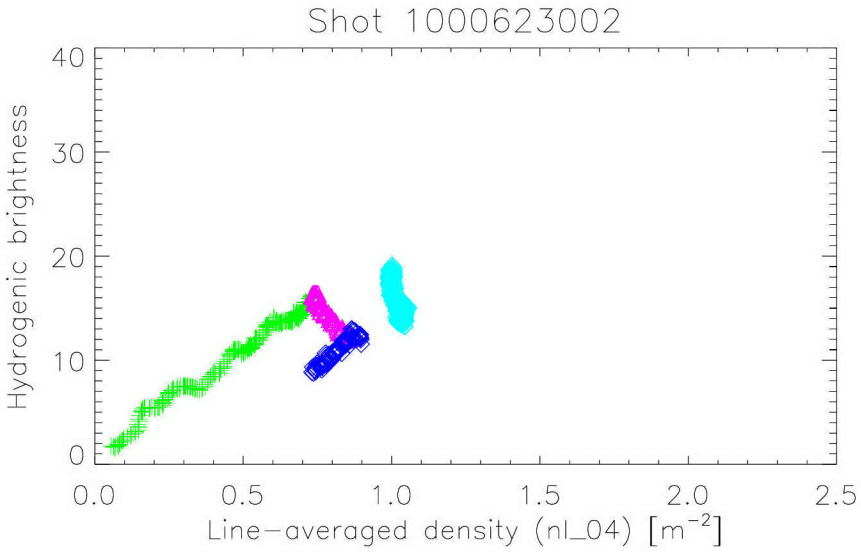

Figure D-4: This is the same type of plot as Fig. D-3, but only for certain time slices during a single shot (1000623002) with a large helium-3 gas puff. There are four separate segments shown, corresponding to different times in the shot (see text).

the earliest segment, but shifted further down (less bright) and to the right (higher density). This means that there is a hydrogenic light "deficit" due to the presence of helium in the discharge. In order for this short segment to fall on the earlier trend at these low brightness levels, the entire line must be shifted over by 0.32 m^{-2}. This portion of the total density can be considered to be from helium. The line-integrated density can usually be related to the central density by a simple proportional factor. In this case, multiplying the line-integrated density by 2.75 matches the central density, so that using the hydrogenic light deficit method, the helium density is estimated to be 0.88×10^{20} m^{-3} for shot 1000623002.

Figure D-5 uses squares to show the results of this analysis for the first four shots of the day (all with fairly large helium gas puffs). This method did not work very well for shots with small amounts of helium. However, an estimate was made for several shots later in the day in order to compare with the other methods — Fig. D-5 uses triangles to show these shots.

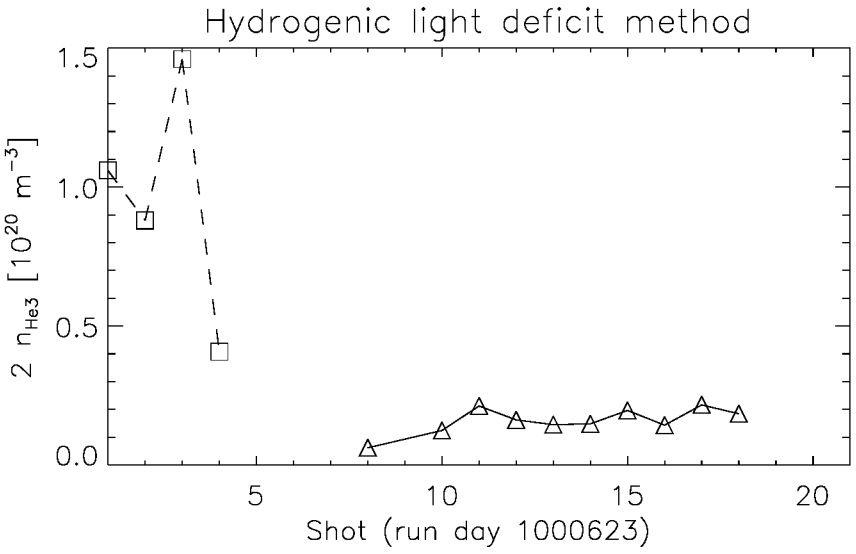

Figure D-5: The estimated electron density from ^{3}He (m^{-3}) using the hydrogenic brightness deficit method (2 electrons for each ^{3}He atom contribute to the core electron density). The first four shots, shown by the squares, had a much stronger difference in the pre- and post-puff times of the shot than did the later shots, indicated by the triangles.

D.1.4 Helium line-radiation emission

Atomic helium emits line radiation at the edge of the plasma, where the temperatures are high enough to excite the electrons in the atom, yet not high enough to completely ionize the atom. The intensity of this radiation can be used as another measure of the helium concentration present in the plasma. Although this is an edge plasma measurement, it is assumed to correlate with the core plasma helium density. For about half of the shots of the 23 June 2000 run day, a McPherson spectrometer was used to measure the Lyman-α line radiation[3] from singly ionized helium-3 ($^3He^+$). Figure D-6 shows the trend through the last half of the run day, with each shot indicated by a plus sign. Although the brightness was measured throughout the shot, for the purpose of comparing the ^{3}He concentration with other methods, only the

[3]The Lyman series of atomic line radiation is from transitions to the ground state ($n = 1$) from higher excited states ($n > 1$). The α line is the first in the series the transition from $n = 2$ to $n = 1$. The photons emitted from this transition for $^3He^+$ have wavelengths of approximately 304 Å, or 30.4 nm. These measurements were also provided by Jim Terry.

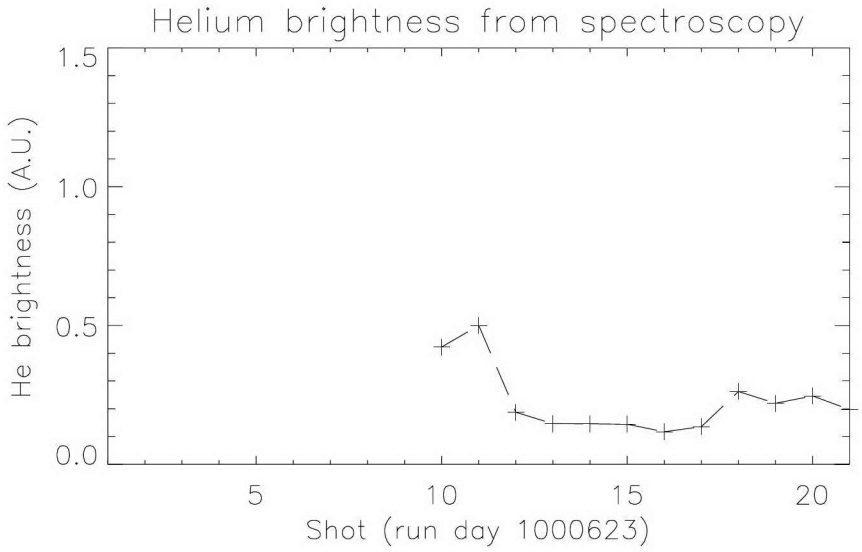

Figure D-6: The helium brightness as measured by observing the Lyman-α radiation from $^3He^+$ at the edge. The magnitude has been rescaled to match the other methods. The spectrometer was only active for the last half of the day (shots 10 to 21).

average value of the helium brightness during the PCI time window is used to obtain a single value for each shot. The relative change from shot to shot can be compared to the other methods, but an absolute calibration in terms of ^{3}He core density cannot be obtained from this spectrometer alone.

D.1.5 Effective charge

A final check can be made by examining a measurement of the effective ion charge $Z_{\text{eff}} = \sum_i Z_i^2 n_i/n_e$ in the plasma calculated using a measurement of the bremsstrahlung radiation and knowledge of the density. However, because the emitted intensity depends on the square of the density, but only linearly in the effective charge, it is difficult to get a quantitative measurement of Z_{eff} without very exact knowledge of the density. There wasn't a large enough variation from shot to shot to learn very much about the helium concentration. In addition, there is a large component of Z_{eff} which comes from high Z impurities, such as molybdenum in C-Mod. This contribution is difficult to isolate. However, the presence of some amount of helium could be

verified by comparing $Z_{\rm eff}$ from the first 21 shots of the day to the last three shots of the day. The first 21 shots were part of the mode conversion experiments, requiring some amount of helium. $Z_{\rm eff}$ was approximately 2 to 2.5 during these shots. The last few shots were devoted to machine "cleanup": i.e., reducing the H/D ratio so that hydrogen minority plasmas could be run the following week. There was no helium puffed during these shots, and $Z_{\rm eff}$ fell to a range of 1.6 to 1.4.

D.1.6 Summary of all methods

Figure D-7 shows the combination of all these methods. The circles connected by thick line (with estimated error bars for each shot) are estimates of the helium density in the core for each shot based on all available methods. Note that only two of these methods give estimates of the actual density (the density rise and the hydrogenic light deficit methods); the rest are scaled to match these two. (The hydrogen deficit method during the later part of the day (triangles) is not very reliable, thus it is not given much weight in the total.)

Ideally, the evolution of the helium-3 density during the course of the shot could be tracked, in order to correlate changes in the PCI observations with changes in the ion concentration mix (the H/D ratio is tracked during the shot). However, even obtaining a reasonable estimate for the average value during the shot is quite difficult, as can be seen in this Appendix. Thus, an average value of the ^{3}He concentration is obtained for each shot by dividing the estimated electron density from helium shown in Fig. D-7 (which is actually $2n_{\rm He3}$) by an average value of the electron density n_e during the steady-state portion of the shot, and then dividing by two to obtain the quantity $n_{\rm He3}/n_e$. The results are shown in Fig. D-8. From this and the spectroscopic H/D measurement, the ion species concentrations for each shot can be used for determining the expected position of the mode-conversion layer for comparison to the PCI data (see Sec. 5.4 and Appendix E), and for use in modeling the plasma and comparing to theory (see Sec. 5.5).

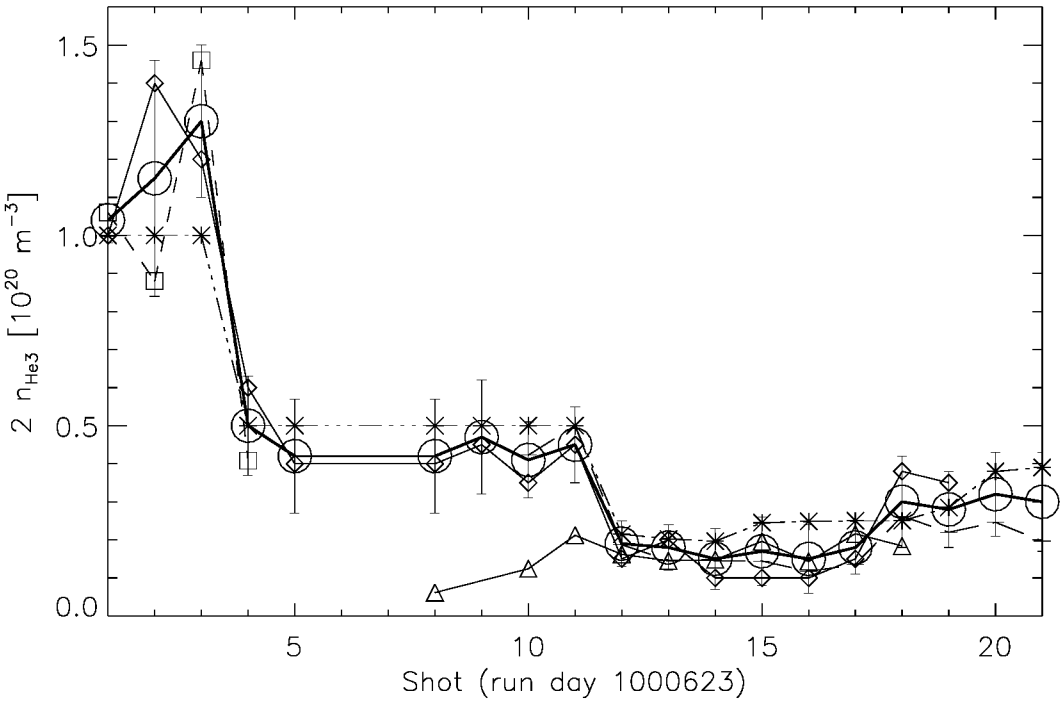

Figure D-7: All methods for determining helium-3 density shown on the same plot. The circles (with accompanying error bars) connected with the thick lines are the estimated helium level for each shot. The axis is labeled "2 n_{He3}" because each atom of ^{3}He contributes two electrons to the central electron density.

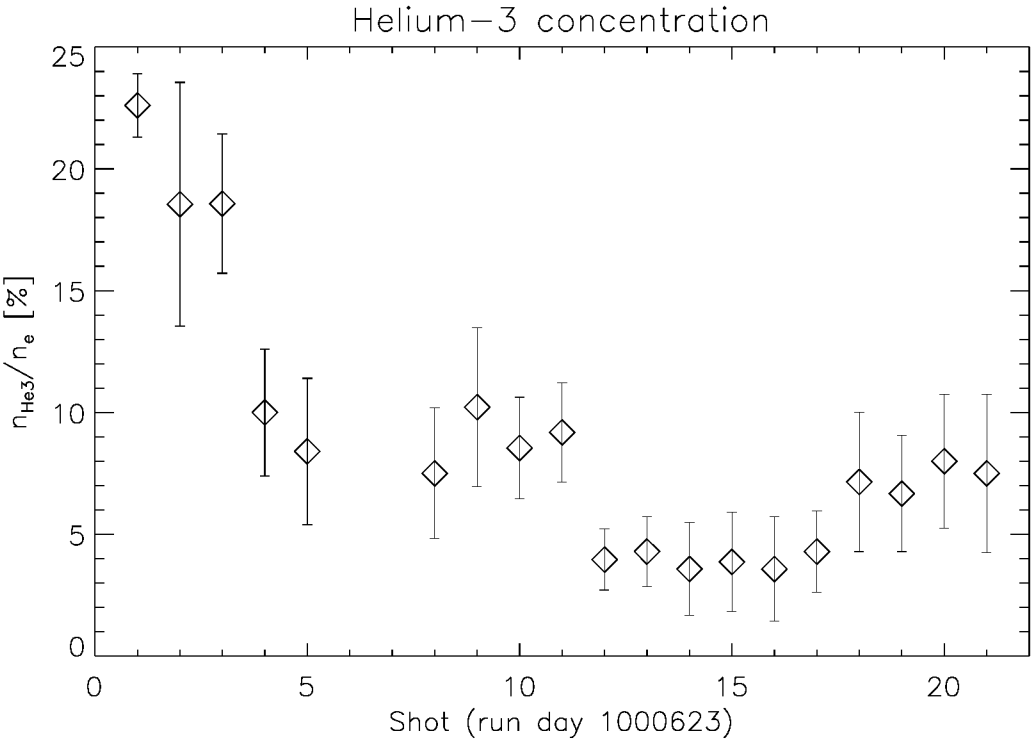

Figure D-8: The estimated ^{3}He concentration (n_{He3}/n_e, in percent) for each of the mode-conversion shots of run day 23 June 2000. The error bars are only rough estimates from the variation shown among the different methods, and could actually be larger.

D.2 Possible future methods for core ion concentration measurements

In order to better characterize the plasma for comparison to theory, the measurements of the core ion concentration mix need to be improved. Some ideas for possible future use on C-Mod are briefly discussed in this section.

(1) A diagnostic which can measure an ion's charge to mass ratio and its energy as it leaves the plasma at the edge was built and operated by Rob Nachtrieb (see Ref. [107]). It incorporates an omegatron and a gridded energy analyzer, and has been used in the past to measure helium-3 in the plasma. There is currently no one at the PSFC to operate it, but should a new student or research scientist revive the omegatron on C-Mod, it may be used as another method to study the helium-3 concentration.

(2) There is another diagnostic currently operational on C-Mod which measures energetic ions from near the edge of the plasma, called a neutral particle analyzer (NPA). The NPA works on the principle of charge exchange, where an ion of a certain energy inside the plasma captures an electron from a passing neutral atom. The energetic ion becomes neutral itself, but retains its kinetic energy. It is then free to cross magnetic field lines and leave the plasma. The NPA captures the atom, strips it of its charge, and uses a parallel magnetic and electric field (which are both perpendicular to the path of the entering particle) to determine its energy and charge to mass ratio. The NPA as currently configured does not have the capability to measure ^{3}He (also it is more difficult for the entire charge exchange process to occur with helium because it needs to capture two electrons to become neutral). Perhaps in the future modifications could be made to allow the NPA to be used as another method for studying ^{3}He concentrations.

(3) Each ion species with a unique charge-to-mass ratio (Z/M) gyrates at a different cyclotron frequency, radiating energy in the ICRF. Normally such ion cyclotron emission (ICE) from the core plasma is weak and difficult to detect. However, if a method for artificially exciting ICE from the core of the plasma could be devised,

and the subsequent radiation could be detected at the edge of the plasma with a receiving antenna, then an estimate of the ion concentrations could be obtained. If the magnetic field at the location of ICE excitation were well-known, then the different frequencies detected could be attributed to the different ion species present in the plasma.

(4) A sample of the core plasma during a shot could be obtained for later analysis. Perhaps this could be achieved by shooting a small, hollow probe at great speed through the center of the plasma, programming it to open midway through its flight to gather plasma ions from the core, and then close again for its departure through the plasma edge. This would be very difficult for high density C-Mod shots — but perhaps in the future a material will be discovered which could withstand the conditions of the core plasma for a brief time.

Appendix E

All the PCI IBW shots

This appendix is a record of all the successful shots from the 23 June 2000 run day with an RF signal in the PCI results. Some of these shots are discussed in more detail in Ch. 5. There are two figures for each shot: the first displays the amplitude of the RF PCI signal across the 12 channels as a function of time, along with various plasma parameters; the second is a plot of the observed wavenumbers (using the observed phase information and knowledge of the channel spacing).

For the amplitude plots, several things are shown. At the top is a contour plot of the PCI signal intensity at the expected RF frequency. The expected RF frequency is determined by the frequency at which the acousto-optical modulators are driven (see Sec. 3.2). For the first half of the day (shots 001 to 014), the modulators were driven at 40.075 MHz, so that the D-port RF signal would show up at approximately 350 kHz. For the second half of the day (shots 014 to 021), the modulators were driven at 40.180 MHz, so that the E-port RF signal would show up at approximately 360 kHz.[1] The bar on the right indicates the contour levels, increasing from the bottom to the top. This shows the spatial structure of the signal, and how it changes as the plasma parameters change. In this contour plot, there are several lines indicating various

[1]The actual RF heterodyne frequency is determined by looking for the maximum signal near the expected frequency in the Fourier spectrum of the PCI data, using a large time window for good frequency resolution. The windowed Fourier transforms are then performed using a time window with a number of samples such that this heterodyne frequency is in the center of one of the frequency bins. The amplitude of this bin is then used for the contour plots.

aspects of the PCI setup and the plasma parameters. The solid lines extending in from the beginning and end of the time window indicate the actual positions of the 12 PCI channels (the first and last channel locations are along the top and bottom of the plot, so there are only 10 lines visible).[2] The (usually steady in time) dotted line is the location of the magnetic axis, as determined from EFIT [3]. The dashed line is the estimated location of the cold plasma ($n_\parallel^2 = S$ for $n_\phi = 10$ and $m_\theta = 0$) mode-conversion layer, indicating how it moves with various plasma parameter changes (the most sensitive usually being the H/D ratio). Note that in all cases it has been shifted by 6 to 12 cm toward the low-field side in order for it to be visible in the contour plot. This is because in all cases, the estimated helium-3 concentration (see Appendix D) was low enough that the PCI viewing window was to the low-field side of the fast wave mode conversion layer. Even if the ^{3}He concentration (as shown in Fig. D-8) is off by a factor of two, so that in the early part of the day the plasmas actually consisted almost entirely of helium-3, the ^{3}He concentration would still not be high enough in the latter part of the day (especially shots 12 through 17) to move the mode conversion layer to within the PCI viewing window, yet a strong IBW-like PCI signal was seen on these shots. A possible explanation for this puzzle is described in Sec. 5.5.4.

Below the contour plot of the PCI amplitude is plotted the relevant RF power signal (i.e., from D-port or E-port) in MW. Next is a contour plot of the density profile (except for shots 5 and 9, where the diagnostic failed) obtained from a measurement of the visible bremsstrahlung radiation and $Z_{\rm eff}$ (the vertical axis is the major radius, the contour levels are shown to the right). After that is plotted the magnetic field at 66 cm major radius, if it is varying in time (otherwise, the toroidal field is indicated in the subtitle of the plot, below the x-axis). Next is a contour plot of the electron temperature using the GPC-ECE diagnostic (see Sec. 4.2), with contour levels shown on the right, increasing from bottom to top. Usually the sawteeth are visible near

[2]What is actually plotted is the grid used in the contour plot, i.e. each space and time point. The time points were usually close enough that they appear as a solid line. However, in Figs. E-31 and E-35, the time window is reduced so that the individual time points are visible.

the center of the plasma on this plot (the vertical axis is major radius). Next is the hydrogen to deuterium (H/D) ratio, as determined from a high-resolution spectrometer (see Appendix D). Finally, the right gap (the separation between the edge of the plasma and the RF limiter) is shown in the bottom plot. The center of the plasma and the right gap are shown because they are indications of the plasma movement within the vacuum vessel. The PCI channels are fixed with respect to the machine, so if the plasma moves around, the PCI signal could move across channels, even if other internal plasma parameters do not change.

The second figure for each shot contains a contour plot showing a two-dimensional Fourier transform of the raw PCI data, in order to construct a k-spectrum. Several hundred time slices are analyzed in order to construct the contour plot. The amplitude of the resulting transform as a function of time and wavenumber bin is shown (with contour levels increasing from bottom to top indicated by the bar on the right). There are thirteen wavenumber bins (the outermost bins are identical — one is a copy of the other, because of spatial aliasing), and when the beam was wide, the resolvable k range was from -4.8 cm^{-1} to 4.84 cm^{-1}. For a part of the run day, a lens was removed from the optical setup on top of the machine (see Fig. 3-1), so that effectively a narrower part of the beam was imaged on the detectors, the channel spacing was decreased, and the observable k range was increased. In this case, the k range was from -9.8 cm^{-1} to 9.8 cm^{-1}. When a strong signal appears exactly in the $k = 0$ bin, that means that there was no discernible phase advance across the 12 channels and it is either a long-wavelength wave, or (more often) some noise source from the laser which affects all channels roughly equally. Below the k-spectrum plot is shown the line-averaged density from interferometry. Below that is plotted the toroidal field (at major radius 66 cm) if it varies in time. Finally, the total RF power (in MW) is plotted at the bottom. This may not be the same as the specific power from either the D-port or E-port antenna as shown in the corresponding PCI signal amplitude plot (i.e. if both transmitters are on simultaneously).

The figure captions point out any unusual features for each shot, and also identify by how much the $n_{\parallel}^2 = S$ layer has been moved in order to show it on the contour

plot. It also gives an estimate of the uncertainty in the position of the $n_\parallel^2 = S$ layer due to the uncertainty in the ^{3}He concentration. The uncertainty in position was not the same in both directions (for example, a 5% decrease in n_{He3}/n_e would move the $n_\parallel^2 = S$ layer further to the HFS than a 5% increase in n_{He3}/n_e would move it to the LFS). However, since this is just a rough estimate, only the larger uncertainty is shown (they were usually different by only a few mm).

It is quite amazing that from the very first shot, and every shot thereafter throughout the day, some sort of RF signal was seen in the PCI viewing window. Both the fast wave and the mode-converted ion Bernstein wave was observed, sometimes simultaneously. The PCI signal amplitude exhibited a complex structure sensitive to small changes in plasma parameters. The k-spectra were usually somewhat simpler, showing a strong short-wavelength IBW like feature, but also showing complex structure, especially with a wide beam. Shots 3, 16, and 17 were tests where half the PCI beam was blocked, so they are not shown. Shots 6, 7, and 22 were failed plasma attempts. Plasma discharges after shot 22 were no longer part of the mode conversion mini-proposal, and had no helium-3 gas puff at all. All other shots for this run day are presented in the rest of this Appendix.

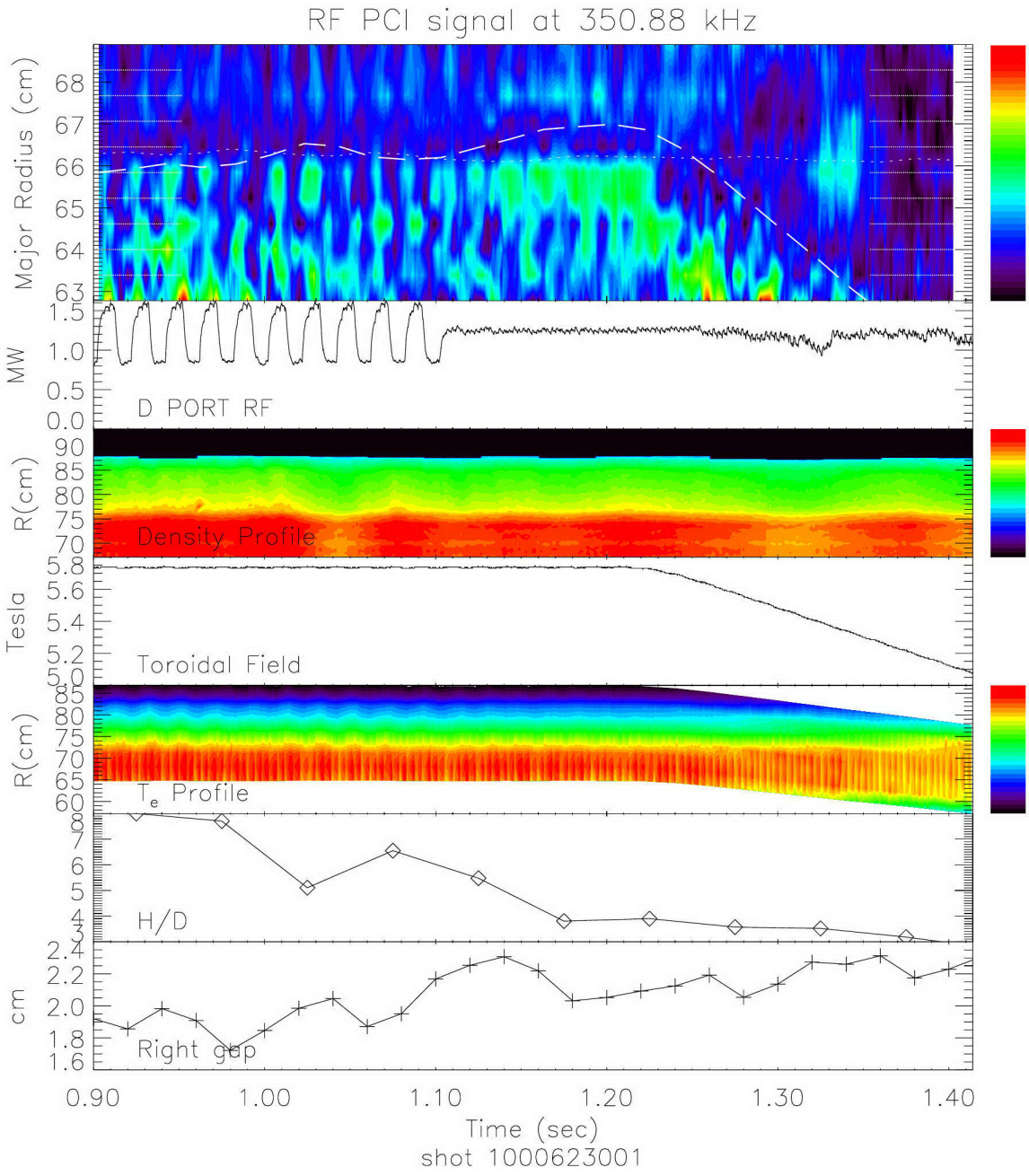

Figure E-1: RF PCI signal amplitude, shot 1000623001. The MC layer has been shifted by 7 cm. The MC position uncertainty is ±0.5 cm. There is a toroidal field ramp-down starting at 1.23 sec, and the amplitude pattern moves in the expected direction.

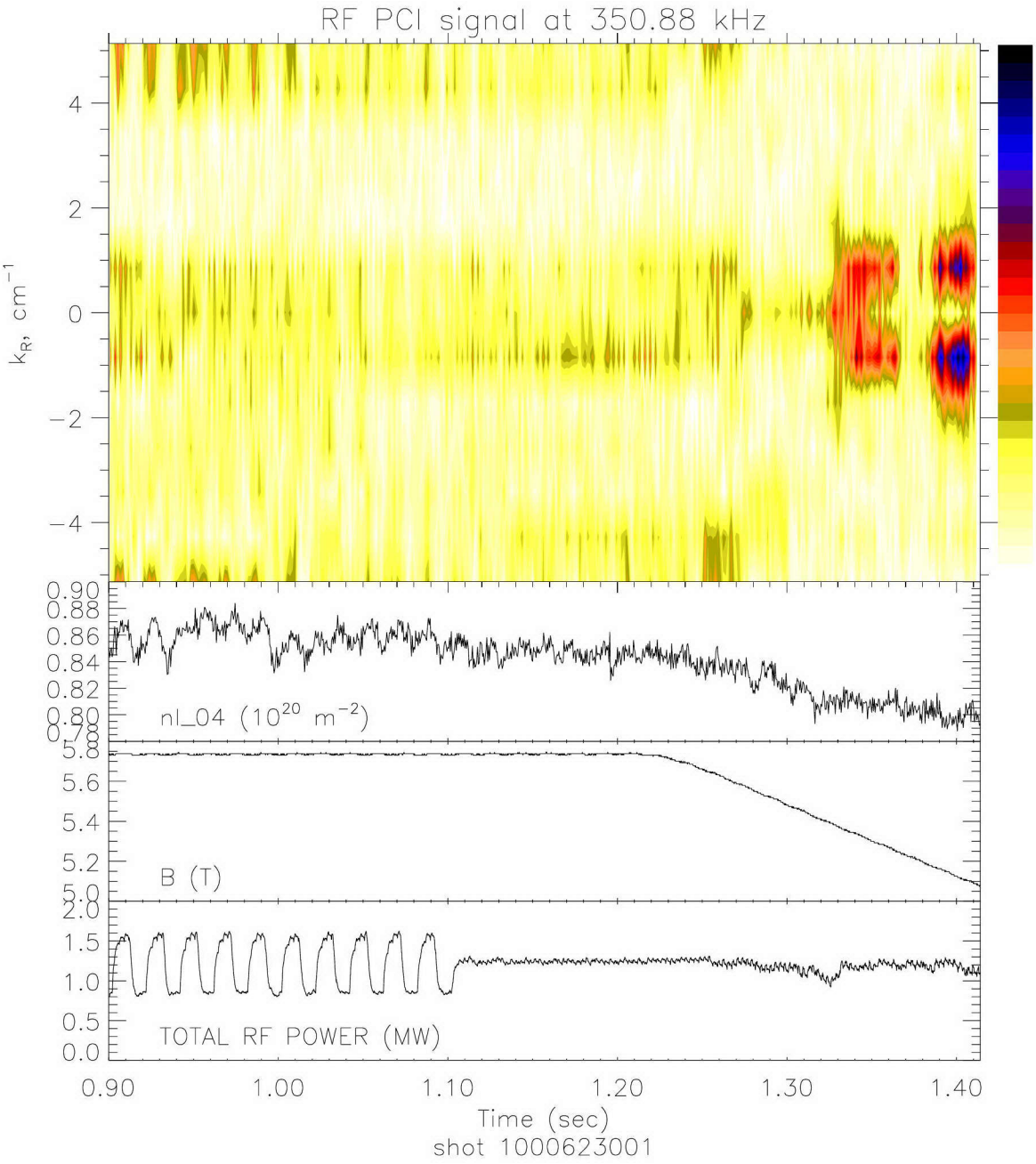

Figure E-2: RF PCI k-spectrum, shot 1000623001. There is a toroidal field ramp-down starting at 1.23 sec, and a strong signal consistent with the presence of both the outgoing and incoming fast wave ($k \simeq \pm 1$ cm^{-1}) is seen after 1.33 sec. The only other scenarios where the fast wave has been observed with the PCI is in peaked density shots (see Ref. [79, 80]).

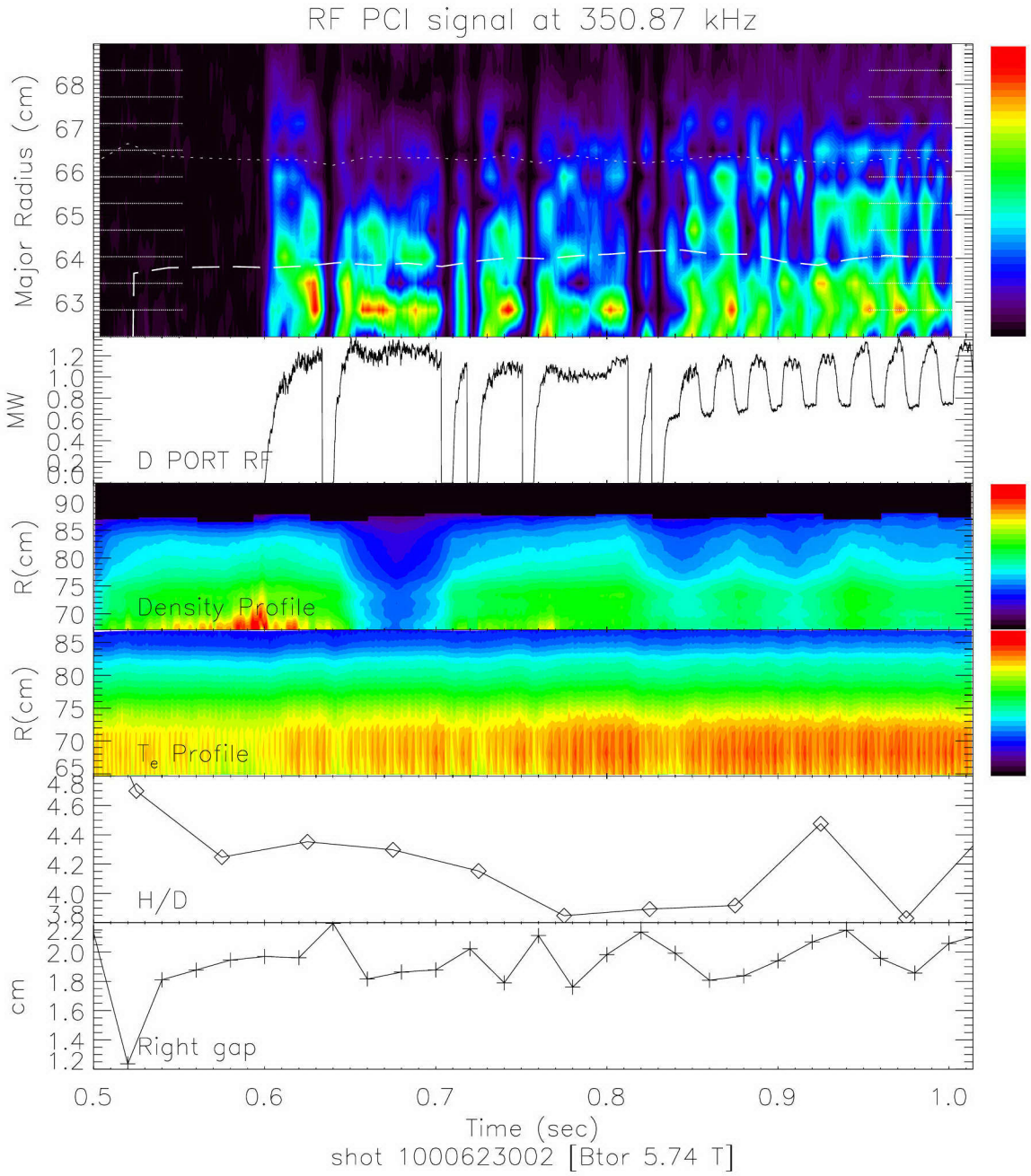

Figure E-3: RF PCI signal amplitude, shot 1000623002. The MC layer has been shifted by 6 cm. MC position uncertainty is ±2 cm.

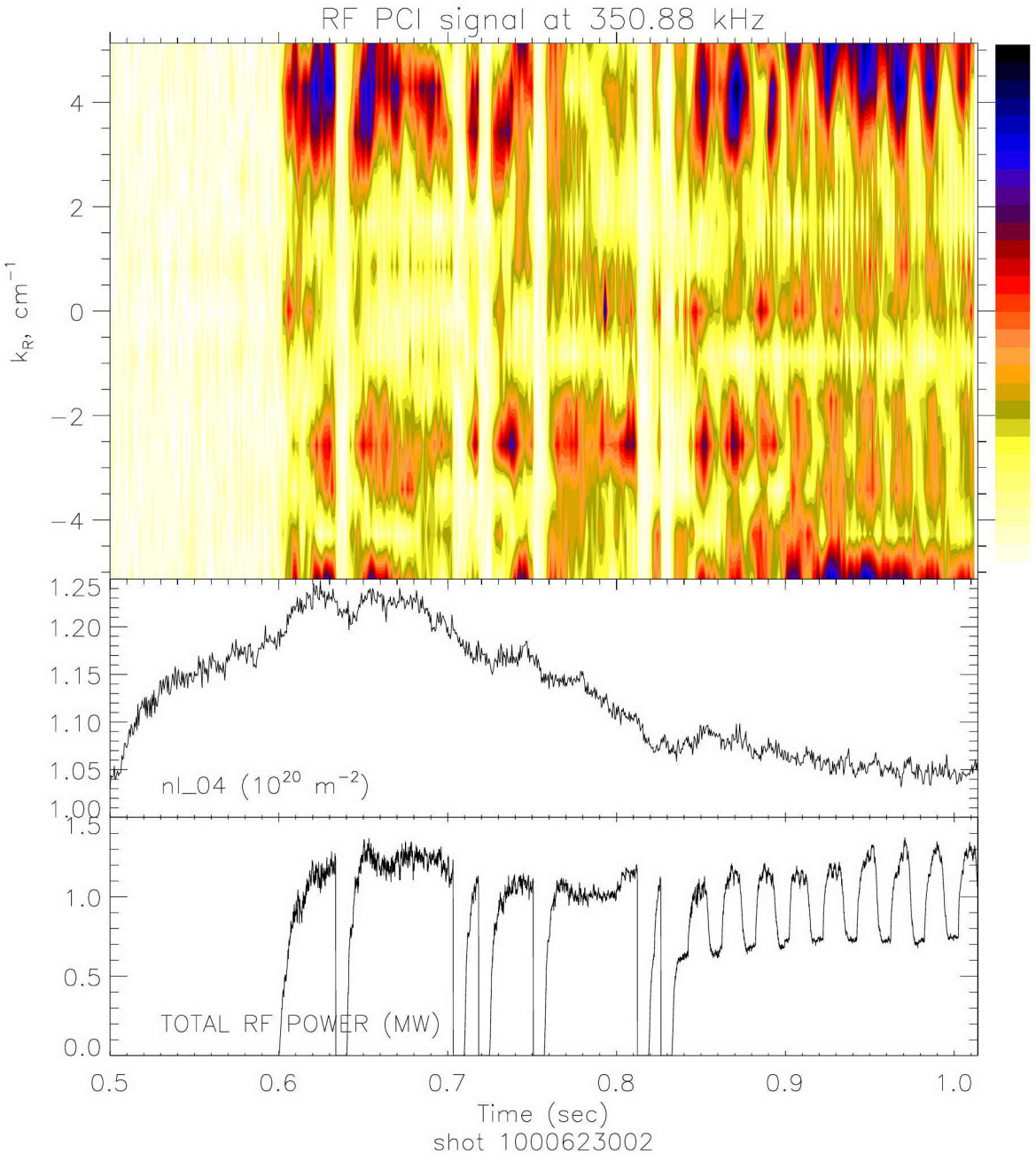

Figure E-4: RF PCI k-spectrum, shot 1000623002. There is an IBW signal from 4 to 5 cm^{-1} during most of the RF pulse.

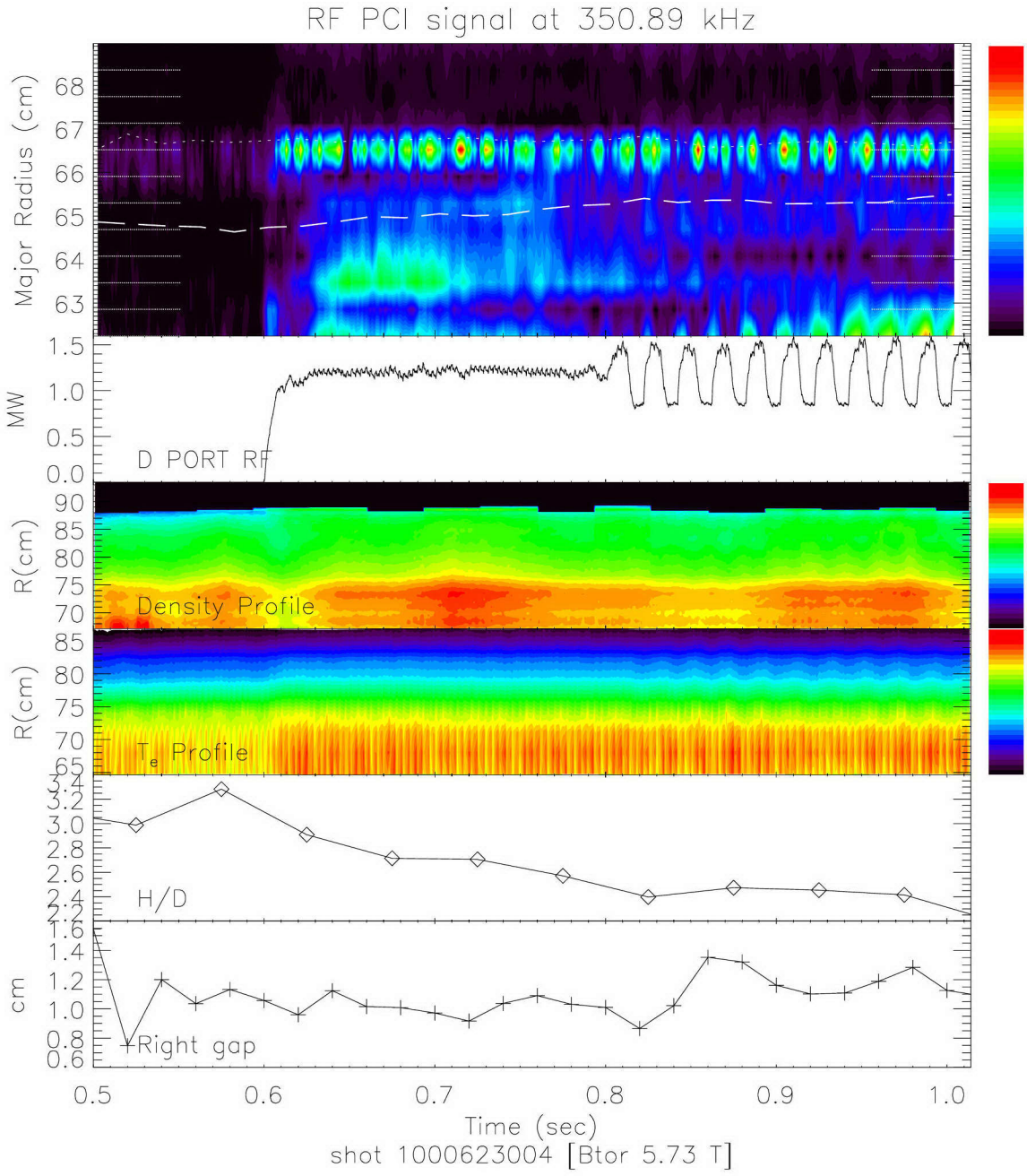

Figure E-5: RF PCI signal amplitude, shot 1000623004. The MC layer has been shifted by 10 cm. MC position uncertainty is ±1.3 cm. There was something wrong with the PCI channel at 66.5 cm for this shot, so the signal there is spurious.

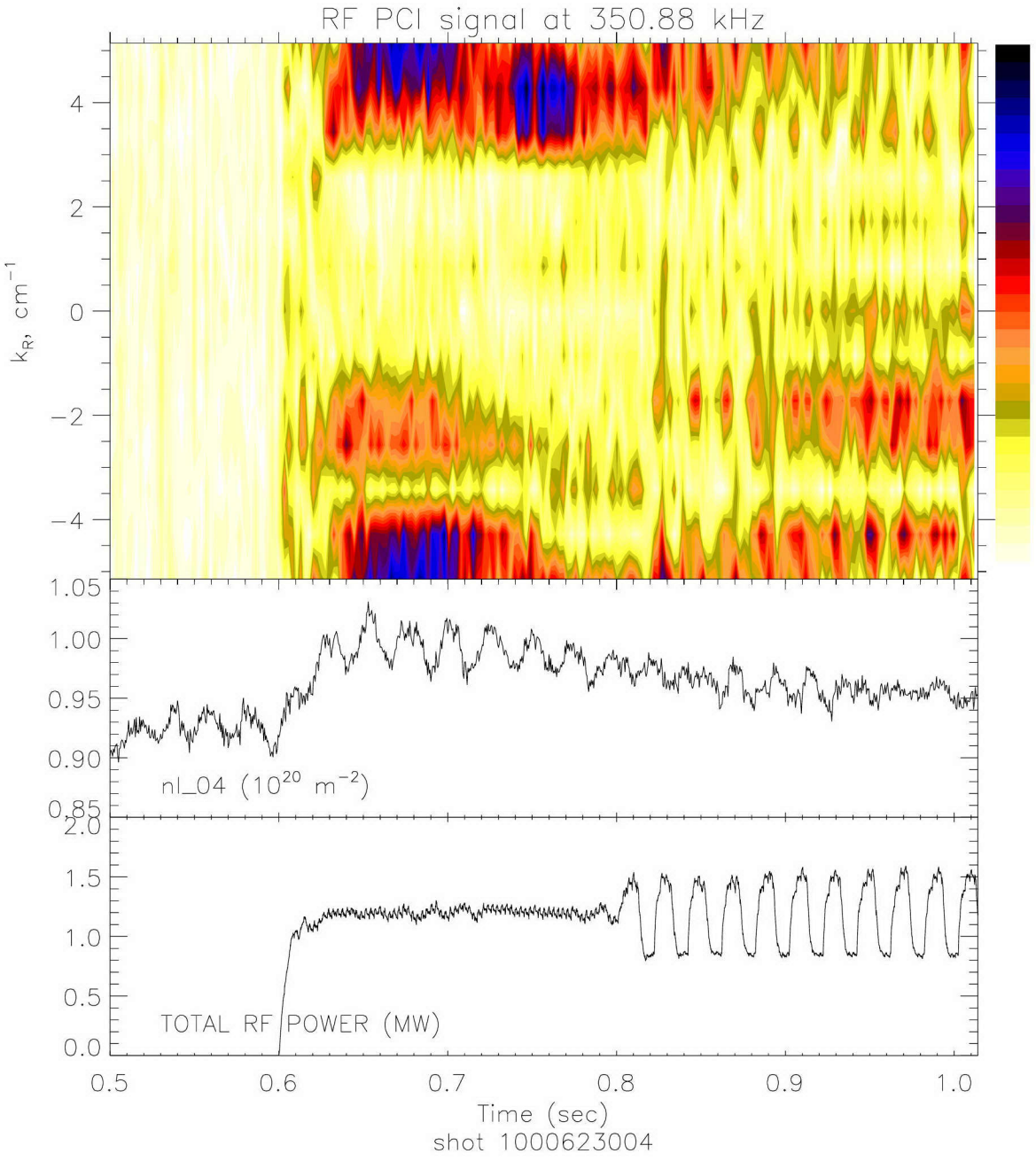

Figure E-6: RF PCI k-spectrum, shot 1000623004. The broad range of signal starting at +3 to +4 cm^{-1} wraps over to -5 and -4 cm^{-1}, due to spatial aliasing.

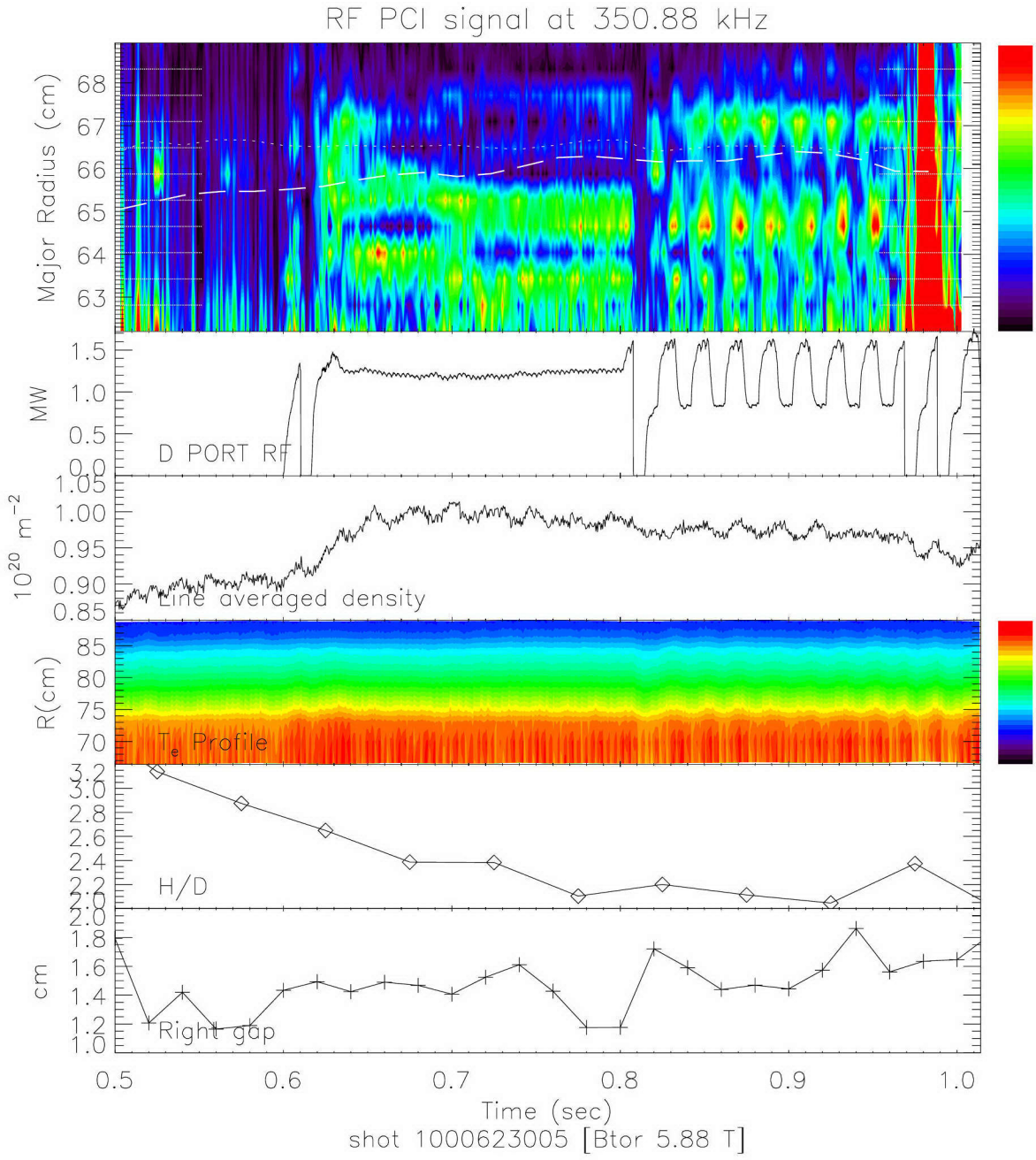

Figure E-7: RF PCI signal amplitude, shot 1000623005. The MC layer has been shifted by 10 cm. MC position uncertainty is ±1.3 cm. There was some laser noise interference, especially after 0.97 sec.

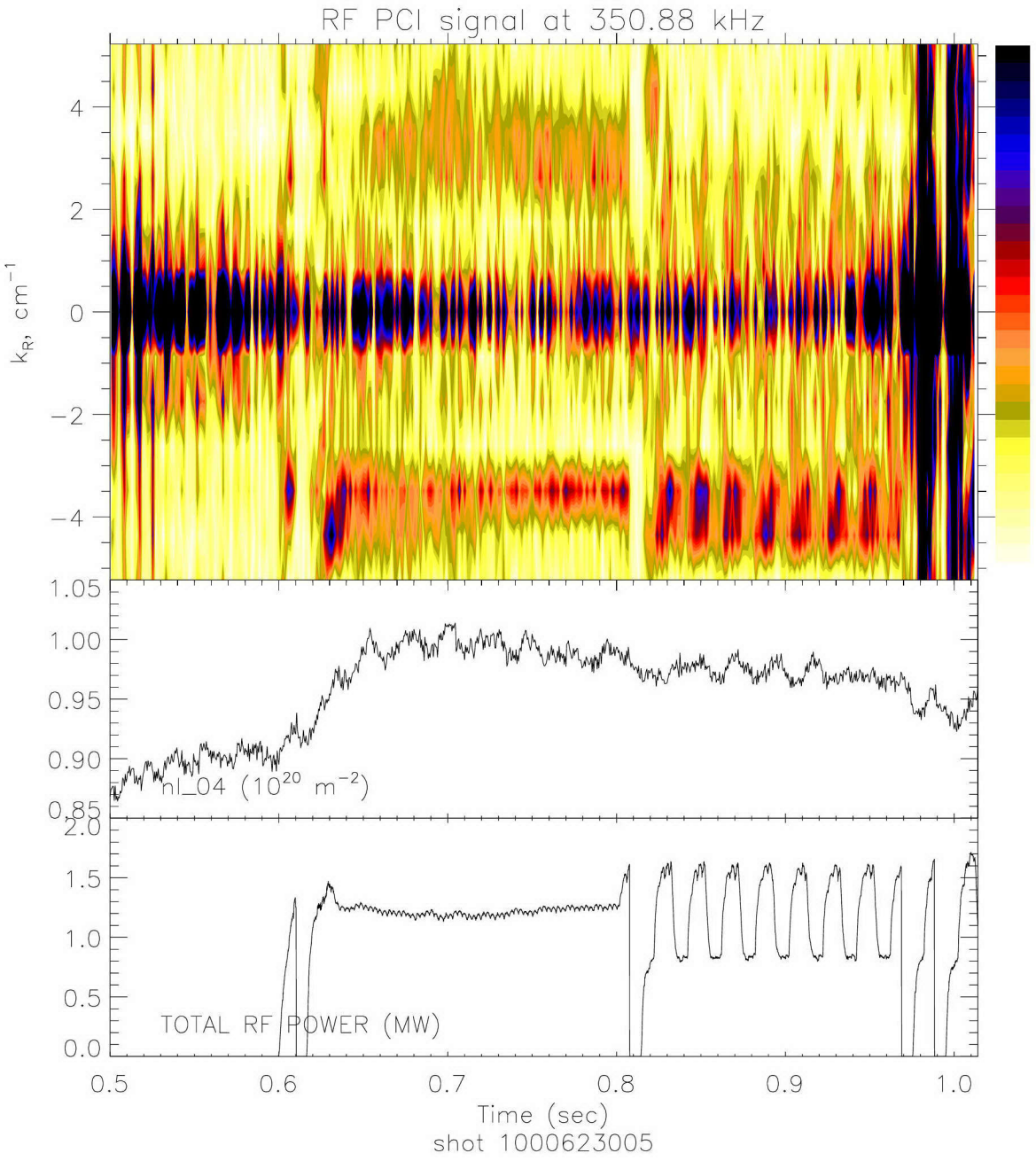

Figure E-8: RF PCI k-spectrum, shot 1000623005. There was some laser noise interference throughout the shot, as can be seen in the $k = 0$ bin. After 0.97 sec, the laser noise became much worse.

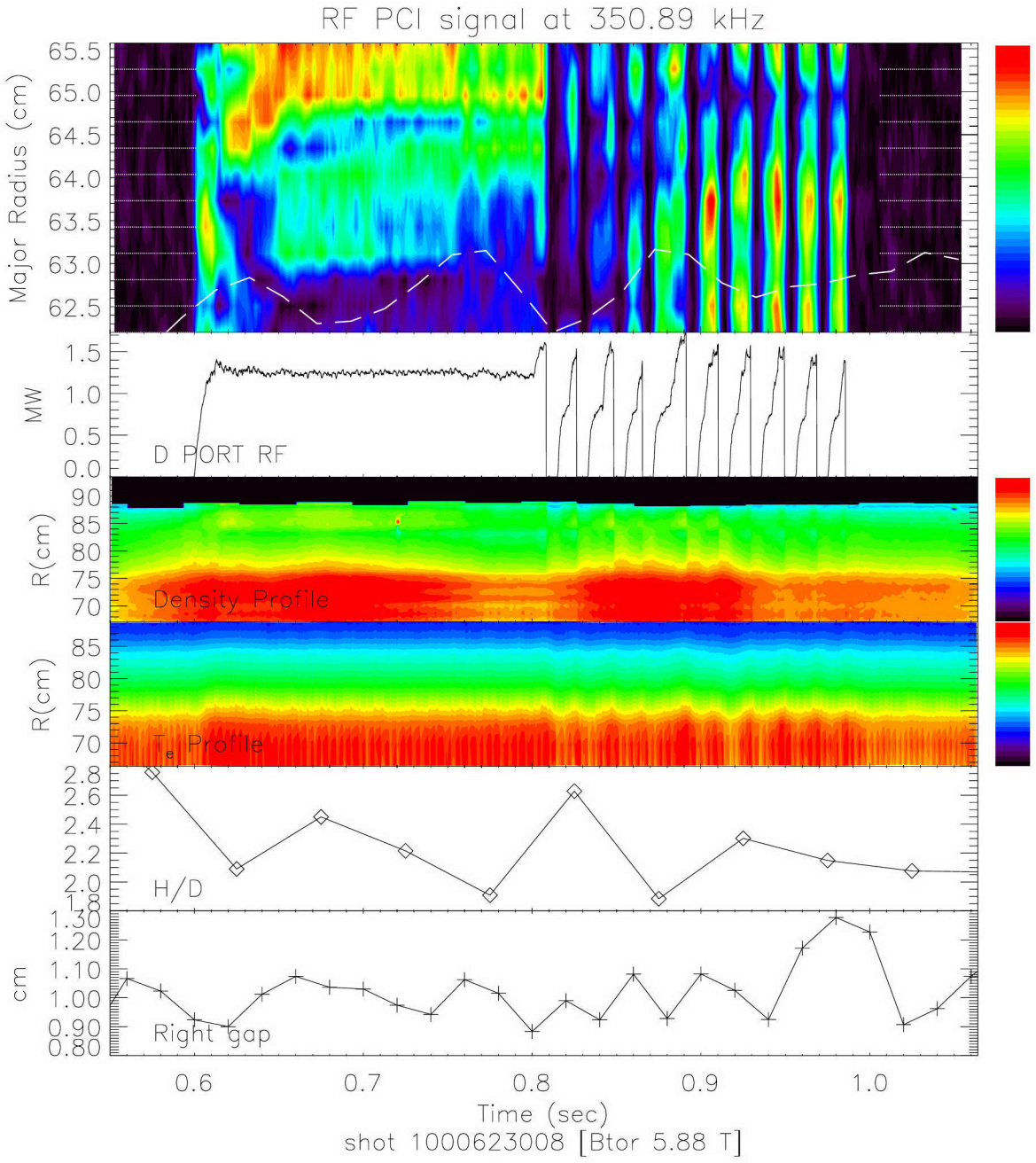

Figure E-9: RF PCI signal amplitude, shot 1000623008. The MC layer has been shifted by 7 cm. MC position uncertainty is ±1.5 cm. The PCI channel spacing has been decreased, so a narrower portion of the plasma is viewed.

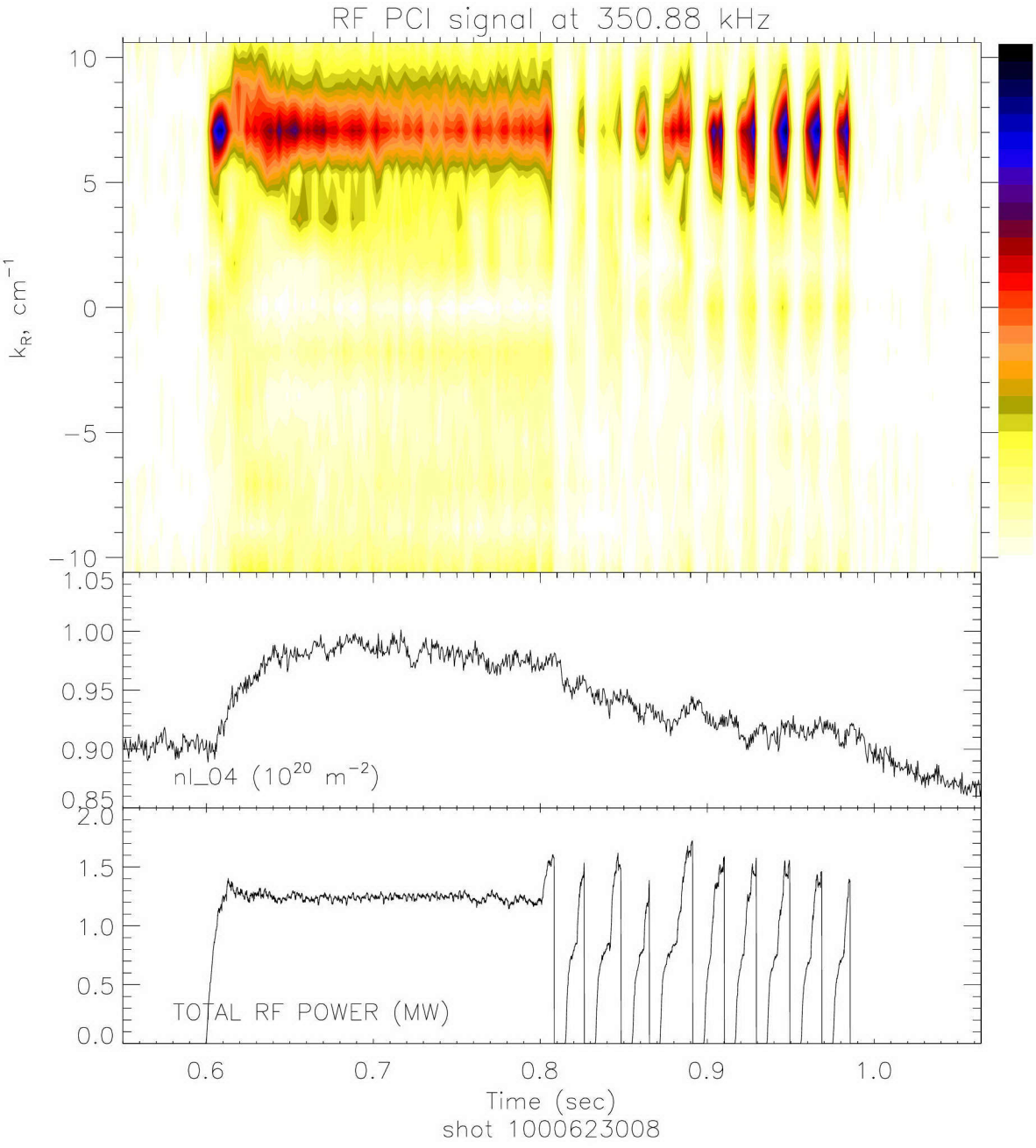

Figure E-10: RF PCI k-spectrum, shot 1000623008. Because the PCI channel spacing was decreased from 0.6 cm to 0.3 cm for this and the next few shots, the k resolution has increased, and the IBW signal is no longer aliased.

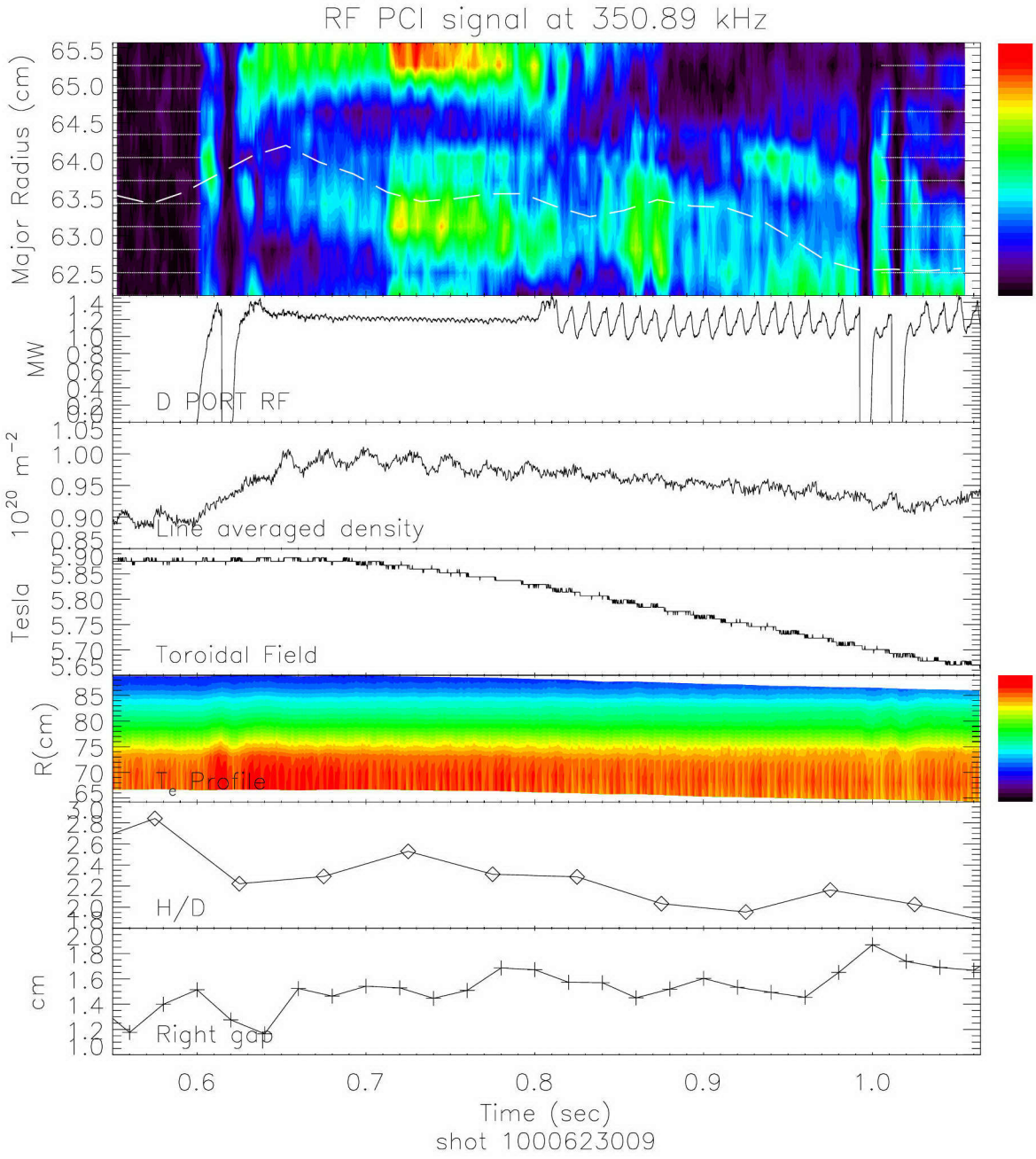

Figure E-11: RF PCI signal amplitude, shot 1000623009. The MC layer has been shifted by 7 cm. MC position uncertainty is ±1.7 cm. There is a toroidal field ramp beginning at 0.7 sec, but the H/D ratio is also changing, so the MC layer movement is not simple. Also, the laser power suddenly increased at 0.71 sec and decreased back to the previous state at 0.82 sec.

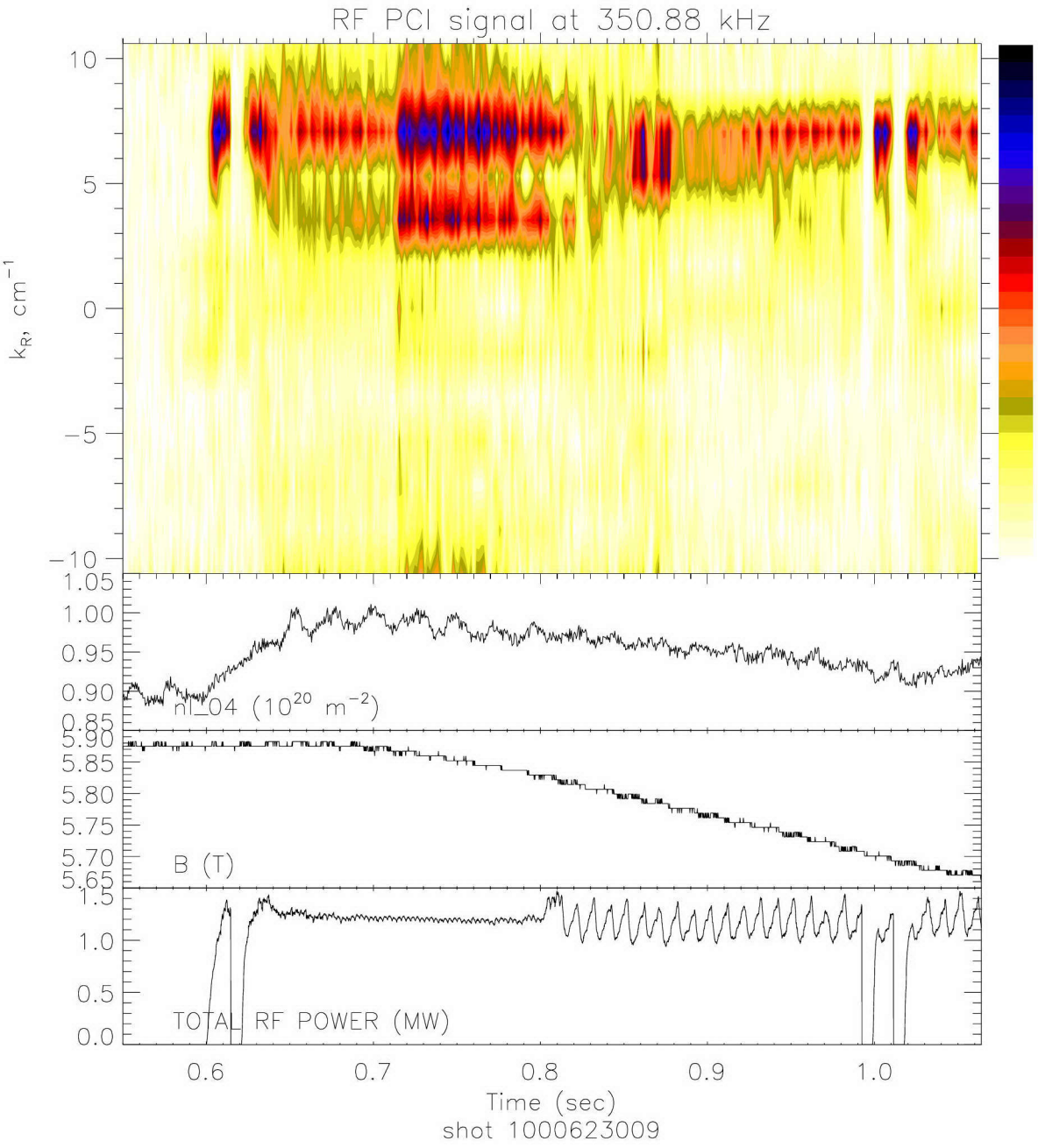

Figure E-12: RF PCI k-spectrum, shot 1000623009. The laser power was higher from the period of 0.71 sec to 0.82 sec, resulting in a stronger PCI signal relative to other times.

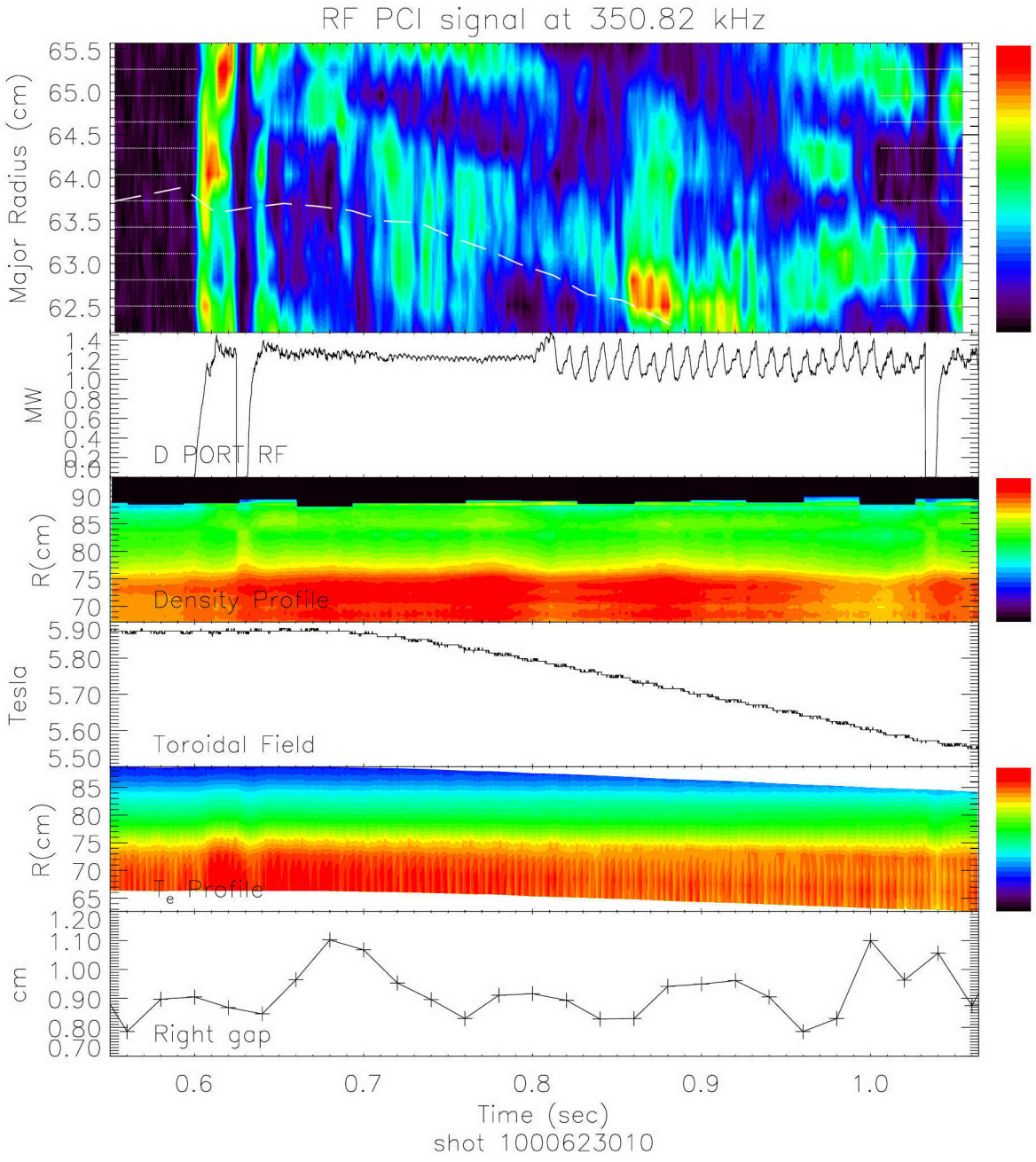

Figure E-13: RF PCI signal amplitude, shot 1000623010. The MC layer has been shifted by 7 cm. MC position uncertainty is ±1 cm. The toroidal field is ramped-down beginning at 0.71 sec.

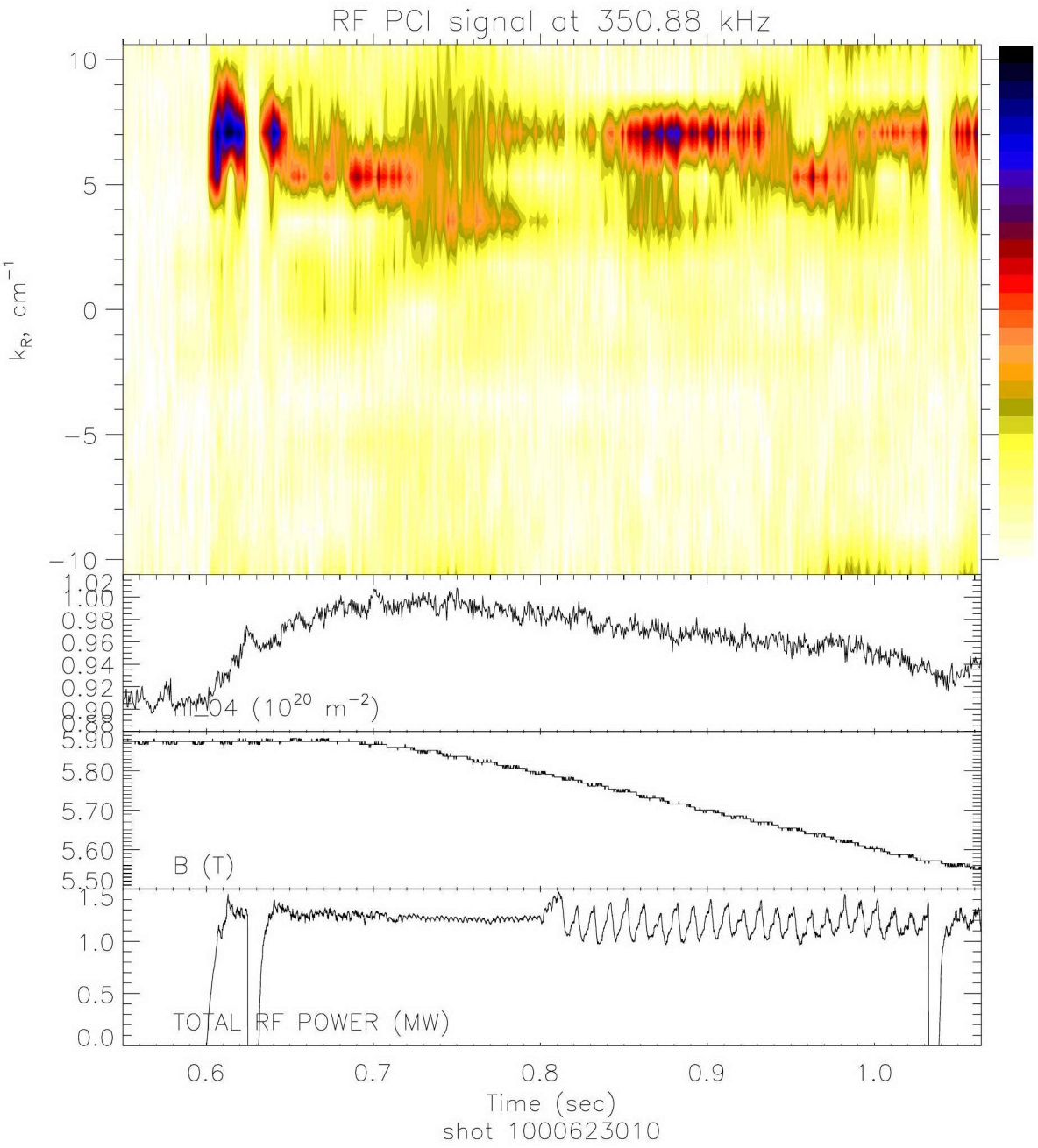

Figure E-14: RF PCI k-spectrum, shot 1000623010.

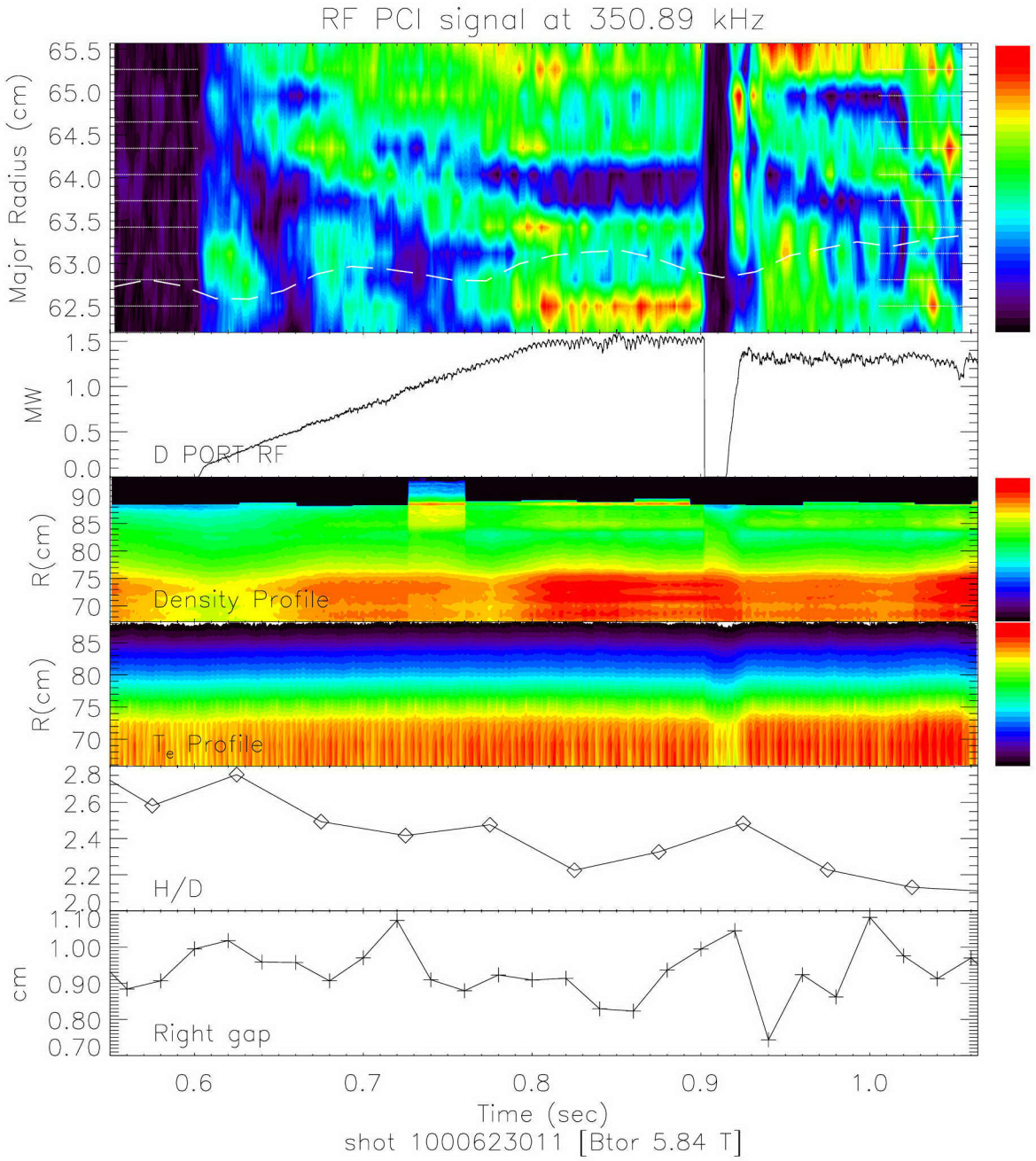

Figure E-15: RF PCI signal amplitude, shot 1000623011. The MC layer has been shifted by 7 cm. MC position uncertainty is ±1 cm.

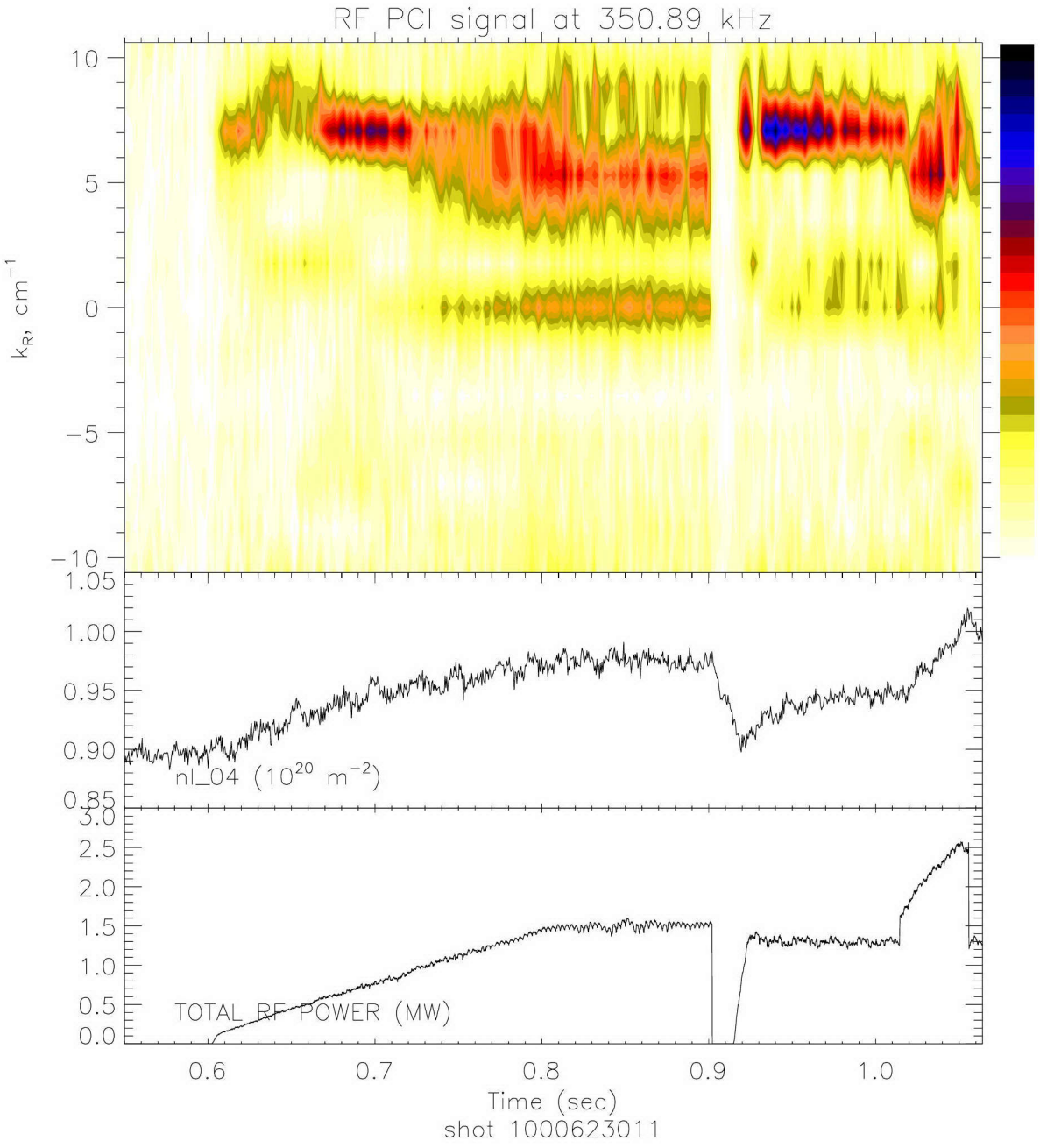

Figure E-16: RF PCI k-spectrum, shot 1000623011. The signal from 0.75 to 0.9 sec in the $k = 0 \pm 0.82$ cm^{-1} bin is possibly due to the fast wave.

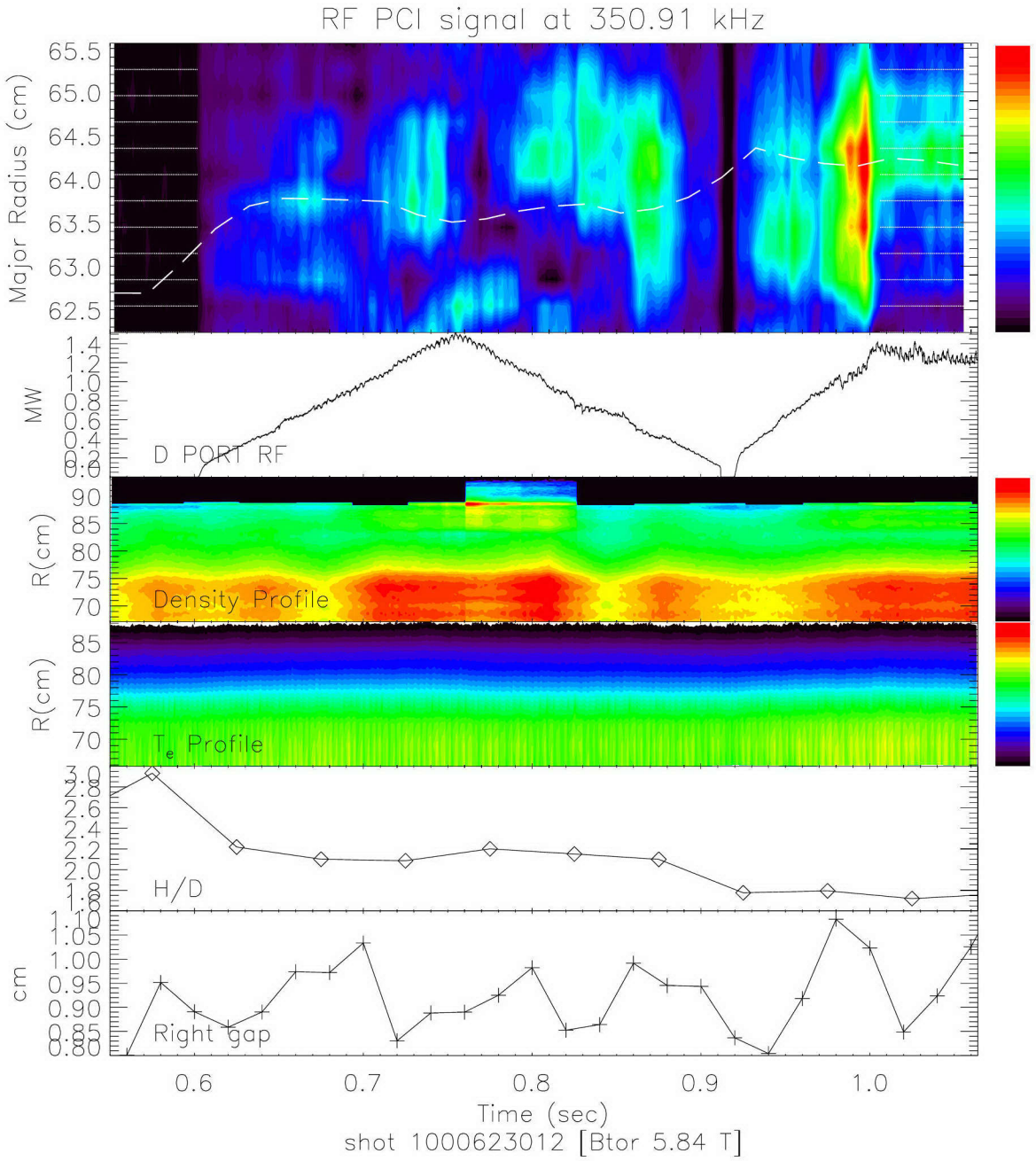

Figure E-17: RF PCI signal amplitude, shot 1000623012. The MC layer has been shifted by 10 cm. MC position uncertainty is ±0.8 cm.

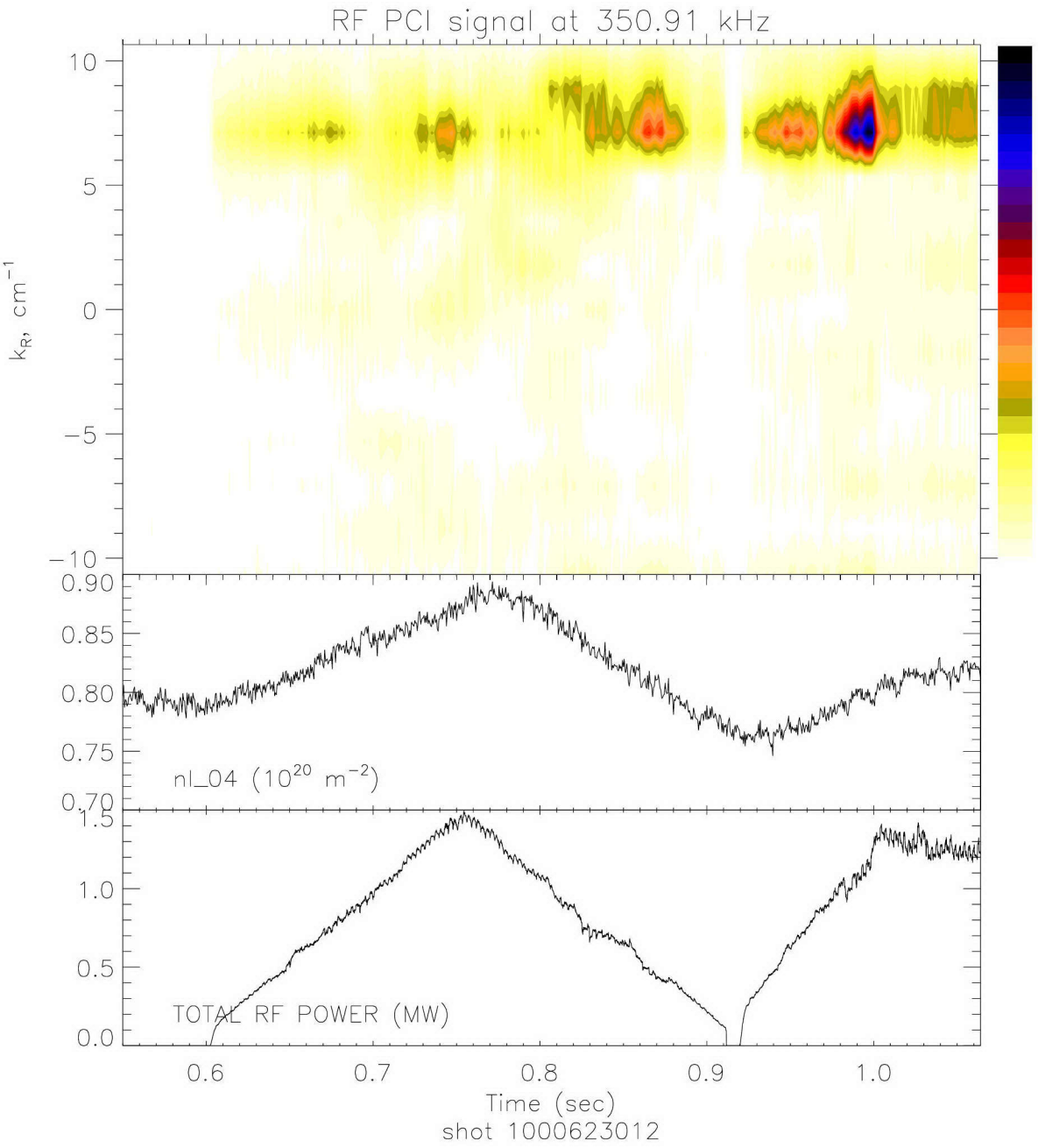

Figure E-18: RF PCI k-spectrum, shot 1000623012.

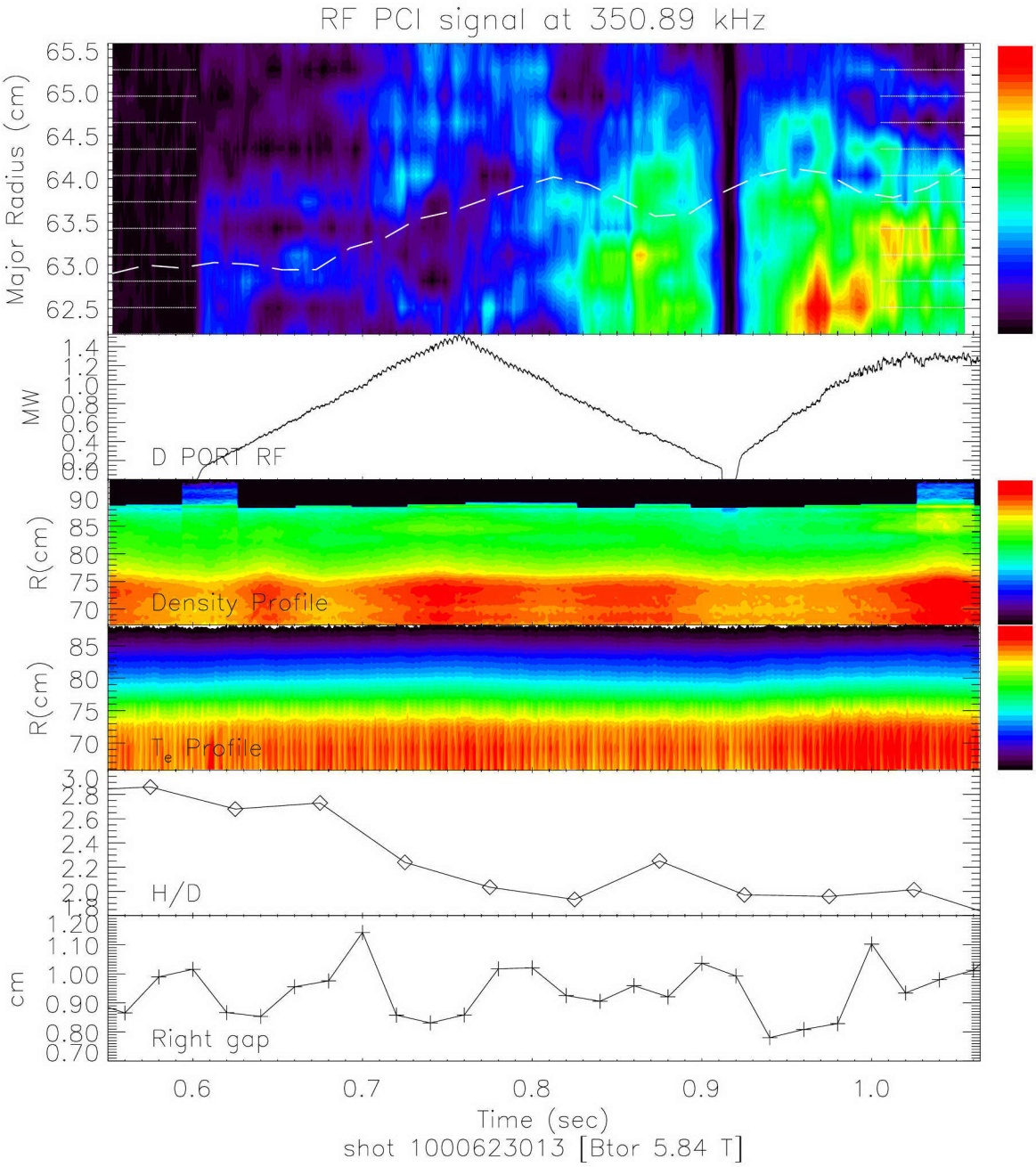

Figure E-19: RF PCI signal amplitude, shot 1000623013. The MC layer has been shifted by 10 cm. MC position uncertainty is ±0.9 cm.

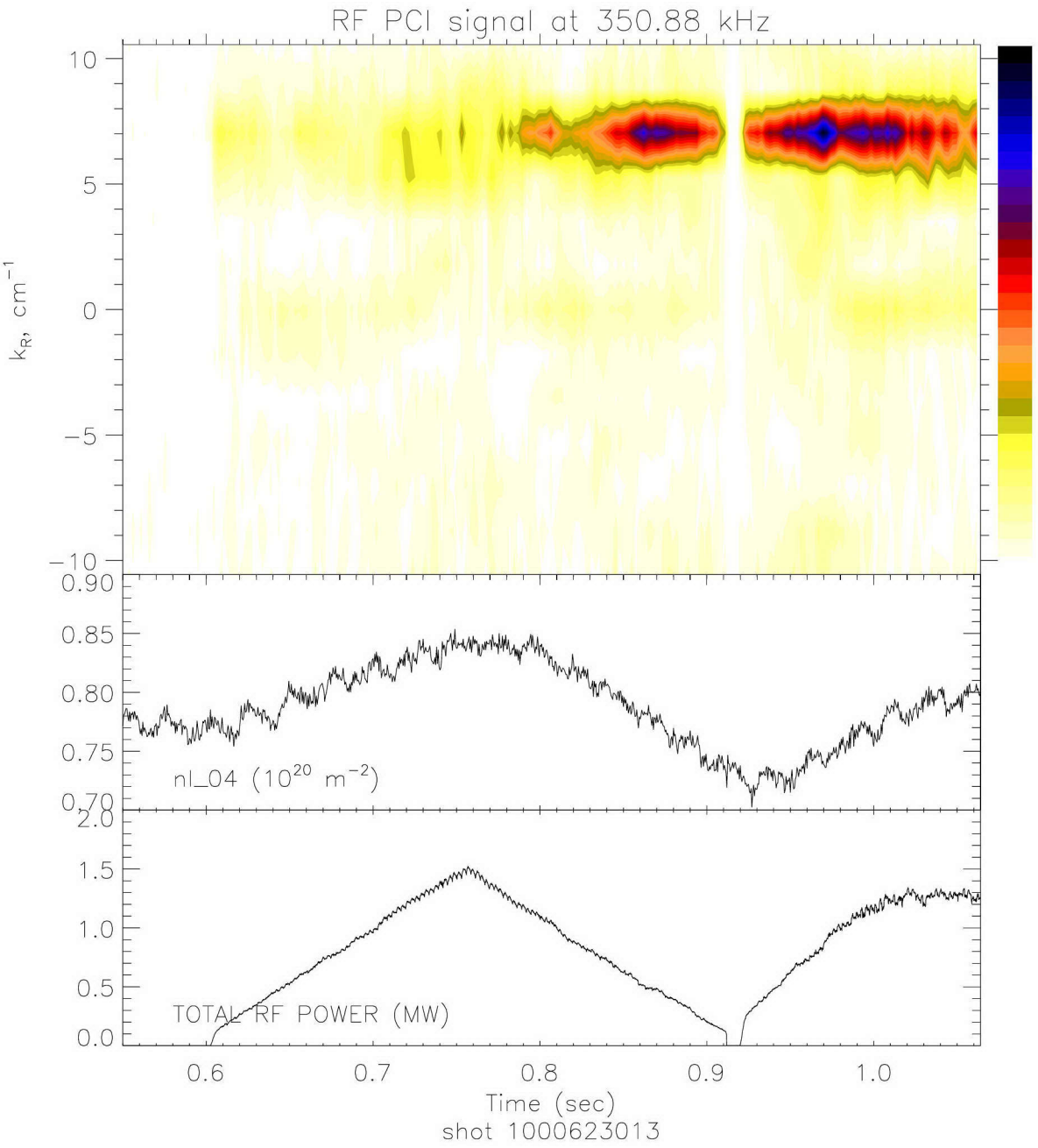

Figure E-20: RF PCI k-spectrum, shot 1000623013.

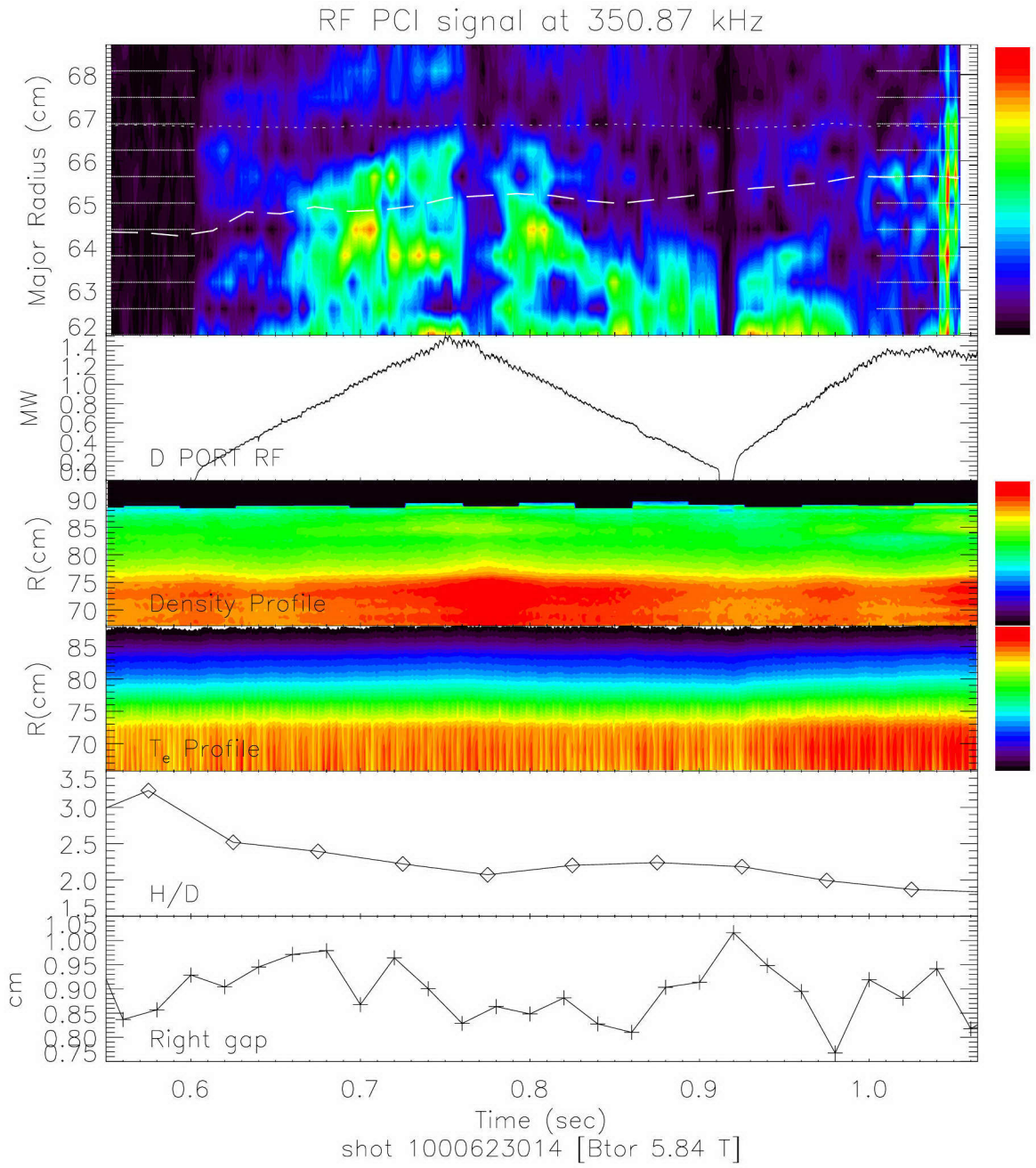

Figure E-21: RF PCI signal amplitude, shot 1000623014. The MC layer has been shifted by 12 cm. MC position uncertainty is ±1.5 cm. Note how the cold plasma MC layer position remains roughly the same while the PCI signal moves further to the LFS as the power ramps up. This may have something to do with temperature dependent IBW propagation characteristics.

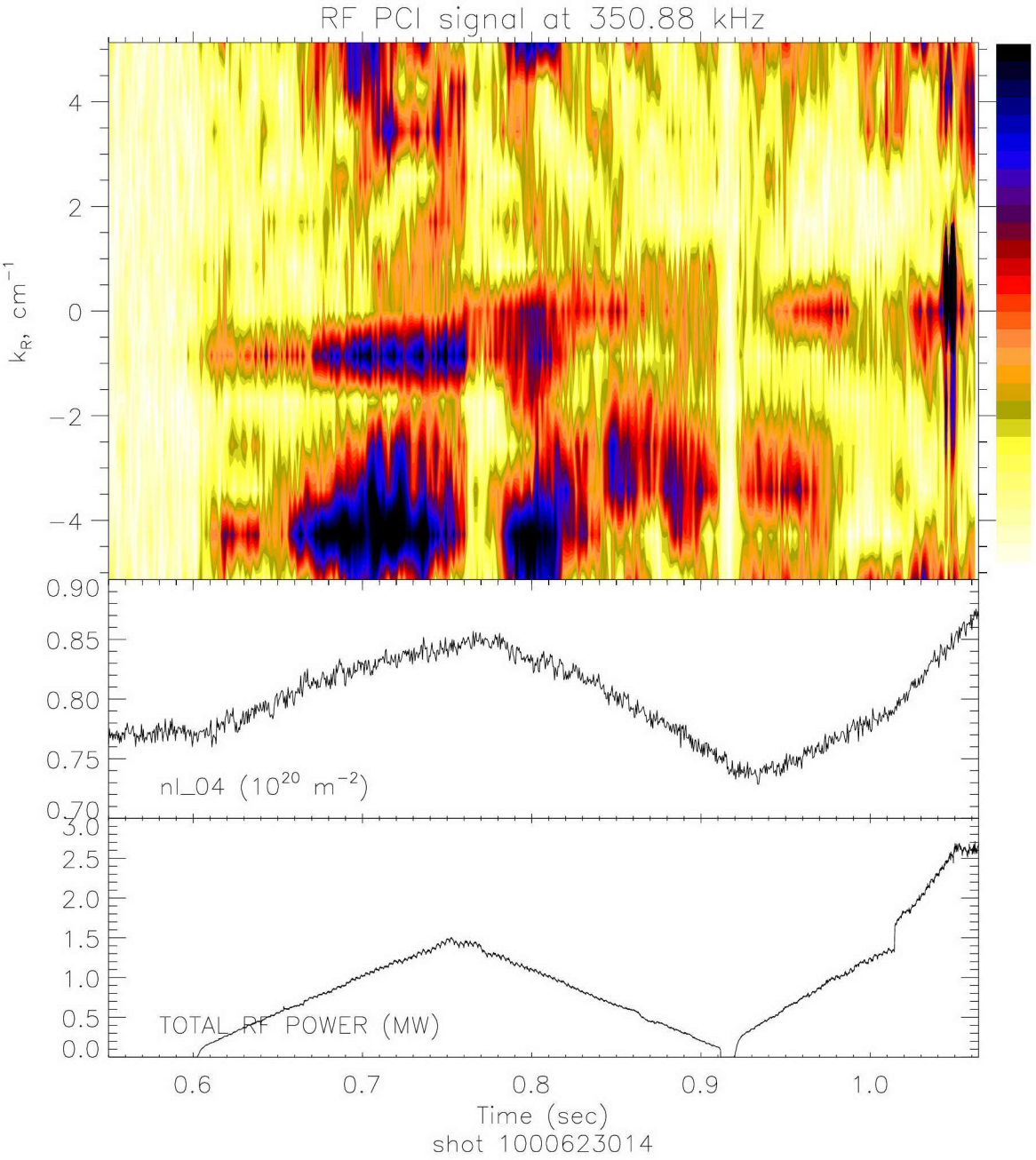

Figure E-22: RF PCI k-spectrum, shot 1000623014. Both a fast wave and IBW are discernible between 0.62 and 0.82 sec.

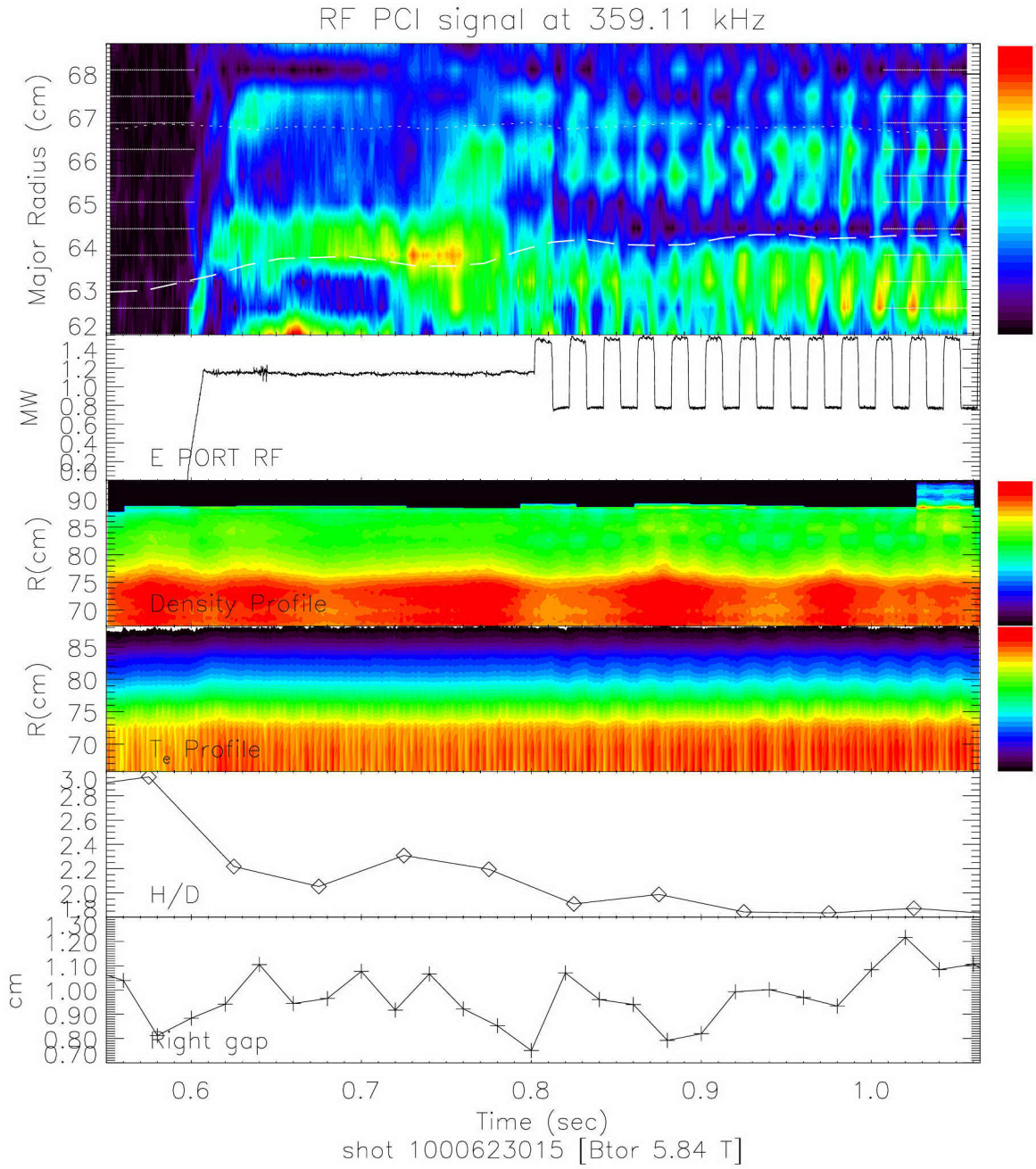

Figure E-23: RF PCI signal amplitude, shot 1000623015. The MC layer has been shifted by 10 cm. MC position uncertainty is ±1.5 cm.

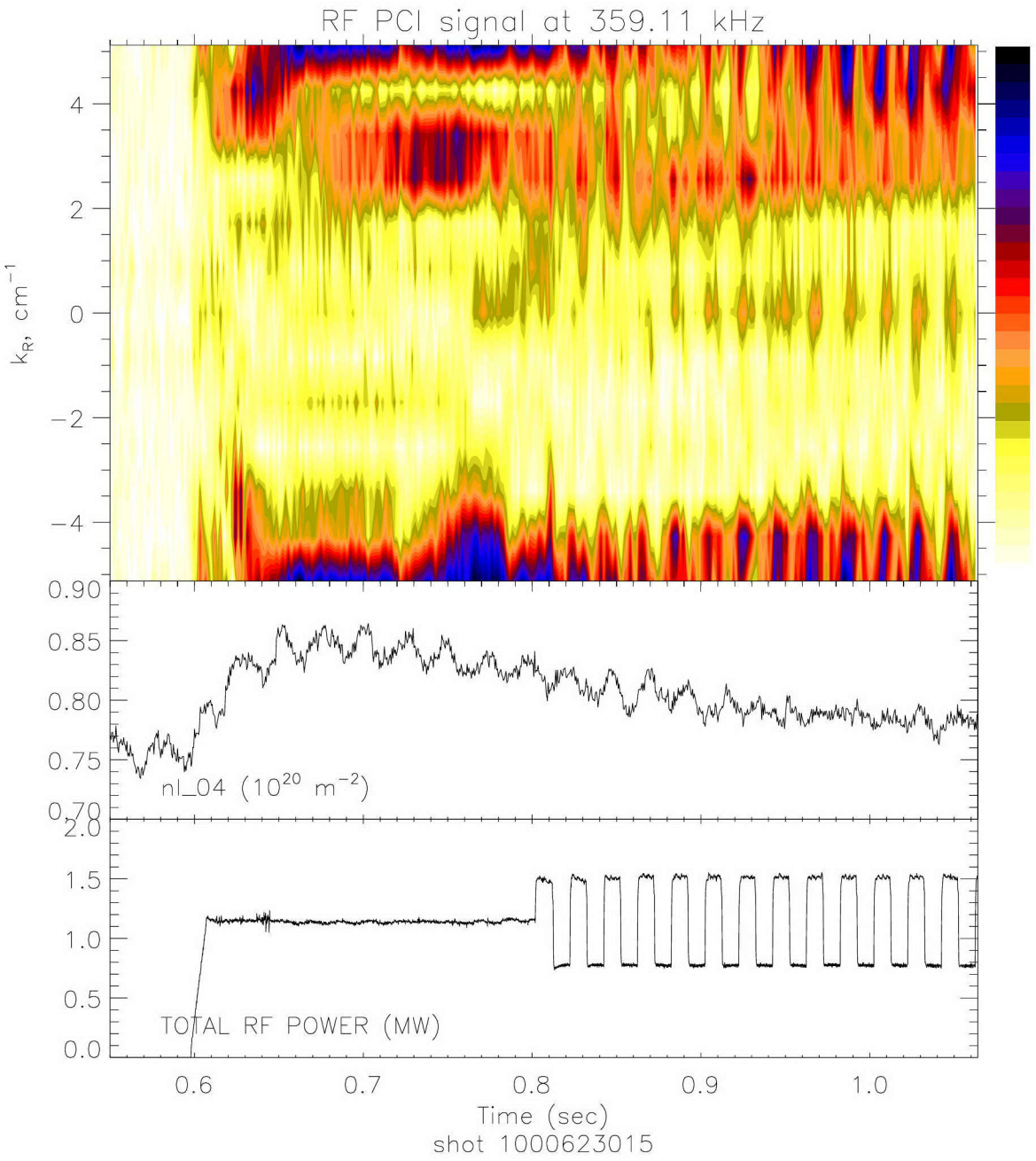

Figure E-24: RF PCI k-spectrum, shot 1000623015.

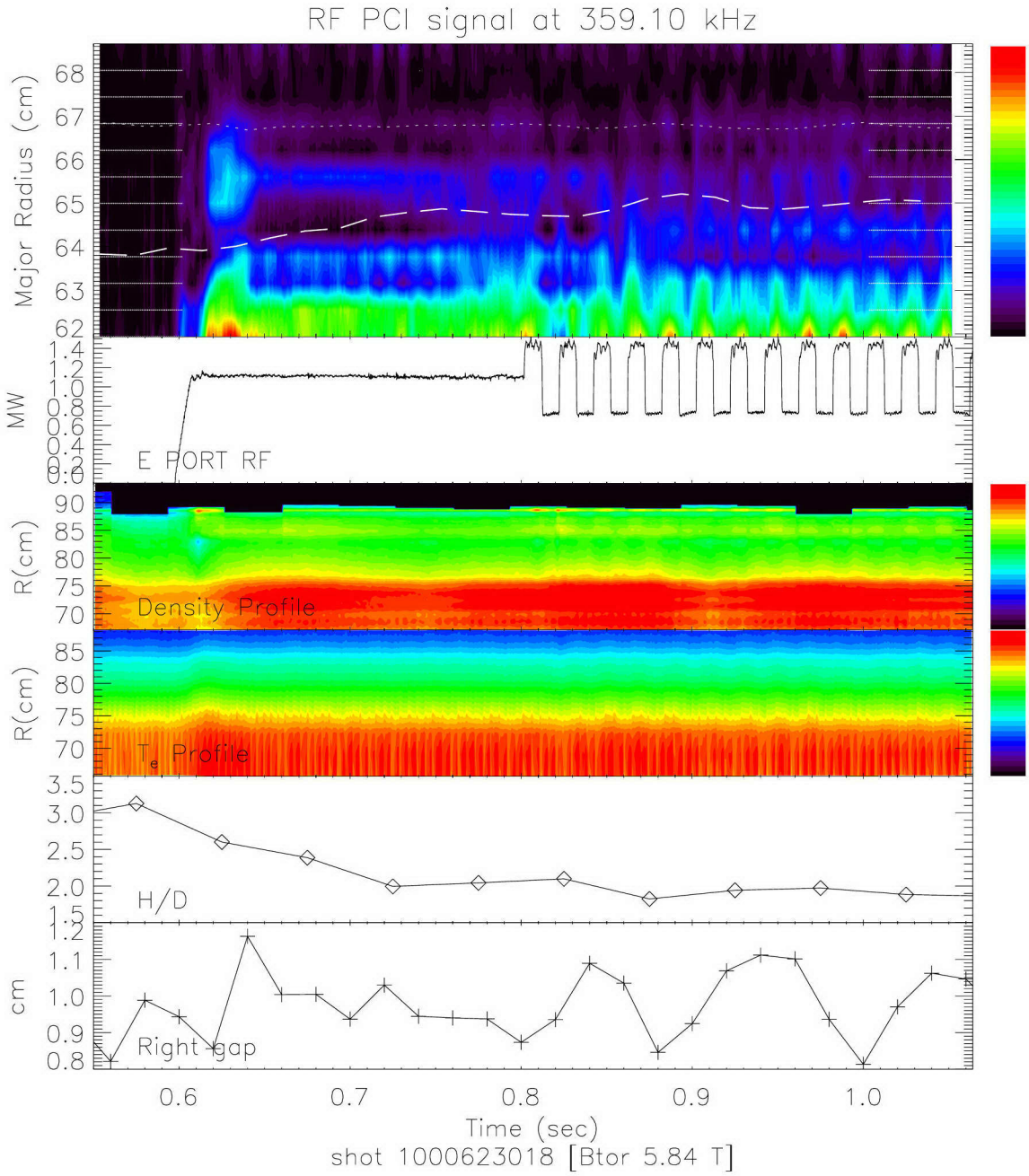

Figure E-25: RF PCI signal amplitude, shot 1000623018. The MC layer has been shifted by 9 cm. MC position uncertainty is ±1.7 cm.

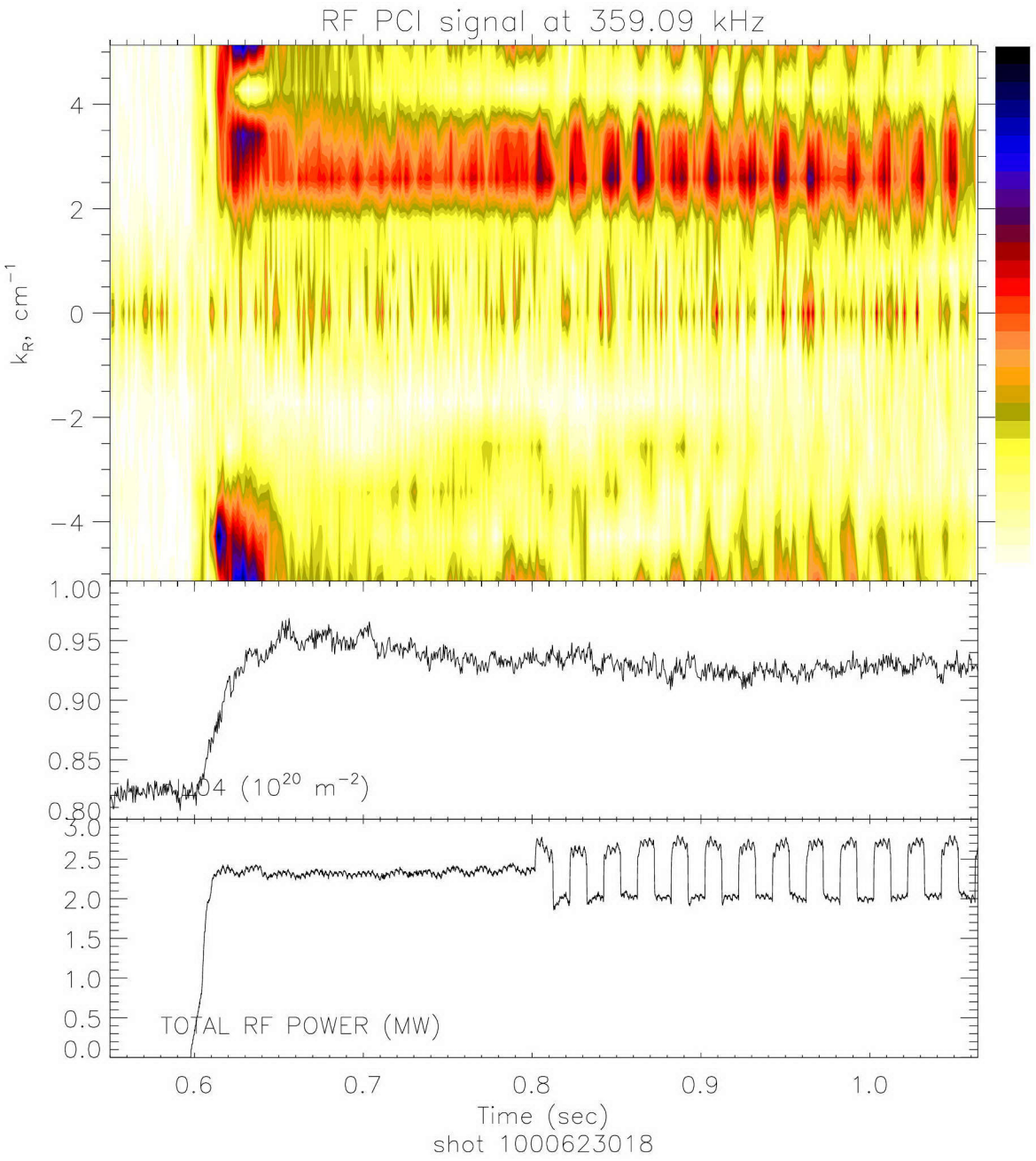

Figure E-26: RF PCI k-spectrum, shot 1000623018.

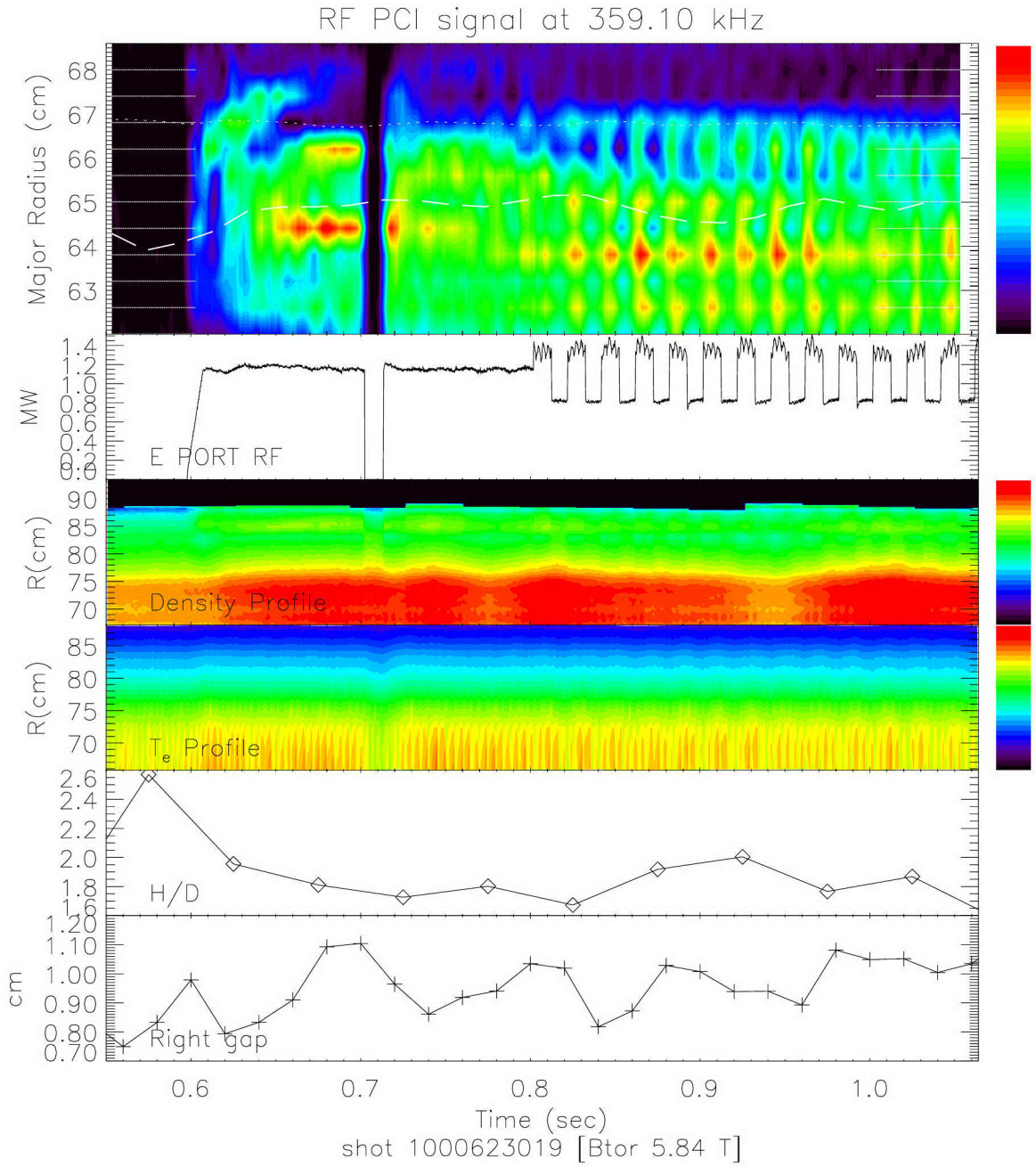

Figure E-27: RF PCI signal amplitude, shot 1000623019. The MC layer has been shifted by 9 cm. MC position uncertainty is ±1.4 cm.

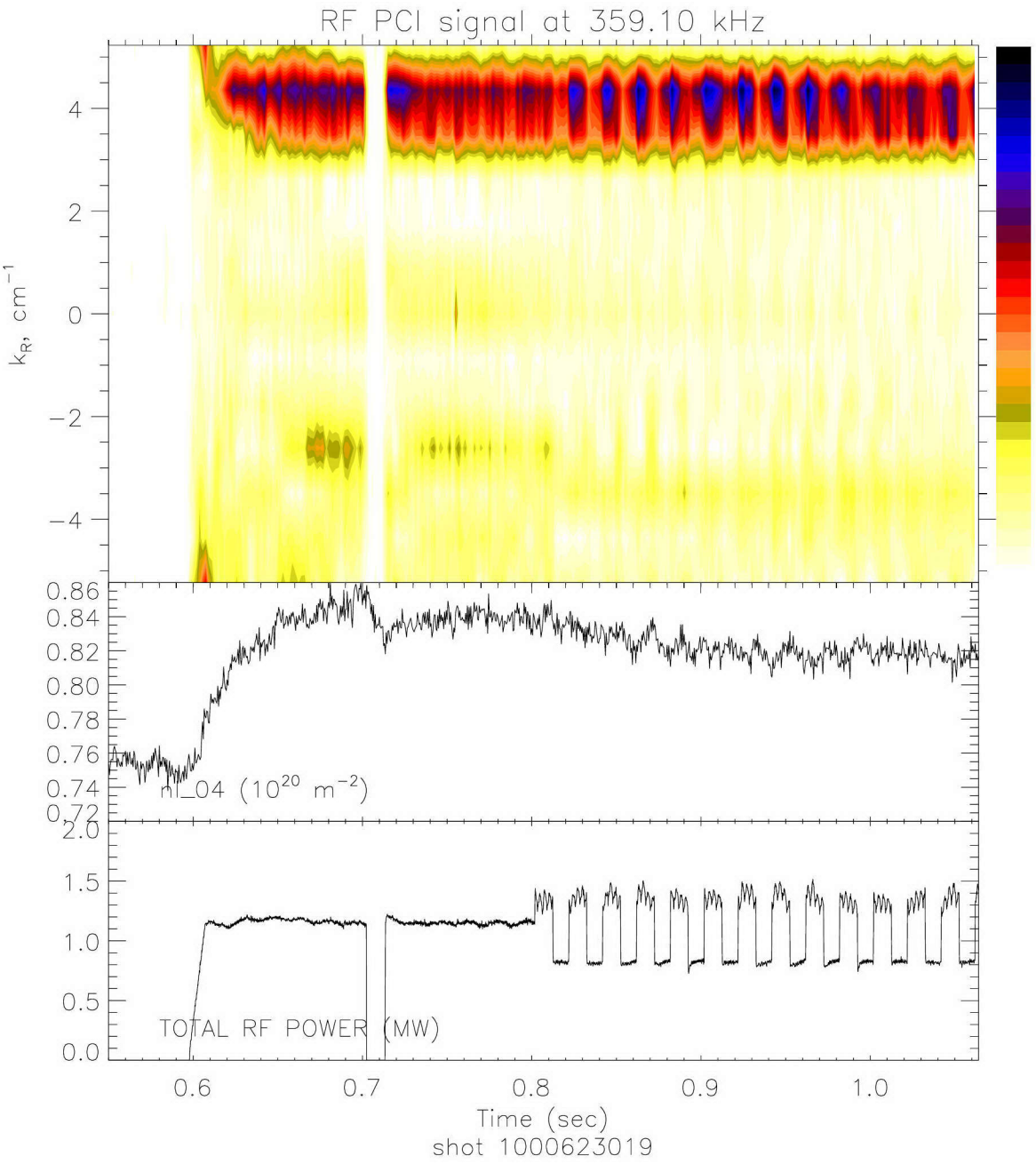

Figure E-28: RF PCI k-spectrum, shot 1000623019.

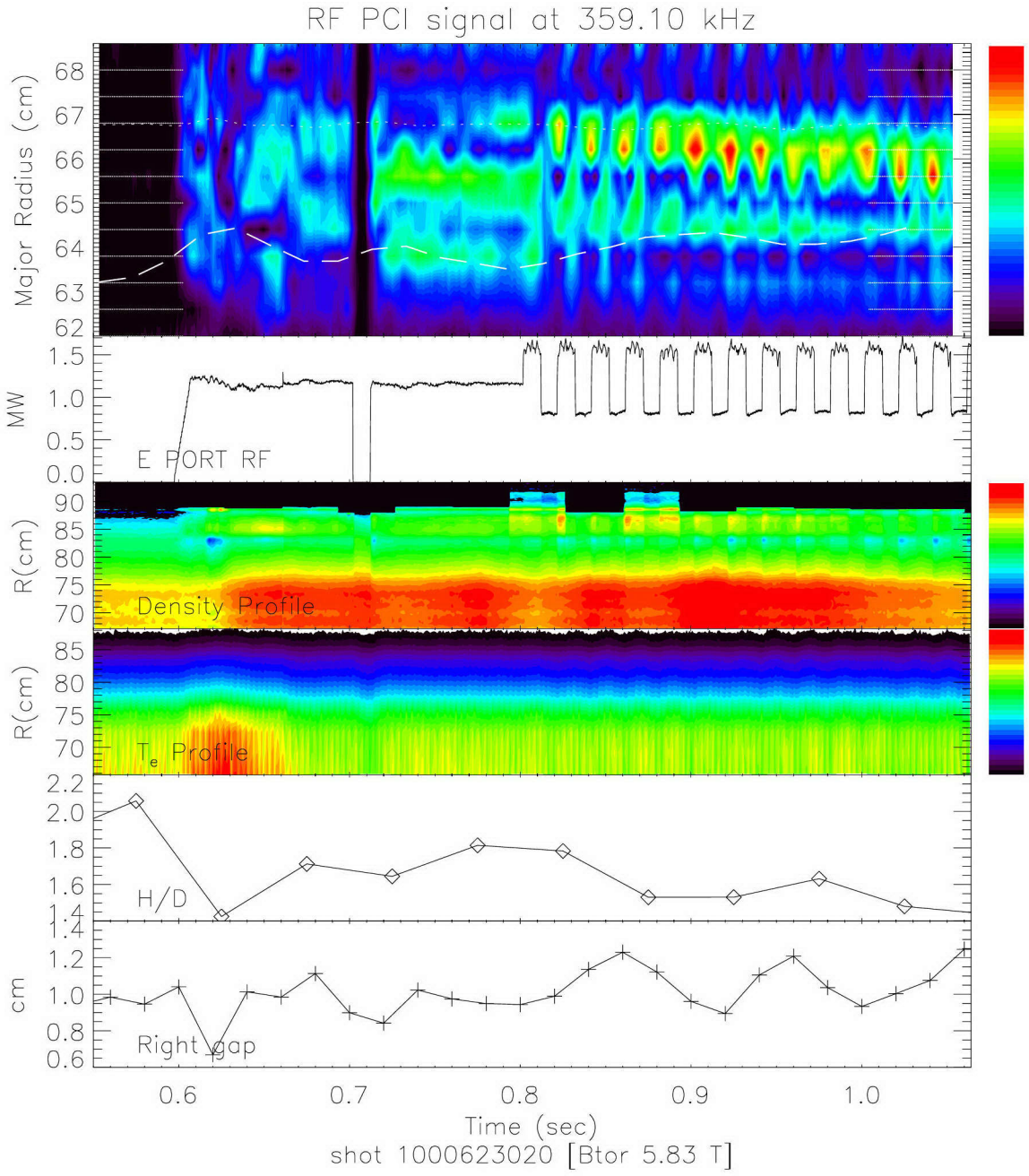

Figure E-29: RF PCI signal amplitude, shot 1000623020 (for the expected RF frequency from the E-port antenna, directly in front of the PCI). The MC layer has been shifted by 7 cm. MC position uncertainty is ±1.5 cm.

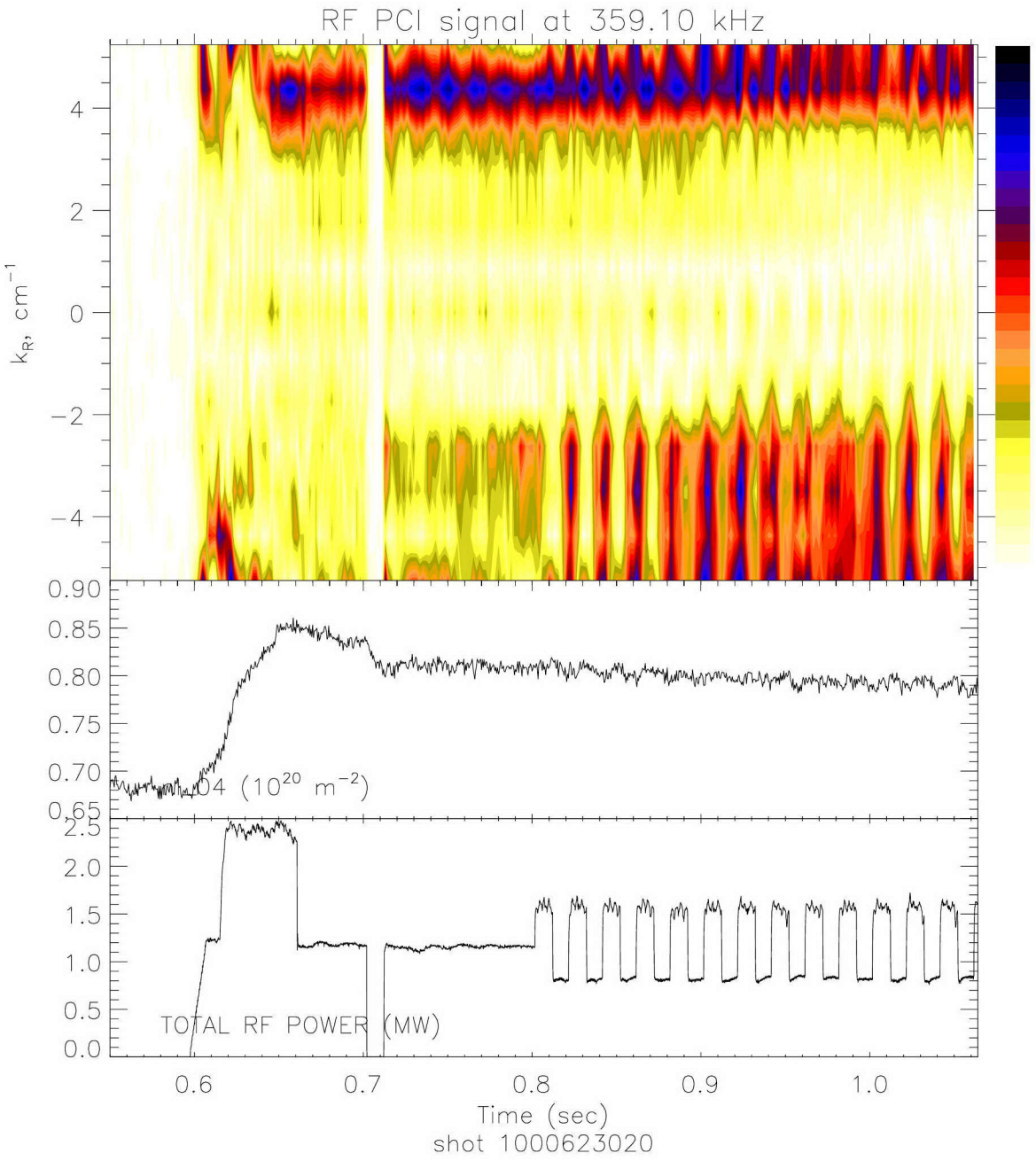

Figure E-30: RF PCI k-spectrum, shot 1000623020 (E-port).

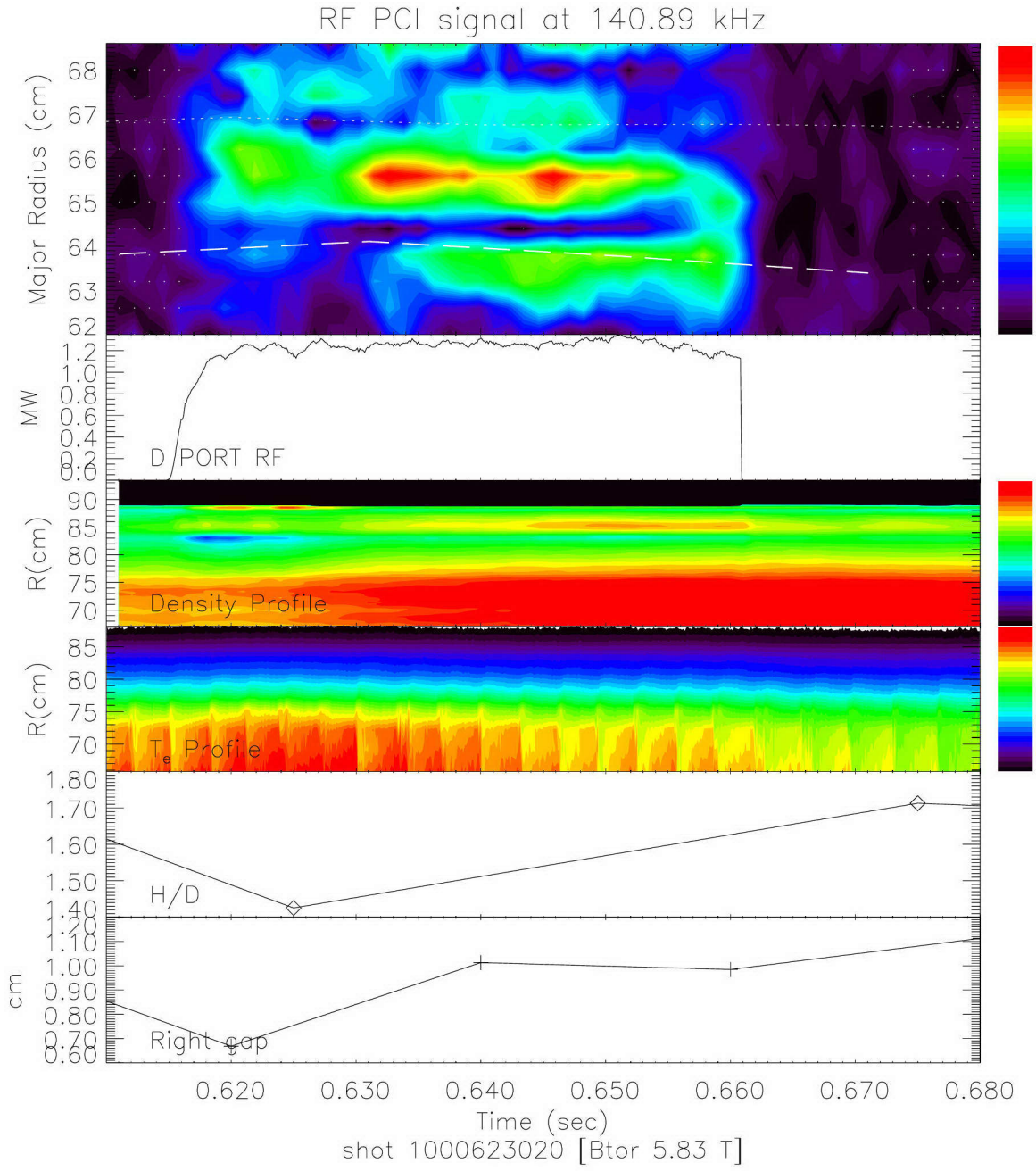

Figure E-31: RF PCI signal amplitude, shot 1000623020 (for the expected RF frequency from the D-port antenna, 36° away from the PCI). The MC layer has been shifted by 7 cm. MC position uncertainty is ±1.4 cm.

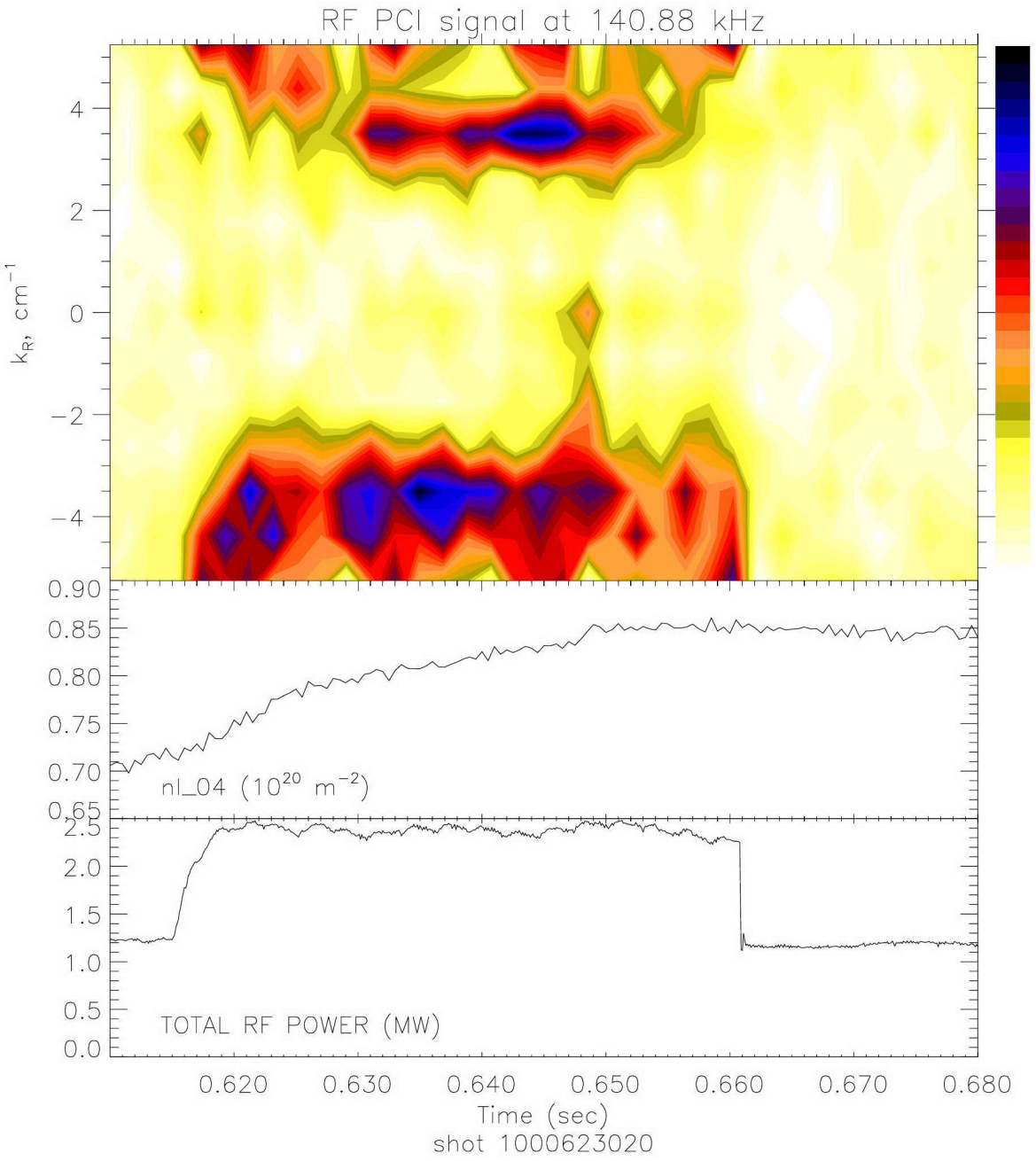

Figure E-32: RF PCI k-spectrum, shot 1000623020 (D-port).

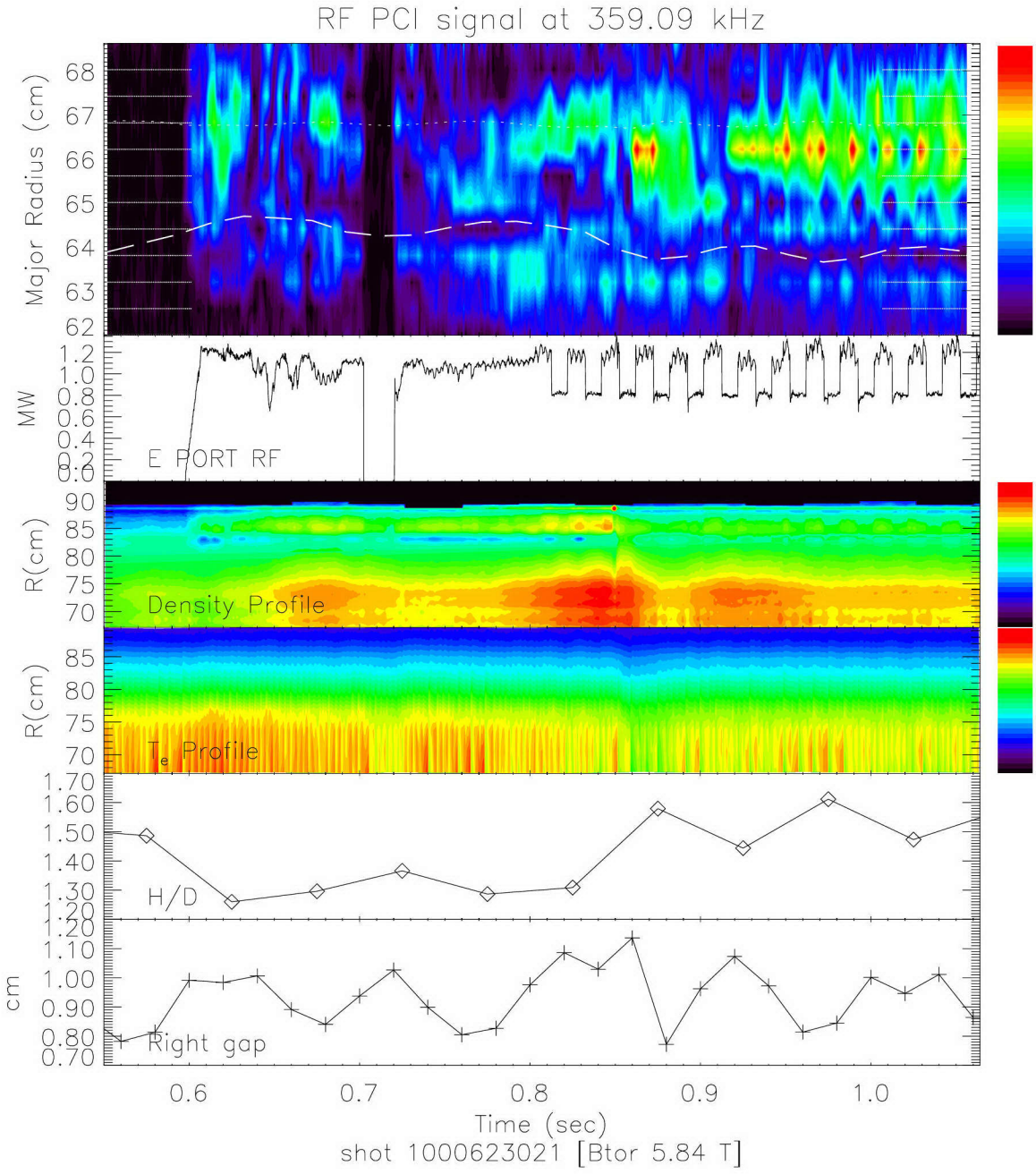

Figure E-33: RF PCI signal amplitude, shot 1000623021 (for the expected RF frequency from the E-port antenna, directly in front of the PCI). The MC layer has been shifted by 7 cm. MC position uncertainty is ±1.9 cm. Shot 21 is very similar to shot 20 except that the plasma current has been increased from 800 kA to 1 MA.

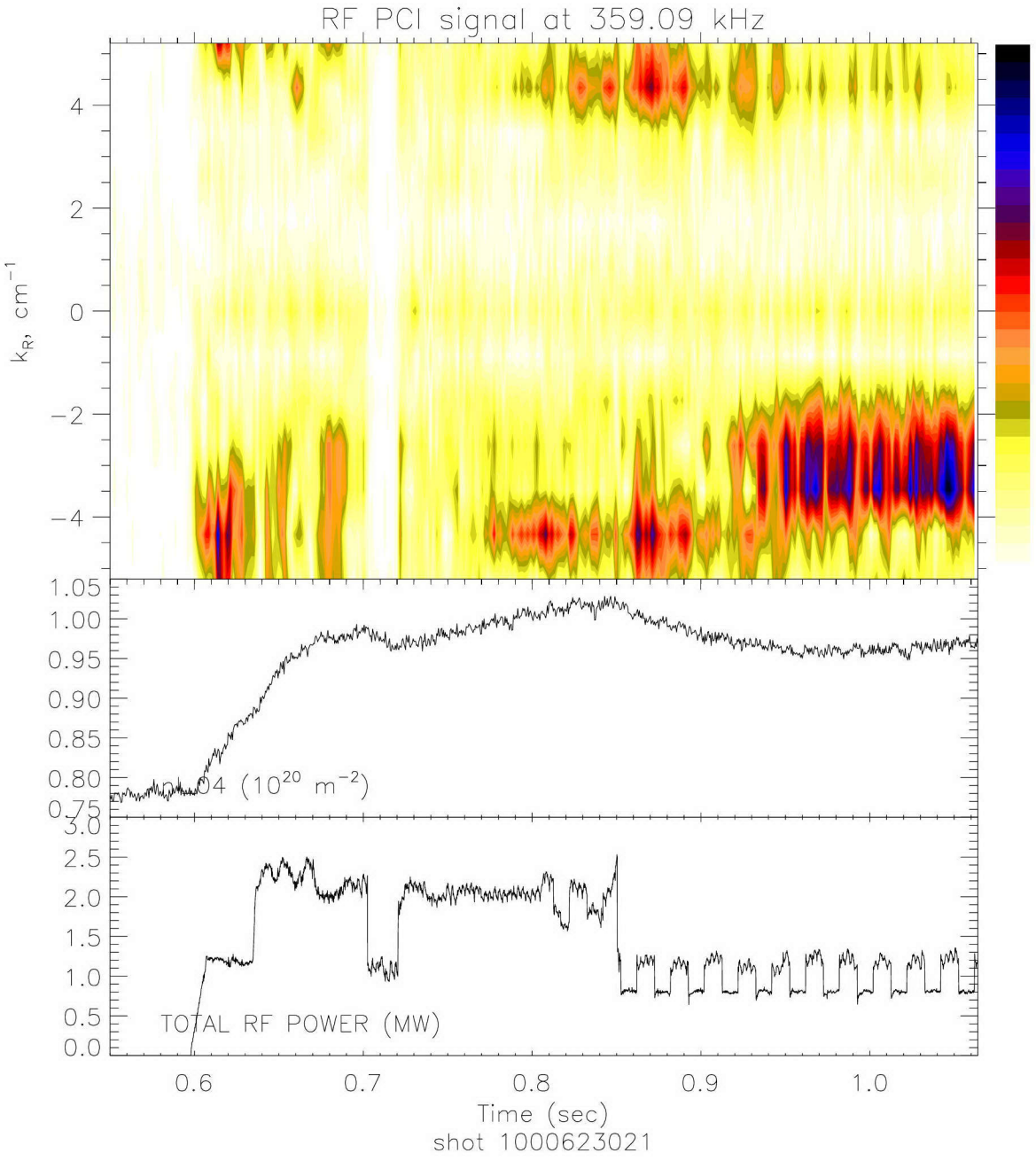

Figure E-34: RF PCI k-spectrum, shot 1000623021 (E-port). Shot 21 is very similar to shot 20 except that the plasma current has been increased from 800 kA to 1 MA.

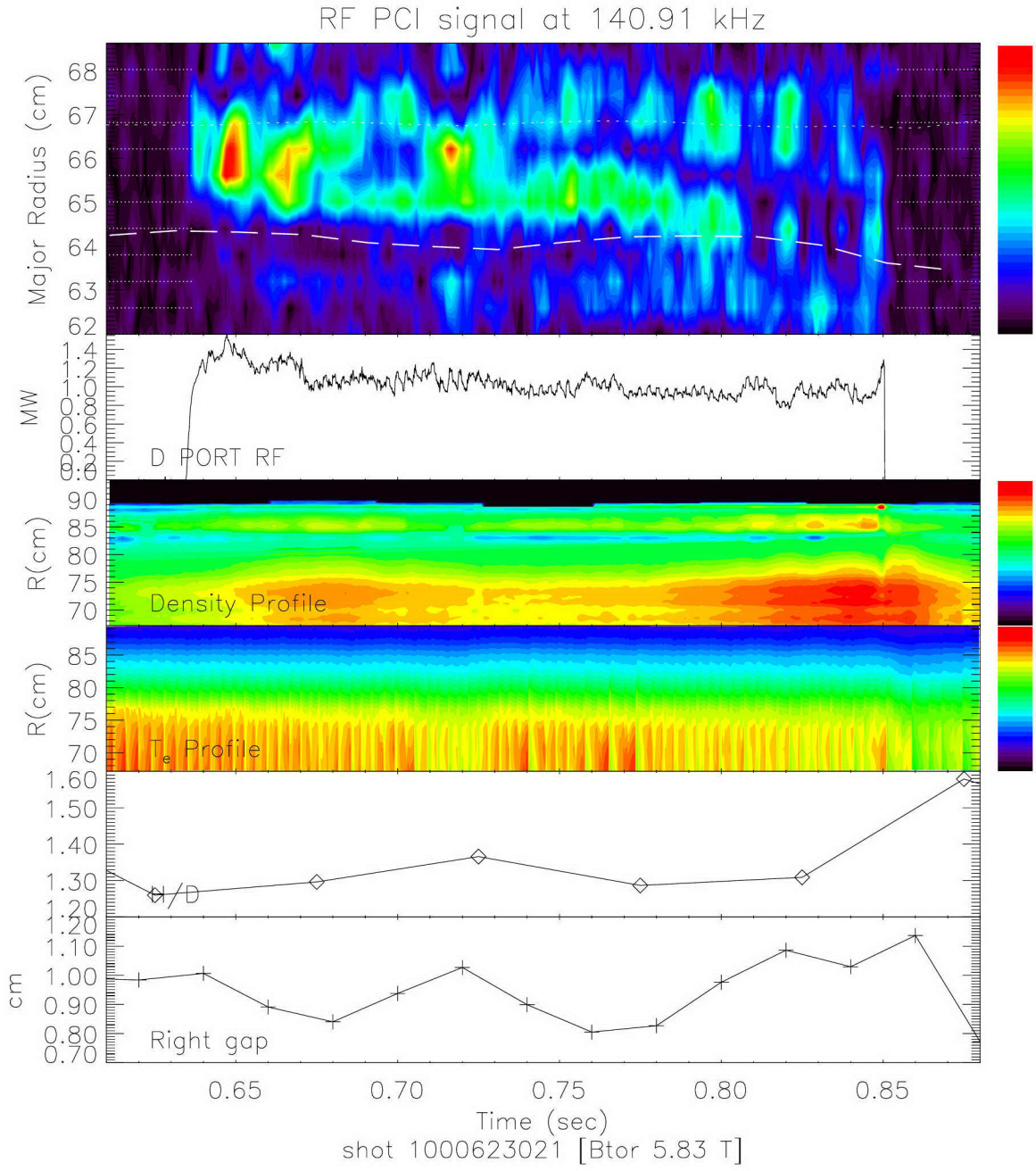

Figure E-35: RF PCI signal amplitude, shot 1000623021 (for the expected RF frequency from the D-port antenna, 36° away from the PCI). The MC layer has been shifted by 7 cm. MC position uncertainty is ±1.9 cm. Shot 21 is very similar to shot 20 except that the plasma current has been increased from 800 kA to 1 MA.

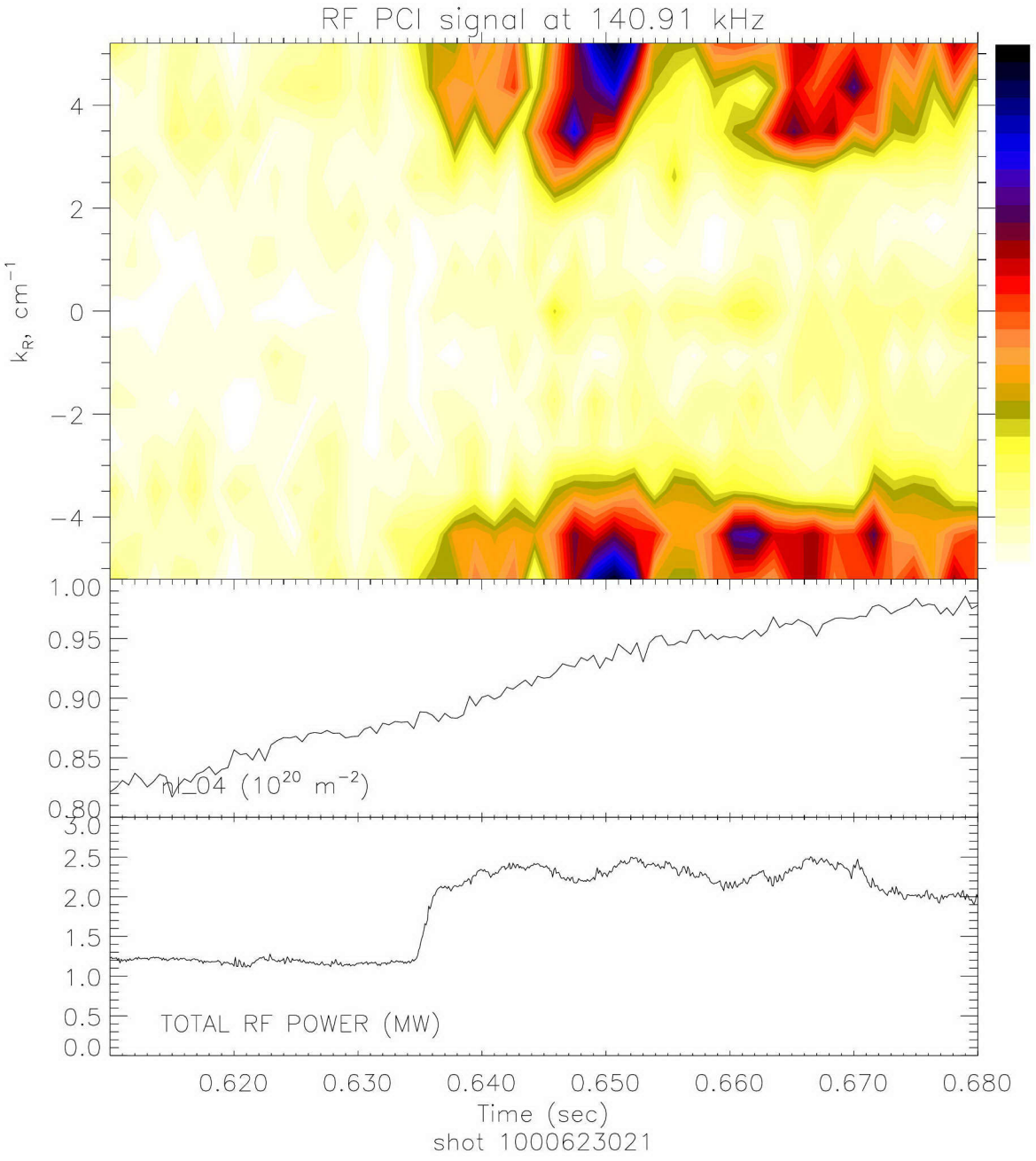

Figure E-36: RF PCI k-spectrum, shot 1000623021 (D-port). Shot 21 is very similar to shot 20 except that the plasma current has been increased from 800 kA to 1 MA.

Bibliography

[1] Donald D. Clayton. *Principles of Stellar Evolution and Nucleosynthesis.* University of Chicago Press, Chicago, 1983.

[2] I.H. Hutchinson et al. First results from Alcator-C-MOD. *Physics of Plasmas*, 1(5):1511–1518, May 1994.

[3] L.L. Lao, H. St. John, R.D. Stambaugh, A.G. Kellman, and W. Pfeiffer. Reconstruction of current profile parameters and plasma shapes in tokamaks. *Nuclear Fusion*, 25(11):1611–1622, November 1985.

[4] Robin Herman. *Fusion: The Search For Endless Energy.* Cambridge University Press, Cambridge, U.K., 1990.

[5] Irving Langmuir. Oscillations in ionized gases. *Proceedings of the National Academy of Sciences*, 14(1):627–637, June 1928.

[6] D.G. Swanson. *Plasma Waves.* Academic Press, Inc., San Diego, 1989.

[7] Marco Brambilla. *Kinetic Theory of Plasma Waves, Homogeneous Plasmas.* Clarendon Press, Oxford University, 1998.

[8] Thomas Howard Stix. *Waves in Plasmas.* American Institute of Physics, New York, 1992.

[9] D.G. Swanson. Radio frequency heating in the ion-cyclotron range of frequencies. *Physics of Fluids*, 28(9):2645–2677, September 1985. Review article.

[10] Burton D. Fried and Samuel D. Conte. *The Plasma Dispersion Function, the Hilbert transform of the Gaussian.* Academic Press, Inc., New York, 1961.

[11] Francis F. Chen. *Introduction to Plasma Physics and Controlled Fusion*, volume 1: Plasma Physics. Plenum Press, New York and London, 2nd edition, 1984.

[12] R. Majeski, J.H. Rogers, S.H. Batha, A. Bers, et al. Ion cyclotron range of frequency experiments in the Tokamak Fusion Test Reactor with fast waves and mode converted ion Bernstein waves. *Physics of Plasmas*, 3(5):2006–2012, May 1996.

[13] Yu.V. Petrov. Current drive by ion Bernstein waves in tokamaks. *Nuclear Fusion*, 34(1):63–74, 1994.

[14] V.F. Bogdanov, V.V. Volkov, K.Yu. Vukolov, N.V. Ivanov, et al. Current drive by ion Bernstein waves in a TO-2 tokamak. *Plasma Physics Reports*, 21(1):1–4, January 1995.

[15] K.H. Burrell. Effects of E x B velocity shear and magnetic shear on turbulence and transport in magnetic confinement devices. *Physics of Plasmas*, 4(5):1499–1518, May 1997.

[16] Keith H. Burrell. Turbulence and sheared flow. *Science*, 281(5384):1816–1817, September 1998.

[17] B.P. LeBlanc, R.E. Bell, S. Bernabei, J.C. Hosea, R. Majeski, M. Ono, C.K. Phillips, J.H. Rogers, G. Schilling, C.H. Skinner, and J.R. Wilson. Direct observation of ion-Bernstein-wave-induced poloidal flow in TFTR. *Physical Review Letters*, 82(2):331–334, January 1999.

[18] Masayuki Ono. Ion Bernstein wave heating research. *Physics of Fluids B*, 5(2):241–280, February 1993. Review article.

[19] Ira B. Bernstein. Waves in a plasma in a magnetic field. *Physical Review*, 109(1):10–21, January 1958.

[20] K.N. Stepanov. Nizkochastotnie kolebaniya plasmi v magnitnom pole. *Zhurnal eksperimental'noy i teoreticheskoy fiziki*, 35:1155–1160, November 1958. [Low-frequency oscillations of a plasma in a magnetic field. *Soviet Physics JETP*, 35:808-811, May 1959].

[21] F.W. Crawford and J.A. Tataronis. Absolute instabilities of perpendicularly propagating cyclotron harmonic plasma waves. *Journal of Applied Physics*, 36(9):2930–2934, September 1965.

[22] S.J. Buchsbaum. Resonance in a plasma with two ion species. *Physics of Fluids*, 3(3):418–420, May-June 1960.

[23] Marco Brambilla. Electron landau damping of ion bernstein waves in tokamak plasmas. *Nuclear Fusion*, 38(12):1805–1817, December 1998.

[24] Marco Brambilla. Numerical simulation of ion cyclotron waves in tokamaks plasmas. *Plasma Physics and Controlled Fusion*, 41(1):1–34, January 1999.

[25] N.D'Angelo and R.W. Motley. Electrostatic oscillations near the ion cyclotron frequency. *Physics of Fluids*, 5(5):633–634, May 1962.

[26] R.W. Motley and N.D'Angelo. Low-frequency oscillations in a potassium plasma. *Physics of Fluids*, 6(3):422–425, March 1963.

[27] M. Porkolab and G.S. Kino. Experimental measurements of electrostatic ion cyclotron waves. In *Proceedings of the seventh international conference on phenomena in ionized gases*, volume II, pages 365–370, Beograd, Yugoslavia, 1966.

[28] A. Hirose, I. Alexeff, and W.D. Jones. Dispersion measurements of electrostatic ion waves in a uniform magnetic field. *Physics of Fluids*, 13(8):2039–2044, August 1970.

[29] E.R. Ault and H. Ikezi. Propagation of ion cyclotron harmonic wave. *Physics of Fluids*, 13(11):2874–2876, November 1970.

[30] T. Ohnuma, S. Miyake, T. Sato, and T. Watari. Propagation of electrostatic ion waves near ion cyclotron harmonics. *Physical Review Letters*, 26(10):541–543, March 1971.

[31] J.P.M. Schmitt. Resonances of an antenna associated with the excitation of ion Bernstein modes. *Physics of Fluids*, 15(11):2057–2060, November 1972.

[32] J.P.M. Schmitt. Wake past an obstacle in a magnetized plasma flow. *Plasma Physics*, 15(7):677–690, July 1973.

[33] J.P.M. Schmitt. Dispersion and cyclotron damping of pure ion Bernstein waves. *Physical Review Letters*, 31(16):982–986, October 1973.

[34] Miklos Porkolab. Plasma heating by fast magnetosonic waves in tokamaks. In Nathaniel J. Fisch, editor, *Advances in Plasma Physics Thomas H. Stix Symposium*, volume 314 of *AIP Conference Proceedings*, pages 99–127, New York, 1994. American Institute of Physics. Invited lecture presented at the Stix Symposium "Advances in Plasma Physics", May 4, 1992.

[35] Miklos Porkolab. On the physics of magnetosonic wave damping on electrons. In Donald B. Batchelor, editor, *Radio Frequency Power in Plasmas*, volume 244 of *AIP Conference Proceedings*, pages 197–200, New York, 1992. American Institute of Physics. (RF Topical Conference at Charleston, SC 1991).

[36] T.H. Stix. Fast-wave heating of a two-component plasma. *Nuclear Fusion*, 15(5):737–754, October 1975.

[37] C.N. Lashmore-Davies, V. Fuchs, A.K. Ram, and A. Bers. Enhanced coupling of the fast wave to electrons through mode conversion to the ion hybrid wave. *Physics of Plasmas*, 4(6):2031–2043, June 1997.

[38] P. Stubbe and A.I. Sukhorukov. On the physics of Landau damping. *Physics of Plasmas*, 6(8):2976–2988, August 1999.

[39] O. Skjæraasen, P.A. Robinson, and A. Melatos. Local transit-time dissipation and Landau damping. *Physics of Plasmas*, 6(9):3435–3441, September 1999.

[40] Thomas O'Neil. Collisionless damping of nonlinear plasma oscillations. *Physics of Fluids*, 8(12):2255–2262, December 1965.

[41] R.J. Goldston and P.H. Rutherford. *Introduction to Plasma Physics*. Institute of Physics, Bristol and Philadelphia, 1995.

[42] Thomas H. Stix. Absorption of plasma waves. *Physics of Fluids*, 3(1):19–32, January-February 1960.

[43] Thomas H. Stix. Radiation and absorption via mode conversion in an inhomogeneous collision-free plasma. *Physical Review Letters*, 15(23):878–882, December 1965.

[44] A.W. Baird III and D.G. Swanson. Experimental investigation of the ion-ion hybrid resonance. *Physics of Fluids*, 12(9):1878–1885, September 1969.

[45] R. Klíma. High-frequency heating in tokamaks. *Nuclear Fusion*, 11(4):357–362, August 1971.

[46] D.G. Swanson. Mode conversion and tunneling at the two-ion hybrid resonance. *Physical Review Letters*, 36(6):316–319, February 1976.

[47] F.W. Perkins. Heating tokamaks via the ion-cyclotron and ion-ion hybrid resonances. *Nuclear Fusion*, 17(6):1197–1224, December 1977.

[48] J. Jacquinot, B.D. McVey, and J.E. Scharer. Mode conversion of the fast magnetosonic wave in a deuterium-hydrogen tokamak plasma. *Physical Review Letters*, 39(2):88–91, July 1977.

[49] Y.C. Ngan and D.G. Swanson. Mode conversion and tunneling in an inhomogeneous plasma. *Physics of Fluids*, 20(11):1920–1937, November 1977.

[50] A.K. Ram and A. Bers. Propagation and damping of mode converted ion-bernstein waves in toroidal plasmas. *Physics of Fluids B*, 3(4):1059–1069, April 1991.

[51] Y. Takase, J.D. Moody, C.L. Fiore, F.S. McDermott, M. Porkolab, and J. Squire. Study of directly launched ion bernstein waves in a tokamak. *Physical Review Letters*, 59(11):1201–1204, September 1987.

[52] Masayuki Ono and King-Lap Wong. Externally launched ion Bernstein wave in the ACT-1 toroidal device. *Physical Review Letters*, 45(13):1105–1108, September 1980.

[53] F. Skiff, M. Ono, and K.L. Wong. Excitation of ion Bernstein waves from loop antennas. *Physics of Fluids*, 31(7):2030–2036, July 1988.

[54] T. Seki and K. Kawahata. High frequency ion Bernstein wave heating in JIPP T-IIU tokamak. In *AIP Conference Proceedings*, volume 244, pages 138–141. American Institute of Physics, January 1992.

[55] R. Cesario, C. Castaldo, V. Pericoli-Ridolfini, et al. Recent results of the ion Bernstein wave heating experiment on FTU. In *AIP Conference Proceedings*, volume 485, pages 100–103. American Institute of Physics, September 1999.

[56] V. Fuchs, A.K. Ram, S.D. Schultz, A. Bers, and C.N. Lashmore-Davies. Mode conversion and electron damping of the fast Alfvén wave in a tokamak at the ion–ion hybrid frequency. *Physics of Plasmas*, 2(5):1637–1647, May 1995.

[57] B. Saoutic, A. Bécoulet, T. Hutter, D. Fraboulet, A.K. Ram, and A. Bers. Mode conversion heating experiments on the tore supra tokamak. *Physical Review Letters*, 76(10):1647–1650, March 1996.

[58] A.K. Ram, A. Bers, S.D. Schultz, and V. Fuchs. Mode conversion of fast Alfvén waves at the ion-ion hybrid resonance. *Physics of Plasmas*, 3(5):1976–1982, May 1996.

[59] I. Monakhov, A. Bécoulet, D. Fraboulet, and F. Nguyen. One-dimensional full wave treatment of mode conversion process at the ion-ion hybrid resonance in a bounded tokamak plasma. *Physics of Plasmas*, 6(3):885–896, March 1999.

[60] Peter O'Shea. *Measurements of ICRF Power Deposition and Thermal Transport with an ECE grating Polychromator on the Alcator C-Mod Tokamak.* PhD thesis, Massachusetts Institute of Technology, March 1997.

[61] P.T. Bonoli, P. O'Shea, et al. Electron heating via mode converted ion Bernstein waves in the Alcator C-Mod tokamak. *Physics of Plasmas*, 4(5):1774–1782, May 1997.

[62] P.T. Bonoli, M. Brambilla, E. Nelson-Melby, et al. Mode conversion electron heating in Alcator C-Mod: Theory and experiment. *Physics of Plasmas*, 7(5):1886–1893, May 2000.

[63] K.G. Budden. *Radio Waves in the Ionosphere: the mathematical theory of the reflection of radio waves from stratified ionised layers*, chapter 21.14-21.16. Cambridge University Press, Cambridge, U.K., 1961.

[64] K.G. Budden. *The Propagation of Radio Waves: the theory of radio waves of low power in the ionosphere and magnetosphere*, chapter 19.4-19.6, pages 591–602. Cambridge University Press, Cambridge, U.K., 1985.

[65] D.B. Batchelor. Budden tunnelling in parallel stratified plasmas. *Plasma Physics*, 22(1):41–55, January 1980.

[66] R.B. White and F.F. Chen. Amplification and absorption of electromagnetic waves in overdense plasmas. *Plasma Physics*, 16(7):565–587, July 1974.

[67] Abhay Ram. Personal communication, 2001.

[68] R.A. Cairns and C.N. Lashmore-Davies. A unified theory of a class of mode conversion problems. *Physics of Fluids*, 26(5):1268–1274, May 1983.

[69] R.A. Cairns and C.N. Lashmore-Davies. Mode conversion of a propagating to nonpropagating wave. *Physics of Fluids*, 29(11):3639–3642, November 1986.

[70] Herbert Buchholz. *The Confluent Hypergeometric Function*, chapter 2.5, pages 20–23. Springer Tracts in Natural Philosophy, Vol. 15. Springer-Verlag, Berlin, Heidelberg, New York, 1969. Trans. by H. Lichtblau and K. Wetzel.

[71] L.J. Slater. *Confluent Hypergeometric Functions*, chapter 1.7.1, pages 11–12. Cambridge University Press, Cambridge, U.K., 1960.

[72] Cornelis A. van Duin and Frans W. Sluijter. Reflection and transmission coefficients for local resonances in a cold magnetoplasma. *Radio Science*, 18(3):337–343, May-June 1983.

[73] K.G. Budden. Resonance tunnelling of waves in a stratified cold plasma. *Philosophical Transactions of The Royal Society of London Series A*, 290(1374):405–433, January 1979.

[74] M. Abramowitz and I.A. Stegun. *Handbook of Mathematical Functions*. Dover, New York, 1970.

[75] E.F. Jaeger, L.A. Berry, E.D'Azevedo, D.B. Batchelor, and M.D. Carter. Advances in full-wave modelling of RF heated, multi-dimensional plasmas. In Tak Kuen Mau and John deGrassie, editors, *14th Topical Conference Radio Frequency Power in Plasmas*, volume 595 of *AIP Conference Proceedings*, pages 369–376, New York, 2001. American Institute of Physics. (Conference in Oxnard, California, May 7–9, 2001).

[76] E.F. Jaeger, L.A. Berry, E.D'Azevedo, D.B. Batchelor, and M.D. Carter. All-orders spectral calculation of radio-frequency heating in two-dimensional toroidal plasmas. *Physics of Plasmas*, 8(5):1573–1583, May 2001.

[77] Henri Weisen. The phase contrast method as an imaging diagnostic for plasma density fluctuations (invited). *Review of Scientific Instruments*, 59(8):1544–1549, August 1988.

[78] Stefano Coda. *An Experimental Study of Turbulence by Phase-Contrast Imaging in the DIII-D Tokamak.* PhD thesis, Massachusetts Institute of Technology, 1997.

[79] Alexander Mazurenko. *Phase Contrast Imaging on the Alcator C-Mod tokamak.* PhD thesis, Massachusetts Institute of Technology, September 2001.

[80] E. Nelson-Melby, A. Mazurenko, M. Porkolab, P.T. Bonoli, and S.J. Wukitch. Phase contrast imaging of ion bernstein and fast waves in Alcator C-Mod. In Tak Kuen Mau and John deGrassie, editors, *14th Topical Conference Radio Frequency Power in Plasmas*, volume 595 of *AIP Conference Proceedings*, pages 90–97, New York, 2001. American Institue of Physics. (Conference in Oxnard, California, May 7–9, 2001).

[81] S.K. Guharay, D.A. Boyd, R.F. Ellis, F.J. Stauffer, and C.J. Lasnier. A 19-channel fast grating polychromator for ECE measurements in the MTX tokamak. *Review of Scientific Instruments*, 61(11):3520–3523, November 1990.

[82] Jon Christian Rost. *Fast ion tails during radio frequency heating on the Alcator C-Mod tokamak.* PhD thesis, Massachusetts Institute of Technology, 1998.

[83] P. Lee, R.J. Taylor, W.A. Peebles, H. Park, C.X. Yu, Y. Xu, Jr. N.C. Luhmann, and S.X. Jin. Observation of mode-converted ion Bernstein waves in the Microtor tokamak. *Physical Review Letters*, 49(3):205–208, July 1982.

[84] H. Park, P.S. Lee, and W.A. Peebles. Tokamak ion temperature determination via CW far-infrared laser scattering from externally excited ion Bernstein waves. *Nuclear Fusion*, 25(10):1399–1411, 1985.

[85] H. Park, Jr. N.C. Luhmann, W.A. Peebles, and R. Kirkwood. Observation of second-harmonic ion Bernstein waves excited by fast-wave mode conversion in the Microtor tokamak. *Physical Review Letters*, 52(18):1609–1612, April 1984.

[86] M. Ono, K.L. Wong, and G.A. Wurden. Harmonic launching of ion Bernstein waves via mode transformation. *Physics of Fluids*, 26(1):298–309, January 1983.

[87] Glen Anthony Wurden. *CO_2 laser scattering on RF waves in ACT-1.* PhD thesis, Princeton University, October 1982.

[88] TFR Group, A. Truc, and D. Gresillon. Observation of fast and slow modes associated with ICRF heating in the TFR tokamak by CO_2 laser scattering. *Nuclear Fusion*, 22(12):1577–1587, 1982.

[89] Y. Takase, C.L. Fiore, F.S. McDermott, J.D. Moody, M. Porkolab, T. Shepard, and J. Squire. Study of mode-converted and directly-excited ion Bernstein waves by CO_2 laser scattering in Alcator C. Number 159 in Application of Radio-Frequency Power to Plasmas, pages 266–269, New York, 1987. American Institute of Physics.

[90] Yu. Petrov, A. Bécoulet, and I. Monakhov. Coupled full-wave and ray-tracing numerical treatment of mode conversion in a tokamak plasma. *Physics of Plasmas*, 7(3):911–922, March 2000.

[91] E. Nelson-Melby, A. Mazurenko, M. Porkolab, P.T. Bonoli, A.E. Hubbard, A. Ram, S.J. Wukitch, M. Brambilla, and G. Taylor. Observations of mode-converted ion Bernstein waves in Alcator C-Mod with phase contrast imaging diagnostic. In *Bulletin of the American Physical Society*, volume 45, page 189. American Institute of Physics, 2000.

[92] A. Mazurenko, E. Nelson-Melby, M. Porkolab, S.J. Wukitch, G.A. Hallock, and A.J. Shugart. Fluctuations and fast wave measurements by the phase contrast imaging on alcator c-mod. In *Bulletin of the American Physical Society*, volume 45, page 318. American Institue of Physics, 2000.

[93] A. Jaun, T. Hellsten, and S.C. Chiu. Toroidal mode conversion in the ICRF. *Nuclear Fusion*, 38(2):153–162, February 1998.

[94] A. Jaun, T. Hellsten, and S.C. Chiu. Ion-Bernstein wave mode-conversion in a hot tokamak plasma. In T. Intrator and P. Ryan, editors, *12th Topical Conference Radio Frequency Power in Plasmas*, volume 403 of *AIP Conference*

Proceedings, pages 281–284, New York, 1997. American Institute of Physics. (Conference in Savannah, Georgia, April 1–4, 1997).

[95] E.F. Jaeger, M.D. Carter, L.A. Berry, D.B. Batchelor, C.B. Forest, and H. Weitzner. Co-counter asymmetry in fast wave heating and current drive. *Nuclear Fusion*, 38(1):1–12, January 1998.

[96] V.A. Svidzinski and D.G. Swanson. Possibility of a direct solution of Vlasov-Maxwell equations in tokamaks in the ion cyclotron range of frequencies. *Physics of Plasmas*, 8(2):463–474, February 2001.

[97] Marco Brambilla. A full wave code for ion cyclotron waves in toroidal plasmas. Technical Report IPP 5/66, Max-Planck-Institut für Plasmaphysik, Garching bei München, February 1996.

[98] A. Ram and A. Bers. Coupling theory for ICRF heating of large tokamaks. *Nuclear Fusion*, 24(6):679–695, June 1984.

[99] Steve Wukitch. Personal communication, 2001.

[100] James Christian Reardon. *RF edge physics on the Alcator C-Mod tokamak.* PhD thesis, Massachusetts Institute of Technology, April 1999.

[101] G. Taylor, B. LeBlanc, C.K. Phillips, G. Schilling, J.R. Wilson, et al. Electron power deposition during ICRF heating on C-Mod. In *Bulletin of the American Physical Society*, page 256. American Institute of Physics, 1999.

[102] F. Reif. *Fundamentals of Statistical and Thermal Physics.* McGraw-Hill, New York, 1965.

[103] Chairman Roger Gaudry. Canada's energy opportunities. Technical Report 23, Science Council of Canada, Ottawa, Ontario, March 1975.

[104] E.A. Alsema and M. van Brummelen. Less CO_2 through PV; study into the maximum feasible energy generation and CO_2 emission reduction using solar cell systems in the Netherlands up to 2020. Technical report, University of

Utrecht, Dept. Natural Science and Symbiosis, November 1992. Commissioned by the Ministry of Economic Affairs. (In Dutch).

[105] Richard A. Kerr. Oil outlook: USGS optimistic on world oil prospects. *Science*, 289(5477):237, 14 July 2000.

[106] David Bodansky. *Nuclear Energy: Principles, Practices, and Prospects.* American Institute of Physics, New York, 1996.

[107] Robert Thomas Nachtrieb. *Ion Mass Spectrometry on the Alcator C-Mod tokamak.* PhD thesis, Massachusetts Institute of Technology, 2000.